

University of Exeter  
College of Engineering, Mathematics and Physical Sciences

# Towards a computational tool for the management of natural capital

Kevin Bolton

29<sup>th</sup> March 2023

Supervised by Professor Stuart Townley and Dr. Markus Mueller

Submitted by Kevin Bolton, to the University of Exeter as a thesis for the degree of Doctor of Philosophy in Mathematics, 29<sup>th</sup> March 2023.

This thesis is available for Library use on the understanding that it is copyright material and that no quotation from the thesis may be published without proper acknowledgement.

I certify that all material in this thesis which is not my own work has been identified and that no material has previously been submitted and approved for the award of a degree by this or any other University.

(Signature) .....

# Abstract

The strive toward the equitable and sustainable use of land to satisfy our material, cultural and fundamental needs is a defining challenge of our time. Computational tools enable and assist the planning and assessment of policy decisions for decision-makers who look to meet these needs. One such need is the transition to a low-carbon economy while continuing to meet today's social, economic and environmental priorities for society whilst being mindful of the needs of future generations. *Ecosystem services* encompass the provisions humans attain from natural assets, and the global stock of natural resources (Millennium Ecosystem Assessment, 2005). In its bid to transition to a low-carbon economy, Cornwall Council published a comprehensive policy plan through its *Environmental Growth Strategy* (Cornwall Council, 2016). Within this strategy, Cornwall Council identified the need for an environmental management system to support environmental growth, whilst incorporating the construction of 52,500 new homes by 2030. These new housing developments will have a lasting effect on the hydrological characteristic behaviour of Cornish river basins. This thesis presents a proof of concept proposal to apply well-established practices and learnings from the *Facilities Management* industry to enable holistic management of a portfolio of natural assets. This prototype study demonstrates how one can begin to consider the wider consequences of policy decisions through a data dashboard for use by public and private officials. Beneath this dashboard, a computational tool could calculate multiple plausible tailored scenarios with its results presented to the dashboard. This thesis introduces a computational tool in the form of a hydrological model. The construction of this computational tool draws upon the current mathematical literature. The 2017 flooding event in Coverack, Cornwall (Falmouth Packet Website, 2017), is utilised as a case study. Such a tool would prove useful in the mitigation of potential, unintended, flooding events as new housing projects commence. The key outcome of this work highlights the opportunity to democratise state-of-the-art mathematical and environmental models through a larger environmental management system tool. In constructing this hydrological tool, a starting point for this larger management tool, a novel modelling technique is developed that significantly reduces the time it takes for the results to compute, whilst maintaining an accurate output.

# Acknowledgements

Firstly, I wish to thank Professor Stuart Townley and Dr. Markus Mueller. Your guidance and insight was invaluable and the patience you have shown to see me through this project is greatly appreciated. Thank you also to Kevin Fitzpatrick and Graham Morris for your initial mentorship and energy in guiding me through the world of Facilities Management at the beginning of this work.

Diolch i'r chriw Abertawe - Ian, Morgan, Jon, Rhi and Evan (I had to at least put *some* Welsh in!). Thank you also to Kayleigh and Jess. I will forever be grateful for the love, friendship and belief you have all shown me. Thank you to the Jolly Sailor crew, there are way too many of you to name! The camaraderie you fostered helped keep me grounded on the most difficult days.

Thank you to my therapist, Nicky. The work we have done and continue to do to gently deconstruct the unhelpful thoughts and behaviours is another PhD in itself. Without your support, I would never have been able to complete this work in a self-compassionate way.

My final and *most important* thank you is to my parents, Mam and Den. When I first began my formal academic education you made sure I knew my numbers, shapes and colours. You saw me through my education and fostered my love of learning in general. That is one of the greatest gifts I will ever receive. I intend to put it to good use. Rydw i'n caru ti.

# Contents

<b>Acknowledgements</b>	<b>3</b>
<b>List of Tables</b>	<b>11</b>
<b>List of Figures</b>	<b>14</b>
<b>I Introduction and Mathematical Background</b>	<b>31</b>
<b>1 Introduction</b>	<b>32</b>
1.1 Research Background . . . . .	32
1.1.1 A Green Economy . . . . .	32
1.1.2 Sustainable Development . . . . .	33
1.1.3 Natural Capital . . . . .	34
1.1.4 The Ecosystem Services Concept . . . . .	35
1.1.5 The Environmental Growth Strategy . . . . .	36
1.1.5.1 Target Outcome 4 . . . . .	37
1.1.6 Motivation . . . . .	38
1.2 A Case Study: Coverack, Cornwall . . . . .	41
1.3 Thesis Motivation and Aims . . . . .	44
1.3.1 Thesis Objectives and Research Questions . . . . .	45
1.4 Thesis Structure . . . . .	47
<b>2 A Literature Review on Hydrological Modelling</b>	<b>49</b>
2.1 Introduction . . . . .	49
2.2 Modelling concepts of hydrological processes . . . . .	50
2.2.1 Interception Component . . . . .	52
2.2.2 Unsaturated Zone Component . . . . .	58
2.2.3 Surface Runoff and Routing Component . . . . .	63
2.2.4 Snowmelt Component . . . . .	70
2.2.5 Evapotranspiration Component . . . . .	72
2.2.6 Saturated Zone Component . . . . .	77
2.3 Computational mesh types . . . . .	78
2.4 Semi-Distributed Models . . . . .	79
2.4.1 DPHM-RS . . . . .	79
2.4.2 HRCDHM . . . . .	80
2.4.3 SLURP . . . . .	81
2.4.4 SWAT . . . . .	81

---

2.4.5	TOPNET . . . . .	81
2.4.6	WATBAL . . . . .	81
2.5	Fully Distributed Models . . . . .	85
2.5.1	CREST . . . . .	85
2.5.2	IHDM . . . . .	86
2.5.3	ISBA . . . . .	86
2.5.4	LISFLOOD . . . . .	86
2.5.5	MIKE SHE . . . . .	86
2.5.6	MISBA . . . . .	87
2.5.7	PAWS . . . . .	87
2.5.8	SHE . . . . .	87
2.5.9	THALES . . . . .	88
2.5.10	TOPMODEL . . . . .	88
2.5.11	tRIBS . . . . .	88
2.5.12	WATFLOOD . . . . .	89
2.6	Literature Gap . . . . .	89
2.7	My Modelling Approach . . . . .	90
2.7.1	Interception Component . . . . .	92
2.7.2	Unsaturated Zone Component . . . . .	92
2.7.3	Overland Flow and Routing Component . . . . .	93
2.7.4	Snowmelt Component . . . . .	94
2.7.5	Evapotranspiration Component . . . . .	94
2.7.6	Saturated Zone Component . . . . .	95
2.8	Summary . . . . .	95
<b>3</b>	<b>Underlying Modelling Foundation</b>	<b>98</b>
3.1	Introduction . . . . .	98
3.2	The Riemann Problem . . . . .	99
3.2.1	An Initial Value Problem using a Linear Advection Equation . . . . .	99
3.2.2	The Riemann Problem: A Linear Case . . . . .	99
3.2.3	The Riemann Problem: A multivariate case . . . . .	101
3.2.3.1	A General Solution Structure . . . . .	101
3.2.3.2	A $2 \times 2$ system example . . . . .	103
3.3	Conservation Laws . . . . .	105
3.3.1	Rankine-Hugoniot Conditions . . . . .	105
3.3.2	Elementary-Wave Solutions of the Riemann Problem . . . . .	106
3.4	Godunov's Numerical Method . . . . .	107
3.4.1	A Conservative Method . . . . .	108
3.4.2	Defining a local Riemann problem . . . . .	108
3.4.3	Transparent Boundary Conditions . . . . .	109
3.4.4	Timestep choice . . . . .	110
3.4.5	Godunov's Method . . . . .	111
3.4.6	Two-dimensional finite volume method . . . . .	113
3.4.6.1	The Godunov Finite Volume Method . . . . .	114

3.5	Total Variation Diminishing Methodology . . . . .	116
3.5.1	Flux Limiters . . . . .	116
3.6	Infiltration Modelling . . . . .	117
3.6.1	The Green-Ampt Model . . . . .	117
3.6.1.1	Green-Ampt infiltration model . . . . .	123
3.6.1.2	Green-Ampt: A worked example . . . . .	126
3.6.2	The SCS Method . . . . .	129
3.6.2.1	SCS Curve Number Method . . . . .	131
3.7	Summary . . . . .	134
 <b>II Model Construction &amp; Validation</b>		<b>135</b>
 4	 <b>Model Construction</b>	 <b>136</b>
4.1	Introduction . . . . .	136
4.2	Computational Domain . . . . .	137
4.2.1	Computational Mesh . . . . .	137
4.2.2	Defining land-use types . . . . .	137
4.2.3	Land-Use Image Processing . . . . .	138
4.2.3.1	Lower resolution categorisations . . . . .	138
4.2.4	Green-Ampt Soil Parameter . . . . .	139
4.2.5	Model Resolution Considerations . . . . .	139
4.3	Construction of the Hydrological Model . . . . .	148
4.3.1	Governing Equations . . . . .	148
4.3.1.1	Integral form of the Governing Equation . . . . .	149
4.3.2	HLLC approximate Riemann Solvers . . . . .	153
4.3.2.1	Estimating flux transfer across pixel boundaries . . . . .	155
4.3.2.2	Riemann State Construction . . . . .	156
4.3.2.3	Surface Reconstruction Method . . . . .	157
4.3.3	Source term discretisation . . . . .	157
4.3.4	Friction term discretisation . . . . .	158
4.3.4.1	Estimating the Manning Parameter . . . . .	161
4.3.5	Infiltration Model . . . . .	164
4.3.5.1	Green-Ampt Approximation . . . . .	165
4.3.5.2	Applying the SCS Method . . . . .	176
4.3.6	Boundary Conditions . . . . .	178
4.3.7	Interception Parameters . . . . .	178
4.3.8	Model Calibration . . . . .	179
4.3.8.1	Manning coefficient in the Shallow Water Equations . . . . .	180
4.3.8.2	Green-Ampt . . . . .	180
4.3.8.3	SCS . . . . .	181
4.3.8.4	Interception Parameter . . . . .	182
4.3.9	Model limitations and Future work . . . . .	183
4.4	Summary . . . . .	185

<b>5</b>	<b>Modelling Performance Analysis</b>	<b>187</b>
5.1	Introduction . . . . .	187
5.2	Sampled Computational Meshes . . . . .	188
5.3	Common Model Parameters & Inputs . . . . .	191
5.4	North-Eastern Sub Region . . . . .	192
5.4.1	Spatial Distribution: Local Terrain . . . . .	192
5.4.2	Spatial Distribution: Land-Use . . . . .	193
5.4.3	Simulation Run Times . . . . .	196
5.4.4	Overland Flow Distribution . . . . .	196
5.4.5	Patch Analysis . . . . .	198
5.4.5.1	Patch #05 . . . . .	199
5.4.5.2	Patch #15 . . . . .	199
5.4.5.3	Patch #32 . . . . .	200
5.4.5.4	Patch #48 . . . . .	200
5.4.5.5	Patch #64 . . . . .	200
5.5	Northern Sub Region . . . . .	211
5.5.1	Spatial Distribution: Local Terrain . . . . .	211
5.5.2	Spatial Distribution: Land-Use . . . . .	211
5.5.3	Simulation Run Times . . . . .	214
5.5.4	Overland Flow Distribution . . . . .	214
5.5.5	Patch Analysis . . . . .	217
5.5.5.1	Patch #03 . . . . .	221
5.5.5.2	Patch #07 . . . . .	221
5.5.5.3	Patch #11 . . . . .	221
5.5.5.4	Patch #23 . . . . .	221
5.5.5.5	Patch #40 . . . . .	222
5.5.5.6	Patch #41 . . . . .	226
5.5.5.7	Patch #42 . . . . .	226
5.6	Summary . . . . .	230
<b>III</b>	<b>Simulation &amp; Analysis</b>	<b>232</b>
<b>6</b>	<b>Non-Uniform Model Input Analysis</b>	<b>233</b>
6.1	Introduction . . . . .	233
6.2	Non-Uniform Model Input . . . . .	233
6.3	Scenario 1 - Central Region . . . . .	236
6.3.1	Movement 20m . . . . .	236
6.3.2	Static 20m . . . . .	242
6.3.3	Movement 50m . . . . .	247
6.3.4	Static 50m . . . . .	252
6.4	Scenario 2 - South Eastern Region . . . . .	257
6.4.1	Movement 20m . . . . .	257
6.4.2	Static 20m . . . . .	261
6.4.3	Movement 50m . . . . .	265

6.4.4	Static 50m . . . . .	269
6.5	Summary . . . . .	274
<b>7</b>	<b>Simulation Modelling: Coverack, Cornwall</b>	<b>275</b>
7.1	Introduction . . . . .	275
7.2	The Coverack Flooding Event: An Overview . . . . .	276
7.3	Sub-Region Domain Definitions . . . . .	278
7.4	A Perspective from a Hypothetical Cornwall Council Policy Planner . . . . .	280
7.5	Modelling Simulation Scenarios . . . . .	281
7.5.1	Control Simulation . . . . .	281
7.5.2	Scenario I: Soil parameter changes . . . . .	281
7.5.3	Scenario II: Land-Use parameter change . . . . .	281
7.5.4	Scenario III: Open “Sluice” parameter . . . . .	281
7.5.5	Scenario IV: Soil and land-use parameter changes . . . . .	281
7.5.6	Scenario V: Soil parameter change with an open “Sluice” . . . . .	281
7.5.7	Scenario VI: Land-use parameter change with an open “Sluice” . . . . .	282
7.5.8	Scenario VII: Soil and land-use parameter changes with an open “Sluice” . . . . .	282
7.6	Modelling Analysis . . . . .	282
7.6.1	Coverack . . . . .	282
7.6.2	Northern Coverack . . . . .	283
7.6.3	North-Eastern Coverack . . . . .	283
7.6.4	Southern Coverack . . . . .	286
7.6.5	Western Coverack . . . . .	286
7.7	Discussion . . . . .	291
7.8	Summary . . . . .	293
<b>IV</b>	<b>Conclusions</b>	<b>294</b>
<b>8</b>	<b>Conclusion</b>	<b>295</b>
8.1	Introduction . . . . .	295
8.2	Thesis Summary . . . . .	295
8.3	Research Contribution . . . . .	297
8.4	Future Research Recommendations . . . . .	298
<b>Appendix</b>		<b>299</b>
A	Modelling foundations . . . . .	300
A.1	Fundamental properties of Hyperbolic Partial Differential Equations	300
A.1.1	Quasi-Linear Equations . . . . .	300
A.1.2	Fundamentals of Hyperbolic Systems . . . . .	301
A.1.2.1	Characteristic and the General Solution structure	301
A.1.3	Linear Hyperbolic Systems . . . . .	302
A.1.3.1	Diagonalisation and Characteristic Variables . . . . .	302
A.1.3.2	A Diagonalisable System . . . . .	303
A.1.3.3	Characteristic Variables . . . . .	303



A.1.4	The Riemann Problem in Linearised Gas Dynamics . . . . .	305
A.2	Numerical Modelling and the Upwind Scheme . . . . .	307
A.2.1	Numerical Modelling and Discretisation . . . . .	307
A.2.2	Derivative Approximations . . . . .	308
A.2.3	A finite difference approximation to the advection equation	309
A.2.4	The CFL Condition . . . . .	311
A.2.5	A Truncation Analysis . . . . .	313
A.2.6	Alternative Numerical Schemes . . . . .	314
A.3	Conservation Laws . . . . .	316
A.3.1	Integral Form of Conservation Laws . . . . .	317
A.3.2	Non-linear hyperbolic conservation laws: Common Prop- erties . . . . .	318
A.3.3	Constructing Solutions on the Characteristic . . . . .	319
A.3.4	Wave Steepening Behaviour . . . . .	321
A.3.5	Shockwaves . . . . .	323
A.3.5.1	Examples of Discontinuous Solutions . . . . .	324
A.3.6	Rarefaction Waves . . . . .	325
A.3.7	A Riemann Problem for the Burgers Equation . . . . .	327
A.3.7.1	The Riemann Problem in Linearised Gas Dynam- ics: Part II . . . . .	329
A.3.8	Generalised Riemann Invariants . . . . .	331
A.3.8.1	Shock Wave Solution . . . . .	331
A.3.8.2	Rarefaction Wave Solution . . . . .	331
A.4	Godunov's Numerical Method . . . . .	332
A.4.1	One-dimensional finite volume method . . . . .	332
A.4.2	Godunov's Method: Interpretation 1 . . . . .	334
A.4.3	Godunov's Method: Interpretation 2 . . . . .	335
A.5	Total Variation Diminishing Methodology . . . . .	337
B	Infiltration Modelling . . . . .	341
B.1	From First Principles - Richards Equation . . . . .	342
B.2	Richards Equation - A qualitative analysis . . . . .	344
B.3	The SCS Method: Terminology . . . . .	346
B.3.1	Hydrological Soil Group . . . . .	346
B.3.2	Antecedent Moisture Conditions . . . . .	346
C	Land-Use Image Processing . . . . .	348
C.1	20m Resolution . . . . .	348
C.2	50m Resolution . . . . .	350
D	Green-Ampt approximation Tabulated Data . . . . .	352
E	Simulation Run Time Raw Data . . . . .	358
F	Min, Max and Average Raw Data . . . . .	360
G	Contour Overland Flow II . . . . .	366
H	Patch-Pixel Composition Raw Data . . . . .	368
I	Model Performance Analysis . . . . .	370
I.1	North Eastern Patch Analysis . . . . .	370

	I.1.1	Patch #23 . . . . .	370
	I.1.2	Patch #56 . . . . .	371
I.2		Northern Patch Analysis . . . . .	371
	I.2.1	Patch #15 . . . . .	371
	I.2.2	Patch #24 . . . . .	372
	I.2.3	Patch #25 . . . . .	372
	I.2.4	Patch #32 . . . . .	372
	I.2.5	Patch #39 . . . . .	373
	I.2.6	Patch #49 . . . . .	373
	I.2.7	Patch #58 . . . . .	374
J		Non-Uniform Model Input Analysis: Scenario 3 - North West . . . . .	384
	J.1	Movement 20m . . . . .	384
	J.2	Static 20m . . . . .	389
	J.3	Movement 50m . . . . .	394
	J.4	Static 50m . . . . .	399
<b>Bibliography</b>			<b>404</b>

# List of Tables

1.1	An overview of ecosystem service categories, their definitions and examples (Millennium Ecosystem Assessment, 2005). . . . .	35
1.2	Components of positive well-being attributed to well-functioning ecosystem services (Millennium Ecosystem Assessment, 2005). . . . .	36
1.3	A description of the watercourses in Coverack. Table adapted from (Environment Agency and Cornwall Council, 2018, pg.4). . . . .	41
2.1	Key literature methods and tools related to the interception component of a hydrological model. . . . .	54
2.2	Key literature methods and tools related to the unsaturated zone component of a hydrological model. . . . .	60
2.3	Key literature methods and tools related to the surface runoff and routing component of a hydrological model. . . . .	66
2.4	A summary of semi-distributed physically based hydrological models and their discretisation approaches with their principle reference. . . . .	80
2.5	A summary of fully distributed physically based hydrological models and their discretisation approaches with their principle reference. . . . .	82
3.1	Green-Ampt infiltration parameters for various soil characterisations from Rawls et al. (1983). Parameter values $ \psi_a $ and b come from analysis of 1845 soils from Clapp and Hornberger (1978). . . . .	120
3.2	Formulae required to implement the Green-Ampt, Horton and Philip point infiltration models. Model parameters are given in brackets below the model name. . . . .	122
3.3	Runoff calculations from applying the Green-Ampt infiltration model. Copied from table 4 in (Tarboton, 2003, Chapt. 5 pg. 28). . . . .	127
3.4	Antecedent moisture classifications for the SCS method of rainfall abstraction. 131	
3.5	Runoff curve numbers for given typical agricultural, suburban and urban land-uses. Adapted from tables 2-2a - 2-2d (Natural Resources Conservation Service, 1986, Chapt. 2 pgs. 5-8). . . . .	132
4.1	Values of Manning’s Roughness Coefficient used for each land-use category. Retrieved from table 5-6 in (Chow et al., 1988, pg. 113). . . . .	163
4.2	A table displaying the total time taken to execute a single timestep of the model when the Newton Raphson method was applied. This single timestep was scaled by a factor to estimate the likely time the model would take to resolve assuming the computational effort was consistent. . . . .	166

4.3	The total area of the model pixel resolutions in square metres and acres broken down into the sub-urban land-use components. . . . .	176
4.4	The total area of the model pixel resolutions in square metres and acres broken down into the urban land-use components. . . . .	177
4.5	Curve number calculations for the sub-urban and urban regions, using the values from Table 3.5. . . . .	177
4.6	The maximum potential storage for a sub-urban and urban land-use pixel. .	177
4.7	Formulae to calculate the total simulated runoff in a sub-urban and urban land-use pixel using the revised initial abstraction value $I_a = 0.05$ . . . . .	177
5.1	A summary of the orthogonal grid mesh utilised within the computational model. . . . .	188
5.3	Total precipitation input values for the entire simulation as well as a break down of input by timestep and pixel-definition. . . . .	191
5.2	Input arguments for both simulation runs. . . . .	192
5.4	Land-use abbreviations, colour code, model parameter and spatial coverage of the sampled computational domain given as a percentage. . . . .	193
5.5	Pixel column and row boundaries which defined analysis regions to calculate the minimum, maximum and average mean water depths at non-zero output pixels in Figures 5.5 and F.1 for the north-eastern sub-region. . . . .	197
5.6	Land-Use abbreviations, colour code, model parameter and spatial coverage of the second sampled computational domain given as a percentage. . . . .	211
5.7	Pixel column and row boundaries which defined analysis regions to calculate the minimum, maximum and average mean water depths at non-zero output pixels in Figures 5.17 and F.2 for the northern sub-region. . . . .	215
5.8	The minimum, maximum and average mean water depth value [cm] difference of the 50m and 50m adjusted model resolutions against the 20m model resolution for each patch reviewed in Section 5.4. . . . .	231
5.9	The minimum, maximum and average mean water depth value [cm] difference of the 50m and 50m adjusted model resolutions against the 20m model resolution for each patch reviewed in Section 5.5. . . . .	231
6.1	The minimum, maximum and average mean water depth output [cm] differences between the 20m and 50m model variants for different input and spatial scenarios reviewed in Sections 6.3, 6.4 and J. . . . .	274
7.1	Coverack Storm inputs estimated from Figure 7.2. Lower bound, upper bound and median estimates using the Met Office's investigation. . . . .	278
7.2	Sub-region pixel boundary definitions (inclusive) for the 20m resolution model.	278
A.1	A comparison between the structures of the linear hyperbolic systems in Sections 3.2.1 and A.1.3.1. . . . .	304
A.2	Common forms of flux/slope limiter functions $\phi$ , the majority of which are second-order TVD. . . . .	339
A.2	Common forms of flux/slope limiter functions $\phi$ , the majority of which are second-order TVD. . . . .	340

B.3	Adjustment scaling parameters for varying soil moisture conditions. Adapted from Ward and Trimble (2003). . . . .	347
D.4	Raw value comparison between the full and approximate Green-Ampt infiltration model using the Sand parameter values. . . . .	352
D.5	Raw value comparison between the full and approximate Green-Ampt infiltration model using the Loamy Sand parameter values. . . . .	352
D.6	Raw value comparison between the full and approximate Green-Ampt infiltration model using the Sandy Loam parameter values. . . . .	353
D.7	Raw value comparison between the full and approximate Green-Ampt infiltration model using the Loam parameter values. . . . .	353
D.8	Raw value comparison between the full and approximate Green-Ampt infiltration model using the Silt Loam parameter values. . . . .	354
D.9	Raw value comparison between the full and approximate Green-Ampt infiltration model using the Sandy Clay Loam parameter values. . . . .	354
D.10	Raw value comparison between the full and approximate Green-Ampt infiltration model using the Clay Loam parameter values. . . . .	355
D.11	Raw value comparison between the full and approximate Green-Ampt infiltration model using the Silty Clay Loam parameter values. . . . .	355
D.12	Raw value comparison between the full and approximate Green-Ampt infiltration model using the Sandy Clay parameter values. . . . .	356
D.13	Raw value comparison between the full and approximate Green-Ampt infiltration model using the Silty Clay parameter values. . . . .	356
D.14	Raw value comparison between the full and approximate Green-Ampt infiltration model using the Clay parameter values. . . . .	357
E.1	Model simulation times for each individual run for 20m and 50m resolutions in seconds with a scaling factor calculation for the north-eastern region. . .	358
E.2	Model simulation times for each individual run for 20m and 50m resolutions in seconds with a scaling factor calculation for the northern region. . . . .	359
F.1	Min, Max and Average of mean water depths at non-zero pixels for north-eastern region. . . . .	360
F.2	Min, Max and Average of mean water depths at non-zero pixels for northern region. . . . .	363
H.1	Patch pixel composition split by land-use type for the north-eastern region.	368
H.2	Patch pixel composition split by land-use type for the northern region. . . .	369

# List of Figures

1.1	A Venn diagram illustrating overarching aims for environmental, social and economic needs. Their interactions illustrate the benefits society obtains from achieving just two needs. Finally, the central overlap illustrates sustainability when decisions are bearable, viable and equitable for all. Image obtained from Dréo (2006). . . . .	34
1.2	An illustrative diagram showing the interdependence of each theme within the Environmental Growth Strategy. Obtained from (Cornwall Council, 2016, pg. 24). . . . .	37
1.3	One actionable target discussed within the Environmental Growth Strategy to achieve the “Understanding Cornwall” ambition. This target is further broken down into actionable items to fulfil the goal of growing natural assets. Obtained from (Cornwall Council, 2016, pg. 27). . . . .	38
1.4	An illustrative example of the MyFM dashboard global page which was in development at NJW Ltd. Client company names and relevant information have been redacted. . . . .	39
1.5	An illustrative example of the MyFM dashboard ‘drilled down’ from the global page in figure 1.4 as seen by the breadcrumb trail labelled in box E. . . . .	39
1.6	Location of England, Cornwall and the village of Coverack. . . . .	42
1.7	Images showing the extent of the flooding experienced in Coverack on 18 <sup>th</sup> July 2017. . . . .	43
1.8	The local watercourse surrounding Coverack. Figure obtained from (Environment Agency and Cornwall Council, 2018) which conducted a wider study on the specific causes of the flooding. . . . .	43
2.1	An illustrative diagram highlighting how each physical process models interrelate within the greater hydrological model. Obtained from Refsgaard and Storm (1995). . . . .	51
2.2	Surface water runoff is generated when the infiltration capacity of the underlying soil cannot keep up with the precipitation input rate. If the precipitation rate is less than or equal to infiltration rate, then no surface runoff occurs (2.2a). If the soil is completely saturated then no infiltration will occur and so the surface runoff rate will equal the precipitation rate (2.2b). If there is capacity to absorb some of the precipitation but the rate of infiltration is lower than the precipitation rate then total surface runoff is the difference between precipitation input rate and infiltration rate (2.2c). Illustrations adapted from Dunne and Leopold (1978). . . . .	65

2.3	Figure a) shows the relationship between the ratio of actual evapotranspiration ( $E_{at}$ ) to potential evapotranspiration ( $E_p$ ) and the ratio between the soil moisture content minus the soil moisture content referenced at wilting point ( $\theta - \theta_w$ ) to the soil moisture content at field capacity minus the soil moisture content referenced at wilting point ( $\theta_F - \theta_w$ ). Similarly, figure b) illustrates the relationship between the ratio of actual soil evaporation realised ( $E_s$ ) against its potential evaporation ( $E_p$ ). This ratio is compared among various soil moisture content references as defined previously. $\theta_M$ defines the irreducible soil moisture content. Obtained from Refsgaard and Storm (1995). . . . .	74
3.1	A diagram of the initial data or <b>Riemann states</b> for the Riemann problem. At $t = 0$ the initial data consists of two constant states separated at a discontinuity $x = 0$ . . . . .	100
3.2	A pictorial representation for the solution to the Riemann Problem in the $x - t$ plane for the linear advection equation where the characteristic speed $a > 0$ . . . . .	100
3.3	The solution structure for the general $m \times m$ Riemann problem of a linear hyperbolic system with constant coefficients. . . . .	102
3.4	The solution structure for the $2 \times 2$ Riemann problem of a linear hyperbolic system with constant coefficients. . . . .	104
3.5	One may find the solution to the Riemann problem for the $2 \times 2$ linear hyperbolic system by tracing along the dashed horizontal line at $t = t^*$ . . . . .	104
3.6	Rankine-Hugoniot conditions for a single discontinuity of speed $S_i$ . The two constant states $\mathbf{U}_l$ and $\mathbf{U}_r$ are connected via a system of conservation laws. . . . .	105
3.7	A solution structure for the Riemann problem within a non-linear system of conservation laws. . . . .	107
3.8	The computation of a Godunov intercell flux for a linear hyperbolic system with constant coefficients. . . . .	111
3.9	A two-dimensional Cartesian domain discretised into finite volumes $\Omega_{i,j}$ with an area of $\Delta x \times \Delta y$ . Each computational pixel has four intercell boundaries (anti-clockwise) $\mathbf{F}_{i-\frac{1}{2},j}$ , $\mathbf{G}_{i,j-\frac{1}{2}}$ , $\mathbf{F}_{i+\frac{1}{2},j}$ , and $\mathbf{G}_{i,j+\frac{1}{2}}$ . . . . .	115
3.10	A stencil for the Godunov finite volume scheme during the linear equation with positive velocity components $a_1$ and $a_2$ . The arrow denotes the direction of the velocity vector. . . . .	116
3.11	Infiltration excess runoff profiles. (a) Moisture content vs. depth profiles and (b) Runoff generation time series. Adapted from Bras (1990); Tarboton (2003). . . . .	118
3.12	Pictorial representation of the Green-Ampt model idealisation where the wetting front penetrates into the soil profile. Initial moisture content is denoted $\theta_0$ . Saturation moisture content, denoted $\theta_s$ , is equivalent to porosity $n$ . $L$ represented the distance between the wetting front and surface at any given timestep ( $t^{(3)}$ here). Adapted from figure 39 (Tarboton, 2003, Chapter 5:10). . . . .	119

3.13	Green-Ampt infiltration model flow chart to calculate the infiltration and runoff generated under various surface water input intensities. Adapted from (Tarboton, 2003, Chapt. 5 pg. 21) . . . . .	125
3.14	Results to the SCS runoff equations with precipitation [in] plotted against direct runoff [in]. Obtained from (Tarboton, 2003, Chapter 5:42 Figure 48).	130
4.1	The location of the digital terrain model data obtained for the Coverack case study within the Lizard Peninsula (Environment Agency, 2017). . . . .	141
4.2	Dudley land-use overlay on DEFRA’s MAGIC map (Department for Environment, Food & Rural Affairs, 2002a) 4.2a and 4.2b with the land-use key in its table of contents 4.2c. . . . .	142
4.3	Locations of where RGB pixel samples were taken for image processing using the Dudley Stamp Map from Department for Environment, Food & Rural Affairs (2002c). . . . .	143
4.4	Binary outputs after image processing for each land use definition. . . . .	144
4.5	The outcome from the land-use image processing procedure using the original MAGIC map Dudley overlay. . . . .	145
4.6	The outcome from the land-use image processing procedure using the 20m resolution variant of the MAGIC map Dudley overlay. . . . .	145
4.7	The outcome from the land-use image processing procedure using the 50m resolution variant of the MAGIC map Dudley overlay. . . . .	146
4.8	A screenshot from the “Soilscapes” platform developed by Cranfield University to describe the underlying soil within the British Isles. Two soil types cover the computational region and are defined in the Soilscapes web platform as: 1. Soilscape 7 (Brown): “Freely draining slightly acidic but base-rich soils”; and 2. Soilscape 17 (Green): “Slowly permeable seasonally wet acid loamy and clayey soils” (Cranfield Soil and Agrifood Institute, 2023).	147
4.9	Illustration of a shallow flow bed topography modelled by equation (4.1) with vector terms (4.2). . . . .	150
4.10	Flux function vectors across the boundary of control volume $\Omega$ . . . . .	151
4.11	A visualisation of the finite volume method in the $(x, t)$ computational domain. The cell average $Q_i^{(k)}$ is updated by the fluxes $\mathbf{f}_{i\pm\frac{1}{2}}$ at the cell boundaries. . . . .	152
4.12	A visualisation of the finite volume method in the $(x, t)$ computational domain as it moves forward a single timestep. . . . .	152
4.13	HLLC solution structure for the Riemann Problem . . . . .	153
4.14	A visualisation of the finite volume method in the $(x, t)$ computational domain. The cell average $Q_i^{(k)}$ is updated by the fluxes $\mathbf{f}_{i\pm\frac{1}{2}}$ at the cell boundaries. . . . .	155
4.15	A comparison between the full and approximate Green-Ampt model for the Sand soil parameter. . . . .	170
4.16	A comparison between the full and approximate Green-Ampt model for the Loamy Sand soil parameter. . . . .	170
4.17	A comparison between the full and approximate Green-Ampt model for the Sandy Loam soil parameter. . . . .	171



4.18	A comparison between the full and approximate Green-Ampt model for the Loam soil parameter. . . . .	171
4.19	A comparison between the full and approximate Green-Ampt model for the Silt Loam soil parameter. . . . .	172
4.20	A comparison between the full and approximate Green-Ampt model for the Sandy Clay Loam soil parameter. . . . .	172
4.21	A comparison between the full and approximate Green-Ampt model for the Clay Loam soil parameter. . . . .	173
4.22	A comparison between the full and approximate Green-Ampt model for the Silty Clay Loam soil parameter. . . . .	173
4.23	A comparison between the full and approximate Green-Ampt model for the Sandy Clay soil parameter. . . . .	174
4.24	A comparison between the full and approximate Green-Ampt model for the Silty Clay soil parameter. . . . .	174
4.25	A comparison between the full and approximate Green-Ampt model for the Clay soil parameter. . . . .	175
5.1	A depiction of the computational mesh for the 20m 5.1a and 50m 5.1b resolution variants. Pixel column indices are located to the top and bottom of figure 5.1a and bottom of 5.1b. Pixel row indices are located to the left and right of 5.1a and left of the computational grid in 5.1b. The patch indexing convention used in this section is highlighted in figure 5.1c. Each patch is defined by the thicker black grid which overlays each respective pixel grid seen in grey. Patch #1, shaded in grey, is an example of a patch where the outputs are averaged to ensure an even comparison between both model resolutions. Patch dimensions and the area of the region are highlighted in each sub-figure. . . . .	190
5.2	A pictorial overview of the topological structure of the full computational domain as well as the first study region used for model analysis. . . . .	194
5.3	The land-use spatial distributions used within each model variants. Labels on the axes represent the row and column indices for each pixel within the computational domain. Figure 5.3a shows the entire computational domain at 20m resolution. 5.3c is a zoomed in picture of the orange square in 5.3a. Similarly, figure 5.3b is the full computational domain at 50m resolution with its orange square highlighted in 5.3d. The land-use categories are abbreviated to the right of each figure. Table 5.4 defines each land-use category. . . . .	195
5.4	The total time in seconds it took for each of fifty simulation runs for both the 20m (blue) and 50m (red) model resolutions to complete. . . . .	196
5.5	The minimum, maximum and average mean water depths at non-zero output pixels within the north-eastern sub-region outlined in Figure 5.3 for both model resolutions. Sub-figures (a) and (b) show the values for two of the five regions where water is present as seen in Figure 5.6 as well as the entire domain (c). . . . .	202

5.6	An evolution of the average water depth overland flow throughout the 20m resolution model simulation. . . . .	203
5.7	A comparison of the normalised average water depth output between the 20m (blue) and 50m (red) resolutions. The normalisation utilises the maximum average value at any timestep within the patch. The number of timesteps goes across the $x$ -axis of each subplot. Their plot placement corresponds to the patch numbers in figure 5.1c. . . . .	204
5.8	A comparison of the absolute average water depth values between the 20m (blue) and 50m (red) resolutions. . . . .	205
5.9	Patch 5 - Original land composition within the 20m (5.9a) and 50m (5.9b) resolution models along with an adjusted 50m resolution patch (5.9c) with absolute water depth values for each model (5.9d) and relative 50m output values compared with the 20m model (5.9e). . . . .	206
5.10	Patch 15 - Original land composition within the 20m (5.10a) and 50m (5.10b) resolution models along with an adjusted 50m resolution patch (5.10c) with absolute water depth values for each model (5.10d) and relative 50m output values compared with the 20m model (5.10e). . . . .	207
5.11	Patch 32 - Original land composition within the 20m (sub-figure 5.11a) and 50m (5.11b) resolution models along with an adjusted 50m resolution patch (5.11c) with absolute water depth values for each model (5.11d) and relative 50m output values compared with the 20m model (5.11e). . . . .	208
5.12	Patch 48 - Original land composition within the 20m (5.12a) and 50m (5.12b) resolution models with absolute water depth values for each model (5.12c) and relative 50m output values compared with the 20m model (5.12d). . . . .	209
5.13	Patch 64 - Original land composition within the 20m (5.13a) and 50m (5.13b) resolution models along with an adjusted 50m resolution patch (5.13c) with absolute water depth values for each model (5.13d) and relative 50m output values compared with the 20m model (5.13e). . . . .	210
5.14	A pictorial overview of the topological structure of the full computational domain as well as the second study region used for the model analysis. . . . .	212
5.15	The land-use spatial distributions used within each model variants. Labels on the axes represent the row and column indices for each pixel within the computational domain. . . . .	213
5.16	The total time in seconds it took for each of fifty simulation runs for both the 20m (blue) and 50m (red) model resolutions to complete. . . . .	214
5.17	An evolution of the average water depth overland flow throughout the 20m resolution model simulation. . . . .	216
5.18	The minimum, maximum and average mean water depths at non-zero output pixels within the northern sub-region outlined in Figure 5.14 for both model resolutions. Sub-figures (a) and (b) show the values for two of the seven regions where water is present as seen in Figure 5.17 as well as the entire domain (c). . . . .	218

5.19	A comparison of the normalised average water depth output between the 20m (blue) and 50m (red) resolutions. The normalisation utilises the maximum average value at any timestep within the patch. The number of timesteps goes across the $x$ -axis of each subplot. Their plot placement corresponds to the patch numbers in figure 5.1c. . . . .	219
5.20	A comparison of the absolute average water depth values between the 20m (blue) and 50m (red) resolutions. . . . .	220
5.21	Patch 3 - Original land composition within the 20m (5.21a) and 50m (5.21b) resolution models with absolute water depth values for each model (5.21c) and relative 50m output values compared with the 20m model (5.21d). . . . .	222
5.22	Patch 7 - Original land composition within the 20m (5.22a) and 50m (5.22b) resolution models along with an adjusted 50m resolution patch (5.22c) with absolute water depth values for each model (5.22d) and relative 50m output values compared with the 20m model (5.22e). . . . .	223
5.23	Patch 11 - Original land composition within the 20m (5.23a) and 50m (5.23b) resolution models along with an adjusted 50m resolution patch (5.23c) with absolute water depth values for each model (5.23d) and relative 50m output values compared with the 20m model (5.23e). . . . .	224
5.24	Patch 23 - Original land composition within the 20m (5.24a) and 50m (5.24b) resolution models along with an adjusted 50m resolution patch (5.24c) with absolute water depth values for each model (5.24d) and relative 50m output values compared with the 20m model (5.24e). . . . .	225
5.25	Patch 40 - Original land composition within the 20m (5.25a) and 50m (5.25b) resolution models along with an adjusted 50m resolution patch (5.25c) with absolute water depth values for each model (5.25d) and relative 50m output values compared with the 20m model (5.25e). . . . .	227
5.26	Patch 41 - Original land composition within the 20m (5.26a) and 50m (5.26b) resolution models along with an adjusted 50m resolution patch to match more closely proportionally with the 20m model (5.26c) with absolute water depth values for each model (5.26d) and relative 50m output values compared with the 20m model (5.26e). . . . .	228
5.27	Patch 42 - Original land composition within the 20m (5.27a) and 50m (5.27b) resolution models along with an adjusted 50m resolution patch to match more closely proportionally with the 20m model (5.27c) with absolute water depth values for each model (5.27d) and relative 50m output values compared with the 20m model (5.27e). . . . .	229
6.1	Spatial and Temporal Inputs. . . . .	235
6.2	Scenario 1 - Central moving storm - 20m resolution model. Each row presents individual timesteps $\Delta t = 01 : 30$ , $\Delta t = 04 : 30$ and $\Delta t = 06 : 00$ . Sub-figures (a), (e) and (i) show the evolution of the fictitious storm during the simulation. Sub-figures (b), (f) and (j) show the average water depth at their given timesteps. Sub-figures (c), (g) and (k) depict the mean unit-width horizontal flux in the $x$ -direction. Sub-figures (d), (h) and (l) depict the mean unit-width horizontal flux in the $y$ -direction. . . . .	238

- 
- 6.3 Scenario 1 - Central moving storm - 20m resolution model. Each row presents individual timesteps  $\Delta t = 07 : 30$  and  $\Delta t = 12 : 00$ . Sub-figures (a) and (e) show the evolution of the fictitious storm during the simulation. Sub-figures (b) and (f) show the average water depth at their given timesteps. Sub-figures (c) and (g) depict the mean unit-width horizontal flux in the  $x$ -direction. Sub-figures (d) and (h) depict the mean unit-width horizontal flux in the  $y$ -direction. . . . . 239
- 6.4 Scenario 1 - Central moving storm - 20m resolution model. Each row presents individual timesteps  $\Delta t = 24 : 00$ ,  $\Delta t = 30 : 00$  and  $\Delta t = 37 : 00$ . Sub-figures (a), (e) and (i) show the evolution of the fictitious storm during the simulation. Sub-figures (b), (f) and (j) show the average water depth at their given timesteps. Sub-figures (c), (g) and (k) depict the mean unit-width horizontal flux in the  $x$ -direction. Sub-figures (d), (h) and (l) depict the mean unit-width horizontal flux in the  $y$ -direction. . . . . 240
- 6.5 Scenario 1 - Central moving storm - 20m resolution model. Each row presents individual timesteps  $\Delta t = 42 : 00$  and  $\Delta t = 48 : 00$ . Sub-figures (a) and (e) show the evolution of the fictitious storm during the simulation. Sub-figures (b) and (f) show the average water depth at their given timesteps. Sub-figures (c) and (g) depict the mean unit-width horizontal flux in the  $x$ -direction. Sub-figures (d) and (h) depict the mean unit-width horizontal flux in the  $y$ -direction. . . . . 241
- 6.6 Scenario 1 - Central static storm - 20m resolution model. Each row presents individual timesteps  $\Delta t = 01 : 30$ ,  $\Delta t = 04 : 30$  and  $\Delta t = 06 : 00$ . Sub-figures (a), (e) and (i) show the evolution of the fictitious storm during the simulation. Sub-figures (b), (f) and (j) show the average water depth at their given timesteps. Sub-figures (c), (g) and (k) depict the mean unit-width horizontal flux in the  $x$ -direction. Sub-figures (d), (h) and (l) depict the mean unit-width horizontal flux in the  $y$ -direction. . . . . 243
- 6.7 Scenario 1 - Central static storm - 20m resolution model. Each row presents individual timesteps  $\Delta t = 07 : 30$  and  $\Delta t = 12 : 00$ . Sub-figures (a) and (e) show the evolution of the fictitious storm during the simulation. Sub-figures (b) and (f) show the average water depth at their given timesteps. Sub-figures (c) and (g) depict the mean unit-width horizontal flux in the  $x$ -direction. Sub-figures (d) and (h) depict the mean unit-width horizontal flux in the  $y$ -direction. . . . . 244
- 6.8 Scenario 1 - Central static storm - 20m resolution model. Each row presents individual timesteps  $\Delta t = 24 : 00$ ,  $\Delta t = 30 : 00$  and  $\Delta t = 37 : 00$ . Sub-figures (a), (e) and (i) show the evolution of the fictitious storm during the simulation. Sub-figures (b), (f) and (j) show the average water depth at their given timesteps. Sub-figures (c), (g) and (k) depict the mean unit-width horizontal flux in the  $x$ -direction. Sub-figures (d), (h) and (l) depict the mean unit-width horizontal flux in the  $y$ -direction. . . . . 245

- 
- 6.9 Scenario 1 - Central static storm - 20m resolution model. Each row presents individual timesteps  $\Delta t = 42 : 00$  and  $\Delta t = 48 : 00$ . Sub-figures (a) and (e) show the evolution of the fictitious storm during the simulation. Sub-figures (b) and (f) show the average water depth at their given timesteps. Sub-figures (c) and (g) depict the mean unit-width horizontal flux in the  $x$ -direction. Sub-figures (d) and (h) depict the mean unit-width horizontal flux in the  $y$ -direction. . . . . 246
- 6.10 Scenario 1 - Central moving storm - 50m resolution model. Each row presents individual timesteps  $\Delta t = 01 : 30$ ,  $\Delta t = 03 : 00$  and  $\Delta t = 06 : 00$ . Sub-figures (a), (e) and (i) show the evolution of the fictitious storm during the simulation. Sub-figures (b), (f) and (j) show the average water depth at their given timesteps. Sub-figures (c), (g) and (k) depict the mean unit-width horizontal flux in the  $x$ -direction. Sub-figures (d), (h) and (l) depict the mean unit-width horizontal flux in the  $y$ -direction. . . . . 248
- 6.11 Scenario 1 - Central moving storm - 50m resolution model. Each row presents individual timesteps  $\Delta t = 10 : 30$  and  $\Delta t = 18 : 00$ . Sub-figures (a) and (e) show the evolution of the fictitious storm during the simulation. Sub-figures (b) and (f) show the average water depth at their given timesteps. Sub-figures (c) and (g) depict the mean unit-width horizontal flux in the  $x$ -direction. Sub-figures (d) and (h) depict the mean unit-width horizontal flux in the  $y$ -direction. . . . . 249
- 6.12 Scenario 1 - Central moving storm - 50m resolution model. Each row presents individual timesteps  $\Delta t = 24 : 00$ ,  $\Delta t = 30 : 00$  and  $\Delta t = 36 : 00$ . Sub-figures (a), (e) and (i) show the evolution of the fictitious storm during the simulation. Sub-figures (b), (f) and (j) show the average water depth at their given timesteps. Sub-figures (c), (g) and (k) depict the mean unit-width horizontal flux in the  $x$ -direction. Sub-figures (d), (h) and (l) depict the mean unit-width horizontal flux in the  $y$ -direction. . . . . 250
- 6.13 Scenario 1 - Central moving storm - 20m resolution model. Each row presents individual timesteps  $\Delta t = 42 : 00$  and  $\Delta t = 48 : 00$ . Sub-figures (a) and (e) show the evolution of the fictitious storm during the simulation. Sub-figures (b) and (f) show the average water depth at their given timesteps. Sub-figures (c) and (g) depict the mean unit-width horizontal flux in the  $x$ -direction. Sub-figures (d) and (h) depict the mean unit-width horizontal flux in the  $y$ -direction. . . . . 251
- 6.14 Scenario 1 - Central static storm - 50m resolution model. Each row presents individual timesteps  $\Delta t = 01 : 30$ ,  $\Delta t = 03 : 00$  and  $\Delta t = 06 : 00$ . Sub-figures (a), (e) and (i) show the evolution of the fictitious storm during the simulation. Sub-figures (b), (f) and (j) show the average water depth at their given timesteps. Sub-figures (c), (g) and (k) depict the mean unit-width horizontal flux in the  $x$ -direction. Sub-figures (d), (h) and (l) depict the mean unit-width horizontal flux in the  $y$ -direction. . . . . 253

- 
- 6.15 Scenario 1 - Central static storm - 50m resolution model. Each row presents individual timesteps  $\Delta t = 10 : 30$  and  $\Delta t = 18 : 00$ . Sub-figures (a) and (e) show the evolution of the fictitious storm during the simulation. Sub-figures (b) and (f) show the average water depth at their given timesteps. Sub-figures (c) and (g) depict the mean unit-width horizontal flux in the  $x$ -direction. Sub-figures (d) and (h) depict the mean unit-width horizontal flux in the  $y$ -direction. . . . . 254
- 6.16 Scenario 1 - Central static storm - 50m resolution model. Each row presents individual timesteps  $\Delta t = 24 : 00$ ,  $\Delta t = 30 : 00$  and  $\Delta t = 36 : 00$ . Sub-figures (a), (e) and (i) show the evolution of the fictitious storm during the simulation. Sub-figures (b), (f) and (j) show the average water depth at their given timesteps. Sub-figures (c), (g) and (k) depict the mean unit-width horizontal flux in the  $x$ -direction. Sub-figures (d), (h) and (l) depict the mean unit-width horizontal flux in the  $y$ -direction. . . . . 255
- 6.17 Scenario 1 - Central static storm - 50m resolution model. Each row presents individual timesteps  $\Delta t = 42 : 00$  and  $\Delta t = 48 : 00$ . Sub-figures (a) and (e) show the evolution of the fictitious storm during the simulation. Sub-figures (b) and (f) show the average water depth at their given timesteps. Sub-figures (c) and (g) depict the mean unit-width horizontal flux in the  $x$ -direction. Sub-figures (d) and (h) depict the mean unit-width horizontal flux in the  $y$ -direction. . . . . 256
- 6.18 Scenario 3 - South-eastern moving storm - 20m resolution model. Each row presents individual timesteps  $\Delta t = 01 : 30$  and  $\Delta t = 06 : 00$ . Sub-figures (a) and (e) show the evolution of the fictitious storm during the simulation. Sub-figures (b) and (f) show the average water depth at their given timesteps. Sub-figures (c) and (g) depict the mean unit-width horizontal flux in the  $x$ -direction. Sub-figures (d) and (h) depict the mean unit-width horizontal flux in the  $y$ -direction. . . . . 258
- 6.19 Scenario 3 - South-eastern moving storm - 20m resolution model. Each row presents individual timesteps  $\Delta t = 12 : 00$  and  $\Delta t = 18 : 00$ . Sub-figures (a) and (e) show the evolution of the fictitious storm during the simulation. Sub-figures (b) and (f) show the average water depth at their given timesteps. Sub-figures (c) and (g) depict the mean unit-width horizontal flux in the  $x$ -direction. Sub-figures (d) and (h) depict the mean unit-width horizontal flux in the  $y$ -direction. . . . . 259
- 6.20 Scenario 1 - Central moving storm - 20m resolution model. Each row presents individual timesteps  $\Delta t = 24 : 00$ ,  $\Delta t = 30 : 00$  and  $\Delta t = 48 : 00$ . Sub-figures (a), (e) and (i) show the evolution of the fictitious storm during the simulation. Sub-figures (b), (f) and (j) show the average water depth at their given timesteps. Sub-figures (c), (g) and (k) depict the mean unit-width horizontal flux in the  $x$ -direction. Sub-figures (d), (h) and (l) depict the mean unit-width horizontal flux in the  $y$ -direction. . . . . 260

- 6.21 Scenario 3 - South-eastern static storm - 20m resolution model. Each row presents individual timesteps  $\Delta t = 01 : 30$  and  $\Delta t = 06 : 00$ . Sub-figures (a) and (e) show the evolution of the fictitious storm during the simulation. Sub-figures (b) and (f) show the average water depth at their given timesteps. Sub-figures (c) and (g) depict the mean unit-width horizontal flux in the  $x$ -direction. Sub-figures (d) and (h) depict the mean unit-width horizontal flux in the  $y$ -direction. . . . . 262
- 6.22 Scenario 3 - South-eastern static storm - 20m resolution model. Each row presents individual timesteps  $\Delta t = 12 : 00$  and  $\Delta t = 18 : 00$ . Sub-figures (a) and (e) show the evolution of the fictitious storm during the simulation. Sub-figures (b) and (f) show the average water depth at their given timesteps. Sub-figures (c) and (g) depict the mean unit-width horizontal flux in the  $x$ -direction. Sub-figures (d) and (h) depict the mean unit-width horizontal flux in the  $y$ -direction. . . . . 263
- 6.23 Scenario 3 - South-eastern static storm - 20m resolution model. Each row presents individual timesteps  $\Delta t = 24 : 00$ ,  $\Delta t = 30 : 00$  and  $\Delta t = 48 : 00$ . Sub-figures (a), (e) and (i) show the evolution of the fictitious storm during the simulation. Sub-figures (b), (f) and (j) show the average water depth at their given timesteps. Sub-figures (c), (g) and (k) depict the mean unit-width horizontal flux in the  $x$ -direction. Sub-figures (d), (h) and (l) depict the mean unit-width horizontal flux in the  $y$ -direction. . . . . 264
- 6.24 Scenario 3 - South-eastern moving storm - 50m resolution model. Each row presents individual timesteps  $\Delta t = 01 : 30$ ,  $\Delta t = 06 : 00$  and  $\Delta t = 12 : 00$ . Sub-figures (a), (e) and (i) show the evolution of the fictitious storm during the simulation. Sub-figures (b), (f) and (j) show the average water depth at their given timesteps. Sub-figures (c), (g) and (k) depict the mean unit-width horizontal flux in the  $x$ -direction. Sub-figures (d), (h) and (l) depict the mean unit-width horizontal flux in the  $y$ -direction. . . . . 266
- 6.25 Scenario 3 - South-eastern moving storm - 50m resolution model. Each row presents individual timesteps  $\Delta t = 13 : 30$  and  $\Delta t = 24 : 00$ . Sub-figures (a) and (e) show the evolution of the fictitious storm during the simulation. Sub-figures (b) and (f) show the average water depth at their given timesteps. Sub-figures (c) and (g) depict the mean unit-width horizontal flux in the  $x$ -direction. Sub-figures (d) and (h) depict the mean unit-width horizontal flux in the  $y$ -direction. . . . . 267
- 6.26 Scenario 3 - South-eastern moving storm - 50m resolution model. Each row presents individual timesteps  $\Delta t = 30 : 00$ ,  $\Delta t = 36 : 00$ ,  $\Delta t = 42 : 00$  and  $\Delta t = 48 : 00$ . Sub-figures (a), (e), (i) and (m) show the evolution of the fictitious storm during the simulation. Sub-figures (b), (f), (j) and (n) show the average water depth at their given timesteps. Sub-figures (c), (g) (k) and (o) depict the mean unit-width horizontal flux in the  $x$ -direction. Sub-figures (d), (h), (l) and (p) depict the mean unit-width horizontal flux in the  $y$ -direction. . . . . 268

6.27	Scenario 3 - South-eastern static storm - 50m resolution model. Each row presents individual timesteps $\Delta t = 01 : 30$ , $\Delta t = 06 : 00$ and $\Delta t = 12 : 00$ . Sub-figures (a), (e) and (i) show the evolution of the fictitious storm during the simulation. Sub-figures (b), (f) and (j) show the average water depth at their given timesteps. Sub-figures (c), (g) and (k) depict the mean unit-width horizontal flux in the $x$ -direction. Sub-figures (d), (h) and (l) depict the mean unit-width horizontal flux in the $y$ -direction. . . . .	270
6.28	Scenario 3 - South-eastern static storm - 50m resolution model. Each row presents individual timesteps $\Delta t = 13 : 30$ and $\Delta t = 24 : 00$ . Sub-figures (a) and (e) show the evolution of the fictitious storm during the simulation. Sub-figures (b) and (f) show the average water depth at their given timesteps. Sub-figures (c) and (g) depict the mean unit-width horizontal flux in the $x$ -direction. Sub-figures (d) and (h) depict the mean unit-width horizontal flux in the $y$ -direction. . . . .	271
6.29	Scenario 3 - South-eastern static storm - 50m resolution model. Each row presents individual timesteps $\Delta t = 30 : 00$ and $\Delta t = 36 : 00$ . Sub-figures (a) and (e) show the evolution of the fictitious storm during the simulation. Sub-figures (b) and (f) show the average water depth at their given timesteps. Sub-figures (c) and (g) depict the mean unit-width horizontal flux in the $x$ -direction. Sub-figures (d) and (h) depict the mean unit-width horizontal flux in the $y$ -direction. . . . .	272
6.30	Scenario 3 - South-eastern static storm - 50m resolution model. Each row presents individual timesteps $\Delta t = 42 : 00$ and $\Delta t = 48 : 00$ . Sub-figures (a) and (e) show the evolution of the fictitious storm during the simulation. Sub-figures (b) and (f) show the average water depth at their given timesteps. Sub-figures (c) and (g) depict the mean unit-width horizontal flux in the $x$ -direction. Sub-figures (d) and (h) depict the mean unit-width horizontal flux in the $y$ -direction. . . . .	273
7.1	A radar-gauge precipitation accumulation difference of the thunderstorm event over Coverack (Harrison et al., 2017; Environment Agency and Cornwall Council, 2018). . . . .	277
7.2	Hyteographs for the Coverack storm event (blue) and the 0.1% Annual Exceedance Probability event (green) (Environment Agency and Cornwall Council, 2018). . . . .	277
7.3	Original 20m resolution land-use map. . . . .	279
7.4	Defined sub-regions for the 20m resolution computational domain. . . . .	279
7.5	Mean water depth values averaged across each land-use for each modelling scenario within the Coastal Coverack sub-region. . . . .	284
7.6	Mean water depth values averaged across each land-use for each modelling scenario within the Northern Coverack sub-region. . . . .	285
7.7	Mean water depth values averaged across each land-use for each modelling scenario within the North-Eastern Coverack sub-region. . . . .	287
7.8	Mean water depth values averaged across each land-use for each modelling scenario within the southern Coverack sub-region. . . . .	288



7.9	Mean water depth values averaged across each land-use for each modelling scenario within the Western Coverack sub-region. . . . .	290
A.1	An illustration of the characteristics present for the linear advection equation with characteristic speed $a > 0$ . The initial position $x_0$ is a fixed initial condition at $t = 0$ . . . . .	302
A.2	A diagrammatic version of the solution to the linearised gas dynamics Riemann problem. Here the density $\rho(x, t)$ and velocity $u(x, t)$ profiles at $t = 1$ are shown. Initial parameter values are $p_0 = 1$ , $\alpha = 1$ with $(\rho_l, u_l) = (1, 0)$ and $(\rho_r, u_r) = (0.5, 0)$ . . . . .	307
A.3	An illustration of all three finite difference approximations to the first derivative of function $f(x)$ about the point $x_0$ ; backward (orange), central (purple) and forward (blue). The true derivative is the line tangent to the curve at $f(x_0)$ in black. . . . .	309
A.4	Discretisation of a finite difference approximation in the $x - t$ domain, with a regular mesh of intervals $\Delta x \times \Delta t$ . . . . .	310
A.5	Grid mesh blueprint of the first-order upwind scheme with positive propagation speed $a$ . Upwind direction is to the left. . . . .	312
A.6	A control volume in the $x-t$ plane, $V = [x_l, x_r] \times [t^{(1)}, t^{(2)}]$ . . . . .	317
A.7	Standard characteristic curves for a non-linear hyperbolic conservation system. . . . .	319
A.8	Wave steepening distortion phenomena in a non-linear hyperbolic conservation system. Part (a) shows the initial solution profile. Part (b) displays the corresponding characteristics of the initial solutions. . . . .	322
A.9	The initial discontinuous data (a), system characteristics (b) and solution on the $x - t$ plane for the inviscid Burgers equation (c). . . . .	325
A.10	The initial expansive discontinuous data (a), system characteristics (b) and rarefaction shock solution on the $x-t$ plane for the inviscid Burgers equation (c). . . . .	327
A.11	A non-centred rarefaction wave with expansive smooth initial data (a) and characteristics picture in $x - t$ plane (b). . . . .	328
A.12	A centred rarefaction wave with expansive discontinuous initial data (a), characteristic picture (b) and the rarefaction solution on the $x - t$ plane which satisfies the entropy condition (c). . . . .	328
A.13	A typical solution for the inviscid Burgers equation where; (a) general solution structure (single wave, shock/rarefaction); (b) shock wave solution; (c) rarefaction wave solution. . . . .	329
A.14	Two elementary wave solutions of the Riemann problem: (a) a shock wave characteristic with speed $S_i$ and (b) a rarefaction wave. . . . .	332
A.15	A discretisation illustration for the computational domain $[0, N] \times [0, T]$ into $n$ finite volumes. $x_{i-\frac{1}{2}}$ and $x_{i+\frac{1}{2}}$ denote the intercell boundaries of pixel $x_i$ . . . . .	333
A.16	A representation of piece-wise constant distribution of information at time step $t^{(k)}$ . . . . .	334

A.17	A stencil of Godunov’s method for the linear advection equation where speed $a > 0$ . Solutions to the Riemann problem are averaged within cell $I_i$ .	335
A.18	Graphical representation outputs (blue) along with the admissible second-order TVD region (grey). Obtained from Wikipedia (2022).	341
B.19	Surface runoff pictorial representation when water input is greater than infiltration capacity. Adapted from Dunne and Leopold (1978); Tarboton (2003).	342
B.20	A control unsaturated soil volume considered when constructing the continuity equation. Adapted from Chow et al. (1988); Tarboton (2003).	343
B.21	Saturation excess runoff generation illustration. (a) shows the moisture content vs. depth profile. (b) A time series of runoff generation when a soil is saturated. Adapted from Bras (1990); Tarboton (2003).	345
C.22	Locations of where RGB pixel samples were taken for image processing using the Dudley Stamp Map from Department for Environment, Food & Rural Affairs (2002c).	348
C.23	Binary outputs after image processing for each land use definition.	349
C.1	Locations of where RGB pixel samples were taken for image processing using the Dudley Stamp Map from Department for Environment, Food & Rural Affairs (2002c).	350
C.2	Binary outputs after image processing for each land use definition.	351
F.1	The minimum, maximum and average mean water depths at non-zero output pixels within the north-eastern sub-region outlined in Figure 5.3 for both model resolutions for the remaining three of the five regions not depicted in Figure 5.5.	362
F.2	The minimum, maximum and average mean water depths at non-zero output pixels within the northern sub-region outlined in Figure 5.14 for both model resolutions for the remaining five of the seven regions not depicted in Figure 5.18.	365
G.1	An evolution of the average water depth overland flow throughout the 50m resolution model simulation.	366
G.2	An evolution of the average water depth overland flow throughout the 50m resolution model simulation.	367
I.3	Patch 23 - Original land composition within the 20m (I.3a) and 50m (I.3b) resolution models along with an adjusted 50m resolution patch (I.3c) with absolute water depth values for each model (I.3d) and relative 50m output values compared with the 20m model (I.3e).	375
I.4	Patch 56 - Original land composition within the 20m (I.4a) and 50m (I.4b) resolution models along with an adjusted 50m resolution patch (I.4c) with absolute water depth values for each model (5.9d) and relative 50m output values compared with the 20m model (I.4e).	376
I.5	Patch 15 - Original land composition within the 20m (I.5a) and 50m (I.5b) resolution models with absolute water depth values for each model (I.5c) and relative 50m output values compared with the 20m model (I.5d).	377

I.6	Patch 24 - Original land composition within the 20m (I.6a) and 50m (I.6b) resolution models along with an adjusted 50m resolution patch (I.6c) with absolute water depth values for each model (I.6d) and relative 50m output values compared with the 20m model (I.6e). . . . .	378
I.7	Patch 25 - Original land composition within the 20m (I.7a) and 50m (I.7b) resolution models along with an adjusted 50m resolution patch (I.7c) with absolute water depth values for each model (I.7d) and relative 50m output values compared with the 20m model (I.7e). . . . .	379
I.8	Patch 32 - Original land composition within the 20m (I.8a) and 50m (I.8b) resolution models along with an adjusted 50m resolution patch (I.8c) with absolute water depth values for each model (I.8d) and relative 50m output values compared with the 20m model (I.8e). . . . .	380
I.9	Patch 39 - Original land composition within the 20m (sub-figure I.9a) and 50m (sub-figure I.9b) resolution models along with an adjusted 50m resolution patch to match more closely proportionally with the 20m model (sub-figure I.9c) with absolute water depth values for each model (sub-figure I.9d) and relative 50m output values compared with the 20m model (sub-figure I.9e). . . . .	381
I.10	Patch 49 - Original land composition within the 20m (I.10a) and 50m (I.10b) resolution models along with an adjusted 50m resolution patch (I.10c) with absolute water depth values for each model (I.10d) and relative 50m output values compared with the 20m model (I.10e). . . . .	382
I.11	Patch 58 - Original land composition within the 20m (I.11a) and 50m (I.11b) resolution models along with an adjusted 50m resolution patch (I.11c) with absolute water depth values for each model (I.11d) and relative 50m output values compared with the 20m model (I.11e). . . . .	383
J.12	Scenario 2 - North-western moving storm - 20m resolution model. Each row presents individual timesteps $\Delta t = 01 : 30$ , $\Delta t = 06 : 00$ and $\Delta t = 12 : 00$ . Sub-figures (a), (e) and (i) show the evolution of the fictitious storm during the simulation. Sub-figures (b), (f) and (j) show the average water depth at their given timesteps. Sub-figures (c), (g) and (k) depict the mean unit-width horizontal flux in the $x$ -direction. Sub-figures (d), (h) and (l) depict the mean unit-width horizontal flux in the $y$ -direction. . . . .	385
J.13	Scenario 2 - North-western moving storm - 20m resolution model. Each row presents individual timesteps $\Delta t = 16 : 30$ and $\Delta t = 24 : 00$ . Sub-figures (a) and (e) show the evolution of the fictitious storm during the simulation. Sub-figures (b) and (f) show the average water depth at their given timesteps. Sub-figures (c) and (g) depict the mean unit-width horizontal flux in the $x$ -direction. Sub-figures (d) and (h) depict the mean unit-width horizontal flux in the $y$ -direction. . . . .	386

- 
- J.14 Scenario 2 - North-western moving storm - 20m resolution model. Each row presents individual timesteps  $\Delta t = 30 : 00$  and  $\Delta t = 36 : 00$ . Sub-figures (a), (e) and (i) show the evolution of the fictitious storm during the simulation. Sub-figures (b), (f) and (j) show the average water depth at their given timesteps. Sub-figures (c), (g) and (k) depict the mean unit-width horizontal flux in the  $x$ -direction. Sub-figures (d), (h) and (l) depict the mean unit-width horizontal flux in the  $y$ -direction. . . . . 387
- J.15 Scenario 2 - North-western moving storm - 20m resolution model. Each row presents individual timesteps  $\Delta t = 42 : 00$  and  $\Delta t = 48 : 00$ . Sub-figures (a) and (e) show the evolution of the fictitious storm during the simulation. Sub-figures (b) and (f) show the average water depth at their given timesteps. Sub-figures (c) and (g) depict the mean unit-width horizontal flux in the  $x$ -direction. Sub-figures (d) and (h) depict the mean unit-width horizontal flux in the  $y$ -direction. . . . . 388
- J.16 Scenario 2 - North-western static storm - 20m resolution model. Each row presents individual timesteps  $\Delta t = 01 : 30$ ,  $\Delta t = 06 : 00$  and  $\Delta t = 12 : 00$ . Sub-figures (a), (e) and (i) show the evolution of the fictitious storm during the simulation. Sub-figures (b), (f) and (j) show the average water depth at their given timesteps. Sub-figures (c), (g) and (k) depict the mean unit-width horizontal flux in the  $x$ -direction. Sub-figures (d), (h) and (l) depict the mean unit-width horizontal flux in the  $y$ -direction. . . . . 390
- J.17 Scenario 2 - North-western static storm - 20m resolution model. Each row presents individual timesteps  $\Delta t = 16 : 30$  and  $\Delta t = 24 : 00$ . Sub-figures (a) and (e) show the evolution of the fictitious storm during the simulation. Sub-figures (b) and (f) show the average water depth at their given timesteps. Sub-figures (c) and (g) depict the mean unit-width horizontal flux in the  $x$ -direction. Sub-figures (d) and (h) depict the mean unit-width horizontal flux in the  $y$ -direction. . . . . 391
- J.18 Scenario 2 - North-western static storm - 20m resolution model. Each row presents individual timesteps  $\Delta t = 30 : 00$  and  $\Delta t = 36 : 00$ . Sub-figures (a), (e) and (i) show the evolution of the fictitious storm during the simulation. Sub-figures (b), (f) and (j) show the average water depth at their given timesteps. Sub-figures (c), (g) and (k) depict the mean unit-width horizontal flux in the  $x$ -direction. Sub-figures (d), (h) and (l) depict the mean unit-width horizontal flux in the  $y$ -direction. . . . . 392
- J.19 Scenario 2 - North-western static storm - 20m resolution model. Each row presents individual timesteps  $\Delta t = 42 : 00$  and  $\Delta t = 48 : 00$ . Sub-figures (a) and (e) show the evolution of the fictitious storm during the simulation. Sub-figures (b) and (f) show the average water depth at their given timesteps. Sub-figures (c) and (g) depict the mean unit-width horizontal flux in the  $x$ -direction. Sub-figures (d) and (h) depict the mean unit-width horizontal flux in the  $y$ -direction. . . . . 393

- 
- J.20 Scenario 2 - North-western moving storm - 50m resolution model. Each row presents individual timesteps  $\Delta t = 01 : 30$ ,  $\Delta t = 06 : 00$  and  $\Delta t = 12 : 00$ . Sub-figures (a), (e) and (i) show the evolution of the fictitious storm during the simulation. Sub-figures (b), (f) and (j) show the average water depth at their given timesteps. Sub-figures (c), (g) and (k) depict the mean unit-width horizontal flux in the  $x$ -direction. Sub-figures (d), (h) and (l) depict the mean unit-width horizontal flux in the  $y$ -direction. . . . . 395
- J.21 Scenario 2 - North-western moving storm - 50m resolution model. Each row presents individual timesteps  $\Delta t = 18 : 00$  and  $\Delta t = 24 : 00$ . Sub-figures (a) and (e) show the evolution of the fictitious storm during the simulation. Sub-figures (b) and (f) show the average water depth at their given timesteps. Sub-figures (c) and (g) depict the mean unit-width horizontal flux in the  $x$ -direction. Sub-figures (d) and (h) depict the mean unit-width horizontal flux in the  $y$ -direction. . . . . 396
- J.22 Scenario 2 - North-western moving storm - 50m resolution model. Each row presents individual timesteps  $\Delta t = 30 : 00$  and  $\Delta t = 36 : 00$ . Sub-figures (a) and (e) show the evolution of the fictitious storm during the simulation. Sub-figures (b) and (f) show the average water depth at their given timesteps. Sub-figures (c) and (g) depict the mean unit-width horizontal flux in the  $x$ -direction. Sub-figures (d) and (h) depict the mean unit-width horizontal flux in the  $y$ -direction. . . . . 397
- J.23 Scenario 2 - North-western moving storm - 50m resolution model. Each row presents individual timesteps  $\Delta t = 42 : 00$  and  $\Delta t = 48 : 00$ . Sub-figures (a) and (e) show the evolution of the fictitious storm during the simulation. Sub-figures (b) and (f) show the average water depth at their given timesteps. Sub-figures (c) and (g) depict the mean unit-width horizontal flux in the  $x$ -direction. Sub-figures (d) and (h) depict the mean unit-width horizontal flux in the  $y$ -direction. . . . . 398
- J.24 Scenario 2 - North-western static storm - 50m resolution model. Each row presents individual timesteps  $\Delta t = 01 : 30$ ,  $\Delta t = 06 : 00$  and  $\Delta t = 12 : 00$ . Sub-figures (a), (e) and (i) show the evolution of the fictitious storm during the simulation. Sub-figures (b), (f) and (j) show the average water depth at their given timesteps. Sub-figures (c), (g) and (k) depict the mean unit-width horizontal flux in the  $x$ -direction. Sub-figures (d), (h) and (l) depict the mean unit-width horizontal flux in the  $y$ -direction. . . . . 400
- J.25 Scenario 2 - North-western static storm - 50m resolution model. Each row presents individual timesteps  $\Delta t = 18 : 00$  and  $\Delta t = 24 : 00$ . Sub-figures (a) and (e) show the evolution of the fictitious storm during the simulation. Sub-figures (b) and (f) show the average water depth at their given timesteps. Sub-figures (c) and (g) depict the mean unit-width horizontal flux in the  $x$ -direction. Sub-figures (d) and (h) depict the mean unit-width horizontal flux in the  $y$ -direction. . . . . 401

J.26 Scenario 2 - North-western static storm - 50m resolution model. Each row presents individual timesteps  $\Delta t = 30 : 00$  and  $\Delta t = 36 : 00$ . Sub-figures (a) and (e) show the evolution of the fictitious storm during the simulation. Sub-figures (b) and (f) show the average water depth at their given timesteps. Sub-figures (c) and (g) depict the mean unit-width horizontal flux in the  $x$ -direction. Sub-figures (d) and (h) depict the mean unit-width horizontal flux in the  $y$ -direction. . . . . 402

J.27 Scenario 2 - North-western static storm - 50m resolution model. Each row presents individual timesteps  $\Delta t = 42 : 00$  and  $\Delta t = 48 : 00$ . Sub-figures (a) and (e) show the evolution of the fictitious storm during the simulation. Sub-figures (b) and (f) show the average water depth at their given timesteps. Sub-figures (c) and (g) depict the mean unit-width horizontal flux in the  $x$ -direction. Sub-figures (d) and (h) depict the mean unit-width horizontal flux in the  $y$ -direction. . . . . 403

Part I.

**Introduction and Mathematical  
Background**

# 1. Introduction

## 1.1. Research Background

The strive towards the equitable and sustainable use of land to reach our material, cultural and fundamental needs is a defining challenge of our time. This ambitious goal requires that the private, public and other sectors all work cohesively together as one. Computational tools enable the construction and testing of the potential effects and consequences as a result of policy and industrial drivers in the UK. Sustainability metrics, agreed by stakeholders, can assess and drive sustainability practices to optimally use land in an equitable way.

This section begins by defining what it means to be a green economy (Section 1.1.1) and how this links to sustainable development (1.1.2). A discussion on what “natural capital” means will follow (1.1.3) and how this idea naturally lends itself to the “Ecosystem Services Concept” (1.1.4). Drawing on these definitions, Cornwall Council’s “Environmental Growth Strategy” (1.1.5) and specifically its fourth target (1.1.5.1) is outlined. A parallel is drawn between the concept of “facilities management” and “ecosystem services” to further motivate the thesis in Section 1.1.6. A case study is provided in Section 1.2 which will look at the fishing community of Coverack, Cornwall, to further demonstrate the need of such a computational tool. Section 1.3 will outline the aims of this thesis, using the sections presented above to guide the work. Section 1.4 will conclude this chapter by outlining the overall structure of this thesis.

### 1.1.1. A Green Economy

An economy which deliberately acts to decrease environmental risk, degradation and minimise ecological decline is defined to be a *green economy*. Recognition that an economic system is green depends on the efficient use of resources as well as fairness in the distribution of investment. Equitable shares of stocks and resources on global, regional and local scales derives an economy which consumes resources efficiently, is low carbon and ensures social inclusivity (United Nations Environment Programme, 2011).

What uniquely distinguishes a green economy from other economies is its focus on valuing natural capital and ecosystem services as having an economic and societal impact. The relationship between natural assets and their functions can be understood and this understanding can be utilised to serve the population at large (The Economics of Ecosystems and Biodiversity, 2010; Runnalls, 2011).



Various definitions of a green economy exist. The International Chamber of Commerce, an organisation that represents global business, defines a green economy as “*an economy in which economic growth and environmental responsibility work together in a mutually reinforcing fashion while supporting progress on social development*” (United Nations Department of Economic and Social Affairs, 2013; International Chamber of Commerce, 2016). A separate approach to defining a green economy is by focusing on multiple industrial sectors, namely, *renewable energy, green infrastructure, sustainable transport* as well as *water, waste and land management* (Burkart, 2009).

A **green economy** sets out policies to deliberately decrease environmental risk, degradation and minimise ecological decline. Its core purpose is to set a policy course which is environmentally friendly but also meets the socio-economic needs of the present whilst not being a detrimental to the needs of future generations (Courant et al., 1928).

Social, economic and environmental needs are equally complex in their own right, yet their simultaneous influence and dependence on one another adds further complexity. The pursuit of ascertaining a homeostasis between these three competing needs which benefits both humans and ecosystems is more commonly referred to as **sustainable development**.

### 1.1.2. Sustainable Development

In 1987, the World Commission on Environment and Development (WCED) released a book entitled “*Our Common Future*” with the sole aim of streamlining environmental policy into the forefront of priorities for national governments. It is more commonly referred to as the *Brundtland report*<sup>1</sup>. This literature piece modernised the concept of sustainable development and normalised the language within environmental policy decision making (World Commission on Environment and Development, 1987). Within the report is their regularly referenced definition of sustainable development

“Development that meets the needs of the present without compromising the ability of future generations to meet their own needs”

Poverty was recognised as a hindrance to sustainability efforts and increasing environmental resource stresses, further highlighting the need of balance between economic and ecological progress (Pyla, 2012). As the concept of sustainable development continued, focus shifted toward the interrelationships and cohesion between economic, societal and environmental goals in order to protect human society for future generations. The term “sustainability” is often associated with the target of equilibrium between humans and nature, whereas “sustainable development” is the holistic approach and processes which are the means to an end in developing sustainable practices (Shaker, 2015). Each domain’s goals and their relationships form the “three pillars of sustainability” as seen in Figure 1.1.

---

<sup>1</sup>This name recognised the work of Gro Harlem Brundtland’s, a former Prime Minister of Norway, the chair of the WCED at the time.

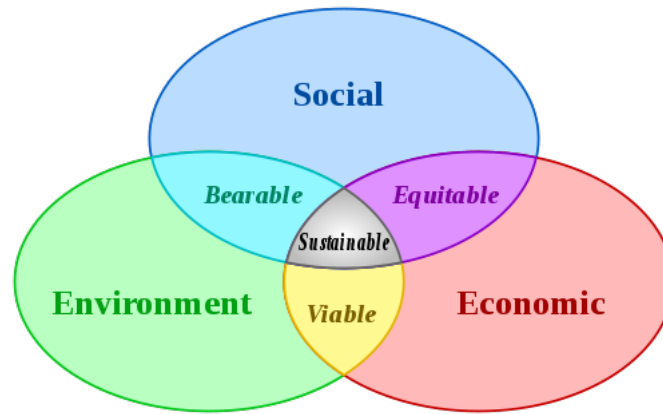


Figure 1.1.: A Venn diagram illustrating overarching aims for environmental, social and economic needs. Their interactions illustrate the benefits society obtains from achieving just two needs. Finally, the central overlap illustrates sustainability when decisions are bearable, viable and equitable for all. Image obtained from Dréo (2006).

Efforts in defining sustainable development theory have been widely criticised and are subject to cynicism. Using terminology and understanding of sustainable development, one can argue that non-renewable resource use is entirely unsustainable, as any consumption of such resources depletes the finite stock Earth has. One can then reasonably imply that the Industrial Revolution is unquestionably unsustainable (Turner, 1988; Georgescu-Roegen, 1971; Rifkin and Howard, 1980; Daly, 1991). There have also been suggestions that incorporating economic development into the concept of environmental conservation was simply a way to promote “business as usual” and use “green terminology” as a way to increase public relations globally (O’Riordan, 1988; Perez-Carmona, 2013).

### 1.1.3. Natural Capital

*Natural capital* is an umbrella phrase describing the global stock of natural resources of which, when combined, deliver a benefit to the human population. The book, “*Small is Beautiful*”, authored by Ernst Friedrich Schumacher, first introduced the concept of natural capital in 1973 (Schumacher, 2010). Such examples of resources include the geological and soil structure beneath an area of local interest, air, water and every living organism. Any asset which provides a benefit to the human species through free goods and/or services is defined to be a part of an *ecosystem service*, described in more detail in Section 1.1.4.

The global economy is entirely dependent on the supply and demand of natural resources and services. Hawken et al. (1999) argued that the next “industrial revolution” is entirely dependent on recognising the fundamental role natural resources have on our way of life and changing our perspective and consumption of these resource to ensure it is sustainable. We are currently living through this revolution. U.S. legislature referred to as the “Green New Deal” has been proposed by primary sponsors Rep. Alexandria Ocasio-Cortez (D-

NY) and Sen. Ed Markey (D-MA) (Meyer, 2019; Whyte, 2019). This has inspired other political parties within the international community to publish their version of a “Green New Deal”, such as the Labour party in the U.K. as part of their 2019 General Election campaign (Varoufakis and Adler, 2019; Harvey, 2019). Most recently, UK Labour party leader Sir Keir Starmer has proposed a publicly-owned green energy company (UK Labour Party, 2022).

#### 1.1.4. The Ecosystem Services Concept

Humans gain a vast and varied range of benefits from their surrounding natural environment via well-functioning ecosystems. Such provisions from natural assets are described as *ecosystem services*. The food we have available from crops, spices etc., the ability to generate energy from hydropower and biomass sources to carbon sequestration and climate regulation are just a few examples of how humans do benefit from natural assets. Ecosystem services encompass the benefits the human species receives from an ecosystem - the dynamic interaction between plant, animal and micro-organism communities, as well as the non-living environment working as a cohesive unit. This concept was relatively benign until the publication of the Millennium Ecosystem Assessment (2005). Within this synthesis, the services provided by ecosystems have been separated into four general branches dependent upon their actual function. These categories and their examples are outlined in Table 1.1 below. Table 1.2 introduces the components of human well-being which are linked to these services.

Table 1.1.: An overview of ecosystem service categories, their definitions and examples (Millennium Ecosystem Assessment, 2005).

Service	Definition	Examples
<b>Cultural</b>	Non-material prosperity people gain from ecosystems through aesthetic experiences	Spiritual enhancement, science, education etc.
<b>Provisional</b>	Any product which can be retrieved from an ecosystem.	Hydropower, biomass fuel, timber, food etc.
<b>Regulating</b>	Benefits humans may obtain from the regulation of an ecosystem process	Regulation of climate, flooding, disease etc.
<b>Supporting</b>	The fundamental ecological recycling processes from which the remaining three services depend on.	Nutrient cycling, soil formation, primary production etc.

Despite policies in recent decades which aim to slow down the degradation of the environment, 30% of UK ecosystem services are in decline (UK National Ecosystem Assessment, 2014). Well functioning ecosystems require a cohesion between natural habitats and the supporting of plants and animals which have failed to be provided (Lawton et al., 2010). The Department for Environment and Rural Affairs constructed a range of environmental “indicators” in order to track the health of the natural environment, so that a base of evidence can be obtained for policy making purposes. Following the creation of the indicators, an indicator assessment was introduced in May 2013 and subsequently revised annually (Department for Environment Food and Rural Affairs, 2013).

Table 1.2.: Components of positive well-being attributed to well-functioning ecosystem services (Millennium Ecosystem Assessment, 2005).

Category	Units of well-being
Security	Personal, secure access to basic amenities. Protection from disasters (natural or otherwise) etc.
Basic materials	Sufficient salary. Access to nutritious food. Shelter etc.
Health	Strength. Feeling well. Access to clean air and water etc.
Positive social relations	Social cohesion. Mutual respect. Ability to help out one another etc.

In a similar vein, Richardson et al. (2015) published a regional environment indicator report for Cornwall. Within the document are three overarching sections labelled “The Natural Environment”, “Green Economy” and “Health and Well-being”. Indicators under the “Natural Environment” section include “conservation priorities” and “water quality”. The “Green Economy” section contains indicators focusing on carbon dioxide levels and energy use whilst the final section looks at food and fuel poverty and general environmental quality (light/air pollution etc.). Focusing on thirteen indicators, these were then split into appropriate measures which looked at the overall trend within the county. Of the thirty one measures looked at, four were improving, two were declining and the rest either showed little change or no result due to insufficient data.

### 1.1.5. The Environmental Growth Strategy

A significant challenge facing governing bodies is deciding how to transition to a low-carbon green economy whilst meeting the social, economic and environmental needs of society now, as well as being mindful of the needs of future generations.

Cornwall council has developed a comprehensive policy plan to tackle these issues which were published in its *Environmental Growth Strategy* (EGS) (Cornwall Council, 2016). This report set out the council’s approach to deliver the economic and social needs of Cornwall through a net increase in its natural capital and ecosystem services. A crucial component towards the strategy’s success is how much environmental growth is realised in Cornwall. The council’s strategic direction is centered on four “ambitions” it wishes to fulfil by 2065.

- Experiencing Cornwall - Technology is at the forefront of attention in our daily lives. Targets within this ambition look to (re-)establish a close relationship between Cornish residents and nature to ascertain and maintain the psychological benefits one can receive.
- Understanding Cornwall - Target outcomes within this theme assess the suitability of the institutional decision making structures regularly used in the management of

modern society. It also highlights the data deficits that the council has which may be vital when determining the most beneficial locations and industrial sectors for investment.

- Valuing Cornwall - Targets here look to embed environmental and sustainable society thinking into our everyday lives.
- Achieving Environmental Growth - Here, specific case studies have been identified as being critical to realising environmental growth.

These ambitions are not exclusive but actually mutually interdependent on one another. This is usefully illustrated in Figure 1.2.

#### 1.1.5.1. Target Outcome 4

One pressing policy issue within political discourse is housing and how we can integrate their construction to meet demand whilst being environmentally sustainable. The UK government has estimated that between 225,000 and 275,000 new homes are needed annually to keep up with population growth as well as tackling current demand (Department for Communities and Local Government, 2017).

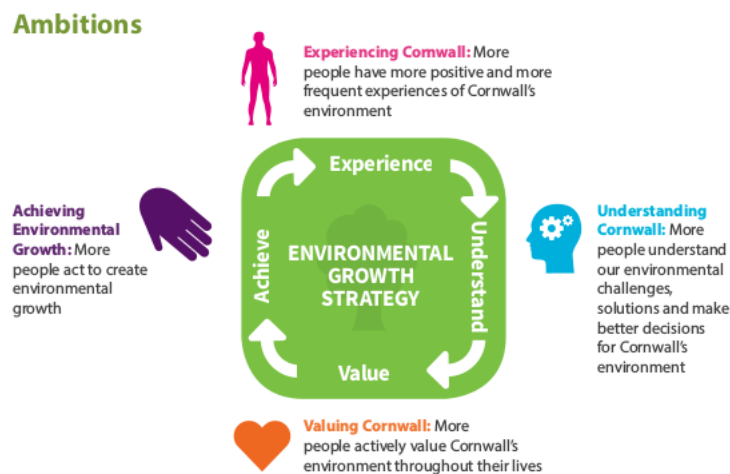


Figure 1.2.: An illustrative diagram showing the interdependence of each theme within the Environmental Growth Strategy. Obtained from (Cornwall Council, 2016, pg. 24).

Legislation by the UK government devolved flood risk management responsibilities to Local Lead Flood Authorities (LLFA), of which Cornwall council is one for the region (Department for Communities and Local Government, 2010). Within the Environmental Growth Strategy, Cornwall council have incorporated the construction of 52,500 new homes by 2030 (Cornwall Council, 2016). Undoubtedly this will have a lasting effect on the hydrological characteristic behaviour of Cornwall's river basins.

To achieve each ambition, actionable targets are highlighted within the EGS. Under the "Understanding Cornwall" ambition, a need to construct a management system which can

aid in ecosystem analytics to support environmental growth was identified. This target outcome is further broken down into actionable items, which are all outlined in Figure 1.3 below.


- 
- Target outcome 4:**  
Cornwall has an environmental management system that supports environmental growth
- For this we need:**
- a) A high quality, user-friendly, accessible management system to inform personal and collective decisions that affect Cornwall's environment.
  - b) Maps and information at a variety of scales to identify the environmental growth opportunities across Cornwall.
  - c) Dynamic management methods to inform the planning, prioritisation and delivery of public, private and community environmental investments.
  - d) Information to identify the environmental trends, risks and opportunities across Cornwall.
  - e) Information to improve our understanding of the social, economic and environmental value of Cornwall's environmental assets.
  - f) Information to monitor the goods and services provided by Cornwall's environment.
  - g) Information regarding cumulative impacts, carrying capacity and optimum uses for Cornwall's land, atmosphere, fresh water and sea.
  - h) Information to identify opportunities to work with nature in Cornwall to cope with global changes.
  - i) Information for Cornish businesses regarding their reliance on natural capital and relationship to climate change.
  - j) Supporting information which enables investment in 'ecosystem services' in Cornwall.

Figure 1.3.: One actionable target discussed within the Environmental Growth Strategy to achieve the “Understanding Cornwall” ambition. This target is further broken down into actionable items to fulfil the goal of growing natural assets. Obtained from (Cornwall Council, 2016, pg. 27).

### 1.1.6. Motivation

NJW Ltd., industrial sponsors for this project, were a technological solutions organisation which developed web-based integrated workplace management services. NJW were subject to a merger with Causeway technologies in January 2019 (Causeway technologies, 2022). One stream in which they deliver their “Integrated Workplace Management Solutions” (IWMS) is through their top HAT analytics platform named “Focal365”.

Focal365 provides executives with an insight into their own data sources to leverage performance and access trends to facilitate short and long term strategic planning. This platform improves visibility of clients’ global property portfolio and facilities information via an efficient central portal. It is an easy-to-use application allowing businesses insights into key metrics via maps, drill-downs and dashboards. One such dashboard in Focal365 is known as “My Facilities Management” or “MyFM” for short. Illustrative examples of these dashboards can be seen in Figures 1.4 and 1.5.

The International Facilities Management Association (IFMA) defines facility management

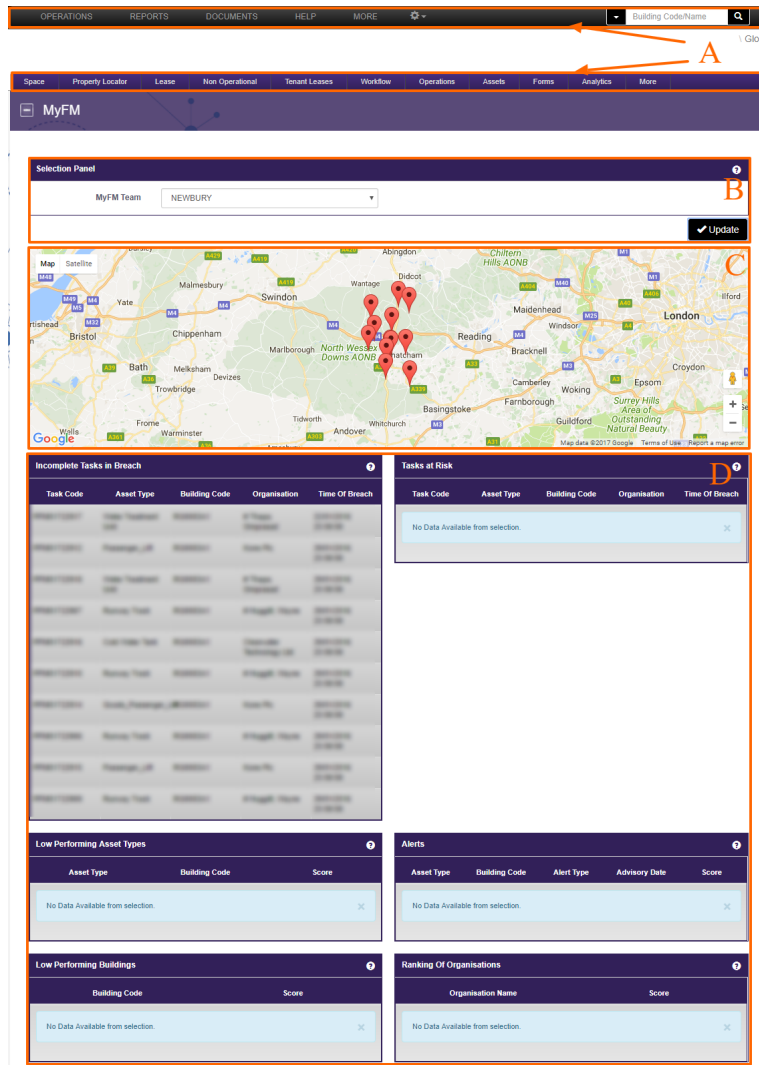


Figure 1.4.: An illustrative example of the MyFM dashboard global page which was in development at NJW Ltd. Client company names and relevant information have been redacted.

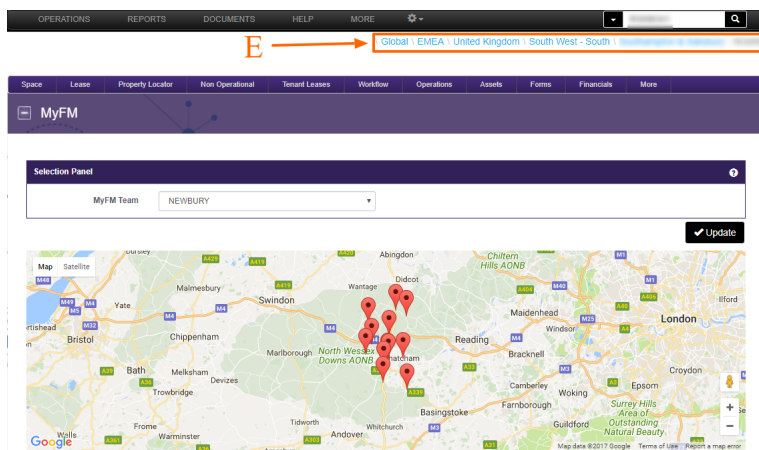


Figure 1.5.: An illustrative example of the MyFM dashboard 'drilled down' from the global page in figure 1.4 as seen by the breadcrumb trail labelled in box E.

as (International Facility Management Association, 1998)

Facility management (FM) is a profession that encompasses multiple disciplines to ensure functionality, comfort, safety and efficiency of the built environment by integrating people, place, process and technology.

A parallel may be drawn between the IFMA definition of facilities management and which can be equally applied to the Ecosystems Services Management concept highlighted in Section 1.1.4. Ecosystem services management encompasses multiple disciplines to ensure the functionality, comfort and benefit of the ecosystem environment by integrating the cultural, provisional, regulating and supporting services.

An objective of facilities management is to provide a support service contributing to the effective and efficient delivery of an organisation's strategic and operational goals while providing a safe and comfortable work environment on a daily basis. Within the facilities management space, such work can be lumped into two broad categories (iFM, 2022).

1. Hard - Relating to building, mechanical and electrical maintenance, fabric maintenance etc.
2. Soft - Relating to people e.g. catering, cleaning, health and safety, security etc.

Similarly, ecosystem services are split into four broad categories of cultural, provisional, regulating and supporting as highlighted in Table 1.2 (page 36).

Understanding the ecosystem services framework allows one to consider the broader objective of governance. To facilitate the transition process toward a sustainable ecosystem, local authorities and other key stakeholders must manage the competing needs of resources key to sustaining human and natural life. For example competing land use resources e.g. the need for over 50,000 houses by 2030 as discussed in Section 1.1.5.1 and water resources. These competing needs need to be considered by managing and mitigating the potential negative impact of human interference and promoting a well-functioning ecosystem.

A dashboard akin to MyFM within Focal365 can aid scientific and policy decision makers with developing integrated impact assessments. In Cornwall Council's case (see Section 1.1.5), they may consider the short to mid term flooding impact of developing housing in a river basin and develop possible mitigation strategies to minimise such consequences.

Facility managers can use MyFM to gain a broad picture on the performance of physical assets in real time using data obtained on these assets in the past. MyFM has the potential to present complex scientific scenario modelling to simplify and aid in understanding the potential ecological impacts of initiatives such as the Environmental Growth Strategy outlined in Section 1.1.5.



Table 1.3.: A description of the watercourses in Coverack. Table adapted from (Environment Agency and Cornwall Council, 2018, pg.4).

Watercourse Name	Route	Type	Catchment area [km <sup>2</sup> ]
North Corner Stream	Due south-west from B3293; discharges into the sea at North Corner	Ordinary watercourse	0.6
North Coverack Stream	Due south-west from “The Coverts”; discharges into sea just south of lower car park	Ordinary watercourse	< 0.5
South Coverack Stream	Due west from Penhallick; discharges into sea at Polcoverack Lane junction with B3294	Main River - lower $\approx$ 230m	2.2

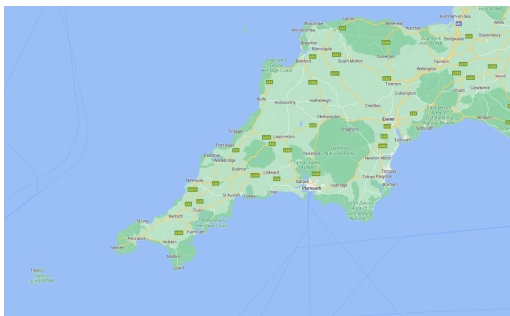
## 1.2. A Case Study: Coverack, Cornwall

Cornwall is located at the most south-western tip of England as illustrated in Figure 1.6a. Coverack is a small coastal village and fishing port located to the east of the Lizard peninsula approximately nine miles south of Falmouth (see Figures 1.6b and 1.6c). Three local watercourses empty the catchment above Coverack. The drainage route flows directly through the village into the sea. Table 1.3 details these three water courses specifically whilst Figure 1.8 highlights their locations.

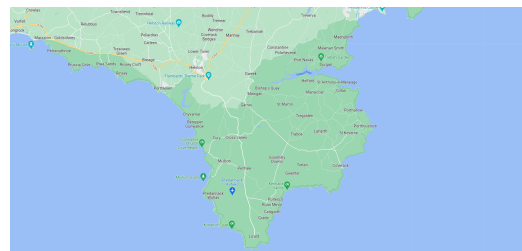
Coverack experienced intense localised rainfall on 18<sup>th</sup> July 2017. The volume of rainfall witnessed meant that the local catchment was not able to cope and resulted in flooding from rivers and surface water causing demonstrable erosion. Figure 1.7 illustrates the ferocity of the flooding event on the day. With over 50,000 new houses due to be constructed by 2030, the built-up environment will affect local flooding management strategies (Cornwall Council, 2016). Average precipitation has increased since 1950 and the rate of this increase has grown since 1980. Human induced climate change is believed to have influenced the intensity of rainfall since 1950. Given that the possibility of more extreme rainfall events is highly likely, modelling Coverack and Cornwall provides an excellent starting point to pilot a land-use flood modelling tool with options to provide a more broader management software package. With the help of software solutions such as “MyFM” highlighted in Section 1.1.6, various stakeholders such as Cornwall Council could potentially easily visualise the impact of policy decisions being driven forward.



(a) Location of Cornwall county in relation to England (Wikipedia, 2021a).



(b) Cornwall county via Google maps (Google Maps, 2017a).



(c) Lizard peninsula showing Coverack to the south-west of Cornwall (Google Maps, 2017b).

Figure 1.6.: Location of England, Cornwall and the village of Coverack.



(a) Flood flow through the B3294 into Coverack (BBC News Website, 2017).



(b) Aerial footage of northern Coverack stream flowing into the sea (BBC News Website, 2017).



(c) Local image showing the flooding extent from the south Coverack stream (Falmouth Packet Website, 2017).

Figure 1.7.: Images showing the extent of the flooding experienced in Coverack on 18<sup>th</sup> July 2017.



Figure 1.8.: The local watercourse surrounding Coverack. Figure obtained from (Environment Agency and Cornwall Council, 2018) which conducted a wider study on the specific causes of the flooding.

### 1.3. Thesis Motivation and Aims

“Sustainable development” refers to the holistic approach and processes that are the means to an end in developing sustainable practices (Shaker, 2015). The “three pillars of sustainability”, illustrated in Figure 1.1 (page 34), refers to the social, environmental and economic needs of a society. Policies which promote all three of these domains may be seen as “sustainable”. A “green economy” sets a policy course that minimises environmental degradation but also meets the socio-economic needs of the present whilst being mindful to the needs of future generations (Courant et al., 1928). “Natural capital” and the concept of “Ecosystem Services” provide a tangible framework to derive metrics that monitor how sustainable proposed policies are.

The wider aim of this thesis is to explore how computational tools can be utilised in the management of natural capital. A holistic computational tool to manage natural capital would give rise to the means of monitoring the sustainability impact proposed policies could have on a given region. Typically those who apply environmental modelling tools for scenario prediction purposes have had many years within their chosen discipline to build their expertise. Policy planners have not had an opportunity to build up this experience to expertly apply models with a full knowledge of its underlying structure and potential pitfalls. A “front-end dashboard” such as “MyFM” discussed in Section 1.1.6 has the potential to democratise access to the most cutting edge modelling techniques. Through a front facing UI, policy planners could test their policy proposals through a “plug and play” feature implemented in it. On the “back-end” of the computational tool would be the most up-to-date environmental models ready to calculate and test a planner’s proposals.

One example of a proposal for sustainable development is Cornwall Council’s “Environmental Growth Strategy” (Section 1.1.5). Within it is an economic transition which decreases reliance on carbon based economic activities. It defines four “ambitions” to promote sustainable growth which have actionable “target outcomes”. Natural assets provide ecosystem services. These services can be quantified to define metrics to aid in the progress monitoring of the target outcomes within the EGS.

Target outcome 4 (Section 1.1.5.1) specifically outlines the Council’s need for an environmental management system to support environmental growth. This thesis aims to catalyse the construction of this environmental management system. Natural capital management is a complex task in its own right. A broader aim of the thesis is to consider how domain-centric language from the “facilities management” industry can be applied to the management of natural capital. The concept of ecosystem services has many high-level parallels with the facilities management industry. For example, the segregation of both concepts into four (cultural, provisional, regulating and supporting) and two (hard and soft) categories respectively. “Service Level Agreements” (SLAs) are widely adopted within the facilities management industry. These are written commitments between a service provider and a customer. SLAs utilise agreed upon metrics which provide clarity to the parties involved and allow them to determine whether a particular agreed upon service has been met (Wieder et al., 2011). This SLA framework could be adopted by

Cornwall Council in the environmental management system to measure the progress of implementation of various schemes and goals within the EGS.

The macro and meso aims of the thesis, illustrating the need for a holistic computational tool to manage natural capital, are given above. The broad and complex nature of these aims demonstrates the opportunity that exists to positively impact and influence the sustainable development framework practices currently in place. To begin achieving this broader objective, one can select a vast array of environmental modelling frameworks to begin constructing the “back-end” of the computational tool. This thesis aims to begin to fulfil the broader objective by focusing on the construction of a hydrological modelling tool that can aid in the construction of new housing development while mitigating any possibly adverse flooding impacts. The motivation for this micro objective, which fits into the broader aims, is provided in the final paragraphs of this section as well as Section 1.3.1. Additional computational components that can help in the development of the wider computational tool, and how they may be linked with this hydrological modelling component, are outlined in Section 8.4 (page 298).

Within the EGS is the need for over 50,000 new homes in Cornwall by 2030. The construction of these homes will severely inhibit the hydrological properties of the river basins which aid flood mitigation. A holistic policy assessment metric within a front-end dashboard would go some way to help decision makers assess the impact and functionality of natural assets. Hydrological modelling is a well-established research field with numerous successful case studies that have enhanced our understanding and ability to plan for flooding disasters. The final aim of this thesis is to present how one can holistically approach flood management through the adoption of a computational tool described above. The Coverack flooding case study (Section 1.2) is an ideal event to showcase this. The thesis objectives and specific research questions are given in Section 1.3.1 below.

It is envisaged that this thesis may be templated to investigate other modelling questions in a natural capital context. For example, Bird diversity and reproductive success in a created wetland (Kačergyè et al., 2021) or the impact of pesticide use on the population of bees (Kleczkowski et al., 2017). The investigation on the application hydrological modelling in a natural capital context begins the striving *“Towards a computational tool for the management of natural capital”*.

### 1.3.1. Thesis Objectives and Research Questions

The aim of this thesis is to explore how a computational tool can be utilised in the management of natural capital. Specifically, how can a hydrological modelling tool be applied in a holistic tool to aid in the policy planning and land-use management in a natural capital context. Three research objectives were defined to achieve the thesis aim. The first objective will develop a hydrological model that can be applied to land-use policy planning scenarios. Research objective 2 will analyse the model performance to determine the most appropriate model parameterisation for the Coverack flood event case study. The final objective will aim to replicate the Coverack flooding event and investigate land-use

scenarios from the “policy planner’s” perspective, and what mitigation measures could be put in place to reduce the flooding risk. It will also introduce how language from the “facilities management” industry can be translated to the natural capital approach to aid policy decision making. These three objectives are broken into specific research questions that are listed below. The chapters that answer these questions are provided in brackets. These objectives were chosen due for them being a computationally interesting problem. They also allow demonstration of hydrological modelling in a novel context and begin developing *towards a computational tool for the management of natural capital*.

RO 1: Modelling. To investigate current hydrological modelling techniques and how they can be applied in the context of land-use management and flood modelling.

RQ 1: What constitutes a hydrological model? (Chapter 2).

RQ 2: What models and techniques exist within the literature and what context are they applied in? (Chapters 2 and 3).

RQ 3: What modelling techniques will be adopted for the hydrological model constructed in this work? (Chapters 2, 3 and 4).

RO 2: Analysis. To investigate, understand and determine the most appropriate model parameters in order to successfully apply the hydrological model in a land-use and flood risk policy context.

RQ 4: How are models validated, verified and calibrated? (Chapters 2 and 4.)

RQ 5: What are the key considerations when deciding between model resolutions? (Chapters 4, 5 and 6)

RQ 6: How does model performance compare between differing model resolutions? (Chapters 5 and 6)

RO 3: A policy planner’s perspective. Taking on the role of a council planner, suggest potential mitigation measures to alter the Coverack watershed’s hydrological properties in order to gain an understanding of how successful these interventions could be.

RQ 7: How is flooding risk assessed? (Chapter 7)

RQ 8: How do mitigation measure proposals from land-use policy affect flood management? (Chapter 7)

---

## 1.4. Thesis Structure

This thesis is structured into four constituent parts. Part I contains the first three chapters: this introduction; a literature review in Chapter 2; and the mathematical background which underpins the work within this thesis in Chapter 3. This introduction motivates this work presented in this thesis. Chapter 2 begins by outlining the six key components which make up a hydrological model. Three of these components will contain a table that outlines the key methodologies and tools utilised within their respective components. These three components will comprise the hydrological model constructed in this work. The chapter continues by describing the computational mesh types available to hydrological models. It will then dive into what constitutes a semi-distributed and fully-distributed hydrological model. The literature gap being filled by this thesis is described and is then followed up by an explanation of the modelling approach that is taken within this work. Chapter 3 will outline the underlying methodology that is used in the hydrological model constructed in Chapter 4. It begins with an overview of what the Riemann problem entails through the prism of the linear advection equation. It expands to its linear and multi-variate cases to derive more in-depth knowledge. The linear advection equation is again used to review Godunov’s numerical method before defining a local Riemann problem that can be solved with this numerical method. This method is expanded to derive the two-dimensional Godunov finite volume method which is the numerical stencil applied within the hydrological model. An overview of Total Variation Diminishing methods is discussed. This chapter concludes with an exploration of point infiltration modelling from first principles and the theory of the Green-Ampt infiltration model and the SCS method.

Part II begins with an outline of the mathematical hydrological model that has been constructed in Chapter 4. First the computational domain is defined. A justification of the methods adopted to represent the surface routing, unsaturated zone and interception components of the model are given, along with a detailed description of how they will be applied. A discussion of how one could calibrate the model and the model’s limitations and potential future work expansions finishes the chapter. Chapter 5 is the concluding chapter in this part of the thesis. It provides an analysis of the model performance between the 20m and 50m model resolution variants, using pre-defined initial conditions. It begins by defining the sampled computational meshes and outlining the common model inputs and parameters. An overview of the local terrain and land-use spatial distribution of the north-eastern sampled mesh is then given before a comparison in model performance between the two model variants considered. This analysis is then repeated for a second sampled domain in the north-central region of the wider computational domain. For both analysis regions, patches have been isolated to highlight the key behaviours.

Part III of this work begins with Chapter 6. This repeats the analysis done in Chapter 5, but non-uniform model inputs are considered which are more “storm-like”. The chapter begins with the construction of a fictitious “storm”. Two scenarios are then reviewed where this storm is applied to different regions of the computational domain. The chapter concludes with a justification of using the 20m model variant over the 50m model variant for Chapter 7. Specific modelling simulations are then considered in Chapter 7 using the

work and understanding attained from Chapters 5 and 6. An overview of the flooding event that took place in Coverack is given in Section 7.2. To aid analysis in the modelling scenarios, the wider computational domain is split into five sub-regions in Section 7.3. Section 7.4 provides additional context to the modelling simulation work and justifies the seven scenarios that are defined in Section 7.5. The analysis for these scenarios is conducted on a sub-region basis in Section 7.6. A discussion of this work then follows in Section 7.7.

Part IV concludes this thesis. Chapter 8 synthesises the work and knowledge attained within this thesis. It begins with an overview of the thesis structure in Section 8.1. A summary of the content in each chapter is given in Section 8.2. Section 8.3 outlines the key research contributions this work has provided. Section 8.4 concludes the chapter with an overview of where this work can be improved and expanded upon.



## 2. A Literature Review on Hydrological Modelling

### 2.1. Introduction

Chapter 1 introduced the broad underlying themes which underpin this thesis. Specifically, humankind's need for equitable and sustainable use of finite resources to reach humanities' material, cultural and fundamental necessities to sustain life. One way of meeting this aim is to set out policies which mitigate and/or decrease environmental and ecological decline while promoting economic growth (Sections 1.1.1 and 1.1.2). The finite global stock of natural resources that humanity uses for its benefits was described by the umbrella phrase *Natural Capital* (Section 1.1.3). The **Ecosystem Services concept** (Section 1.1.4) provided a useful theoretical framework to analyse how humans benefit from its natural resources. Cornwall Council's *Environmental Growth Strategy* (Section 1.1.5) is a comprehensive policy programme which looks to transition to a low-carbon green economy whilst meeting its social, economic and environmental responsibilities. One such responsibility is flood risk management considerations. Within its strategy the council has proposed the construction of 52,500 homes by 2030. In order to consider the probable impact of such developments, the council identified a need for "*an environmental management system that supports environmental growth*" (Section 1.1.5.1), known as "Target outcome 4" in its strategy. A building asset management system **Focal365** was developed by NJW Ltd. to aid their clients in managing their building assets (Section 1.1.6). Their work exists in the *Facilities Management* industry. *Service Level Agreements* are written commitments between a service provider and client. It is the parallel between facilities management and ecosystem services and the potential of applying the concepts and learnings from facilities management which motivates this work. One such parallel is between a Service Level Agreement and target outcome 4. The need for over 50,000 homes by 2030 will severely impact the local hydrological characteristics and functionality and natural assets. In turn this will increase the potential for flooding. A hydrological modelling and flooding impact computational tool which links with a management system could go some way in fulfilling one of Cornwall Council's ambitions. In order to assess the suitability of the computational tool, Coverack in Cornwall (Section 1.2) is a case study within this work due to its recent flood event.

This chapter will review the literature which underpins hydrological modelling. First the individual components of the modelling theory are presented (Section 2.2). Specifically the Interception (2.2.1), Unsaturated Zone (2.2.2), Surface Runoff and Routing (2.2.3),

Snowmelt (2.2.4), Evapotranspiration (2.2.5) and Saturated Zone (2.2.6) components. The first three components will contain a Table outlining the key methodologies and tools present within the literature. These components will comprise the hydrological model constructed in this work. This will be justified in Section 2.7. A summary of computational meshes is given in Section 2.3. An overview of what semi-distributed (Section 2.4) and fully-distributed modelling (Section 2.5) entails is given with specific model summaries presented within each respective section. Section 2.6 will provide the literature gap that this thesis intends to fill. Finally a justification for the modelling approach taken in this work is provided in Section 2.7 using the component templates from Section 2.2 and in the context provided from Chapter 1.

## 2.2. Modelling concepts of hydrological processes

Modelling hydrological systems from first principles may be conducted with one of two methods: 1. Use a finite difference approximation of the partial differential equations which capture the characteristics associated with the mass, momentum and energy balance equations or; 2. Use of empirical equations (Abbott et al., 1986b). For hydrological modelling within a floodplain one must consider the principle components associated with the land-phase of the hydrological cycle namely interception, snowmelt, evapotranspiration, sub-surface runoff, groundwater flow, surface runoff and channel routing.

Figure 2.1 below is an illustration of the physically based and fully distributed MIKE SHE hydrological model (Refsgaard and Storm, 1995). Within this chapter, a selection of physically based hydrological models are reviewed. The differing modelling approaches for each model are highlighted and discussed. An overview of each model's acronym, definition, main references and general computational approach are listed in Tables 2.4 and 2.5 on pages 80 and 82 respectively.

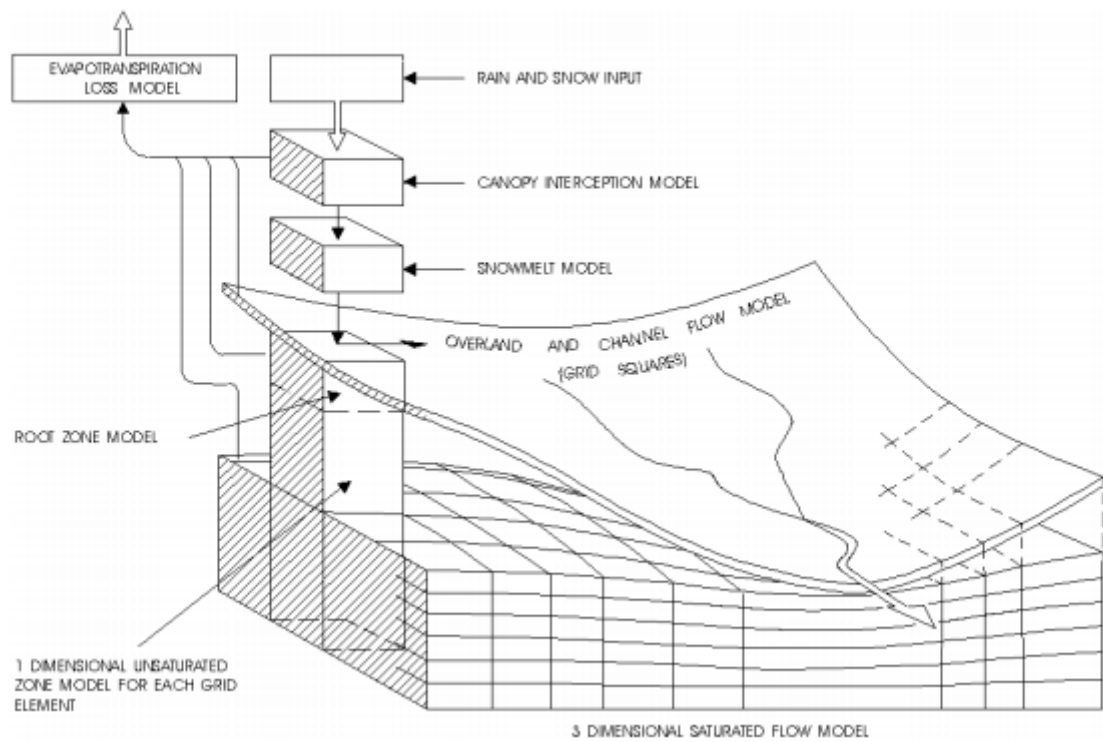


Figure 2.1.: An illustrative diagram highlighting how each physical process models interrelate within the greater hydrological model. Obtained from Refsgaard and Storm (1995).

### 2.2.1. Interception Component

Gross rainfall which descends onto local vegetation within a river's floodplain is temporarily stored on their leaves, forming a thin layer over its surface. It is then redistributed either through evaporation into the atmosphere (interception loss) or finds its way to the ground in one of two ways. The first occurs when the weight of the water volume exceeds the surface tension on its host leaf. Hence under gravity, the water forms into a droplet to fall to the ground, provided it is not intercepted by another, more sheltered, leaf below. The second route towards the ground involves water flowing down the branches and stems of the vegetation, known as stemflow. This redistribution of gross rainfall by vegetation is the concept known as *interception*. *Throughfall*, the occurrence of rainfall directly reaching the ground surface without being intercepted by vegetative surfaces (David et al., 2005), and stemflow, are aggregated together to define *net rainfall*. The key methodologies that relate to the interception component of a hydrological model are listed in Table 2.1 beginning on page 54.

The hydrological process of rainfall interception has a major influence on the management of water resources as well as climate change (Arnell, 2002), particularly in forested areas. Forest regions experience a total annual interception loss of at least 25% of total gross rainfall (Dingman, 2002). This is due to the phenomenon of tall vegetative plants having a higher aerodynamic conductance and thus a much greater evaporation rate (Muzylo et al., 2009).

The earliest attempt of modelling canopy interception came from Ibbitt (1971), used in the TOPNET model. Here, the proportion of precipitation throughfall,  $f(C)$ , is quantified as

$$f(C) = \frac{C}{S} \left( 2 - \frac{C}{S} \right). \quad (2.1)$$

$C$  is the total rainfall intercepted by the canopy.  $S$  is the maximum interception possible (i.e. storage capacity of the canopy). One can then determine the rate of change of interception storage with

$$\frac{dC}{dt} = P(1 - f(C)) - E_{int}C_r f(C). \quad (2.2)$$

$E_{int}$  is the evaporation rate of intercepted water,  $P$  is the total precipitation rate (mm/day) and  $C_r$  is an adjustment factor for intercepted water evaporation.

Rutter et al. (1971) developed the Rutter interception model. Within the hydrological research community, this model is considered the standard reference for rainfall interception (Noilhan and Mahfouf, 1996). A multitude of physically based models such as SHE, DPHMRS, ISBA, MISBA, tRIBS and IHDM have used this model in their development process. Mathematically, the Rutter interception model is

$$\frac{dC}{dt} = (1 - \delta) - E_{int} - k_1 \exp(b(C - S)); \quad \text{where } 0 \leq C \leq S. \quad (2.3)$$

The model parameters from  $C$ ,  $S$  and  $E_{int}$  are as in Equations (2.1) and (2.2).  $\delta$  is a throughfall coefficient.  $\delta$  and the canopy storage capacity  $S$  are related to the “leaf area index” ( $L_{AI}$ ) of the canopy. Finally,  $k_1$  and  $b$  are drainage parameters.

Kristensen and Jensen (1975) expanded the Rutter model by computing the intercepted water capacity and hence the canopy storage. This was then applied to the MIKE SHE model.  $S_{int}$  is the canopy storage capacity parameter and  $L_{AI}$  represents the leaf area index.

$$S = S_{int}L_{AI}. \quad (2.4)$$

The interception component within the LISTFLOOD model is estimated with

$$C = S \left( 1 - \exp \left\{ -\frac{k_2 P \Delta t}{S} \right\} \right), \quad (2.5)$$

where  $k_2$  parametrises vegetation density. This method follows the simple approach proposed by Merriam (1960) and Aston (1979) (Van Der Knijff et al., 2010). Kouwen (1988) utilises the Horton equation (Horton, 1919). This empirical model has also been reproduced by Gash and Shuttleworth (2007). Used in the WATFLOOD/SPL9 model, interception depth is calculated as

$$C = a_w + b_w \cdot P^{n_w}. \quad (2.6)$$

Here,  $a_w$ ,  $b_w$  and  $n_w$  are model parameters which are dependent on canopy vegetation. Another model for rainfall interception was developed by Deardorff (1978). This was applied within the hydrological models ISBA (Noilhan and Planton, 1989; Noilhan and Mahfouf, 1996) and MISBA (Kerkhoven and Gan, 2006).

$$\frac{dC}{dt} = v_{eg} \cdot P - (E_v - E_{int}) - R_r; \quad \text{where } C \ll 0.2 \cdot v_{eg} \cdot L_{AI}. \quad (2.7)$$

Here,  $v_{eg}$  is the fraction of vegetation present.  $E_v$  represents the evaporation from vegetation and  $R_r$  is the surface runoff of intercepted water. To conclude, the PAWS model applies a bucket model to measure canopy interception (Shen and Phanikumar, 2010)

$$\frac{dC}{dt} = \min \left( \frac{S - C}{\Delta t}, P \right). \quad (2.8)$$

Table 2.1.: Key literature methods and tools related to the interception component of a hydrological model.

Leading Reference(s)	Model / Method	Summary	Pros & Cons
Ibbitt (1971); Bandaragoda et al. (2004)	Canopy interception component within TOPNET	<ul style="list-style-type: none"> <li>• TOPNET is a networked version of TOPMODEL that was developed as part of the Distributed Model Intercomparison Project (DMIP) (Smith, 2002).</li> <li>• Each river network reach was topographically derived with spatially distributed sub-basins using the US National Elevation Dataset Digital Elevation Model (DEM).</li> <li>• Rainfall inputs were provided by NEXRAD (Next Generation Weather Radar system).</li> <li>• A wetness index distribution was derived from DEM.</li> <li>• Initial model parameters were estimated via look-up tables based on soils from STATSGO (soil maps for the US State Soil Geographic database) and vegetation (from the 1-km Advanced Very High Resolution Radiometer (AVHRR)).</li> <li>• Model parameters are calibrated using a shuffled complex evolution algorithm (Duan et al., 1993). This looked to minimise the mean square error between the observed and modelled hourly streamflows.</li> <li>• <b>Case Study:</b> The TOPNET model (and the canopy interception component within it) submitted results as part of DMIP. Uncalibrated and calibrated results were presented for five basins: Blue River; Elk River; Baron Fork; Illinois at Watts; and Illinois at Tahlequah</li> </ul>	<ul style="list-style-type: none"> <li>+ This method is much simpler than standard interception models (e.g. those presented in Rutter et al. (1971)).</li> <li>+ This method only requires two parameters: Canopy interception capacity (driven by hourly precipitation and potential evapotranspiration inputs) and an interception evaporation adjustment factor.</li> </ul>

Leading Reference(s)	Model / Method	Summary	Pros & Cons
Rutter et al. (1971)	Predictive model of interception loss in pine canopies.	<ul style="list-style-type: none"> <li>• Total interception loss is calculated as an integral of evaporation rate in time. The water balance equations were used to measure interception loss in a storm. The model assumed the canopy to have capacity to store water on its surface which emptied due to evaporation and drainage.</li> <li>• Two of the model parameters, throughfall <math>p</math> and the minimum quantity of water required to wet all canopy surfaces <math>S</math> would be expected to vary depending on the amount and disposition of the foliage representing the canopy.</li> <li>• The other model parameter, the drainage coefficient <math>b</math>, is dependent on the leaf characteristics and susceptibility to getting wet.</li> <li>• <b>Case Study:</b> A 40 year old plantation spanning 600 trees/ha with mean height of 20m in southeast England was used to test the predictive ability of the interception loss model.</li> <li>• For 8 months, gross rainfall and throughfall were noted in 5 minute time periods along with mean canopy temperature, temperature above the canopy and humidity above the canopy.</li> <li>• A random storm selection was used to analyse and construct a model of the interception process. The storm characteristics used can be found in Table I in Rutter et al. (1971).</li> <li>• Over the following 18 months, rainfall and throughfall were recorded daily. The model agreed well with observed monthly interception losses in a stand of Corsican pine over this period.</li> <li>• Additional details on the background science and modelling may be found in Zinke (1967); Rutter et al. (1975) and Rutter and Morton (1977).</li> </ul>	<ul style="list-style-type: none"> <li>- Model assumed canopy parameters were constant but study acknowledged that it may vary.</li> </ul>

Leading Reference(s)	Model / Method	Summary	Pros & Cons
<p>Merriam (1960); Aston (1979); Kouwen (1988)</p>	<p>Interception component within LISFLOOD model</p>	<ul style="list-style-type: none"> <li>• <b>Case Study:</b> LISFLOOD model applied to Elbe River, the fourth largest in western and central Europe.</li> <li>• Input data at 1-km resolution was used. Data from the Czech Meteorological Institute and German federal meteorological authorities were used to generate an interpolated meteorological input grid for between 1994 and 2002.</li> <li>• Model assumes interception cannot exceed interception storage capacity (the difference between the maximum interception and water accumulated through interception).</li> <li>• An automatic calibration algorithm combining an adaptive partition-based search and downhill simplex method (Szabó, 2006) was used in a semi-distributed manner for the Dresden gauge (which is representative of most of the central Elbe region).</li> <li>• Model fitness was measured using the root mean square error and Nash and Sutcliffe efficiency (Nash and Sutcliffe, 1970).</li> </ul>	<ul style="list-style-type: none"> <li>- A reduced model performance was identified in far downstream channels that are heavily regulated.</li> <li>- Simulation of man-made structures in the model was found to be difficult to do.</li> <li>- The model was only performed in west- and central-European catchments and hadn't been tested in drier (Mediterranean conditions) at the time.</li> </ul>
<p>Deardorff (1978)</p>	<p>A ground surface moisture method</p>	<ul style="list-style-type: none"> <li>• This method was templated against an efficient time-dependent equation for predicting ground surface temperature based on the 'force restore' method from Bhumralkar (1975) and Blackadar (1976).</li> <li>• Specific humidity at the surface is related to the ground surface moisture content rather than the bulk soil moisture content. Hence evaporation in the model "dried" out the ground surface and reduced the evaporation rate from bare soil compared to evapotranspiration.</li> <li>• This paper developed a vegetation layer for the method and tested against observations presented in Penman and Long (1960).</li> <li>• The method allows surface to become moist quickly during rainfall or drier than bulk soil while evaporation occurs.</li> </ul>	<ul style="list-style-type: none"> <li>- Method is not relevant unless the main influences of a vegetation layer are included.</li> </ul>



Leading Reference(s)	Model / Method	Summary	Pros & Cons
Shen and Phanikumar (2010)	Interception component within the Process-based Adaptive Watershed Simulator (PAWS)	<ul style="list-style-type: none"> <li>• A 1D Richards Equation (coupled with a 3D saturated groundwater flow equation) is applied when the model is run under 'normal' conditions.</li> <li>• When heavy rainfall periods on dry surfaces are simulated, the Green-Ampt equation is applied to avoid significant numerical errors in the vertical discretisation of Richards equation.</li> <li>• <b>Case Study:</b> PAWS was applied to the Red Cedar River Watershed (Grand River Watershed, Michigan).</li> <li>• Model utilised a <math>900\text{m} \times 900\text{m}</math> resolution grid. Daily and sub-daily weather data were provided by the National Climatic Data Center (National Climatic Data Center, 2010) and the Michigan Automated Weather Network (Michigan Automated Weather Network, 2010). Elevation of the land was provided via the US National Elevation Dataset (30m resolution).</li> <li>• Eight major rivers from the National Hydrography Dataset were manually selected as the modelled river network. River bed elevations obtained by taking the difference between bank-full river depth and local elevation.</li> <li>• Flow records were retrieved from US gauge 04112500, East Lansing (September 2002 - December 2005) to calibrate the model. Values prior to September 2002 were used for model verification.</li> </ul>	<ul style="list-style-type: none"> <li>- Thin water features (streams, creeks etc.) were difficult to capture for DEM data at 90m resolution.</li> <li>- The model assumes that soil moisture does not travel laterally in the unsaturated zone. This will lead to model deterioration for areas with perched water table dynamics.</li> </ul>

### 2.2.2. Unsaturated Zone Component

Should water droplets avoid being intercepted and evaporated then it will infiltrate the soil and reach the *unsaturated zone*. Typically, this region contains a heterogeneous soil profile extending from the Earth's surface to the groundwater table (Refsgaard and Storm, 1995). Cyclic fluctuations of soil moisture content are regularly observed which is consistent with the temporary storage of precipitation.

Common practice within physically based modelling is to sub-divide the zone into two layers. The *root zone layer* refers to the layer that is closest to the Earth's surface. Evapotranspiration, infiltration and precipitation have a large influence in the high frequency oscillations of soil moisture content characteristic to this region. The lower layer, known as the *transmission zone* closest to the groundwater table, observes much slower soil moisture movement as it percolates into the saturated zone below (Refsgaard and Storm, 1995; Biftu and Gan, 2004). Within the unsaturated zone, flow is assumed to slowly occur in the vertical plane due to the dominance of the gravity in the percolation process. The key methodologies that relate to the unsaturated zone component of a hydrological model are listed in Table 2.2 beginning on page 60.

A popular method to calculate soil moisture content is to first determine the infiltration at a given timestep and utilise a water balance equation to find the soil moisture content and total percolation into the saturation zone. Three types of infiltration modelling methods exist. The first is an empirical method developed by Horton (1940). For pre-storm initial conditions assume the infiltration capacity is  $f_3$ . As a storm event occurs, infiltration begins and the soil capacity follows an exponential decay by multiplicative factor  $k$  toward a steady state capacity  $f_4$  (Tarboton, 2003):

$$f_c(t) = f_4 + (f_3 - f_4)e^{-kt}. \quad (2.9)$$

A second infiltration method involves mathematical models based on physical processes. A common example is Richard's equation. This model looks at one-dimensional flow in the vertical plane. It combines Darcy's law (Whitaker, 1986) and the conservation of mass. The effect of gravity, soil suction and evapotranspiration are all included in this model (Refsgaard and Storm, 1995).

$$C \frac{\partial \psi}{\partial t} = \frac{\partial}{\partial z} \left( K(\theta, z) \frac{\partial \psi}{\partial z} \right) + \frac{\partial K}{\partial z} - S(z). \quad (2.10)$$

Here  $\psi$  represents soil moisture tension,  $t$  and  $z$  are time and the vertical space coordinate respectively.  $K(\theta, z)$  is a hydraulic conductivity parameter,  $C$  is a soil water capacity parameter  $\left( \frac{\partial \theta}{\partial \psi} \right)$ ,  $\theta$  the volumetric soil moisture content and  $S(z)$  a source/sink term from root extraction and soil evaporation. SHE and MIKE SHE are examples of hydrological models which apply this approach for the unsaturated zone components.

An approximation of the physically based infiltration model is the third category. One such approximation model is the ***Green-Ampt*** model (Green and Ampt, 1911).

$$f = K_{\text{sat}} \left( 1 + \frac{|\psi_f| \Delta\theta}{F} \right). \quad (2.11)$$

$K_{\text{sat}}$  is the hydraulic conductivity.  $|\psi_f|$  is the wetting front soil suction head.  $\Delta\theta = n - \theta_0$  represents the difference between the saturation and initial moisture content. Finally,  $F$  is the depth of infiltrated water. Hydrological models WATBAL, TOPNET and R.WATER.FEA utilise the Green-Ampt model within their simulations.

Another physically based approximation model is the Philip model (Philip, 1954). This model quantifies rate of infiltration  $f$  as

$$f = \frac{1}{2} S_p t^{-1/2} + K_p. \quad (2.12)$$

A function of soil suction potential the parameter  $S_p$  is known as sorptivity and  $K_p$  is the hydraulic conductivity. This model is applied within the SLURP, DPHMRS and WATFLOOD/SPL9 hydrological models.

Table 2.2.: Key literature methods and tools related to the unsaturated zone component of a hydrological model.

Leading Reference(s)	Model / Method	Summary	Pros & Cons
Green and Ampt (1911)	Green-Ampt model	<ul style="list-style-type: none"> <li>• Green was one of the first to construct an infiltration model from a scientific foundation. The model related three fundamental constants of soil physics: Specific pore size; Permeability to water, and the Capillary coefficient.</li> <li>• The study explicitly stated the interdependence between soil condition and hydraulic properties to the value of soil constants. These values are susceptible to alteration when disturbed (e.g. from ploughing, rolling etc.)</li> <li>• The study noted that absolute permeability should be independent of the fluid in unsaturated conditions. Given a sufficient amount of water to warrant modification of the soil's capillary passages, it could be done in one of two ways: 1. Either the soil moisture restricts the area of the capillaries where air is passing; 2. Or soils such as clay absorbing moisture to restrict the pore size. These findings were found in a previous study (see reference 1 in Green and Ampt (1911); page 6).</li> <li>• Capillary forces assist hydrostatic pressure. Green investigated three cases where water moved up, down and horizontally. Three formulae were deduced from these experiments.</li> <li>• In an attempt to validate the formulae, an experiment was conducted with a glass tube. It was 1 inch in diameter and 30 inches long and uniformly packed with soil leaving 6 inches at the top of the tube with a copper gauze disc and perforated cork at the lower end. A 10cm water layer was placed on top of the soil column and readings were taken during irregular periods over 60 hours. Three soils were used: friable loam; clay soil; and surface sand. The formula for upward water movement could not be validated in this experiment.</li> </ul>	<p>+ One of the first attempts to build a scientific consensus on soil physics and to obtain quantitative parameters needed to model soil drainage.</p> <p>- One could not guarantee the uniformity of soil structure across experiments when filling the tubes with the same soil. The glass tubes were filled as uniformly as possible. However, experimental data used soil that was 'disturbed' and may not be reflective of soil 'in situ' (in a field for example), disarranging the original soil structure when the samples were collected.</p>

Leading Reference(s)	Model / Method	Summary	Pros & Cons
Horton (1919)	Horton Model	<ul style="list-style-type: none"> <li>• The Horton model was constructed empirically via small catchment studies. It is expressed as a function of time, representing potential infiltration when the rainfall rate is unlimited (when rainfall rate is higher than the potential infiltration rate). The model may be applied to permeable or semi-permeable surfaces.</li> <li>• Horton begins by describing the physics of interception and notes several leaves with sketches from various tree species (Horton (1919); page 4, Figure 2).</li> <li>• The experiments conducted here utilised observations from Seckendorff (reference 1 page 5). Where a continuous storm event lasted from June 12<sup>th</sup> to June 15<sup>th</sup> resulting in a cumulative precipitation event of 52.6mm.</li> <li>• Interception loss as a percentage of precipitation was calculated for Oak, Hemlock, Rye, Aspen Elm, Horse Chestnut, Cherry, Maple, Cherry Stem, Pigweed, Clover, Willow, Ash, Basswood, Evergreen and deciduous forests.</li> <li>• A variety of other data sources were also used in the construction of the model. Horton constructed a 'tree-trunk interceptometer' where a funnel plugged into tree trunks transferred water into a tub covered by a lid. This was based on Ebermayer's experiments from a decade earlier (reference 3 in Horton (1919)). Further data from Adlisburg Switzerland (1889-1890) and Haidenhaus (1890) was used to construct the model.</li> </ul>	<ul style="list-style-type: none"> <li>+ A first attempt in constructing a complete and thorough analysis of interception studies on experimental observations.</li> <li>- Results from this paper may not accurately represent rainfall interception by scattered trees and shrubs over a large area due to the limited quantity of measuring devices.</li> </ul>

Leading Reference(s)	Model / Method	Summary	Pros & Cons
Richards (1931)	Richards Equation	<ul style="list-style-type: none"> <li>Richards equation is a non-linear partial differential equation providing a description on water movement within unsaturated soils in space and time between the atmosphere and aquifer. It is based on the Darcy-Buckingham law representing flow in porous media under variable saturated conditions.</li> <li>Construction of the equation requires the soil hydraulic properties - a set of five parameters capturing soil characteristics. The properties consist of water retention curve parameters from van Genuchten (1980). (<math>\alpha, n, m, \theta_s, \theta_r</math>) are inverse of air entry value <math>[L^{-1}]</math>, pore size distribution, <math>m = 1 - n^{-1}</math>, saturated volumetric soil moisture content and residual volumetric soil moisture content respectively (Angulo-Jaramillo et al., 2000; Inoue et al., 2000; Köhne et al., 2006; Fodor et al., 2011; Younes et al., 2017; Kuraz et al., 2022).</li> </ul>	<ul style="list-style-type: none"> <li>- It is computationally expensive and unpredictable (Short et al., 1995; Tocci et al., 1997; Farthing and Ogden, 2017). There is no guarantee that a solver will converge for given set of parameters.</li> <li>- Papers have criticised its emphasis on the role of capillarity (Germann, 2010) and being “over-simplistic” (Gray and Hassanizadeh, 1991)</li> </ul>
Philip (1954)	Physically-based two term infiltration rate model to solve the one-dimensional Richards equation.	<ul style="list-style-type: none"> <li>Philip’s model assumes Darcy’s law is valid for unsaturated soils in the general form where hydraulic conductivity (<math>K_p</math>) is a unique function of soil moisture content <math>\theta</math>.</li> <li>Experimental data from Green and Ampt (1911); Bodman and Colman (1944); Colman and Bodman (1945); Miller (1951) and Miller and Richard (1952) was used to construct the model.</li> <li>Model assumes that the soil conditions and properties are homogeneous. It also assumes that soil moisture content is distributed uniformly as well as constant.</li> <li>Early infiltration stages the first term of the model (<math>\frac{1}{2} S t^{-1/2}</math>) dominates. The hydraulic conductivity parameter gains influence and increases in importance overtime.</li> <li>Philip expanded on the initial model construction and presented discussions on other properties of the model including: The Profile of Infinity (Philip, 1957a); Moisture Profiles and their relation to conducting experiments (Philip, 1957b); Sorptivity and Algebraic Infiltration equations (Philip, 1957c); and Influence of the Initial Moisture Content (Philip, 1957d)</li> </ul>	<ul style="list-style-type: none"> <li>+ Model is easy to solve and more intuitive in comparison with other infiltration models.</li> <li>- Soils within a field are rarely homogeneous.</li> <li>- Philip’s model will not be able to take into account multi-layered soil system.</li> </ul>

### 2.2.3. Surface Runoff and Routing Component

The surface runoff and routing component of a hydrological simulation models three physical processes. These are the accumulation of water which contributes to surface runoff (a.k.a overland flow), the routing of overland flow to the nearest stream or river channel and the routing of channel flow to a river catchment's outlet.

Two physical phenomena can lead to surface runoff. *Dunne runoff* is a name given to runoff generation when the soil underneath is saturated preventing further infiltration, as illustrated in Figure 2.2b. Figure 2.2c demonstrates the second type of runoff known as *Horton runoff*. Runoff here is generated when the precipitation rate is greater than the infiltration capacity of the soil and thus not all water cannot be absorbed into the Earth's surface. The key methodologies that govern surface runoff and routing of a hydrological model are listed in Table 2.3 beginning on page 66.

TOPMODEL and TOPNET convert the topographic wetness index (equation (2.35), Section 2.2.6) into a distribution function. This distribution allows one to observe areas with similar hydrological properties and how each area within a catchment contributes to overland flow. A model's simulation of individual catchment response then depends on the distribution of similar indices as well as the temporal and spatial input sequences of precipitation rate and evaporation loss (Beven et al., 1995, pg. 644).

Surface runoff within the physically based hydrologic models, ISBA, MISBA and LIST-FLOOD behaves similar to a multi-bucket model scheme. These models take into account the sub-grid heterogeneity of soil moisture capacity and assume it follows a Xinanjiang distribution which defines the distribution of bucket sizes. When a bucket is filled, surface runoff commences (Zhao, 1992; Habets et al., 1999; Kerkhoven and Gan, 2006):

$$F(x) = 1 - \left(1 - \frac{x}{x_{max}}\right)^\beta; \quad 0 \ll x \ll x_{max} \quad (2.13)$$

$$\frac{x_{ave}}{x_{max}} = \frac{1}{\beta + 1} \quad (2.14)$$

$F(x)$  represents the cumulative probability distribution of soil moisture capacity  $x$ . This distribution is defined by the maximum soil moisture capacity,  $x_{max}$ , and average soil moisture capacity  $x_{ave}$ .  $\beta$  is an empirical parameter which defines the maximum bucket size (or soil depth) in each grid.

Physically based models SHE and MIKE SHE implement a two-dimensional diffusion wave approximation of the St. Venant equation to model overland flow

$$\frac{\partial h}{\partial t} + \frac{\partial(uh)}{\partial x} + \frac{\partial(vh)}{\partial y} = \mathbf{q}. \quad (2.15)$$

$h(x, y)$  represents the local water depth,  $t$  time,  $u(x, y)$  and  $v(x, y)$  are the flow velocities in the  $x$  and  $y$  directions respectively. Finally,  $\mathbf{q}(x, y, t)$  is the surface runoff at location  $(x, y)$  and time  $t$ .

A kinematic wave model for routing overland flow is applied in some distributed and semi-distributed models such as IHDM, DPHMRS, HRCHM, TOPNET, THALES, MISBA, LISTFLOOD and R.WATER.FEA. This is defined as

$$\frac{\partial q}{\partial t} + c \frac{\partial q}{\partial x} = cR. \quad (2.16)$$

Here,  $q$  is the surface runoff,  $c$  the kinematic wave velocity and  $R$  the excess water content available for runoff following the application of vertical water balance.

Finally, WATFLOOD applies the continuity equation and utilises a storage routing technique.  $I_1$  and  $I_2$  represents inflow to a given area. Similarly  $O_1$  and  $O_2$  represent outflow.  $S_{1,2}$  captures the total storage of a given area and  $\Delta t$  is a routing timestep:

$$\frac{I_1 + I_2}{2} - \frac{O_1 + O_2}{2} = \frac{S_2 - S_1}{\Delta t}. \quad (2.17)$$

Other overland flow methods include: non-linear hydrologic routing and a response function based on the kinematic wave model (Akram et al., 2014). Other channel routing methods includes the one-dimensional diffusion wave equation (Tipler and Mosca, 2003), an approximate solution of the modified diffusion equation known as the Muskingum-Cunge method (Merkel, 2002; Cunge, 1969) and the kinematic wave model (Lighthill and Whitham, 1955).



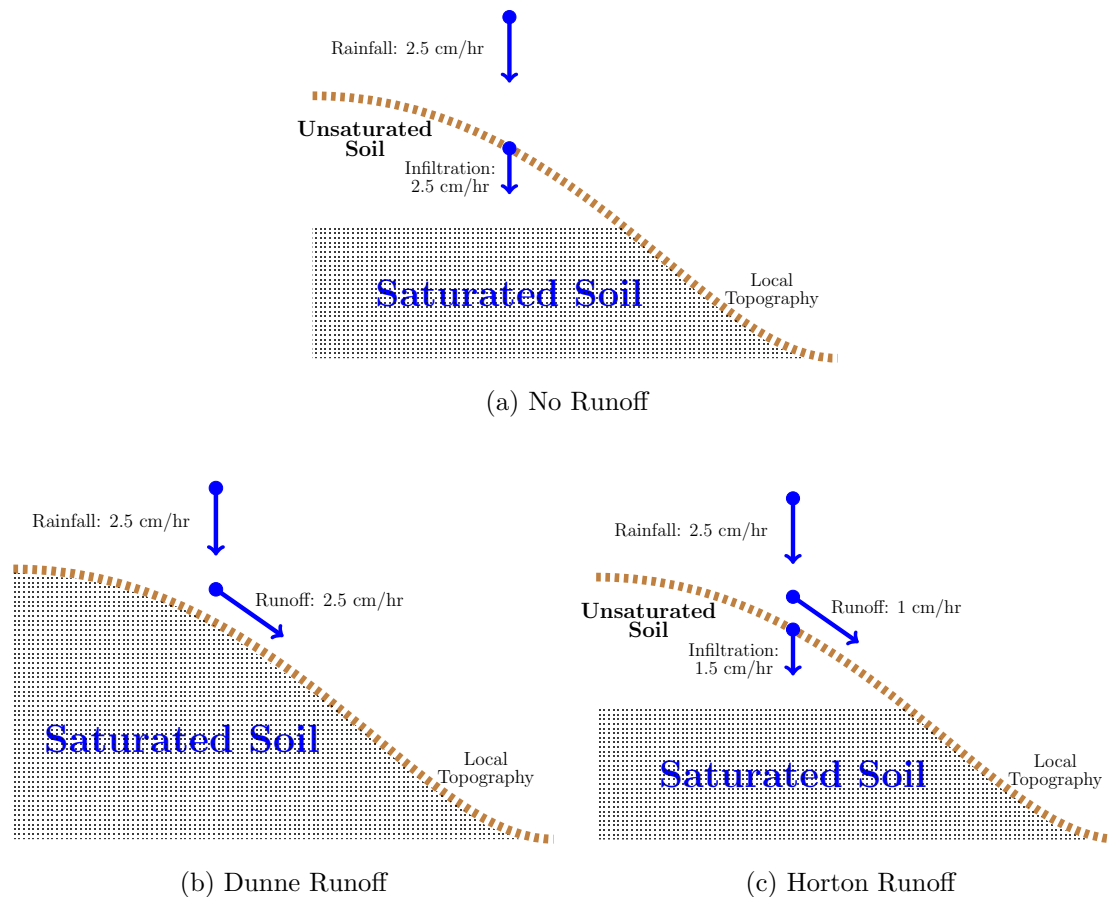


Figure 2.2.: Surface water runoff is generated when the infiltration capacity of the underlying soil cannot keep up with the precipitation input rate. If the precipitation rate is less than or equal to infiltration rate, then no surface runoff occurs (2.2a). If the soil is completely saturated then no infiltration will occur and so the surface runoff rate will equal the precipitation rate (2.2b). If there is capacity to absorb some of the precipitation but the rate of infiltration is lower than the precipitation rate then total surface runoff is the difference between precipitation input rate and infiltration rate (2.2c). Illustrations adapted from Dunne and Leopold (1978).

Table 2.3.: Key literature methods and tools related to the surface runoff and routing component of a hydrological model.

Leading Reference(s)	Model / Method	Summary	Pros & Cons
Zhao (1992); Habels et al. (1999); Kerkhoven and Gan (2006)	Xinanjiang distribution model	<ul style="list-style-type: none"> <li>• Used in ISBA, MISBA and LISFLOOD</li> <li>• Model requires 15 parameters and grouped as: 1. Evapotranspiration parameters; 2. Runoff production parameters; 3. Runoff separation parameters; and 4. Runoff concentration parameters. These are all defined in Zhao (1992, pg. 378)</li> <li>• This model has been validated for hydrological systems within humid and semi-humid regions.</li> <li>• The overall hydrological sub-basin is segmented into a set of sub-basins. An outflow hydrograph for each sub-basin is determined before being combined to determine the outflow of the whole basin Zhao (1992, Fig. 1; pg 372).</li> <li>• Runoff is generated when unsaturated zone reaches field capacity and no further rainfall can infiltrate into the soil. Runoff equals rainfall excess without further loss.</li> <li>• Horton's concept of a constant infiltration rate when field capacity was reached did not match with observed behaviour. A third component, "interflow" was introduced to model to represent variability of infiltration rate.</li> <li>• A point runoff production output is determined on depletion of tension water storage at that point. A tension water capacity curve gives a non-uniform distribution of tension water capacity at each sub-basin Zhao (1992, Fig. 2; pg 374).</li> <li>• Runoff components are separated into three parts: surface runoff, ground water contribution and contribution to interflow.</li> <li>• Classification of the four parameter groups maps one-to-one to different characteristics in optimisation. Parameters within the same group are mutually dependent. Runoff concentration parameters (group 4) have little influence on parameter optimisation in group 3 etc. Hence, group 1 are first to be optimised, then group 2 etc.</li> <li>• Three objective functions are used in the optimisation process: Water balance error equation; Relative absolute error; and Absolute logarithmic error.</li> <li>- Determination of model parameters is extremely difficult due to output sensitivity and dependence of some parameter values on other parameter values.</li> </ul>	<ul style="list-style-type: none"> <li>+ The model has been successfully applied to very large agricultural, pastoral and forest lands of China. It has also performed well on the Bird Creek watershed (an arid region) within the U.S.</li> </ul>

Leading Reference(s)	Model / Method	Summary	Pros & Cons
Abbott et al. (1986a,b)	2D-diffusion wave equation (SHE/MIKE SHE models)	<ul style="list-style-type: none"> <li>• A 2D-diffusion wave solution governs the overland flow component of SHE. It is based on approximation of the St. Venant equations of continuity and momentum (neglecting inertia terms)</li> <li>• The Stricker/Manning resistance coefficients for friction slopes relates velocities to flow depths. The relations are combined and solved with the continuity equation in an explicit finite difference scheme from Preissmann and Zaoui (1979).</li> <li>• Water surface depth that is available as runoff is determined from net rainfall and evaporation rates supplied by interception and evapotranspiration components.</li> <li>• Main model parameters of overland flow component are the Strickler coefficients for friction slopes and the coefficients of discharge for weir formulae. The input data that is needed includes the flow or water level specified at the domain boundaries, man-controlled diversions and discharges and the topography of overland flow plan and channel cross-sections.</li> <li>• Since parameters are based on physical characteristics they do not need to be calibrated in principle. However, a certain amount of calibration is likely to be required as data is obtained on a point scale and may not be representative of the grid scale on which the model parameters are applied.</li> <li>• Vo and Gourbesville (2016) applied the MIKE SHE model to the Vu Gia Thu Bon catchment in Vietnam. They utilised daily data from seven stations for calibration (using data between 1991-2000) and validation (using data between 2001-2010) of the model.</li> <li>• Comparison between observed and simulated discharges saw a Nash-Sutcliffe score of 0.82 and correlation coefficient score of 0.92. Similarly water level comparisons were 0.77 (Nash-Sutcliffe) and 0.89 (correlation coefficient).</li> <li>• A sensitivity ratio was employed to determine the level of influence of each parameter towards river flow and quantify the dependent rate of runoff on change of the parameters (EPA, 2001; Maidment and Hoogerwerf, 2002). Parameter sensitivity analysis was derived from the discharge response at Nong Son and Thanh My stations.</li> <li>• Model assessment metrics included the root mean square error, correlation coefficient and Nash-Sutcliffe coefficient.</li> </ul>	<ul style="list-style-type: none"> <li>+ The 2D diffusion wave equation can incorporate complex topography which influences flow routing.</li> <li>- Calibration of the model with multiple components with mutually dependent parameters is a complex task.</li> </ul>

Leading Reference(s)	Model / Method	Summary	Pros & Cons
Cunge (1969); Merkel (2002)	Muskingum-Cunge Method	<ul style="list-style-type: none"> <li>• The original Muskingum flood wave propagation method assumes that the stage/discharge (H/Q) relationship is one-to-one (Chow, 1959). This assumption lead to a first order differential equation with an analytical solution that does not allow wave damping.</li> <li>• This method gives wave attenuation along a stream. The contradiction of wave attenuation without wave damping was explained from the method being directly derived from finite difference scheme which replaced the partial differential equations in the Saint-Venant equations.</li> <li>• This introduced an artificial attenuation rate of flow by modifying the celerity of resulting waves, an error in the original analytical solution of the governing equations. One is required to determine an artificial damping parameter through trail-and-error calibration.</li> <li>• Parameter coefficients determined this way have no physical basis from the governing equations.</li> <li>• Cunge built on Muskingum method and determined routing parameters based on physical-numerical principles.</li> <li>• The approach by Muskingum was seen as an approximation to a parabolic differential equation. This differential equation is derived from the Saint-Venant equation by neglecting inertia terms in the dynamic equation.</li> <li>• This enables a physical river characteristic term in the form of a diffusion coefficient. Then the analytical solution does not have to assume a one-to-one relationship between stage and discharge. This enables flood wave attenuation terms to be determined. Model parameters may then be determined from physical river characteristics.</li> </ul>	<ul style="list-style-type: none"> <li>+ This method can apply calculations quickly and conveniently on any computational tool.</li> <li>+ Muskingum-Cunge method is strongly stable with excellent convergence for values of Courant number <math>\approx 1</math> (Ponce, 1986).</li> <li>- Method assumes that geometric and hydraulic channel data is representative of the hydrological system under consideration.</li> </ul>

Leading Reference(s)	Model / Method	Summary	Pros & Cons
Lighthill and Whitham (1955)	Kinematic wave model	<ul style="list-style-type: none"> <li>• Kinematic waves describe and define motion without considering the forces giving rise to the motion. Kinematic-wave theory assumes terms in equation of motion are insignificant. It is primarily based on the continuity equation and approximates the dynamic equation.</li> <li>• Kinematic wave model is applicable to overland flow where lateral inflow is continuously added and a large part of the flow.</li> <li>• Shallow water waves are assumed to be long and flat. This implies that the friction slope is equal to the bed slope. Through the equation of motion, steady uniform flow, steady non-uniform flow and unsteady non-uniform flow are insignificant as noted in Miller (1984, Equation 37; page 6).</li> <li>• The friction slope is defined with a uniform flow formula. Discharge is described from a general power relationship <math>Q = \alpha A^m</math>, where <math>\alpha</math> and <math>m</math> are coefficients to be determined. This is solved simultaneously with the unsteady continuity equation with initial and boundary conditions imposed.</li> <li>• Kinematic waves only propagate downstream (unlike dynamic waves which propagate both up- and downstream at a characteristic speed <math>c</math>) (Lighthill and Whitham, 1955; Henderson, 1963, 1966).</li> <li>• Assumptions: 1. <b>Pressure distribution is hydrostatic.</b> This implies that vertical components are negligible. Pressure departs from hydrostatic when bed slope becomes steep (Chow, 1959, pages 32-33). For uniform flow in steep channels, pressure at any depth must be corrected by factor <math>\cos^2 \theta</math>. This provides an indication of the magnitude of errors involved.; 2. <b>Friction approximations:</b> a. Chézy and Manning formulas are commonly used to estimate friction slope in unsteady flow (even though they were developed for steady uniform flow). The exercise in estimating the resistance coefficient is very difficult. An error in the estimation of the coefficient leads to errors in predicted velocity / flow of the same magnitude.; b. Assuming a steady uniform flow allows one to express the longitudinal shear stress using the Chézy formula.</li> <li>• Applying these assumptions to unsteady flow scenarios give reasonable approximations.</li> <li>• In channel-routing applications, kinematics models always predict steeper waves with less dispersion and attenuation than what actually occurs. The effect of error accumulation in some model approximations provide justification against use in some channel-routing scenarios. The error accumulation is caused from the neglecting the secondary slope terms in the equation of motion.</li> </ul>	<ul style="list-style-type: none"> <li>+ Kinematic wave approximations are proven to be an accurate and efficient method to employ in the simulation of storm water runoff (Overton and Meadows, 1976; US Army Corps of Engineers, 1993).</li> <li>- No analytical solutions exist that can be exploited for modelling purposes. Shock formations in the solutions limits the applicability of model in river modelling scenarios. Finite difference method techniques are required. (Lighthill and Whitham, 1955).</li> </ul>

### 2.2.4. Snowmelt Component

During snowy seasons, surface runoff may be produced from the melting of snow, known as *snowmelt*. This process is the most important in regions of higher altitudes, where river basins may reside within mountainous regions. Here, precipitation typically falls as snow and surface runoff is dependent on the supply of heat to melt snow, rather than the timing of precipitation (Ferguson, 1999).

Several energy fluxes act in opposing ways and influence the quantity of meltwater available for runoff at any given time. Heat may be delivered to the snowpack from geothermal sources emanating from the soil below it (Gray and Male, 1981). From above, surface runoff is influenced by the net shortwave radiative flux that is experienced by a snowpack. Net shortwave radiation describes the differences between the energy absorbed by the snowpack from the sun and what is reflected away due to the reflective properties of the snow, referred to as its albedo. Longwave radiation from atmospheric gases such as carbon dioxide and water vapour also have an influence on the snowpack's composition. Typically the net longwave radiation is negative resulting in a loss of energy in the snowpack (Kondratyev, 1969).

As the water from within the snowpack changes phase via evaporation, sublimation or condensation a latent temperature flux, describing the net energy removed from or delivered to a snowpack, may be measured. Similarly, the heat flux experienced due to convection between air and the snowpack is known as the sensible heat flux.

Physically based watershed hydrological models use a snowmelt model to simulate the snow accumulation and melt processes described above. It does this by quantifying the physical phenomena using one of two methods. The first is known as the *temperature index* method which uses air temperature as an index for snow melt. The final method is known as the *energy balance method*, which uses the principles of energy balance and radiation (Singh et al., 2009).

In the temperature index method, a melt factor ( $MF$ ) relates the air temperature  $T_a$  to the snowmelt rate

$$M = MF (T_a - T_{base}).$$

Here,  $M$  represents the snowmelt depth [mm];  $MF$  is the melt factor [ $\text{mm } ^\circ\text{C}^{-1} \text{hr}^{-1}$ ]. This is dependent on the gradient and aspect of the land surface, its vegetation cover and the climate.  $T_a$  is the mean air temperature over time [ $^\circ\text{C}$ ]; finally,  $T_{base}$  is the base temperature at which snow will start to melt [ $^\circ\text{C}$ ]. When there is a strong connection and correlation between the average air temperature and dominant energy component responsible for snowmelt, this method is most applicable. Here,  $(T_a - T_{base})$  is an empirical measure which quantifies the accumulated insolation attained by a snowpack within a given region.

Speers and Versteeg (1982) describe how the temperature index method is used within the LISTFLOOD model. It was also adapted to take into account snowmelt acceleration when rain occurs:

$$M = MF(1 + 0.01P\Delta t)(T_a - T_{base})\Delta t$$

where  $P$  is the rainfall rate [mm/day] and  $\Delta t$  is the time interval [days].

WATFLOOD/SPL9 combined the temperature index and surface radiation budget to construct a radiation-temperature empirical measure (Hamlin, 1996). This measure and the snowmelt depth model, given by Kouwen and Mousavi (2002), provide the snowmelt component of WATFLOOD/SPL9 where  $r_n$  is a factor which converts energy flux density to snowmelt depth [mm hr<sup>-1</sup>].  $R$  is the net radiation experienced by a snowpack [Wm<sup>-2</sup>].

$$M = MF(T_a - T_{base}) + r_n R.$$

A slightly different approach is used by the SWAT model (Arnold et al., 1998). Snowmelt rate is a function of snowpack temperature ( $T_{SP}$ ). Snowmelt only commences when the second soil layer within the model is greater than 0°C:

$$M = (1.52 + 0.54T_{SP})T_a.$$

The energy balance method utilises the one-dimensional energy equation which is applied to a control volume of snow assuming it has an upper and lower interface with the air and ground respectively (Singh et al., 2009). Thus, the transfer of energy from snow surface and snow-soil interface may be quantified with

$$Q_m = -(Q_n + Q_h + Q_e + Q_p + Q_g + U).$$

Here,  $Q_n$  is the net sum of radiation;  $Q_h$  is convective sensible heat flux;  $Q_e$  is the latent heat flux [Jm<sup>-2</sup>];  $Q_p$  is the advective heat from precipitation;  $Q_g$  represents the ground heat flux and  $U$  is the cold content of the snowpack. One may then estimate the total snowmelt with

$$M = \frac{Q_m}{\rho_w \lambda_f \theta},$$

where  $\lambda_f$  represents the latent heat available when ice fuses;  $\rho_w$  is water density and  $\theta$  is the ratio of heat needed to completely melt a snowpack to the heat needed to melt the same quantity of pure ice at 0°C. Operationally, this method is rarely used due to the heavy requirements of a vast quantity of good quality data which is not freely abundant.

### 2.2.5. Evapotranspiration Component

Land surface *evaporation* directly occurs on both soil and vegetation surfaces. The primary energy source to induce latent heat of vaporisation comes from solar radiation. *Transpiration* is a process which begins via water extraction by plants from its roots. This water then makes its way through the stem and reaches the atmosphere through tiny openings within a plant's stomata, tiny holes on the surface of its leaves. The wind velocity and local specific humidity gradient controls how much water vapour is transported away from the evaporative surface. This summation of water loss from a defined area, during a specified time period, due to evaporation from the soil surface and transpiration from vegetation is defined as *evapotranspiration* (Soil Science Glossary Terms Committee, 2008; Kirkham, 2014).

The supply of energy to provide latent heat of vapourisation and the local wind velocity and specific humidity are two significant factors which influence open water evaporation. A third influencing factor includes the supply of water at the evaporative surface itself. If the supply of moisture to a vegetative surface was unlimited, then the evapotranspiration would be referred to as *potential evapotranspiration*. The *actual evapotranspiration* never exceeds its potential as moisture supply is always limited. It is dependent on the moisture content within and on the vegetative surfaces (Rosenberg et al., 1983; Chow et al., 1988; Kirkham, 2014).

To calculate the evapotranspiration component within the hydrological models, the standard techniques involve focusing on the two main influencing processes of latent heat of vapourisation (commonly referred to as the *energy balance method*) and the relationship between wind velocity and specific humidity, referred to as the *aerodynamic method*.

A full derivation of the equation using the energy balance method is provided in Chow et al. (1988, pg. 81–84). The result of the derivation is presented below:

$$E_r = \frac{1}{l_v \rho_v} (R_n - H_s - G). \quad (2.18)$$

$l_v$ ,  $\rho_v$ ,  $R_n$ ,  $H_s$  and  $G$  represent the latent heat from vapourisation, water density, net radiation, sensible heat flux and ground heat flux respectively.

The aerodynamic method looks at the transport rate of water vapour away from the evaporative surface. This transport rate is governed by the wind speed across its surface and the local humidity above it. As with the energy balance method above, a full derivation is provided in Chow et al. (1988, pg. 84–86) and its result is shown below:

$$E_a = B(e_{as} - e_a). \quad (2.19)$$

$B$  is a vapour transfer coefficient,  $e_{as}$  is the saturated vapour pressure and  $e_a$  is the vapour



pressure at air temperature. The evapotranspiration component within the ISBA, MISBA and SLURP hydrological models is calculated by applying the definitions of equations (2.18) and (2.19).

One of the first attempts to model evapotranspiration with the above equations came from Penman (1948). Equations (2.18) and (2.19) separately assume that the supply of heat and the supply of water vapour transport is unlimited. However in reality both are limited and so Chow et al. (1988, pg. 86–88) showed how one can combine both methods for a more realistic evapotranspiration component model. This model has been used in various hydrological simulators such as HRCDHM and tRIBS:

$$E = \left( \frac{\Delta}{\Delta + \gamma} \right) E_r + \left( \frac{\gamma}{\Delta + \gamma} \right) E_a. \quad (2.20)$$

$\Delta$  represents the slope of saturation vapour pressure against a temperature curve.  $\gamma$  is a psychometric constant.

Monteith (1965) adapted Penman's initial contribution leading to

$$E = \frac{1}{l_v} \left( \frac{\Delta(R_n - G) + \gamma l_v E_a}{\Delta + \gamma} \right). \quad (2.21)$$

This variation has been applied in the SWAT, SHE, MIKE SHE, IHDM and tRIBS hydrological models.

Another adaptation of the Penman equation was made by Priestley and Taylor (1972). Present in the hydrological models WATFLOOD/SPL9, SWAT and TOPNET, an empirical approximation of equation (2.20) is made to only require net radiation data. The Priestley-Taylor model mathematically describes potential evapotranspiration as

$$E = \alpha \left( \frac{\Delta}{\Delta + \gamma} \right) (R_n - G) \quad (2.22)$$

with  $\alpha$  representing a multiplying coefficient.

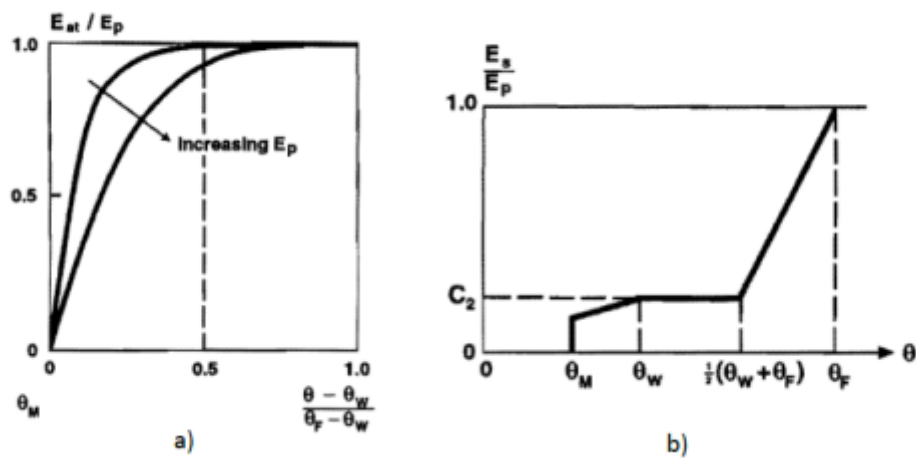


Figure 2.3.: Figure a) shows the relationship between the ratio of actual evapotranspiration ( $E_{at}$ ) to potential evapotranspiration ( $E_p$ ) and the ratio between the soil moisture content minus the soil moisture content referenced at wilting point ( $\theta - \theta_w$ ) to the soil moisture content at field capacity minus the soil moisture content referenced at wilting point ( $\theta_F - \theta_w$ ). Similarly, figure b) illustrates the relationship between the ratio of actual soil evaporation realised ( $E_s$ ) against its potential evaporation ( $E_p$ ). This ratio is compared among various soil moisture content references as defined previously.  $\theta_M$  defines the irreducible soil moisture content. Obtained from Refsgaard and Storm (1995).

A method developed by Kristensen and Jensen (1975) has been utilised in the WATBAL and MIKE SHE hydrological model. This method calculates the actual evapotranspiration from the soil moisture content and potential evaporation shown pictorially in Figure 2.3 above.

The HydroGeoSphere hydrological model (Aquanty Inc., 2015) tweaked the Kristensen-Jensen model so that transpiration rate may be estimated from the relationship between net transpiration capacity between leaf area index ( $f_1(L_{AI})$ ), water content ( $f_2(\theta)$ ), a time-varying root distribution function ( $R_{DF}$ ), a evapotranspiration reference ( $E_p$ ) and canopy evaporation ( $E_c$ ):

$$T_p = f_1(L_{AI}) \cdot f_2(\theta) \cdot R_{DF} \cdot (E_p - E_c). \quad (2.23)$$

The vegetation term is expressed as:

$$f_1(L_{AI}) = \max(0, \min[1, (C_2 + C_1 L_{AI})]), \quad (2.24)$$

with dimensionless fitting parameters  $C_1$  and  $C_2$ . The soil water content function takes the form:

$$f_2(\theta) = \begin{cases} 0 & 0 \leq \theta \leq \theta_{wp}, \\ 1 - \left[ \frac{\theta_{fc} - \theta}{\theta_{fc} - \theta_{wp}} \right]^{C_3} & \theta_{wp} \leq \theta \leq \theta_{fc}, \\ 1 & \theta_{fc} \leq \theta \leq \theta_o \\ \left[ \frac{\theta_{an} - \theta}{\theta_{an} - \theta_o} \right]^{C_3} & \theta_o \leq \theta \leq \theta_{an}, \\ 0 & \theta_{an} \leq \theta. \end{cases} \quad (2.25)$$

Here  $C_3$  is a dimensionless fitting parameter and  $\theta_{an}$ ,  $\theta_{fc}$ ,  $\theta_o$ ,  $\theta_{wp}$  represent the water content at the anoxic limit, at field capacity, at the oxic limit and at the wilting point respectively.

Thus, soil evaporation may be computed depending on which assumptions one is making. If one assumes that evaporation is active provided that potential evapotranspiration,  $E_p$ , has not been diminished by either canopy evaporation,  $E_c$ , nor transpiration  $T_p$  then, given a wetness factor  $\alpha^*$  and an evaporation distribution function  $E_{DF}$ ,

$$E_s = \alpha^* \cdot (E_p - E_c - T_p) \cdot E_{DF}. \quad (2.26)$$

If one assumes that soil evaporation occurs in tandem with transpiration then one will use

$$E_s = \alpha^* \cdot (E_p - E_c) \cdot (1 - f_1(L_{AI})) \cdot E_{DF}. \quad (2.27)$$

The hydrological models WATFLOOD/SPL9 and SWAT implement an empirical model developed by Hargreaves and Samani (1982) to compute the evapotranspiration component

$$E = 0.0075 \cdot R_a \cdot C_t \cdot \delta_t^{0.5} \cdot T_{avg}. \quad (2.28)$$

Here,  $R_a$  is the incoming solar radiation;  $C_t$  is a coefficient for temperature reduction;  $\delta_t$  is the difference between the average monthly maximum and monthly minimum temperature [F];  $T_{avg}$  is the mean temperature within the timestep [F].

Actual evapotranspiration ( $E_a$ ) within the SLURP model is ascertained from the Complementary Relationship Areal Evapotranspiration (CRAE) method from Morton (1983). First an empirical equation using a relationship slope between saturation vapour pressure and temperature curve, along with net radiation is utilised to find the aerial wet-environment evaporation ( $E_w$ ). Potential evaporation ( $E_p$ ) is found by applying equation (2.21), then actual evapotranspiration may be calculated as

$$E_a = 2E_w - E_p. \quad (2.29)$$

A different technique is employed by the LISTFLOOD model based on Supit et al. (1994); Supit and Van Der Goot (2003). Here soil evaporation and transpiration is calculated separately. Actual soil evaporation is approximated by multiplying a reduction factor,  $\alpha_1$ , to the maximum soil evaporation ( $E_{S_{max}}$ ). Similarly, actual transpiration is calculated from the product between a reduction factor,  $\alpha_2$ , and maximum transpiration  $T_{max}$ :

$$E_{S_a} = \alpha_1 \cdot E_{S_{max}} \quad (2.30)$$

$$T_a = \alpha_2 \cdot T_{max} \quad (2.31)$$

Maximum soil evaporation and transpiration may be calculated with

$$E_{S_{max}} = E_{S_0} \cdot e^{-k_{gb} \cdot L_{AI}} \cdot \Delta t \quad (2.32)$$

$$T_{max} = k_{crop} \cdot E_{T_0} \cdot \left(1 - e^{-k_{gb} \cdot L_{AI}}\right) \cdot \Delta t - E_{int} \quad (2.33)$$

where  $k_{crop}$ ,  $k_{gb}$ ,  $E_{T_0}$ ,  $E_{S_0}$  and  $E_{int}$  are parameters for the crop coefficient, extinction coefficient, the reference potential evaporation, potential evaporation from bare soil and the evaporation of intercepted water, respectively.

### 2.2.6. Saturated Zone Component

The *saturated zone* component within hydrological models takes care of subsurface flow in saturated soils as well as ascertaining the height of groundwater. A coupled boundary condition exists between this component and the unsaturated zone. The percolation rate from the unsaturated zone impacts the groundwater table which, when updated, alters the lower boundary conditions for the unsaturated zone.

Fully distributed physically based models (SHE, MIKE SHE and IHDM) utilise a three dimensional groundwater flow equation to model the temporal and spatial variation of hydraulic heads. Typically this model assumes anisotropic conditions with either a heterogeneous or multi-layer aquifer system. This equation is presented by Refsgaard and Storm (1995) as

$$S(x_{i,j}) \frac{\partial h(x_i)}{\partial t} + R(x_{i,j}) = \frac{\partial}{\partial x_i} \left( K(x_{i,j}) H \frac{\partial h(x_i)}{\partial x_i} \right). \quad (2.34)$$

$x_{i,j}$  is the spatial coordinate with subscripts  $(i, j) \in \{1, 2, 3\}$ .  $S(x_{i,j})$  represents specific storage.  $h(x_i)$  is the hydraulic head,  $K(x_{i,j})$  the hydraulic conductivity and  $R(x_{i,j})$  the volumetric flow rate via source and sink terms.

TOPMODEL and DPHMRS, semi-distributed hydraulic models, apply the topographic wetness index attributed to Kirkby and Weyman (1974) and Beven and Kirkby (1979).

$$\ln \left( \frac{\alpha}{\tan \beta} \right). \quad (2.35)$$

This index allows one to study how effects of spatial scale influence hydrological processes.  $\alpha$  parametrises the local upslope area which drains through a given pixel per unit contour length.  $\tan \beta$  is the local slope with its units in radians. Using this index, one can then model the relationship between the average catchment water table depth to the local water table depth as

$$f(\bar{z} - z_i) = \ln \left( \frac{\alpha}{\tan \beta} \right) - \ln(T_0) - A^{-1} \sum_i \left\{ \ln \left( \frac{\alpha}{\tan \beta} \right) - \ln(T_0) \right\}. \quad (2.36)$$

As a soil just saturates  $T_0$  is the local lateral transmissivity.  $\bar{z}$  is the average water table level for the catchment.  $z_i$  is the local water table level and  $A$  is the area of the catchment.

A gravity drainage scheme is used as a saturated zone component for the ISBA and MISBA models (Kerkhoven and Gan, 2005). Here,  $Q$  is sub-surface runoff,  $D$  is depth of the deep soil layer,  $\theta$  is the soil water content and  $\theta_{drain}$  is the minimum soil water content required for drainage to begin.  $C$  is a multiplicative coefficient.

$$Q = C(\theta - \theta_{drain})D. \quad (2.37)$$

Groundwater flow within the LISTFLOOD model is split into an upper and lower zone. Flow from the upper zone to the channel ( $Q_{U_z}$  [mm]) is represented by (Ivanov et al., 2004a)

$$Q_{u_z} = \frac{1}{T_{u_z}} \cdot U_Z \Delta t. \quad (2.38)$$

Here  $T_{u_z}$  is a reservoir constant [days] and  $U_Z$  is the absolute amount of water stored [mm]. Similarly  $T_{l_z}$  and  $L_Z$  is a reservoir constant and absolute water storage for the lower zone with flow from the lower zone ( $Q_{l_z}$ ) given by

$$Q_{l_z} = \frac{1}{T_{l_z}} \cdot L_Z \Delta t. \quad (2.39)$$

Finally, a quasi three-dimensional cascade model method is used by the tRIBS model (Ivanov et al., 2004b):

$$\sum_j Q_{S_{out_j}} = - \sum_j TW_j \tan \beta_j. \quad (2.40)$$

$Q_{S_{out_j}}$  is the outflow flux from a saturated layer with width  $W_j$  along a negative hydraulic gradient (estimated as a local gradient of water table,  $\tan \beta$  and  $\beta$  the local slope of groundwater level). The  $j^{\text{th}}$  index refers to directional values of width and hydraulic gradient.

## 2.3. Computational mesh types

A major influence on physically based hydrological modelling is that of horizontal discretisation resolution. The discretisation schemes can be broadly organised into three categories; 1. Orthogonal grid base; 2. Irregular grid base; and 3. Hydrologic (or grouped) response unit base (Kite and Pietroniro, 1996).

**Orthogonal grid** base discretisation schemes result in dividing a river basin into rectangular segments. A grid resolution may differ within the basin but must be consistent for each given row and/or column in a network array (Abbott et al., 1986b). A Representative Element Area (REA) discretisation scheme was introduced by Wood et al. (1988). Here, spatial variability was assumed to disappear in watershed runoff. Various hydrological models utilise the orthogonal discretisation approach, these include: SHE, WATBAL, MIKE SHE, ISBA, MISBA, LISTFLOOD, WATFLOOD/SPL9, HydroGeoSphere, PAWS and CREST.

Local basin topography and terrain features determine how a river basin is discretised in the *irregular grid* base schemes. Hydrological modelling components are determined via streamlines, equipotential lines or through triangulated irregular networks (TIN). Examples of hydrological models which apply this scheme include THALES, tRIBS and R.WATER.FEA.

**Hydrological response** unit base discretisation schemes are characterised by a river basin being divided into sub-basins defined by an individual drainage network (Biftu and Gan, 2004). Hydrological processes are evaluated at point scale and then aggregated within the sub-basin scale. Examples which use this discretisation method include TOPMODEL, TOPNET, SWAT, HRCDHM, DPHMRS and IHDM. For a **Grouped response** unit base discretisation scheme, a watershed is separated into sub-basins where a grid cell or an agglomeration of cells are represented as a grouped response unit. The SLURP hydrological model utilises this scheme.

## 2.4. Semi-Distributed Models

Unnecessarily large data sets and computational power may be avoided by modelling the essential physics and lumping key hydrological processes at a sub-basin scale. One can use digital terrain elevation data or a digital elevation model to induce the appropriate topographic information for a given river basin. This region may then be divided into a finite number of sub-basins, which need not be equal in their shape and size. Models which apply this approach to simulating river system behaviour are commonly referred to as *semi-distributed* physically based hydrological models. Methods which estimate runoff amounts, such as unit hydrographs, may be used to estimate the streamflows from each of these sub-basins. Semi-distributed models allow for a better detailed picture of a larger watershed whilst still providing a relatively cheap and simple calculation. However, the ability of in-depth understanding of physical processes would be difficult to attain. A summary of semi-distributed models is outlined below with a brief overview of how they came to be. Table 2.4 lists these models along with their primary reference.

### 2.4.1. DPHM-RS

Authored by Biftu and Gan (2001) from the University of Alberta, Canada, the semi-Distributed Physically based Hydrologic Model using Remote Sensing and GIS looked to take advantage of scientific knowledge of the hydrological process and apply newly acquired satellite data information into fully-distributed models. Essential physics of basin hydrology was modelled by using spatial hydrologic information available from remote sensing. It took into account terrain features via topographic information from digital terrain elevation data or a digital elevation model. It looked to estimate some model parameters from field measurements and remote sensing data instead of relying on then traditional parameter calibration techniques. This model divides a river basin into sub-basin components. It computes evapotranspiration, soil moisture and surface runoff using

Table 2.4.: A summary of semi-distributed physically based hydrological models and their discretisation approaches with their principle reference.

Leading Reference(s)	Name	Acronym	Purpose
Biftu and Gan (2001)	semi-Distributed Physically based Hydrologic Model using Remote Sensing and GIS	DPHM-RS	Models essential physics of basin hydrology using spatial hydrologic information available from remote sensing.
Hromadka II and Rao (2021)	Hydrologic Research Center Diffusion Hydrodynamic Model	HRCDHM	Models floodplain and dam break events.
Kite (2019)	Semi-distributed Land Use-based Runoff Processes	SLURP	Simulates hydrological cycle from precipitation to land surface runoff.
Arnold et al. (1998)	Soil and Water Assessment Tool	SWAT	Assesses impact of water management on supply and non-point source pollution in watersheds and large river basins.
National Institute of Water and Atmospheric Research (2011)	-	TOPNET	Simulating catchment water and river flow. Combines TOPMODEL with kinematic wave channel routing algorithm (Goring, 1994).
Yates (1994)	An integrated Water Balance Model	WATBAL	Describes a water balance model in combination with the Priestley-Taylor method (Priestley and Taylor, 1972).

energy and rainfall forcing data in a sub-basin scale.

### 2.4.2. HRCDHM

Developed by hydrologists from the United States Geological Survey, the **H**ydrologic **R**esearch **C**enter **D**iffusion **H**ydrodynamic **M**odel is a coupled one- (or two-) dimensional surface flow model. It is based on the diffusions form of the Navier-Stokes equations and is used in modelling floodplains and dam break events (Hromadka II and Rao, 2021). It was constructed as part of the National Oceanic and Atmospheric Association’s “Distributed Model Intercomparison Project” (DMIP). The hydrological processes of infiltration, percolation, evapotranspiration, surface and subsurface flow are modelled along the vertical axis on a sub-catchment scale. Kinematic channel routing carries flow through a network of sub-catchments to a watershed outlet, providing the capability for spatially distributed flow simulations.



### 2.4.3. SLURP

The **S**emi-distributed **L**and **U**se-based **R**unoff **P**rocesses model simulates the hydrological cycle from the point of precipitation to land water runoff (Kite, 2019). It includes the effects of reservoirs, dams, regulators, water extractions and irrigations schemes. It employs a vertical water balance model to examine the effects of proposed changes in water management within a basin to see what effects external factors such as climate change or changing land cover might have on various water users.

### 2.4.4. SWAT

The **S**oil and **W**ater **A**ssessment **T**ool was initially designed to aid water resource managers to assess the impact of water management on supplies and nonpoint source pollution in watersheds and large river basins (Arnold et al., 1998). It has grown over the past forty years to be used at various scales from a small watershed to a large river basin-scale model. It may simulate the quality and quantity of surface and ground water to predict the environmental impact of land use, land management practices and climate change.

### 2.4.5. TOPNET

A semi-distributed hydrological model for simulating catchment water and river flow, TOPNET was conceived by combining the fully-distributed model TOPMODEL (see Section 2.5.10) with a kinematic wave channel routing algorithm (Goring, 1994). This model could be applied over a large watershed using smaller sub-basins as model elements. Developed by New Zealand’s National Institute of Water and Atmospheric Research, its approach combines the understanding of hydrology and soil science to calculate water availability over time (National Institute of Water and Atmospheric Research, 2011).

### 2.4.6. WATBAL

First introduced by Yates (1994), WATBAL is an acronym for “An integrated **W**ater **B**alance Model for Climate Impact Assessment of River Basin Runoff”. As the name suggests, it describes a water balance model in combination with the Priestly-Taylor method (Priestley and Taylor, 1972) to compute potential evapotranspiration. It was developed with having in mind that it will become an integrated tool for modelling the response of river basins to climate change. The model’s conception was necessary because previous to this there was no accepted method or general approach to properly assess the impact of climate change on water resources. This model was tasked with providing a consistent and sound method for measuring such an impact.

Table 2.5.: A summary of fully distributed physically based hydrological models and their discretisation approaches with their principle reference.

Leading Reference(s)	Name	Acronym	Purpose
Wang et al. (2011)	Couple Routing and Excess Storage model	CREST	Simulates spatial and temporal variation of land surface and subsurface water fluxes and storages.
Beven et al. (1987)	Institute of Hydrology Distributed Model	IHDM	Models flood forecasts for ungauged catchments to predict hydrological effects of land use change.
Mahfouf et al. (1995); Bouilloud et al. (2010)	Interaction between Soil, Biosphere and Atmosphere model	ISBA	Solves water and energy budgets in the vertical direction.
de Roo et al. (2013)	-	LISFLOOD	Aid water policy making and humanitarian aid for the European Commission.
Abbott et al. (1986a,b); Refsgaard and Storm (1995)	-	MIKE SHE	Extension of the SHE model. Simulates water flow, water quality and sediment transport. Utilised in river basin planning, irrigation and drainage etc.
Kerkhoven and Gan (2006)	Modified Interaction between Soil, Biosphere and Atmosphere model	MISBA	ISBA model applied in the Athabasca River basin using historically observed streamflows.

Leading Reference(s)	Name	Acronym	Purpose
Shen and Phanikumar (2010); Shen et al. (2013, 2014)	Process-based Adaptive Watershed Simulator	PAWS	Developed to help water resource management problems.
Abbott et al. (1986a,b)	System Hydrologique Europeen	SHE	Initially constructed to tackle issues where conventional rainfall-runoff models could not.
O'Loughlin (1986); Grayson et al. (1992)	-	THALES	A simple distributed parameter hydrological model simulating Hortonian overland flow utilising TAPES-C analysis of topography as a physically realistic basis for structuring a dynamic model.
Beven et al. (1995); Beven and Freer (2001)	-	TOPMODEL	Constructing a pragmatic and practical forecasting and simulation tool. Development of a theoretical framework where perceived hydrological processes, scale and realism issues and model procedures may be researched.

Leading Reference(s)	Name	Acronym	Purpose
Ralph M Parsons Laboratory (2000)	TIN based Real Integrated Basin Simulator	tRIBS	Developed a distributed model on a TIN mesh to increase efficiency and model execution times.
Kouwen (1986, 1988); Kouwen and Mousavi (2002)	-	WATFLOOD	Optimises use of remotely sensed land cover data, digital elevation models, numerical weather data etc.

## 2.5. Fully Distributed Models

Fully-distributed models estimate a response to an input using either a physics based or conceptual mathematical representation of some given hydrological system. Conceptual models rely on a variant of linear reservoir theory to delay and / or attenuate the routing of runoff generation. Typically runoff generation and routing are not interlinked within the modelling process. Unlike conceptual models, physics-based modelling couples the runoff generation and routing output using equations related to the conservation of mass, momentum and energy to understand the relationship between routing and runoff.

Numerical solutions of governing equations require discrete elements. Three examples of these elements are finite difference, finite element and stream tubes. On a computational level, model parameters are considered as being representative of an average process. Thus some average property is only valid over the computational element used to represent the flow process.

From a model perspective, parameters are representative of the surface / medium at the computational element scale used to solve the governing mathematical equations. A common rule of thumb guide is that as a model applies more coarse grids, the physical significance of the model weakens. For example, runoff depth within a 1km grid cell can only be considered a *generalisation* of the actual runoff process. It may or may not produce physically realistic model output one would expect in observed reality.

Computational power and resource can be easily exceeded when modelling large basins at a fine resolution. This computational limitation often motivates the need to model at a more coarser spatial grid. A common problem often confronted when developing an operational distributed hydrological model for large river basin is how one can parametrise the sub-grid physical processes.

The used structure in Section 2.4 is used in this section. A summary of the fully-distributed models that are present within the research space is presented. Table 2.5 above outlines the fully-distributed models which are to be discussed.

### 2.5.1. CREST

The **C**ouple **R**outing and **E**xcess **S**Torage model (Wang et al., 2011) is a distributed hydrological model which may be used to simulate the spatial and temporal variation of land surface and subsurface water fluxes and storages by cell-to-cell simulation. It was jointly built by the University of Oklahoma and NASA SERVIR. CREST has three useful characteristics 1. a distributed rainfall-runoff generation and cell-to-cell routing, 2. a coupling between runoff generation and routing components via three feedback mechanisms, 3. scalability by representing soil moisture variability and routing processes at the sub-grid scale via a variable infiltration curve and linear reservoirs respectively.

### 2.5.2. IHDM

Authored by Beven et al. (1987) from the Institute of Hydrology, the **I**nstitute of **H**ydrology **D**istributed **M**odel is a physically based catchment model for overland flow, saturated and unsaturated subsurface flow and channel flow. It was created to model flood forecasts for ungauged catchments in order to predict the hydrological effects of land use change.

### 2.5.3. ISBA

ISBA, the **I**nteraction between **S**oil, **B**iosphere and **A**tmosphere model, is a one dimensional physically based scheme. It solves water and energy budgets solely in the vertical direction focusing entirely on land surface processes (Mahfouf et al., 1995; Bouilloud et al., 2010). It forms part of Météo-France’s numerical weather prediction, research and climate atmospheric models **A**ction de **R**echerche **P**etite **E**chelle **G**rade **E**chell (ARPEGE; Courtier and Geleyn (1988), ALADIN; Bubnová et al. (1995)), mesoscale nonhydrostatic (MESO-NH; Lafore et al. (1998)) and Applications of Research to Operations at Mesoscale (AROME; Seity et al. (2011)).

### 2.5.4. LISFLOOD

Created by the European Commission’s Joint Research Center, LISFLOOD was developed to aid water policy making and humanitarian aid (de Roo et al., 2013). It has been built to support each phase of a policy cycle from anticipation to evaluation. It is a grid-based hydrological rainfall runoff routing system which simulates hydrological processes which occur within a river catchment. It models the combined effects of weather and climate change, land use, socio-economic changes on water demand and policy measures for water savings or flood control.

LISFLOOD has acted as the core model of flood and drought simulation efforts within the JRC including the European Flood Awareness System (EFAS; Thielen et al. (2009)), the Global Flood Awareness System (GloFas; Alfieri et al. (2013)) and the European Drought Observatory (EDO; Vogt et al. (2011)). At present, LISFLOOD, is adding to its capabilities to include crop yield and energy production, serving as a model for the Water-Energy-Food-Ecosystem Nexus project.

### 2.5.5. MIKE SHE

MIKE SHE is a descendant of the SHE hydrological model discussed in Section 2.5.8. The Danish international water software development and engineering consultancy firm DHI (Dansk Hydraulisk Institut) continually invested in the research and development of SHE resulting in MIKE SHE.

MIKE SHE is a comprehensive deterministic, distributed and physically-based modelling

method for the simulation of all major hydrological processes that occur in the land phase of the hydrological cycle (Refsgaard and Storm, 1995). It simulates water flow, water quality and sediment transport. Typical application areas include river basin planning, water supply, irrigation and drainage to name a few. It may be applied on various spatial scales from single soil profile infiltration studies to large regions which include several river catchments.

### 2.5.6. MISBA

MISBA is a modification of the ISBA model outlined in Section 2.5.3, where the model could better simulate the sub-surface runoff of the Athabasca River Basin. This model was specifically constructed to simulate historically observed streamflows in the large northern basin of the Athabasca River Basin of 133,000 km<sup>2</sup>. It used gridded meteorological data from a numerical weather prediction model and Canadian GEM model as well as GCSM scale re-analysis data called ERO-40 from ECMWF (Kerkhoven and Gan, 2006).

### 2.5.7. PAWS

Initially developed via Dr. Chaopeng Shen's Ph.D. dissertation topic to help tackle water resource problems, the **P**rocess-based **A**daptive **W**atershed **S**imulator (PAWS) model is a comprehensive computationally-efficient parallel hydrological model designed for large-scale simulations (Shen and Phanikumar, 2010; Shen et al., 2013, 2014).

### 2.5.8. SHE

In the mid 1970s a Danish-French-UK consortium felt that a new hydrological model was needed to tackle increasingly pressing practical hydrological problems. These issues came in the form of impacts of anthropogenic activities on the hydrological cycle as well as water resource development and management. The consortium comprised of DHI (Dansk Hydraulisk Institut), SOGREAH (Société Grenobloise d'Etudes et d'Applications Hydrauliques) and the Institute of Hydrology (UK).

The model known as "SHE" (Systeme Hydrologique Europeen; Abbott et al. (1986a,b)) was developed to tackle issues that conventional rainfall-runoff models could not, especially consequences of man-made changes within a catchment. It was constructed with the vision to be applicable to almost any hydrological problem. A flexible model structure with a distributed structure and physical interpretation of hydrological processes expected to give significant advantages over existing hydrological models for a range of applications that were more complicated in nature.

### 2.5.9. THALES

THALES, named after Thales of Miletos, a Greek philosopher who recognised the influence of topography on runoff generation, developed from the original work of O'Loughlin (1986). It is a simple distributed parameter hydrological model which simulates Hortonian overland flow and runoff from saturated source areas. Typically it is used to determine barriers to modelling of the hydrology within small catchments.

This model is designed to take advantage of TAPES-C (**T**opographic **A**nalysis **P**rograms for the **E**nvironmental **S**ciences: **C**ontour) analysis of topography as a physically realistic basis for structuring a dynamic hydrological model. It is a set of computer programmes which generate a network of interconnected elements on a surface defined by elevation isolines (Grayson et al., 1992).

### 2.5.10. TOPMODEL

TOPMODEL is a product of two overarching goals. 1. The construction of pragmatic and practical forecasting and continuous simulation model. 2. Development of a theoretical framework within which perceived hydrological processes, issues of scale and realism and model procedures may be researched. Parameters are intended to be interpretable physically and the total parameters kept to a minimum. In practice, this model attempts to combine computational and parametric efficiency of a lumped approach with the link to physical theory and possibilities for a more rigorous evaluation offered by a distributed model (Beven et al., 1995).

These objectives led to a popular framework because of its simplicity. It uses a digital terrain model for computational efficiency in predicting distributed hydrological responses whilst also using a topographic index of hydrological similarity using analysis of topographic data. A kinematic wave routing of subsurface flow was also implemented to allow the simulation of dynamically variable upslope contributing areas and replaces the assumption of quasi-steady state saturated zone configuration (Beven and Freer, 2001).

### 2.5.11. tRIBS

tRIBS stands for **T**IN based **R**ead **I**ntegrated **B**asin **S**imulator. It has been constructed using object-oriented programming methodology in C++ allowing for the development and simulation of catchment scale hydrological processes on a *Triangulated Irregular Network* (TIN; Ralph M Parsons Laboratory (2000)).

Researchers from the Ralph M. Parsons Laboratory in the Department of Civil and Environmental Engineering of MIT argue that the common methods of distributed models using terrain inherent within a raster grid leads to large execution times and is highly inefficient. Hence they have developed a distributed hydrological model on a TIN mesh.



### 2.5.12. WATFLOOD

The WATFLOOD model makes optimal use of remotely sensed land cover data, digital elevation models and numerical weather data. Distributed data may be directly incorporated into hydrological modelling without loss of inherent details.

WATFLOOD was initiated by Don McMullen, a hydrometeorologist of the Province of Ontario and Dr. Nick Kouwen as a visitor to the Conservation Authorities Branch of the Ontario Ministry of Natural Resources as a flood forecasting system (Kouwen, 1986, 1988; Kouwen and Mousavi, 2002). It is a set of integrated computer programmes which forecast flood flows and / or do simulations for watershed having response times which range from an hour to several weeks.

## 2.6. Literature Gap

Typically hydrological models within the literature have been applied to watersheds to estimate the response of hydrological systems to intense storm events. The six components which make up a hydrological model have been outlined in Section 2.2. Three of these components will make up the hydrological model constructed in Chapter 4, namely the interception, unsaturated zone and surface routing components. Only three parts are considered due to the computational limitation of my personal PC. Tables 2.1 (page 54), 2.2 (page 60) and 2.3 (page 66) give overviews of the key literature methods and tools for the interception, unsaturated zone and surface routing components of a hydrological model respectively. The methodological similarities and differences between the hydrological model developed in this work and the literature for the relevant components are highlighted in Sections 2.7.1, 2.7.2 and 2.7.3.

Hydrological systems also have a key influence in local wildlife populations and maintaining diverse habitats as well as other important roles in sustaining the local ecology (McCabe, 2011). Hydrological models are typically applied in the literature to understand the spatial and temporal evolution of given storm events over specific time periods with the intention of using it to estimate the hydrological impacts in future. Whilst this motivation of model construction is important and satisfactory on its own, the hydrological model developed in this work is done so with an understanding of the wider role watersheds have on the local environment.

High level strategic goals defined by Cornwall Council through its “Environmental Growth Strategy” (Section 1.1.5) can be achieved holistically through a computational platform which integrates multiple models from different environmental domains that are interdependent. For example, the output from a given hydrological model could be used as an input to modelling frameworks which simulate the wildlife population of a given watershed (McRae et al., 2008). This work is not considered to be replicating the exercise of hydrological model development for its own sake. It is considered to be a small cog in a larger ecosystem management tool. Hence, the construction of the hydrological model is

a first step “*Towards a computational tool for the management of natural capital*”. This tool is intended to be utilised as an aid to policy and decision making. This tool would be comprised of multiple models from different environmental domains whose inputs and outputs are dependent on one another.

Influence and motivation has been taken from the facility management industry considered in Section 1.1.6 to apply methods which align with the high level strategic goals within the ecosystem services field outlined in Section 1.1.4. There are many potential avenues from the EGS one can explore. Ecosystem analytics could be presented on a “front-end” platform, similar to the “MyFM” dashboard from the top HAT analytics platform “Focal365” (1.1.6), to present the possible impacts of proposed policy solutions. The first step toward constructing the “back-end” of this platform is the construction of a hydrological model. This model is motivated by the need to meet the objectives of “Target Outcome 4” (Section 1.1.5.1). This goal looks to construct a management guideline to aid ecosystem analytics to support environmental growth in the long term whilst supporting human needs in the short-medium term through housing construction.

Economic and societal growth is coupled with environmental growth, as outlined in the Environmental Growth Strategy (1.1.5). Natural Capital Accounting is a framework which helps in assessing how these three high-level domains influence one another. The facilities management industry already has an established vernacular which could act as a template to define a new domain specific analytical toolset for the natural capital accounting framework. The use of the wider computational tool described could be applied to further establish and embed this framework. The use of bespoke modelling tools on the “back-end” of the tool makes advanced modelling techniques available to policy makers. Policy makers could apply these models with confidence without the years of training needed to successfully implement them. The perspective of a policy planner interacting with this tool and its “plug-and-play” feature on the “front-end” of the tool is the primary motivation of the scenarios in the simulation modelling outlined in Chapter 7.

## 2.7. My Modelling Approach

How surface runoff is calculated is determined by a hydrological model’s structure. Its governing equations determine how simple or complex these calculations can be. Empirical and statistical hydrological models, typically referred to as “black box” models are the simplest. These models are data driven and their derivation are not built up from a physical reality (Refsgaards and Knudsen, 1996; Sitterson et al., 2017; Beven, 2019). When considering how land-use policy changes will affect the hydrological characteristics of a watershed, an in-depth understanding of these characteristics is vital. Since these empirical models do not offer such an understanding, the hydrological model being developed will not use this approach.

Semi-distributed hydrological models model the essential physics that govern the hydrological properties of a watershed. Key hydrological parameters are lumped together at

sub-basin scales. This limits the amount of data required and reduces the amount of computational power needed to simulate such systems. However, these models are not able to determine the spatial variability of output within a catchment. Key to land-use policy changes and flood risk assessment, the hydrological model constructed in this work must contain this capability. As such, this approach to developing a hydrological model will not be considered.

Fully-distributed hydrological models are conceived from the physical laws and equations that govern the hydrological responses within a watershed. Any output at a given spatial and temporal resolution can be ascertained. The key motivation of this work is centred around a policy planner making land-use policy proposals using a computational tool. A key component of this will be the need for output at various spatial and temporal resolutions which can aid them in this regard. Thus, the hydrological model in this work will be developed using the fully-distributed model framework.

Section 2.2 outlined the six key hydraulic processes which make up a hydrological model. The Interception (Section 2.2.1), Unsaturated Zone (2.2.2), Snowmelt (2.2.4), Evapotranspiration (2.2.5), and Saturated Zone (2.2.6) components influence the amount of water available for surface runoff and routing (Section 2.2.3).

Fully distributed hydrological models couple runoff generation with overland flow routing. As mentioned in Section 2.5, these are key considerations in flood impact analysis. These considerations are fundamental to the hydrological model being built in this work. Such analysis will be made available through a ‘front-end’ dashboard tool that policy planners can utilise where they can access a hydrological modelling tool designed in the ‘back-end’. The construction of this model will be applied to the Coverack flooding case study, outlined in Section 1.2, to analyse its performance and suitability for flood impact management. This is conducted through the perspective of a policy planner using this tool. Due to the ease of implementation, an orthogonal grid mesh structure (reviewed in Section 2.3) will be utilised when constructing the model. The justification of this mesh is expanded upon in Section 4.2.1.

Following the structure from Section 2.2, a summary of the approach taken and reasoning behind the initial hydrological model construction is given. The model developed in this work will run simulations on a standard personal computer<sup>1</sup>. As such, this model will only contain three of the six components which compose a hydrological model, namely the interception, unsaturated zone and surface routing components, to minimise computational expenditure. Similarities and differences between the methodologies used in the model constructed and the models outlined in the literature will be listed for these components. An explanation for the omission of the remaining three components is given in their relevant sections.

---

<sup>1</sup>Machine specification: HP EliteBook 850 G3; 16 GiB memory; Intel®Core™ i5-6200U CPU @ 2.30 GHz × 4; Mesa Intel®HD Graphics 520 (SKL GT2); 512.1 GB disk capacity. Ubuntu 22.01 1 LTS; 64-bit.

### 2.7.1. Interception Component

Section 2.2.1 points to numerous in-depth existing methods which compute the interception of precipitation. Key literature methods and tools related to this component are given in Table 2.1 (page 54). This component will play a key factor in the total input of water available when calculating overland water flow.

Canopy interception within the TOPNET hydrological model utilises a “Wetness Index Distribution” derived from a Digital Elevation Model. This method quantifies terrain driven variations in soil moisture and predicts relative surface wetness, and thus hydrological responsiveness, across a watershed (Ibbitt, 1971; Bandaragoda et al., 2004). Rutter et al. (1971) derived total interception loss as an integral of evaporation rate in time. This method utilised the water balance equations to measure interception loss in a storm. The interception component of LISTFLOOD applied a storage-based equation (Equation (2.5)) (Merriam, 1960; Aston, 1979; Kouwen, 1988). Deardorff (1978) adapted a time-dependent equation for predicting ground surface temperature from Bhumralkar (1975) and Blackadar (1976) to determine surface water availability (demonstrated by Equation (2.7), page 53). Finally, a bucket model approach was used within the PAWS scheme to determine its interception routine (Shen and Phanikumar, 2010).

In order to minimise the overall complexity of the model, none of these methodologies listed will be applied to the hydrological model in this work. Empirical parameters from the literature will be identified and used to represent the interception components for specific land-use categories. Section 4.3.7 discusses these empirical parameters in more detail.

### 2.7.2. Unsaturated Zone Component

Section 2.2.2 summarises the methodology that has been taken within the literature to simulate the unsaturated zone component of a hydrological model. Three methods were illustrated, namely an empirically based mode (e.g. Horton’s), a mathematical model based on physical processes (e.g. Richard’s equation) and a physically based approximations models (e.g. Green-Ampt and Philips models). The hydrological model construction is based upon physical processes. Table 2.2 (page 60) lists the key approaches taken to derive these models.

Green and Ampt (1911) were among the first people to construct a soil infiltration model based on physical principles. Three fundamental constants of soil physics were identified: Specific pore size; Permeability to water; and Capillary Coefficients. Work derived from this model identified multiple parameter options for different soil categories. These are listed in Table 3.1 on page 120. Horton (1919) was one of the first people to attempt to aggregate all scientific research related to infiltration modelling at the time. His model describes how soil infiltration capacity declines as a precipitation event advances. This model generates runoff when precipitation intensity exceeds the soil infiltration capacity. It

was empirically derived from small catchment studies. Richards (1931) constructed a non-linear partial differential equation that describes water movement within unsaturated soils in space and time between the atmosphere and an aquifer. This equation was templated on the Darcy-Buckingham law that represents flow in porous media under varying saturated conditions. Philip's infiltration model (Philip, 1954) is a truncated power series solution where known soil hydraulic properties are applied. This model assumes that Darcy's law is valid for unsaturated soils in a general form where hydraulic conductivity  $K_p$  is a unique function of soil moisture content  $\theta$ .

Unlike the Horton model which has no parameters that are linked to soil hydrological properties, the Green-Ampt model has a robust catalogue of parameters that can be implemented that are physically intuitive. The well established parameter values of the Green-Ampt model, and its simplicity of application, means that it is preferred over Richards equation and Philip's model. Its construction is presented in Section 4.3.5.1.

### 2.7.3. Overland Flow and Routing Component

Overland flow and surface routing is the key hydrological model component when analysing flooding impact due to land-use change. Within Section 2.2.3 two types of surface runoff were defined, namely Horton and Dunne. Table 2.3 (page 60) lists some of the key methodologies constructed to model this behaviour.

One of the first well known surface routing models is the Xinanjiang model. This model is a statistical integral structure which describes surface runoff generation over partial catchment areas (Zhao, 1992; Habets et al., 1999; Kerkhoven and Gan, 2006). Its original version constituted a single parabolic curve to describe soil moisture variation (Jayawardena and Zhou, 2000). Within the literature it has typically been applied and validated mainly in humid and semi-humid regions. A two-dimensional diffusion wave approximation of the shallow water equations comprised the surface routing component of the SHE and MIKE SHE hydrological models (Abbott et al., 1986a,b). The friction component of this approximation applied the Strickler/Manning resistance coefficients that was solved in conjunction with the continuity equation within a finite difference scheme from Preissmann and Zaoui (1979).

The Muskingum-Cunge method (Cunge, 1969; Merkel, 2002) applied physical-numerical principles to determine the surface routing parameters. It combines the continuity equation and a simplified form of the momentum equation. Lighthill and Whitham (1955) introduced the Kinematic wave model. This model describes discharge through a general power relationship. This is solved simultaneously with the unsteady continuity equation as well as the imposition of the initial and boundary conditions. This model is most applicable to overland flow where lateral inflow is continuously added and constitutes a significant part of the flow.

The Xinanjiang distribution model is a statistically-based method constructed without parameters which incorporate any hydrological properties of the watershed. Since the

physical intuition is not embedded within the model it is not considered a preferable candidate in this work. The Muskingum-Cunge method assumes that all the geometric and hydraulic data used to run it is representative of the watershed under consideration. The idea of land-use change / flood risk modelling policy proposals is to disrupt the hydrological properties and affect the discharge response of the watershed. This assumption makes the method unsuitable for use.

Storm events by their very nature are discrete events. The kinematic wave model is best suited to conditions where a continuous input is present. As such, this method has not been considered for the surface routing component of the model in this work. The two-dimensional diffusion wave approximation of the shallow water equations is the final method listed in this section. The model's parameters have the hydrological properties of a system naturally represented within them. It has been successfully implemented into the SHE and MIKE SHE hydrological models (Abbott et al., 1986a,b). These models use an explicit finite difference scheme constructed by Preissmann and Zaoui (1979) to solve the continuity equation along with the Strickler/Manning friction coefficients. The model constructed in this work will apply the Godunov Finite Volume difference scheme instead. The friction component of the model will be resolved from methods developed in Xia et al. (2017) and Xia and Liang (2018). Chapter 3 will present the underlying maths that is present in the construction of this modelling component outlined in Section 4.3.

### 2.7.4. Snowmelt Component

Since the motivation for this work resides from Cornwall Council's "Environmental Growth Strategy" (Section 1.1.5), the potential for snowfall within the area of interest is extremely limited. Cornwall is located on the most south-western part on the island of Great Britain. From the Met Office's own analysis, Cornwall is statistically the least likely part of the island to receive snowfall. It has a mean of nearly seven and a half days of snow or sleet falling within a year (Meteorological Office, 2022), however its modal value is zero days of snow or sleet falling. In view of this information for the area of interest, a snowmelt component will not be implemented in the computational model.

### 2.7.5. Evapotranspiration Component

Evapotranspiration refers to the water lost to the atmosphere via evaporation for the land surface and transpiration from vegetation as highlighted in Section 2.2.5. Within the literature it is common practice to measure this process in units of millimetres per unit time (Allen et al., 1998). Evapotranspiration considers the water loss from water availability that already exists on the land surface. This work looks at the potential flooding impacts from individual storm events as a result of land-use change. Evapotranspiration can have long term future impacts to flow change (Watts et al., 2015), however it does not have an immediate impact on the magnitude of flooding. Hence, the evapotranspiration component is not included in the model construction.

### 2.7.6. Saturated Zone Component

As stated in Section 2.2.6, this component is intrinsically linked with the unsaturated zone via the percolation rate. However, for simplicity, this component will not be considered in the model construction to minimise computational expense and run time.

## 2.8. Summary

Chapter 2 begins the exploration towards the construction of a computational tool in the form of a hydrological model for flood risk. Section 2.2 notes that a hydrological model comprises of six constituent parts. The interception component (Section 2.2.1) refers to redistribution of gross rainfall by vegetation. Key literature methods and tools are given in Table 2.1 (page 54). Interception methods range from the simple application of a “wetness index distribution” employed in TOPNET (Bandaragoda et al., 2004) to the involvement of a 1D Richards Equation used in PAWS (Shen and Phanikumar, 2010). Further interception models from Ibbitt (1971), Rutter et al. (1971), Kristensen and Jensen (1975), Kouwen (1988) and Deardorff (1978) were outlined. Section 2.2.2 reviews the unsaturated zone component of a hydrological model. The key literature tools, methods and their genesis are given in Table 2.2 (page 60). Four methodologies dominate this component. These range from the empirical Horton method (Horton, 1919) to a physical-numerical construction within the Philip model (Philip, 1954). Section 2.2.3 reviews the overland flow routing component of hydrological modelling. This component is fundamental for understanding how flooding impact responses change due to land-use change and intervention. Table 2.3 on page 66 outlines the key methodologies and tools present within the literature. The ISBA, MISBA and LISFLOOD models have all utilised the Xinanjiang distribution model (Zhao, 1992; Habets et al., 1999; Kerkhoven and Gan, 2006). This model determines a catchment response by sub-dividing the basins into sub-basins and accumulating the responses of these basins. SHE and MIKE SHE models adopt the 2D-diffusion wave solution to govern overland flow (Abbott et al., 1986a,b). Also outlined is the physical-numerical Muskingum-Cunge method (Cunge, 1969; Merkel, 2002) outlining the stage/discharge relationship and the Kinematic wave model (Lighthill and Whitham, 1955) which describes waves without consideration of the forces giving rise to the motion.

Section 2.2.4 looked at the snowmelt component of hydrological models, typically present in higher altitude regions. Two main methods were outlined, the temperature index and energy balance method. Evapotranspiration, the summation of water loss from a defined area during a specific time period, was discussed in Section 2.2.5. The aerodynamic method, focusing on the relationship between wind velocity and specific humidity, and the energy balance method, which looks at the main influencing processes of latent heat were discussed in that section. Subsurface flow within saturated soils is covered by the saturated zone component in a hydrological model (Section 2.2.6). One method to represent this is a three-dimensional groundwater flow equation (Refsgaard and Storm, 1995). Another way to model this component is through the topographic wetness index (Kirkby and

Weyman, 1974). A gravity drainage scheme (Kerkhoven and Gan, 2005) and a quasi three-dimensional cascade model (Ivanov et al., 2004b) have also been used. These final three hydrological modelling components are introduced but no tables outlining their key literature methods and tools were given. Due to the level complexity required to incorporate all six components into a hydrological model and the fact that the model would be applied to a personal machine, these components will not be included in the initial construction of the hydrological model. This decision is justified in Section 2.7.

A brief review of computational mesh types was presented in Section 2.3. Sections 2.4 and 2.5 outlined the advantages and drawbacks of semi-distributed and fully-distributed hydrological models respectively. These modelling structures fundamentally govern how surface runoff is calculated within a hydrological model. Within both sections, examples of specific models and their origins were mentioned. Section 2.6 identified the opportunity to apply hydrological models from within the literature in a new way. Through the application of a “front-end dashboard”, those with little to no understanding of how to successfully apply a hydrological model for policy planning contexts could have access to these tool. There is a wide scope that the development of the hydrological model and its output could be interlinked with other environmental models to assess the wider role watershed responses have on the local environment.

Using the knowledge available from the literature and the context in which this hydrological model is to be constructed, Section 2.7 justified the modelling approach taken within this work on a component-by-component basis. It began by reviewing the underlying structure of a hydrological model. A fully-distributed model will be adopted for the hydrological model in this thesis as these models are conceived from physical laws and equations where outputs are given at spatial and temporal resolutions. As the key motivation of this work centres around land-use policy planning and flood risk assessment it is viewed that this modelling structure is the most suitable for the context. The interception component of a hydrological model is a key factor in the total input of water available when calculating overland flow. An empirical approach will be adopted to represent this component to minimise the overall complexity of the model. The Green-Ampt model is adopted for the unsaturated zone component of the model due to its well established and robust catalogue of parameters that are physically intuitive and can be easily applied. The overland flow and routing component will apply the 2D diffusion wave approximation to the shallow water equations. It will apply the Godunov Finite Volume difference scheme with the friction component modelled from Xia et al. (2017) and Xia and Liang (2018). The remaining three modelling components are not included in the construction of the hydrological model. Their justifications are given in Sections 2.7.4, 2.7.5 and 2.7.6 for the Snowmelt, Evapotranspiration and Saturated Zone components respectively.

This chapter has determined what comprises a hydrological model (**RQ1**). It has also given a comprehensive review of the modelling techniques and contexts in which they are applied (**RQ2**). Section 2.7 has determined the approach and techniques that will be applied to construct a hydrological model in this work (**RQ3**). Finally, Tables 2.1, 2.2 and 2.3 have begun to outline how models are validated, verified and calibrated in



their specific contexts (**RQ4**). Chapter 3 will discuss the underlying methodology which underpins the hydrological model that is constructed in this work. Chapter 4 will outline the construction of the model based on the review conducted within this chapter.

# 3. Underlying Modelling Foundation

## 3.1. Introduction

Chapter 1 provided the themes on which this thesis is based. In particular, humankind’s need to equitably and sustainably use finite resources to attain our material, cultural and fundamental needs. Cornwall Council set a comprehensive policy platform looking to transition to a low-carbon green economy to meet its own needs (Section 1.1.5). One of its key aims is to construct 52,500 homes by 2030. This will have a significant impact on the local flood-plain hydrological characteristics and so an “environmental management system” to support environmental growth was also included. Many academic parallels exist between this proposed management platform and the “facilities management” industry (Section 1.1.6). Within this thesis it is proposed that a portfolio management dashboard such as *MyFM* could be utilised as a policy guidance tool to inform policy makers of the potential flooding impacts on proposed development sites. Underneath this front-end dashboard would be the hydrological modelling computational tool. Chapter 2 reviewed the literature from which such a hydrological model could be developed. Section 2.2 looked at the individual components that can make up a hydrological model. Section 2.3 gave an overview of the computational mesh options available to a hydrological model. Sections 2.4 and 2.5 illustrated the two main categories of hydrological models, semi-distributed and fully-distributed, respectively, utilising specific model examples from the literature. Section 2.6 outlined the research gap this thesis intends to fill. Finally, Section 2.7 justified the approach taken in constructing the hydrological model in this work. The reasoning provided was given in context of the specific case study chosen, highlighted in Section 1.2.

In this chapter, the underlying modelling theory which underpins the computational hydrological model developed in Chapter 4 is given. References to Appendices A and B are provided throughout to point the user to the underlying mathematical theory of the modelling techniques discussed in this chapter. To begin, a review of the properties of the Riemann problem are given from the perspective of the linear advection equation in Section 3.2. This understanding is expanded to the linear and multivariate cases (Sections 3.2.2 and 3.2.3 respectively) where a general solution structure to the Riemann problem (Section 3.2.3.1) is given as well as an illustration of the  $2 \times 2$  case. Godunov’s numerical method is introduced in Section 3.4.1 with its application to local Riemann problems to solve the linear advection equation. This methodology is built upon to discuss the two-dimensional Godunov first-order upwind method (Section 3.4.6). A brief overview on Total Variation Diminishing theory is given in Section 3.5. This chapter will conclude by looking into the background of point infiltration modelling from first principles (Section

3.6) with an emphasis on the *Green-Ampt* infiltration model (Section 3.6.1) and the *SCS Method* (Section 3.6.2) for non-urban and urban regions respectively.

## 3.2. The Riemann Problem

### 3.2.1. An Initial Value Problem using a Linear Advection Equation

Consider the time-dependent one-dimensional linear advection equation and initial condition

$$\begin{cases} u_t + au_x = 0, & -\infty \leq x \leq \infty, \quad t > 0 \\ u(x, 0) = u_0(x). \end{cases} \quad (3.1)$$

Here, Equation (3.1) admits a solution  $u = f(x - at)$ , which moves at speed  $a$ .  $a$  is more commonly referred to as the constant wave propagation speed. At initial time  $t = 0$ ,  $u$  is solely a function in the spatial domain and denoted  $u_0(x)$ . The simplicity of problem (3.1) is the foundation to build an understanding of what the Riemann problem is. An understanding of the basic hyperbolic partial differential equation properties such as its characteristic and the general solution structure is given in Appendix (A.1.2; page 301).

### 3.2.2. The Riemann Problem: A Linear Case

The Riemann problem is a special case of an initial value problem. Using the linear advection equation from (3.1) let us redefine the initial condition as follows

$$\begin{cases} u_t + au_x = 0 \\ u(x, 0) = u_0(x) = \begin{cases} u_l & \text{if } x < 0 \\ u_r & \text{if } x > 0. \end{cases} \end{cases} \quad (3.2)$$

Shown in Figure 3.1 are the two constant values  $u_l$  (left) and  $u_r$  (right) of the discontinuity at  $x = 0$ . The constant values are often times referred to as the left and right *Riemann states*.

Using the *method of characteristics* analytical technique (discussed in Appendix (A.1.2.1; page 301)), all the points on the initial profile may be expected to propagate a distance  $at$  in time  $t$ . More specifically, the initial discontinuity at  $x = 0$  should propagate a distance  $at$  in time  $t$ . This specific characteristic curve at the discontinuity defines a boundary between characteristic curves to the left with solution  $u_l$  and characteristics to the right with solution  $u_r$ . This solution structure is highlighted in Figure 3.2. A detailed summary of the general solution structure is in Appendix (A.1.2.1). As the initial conditions

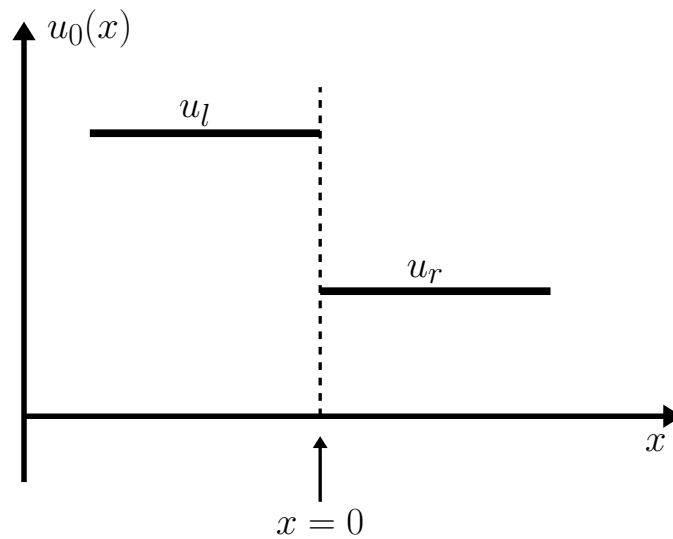


Figure 3.1.: A diagram of the initial data or *Riemann states* for the Riemann problem. At  $t = 0$  the initial data consists of two constant states separated at a discontinuity  $x = 0$ .

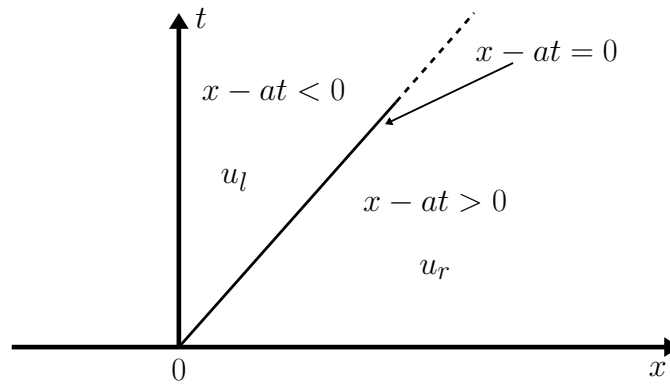


Figure 3.2.: A pictorial representation for the solution to the Riemann Problem in the  $x-t$  plane for the linear advection equation where the characteristic speed  $a > 0$ .

are constant on either side of the characteristic curve, one may define the solution to the Riemann problem presented in (3.2) as

$$u(x, t) = u_0(x - at) = \begin{cases} u_l & \text{if } x - at < 0 \\ u_r & \text{if } x - at > 0. \end{cases} \quad (3.3)$$

Illustrated in Figure 3.2 is the solution described in (3.3) in the  $x-t$  plane. One may draw a characteristic through a point  $x_0$  on the  $x$ -axis. Since  $a$  is constant, each characteristic is parallel to one another. The characteristic which passes through the discontinuity  $x = 0$  defines the boundary from which the solution changes.

### 3.2.3. The Riemann Problem: A multivariate case

Sections 3.2.1 - 3.2.2 discussed the linear Riemann problem by considering a linear advection equation in one-spatial dimension. This section will build on this analysis by expanding this understanding to the multivariate Riemann problem using a set of  $m$  hyperbolic PDEs expressed as

$$\mathbf{U}_t + \mathbf{A}\mathbf{U}_x = \mathbf{0}, \quad (3.4)$$

with coefficient entries in  $\mathbf{A}$  all constant. Using the assumption of hyperbolicity the matrix  $\mathbf{A}$  has  $m$  real eigenvalues  $\lambda^{(i)}$  with corresponding linearly independent eigenvectors  $\mathbf{e}^{(i)}$  where  $i \in \{1, \dots, m\}$ . The general theory relating to linear hyperbolic systems may be viewed in Appendix (A.1.3; page 302). Consider the Riemann problem for the hyperbolic, constant coefficient system (3.4), mathematically expressed as

$$\begin{cases} \mathbf{U}_t + \mathbf{A}\mathbf{U}_x = \mathbf{0}, & -\infty < x < \infty, t > 0 \\ \mathbf{U}(x, 0) = \mathbf{U}^{(0)}(x) = \begin{cases} \mathbf{U}_l & x < 0, \\ \mathbf{U}_r & x > 0. \end{cases} \end{cases} \quad (3.5)$$

The above problem (3.5) is a generalised expression of (3.2). It is assumed that the system is strictly hyperbolic. As such the real and distinct eigenvalues are ordered as

$$\lambda^{(1)} < \lambda^{(2)} < \dots < \lambda^{(m)}. \quad (3.6)$$

#### 3.2.3.1. A General Solution Structure

Figure 3.3 pictorially represents the solution structure of the Riemann problem (3.5) in the  $x-t$  plane.  $m$  waves emerge from the origin. Each wave relates to each eigenvalue  $\lambda^{(i)}$ . Every wave  $i$  contains a **jump discontinuity** in  $\mathbf{U}$  propagating with speed  $\lambda^{(i)}$ . To the left of the  $\lambda^{(1)}$ -wave, the solution is simply the initial data  $\mathbf{U}_l$ . Similarly, to the right of the  $\lambda^{(m)}$ -wave is the solution  $\mathbf{U}_r$ .

The problem before us is to construct a solution between the internal sections from the  $\lambda^{(1)}$ - and  $\lambda^{(m)}$ -waves. Utilising the fact that the eigenvectors  $\mathbf{E}^{(1)}, \dots, \mathbf{E}^{(m)}$  are linearly independent, one can expand the constant left and right states as linear combinations of

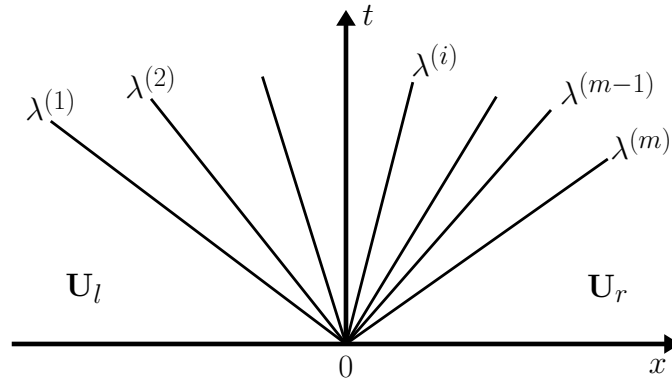


Figure 3.3.: The solution structure for the general  $m \times m$  Riemann problem of a linear hyperbolic system with constant coefficients.

these eigenvectors i.e.

$$\mathbf{U}_l = \sum_{i=1}^m a_i \mathbf{E}^{(i)}, \quad \mathbf{U}_r = \sum_{i=1}^m b_i \mathbf{E}^{(i)}, \quad (3.7)$$

with constant coefficients  $a_i, b_i$ . The fundamental theory used here is discussed in Appendix (A.1.3.1; page 302). Considering the problem in terms of its characteristic variables we have  $m$  scalar Riemann problems for the PDEs

$$\frac{\partial w_i}{\partial t} + \lambda^{(i)} \frac{\partial w_i}{\partial x} = 0. \quad (3.8)$$

Using a similarity argument one may translate the initial conditions of the Riemann problem in (3.2) to give the initial conditions for the characteristic equation (3.9). Equivalently, the solution for the characteristic equation may be reached by comparing and contrasting the solution of the linear advection equation (3.3) to yield (3.10).

$$w_i^{(0)} = \begin{cases} a_i & \text{if } x < 0 \\ b_i & \text{if } x > 0. \end{cases} \quad (3.9)$$

Hence comparing the solution structure from the scalar Riemann problems each characteristic variable has the solution

$$w_i(x, t) = w_i^{(0)}(x) = \begin{cases} a_i & \text{if } x - \lambda^{(i)}t < 0 \\ b_i & \text{if } x - \lambda^{(i)}t > 0. \end{cases} \quad (3.10)$$

For any given point  $(x, t)$  there exists an eigenvalue  $\lambda^{(I)}$  such that  $\lambda^{(I)} < x/t < \lambda^{(I+1)}$ . In other words,  $x - \lambda^{(i)}t > 0$ ,  $\forall i$  such that  $i \leq I$ . Note here that  $x/t$  may also be less than (or greater than) every single eigenvalue. As such the final solution of the Riemann problem may be written in terms of the original variables as

$$\mathbf{U}(x, t) = \sum_{i=I+1}^m a_i \mathbf{E}^{(i)} + \sum_{i=1}^I b_i \mathbf{E}^{(i)}, \quad (3.11)$$

where the integer  $I = I(x, t)$  is the maximum value of the sub-index  $i$  for which  $x - \lambda^{(i)}t > 0$ .

### 3.2.3.2. A $2 \times 2$ system example

To illustrate the theory that is presented in Section 3.2.3.1 consider a general  $2 \times 2$  linear hyperbolic system. Figure 3.4 shows two waves emerging from the origin  $(0, 0)$  in the  $(x, t)$  plane with speeds equal to  $\lambda^{(1)}$  and  $\lambda^{(2)}$ .

To the left of  $dx/dt = \lambda^{(1)}$  is the initial state  $\mathbf{U}_l = a_1 \mathbf{E}^{(1)} + a_2 \mathbf{E}^{(2)}$ . Similarly, the initial state  $\mathbf{U}_r = b_1 \mathbf{E}^{(1)} + b_2 \mathbf{E}^{(2)}$  is the solution to the right of the ODE  $dx/dt = \lambda^{(2)}$ . The section to the right of the left wave and left of the right wave is most commonly referred to as the *star region* with the solution denoted  $\mathbf{U}_*$ . Its value is determined by considering the pathway of the two waves which emanate from the origin of the initial discontinuity.

Starting from a point  $P_*(x, t)$  within the star region we trace along the characteristic curves with speeds  $\lambda^{(1)}$  and  $\lambda^{(2)}$ . These characteristics are represented by the dashed lines in Figure 3.4 and are parallel to the characteristics which pass through the origin. The characteristic curves which pass through  $P_*$  also pass through the initial points  $x_0^{(1)} = x - \lambda^{(1)}t$  and  $x_0^{(2)} = x - \lambda^{(2)}t$ .

The solution may be expressed in the form of (3.11) and now one must select the correct corresponding coefficients which satisfy these characteristic curves. A time  $t^*$  and point  $x_l$  to the left of the slowest wave is chosen so that  $\mathbf{U}(x_l, t^*) = \mathbf{U}_l$ . Highlighted in Figure 3.5

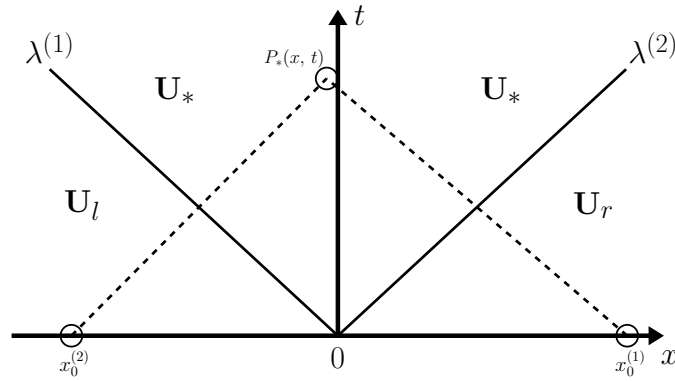


Figure 3.4.: The solution structure for the  $2 \times 2$  Riemann problem of a linear hyperbolic system with constant coefficients.

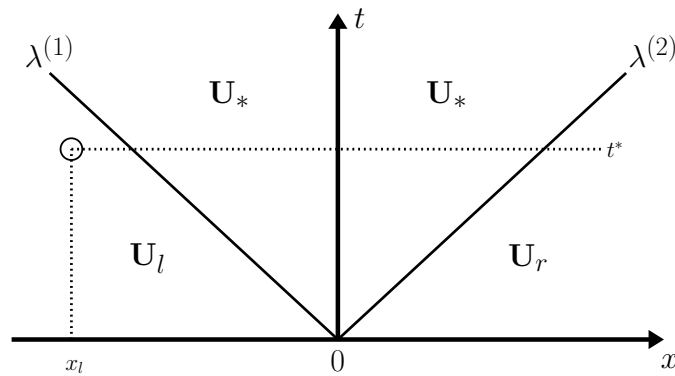


Figure 3.5.: One may find the solution to the Riemann problem for the  $2 \times 2$  linear hyperbolic system by tracing along the dashed horizontal line at  $t = t^*$ .

is the starting point  $(x_l, t^*)$ . Since this is to the left of the  $\lambda^{(1)}$ -wave every coefficient is  $a_i$ . As we trace the horizontal line  $t = t^*$  we eventually pass the wave  $dx/dt = \lambda^{(1)}$ , where  $x - \lambda^{(1)}t$  changes sign (as expressed in (3.10)). As such the constant coefficient changes from  $a_1$  to  $b_1$ . Hence, the solution within the entire star region between the two waves is

$$\mathbf{U}_*(x, t) = b_1 \mathbf{E}^{(1)} + a_2 \mathbf{E}^{(2)}. \quad (3.12)$$

Continuing to move rightward one eventually crosses the  $\lambda^{(2)}$  wave where  $x - \lambda^{(2)}t$  changes from negative to positive. Again, utilising the result in (3.10) the right initial state i.e. the solution to the right of the fastest wave speed is obtained,

$$\mathbf{U}_r(x, t) = b_1 \mathbf{E}^{(1)} + b_2 \mathbf{E}^{(2)}. \quad (3.13)$$



### 3.3. Conservation Laws

#### 3.3.1. Rankine-Hugoniot Conditions

Within a one-dimensional fluid flow, the relationship between two different fluid characteristics on either side of a shock wave is known as the *Rankine-Hugoniot conditions* or *Rankine-Hugoniot jump conditions*. This is named after the work produced by William J. M. Rankine and Pierre H. Hugoniot (Rankine, 1870; Hugoniot, 1887, 1889; Salas, 2006).

Given a system of hyperbolic conservation laws

$$\mathbf{U}_t + \mathbf{F}(\mathbf{U})_x = \mathbf{0}, \quad (3.14)$$

with a discontinuous wave solution of speed  $S_i$  and corresponding characteristic speed  $\lambda_i(\mathbf{U})$ , the Rankine-Hugoniot conditions state that the difference in flux either side of the discontinuity is equal to the product between the difference in respective states immediately to the left and right of the discontinuity and the wave solution of speed  $S_i$  i.e.

$$\Delta \mathbf{F} = S_i \Delta \mathbf{U} \quad (3.15)$$

where

$$\Delta \mathbf{U} \equiv \mathbf{U}_r - \mathbf{U}_l, \Delta \mathbf{F} \equiv \mathbf{F}_r - \mathbf{F}_l, \mathbf{F}_r = \mathbf{F}(\mathbf{U}_r), \mathbf{F}_l = \mathbf{F}(\mathbf{U}_l).$$

$\mathbf{U}_l$  and  $\mathbf{U}_r$  denote the states immediately to the left and right of the discontinuity respectively. Figure 3.6 shows these conditions for the case of a single discontinuity.

Typically, it is difficult to be able to determine speed  $S_i$  as a function of initial states.

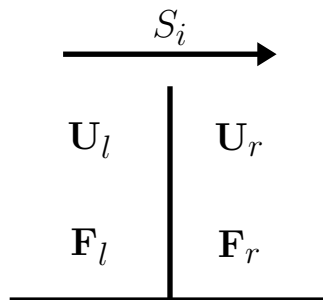


Figure 3.6.: Rankine-Hugoniot conditions for a single discontinuity of speed  $S_i$ . The two constant states  $\mathbf{U}_l$  and  $\mathbf{U}_r$  are connected via a system of conservation laws.

When we consider a linear system with constant coefficients such as Equation (3.4) at the top of Section 3.2.3 on page 101 with eigenvalues  $\lambda_i$ ,  $i \in \{1, \dots, m\}$ . Its Rankine-Hugoniot conditions across the discontinuous wave of speed  $S_i \equiv \lambda_i$  is

$$\Delta \mathbf{F} = \mathbf{A} \Delta \mathbf{U} = \lambda_i (\Delta \mathbf{U})_i. \quad (3.16)$$

These conditions allow us to construct solutions of the Riemann problem for a hyperbolic system more efficiently.

### 3.3.2. Elementary-Wave Solutions of the Riemann Problem

Consider a quasi-linear hyperbolic system

$$\mathbf{W}_t + \mathbf{A}(\mathbf{W}) \mathbf{W}_x = \mathbf{0}, \quad (3.17)$$

where

$$\mathbf{W} = [\omega_1, \omega_2, \dots, \omega_m]^T. \quad (3.18)$$

Consider applying a solution to the Riemann problem for a general  $m \times m$  non-linear hyperbolic system with initial data  $\mathbf{U}_l$ ,  $\mathbf{U}_r$  and the Initial Value Problem:

$$\begin{cases} \mathbf{U}_t + \mathbf{F}(\mathbf{U})_x = \mathbf{0} \\ \mathbf{U}(x, 0) = \mathbf{U}_0(x) = \begin{cases} \mathbf{U}_l, & \text{if } x < 0 \\ \mathbf{U}_r, & \text{if } x > 0. \end{cases} \end{cases} \quad (3.19)$$

Section 3.3 outlines all the relevant theory needed to reach Equation (3.19). A similarity solution of Equation (3.11) to Equation (3.17) is composed of  $m + 1$  constant states with  $m$  waves separating it. This solution is denoted as  $\mathbf{U}(x/t)$  and illustrated in Figure 3.7.

For each wave an eigenvalue,  $\lambda_i$ , defines a wave family. Within a linear system with constant coefficients, each wave discontinuity of speed  $S_i = \lambda_i$  defines a linearly degenerate field. In non-linear systems, wave discontinuities may present themselves as shock waves or contact waves. They may also transition smoothly as rarefactions. The definition of these waves depends solely on the Riemann states of the Riemann problem for each specific wave. Each of the three wave possibilities and their solutions are considered in Appendix Sections (A.3.4) - (A.3.6).

Assuming the Riemann states  $\mathbf{U}_l$  and  $\mathbf{U}_r$  are connected by a single wave and all other waves contain zero strength, the solution of the Riemann problem consists of a single

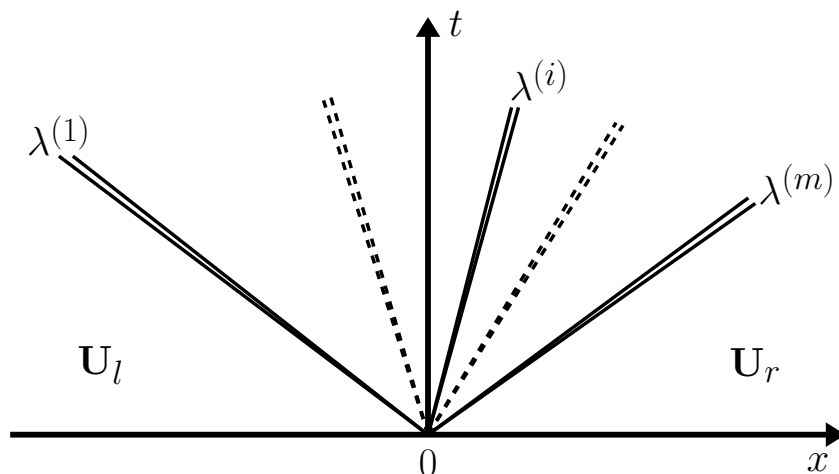


Figure 3.7.: A solution structure for the Riemann problem within a non-linear system of conservation laws.

non-trivial wave. In practice, a common approach is to select constant states that reside either side of a contact wave and if it is a discontinuity, results in either a shock or contact wave.

### 3.4. Godunov's Numerical Method

When considering the simulation of flooding events one has to consider the wetting and drying processes on complex terrain and adjacent grid pixels. Such scenarios are likely to contain solutions with discontinuities such as shock waves. Specific constraints on the mathematical formulations of governing equations and individual numerical schemes are needed to be able to solve such problems.

One such constraint is that variables within the governing equations must be *conserved*. It is not within this work's remit to explain why this is the case. However, work by Hou and LeFloch (1994) highlights in depth that non-conservative variables do not capture the required behaviour at a discontinuous wet-dry interface.

A fundamental result from Lax and Wendroff (1960) states that if conservative numerical methods are convergent then they converge to a weak solution of the conservation law. When considering the modelling of flooding scenarios, pixels are likely to begin dry and become wet. This is a common example of shock wave behaviour. To capture such properties, a conservative numerical method is needed.

Consider the scalar conservation law of the linear advection equation (3.1) in integral form

$$\int (u dx - f dt) = 0, \quad (3.20)$$

where for a given rectangular control volume  $[x_1, x_2] \times [t_1, t_2]$ ,

$$\int_{x_1}^{x_2} u(x, t_2) dx = \int_{x_1}^{x_2} u(x, t_1) dx + \int_{t_1}^{t_2} f(u(x_1, t)) dt - \int_{t_1}^{t_2} f(u(x_2, t)) dt. \quad (3.21)$$

### 3.4.1. A Conservative Method

For the scalar conservation law (3.20), a conservative numerical method takes the form

$$u_i^{(k+1)} = u_i^{(k)} + \frac{\Delta t}{\Delta x} \left( f_{i-\frac{1}{2}} - f_{i+\frac{1}{2}} \right), \quad (3.22)$$

where the numerical flux  $f_{i+\frac{1}{2}}$  is an approximation to the physical flux  $f(u)$  defined as

$$f_{i+\frac{1}{2}} = f_{i+\frac{1}{2}} \left( u_{i-a_l}^{(k)}, \dots, u_{i+a_r}^{(k)} \right). \quad (3.23)$$

$a_l, a_r$  are two non-negative integers. A fundamental property of the numerical flux is the **consistency** condition

$$f_{i+\frac{1}{2}}(v, \dots, v) = f(v). \quad (3.24)$$

In other words, if all the numerical flux arguments in (3.23) equate to  $u^{(k)}$  then the numerical flux is identical to the physical flux. Further analysis of this property may be seen in LeVeque (1992). One may also derive a second conservative method:

$$u_i^{(k+1)} = u_i^{(k)} + \frac{\Delta t}{\Delta x} \left[ f_{i-\frac{1}{2}} - f_{i+\frac{1}{2}} \right], \quad (3.25)$$

where

$$f_{i-\frac{1}{2}} = \frac{1}{\Delta t} \int_0^{\Delta t} f \left( \tilde{u} \left( x_{i-\frac{1}{2}}, t \right) \right) dt, \quad f_{i+\frac{1}{2}} = \frac{1}{\Delta t} \int_0^{\Delta t} f \left( \tilde{u} \left( x_{i+\frac{1}{2}}, t \right) \right) dt \quad (3.26)$$

are the intercell fluxes defined as time integral averages. Further information on the derivation of Equation (3.25) is in Appendix (A.4.3; page 335).

### 3.4.2. Defining a local Riemann problem

Sergei K. Godunov was first to expand on the conservative numerical modelling of a first-order upwind scheme by **Courant, Isaac and Rees** Courant et al. (1952) by extending the analysis to non-linear hyperbolic laws. Further literature on the **CIR** scheme can be

found at (Toro et al., 1994, pg. 168) and references therein.

The specific numerical modelling begins with a conservative method of the form shown in Equation (3.22) in Section 3.4.1. The intercell numerical fluxes,  $f_{i-\frac{1}{2}}$  and  $f_{i+\frac{1}{2}}$ , are calculated via solutions of local Riemann problems.

One fundamental assumption needed for this computation is that, at a given timestep  $k$ , initial data is a piece-wise constant distribution. It is more convenient to think at timestep  $k$ , that data are pairs of constant states  $(u_i^{(k)}, u_{i+1}^{(k)})$  with a discontinuity at the intercell boundary  $x_{i+\frac{1}{2}}$ .

From this construction, one can define the **local Riemann problem** at the given timestep  $k$  at each intercell boundary  $x_{i+\frac{1}{2}}$  as RP  $(u_i^{(k)}, u_{i+1}^{(k)})$  with initial data  $(u_i^{(k)}, u_{i+1}^{(k)})$  i.e.

$$\begin{cases} u_t + f(u)_x = 0 \\ u(x, 0) = u_0(x) = \begin{cases} u_i^{(k)} & \text{if } x < 0, \\ u_{i+1}^{(k)} & \text{if } x > 0. \end{cases} \end{cases} \quad (3.27)$$

This local Riemann problem definition may be applied numerous times to determine a solution for the **global** problem at timestep  $k + 1$ .

### 3.4.3. Transparent Boundary Conditions

The conservative method (3.25) may be computed for pixels  $i \in \{2, \dots, n-1\}$ . For each corresponding Riemann problem the fluxes are defined at the intercell boundaries  $x_{i-\frac{1}{2}}$  and  $x_{i+\frac{1}{2}}$ . For pixels 1 and  $n$ , each only contain one intercell flux to the right and left of each respective cell.

Consider the left boundary at  $i = 1$  where  $f_{\frac{3}{2}}$  exists but  $f_{\frac{1}{2}}$  does not. One can specify a **fictitious cell** at  $i = 0$  with a cell average  $u_0^{(k)}$  at each timestep. From this construction, define a Riemann problem RP  $(u_0^{(k)}, u_1^{(k)})$  which can be solved to determine the intercell flux  $f_{\frac{1}{2}}$ . This construction can be emulated on the right hand boundary. Define a fictitious cell  $i = n + 1$  and cell average  $u_{n+1}^{(k)}$  so that the Riemann problem RP  $(u_n^{(k)}, u_{n+1}^{(k)})$  may be resolved to find the intercell flux  $f_{n+\frac{1}{2}}$ .

It is common practice to define the cell averages of the fictitious pixels as data at the cell averages adjacent to the boundaries i.e.

$$u_0^{(k)} = u_1^{(k)}, \quad u_{n+1}^{(k)} = u_n^{(k)}. \quad (3.28)$$

Defining the boundary condition this way will see no disturbances caused at the boundaries. Waves will go through the intercell fluxes  $f_{\frac{1}{2}}$  and  $f_{n+\frac{1}{2}}$  as if they were not there.

These are typically referred to as *transparent* or *transmissive* boundary conditions.

### 3.4.4. Timestep choice

Explicit time integration schemes timestep choice are restricted due to the numerical domain of dependence. This is outlined further in Appendix Sections (A.2.1) - (A.2.4). Similar constraints exist in conservative methods. For Godunov's method, the choice  $\Delta t$  is dependent on the Courant number  $C$ .

For non-linear problems, at each time steps, multiple wave speeds exist and thus multiple associated Courant numbers need to be considered. When discussing the second interpretation of Godunov's method (Equation (3.25); its derivation is outlined further in Appendix A.4.3), it is implicitly assumed that the solution to the local Riemann problem is constant along the intercell boundaries. Hence, the fastest wave at any given timestep travels for at most a single cell length,  $\Delta x$ , within timestep  $\Delta t$ . Representing the maximum wave speed through the domain at  $t = k$  as  $S_{\max}^{(k)}$ , the *maximum Courant number*  $C_{\text{cfl}}$ , known as the *CFL coefficient* is defined as

$$C_{\text{cfl}} = \frac{\Delta t S_{\max}^{(k)}}{\Delta x}. \quad (3.29)$$

$\Delta t$  is determined so that

$$0 < C_{\text{cfl}} < 1. \quad (3.30)$$

Hence,

$$\Delta t = \frac{C_{\text{cfl}} \Delta x}{S_{\max}^{(k)}}. \quad (3.31)$$

Estimating the maximum speed  $S_{\max}^{(k)}$  can be very difficult and frustrating when simulating realistic scenarios. Possible estimation methods could include:

1. Obtain the absolute value maximum characteristic speed  $u_i^{(k)}$  out of the  $n + 2$  available at any timestep  $k$ ;
2. Find the absolute value speed  $S_{i+\frac{1}{2}}^{(k)}$  from the Riemann problem solution at every timestep  $k$  as this information is available through the flux estimation computation. One has to take account as to the wave behaviour and so intercell speed would be defined as

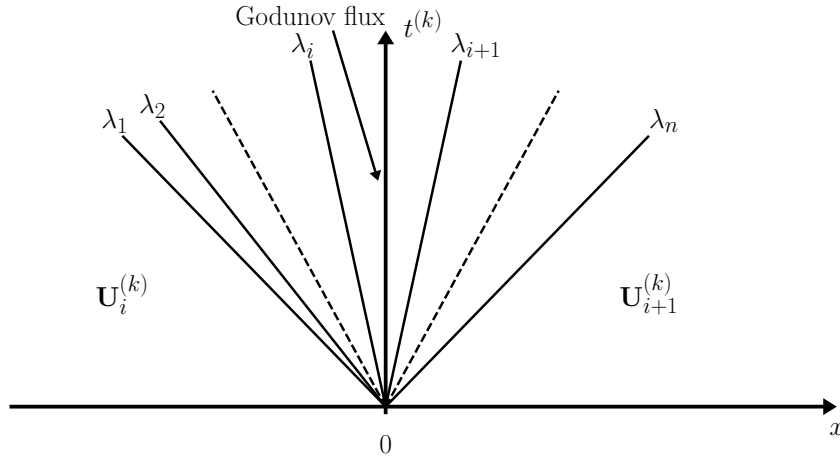


Figure 3.8.: The computation of a Godunov intercell flux for a linear hyperbolic system with constant coefficients.

$$S_{i+\frac{1}{2}}^{(k)} = \begin{cases} \left| \frac{1}{2} (u_i^{(k)} + u_{i+1}^{(k)}) \right| & \text{(Shock)} \\ \max \left( |u_i^{(k)}|, |u_{i+1}^{(k)}| \right) & \text{(Rarefaction)}. \end{cases} \quad (3.32)$$

From (3.32) one may then define the maximum wave speed at  $t = k$  as

$$S_{\max}^{(k)} = \max_i \left\{ S_{i+\frac{1}{2}}^{(k)} \right\} \quad \text{where } i \in \{0, \dots, n+1\}. \quad (3.33)$$

By choosing the CFL coefficient, the timestep  $\Delta t$  is determined as illustrated in (3.31). Typically the empirical value  $C_{\text{cfl}} = 0.9$  is used for the linear stability condition  $|c| \leq 1$ .

### 3.4.5. Godunov's Method

Consider the constant coefficient, linear hyperbolic system written in conservative form as

$$\mathbf{U}_t + \mathbf{F}(\mathbf{U})_x = \mathbf{0}, \quad \mathbf{F}(\mathbf{U}) = \mathbf{A}\mathbf{U}. \quad (3.34)$$

A more general review of quasi-linear hyperbolic equations is given in Appendix (A.1.1). A Godunov first-order upwind method applies the conservative formula (3.25). To determine the intercell numerical flux,

$$\mathbf{F} \left( \mathbf{U}_{i+\frac{1}{2}}(0) \right), \quad (3.35)$$

the solution of the local Riemann problem,  $\text{RP} \left( \mathbf{U}_i^{(k)}, \mathbf{U}_{i+1}^{(k)} \right)$ , denoted  $\mathbf{U}_{i+\frac{1}{2}}(x/t)$  is needed. In this instance,  $\mathbf{U}_{i+\frac{1}{2}}(0)$  is the value of the solution at  $x/t = 0$ . This is pictured in Figure 3.8.

In Section 3.2.3 the general solution structure of the Riemann problem in the  $x - t$  plane where each wave relates to an eigenvalue  $\lambda^{(i)}$  with an associated eigenvector was discussed. This work also allowed the expansion of the left and right states as linear combinations of the eigenvectors.

Building on the work described above, expand the initial Riemann states with constant coefficients  $a_j, b_j$

$$\mathbf{U}_i^{(k)} = \sum_{j=1}^n a_j \mathbf{E}^{(j)}, \quad \mathbf{U}_{i+1}^{(k)} = \sum_{j=1}^n b_j \mathbf{E}^{(j)}. \quad (3.36)$$

Thus, at any point in the  $x - t$  plane the general solution is given by

$$\mathbf{U}_{i+\frac{1}{2}}(x/t) = \sum_{j=1}^I b_j \mathbf{E}^{(j)} + \sum_{j=I+1}^n a_j \mathbf{E}^{(j)}. \quad (3.37)$$

$I$  is the largest integer where  $I \in [1, n]$  such that  $\lambda^{(I)} \leq x/t$ .

The Godunov flux at  $x/t = 0$  requires an integer  $I$  such that  $\lambda^{(I)} \leq 0$  and  $0 \leq \lambda^{(I+1)}$ . Provided this criteria is met, one can then use (3.37) to determine a solution as either

$$\mathbf{U}_{i+\frac{1}{2}}(0) = \mathbf{U}_i^{(k)} + \sum_{j=1}^I (b_j - a_j) \mathbf{E}^{(j)} \quad (3.38)$$

or

$$\mathbf{U}_{i+\frac{1}{2}}(0) = \mathbf{U}_{i+1}^{(k)} - \sum_{j=I+1}^n (b_j - a_j) \mathbf{E}^{(j)}. \quad (3.39)$$

The discontinuous jump across wave  $j$  with eigenvalue  $\lambda^{(j)}$  is captured by the difference between the constant coefficients  $(b_j - a_j)$ . The solution to the Riemann problem at  $x/t = 0$  is interpreted as the left initial state  $\mathbf{U}_i^{(k)}$  summed with every wave jump across waves of negative or zero speed. Similarly, (3.39) begins with the right initial state  $\mathbf{U}_{i+1}^{(k)}$  minus the wave jumps across each wave of non-negative speeds.

A full solution structure may be ascertained by combining (3.38) and (3.39)

$$\mathbf{U}_{i+\frac{1}{2}} = \frac{1}{2} \left( \mathbf{U}_i^{(k)} + \mathbf{U}_{i+1}^{(k)} \right) - \frac{1}{2} \sum_{j=1}^m \text{sign}(\lambda^{(j)} (b_j - a_j)) \mathbf{E}^{(j)}. \quad (3.40)$$

Finally, one can implement any solution structure (3.38) - (3.40) to obtain the Godunov



intercell flux (3.35), which when applied respectively with eigendecomposition are

$$\mathbf{F}_{i+\frac{1}{2}} = \mathbf{F}_i^{(k)} + \sum_{j=1}^I (b_j - a_j) \lambda^{(j)} \mathbf{E}^{(j)}, \quad (3.41)$$

$$\mathbf{F}_{i+\frac{1}{2}} = \mathbf{F}_{i+1}^{(k)} - \sum_{j=I+1}^n (b_j - a_j) \lambda^{(j)} \mathbf{E}^{(j)}, \quad (3.42)$$

$$\mathbf{F}_{i+\frac{1}{2}} = \frac{1}{2} \left( \mathbf{F}_i^{(k)} + \mathbf{F}_{i+1}^{(k)} \right) - \frac{1}{2} \sum_{j=1}^m (b_j - a_j) |\lambda^{(j)}| \mathbf{E}^{(j)}. \quad (3.43)$$

Toro et al. (1994) (pg. 192-193) shows two further ways in which the Godunov flux may be written.

### 3.4.6. Two-dimensional finite volume method

Highlighted in Section 2.2.3, at least two dimensions are needed to understand the spatial variance of overland flow. Methodology on how conservative methods may be used over a finite control volume in a single dimension are considered in Appendix (A.4.1). The method outlined in this section is an extension of this.

Consider the time-dependent two-dimensional conservation law

$$\mathbf{U}_t + \mathbf{F}(\mathbf{U}_x) + \mathbf{G}(\mathbf{U}_y) = \mathbf{0}. \quad (3.44)$$

The domain is constructed so that the boundaries of each pixel align with the coordinate directions of the computational cell  $\Omega_{i,j}$ , where  $i, j$  refer to the positions of the x- and y-directions respectively. Each pixel has an area of  $\Delta x \times \Delta y$ . The cell average  $\mathbf{U}_{(i,j)}^{(k)}$  is located in the centre of the cell, thus giving its name to *cell centred methods*.

Figure 3.9 highlights the computational domain and the intercell boundaries which correspond to an individual numerical flux. From this construction, the explicit finite volume scheme to solve (3.44) would be

$$\mathbf{U}_{(i,j)}^{(k+1)} = \mathbf{U}_{(i,j)}^{(k)} + \frac{\Delta t}{\Delta x} \left( \mathbf{F}_{(i-\frac{1}{2},j)} - \mathbf{F}_{(i+\frac{1}{2},j)} \right) + \frac{\Delta t}{\Delta y} \left( \mathbf{G}_{(i,j-\frac{1}{2})} - \mathbf{G}_{(i,j+\frac{1}{2})} \right). \quad (3.45)$$

In this example, the cell average in  $\Omega_{i,j}$  is updated from  $t = k \rightarrow t = k + 1$  in a single timestep by considering every intercell boundary flux contribution. This is a natural extension of the one-dimensional conservative formula (3.22) discussed in Section 3.4.1. The most simple upwind finite volume method may be demonstrated through applying

the Godunov first-order upwind flux across each intercell boundary (presented in detail in Appendix Sections A.4.2 and A.4.3). Namely one can define the intercell boundary fluxes as

$$\mathbf{F}_{(i+\frac{1}{2},j)} = \mathbf{F} \left( \mathbf{U}_{(i+\frac{1}{2},j)}(0) \right), \quad \mathbf{G}_{(i,j+\frac{1}{2})} = \mathbf{G} \left( \mathbf{U}_{(i,j+\frac{1}{2})}(0) \right), \quad (3.46)$$

where  $\mathbf{U}_{(i+\frac{1}{2},j)}(x/t)$  is the solution to the Riemann problem

$$\begin{cases} \mathbf{U}_t + \mathbf{F}(\mathbf{U})_x = \mathbf{0}, \\ \mathbf{U}(x, 0) = \begin{cases} \mathbf{U}_{(i,j)}^{(k)} & \text{if } x < 0, \\ \mathbf{U}_{(i+1,j)}^{(k)} & \text{if } x > 0. \end{cases} \end{cases} \quad (3.47)$$

$\mathbf{U}_{(i,j+\frac{1}{2})}(x/t)$  is the solution to the Riemann problem

$$\begin{cases} \mathbf{U}_t + \mathbf{G}(\mathbf{U})_y = \mathbf{0}, \\ \mathbf{U}(x, 0) = \begin{cases} \mathbf{U}_{(i,j)}^{(k)} & \text{if } y < 0, \\ \mathbf{U}_{(i,j+1)}^{(k)} & \text{if } y > 0. \end{cases} \end{cases} \quad (3.48)$$

### 3.4.6.1. The Godunov Finite Volume Method

Consider the linear advection equation with constant positive velocity coefficients  $a_1, a_2$

$$u_t + f(u)_x + g(u)_y = 0, \quad f(u) = a_1 u, \quad g(u) = a_2 u. \quad (3.49)$$

By applying the first interpretation of Godunov's method (Equation (3.22); additional details in Appendix (A.4.2); page 334) one will obtain

$$u_{(i,j)}^{(k+1)} = u_{(i,j)}^{(k)} + c_1 \left( u_{(i-1,j)}^{(k)} - u_{(i,j)}^{(k)} \right) + c_2 \left( u_{(i,j-1)}^{(k)} - u_{(i,j)}^{(k)} \right), \quad (3.50)$$

where the Courant numbers in the x- and y-directions respectively are

$$c_1 = \frac{a_1 \Delta t}{\Delta x}; \quad c_2 = \frac{a_2 \Delta t}{\Delta y}. \quad (3.51)$$

Figure 3.10 illustrates the computational stencil. The point  $(i, j)$  is the centre of the stencil with pixel average  $u_{(i,j)}^{(k)}$ . Typically, the cell averages  $u_{(i-1,j)}^{(k)}$  and  $u_{(i,j-1)}^{(k)}$  are the

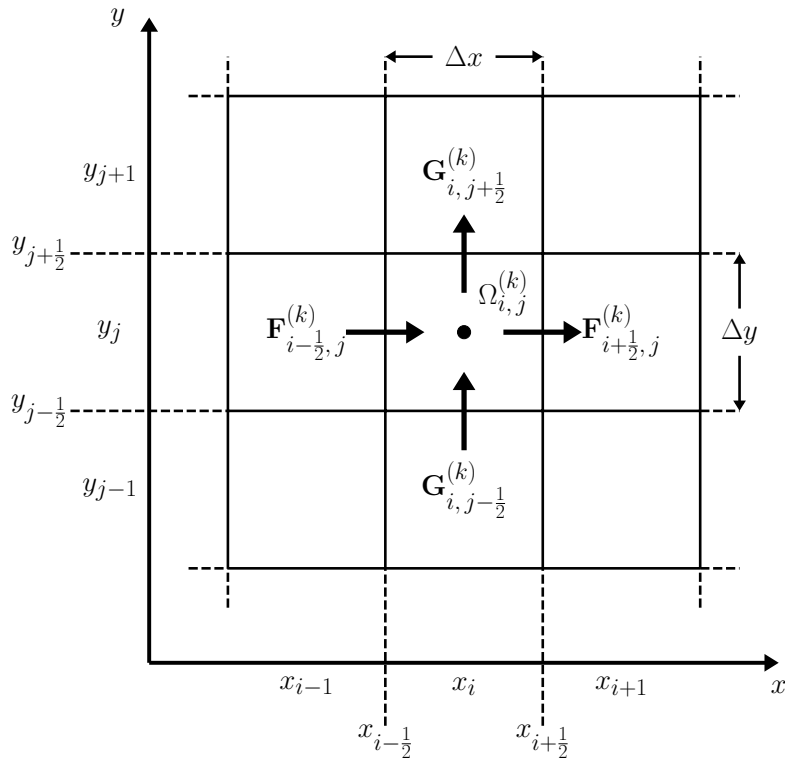


Figure 3.9.: A two-dimensional Cartesian domain discretised into finite volumes  $\Omega_{i,j}$  with an area of  $\Delta x \times \Delta y$ . Each computational pixel has four intercell boundaries (anti-clockwise)  $\mathbf{F}_{i-\frac{1}{2},j}$ ,  $\mathbf{G}_{i,j-\frac{1}{2}}$ ,  $\mathbf{F}_{i+\frac{1}{2},j}$ , and  $\mathbf{G}_{i,j+\frac{1}{2}}$ .

upwind values in the  $x$ - and  $y$ -directions respectively and are used to update the cell averages.

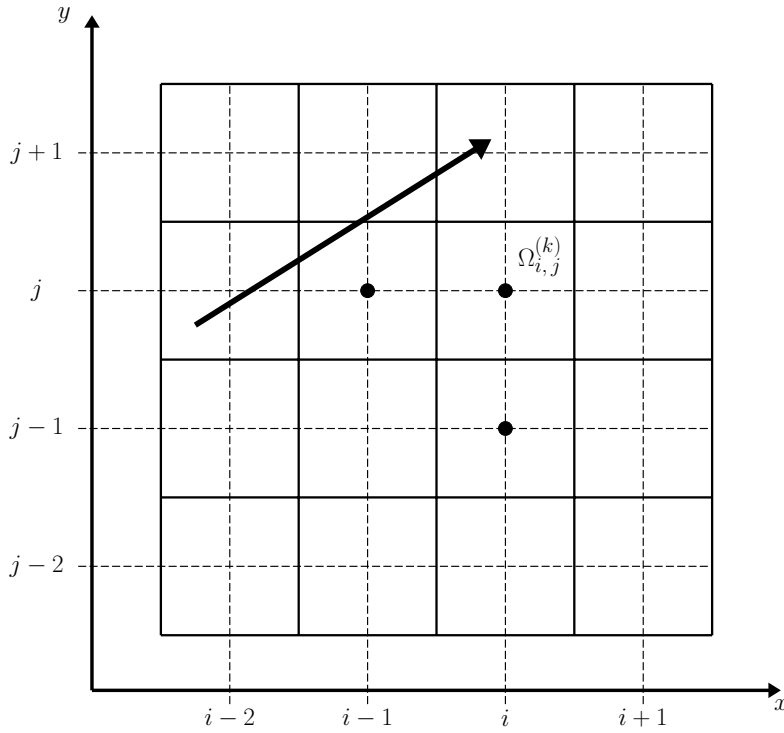


Figure 3.10.: A stencil for the Godunov finite volume scheme during the linear equation with positive velocity components  $a_1$  and  $a_2$ . The arrow denotes the direction of the velocity vector.

## 3.5. Total Variation Diminishing Methodology

### 3.5.1. Flux Limiters

Shocks, discontinuities or abrupt changes in the solution domain may result in unpredictable oscillations within high order spatial discretisation schemes. **Flux limiters** are specific numerical applications of total variation diminishing theory. The purpose of a flux limiter is to steer clear from spurious oscillations which would normally occur due to shocks, discontinuities and/or sharp changes in the solution domain. The same underlying theory may also be referred to as **slope limiters** referring to the situation when a limiter acts on system states such as pressure, velocity etc.

When numerically approximating scientific phenomena, one requires the results to be feasible physically and meaningful. Typically limiters are used when solving PDEs in high resolution methods where a sharp wave front is present. To understand how flux limiters are applied, consider the forward difference approximation for the linear advection equation (derived and discussed in Appendix (A.2.3)),

$$\frac{du_i}{dt} + \frac{1}{\Delta x_i} \left( f \left( u_{i+\frac{1}{2}} \right) - f \left( u_{i-\frac{1}{2}} \right) \right) = 0, \quad (3.52)$$

where  $a = 1$  and  $f(u_j)$  is some intercell boundary flux at  $x_j$ . Provided that these intercell fluxes may be calculated using low and high resolutions schemes, then a flux limiter may

switch between the schemes depending on the gradients close to the particular cell as follows

$$\begin{cases} f\left(u_{i+\frac{1}{2}}\right) = f_{i+\frac{1}{2}}^{low} - \phi(r_i) \left(f_{i+\frac{1}{2}}^{low} - f_{i+\frac{1}{2}}^{high}\right) \\ f\left(u_{i-\frac{1}{2}}\right) = f_{i-\frac{1}{2}}^{low} - \phi(r_{i-1}) \left(f_{i-\frac{1}{2}}^{low} - f_{i-\frac{1}{2}}^{high}\right). \end{cases} \quad (3.53)$$

Here,  $f_j^{low}$ ,  $f_j^{high}$  and  $\phi(r)$  denote a low resolution flux, high resolution flux and the flux limiter function respectively and  $r$  is the ratio of successive gradients on the solution mesh

$$r_j = \frac{u_j - u_{j-1}}{u_{j+1} - u_j}. \quad (3.54)$$

The limiter function is constructed so that its output is non-negative i.e.  $\phi(r) \geq 0$ . When the limiter is zero, the flux is determined from the low resolution scheme due to either a sharp or zero gradient, or opposite slopes. If the limiter is equal to one, the solution is smooth and a high resolution scheme may be applied. Many limiter functions exist in the literature and are outlined in Appendix (A.5).

Each limiter limits actions in forward and backward gradients and being second order TVD means that they are designed such that they pass through the TVD region, guaranteeing scheme stability and satisfying the following:

- $r \leq \phi(r) \leq 2r, \quad 0 \leq r \leq 1,$
- $1 \leq \phi(r) \leq r, \quad 1 \leq r \leq 2,$
- $1 \leq \phi(r) \leq 2, \quad r > 2,$
- $\phi(1) = 1.$

For this thesis specifically, the *minmod* limiter (3.55), first constructed and presented in Roe (1986), will be applied. This is considered in Section 4.3.2.3.

$$\phi_{mm}(r) = \max[0, \min(1, r)], \quad \lim_{r \rightarrow \infty} \phi_{mm}(r) = 1. \quad (3.55)$$

## 3.6. Infiltration Modelling

### 3.6.1. The Green-Ampt Model

The *Green-Ampt* (Green and Ampt, 1911) model is one of many which approximate the infiltration and runoff process. An overview of the theory which underpins infiltration and runoff modelling may be found in Appendix (B.2; page 344).

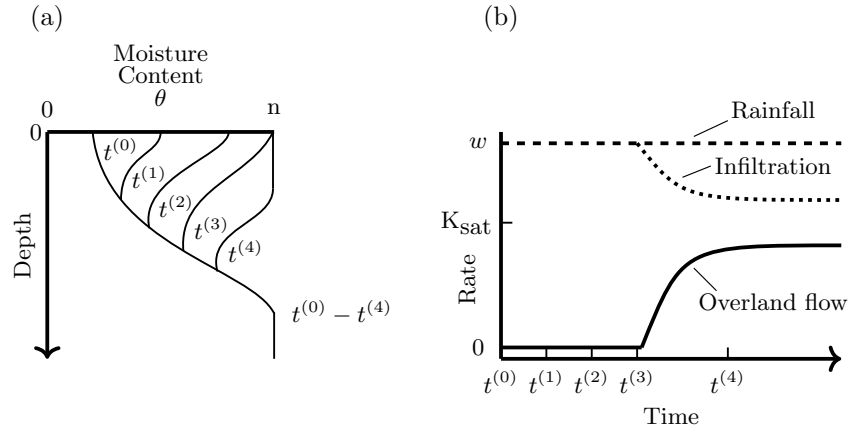


Figure 3.11.: Infiltration excess runoff profiles. (a) Moisture content vs. depth profiles and (b) Runoff generation time series. Adapted from Bras (1990); Tarboton (2003).

Curved soil moisture profiles shown in Figure 3.11 are approximated using the Green-Ampt model as a solution to Richards equation with a sharp boundary between saturation conditions. Initial moisture content is defined as  $\theta = \theta_0$  and saturated condition  $\theta = n$  just below and above the wetting front respectively. Figure 3.12 illustrates this scenario. Assume that moisture content is uniform over depth and define  $L$  to be the depth from the surface to the wetting front.  $\Delta\theta = n - \theta_0$  is the difference between initial and saturation moisture content. We may then define the depth of infiltrated water after initial infiltration as

$$F = L\Delta\theta. \quad (3.56)$$

The Green-Ampt model assumes that surface water input is infinite in supply and that the ponding depth is small. As such, the hydraulic gradient contribution from the ponding depth at the surface is minimal. At the depth just below the wetting front, soil is at its initial unsaturated condition and has a suction head  $|\psi_f|$ . From the surface to just below the wetting front, infiltration is driven by the hydraulic head difference

$$h = -(L + |\psi_f|). \quad (3.57)$$

Dividing the hydraulic head difference (3.57) by the wetting front depth,  $L$ , yields the hydraulic gradient

$$\frac{dh}{dz} = -\frac{L + |\psi_f|}{L}. \quad (3.58)$$

Now applying Darcy's equation and using (3.56) to obtain the infiltration capacity

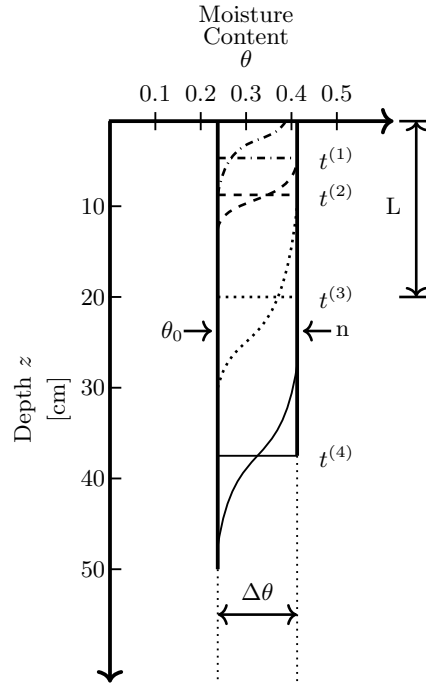


Figure 3.12.: Pictorial representation of the Green-Ampt model idealisation where the wetting front penetrates into the soil profile. Initial moisture content is denoted  $\theta_0$ . Saturation moisture content, denoted  $\theta_s$ , is equivalent to porosity  $n$ .  $L$  represented the distance between the wetting front and surface at any given timestep ( $t^{(3)}$  here). Adapted from figure 39 (Tarboton, 2003, Chapter 5:10).

$$\begin{aligned}
 f_c &= K_{\text{sat}} \left( 1 + \frac{|\psi_f|}{L} \right) \\
 &= K_{\text{sat}} \left( 1 + \frac{P}{F} \right)
 \end{aligned} \tag{3.59}$$

where  $P = |\psi_f| \Delta \theta$ . Equation (3.59) is an expression for the reduction of infiltration capacity as a function of infiltrated depth  $f_c(F)$ . One may estimate the soil moisture characteristic with the initial moisture content parameter,  $\psi_f = \psi(\theta_0)$ .

Rawls et al. (1993) suggests calculating  $|\psi_f|$  from air entry pressure using the parameters  $\psi_a$  and  $b$  from Table 3.1 and the formula

$$|\psi_f| = \left( \frac{2b + 3}{2b + 6} \right) |\psi_a|. \tag{3.60}$$

Table 3.1.: Green-Ampt infiltration parameters for various soil characterisations from Rawls et al. (1983). Parameter values  $|\psi_a|$  and  $b$  come from analysis of 1845 soils from Clapp and Hornberger (1978).

Soil Texture	Porosity $n$	Effective Porosity $\theta_e$	Wetting front soil suction head $\psi_f$ [cm]	Hydraulic conductivity $K_{\text{sat}}$ [cm/hr]	$ \psi_a $ [cm]	$b$
<b>Sand</b>	0.437 (0.374 - 0.500)	0.417 (0.354 - 0.480)	4.95 (0.97-25.36)	11.78	12.1 (14.3)	4.05 (1.78)
<b>Loamy Sand</b>	0.437 (0.363 - 0.506)	0.401 (0.329 - 0.473)	6.13 (1.35 - 27.94)	2.99	9 (12.4)	4.38 (1.47)
<b>Sandy Loam</b>	0.453 (0.351 - 0.555)	0.412 (0.283 - 0.541)	11.01 (2.67 - 45.47)	1.09	21.8 (31.0)	4.9 (1.75)
<b>Loam</b>	0.463 (0.375 - 0.551)	0.434 (0.334 - 0.534)	8.89 (1.33 - 59.38)	0.34	47.8 (51.2)	5.39 (1.87)
<b>Silt Loam</b>	0.501 (0.420 - 0.582)	0.486 (0.394 - 0.578)	16.68 (2.92 - 95.39)	0.65	78.6 (51.2)	5.3 (1.96)
<b>Sandy Clay Loam</b>	0.398 (0.332 - 0.464)	0.330 (0.235 - 0.425)	21.85 (4.42 - 108.0)	0.15	29.9 (37.8)	7.12 (2.43)
<b>Clay Loam</b>	0.464 (0.409 - 0.519)	0.309 (0.279 - 0.501)	20.88 (4.79 - 91.10)	0.1	63 (51.0)	8.52 (3.44)
<b>Silty Clay Loam</b>	0.471 (0.418 - 0.524)	0.432 (0.347 - 0.517)	27.30 (5.67 - 131.50)	0.1	35.6 (37.8)	7.75 (2.77)
<b>Sandy Clay</b>	0.430 (0.370 - 0.490)	0.321 (0.207 - 0.435)	23.90 (4.08 - 140.2)	0.06	15.3 (17.3)	10.4 (1.64)
<b>Silty Clay</b>	0.479 (0.425 - 0.533)	0.423 (0.334 - 0.512)	29.22 (6.13 - 139.4)	0.05	49 (62.0)	10.4 (4.45)
<b>Clay</b>	0.475 (0.427 - 0.523)	0.385 (0.269 - 0.501)	31.63 (6.39 - 156.5)	0.03	40.5 (39.7)	11.4 (3.7)

Now, given a surface water input rate  $w$ , prior to surface ponding, the cumulative infiltration is  $F = wt$ . When infiltration decreases to the point where it equals water input rate,  $f_c = w$ , ponding will commence. Thus setting this condition to Equation (3.59) and solving for  $F$  gives the cumulative infiltration at ponding as

$$F_p = \frac{K_{\text{sat}}|\psi_f|\Delta\theta}{w - K_{\text{sat}}}. \quad (3.61)$$

The time taken to reach a ponding state is

$$t_p = \frac{F_p}{w} = \frac{K_{\text{sat}}|\psi_f|\Delta\theta}{w(w - K_{\text{sat}})}. \quad (3.62)$$

Infiltration rate is the derivative of cumulative infiltration in the Green-Ampt model and limited by infiltration capacity and so infiltration after ponding is



$$f(t) = \frac{dF}{dt} = f_c(t) = K_{\text{sat}} \left( 1 + \frac{P}{F} \right). \quad (3.63)$$

Applying the separation of variables technique, one may integrate from an initial cumulative infiltration depth  $F_p$  at time  $t_p$  (from Equations (3.61) and (3.62)) to a final cumulative infiltration depth  $F$  at time  $t$  to obtain the cumulative infiltration under ponded conditions as

$$t - t_p = \frac{F - F_p}{K_{\text{sat}}} + \frac{P}{K_{\text{sat}}} \ln \left( \frac{F_p + P}{F + P} \right). \quad (3.64)$$

One cannot obtain an explicit function for the cumulative infiltration after ponding, but it may be solved numerically for any given time after an initial ponding time  $t_p$  to obtain the cumulative infiltration as a function of time.

Empirical observations show that as infiltration capacity decreases, the prevalence of surface runoff increases over time. As the Green - Ampt model naturally models infiltration capacity as a function of cumulative infiltrated depth, this model naturally encapsulates the relationship between infiltration capacity and runoff. Cumulative infiltrated depth may be considered a state variable and so variability in infiltration rate is reduced when it is not dependent on variable rainfall rates, typically referred to as the infiltrability-depth approximation (Smith, 2002) .

As well as the Green-Ampt model, Table 3.2 highlights formulae from the Horton and Philip models used in infiltration modelling. These two models measure decreasing infiltration capacity explicitly as a function of time, thus being completely de-coupled from cumulative infiltration depth. More information on these models may be found in (Tarboton, 2003, pg. Chapter 5: 13-18). In this work, the Green-Ampt model is used as the infiltrability-depth approximate provides a more intuitive and physically sound basis for applying infiltration modelling.

A working example of how the Green-Ampt model is used in practise will be discussed in Section 3.6.1.1.

Table 3.2.: Formulae required to implement the Green-Ampt, Horton and Philip point infiltration models. Model parameters are given in brackets below the model name.

Model	Infiltration Capacity	Cumulative Infiltration at Ponding	Cumulative Infiltration under ponded conditions
<b>Green-Ampt</b> ( $K_{\text{sat}}, P$ )	$f_c = K_{\text{sat}} \left( 1 + \frac{P}{F} \right)$	$F_p = \frac{K_{\text{sat}} P}{w - K_{\text{sat}}}$ $w > K_{\text{sat}}$	Solve implicitly for F $t - t_p = \frac{F - F_p}{K_{\text{sat}}} + \frac{P}{K_{\text{sat}}} \ln \left( \frac{F_p + P}{F + P} \right)$
<b>Horton</b>  ( $k, f_0, f_1$ )	Given F, solve implicitly for $f_c$ $F = \frac{f_0 - f_c}{k} = \frac{f_1}{k} \ln \left( \frac{f_c - f_1}{f_0 - f_1} \right)$	$F_p = \frac{f_0 - w}{k} - \frac{f_1}{k} \ln \left( \frac{w - f_1}{f_0 - f_1} \right)$  $f_c < w < f_0$	Solve for time offset $t_o$ first $F_p = f_1 (t_s - t_o) + \frac{f_0 - f_1}{k} (1 - \exp[-k(t_p - t_o)])$ then $F = f_1 (t - t_o) + \frac{f_0 - f_1}{k} (1 - \exp[-k(t_p - t_o)])$
<b>Philip</b>  ( $K_p, S_p$ )	$f_c = K_p + \frac{K_p S_p}{\sqrt{S_p^2 + 4K_p F - S_p}}$	$F_p = \frac{S_p^2 (w - K_p/2)}{2 (w - K_p)^2}$  $w > K_p$	Solve for time offset $t_o$ first $t_o = t_s - \frac{1}{4K_p^2} \left( \sqrt{S_p^2 + 4K_p F_s - S_p} \right)^2$ then $F = S_p (t - t_o)^{0.5} + K_p (t - t_o)$

### 3.6.1.1. Green-Ampt infiltration model

Within standard practical applications the Green-Ampt model parameters  $K_{\text{sat}}$  and  $P$  are utilised as empirical parameters where the values are determined by how they best fit the infiltration data or the ratio between measured rainfall to measured surface runoff. Equation (3.63) empirically describes the reduction of infiltration capacity as a function of cumulative infiltrated depth, where it was derived from a physical logic.

Given a time series of the surface water inputs, and soil conditions represented in terms of the infiltration model parameters, the infiltration capacity function  $f_c(t)$  provides the starting point to calculate runoff at a given location.

Typically infiltration problems look to answer the following question: Given a surface water input time series and the necessary parameters for the infiltration model, what is the ponding time and the infiltration after the occurrence of ponding, and what runoff (if any) was generated?

Surface water input is represented discretely where the input to the model is the time average surface water input per time interval. More detail in the output can be achieved by reducing the time interval as small as needed thus providing more granular input information. The output of the model is the runoff generated from excess surface water input over the infiltration capacity integrated over each time interval. Due to the dependence of the infiltration capacity on the cumulative infiltrated depth  $F$ , the capacity reduces as time evolves. Thus  $F$  is considered a state variable in this modelling approach.

Consider a series of time intervals where the general interval  $k$  goes from  $t = (k - 1)\Delta t$  to  $t = k\Delta t$ .  $\omega_t$  is the surface water input intensity and considered constant throughout the time interval.  $F_t$  is the initial cumulative infiltration depth at the start of the interval. The Green-Ampt infiltration capacity is then evaluated using Equation (3.63). Given an initial cumulative infiltration depth and surface water input  $\omega_t$  the goal is to obtain the total water infiltration within the interval  $f_t$  and the resulting cumulative infiltration at the end of the interval  $F_{t+\Delta t}$  as well as the runoff  $r_t$  generated during the time interval.

The infiltration model is initialised using  $F_0$  as the storm begins and continues throughout each time interval during the entire duration of the surface water input time series. Throughout this time three potential ponding scenarios need to be considered:

1. Ponding occurs throughout the interval.
2. No ponding occurs throughout the interval.
3. Ponding begins part-way through the interval.

Infiltration capacity will be monotonically decreasing with time. Once ponding has occurred with a given surface water input intensity, it will continue. Ponding will not cease part way through an interval, but may stop at the end of an interval when the surface water input intensity changes.

Figure 3.13 shows the algorithmic approach one can apply to determine the infiltration and runoff generated under variable surface water input intensity. In the next section, the methodology of the Green-Ampt model is illustrated with a worked-example from Tarboton (2003).

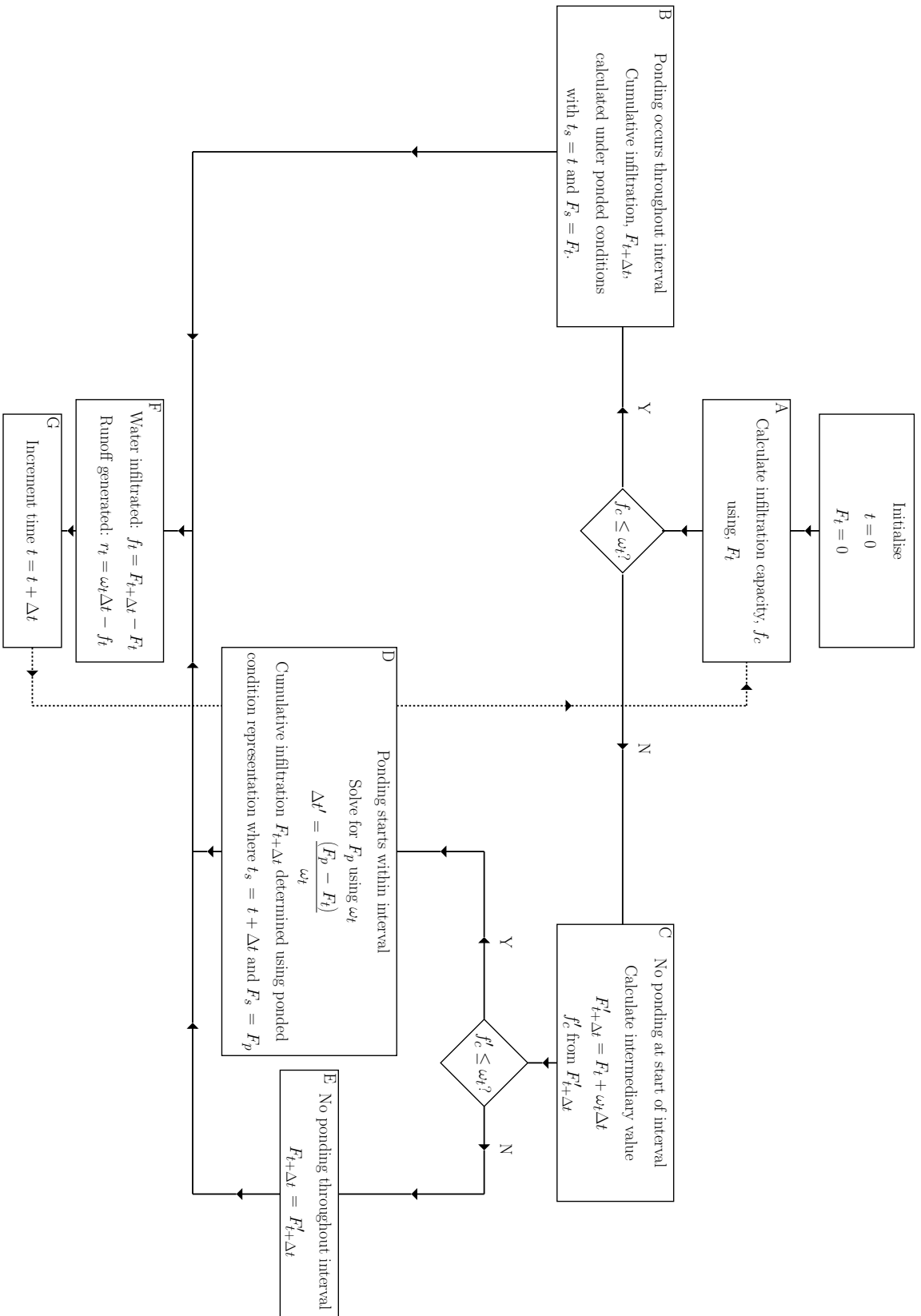


Figure 3.13.: Green-Ampt infiltration model flow chart to calculate the infiltration and runoff generated under various surface water input intensities. Adapted from (Tarboton, 2003, Chapt. 5 pg. 21)

### 3.6.1.2. Green-Ampt: A worked example

Column 2 of Table 3.3 on page 127 lists the rainfall total and intensity for over the course of two hours. Each timestep is split into 15 minute intervals or 0.25 hours. The goal here is to determine the runoff per timestep on an area of sandy loam with an initial moisture content equal to the field capacity. Table 3.3 lists the results of applying the Green-Ampt model and here the process of how it is applied is outlined.

From Table 3.1, sandy loam soil has the parameter values  $n = 0.453$  (porosity),  $\theta_e = 0.412$  (effective porosity),  $\psi_f = 11.01$  (wetting front soil suction head) and  $K_{\text{sat}} = 1.09$  (hydraulic conductivity). Further, the parameters  $|\psi_a| = 21.8$  and  $b = 4.9$  are needed from the table.

A residual moisture content value is determined by taking the difference between the porosity and the effective porosity,  $n - \theta_e = 0.453 - 0.412 = 0.041 = \theta_r$ .

Inverting Clapp and Hornberger's (Clapp and Hornberger, 1978) simplification of Brooks and Corey functions equation seen in (Tarboton, 2003, Chapt. 4 pg. 16) to define the field capacity as the moisture content responding to a pressure head,  $\psi = -340$  cm

$$\theta = n \left( \frac{|\psi|}{|\psi_a|} \right)^{-1/b}. \quad (3.65)$$

Hence field capacity using (3.65) is  $\theta_{fc} = 0.259$ . Since  $\theta_{fc} > \theta_r$  it is consistent that moisture content is reached after roughly three days of drainage. Now calculate a parameter P which is the pressure head multiplied by the change in moisture content

$$P = |\psi_f| (n - \theta_{fc}) = 2.14\text{cm}. \quad (3.66)$$

Since the time interval is 15 minutes,  $\Delta t = 0.25\text{hrs}$ . One can then calculate the rainfall intensity per timestep by multiplying  $\Delta t$  with the total rainfall per timestep in column 2 of Table 3.3. All the initial calculations required to begin applying the Green-Ampt model has been completed using the flow chart in Figure 3.13.

Initially  $F = 0$  and  $f_c = \infty$ , thus ponding does not occur at  $k = 0$ . We move from box A to C

$$F'_{t+\Delta t} = F_t + \omega_t \Delta t = 0 + 0.3 = 0.3\text{cm}. \quad (3.67)$$

(3.67) is the preliminary cumulative infiltration under the assumption of no ponding. Thus the corresponding value  $f'_{t+\Delta t}$  is

Table 3.3.: Runoff calculations from applying the Green-Ampt infiltration model. Copied from table 4 in (Tarboton, 2003, Chapt. 5 pg. 28).

	<b>Time</b> [h]	<b>RF</b> <b>Increment</b> [cm]	<b>RF</b> <b>Intensity</b> [cm/h]	$F_t$ [cm]	$f_c$ [cm/h]	$F'$ [cm]	$f'_c$ [cm/h]	$F_p$ [cm]	$dt'$ [h]	$t_s$ [h]	$F_{t+\Delta t}$ [cm]	$g(F)$ [cm]	<b>Infiltration</b> [cm]	<b>Runoff</b> [cm]
	0	0.3	1.2	0	$\infty$	0.300	8.867				0.3000		0.300	0.000
	0.25	0.4	1.6	0.300	8.867	0.700	4.423				0.700		0.400	0.000
	0.50	0.5	2.0	0.700	4.423	1.200	3.034				1.200		0.500	0.000
	0.75	0.6	2.4	1.200	3.034	1.800	2.386	1.781	0.242	0.992	1.79995	0.000	0.59995	0.00005
<b>Ponding</b>	1.00	0.7	2.8	1.800	2.386			1.800	0.000	1.000	2.354	0.000	0.554	0.146
	1.25	0.8	3.2	2.354	2.081			2.354	0.000	1.250	2.851	0.000	0.497	0.303
	1.50	0.4	1.6	2.851	1.908	3.251	1.808				3.251		0.400	0.000
<b>Ponding</b>	1.75	0.6	2.4	3.251	1.808			3.251	0.000	1.750	3.692	0.000	0.441	0.159
	2.00	0.6	2.4	3.692	1.722			3.692	0.000	2.000	4.114	0.000	0.422	0.178

$$f'_{t+\Delta t} = K_{\text{sat}} \left( 1 + \frac{P}{F} \right) = 1.09 \left( 1 + \frac{2.14}{0.3} \right) = 8.867 \text{ cm/h.} \quad (3.68)$$

As  $f'_{t+\Delta t} > \omega_t$  we move from box C to E where the cumulative infiltration is set to the preliminary value. Moving onto box F to determine the total water infiltrated and the runoff generated at the timestep. Moving from Box F to Box G to increment the time by  $\Delta t$  and move back to Box A.

No ponding occurs during the first three timesteps of the calculation. Following the flow chart (A->C->E->F->G->A) until the fourth time interval between 0.75 and 1 hrs.

At this point the infiltration capacity is calculated to be

$$f'_{t+\Delta t} = K_{\text{sat}} \left( 1 + \frac{P}{F} \right) = 1.09 \left( 1 + \frac{2.14}{1.8} \right) = 2.386 \text{ cm/h.} \quad (3.69)$$

Here  $f'_{t+\Delta t} < \omega_t = 2.4 \text{ cm / hr}$ . Thus ponding begins at the start of this interval and we move onto box D. We then calculate the cumulative infiltration at ponding using

$$F_p = \frac{K_{\text{sat}} P}{(\omega_t - K_{\text{sat}})} = \frac{1.09 \times 2.14}{(2.4 - 1.09)} = 1.781 \text{ cm.} \quad (3.70)$$

The time taken at which ponding begins within the interval is calculated as

$$\Delta t' = \frac{(F_p - F_t)}{\omega_t} = \frac{(1.781 - 1.2)}{2.4} = 0.242 \text{ hours.} \quad (3.71)$$

Hence ponding begins at  $0.75 + 0.242 = 0.992 \text{ hrs}$ . Infiltration under ponded conditions occurs for 0.008 hours within this time interval. The cumulative infiltration is calculated during this period by solving (3.72) numerically,  $g(F) = 0$  (e.g. using the Newton Rhapson method (Gerald, 1978))

$$g(F) = 0 = t - t_s - \frac{F - F_s}{K_{\text{sat}}} - \frac{P}{K_{\text{sat}}} \ln \left( \frac{F_s + P}{F + P} \right) \quad (3.72)$$

This results in  $F_{t+\Delta t} = 1.79995 \text{ cm}$ . Moving onto box F to calculate the infiltration within the timestep  $f_t = F_{t+\Delta t} - F_t = 1.7995 - 1.2 = 0.59995 \text{ cm}$ . Since the rainfall input during the timestep is 0.6cm the total runoff is 0.00005cm as seen in the final column of Table 3.3.

At the beginning of the fifth timestep the infiltration capacity is  $f_c = 2.386 \text{ cm} < \omega_t$  and so infiltration under ponded conditions is beginning at the start of the timestep. The calculation is exactly the same as (3.72) except for the starting values  $F_s$  and  $t_s$  which are taken at the beginning of the timestep.



At the sixth time interval ( $k = 1.25$ ).  $F_t = 2.354$  cm leading to an infiltration capacity  $f_c = 2.081$  cm / hr  $< \omega_t = 3.2$  cm / hr. Thus we follow through to box B to determine the cumulative infiltration under ponded conditions.

At the start of the seventh interval ponding has ceased as  $\omega_t = 1.6 < 1.908$  cm / hr  $= f_c$  with a cumulative infiltration of 2.851cm. Following through to box C and calculate the preliminary infiltration at the end of the time interval as  $F'_{t+\Delta t} = 3.251$  cm as detailed in the initial timestep. Using this preliminary value the infiltration capacity value of 1.808 cm / hr is obtained. This is greater than the rainfall rate and so no ponding occurs through the interval. One then moves onto box E through to F and then G.

At the beginning of the penultimate timestep the rainfall rate has increased to  $\omega_t = 2.4$  cm / hr with a cumulative infiltration of 3.251 cm. Thus the infiltration capacity is 1.808 cm / hr, a little less than the rainfall rate and so ponding has begun once more. Following through to box B, one will calculate the cumulative infiltration as well as the total infiltration within the time interval and runoff (box F), the values of which can be viewed in Table 3.3.

### 3.6.2. The SCS Method

The Green-Ampt model described in Section 3.6.1 is a point infiltration model which quantifies the physics of the infiltration phenomena from Richards equation in a simplified manner. Due to the impervious surface present within sub-urban and urban areas, it is not practical to use such a model to calculate infiltration. As such, another way to calculate rainfall abstraction is through empirical methods. One such method is the *SCS method* constructed by the Soil Conservation Service in 1972 (Chow et al., 1988).

Considering a single rainfall storm event in isolation, the total direct runoff  $Q$  is less than or equal to the precipitation depth  $P$ . Once runoff has commenced, water depth within the watershed is  $F_a \leq S$  where  $S$  is the maximum possible water retention. An initial amount of rainfall will occur where no runoff is present known as the initial abstraction  $I_a$ , thus resulting a potential runoff amount of  $P - I_a$ . The SCS method suggests that the ratio between runoff and potential maximum runoff equals the ratio between depth of water retained in the water shed over the potential maximum retention

$$\frac{Q}{P - I_a} = \frac{F_a}{S}. \quad (3.73)$$

Using conservation of mass,

$$P = Q + I_a + F_a, \quad (3.74)$$

the total runoff from a storm may be determined with

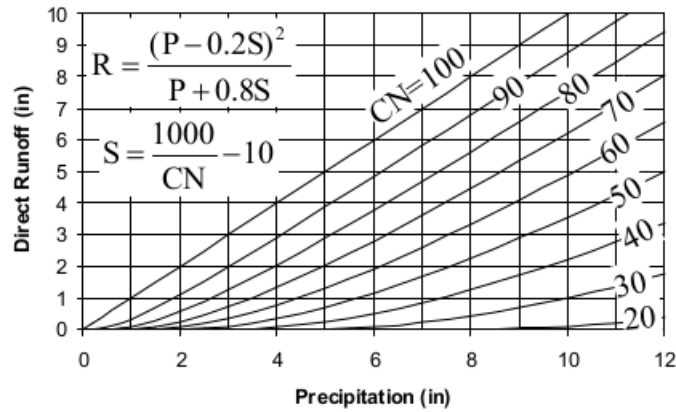


Figure 3.14.: Results to the SCS runoff equations with precipitation [in] plotted against direct runoff [in]. Obtained from (Tarboton, 2003, Chapter 5:42 Figure 48).

$$Q = \frac{(P - I_a)^2}{P - I_a + S}. \quad (3.75)$$

Through small experimental watersheds, the empirical relation of  $I_a = 0.2S$  was determined by the Soil Conservation Service. Hence (3.75) becomes

$$Q = \frac{(P - 0.2S)^2}{P + 0.8S}. \quad (3.76)$$

Data from multiple watersheds was collated and presented as seen in Figure 3.14, where  $R = Q$ . These plots were standardised with a dimensionless *curve number* (CN), where impervious surfaces have a curve number ( $CN = 100$ ) and values below 100 are for natural surfaces. A relation between the curve number and maximum potential water retention  $S$  (with units of inches) was determined to be

$$S = \frac{1000}{CN} - 10. \quad (3.77)$$

Figure 3.14 shows curve numbers for *normal antecedent moisture conditions* (AMC II). Antecedent moisture condition is an empirical measure to account for the fact that runoff quantity is dependent on the presence (or lack thereof) of moisture in the watershed currently. More details on how this index was constructed may be found in Linsey et al. (1982).

The curve number for dry conditions (AMC I) may be calculated as

$$CN_I = \frac{4.2CN_{II}}{10 - 0.058CN_{II}}. \quad (3.78)$$

Table 3.4.: Antecedent moisture classifications for the SCS method of rainfall abstraction.

AMC Group	Total 5 day antecedent rainfall [in]	
	Dormant Season	Growing Season
<b>I</b>	< 0.5	< 1.4
<b>II</b>	0.5 - 1.1	1.4 - 2.1
<b>III</b>	> 1.1	> 2.1

Similarly, curve numbers for wetter scenarios (AMC III) are determined using the formula

$$CN_{III} = \frac{23CN_{II}}{10 + 0.13CN_{II}}. \quad (3.79)$$

where  $CN_{II}$  is the curve number for normal moisture conditions. Table 3.4 shows AMC value range classifications. Table 3.5 shows tabulated curve numbers by the SCS characterised by soil type and land-use definition. Four soil groups are used to characterise runoff potential

**Group A:** Low runoff potential. Soils with high infiltration capacity, even when thoroughly wet. E.g. deep sand, deep loess and aggregated silts.

**Group B:** Moderate runoff potential. Soils have moderate infiltration capacity when thoroughly wet. E.g. shallow loess and aggregated silts.

**Group C:** High runoff potential. Soils have low infiltration capacity when thoroughly wet. E.g. clay loams, shallow sandy loam, soils low in organic matter and soils high in clay.

**Group D:** Very high runoff potential. Soils have very low infiltration capacity if thoroughly wet. E.g. soils which swell significantly when set. E.g. heavy plastic clays and particular saline soils.

Despite the limitation in physical basis, due to the availability of curve number values in soil maps etc., this method is used often in practise. A more detailed discussion of how the SCS method is implemented for specific land-use types within the model may be found in Section 4.3.5.2.

### 3.6.2.1. SCS Curve Number Method

In Section 4.2.3 the six land-use types defined will be used in the simulation of the computational domain. Four of these land-use types: Arable; Grassland; Rough Grazing; and Woodland; may be considered as ‘natural’ and the Green-Ampt method discussed above is

Table 3.5.: Runoff curve numbers for given typical agricultural, suburban and urban land-uses. Adapted from tables 2-2a - 2-2d (Natural Resources Conservation Service, 1986, Chapt. 2 pgs. 5-8).

Land Use Category		Hydrological Soil Group			
		A	B	C	D
<b>Cultivated land</b>	w/out conservation treatment	72	81	88	99
	w/ conservation treatment	62	71	78	81
<b>Pasture or range land</b>	Poor condition	68	79	86	89
	Good condition	39	61	74	80
<b>Meadow</b>	Good condition	30	58	71	78
<b>Woodland</b>	thin stand, poor cover, no mulch	45	66	77	83
	Good cover	25	55	70	77
<b>Open space</b> (parks/lawns etc)	Good condition (> 75% cover)	39	61	74	80
	Fair condition (50% – 75% grass cover)	49	69	79	84
<b>Commercial/Business areas</b> (85% impervious)		89	92	94	95
<b>Industrial areas</b> (72% impervious)		81	88	91	93
<b>Residential</b>					
<b>Average lot size</b> [acres]	<b>Average impermeability</b> [%]				
≤ 1/8	65	77	85	90	92
1/4	38	61	75	83	87
1/3	30	57	72	81	87
1/2	25	54	70	80	85
1	20	51	68	79	84
<b>Paved areas</b> (Car parks, roofs, driveways etc.)		98	98	98	98
<b>Streets/Roads</b>	Paved with curbs and storm drainage	98	98	98	98
	Gravel	76	85	89	91
	Dirt	72	82	87	89

used to estimate the cumulative infiltration at each time step with appropriate parameters. However, ‘sub-urban’ and ‘urban’ land-use types require a different method to determine the total abstraction of surface water through storm drainage solutions present within built up areas.

The *Curve Number Method* is an often used empirical method used to predict direct runoff and/or infiltration from rainfall excess (Natural Resources Conservation Service, 1986). Developed by the USDA Natural Resources Conservation Service (formerly known as the Soil Conservation Service, or SCS), a runoff curve number was constructed via an empirical analysis of runoff from small catchment and hillslope plots surveyed by the USDA. The runoff equation is defined as

$$Q = \begin{cases} 0 & \text{if } P \leq I_a \\ \frac{(P - I_a)^2}{P - I_a + S} & \text{if } P > I_a, \end{cases} \quad (3.80)$$

for runoff  $Q$  [in]; rainfall  $P$  [in]; potential soil maximum soil moisture retention after runoff begins  $S$  [in]; and initial abstraction  $I_a$  [in] generally assumed to be  $I_a = 0.2S$ . However, research suggests that  $I_a = 0.05S$  may be more appropriate in urban watersheds where the curve number (CN) is updated to reflect evolving conditions (Woodward et al., 2003).

The relationship between potential maximum soil retention and the runoff curve number, CN, is

$$S = \frac{1000}{CN} - 10. \quad (3.81)$$

$CN \in [30, 100]$  where lower numbers refer to lower runoff potential while larger values indicate higher runoff potential. Figure 3.14 plots the solutions to Equation (3.80).

The curve number is a dimensionless parameter indicating the runoff response characteristic of a drainage basin. The value is dependent on multiple factors including the soil type, soil infiltration capability, land-use, the hydrological soil group and the antecedent moisture condition. A brief discussion on the hydrological soil group definition and the antecedent moisture condition is given below.

## 3.7. Summary

Chapter 3 outlines the underlying methodology that is implemented within the hydrological model that is constructed in Chapter 4. The fundamental mathematics which underpin the methods presented within this chapter may be found in Appendices A and B. Section 3.2 outlines the Riemann problem. The Riemann problem is introduced through the initial value problem of the linear advection equation (Section 3.2.1). It is expanded into the linear case (Section 3.2.2) where Riemann states are defined. Section 3.2.3 expands on the analysis further and looks at the Riemann problem for the multi-variate case. It discusses the general solution structure to the Riemann problem (Section 3.2.3.1) and provides a  $2 \times 2$  example to solidify the understanding of the solution structure. Section 3.3.1 begins by discussing how the efficient construction of solutions to the Riemann problem in a hyperbolic system can be obtained through the application of the Rankine-Hugoniot conditions. Section 3.3.2 introduces the common wave solutions to the Riemann problem. These are the shock, contact and rarefaction waves.

Godunov's numerical method is presented with application to the linear advection equation in its integral (Equation (3.20)) and differential (Equation (3.22)) forms in Section 3.4.1. Building on the differential form of the linear advection equation, a local Riemann problem is defined in Section 3.4.2 which can be applied ad-infinitum to solve the global problem at the next timestep. The boundary condition and timestep considerations are outlined in Sections 3.4.3 and 3.4.4 respectively. Section 3.4.6 expands the Godunov first-order upwind method from one-dimension into two-dimensions. This is the numerical modelling stencil that will be used in the hydrological model in Chapter 4. The purpose of Total Variation Diminishing methods is discussed through the prism of flux limiters in Section 3.5.

Chapter 3 concludes with Section 3.6, a comprehensive overview of the modelling techniques that will be employed for the infiltration component of the hydrological model. It begins with an summary of the underlying theory of the Green-Ampt infiltration model (Section 3.6.1). It continues on with a discussion of how the model is applied (Section 3.6.1.1), before diving into a worked example (Section 3.6.1.2). For impervious regions of a watershed, the SCS method will be applied to abstract water input from the system. Its construction, key parameters and implementation as an empirical method to predict direct runoff from rainfall excess is considered in Section 3.6.2. Total runoff is determined using the conservation of mass equation (Equation 3.74). A "Curve Number" empirical parameter is needed to predict infiltration from rainfall excess. This is a dimensionless parameter that indicates the runoff response characteristic of a drainage basin. This parameter is established through a formulae defined by "Antecedent moisture classifications". Soil groups are categorised into four depending on their runoff potential. Typical runoff curve numbers are given in Table 3.5 (page 132). The relationship between the potential maximum soil retention and runoff curve number is given by Equation (3.81).

This chapter outlined the modelling techniques that exist in literature (**RQ2**) that will be explicitly applied to the hydrological model construction in Chapter 4 (**RQ4**).

## Part II.

# Model Construction & Validation

## 4. Model Construction

### 4.1. Introduction

Chapter 1 outlined humankind’s need to equitably and sustainably use finite resources to meet its material, cultural and fundamental needs. Cornwall Council set a comprehensive policy plan through its *Environmental Growth Strategy* (Section 1.1.5) to meet its needs. Within its strategy the council identified the need for an “environmental management system” to aid in the management of environmental growth. Using the parallels between “facilities management” and this proposed platform (Section 1.1.6) a computational tool in the form of a hydrological model was proposed. This computational tool aims to help policy makers consider the potential flood risks associated with the construction of housing developments which will affect the hydrological characteristics of a local flood plain. Chapter 2 reviewed the literature behind hydrological modelling. Chapter 3 highlighted the mathematical theory which underpins the model that is defined within this chapter.

This chapter begins by defining the hydrological model’s computational mesh (Section 4.2.1) and land-use types (Section 4.2.2) used in this work. How these land-use definitions are implemented into the model will be given in Section 4.2.3. A justification of the method used to represent the surface runoff and routing component (Section 2.2.3) of the model is given in Section 4.3. Section 4.3.1 defines the governing equations of the model. An approximate Riemann solver will be introduced in Section 4.3.2. The routing component will be finalised with the source and friction discretisation terms in Sections 4.3.3 and 4.3.4 respectively. A justification of the methods adopted for the unsaturated zone component (Section 2.2.2) of the model is considered in Section 4.3.5, looking at the Green-Ampt model (Section 4.3.5.1) and the SCS Method (Section 4.3.5.2). The model’s boundary condition is outlined in Section 4.3.6. Section 4.3.7 justifies the approach taken for the interception component of the hydrological model. The chapter concludes with an overview of how one can calibrate the model (Section 4.3.8) and an outline of the model’s limitations and how it can be expanded (Section 4.3.9). References to Appendix Sections C and D are present within the chapter providing the reader supplementary material.



## 4.2. Computational Domain

### 4.2.1. Computational Mesh

The LiDAR Composite Digital Terrain Model (DTM) from the Environment Agency (2017) at a two metre resolution was downloaded. Specifically, the tile “SW71NE” was extracted. This covers the south-east corner of the Lizard peninsula containing Coverack. Figure 4.1; page 141 highlights the region where the DTM data was extracted.

The data provided contained spatial meta-data in the form of a Universal Transverse Mercator (UTM; Wikipedia (2021b)), a standardised map projection system to assign locations on the Earth’s surface. This form naturally lends itself to an orthogonal computational mesh. Given that this work is more specifically looking to the feasibility of constructing a long-term sustainable planning system through computational tools, the orthogonal system is adopted, despite there being more precise ways to develop a computational mesh to construct more accurate methods as outlined in Section 2.3.

### 4.2.2. Defining land-use types

To consider the potential flooding effect of Coverack specific land-use types, which will have differing hydrological characteristics, need to be defined. When first considering how to implement land-use into the model one may begin by looking at the UK Centre for Ecology & Hydrology’s Land Cover Map project (Morton et al., 2020). Core users of this project include governmental departments, researchers, councils, charities etc., for a wide range of applications. However, in point 8. of its user guidance it stresses the key difference between land cover and land-use:

*8. What is the difference between Land Cover and Land Use?*

*Our Land Cover Maps (LCMs) map Land Cover. They do this by describing the physical material on the surface of the United Kingdom. Whilst land cover may be synonymous with land use, this is not always the case. An arable crop cover denotes arable land use, but often land use cannot be inferred, for example grass used for recreation is similar to that which is grazed.*

From this subtle point that land cover cannot infer land use, this approach was ruled out as land-use is a key factor in this study.

A comprehensive survey of land use known as the “Land Utilisation Survey of Britain” was first conducted by Sir Laurence Dudley Stamp in the 1930s (Stamp, 1937). A large swathe of governmental policy has been derived from Stamp’s survey work. Over the past decade a lot of work has gone into digitising historic land use maps, one such example comes from Baily (2007). An electronic record of this survey may be found on Department for Environment, Food & Rural Affairs’s “MAGIC” platform (Department for Environment, Food & Rural Affairs, 2002c). This MAGIC website provides authoritative geographic

information on the natural environment provided by various governmental departments. It covers rural, urban, coastal and marine environments across the isle of Great Britain. This information is presented as an interactive map with various mapping tools.

In this work the “Magic Map” (Department for Environment, Food & Rural Affairs, 2002a) was accessed at the grid reference “OSGB36” with a scale of approximately 1:40000. The Dudley Stamp Land Use Inventory overlay in the landscape section of the table of contents drop down menu was applied. Figure 4.2; page 142 shows the output of this overlay. The black box in Figure 4.2b highlights the section of map being applied in this study. Figure 4.2c is a key which outlines the land-utilisation categories from the survey.

Specifically, this map shows a pre-war land survey where data was scanned and digitised at a 1km resolution with eight land-use classifications. Cross referencing the case-study region in the black box of sub-figure 4.2b with the key in sub-figure 4.2c. Every land-use category is present except for the “Orchard” land-use type. Hence in this study, the remaining land-use categories from the Dudley map, namely **Rough Grazing**, **Urban**, **Water**, **Arable**, **Suburban**, **Grassland** and **Woodland** will be utilised.

### 4.2.3. Land-Use Image Processing

The data used to construct the overlay seen in Figure 4.2a; page 142 was not available to download as stated on their webpage (Department for Environment, Food & Rural Affairs, 2002b). Hence an alternative approach was taken to define land-use categories using the overlay.

Using the key in Figure 4.2c; page 142, RGB samples were taken from the black box in Figure 4.2b. These locations can be seen in Figure 4.3; page 143 for each land use category. Using these RGB samples, a binary image was created to determine the location of each land use type within the region. White space in Figure 4.4 highlights the presence of a given land-use type.

These binary datasets were summed to locate any missing data points (shown as black points in Figures 4.5a and 4.5b). A MATLAB fill missing function for nearest column 4.5c and nearest row 4.5d were applied to complete the land-categorisation process.

#### 4.2.3.1. Lower resolution categorisations

The land-use imaging process described in 4.2.3 was also applied for the 20m and 50m resolution models. The related figures can be seen in the appendices C.1 (page 348) and C.2 (page 350).

To create a lower resolution version of the model, a MATLAB block processing function was applied to the original Dudley land-use map in Figure 4.2b as well as the terrain, surface and cover data obtained from Section 4.2.1. Within this work the block processing function takes an input image ‘A’ and applies an averaging calculation to a distinct block

of size  $m \times n^1$  to obtain an output image ‘B’. Figures 4.6 and 4.7 show these lower resolution domains and resulting land-use categories which will be used in the model.

#### 4.2.4. Green-Ampt Soil Parameter

To successfully implement the Green-Ampt model, outlined in Section (3.6.1; page 117) one needs to define a set of parameters related to at least one soil type. These parameters are presented in Table 3.1 (page 120). A simple soil dataset was compiled by Cranfield University in its “Soilscapes” web platform. A screenshot of the computational domain within this tool is shown in Figure 4.8. Two soil types cover this region and are defined in the Soilscapes web platform as: 1. Soilscape 7 (Brown): “Freely draining slightly acidic but base-rich soils”; and 2. Soilscape 17 (Green): “Slowly permeable seasonally wet acid loamy and clayey soils” (Cranfield Soil and Agrifood Institute, 2023). To maintain model simplicity, only the parameters associated with the “Sandy Loam” soil texture in Table 3.1 will be used for the simulation and analysis exercises in Chapters 5, 6, and 7. This category is most closely aligned with the “Soilscape 7”.

#### 4.2.5. Model Resolution Considerations

Higher resolution models (e.g. the 2m LiDAR DTM discussed in Section 4.2.1) can provide detailed output and enable analyses on a granular level. However, a vast amount of good quality data is needed to corroborate this model. In this work, data at this resolution was not available in sufficient quantity to justify the application of a 2m hydrological model. Higher resolution models improve model accuracy and enable small scale processes to be simulated. This in turn reduces dependence on uncertain parameterisations. However, the choice in model resolution is limited by the computational power available to the modeller. A model at this resolution will utilise an extensive amount of computational expenditure. The computational capacity available to run the model is limited to what is available on my personal machine. Therefore it is unfeasible to construct the 2m variant of the hydrological model in this work.

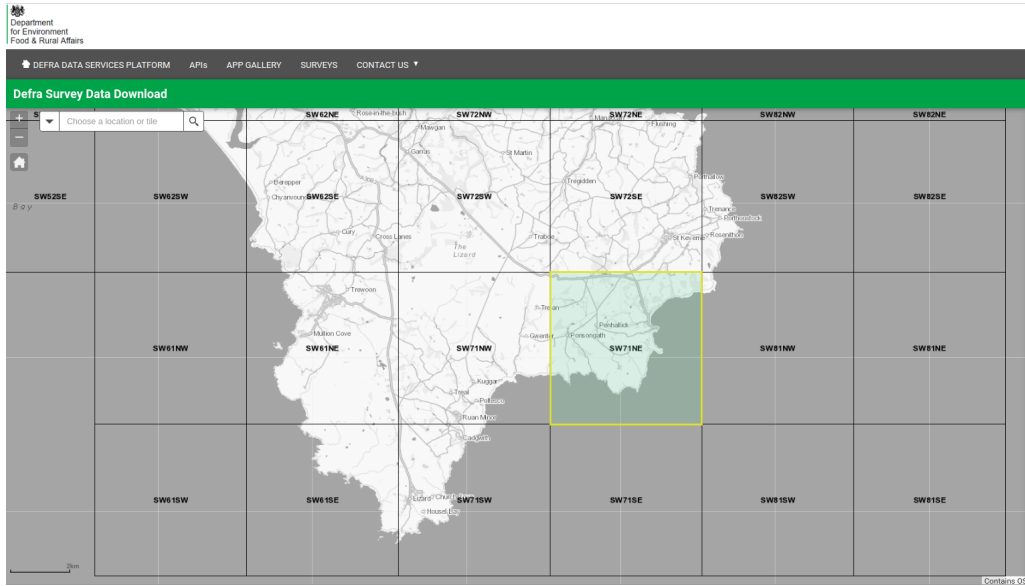
Lower resolution models (e.g. 100m+) would lose too much land-use information. Land-use data obtained from the “MAGIC” map is well resolved, but not resolved highly enough. Applying a filter to obtain 100m resolution land-use data would lose too much land-use information and would not be beneficial in the context of land-use planning and flood risk management.

A compromise is sought to obtain a resolution which does not lose so much information as to be unusable, but not too high so that it is too computationally expensive to run. Typically, a large individual house will have a plot size of 400m<sup>2</sup> (Scottish Government, 2023). Similarly, a street of houses could cover a plot region of 2500m<sup>2</sup>. Modelling at this scale will allow one to analyse scenarios for a lesser computational cost. However,

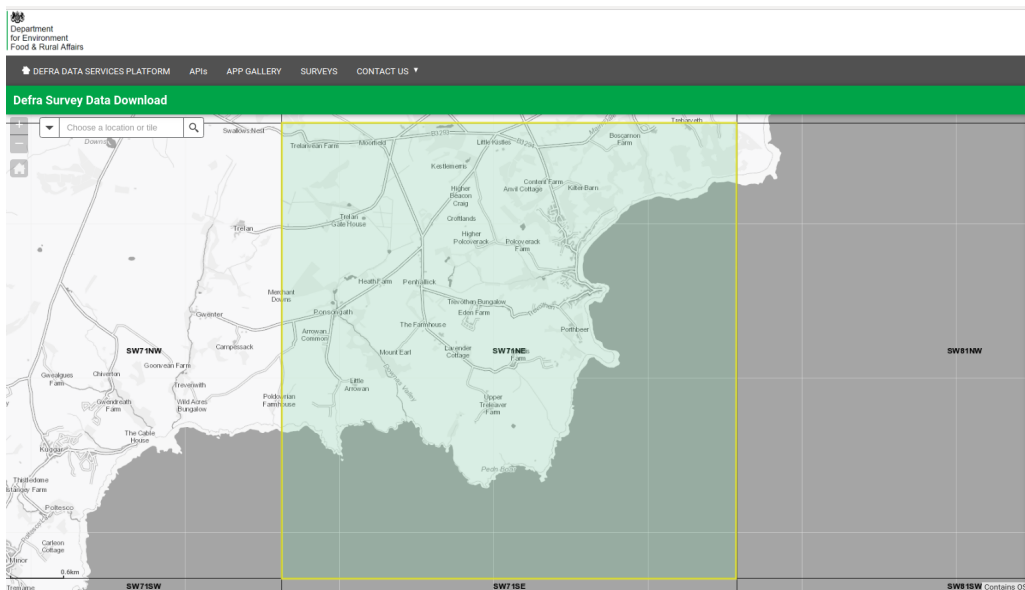
---

<sup>1</sup>Here,  $(m, n)$  define the number of rows and columns in the block.

the resolution is not so low that too much information is lost to render the simulations redundant. Therefore, the 20m and 50m resolution variants of the hydrological model constructed in this chapter will be compared.

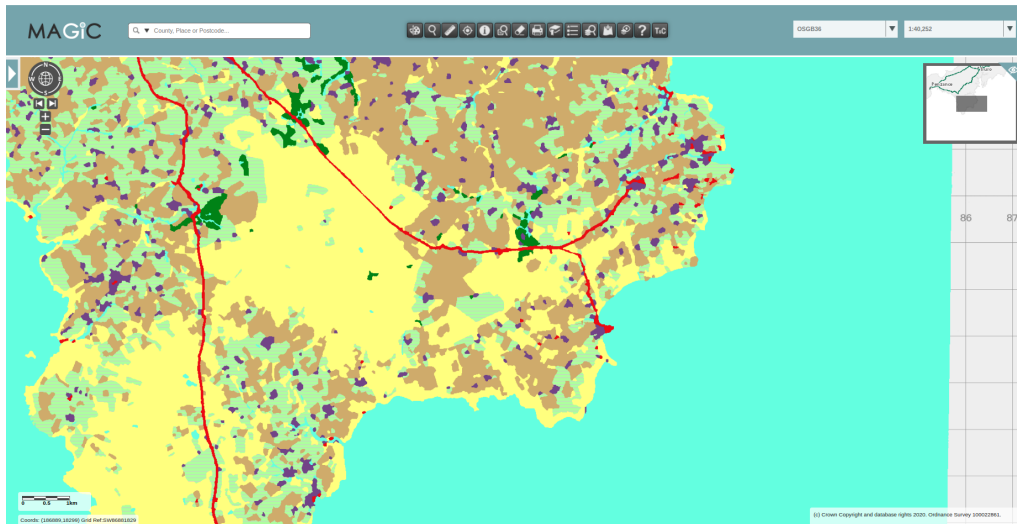


(a) Location of tile “SW71NE” in relation to the Lizard Peninsula in the Environment Agency’s data survey platform.

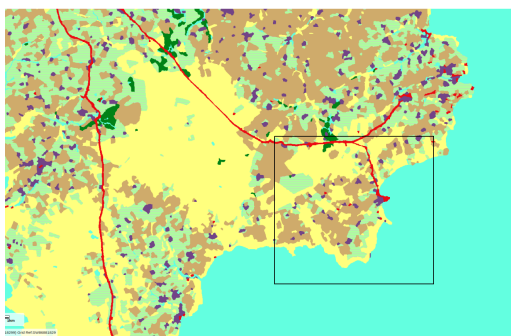


(b) A zoomed in view of tile “SW71NE” highlighted in sub-figure 4.1.a.

Figure 4.1.: The location of the digital terrain model data obtained for the Coverack case study within the Lizard Peninsula (Environment Agency, 2017).



(a) A screenshot of the full MAGIC Map platform (Department for Environment, Food & Rural Affairs, 2002a).



(b) A screenshot of the MAGIC Map platform where the black box indicates the region where land-use information will be extracted.



(c) The Dudley Stamp Land Use key which is located in the MAGIC platform's table of contents.

Figure 4.2.: Dudley land-use overlay on DEFRA's MAGIC map (Department for Environment, Food & Rural Affairs, 2002a) 4.2a and 4.2b with the land-use key in its table of contents 4.2c.

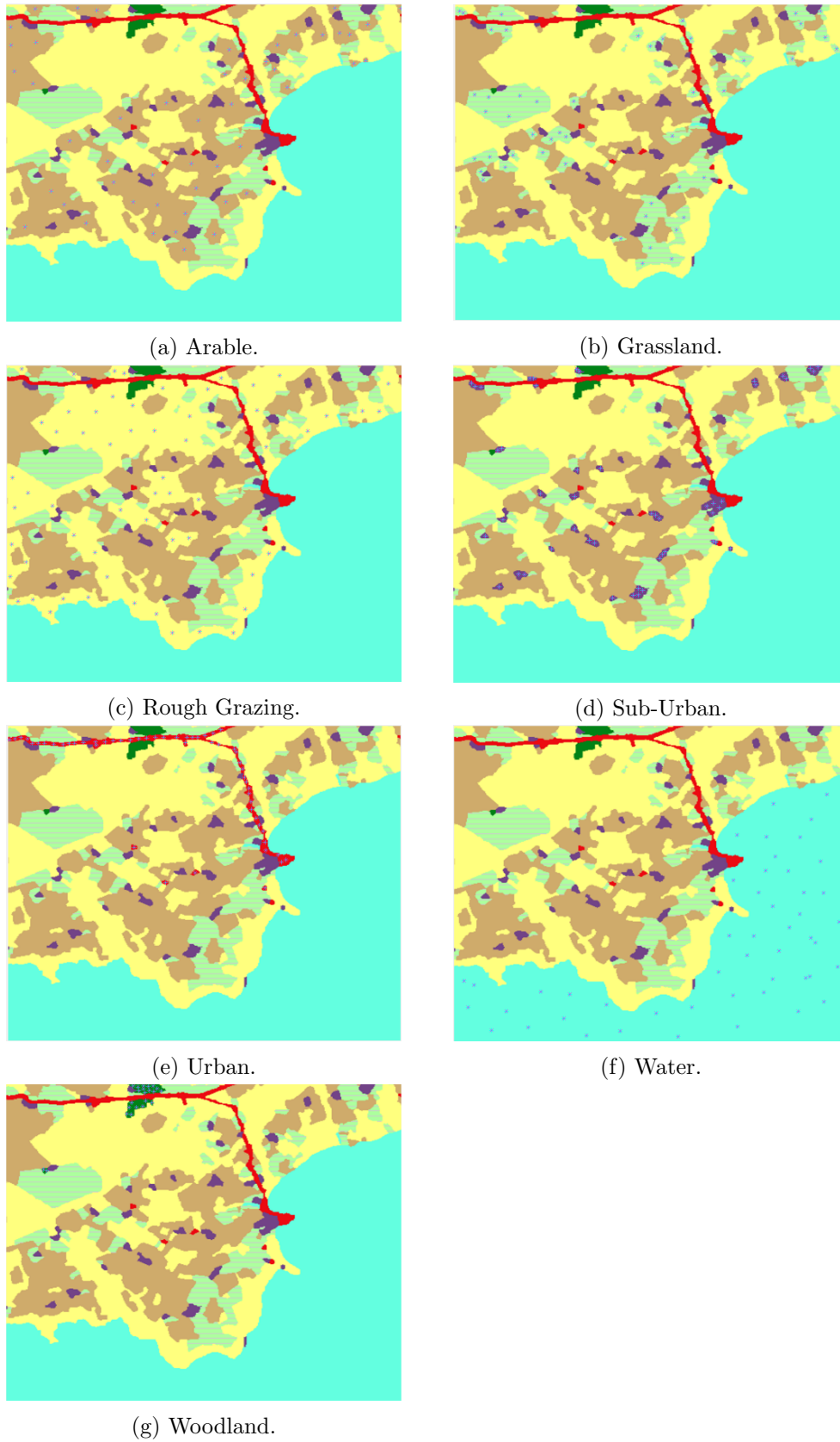


Figure 4.3.: Locations of where RGB pixel samples were taken for image processing using the Dudley Stamp Map from Department for Environment, Food & Rural Affairs (2002c).

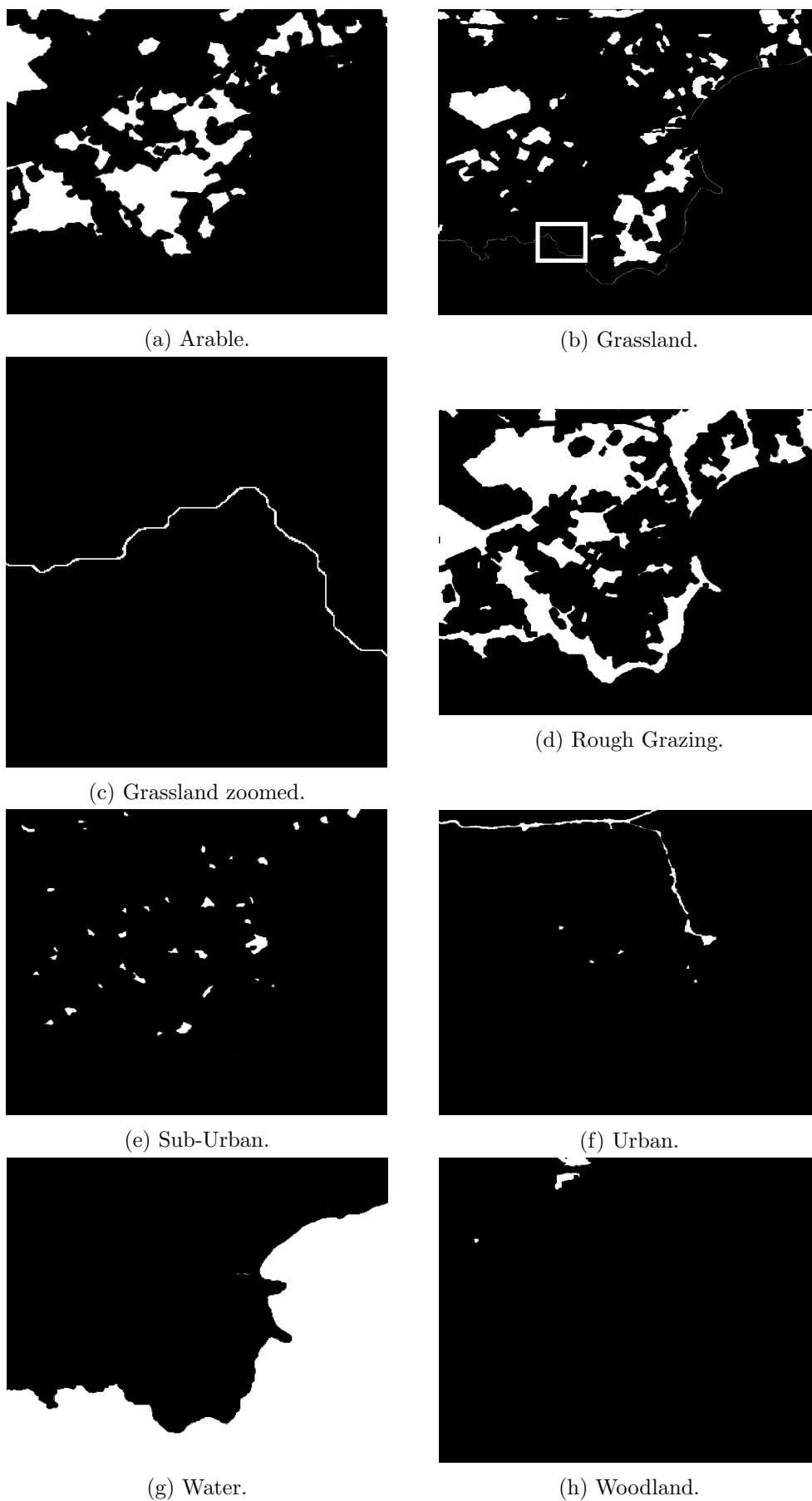
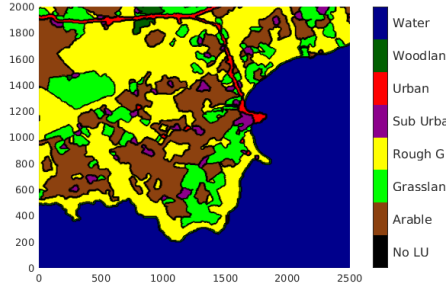


Figure 4.4.: Binary outputs after image processing for each land use definition.

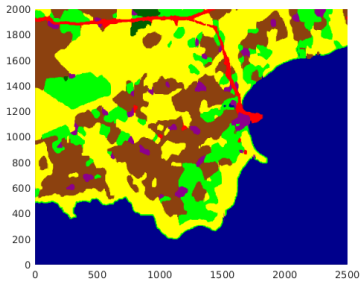




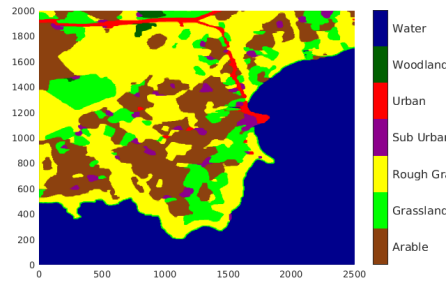
(a) Summation of all binary land uses from figure 4.4.



(b) Land Use before fillmissing function.



(c) Land Use - fill missing function, nearest column entry.

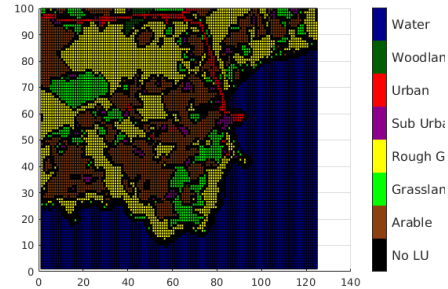


(d) Land Use - fill missing function, nearest row entry.

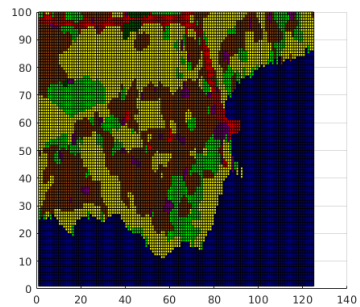
Figure 4.5.: The outcome from the land-use image processing procedure using the original MAGIC map Dudley overlay.



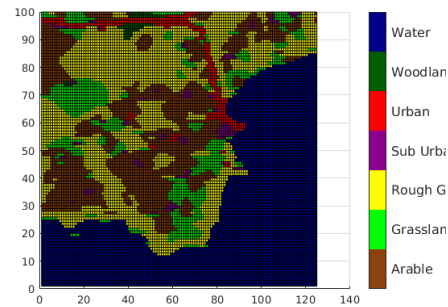
(a) Summation of all binary land uses from figure C.23.



(b) Land Use before fillmissing function.



(c) Land Use - fill missing function, nearest column entry.

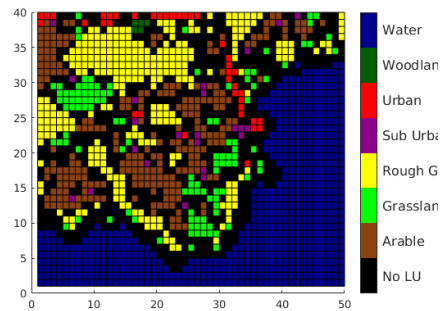


(d) Land Use - fill missing function, nearest row entry.

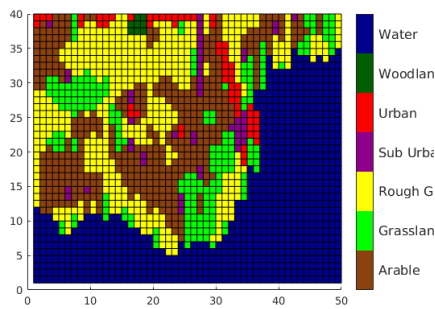
Figure 4.6.: The outcome from the land-use image processing procedure using the 20m resolution variant of the MAGIC map Dudley overlay.



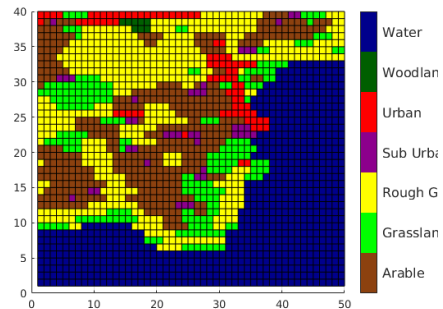
(a) Summation of all binary land uses from figure C.2.



(b) Land Use before fillmissing function.



(c) Land Use - fill missing function, nearest column entry.



(d) Land Use - fill missing function, nearest row entry.

Figure 4.7.: The outcome from the land-use image processing procedure using the 50m resolution variant of the MAGIC map Dudley overlay.

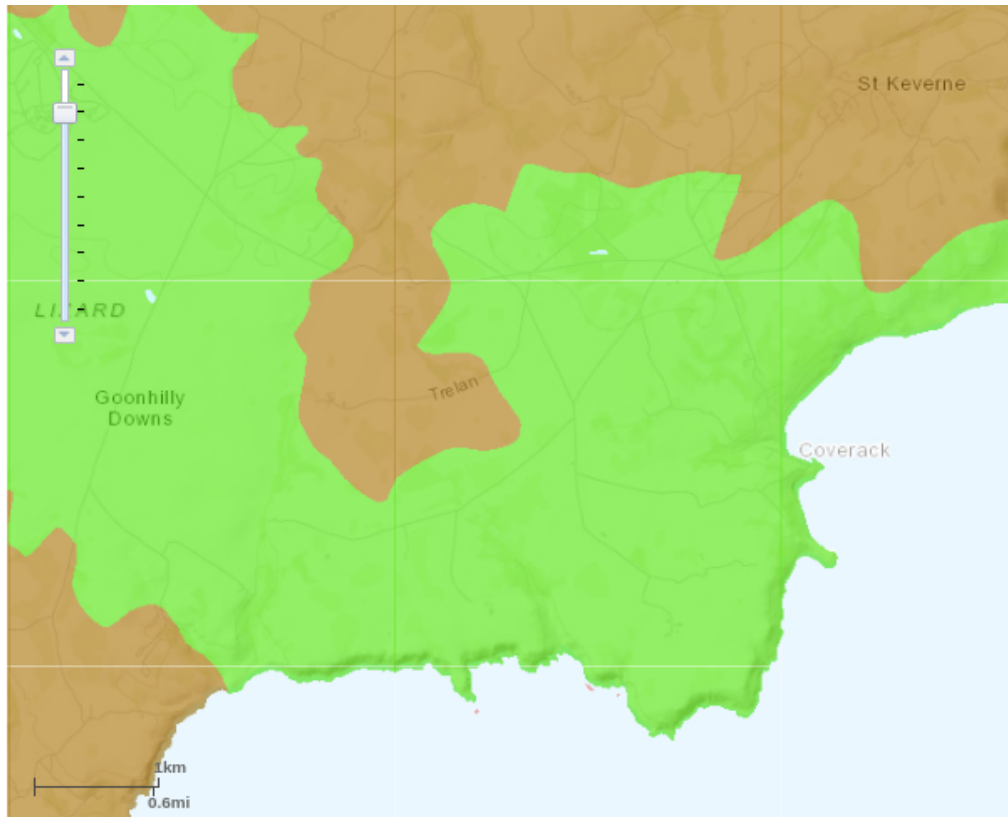


Figure 4.8.: A screenshot from the “Soilscapes” platform developed by Cranfield University to describe the underlying soil within the British Isles. Two soil types cover the computational region and are defined in the Soilscapes web platform as: 1. Soilscape 7 (Brown): “Freely draining slightly acidic but base-rich soils”; and 2. Soilscape 17 (Green): “Slowly permeable seasonally wet acid loamy and clayey soils” (Cranfield Soil and Agrifood Institute, 2023).

### 4.3. Construction of the Hydrological Model

Precipitation that is not intercepted by vegetation, or infiltrated into the soil, transfers itself to surface water reservoirs (e.g. streams, rivers, lakes etc.) across the land surface. This process is known as *surface runoff*. Approximately one third of precipitation results in surface runoff while the remaining two thirds are either transpired, evaporated or infiltrated into the soil surface below (Perlman, 2016). Surface runoff is a critical balancing component of the hydrological cycle. The combination of soil saturation excess and infiltration excess determines how much surface runoff is generated (Yang et al., 2015). Surface runoff modelling allows one to visualise how changes in land surface composition, vegetation and meteorological events affect water systems. Physically-based governing equations allows one to model runoff spatially and temporally at a desired resolution. The structure of these physical models are derived from physics-based laws meaning that the hydrological properties of a watershed are already encoded within it, making it more realistic. The use of 2D depth-averaged shallow water equation models is common place within the literature (Delis and Nikolos, 2021). It is also spatially intuitive when applied to an orthogonal grid mesh (as decided on in Section 2.7). As such, the shallow water equations will be used to govern the surface routing component of the hydrological model within this work.

The non-linear shallow water equations have been proven useful in simulating long wave hydrodynamics when one neglects the vertical acceleration of water particles and assumes flow to be nearly horizontal. Given the hydrostatic nature of the equations, hyperbolic integral formulation of the non-linear shallow water equations provide an accurate model for steep-fronted flows such as flash floods, dam breaks, etc. Utilising the theory outlined in Chapter 3 a model is constructed which will simulate potential flooding scenarios in the case study region highlighted in Section 1.2.

#### 4.3.1. Governing Equations

One may derive the 2D non-linear shallow water equations by depth-integrating the three-dimensional Reynolds-averaged Navier-Stokes equations (Reynolds, 1895) while neglecting vertical acceleration of water particles. Assuming the pressure distribution to be hydrostatic (White, 2008) in matrix form this derivation is written as

$$\frac{\partial \mathbf{q}}{\partial t} + \frac{\partial \mathbf{f}}{\partial x} + \frac{\partial \mathbf{g}}{\partial y} = \mathbf{S}, \quad (4.1)$$

where

$$\mathbf{q} = \begin{bmatrix} h \\ uh \\ vh \end{bmatrix}; \mathbf{f} = \begin{bmatrix} uh \\ hu^2 + \frac{1}{2}gh^2 \\ huv \end{bmatrix}; \mathbf{g} = \begin{bmatrix} hv \\ huv \\ hv^2 + \frac{1}{2}gh^2 \end{bmatrix}; \mathbf{S} = \begin{bmatrix} r - f \\ gh \left( S_{0x} - \frac{\tau_{zx}}{\rho} \right) \\ gh \left( S_{0y} - \frac{\tau_{zy}}{\rho} \right) \end{bmatrix}. \quad (4.2)$$

In this definition the Coriolis effects, viscous terms and surface stresses are assumed to be negligible. The first entry of each vector denotes the components of the continuity equation. The middle and final vector entries are components of the fluid momentum in the  $x$ - and  $y$ - directions respectively.

Here  $t$  is the time parameter,  $(x, y)$  are the standard Cartesian coordinates in the horizontal direction.  $\mathbf{q}$  denotes the conserved flow variable one is interested in modelling.  $\mathbf{f}$  and  $\mathbf{g}$  characterise the flux vectors in their respective  $x$ - and  $y$ - directions.  $\mathbf{S}$  contains the remaining source and sink terms.  $h$  denotes the average depth of a vertical water column.  $u$  and  $v$  are the depth-averaged velocity components in two Cartesian directions,  $g \approx 9.81\text{ms}^{-2}$  is gravitation acceleration;  $\rho$  is water density; and  $\tau_{zx}$  and  $\tau_{zy}$  are bed friction stress terms representing the energy dissipation due to bed roughness on the flow and is estimated empirically with the formulae

$$\begin{aligned} \tau_{zx} &= \rho C_f u \sqrt{u^2 + v^2} \\ \tau_{zy} &= \rho C_f v \sqrt{u^2 + v^2} \\ \text{and } C_f &= \frac{gn^2}{h^{1/3}}. \end{aligned} \quad (4.3)$$

Here,  $n$  represents the manning coefficient.  $z$  is the local surface elevation using sea level as a datum point.  $S_{0x}$  and  $S_{0y}$  represent the local bed gradients while  $S_{fx}$  and  $S_{fy}$  denote the local friction slopes in their respective directions. It is commonplace to write the water surface elevation as the sum of the local surface elevation and water depth namely  $\eta = h + z$ .  $r$  is the net local input of water from rainfall. Finally,  $f$  is the local water abstraction parameters, primarily infiltration influences within this work. Each of these parameters described here are illustrated in Figure 4.9.

#### 4.3.1.1. Integral form of the Governing Equation

Consider the *volume* within a vertical column of fluid. The domain of interest is partitioned into *control volumes* denoted  $\Omega_{(i,j)}$ . Here  $\mathbf{q}_{(i,j)}$  is the average of all conserved flow variables within the defined control volume. Taking the integral of Equation (4.1) with respect to the control volume yields

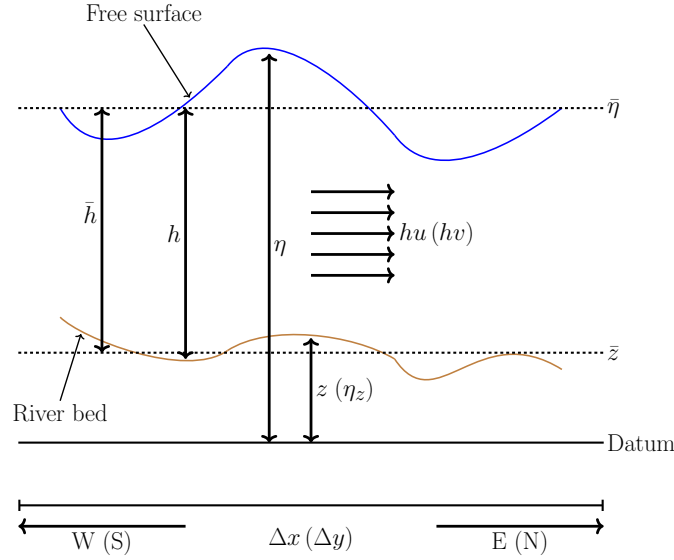


Figure 4.9.: Illustration of a shallow flow bed topography modelled by equation (4.1) with vector terms (4.2).

$$\frac{\partial}{\partial t} \int_{\Omega(i,j)} \mathbf{q}_{(i,j)} \partial\Omega_{(i,j)} + \underbrace{\int_{\Omega(i,j)} \left( \frac{\partial \mathbf{f}}{\partial x} + \frac{\partial \mathbf{g}}{\partial y} \right) \partial\Omega_{(i,j)}}_{\blacklozenge} = \int_{\Omega(i,j)} \mathbf{S}_{(i,j)} \partial\Omega_{(i,j)}. \quad (4.4)$$

One may then apply *Green's theorem* (actually proved by Bernhard Riemann (1851) Riley et al. (2010)) to rewrite ( $\blacklozenge$ ) in (4.4) as ( $\clubsuit$ ) in (4.5) as

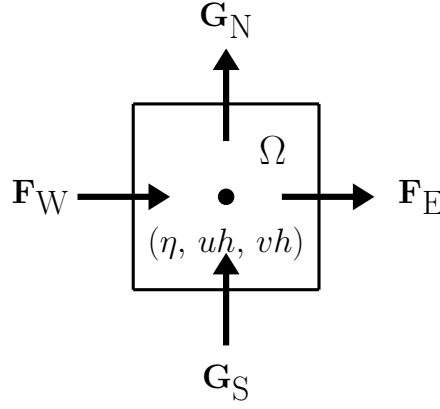
$$\frac{\partial}{\partial t} \int_{\Omega(i,j)} \mathbf{q}_{(i,j)} \partial\Omega_{(i,j)} + \underbrace{\oint_S (\mathbf{f} dy - \mathbf{g} dx)}_{\clubsuit} = \int_{\Omega(i,j)} \mathbf{S}_{(i,j)} \partial\Omega_{(i,j)}. \quad (4.5)$$

Here  $S$  is the boundary of the volume  $\Omega$ . Within the Cartesian mesh evaluating the surface integral term in (4.5) gives

$$\oint_S (\mathbf{f} dy - \mathbf{g} dx) = (\mathbf{F}_E - \mathbf{F}_W) \Delta y + (\mathbf{G}_N - \mathbf{G}_S) \Delta x. \quad (4.6)$$

$\mathbf{F}_W$ ,  $\mathbf{F}_E$ ,  $\mathbf{G}_N$  and  $\mathbf{G}_S$  are flux function vectors pointing outward from volume  $\Omega$ , in the  $x$ - and  $y$ -directions respectively, as illustrated in Figure 4.10.  $\Delta x$  and  $\Delta y$  are the side lengths of the control volume in the Cartesian grid mesh. The conserved flow variables in  $\mathbf{q}$  are assumed to reside in the cell centre.

Applying this surface integral definition (4.6) into (4.5) yields the explicit forward time conservative finite volume formula


 Figure 4.10.: Flux function vectors across the boundary of control volume  $\Omega$ 

$$\mathbf{q}_{(i,j)}^{(k+1)} = \mathbf{q}_{(i,j)}^{(k)} - \frac{\Delta t}{\Delta x} (\mathbf{f}_E - \mathbf{f}_W) - \frac{\Delta t}{\Delta y} (\mathbf{g}_N - \mathbf{g}_S) + \Delta t \left( \mathbf{r}_{(i,j)}^{(k)} + \mathbf{S}_{z_{(i,j)}}^{(k)} + \mathbf{s}_{f_{(i,j)}}^{(k+1)} \right). \quad (4.7)$$

Superscript  $(k)$  and  $(k+1)$  refer to the time-dependence of variables, written in brackets to distinguish it from exponents. Subscript  $(i, j)$  is the cell index in the  $x$ - and  $y$ - directions respectively.  $\Delta t$  denotes the timestep used in the numerical approximation. Finally,  $\mathbf{f}_W$ ,  $\mathbf{f}_E$ ,  $\mathbf{g}_N$  and  $\mathbf{g}_S$  denote the numerical fluxes through the west, east, north and south cell interfaces of volume  $\Omega$  respectively.

The source term in  $\mathbf{S}_{(i,j)}$ , in (4.5), is split into three distinct components. The first component,  $\mathbf{r}_{ij}^{(k)} = r_{ij}^{(k)} - f_{ij}^{(k)}$ , is the net quantity of water within cell volume  $\Omega_{ij}$  at time  $t = k$ . The second component is the local elevation gradient in the  $x$ - and  $y$ - directions,  $\mathbf{S}_{z_{ij}}^{(k)}$ . Both the net water quantity and elevation gradient require values at the current timestep to be evaluated. The final friction source term,  $\mathbf{S}_{\mathbf{f}_{ij}}^{(k+1)}$ , is treated implicitly as it involves conserved flow variables at the time level of interest  $t = k + 1$ . The column vector definitions of these source terms are defined below as

$$\mathbf{r}_{ij}^{(k)} = \begin{bmatrix} r_{ij}^{(k)} - f_{ij}^{(k)} \\ 0 \\ 0 \end{bmatrix}; \quad \mathbf{S}_{z_{ij}}^{(k)} = \begin{bmatrix} 0 \\ ghS_{0x} \\ ghS_{0y} \end{bmatrix}; \quad \mathbf{S}_{\mathbf{f}_{ij}}^{(k+1)} = - \begin{bmatrix} 0 \\ gh \frac{\tau_{zx}}{\rho} \\ gh \frac{\tau_{zy}}{\rho} \end{bmatrix}. \quad (4.8)$$

Figure 4.11 represents the spatial element of Equation (4.7) while the time marching element of the scheme is captured by Figure 4.12.

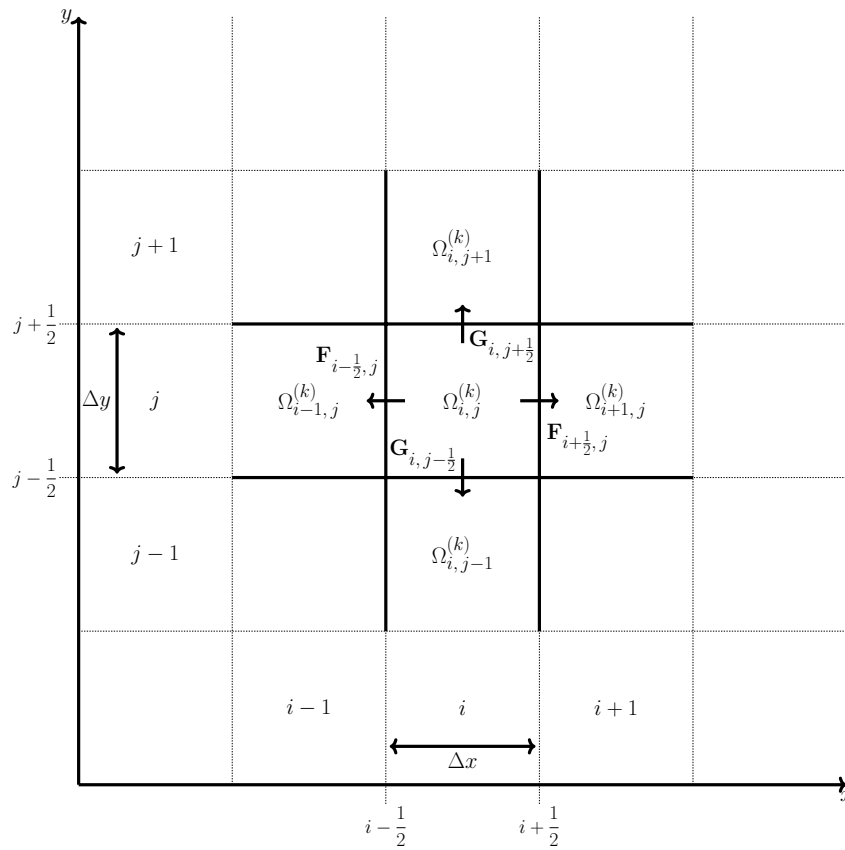


Figure 4.11.: A visualisation of the finite volume method in the  $(x, t)$  computational domain. The cell average  $Q_i^{(k)}$  is updated by the fluxes  $\mathbf{f}_{i\pm\frac{1}{2}}$  at the cell boundaries.

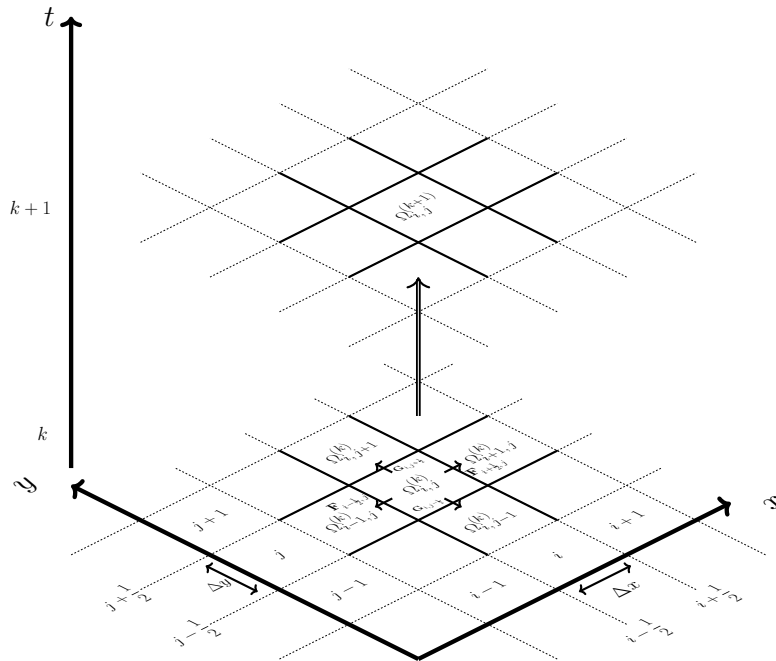


Figure 4.12.: A visualisation of the finite volume method in the  $(x, t)$  computational domain as it moves forward a single timestep.

The two-dimensional shallow water equations (4.1) are modelled by applying the first-



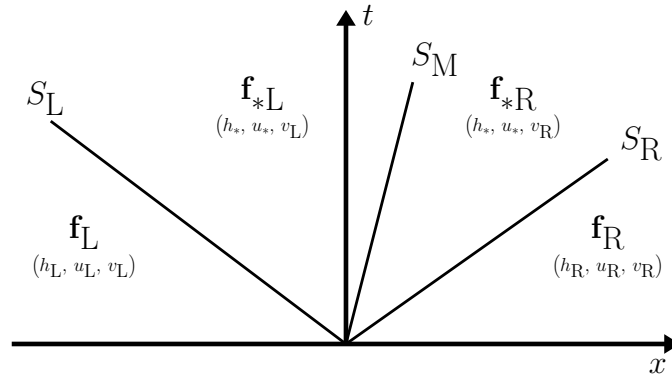


Figure 4.13.: HLLC solution structure for the Riemann Problem

order Godunov finite volume method from Toro (1999). The model's foundation is based on Liang and Borthwick (2009) with suitable modifications described within Xia et al. (2017) and Xia and Liang (2018). The specific methodologies within these articles are outlined below.

#### 4.3.2. HLLC approximate Riemann Solvers

Appendix A.3.8 highlights the general theory of Riemann Solvers and more specifically the HLLC solver (Toro et al., 1994; Toro, 1999, 2001). The HLLC solver is the chosen numerical method due to its applicability to wet-dry interfaces and ease of application. Applying the solution structure in Equation (3.47) on page 114 to the interface flux at the western pixel boundary gives:

$$\mathbf{f}_w = \begin{cases} \mathbf{f}_L & \text{if } 0 \leq S_L, \\ \mathbf{f}_{*L} & \text{if } S_L \leq S_M, \\ \mathbf{f}_{*R} & \text{if } S_M \leq S_R, \\ \mathbf{f}_R & \text{if } S_R \leq 0. \end{cases} \quad (4.9)$$

Here  $\mathbf{f}_L = \mathbf{f}(\mathbf{q}_L)$  and  $\mathbf{f}_R = \mathbf{f}(\mathbf{q}_R)$  are evaluated using the local Riemann states, discussed in Section 3.4.2. Implementing a piece-wise linear approximation using the central pixel values one may estimate the face values of the wave. The contact wave is estimated by the left and right fluxes  $\mathbf{f}_{*L}$  and  $\mathbf{f}_{*R}$  respectively.  $S_L$ ,  $S_M$  and  $S_R$  represent the wave speed estimates of the left, contact (middle) and right waves, respectively.

When considering the flux in the  $x$ -direction, the contact wave due to the existence of the  $y$ -direction momentum equation is always a shear wave. Crossing the contact wave the tangential velocity  $v$  changes in a discontinuous nature, while  $u$  and  $h$  stay constant (Toro et al., 1994).

Consider the flux expression definitions in Figure 4.13 above. Define the middle region fluxes either side of the contact wave, using the left and right tangential velocity components of the Riemann states  $v_L$  and  $v_R$  respectively, as

$$\mathbf{f}_{*L} = \begin{bmatrix} f_{*1} \\ f_{*2} \\ v_L f_{*1} \end{bmatrix} \quad \text{and} \quad \mathbf{f}_{*R} = \begin{bmatrix} f_{*1} \\ f_{*2} \\ v_R f_{*1} \end{bmatrix}. \quad (4.10)$$

Using the HLL formula defined in Harten (1983) the middle region fluxes are calculated with

$$\mathbf{f}_* = \frac{S_R \mathbf{f}_L - S_L \mathbf{f}_R + S_L S_R (\mathbf{q}_R - \mathbf{q}_L)}{S_R - S_L}. \quad (4.11)$$

To approximate the flux at the western interface of the pixel (Equation (4.9)) the wave speed estimates at the boundaries are needed. Approximations outlined in Fraccarollo and Toro (1995) are used, which includes the dry bed options using the two-rarefaction approximate Riemann solver. The left wave speed approximation may be determined from

$$S_L = \begin{cases} u_R - 2\sqrt{gh_R} & \text{if } h_L = 0, \\ \min(u_L - \sqrt{gh_L}, u_* - \sqrt{gh_*}) & \text{if } h_L > 0. \end{cases} \quad (4.12)$$

Similarly the right wave speed estimate formula is

$$S_R = \begin{cases} u_L + 2\sqrt{gh_L} & \text{if } h_R = 0, \\ \min(u_R + \sqrt{gh_R}, u_* + \sqrt{gh_*}) & \text{if } h_R > 0. \end{cases} \quad (4.13)$$

given the left  $(u_L, h_L)$  and right  $(u_R, h_R)$  Riemann states of a local Riemann problem with

$$u_* = 0.5(u_L + u_R) + \sqrt{gh_L} - \sqrt{gh_R} \quad (4.14)$$

$$h_* = g^{-1} \left[ 0.5 \left( \sqrt{gh_L} + \sqrt{gh_R} \right) + 0.25(u_L - u_R) \right]^2. \quad (4.15)$$

The recommendation from Toro et al. (1994) in general problems with dry-bed scenarios is to calculate the middle wave speed with

$$S_M = \frac{S_L h_R (u_R - S_R) - S_R h_L (u_L - S_L)}{h_R (u_R - S_R) - h_L (u_L - S_L)}. \quad (4.16)$$

The methodology outlined in this Section 4.3.2 is applied to approximate the other interface fluxes  $\mathbf{f}_E$ ,  $\mathbf{g}_N$  and  $\mathbf{g}_S$  with their corresponding parameters.

## 4.3.2.1. Estimating flux transfer across pixel boundaries

To estimate the net flux of water through cell  $\Omega_{(i,j)}$ , from Equation (4.7) at time  $t = k + 1$ , one focuses on the water transfer across the boundaries of the cell of interest. Each estimated flux is then multiplied by the appropriate spatial interval and summed to approximate the overall flux. In this model outline the process is described using the net flux contributions across the *western* cell boundary  $\mathbf{f}_W$ . This border separates cell  $\Omega_{(i,j)}$  from  $\Omega_{(i-1,j)}$  as outlined by the red box in Figure 4.14. The common practice in the literature to denote this cell boundary with the index  $(i - \frac{1}{2}, j)$  will be followed. The conserved flow variables of the two adjacent pixels are  $\mathbf{q}_{(i-1,j)}^{(k)}$  and  $\mathbf{q}_{(i,j)}^{(k)}$  respectively.

At its core this type of net flux calculation may be reduced down to a Riemann problem, such as the one described in Section 3.2.3. This Riemann problem is governed by the conservation equation (4.1) with piecewise constant initial values  $\mathbf{q}_{(i-1,j)}^{(k)}$  and  $\mathbf{q}_{(i,j)}^{(k)}$ . In the sections below techniques outlined in Chapter 3 from Toro et al. (1994); Toro (1999); Liang and Marche (2009); Xia et al. (2017); Xia and Liang (2018) are applied. The HLLC Riemann solver has become a de-facto method within the literature due to its relative ease of implementation as well as its suitability for solving “wet-dry” boundary scenarios, a common obstacle within overland flow modelling (Toro et al., 1994). To begin the set up, work needed to successfully implement the HLLC Riemann solver is discussed.

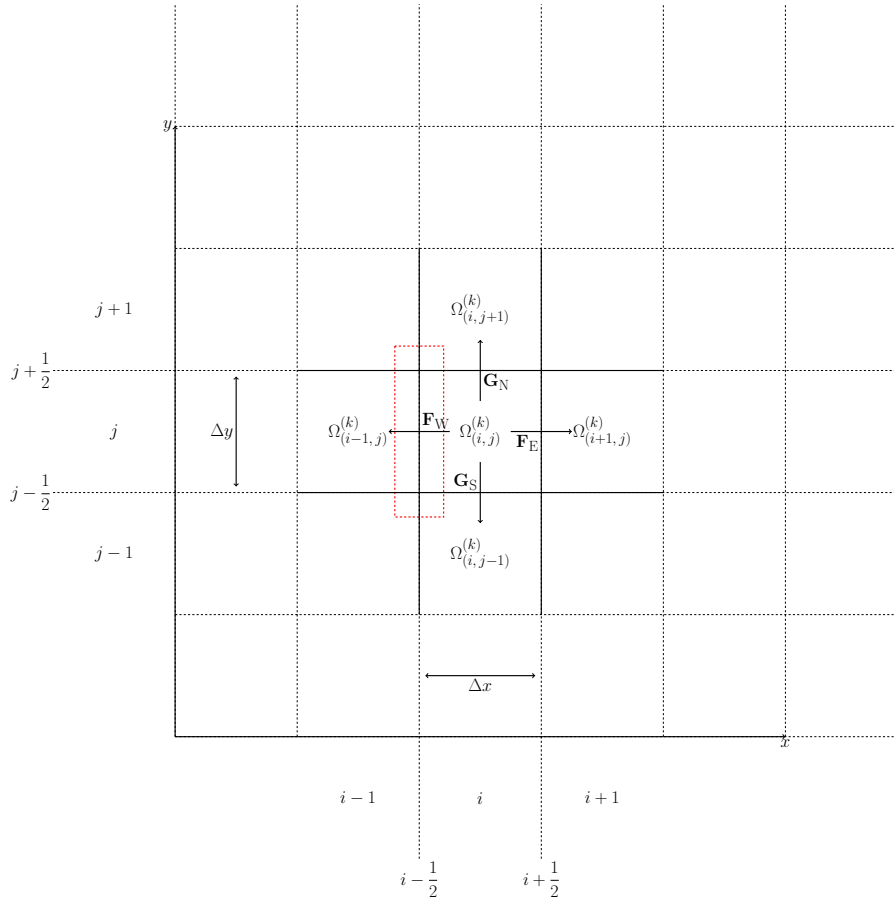


Figure 4.14.: A visualisation of the finite volume method in the  $(x, t)$  computational domain. The cell average  $Q_i^{(k)}$  is updated by the fluxes  $\mathbf{f}_{i\pm\frac{1}{2}}$  at the cell boundaries.

### 4.3.2.2. Riemann State Construction

To calculate the net flux going across the western flux boundary, the water surface elevation just to the left and right of  $(i - \frac{1}{2}, j)$  respectively denoted  $\eta_L$  and  $\eta_R$  is required. Also needed is the bed elevation  $z_L$  and  $z_R$  as well as conserved flow variables  $\mathbf{q}_L$  and  $\mathbf{q}_R$ . The left and right Riemann states for water surface elevation are defined as:

$$\begin{cases} \eta_L = \eta_{(i-1, j)} + \max \left[ 0, \min \left( z_{(i, j)} - z_{(i-1, j)} - \delta z, \eta_{(i, j)} - \eta_{(i-1, j)} \right) \right], \\ \eta_R = \eta_{(i, j)} + \max \left[ 0, \min \left( z_{(i-1, j)} - z_{(i, j)} + \delta z, \eta_{(i-1, j)} - \eta_{(i, j)} \right) \right], \end{cases} \quad (4.17)$$

where the definition of  $\delta z$  is given in Section 4.3.2.3. Using the water surface elevation Riemann states in (4.17), define the left and right bed surface elevation

$$\begin{cases} z_L = \eta_L - h_{(i-1, j)}, \\ z_R = \eta_R - h_{(i, j)}. \end{cases} \quad (4.18)$$

Using the left and right bed surface elevations in (4.18), apply a common bed elevation at the boundary as recommended in Audusse et al. (2004),

$$z_f = \max(z_L, z_R) \equiv \max(z_{(i-1, j)}, z_{(i, j)}). \quad (4.19)$$

The common bed elevation (4.19) is then utilised to define the left and right flow variable Riemann state components of water depth, ensuring non-negative values

$$\begin{cases} h_L = \max(0, \eta_L - z_f), \\ h_R = \max(0, \eta_R - z_f). \end{cases} \quad (4.20)$$

Unit-width discharges in the  $x$ - (4.21) and  $y$ - (4.22) directions are defined as follows:

$$\begin{cases} [hu]_L = h_L \cdot u_{(i-1, j)}, \\ [hu]_R = h_R \cdot u_{(i, j)}, \end{cases} \quad (4.21)$$

$$\begin{cases} [hv]_L = h_L \cdot v_{(i-1, j)}, \\ [hv]_R = h_R \cdot v_{(i, j)}. \end{cases} \quad (4.22)$$

Here,  $u_{(i, j)} = [hu]_{(i, j)} / h_{(i, j)}$  and similarly defined for  $u_{(i-1, j)}$ ,  $v_{(i-1, j)}$  and  $v_{(i, j)}$ .

### 4.3.2.3. Surface Reconstruction Method

The Riemann states either side of a contact wave need to be determined in order to implement the HLLC solver outlined in Section 4.3.2. To do this, a method proposed by Xia et al. (2017) known as the *Surface Reconstruction Method* is applied. To begin reconstructing the bed surface elevations of adjacent pixels separated by the boundary of the control volume one may use:

$$\begin{cases} z_{(i-\frac{1}{2},j)-} = z_{(i-1,j)} + \mathbf{r}_{(i-1,j)} \Phi(\mathbf{r}_{(i-1,j)}) \nabla z_{(i-1,j)}, \\ z_{(i-\frac{1}{2},j)+} = z_{(i,j)} + \mathbf{r}_{(i,j)} \Phi(\mathbf{r}_{(i,j)}) \nabla z_{(i,j)}. \end{cases} \quad (4.23)$$

Equation (4.23) determines whether the terrain between two adjacent cells is continuous or not.  $\nabla z_{(i,j)}$  is a first order approximation of the bed gradient and is restricted by the minmod gradient limiter

$$\Phi(r_{(i,j)}) = \max[0, \min(r_{(i,j)}, 1)] \quad \text{where} \quad r_{(i,j)} = \frac{z_{(i+1,j)} - z_{(i,j)}}{z_{(i,j)} - z_{(i-1,j)}}, \quad (4.24)$$

as discussed in Section 3.5. In this instance, the distance between the boundary and cell centre in the  $x$ -direction is  $\mathbf{r}_{(i,j)} = \Delta x/2$ . Similarly in the  $y$ -direction,  $\mathbf{r}_{(i,j)} = \Delta y/2$ . One then can calculate the difference between bed elevations from adjacent cells using

$$\delta z = z_{(i-\frac{1}{2},j)+} - z_{(i-\frac{1}{2},j)-}. \quad (4.25)$$

The bed elevation difference in (4.25) is then applied to Equation (4.17) to determine the left and right Riemann states needed for the simulation.

### 4.3.3. Source term discretisation

Using the left Riemann state for water depth defined by Equation (4.20) and common bed elevation by (4.19) one may define the *bed source* terms as

$$\mathbf{S}_z = \begin{bmatrix} 0 \\ \frac{1}{\Delta x \cdot \Delta y} \sum \frac{1}{2} g (h_i + h_{(L,B)}) (z_i - \bar{z}_{(f,B)}) \end{bmatrix}. \quad (4.26)$$

where  $B$  is a place holder for one of the cardinal directions  $B = \{N, S, E, W\}$  and  $h_{(L,B)}$  are the respective left water depth Riemann states at the cell boundaries.

$\bar{z}_{(f,B)}$  is a local bed modification scheme defined to prevent numerical instability of a solution when at rest. It is defined as

$$\bar{z}_{(f,B)} = z_{(f,B)} - \Delta z, \quad (4.27)$$

where without loss of generality

$$\Delta z = \begin{cases} \max(0, z_{(f,B)} - \eta_{(i,j)}) & \text{if } h_{(i+1,j)} < \epsilon_h, \\ \max(0, \min(\delta z, z_{(f,B)} - \eta_{(i,j)})) & \text{if } h_{(i+1,j)} > \epsilon_h. \end{cases} \quad (4.28)$$

$\epsilon_h$  is an infinitesimal value defining the threshold of when a cell is deemed to be “dry”. Xia et al. (2017) is followed in defining this threshold as  $\epsilon_h = 10^{-10}$ .

#### 4.3.4. Friction term discretisation

Standard practice within shallow water modelling is to treat the friction component of the governing equation (4.1) implicitly (Fiedler and Ramirez, 2000; Liang and Borthwick, 2009; Costabile et al., 2013). Friction terms may be numerically approximated using methods such as Newton-Raphson (Xia et al., 2017). However within this work, the method outlined in Xia and Liang (2018) is followed. This method calculates the friction term explicitly after some algebraic manipulation. Consider the momentum components of the governing equation in scalar form:

$$q_x^{(k+1)} = q_x^{(k)} + \Delta t A_x - \Delta t g n^2 \left(h^{(k)}\right)^{-7/3} q_x^{(k+1)} \sqrt{\left(q_x^{(k+1)}\right)^2 + \left(q_y^{(k+1)}\right)^2}, \quad (4.29)$$

$$q_y^{(k+1)} = q_y^{(k)} + \Delta t A_y - \Delta t g n^2 \left(h^{(k)}\right)^{-7/3} q_y^{(k+1)} \sqrt{\left(q_x^{(k+1)}\right)^2 + \left(q_y^{(k+1)}\right)^2}. \quad (4.30)$$

Here  $(q_x, q_y) = (hu, hv)$  are the unit-width discharges in the  $x$ - and  $y$ -directions respectively.  $A_x$  and  $A_y$  are the momentum components computed at time  $t = k$  as discussed in Sections 4.3.2.3 and 4.3.3,  $-(\Delta x \cdot \Delta y)^{-1} \sum \mathbf{f}_B(\mathbf{q}^{(k)}) + \mathbf{s}_z^{(k)}$ . It is evident that Equations (4.29) and (4.30) are respective non-linear functions of  $(q_x, q_y)$ . Reforming these Equations to isolate the unit-width discharges at the next timestep

$$q_x^{(k+1)} \left\{ 1 + \Delta t g n^2 \left(h^{(k)}\right)^{-7/3} \sqrt{\left(q_x^{(k+1)}\right)^2 + \left(q_y^{(k+1)}\right)^2} \right\} = q_x^{(k)} + \Delta t A_x, \quad (4.31)$$

$$q_y^{(k+1)} \left\{ 1 + \Delta t g n^2 \left(h^{(k)}\right)^{-7/3} \sqrt{\left(q_x^{(k+1)}\right)^2 + \left(q_y^{(k+1)}\right)^2} \right\} = q_y^{(k)} + \Delta t A_y. \quad (4.32)$$

Making the simple definitions  $m_x = q_x^{(k)} + \Delta t A_x$ ;  $m_y = q_y^{(k)} + \Delta t A_y$  and dividing (4.31) with (4.32) yields the ratio

$$\frac{q_x^{(k+1)}}{q_y^{(k+1)}} = \frac{m_x}{m_y}. \quad (4.33)$$

Taking ratio (4.33) and substitute it into (4.31) gives

$$q_x^{(k+1)} \left\{ 1 + \Delta t g n^2 \left( h^{(k)} \right)^{-7/3} \sqrt{\left( q_x^{(k+1)} \right)^2 + \left( \frac{m_y}{m_x} \right)^2 \left( q_x^{(k+1)} \right)^2} \right\} = m_x. \quad (4.34)$$

Now consider the cases where  $q_x^{(k+1)}$  is positive and non-positive. If:

1.  $q_x^{(k+1)} > 0$ , equation (4.34) takes the form

$$q_x^{(k+1)} + \left( q_x^{(k+1)} \right)^2 \Delta t g n^2 \left( h^{(k)} \right)^{7/3} \sqrt{1 + \left( \frac{m_y}{m_x} \right)^2} = m_x; \quad (4.35)$$

2. Otherwise  $q_x^{(k+1)} < 0$  and

$$q_x^{(k+1)} - \left( q_x^{(k+1)} \right)^2 \Delta t g n^2 \left( h^{(k)} \right)^{7/3} \sqrt{1 + \left( \frac{m_y}{m_x} \right)^2} = m_x. \quad (4.36)$$

Equations (4.35) and (4.36) are quadratic expressions for the unit-width discharge in the  $x$ -direction at time level  $t = k + 1$ . Each equation has two roots and so four potential values are eligible solutions mathematically. To identify a suitable root solution, consider the physical plausibility of the roots. For example, for (4.35):

$$q_x^{(k+1)} = \frac{1 \pm \sqrt{1 + 2m_x \alpha}}{-\alpha}, \quad (4.37)$$

where

$$\alpha = 2\Delta t g n^2 \left( h^{(k)} \right)^{-7/3} \sqrt{1 + \left( \frac{m_y}{m_x} \right)^2}. \quad (4.38)$$

Similarly, assuming non-positive unit-width discharge, the roots to the quadratic expression (4.36) are:

$$q_x^{(k+1)} = \frac{1 \pm \sqrt{1 - 2m_x \alpha}}{\alpha}. \quad (4.39)$$

The physical interpretations of the roots in (4.37) are discussed. First assume  $m_x > 0$  then  $(4.37)^+$  will be negative<sup>2</sup>. This directly contradicts the initial assumption that the unit-width discharge is positive and so cannot be a physically permissible root. For both roots of (4.39), the unit-width discharges are positive provided they are real, contradicting the initial assumption of non-positivity and so can be rejected. The final root  $(4.37)^-$  is positive and consistent with the original assumption. Thus its derivation is the only physically plausible root for positive  $m_x$ .

Assuming  $m_x < 0$ , one may determine that the root  $(4.39)^-$  is the only possible root using an analogous analysis above. One may then combine  $(4.37)^-$  and  $(4.39)^-$  into a single expression for the unit-width discharge at time  $t = k + 1$  as

$$q_x^{(k+1)} = \frac{m_x + m_x \sqrt{1 + 2m_x \alpha}}{-m_x \alpha}. \quad (4.40)$$

An explanation of how both of these roots may be combined can be found in Xia and Liang (2018). Two further considerations are needed before conclusively defining the unit-width discharge. The first is for extremely small water depth  $h^{(k)}$  contained within  $\alpha$ . If this were to occur, the calculation may require a computational precision a machine cannot accommodate and thus introduce numerical instability. A preventative measure is utilised by transferring  $(h^{(k)})^{-1}$  into the square root of  $m_x \alpha$  to give

$$q_x^{(k+1)} = \frac{m_x - m_x \sqrt{1 + 4\Delta t g n^2 (h^{(k)})^{-4/3} \sqrt{\left(\frac{m_x}{h^{(k)}}\right)^2 + \left(\frac{m_y}{h^{(k)}}\right)^2}}{-2\Delta t g n^2 (h^{(k)})^{-4/3} \sqrt{\left(\frac{m_x}{h^{(k)}}\right)^2 + \left(\frac{m_y}{h^{(k)}}\right)^2}}. \quad (4.41)$$

One final consideration is when a denominator of a solution equals zero. If this is an actuality, one can use either Equation (4.35) or (4.36) and set  $q_x^{(k+1)} = m_x$ . To conclude, the physically admissible unit-width discharge in the horizontal  $x$ -direction is

$$q_x^{(k+1)} = \begin{cases} m_x & \text{if } m_x \alpha < \epsilon_h, \\ \frac{m_x - m_x \sqrt{1 + 4\Delta t g n^2 (h^{(k)})^{-4/3} \sqrt{\left(\frac{m_x}{h^{(k)}}\right)^2 + \left(\frac{m_y}{h^{(k)}}\right)^2}}{-2\Delta t g n^2 (h^{(k)})^{-4/3} \sqrt{\left(\frac{m_x}{h^{(k)}}\right)^2 + \left(\frac{m_y}{h^{(k)}}\right)^2}} & \text{if } m_x \alpha \geq \epsilon_h. \end{cases} \quad (4.42)$$

By identical analysis, the unit-width discharge located in the quadratic expression (4.32)

---

<sup>2</sup>(4.37)<sup>+</sup> denotes the root with addition operator  $\frac{1 + \sqrt{1 + 2m_x \alpha}}{-\alpha}$ , similarly (4.37)<sup>-</sup> denotes the root with the subtraction operator,  $\frac{1 - \sqrt{1 + 2m_x \alpha}}{-\alpha}$



for the horizontal  $y$ -direction has the physically admissible solution

$$q_y^{(k+1)} = \begin{cases} m_y & \text{if } m_y \alpha < \epsilon_h, \\ \frac{m_y - m_y \sqrt{1 + 4\Delta t g n^2 (h^{(k)})^{-4/3} \sqrt{\left(\frac{m_x}{h^{(k)}}\right)^2 + \left(\frac{m_y}{h^{(k)}}\right)^2}}}{-2\Delta t g n^2 (h^{(k)})^{-4/3} \sqrt{\left(\frac{m_x}{h^{(k)}}\right)^2 + \left(\frac{m_y}{h^{(k)}}\right)^2}} & \text{if } m_y \alpha \geq \epsilon_h. \end{cases} \quad (4.43)$$

#### 4.3.4.1. Estimating the Manning Parameter

In equation (4.3), a reference to the manning coefficient was stated. A brief outline of the history which gave rise to this parameter is given as well as a description on how it is implemented in the model.

In 1889, Irish Engineer Robert Manning presented the ‘‘Manning formula’’<sup>3</sup> built on from the work of Philippe Gauckler in 1867 (Manning, 1891). It is an empirical formula used to estimate the average velocity of a liquid flowing in a channel that is open to atmospheric pressure; or put more simply, open channel flow. Further details specific to this formula can be found in chapter 5-6 of Chow et al. (1988).

The greatest difficulty in implementing this formula comes from the estimation of the roughness coefficient (or Manning coefficient),  $n$ . There is no agreed upon process to select an appropriate value within the literature. Typically, four guiding principles are used:

1. Understand the factors which affect the value of  $n$ . How does the basic knowledge of the problem one is trying to solve help reduce the candidate values of  $n$ ?
2. Consult a table of typical coefficient values with varying channel types.
3. Examine and understand the appearance of typical channels with known roughness coefficients.
4. Determine the value of  $n$  through analytical processes based on theoretical velocity distribution in a channel cross section.

Engineers typically consider ten factors which can influence this roughness coefficient. These are *Surface Roughness*; *Vegetation*; *Channel Irregularity*; *Channel Alignment*; *Silting and Scouring*; *Obstruction*; *Channel Shape and Size*; *Stage and Discharge*; *Seasonal Discharge* and *Suspended Material and Bed Load*. A more thorough explanation of these factors are highlighted in (Chow et al., 1988, Chapt. 5-8).

Noting that several factors can influence the value of this roughness coefficient, Cowan

<sup>3</sup>It is also referred to as the ‘‘Gauckler–Manning’’ or ‘‘Gauckler-Manning-Strickler’’ formula

(1956) put forward a formula to compute the value of  $n$  as

$$n = (n_0 + n_1 + n_2 + n_3 + n_4) m_5. \quad (4.44)$$

Table 5-5 in (Chow et al., 1988, pg. 109) provides possible values one can use to compute the roughness coefficient. The parameters in Equation (4.44) are as follows:  $n_0$  is the basic  $n$  value for a straight uniform smooth channel;  $n_1$  captures the effect of surface irregularities;  $n_2$  covers variations in shape and size of the channel cross section.  $n_3$  represents any obstructions present;  $n_4$  provides a value for vegetation and flow conditions; and  $m_5$  is a correction factor that is dependent on the meandering of a channel. Further to that table, a table of Manning's Roughness coefficients was constructed by Robert Horton in 1916 (Chow et al., 1988) which lists the minimum, normal and maximum values of  $n$  depending on the description of channel type. Table 4.1 below extracts values from a more complete table 5-6 in (Chow et al., 1988, pgs. 110-114) and relates it to the land-use category descriptions used in this work. Throughout every simulation, the "normal" value was applied.

Table 4.1.: Values of Manning's Roughness Coefficient used for each land-use category. Retrieved from table 5-6 in (Chow et al., 1988, pg. 113).

Region	Channel Type	Land-Use	Description	Min	Normal	Max
Flood Plain	Natural Stream	Arable	Cultivated area, Mature Field Crops	0.03	0.04	0.05
Flood Plain	Natural Stream	Grassland	Pasture, No brush, Short Grass	0.025	0.03	0.035
Flood Plain	Natural Stream	Rough Grazing	Pasture, No brush, High Grass	0.03	0.035	0.05
Built up channel	Urban	Sub-Urban	Composition: 20% Roads; 30% Woodland; 50% Residential/Urban	-	0.0541	-
Built up channel	Urban	Urban	Non-metal, Asphalt, Smooth	0.013	0.013	-
Flood Plain	Natural Stream	Woodland	Trees, Dense Willows, Summer, Straight	0.11	0.15	0.2

### 4.3.5. Infiltration Model

Out of the six land-use types that are considered in this work (discussed in Section (4.2.3)), four surfaces are considered ‘permeable’, *Arable*, *Grassland*, *Rough Grazing* and *Woodland* (as illustrated in Figure (4.2c), page 142). Four potential candidate models exist that may be used to model the infiltration component of a hydrological model for permeable surfaces. These are the Green-Ampt model (Green and Ampt, 1911), Horton’s model (Horton, 1919), Richards equation (Richards, 1931), and Philip’s model (Philip, 1954). A summary of these models may be viewed in Table (2.2; page 60).

As noted in Section 2.6, the purpose of this work is to construct a hydrological model that will work *towards* a computational tool to aid in the management of natural systems. In the context of land-use management planning it is vital to understand the underlying hydrological properties of the watershed to ascertain how decisions involving converting land-use cases could affect local flooding risk in the near and longer term. The Horton model explains how soil infiltration capacity declines throughout a precipitation event and runoff is generated only when rainfall intensity exceeds infiltration capacity. This model models infiltration capacity as a function of time and is physically decoupled from the physical parameters, and hydrological characteristics, that would underpin differing soil types. Similarly the Philip model also calculates infiltration capacity as a function of time. Due to the need for physical consideration of the hydrological characteristics in this use case, the Horton and Philip models were deemed unsuitable.

Both the Green-Ampt model and Richards equation contain parameters which capture the hydraulic qualities of the soil to provide a physically coupled model. Obtaining a solution to Richards equation is one of the most challenging problems in hydrological modelling (Farthing and Ogden, 2017). Such a solution has been noted as computationally expensive and unpredictable since there is no guarantee of a solver converging given a set of parameters (Short et al., 1995; Tocci et al., 1997). Also, the need for field observations to quantify the soil hydraulic properties needed for the equation present practical limitations for this work. As such, the Richards equation was also deemed unsuitable.

The Green-Ampt model on the other hand is a simple model where its parameters may be obtained from the physical properties of the soil. A parameter table for differing soil types is already present in the literature (as seen in Table (3.1); page 120). The model has been shown to produce satisfactory results for profiles where hydraulic conductivity increases with depth; for soils having non-uniform initial water contents (particularly useful if one wishes to consider different management scenarios after a heavy rainfall); and for profiles that become dense with depth etc. (Gupta, 2017). It is for these reasons that the Green-Ampt model was developed to represent the unsaturated zone component of the hydrological model within this work. Its construction is discussed in Section (4.3.5.1). The initial construction of the model involved the implementation of the Newton-Raphson method to take into account the ponded-infiltration scenario. Simulation of a single timestep would take forty minutes to execute due to the implicit nature to resolve numerically. A new approach is developed to replace the Newton-Raphson component of

the Green-Ampt model. It will be shown that for each soil texture tested there is good agreement in output between the full and approximate models using the worked example, outlined in Section 3.6.1.2 (page 126), to compare them. At the time of writing, there was no evidence found within the literature that this approach has been utilised in this context before. It is believed that the approach outlined below is a novel interpretation of implementing the Green-Ampt method.

The remaining two land-use types that have ‘impermeable’ surfaces are the *sub-urban* and *urban* categories. The Green-Ampt model was designed for natural environments and not built-up regions. As such a separate method to calculate runoff abstraction and runoff rate is required for these two remaining categories. Three potential candidate methods were considered for this task. These are the Rational Method (Rossmiller, 1980; Mishra and Singh, 2003), Cook’s Method (Miller, 1994) and the SCS Method (S.C.S, 1972; Kouwen, 1988).

The Rational Method employs an empirical formula in an urban setting to compute peak runoff rates to design drainage infrastructure. Rainfall amount, intensity, catchment conditions and human activity are all considered to determine runoff amount. It is most useful when considering relatively small areas such as roof tops and parking lots. Its use is restricted to areas of less than 8km<sup>2</sup> (Miller, 1994). The method assumes the rainfall is uniformly distributed over a watershed and its rainfall intensity is constant. In the case of land-use planning one is not afforded the luxury of assuming that rainfall rate will be constant. From this assumption alone, this method is discounted. Cook’s Method is similar to the Rational Method, except that it parametrises four specific catchment size and conditions. These are *Relief*, *Soil infiltration*, *Vegetation cover*, and *Surface Storage*. These values may be seen in Chapter 2, Table 2.7 in Miller (1994). However, again given the underlying assumption of a uniform rainfall distribution and rainfall intensity and its unsuitability for use in land management contexts, this method is also discarded.

The final candidate, the SCS Method, is an already widely used and accepted method for predicting runoff and infiltration (Natural Resources Conservation Service, 1986). This model is simple in its concept and requires only the curve number (CN) as a parameter. The model inputs are well documented in literature and it does not require an initial assumption for a uniform rainfall distribution and constant rainfall intensity rate. It is for these reasons, that this method is adopted for calculating the infiltration component of the hydrological model for the sub-urban and urban areas within the computational domain. The application of the SCS Method is presented in Section (4.3.5.2).

#### **4.3.5.1. Green-Ampt Approximation**

Chapter 5 presents an analysis on the model performance that is described within this chapter. This analysis considers both resolution variants outlined in Section 4.2.3. When conducting this analysis initially, the model implemented the Newton Raphson method during ponding scenarios as it was laid out in Section 3.6.1.2. The parameters for these simulation comparisons is outlined in Section 5.4. When comparing the original and

Table 4.2.: A table displaying the total time taken to execute a single timestep of the model when the Newton Raphson method was applied. This single timestep was scaled by a factor to estimate the likely time the model would take to resolve assuming the computational effort was consistent.

<b>Record Type</b>	<b>Timestep #</b>	<b>Seconds</b>	<b>Time</b> [DD:HH:MM:SS]
<b>Measured</b>	1	2438.38	00:00:40:38
<b>Estimate</b>	5	12191.9	00:03:23:12
<b>Estimate</b>	10	24383.82	00:06:46:23
<b>Estimate</b>	50	121919	01:09:51:59

approximate Green-Ampt models, the words “overestimate” and “underestimate” are used to relate between both models as opposed to between a model and observation data. This nomenclature is also used in the analysis between the 20m and 50m model variants in Chapters 5 and 6.

Table 4.2 documents the time taken for a single timestep to complete. The time taken to execute a single timestep was scaled by a factor to estimate the time it would take to resolve assuming that the level of computational performance was consistent. Upon investigation into the model, the ponded infiltration calculation using the Newton-Raphson method was the primary culprit in the infeasibility of the time taken to compute, given its implicit approach to numerical resolving.

To resolve this issue, the Newton-Raphson method within the Green-Ampt model is replaced with an approximate method to minimise the computational demand needed. Boxes B and D in Figure 3.13 in Section 3.6.1.1 are the two areas within the model flow where the Newton Raphson method is utilised.

If the rainfall rate  $r(k)$  is less than the infiltration capacity, one again calculates the intermediary infiltration capacity, using Equation (3.59) on page 119, with the intermediary total infiltration  $F'_{t+\Delta t}$  (Figure 3.13, box C; page 125). If the rainfall rate is less than the intermediary infiltration capacity value ( $f'_c(k)$ ) then the entire volume of rainfall in that timestep is infiltrated.

If a given rainfall rate is greater than  $f'_c(k)$ , then Equation (3.62) is used to determine the cumulative infiltration at the point when ponding commences. The time taken within the interval for ponding to occur is also calculated. The total amount of rainfall input which occurs during ponding equates to

$$rf_r(k) = r(k) \Delta t \left( 1 - \frac{t'_k}{\Delta t} \right). \quad (4.45)$$

$r(k)\Delta t$  is a product between the rainfall rate at timestep  $k$  and the temporal interval for the computation. This gives the total amount of rainfall input expected over a given timestep. The term inside the brackets gives the proportion of time remaining during the ponding event. When ponding begins, the infiltration is assumed to occur at a rate equal to the intermediate infiltration capacity value ( $f'_c(k)$ ). Hence the total amount of infiltration during ponding is

$$F_{pp} = (\Delta t - t'_k)f'_c(k). \quad (4.46)$$

Thus the respective total infiltration and runoff is equal to

$$F_c(k) = F(t'k) + F_{pp} \quad (4.47)$$

$$rf_o(k) = rf_r(k) - F_{pp}. \quad (4.48)$$

If initially the rainfall rate is greater than the infiltration capacity (box B; Figure 3.13), one assumes that infiltration occurs at a linear rate according to its capacity and ponding occurs throughout the interval

$$F_A = F(k-1) + f_c(k)r(k)\Delta t. \quad (4.49)$$

In Section 3.6.1.1, the model flow was illustrated using a worked example taken from Tarboton (2003) with the flow chart figure 3.13 on page 125.

Table 3.1; page 120 notes the soil parameters used in the full Green-Ampt model described in Section 3.6.1.1. The approximate Green-Ampt model described in this section is compared against the full model using the rainfall input increments from Table 3.3; page 127.

For each of the soil types below three figures are presented. The first shows the infiltration capacity for both the full model (blue squares) and approximate model (black asterisks). The second shows the percentage error difference of the infiltration capacity between the two models. The final plot depicts the total surface runoff per timestep for each model respectively. To compliment these figures, the raw data for these graphs may be found in appendix D.

Figures 4.15a - 4.15c; page 170 compares the full model to the approximate model with the sand soil type parameters, with the results from these simulations listed in Table D.4; page 352. There were no discrepancies to be found between the models when considering this soil type. Similarly for the Loamy Sand soils, Figures 4.16a - 4.16b; page 170 and Table D.5; page 352, the approximate infiltration model absorbed all the incoming rainfall inputs from the worked example.

The approximate model absorbed a little more rainfall compared to the full model, as seen between Figures 4.17a - 4.17c; page 171 and Table D.6; page 353. This left runoff in the approximate model to slightly underestimate the full model, but the relative magnitudes between the timesteps for each model performed similarly. There was minimal discrepancy between the infiltration capacities for the models using the Sandy Loam parameters.

For the Loam soil type, the approximate model overestimated the rainfall runoff rate by 7.9% on the second timestep ( $\Delta t = 0.5$ ) resulting in a 10% difference between the runoff outputs at the same point of the model. Despite this, as the simulation progressed difference between the approximate and full model was below 1% during the second half of the run as illustrated in Figures 4.18a – 4.18c; page 171 and Table D.7; page 353.

The difference in infiltration capacity between the two models oscillated around 1% for the silty loam soil parameters. The approximate model infiltrated too little water at  $\Delta t = 0.75$  and a little more for the remaining timesteps. This resulted in an overestimate of runoff to begin with and then an underestimation of runoff for the remaining time. As seen in previous soil types beforehand, Figures 4.19a – 4.19c show the relative magnitudes between both models does perform well, with Table D.8 presenting the specific values.

During the Sandy Clay Loam simulations, the approximate model consistently slightly underestimated the infiltration capacity. The difference between this underestimation began at just below 12% and shrank as the simulation ran where at the final timestep a difference of 4% was recorded. The sensitivity of the Newton-Raphson method in the implicit nature of infiltration of ponded conditions is reflected in the runoff output at the first timestep in 4.20a; page 172, where a lot less water is infiltrated into the soil compared to its approximate counterpart. Apart from this first timestep, the runoff outputs for each model performed similarly, as depicted by Figures 4.20a - 4.20c and Table D.9; page 354.

When the Clay Loam infiltration parameters were implemented into the approximate model, the model began to slightly overestimate the infiltration capacity by 10%, but then slightly underestimate the full model though consistently close the difference between the two models. This initial overestimation is seen with the lower runoff output on the first timestep  $\Delta t = 0.25$  in Figure 4.21c; page 173. However for the remaining timesteps, the runoff values between the two models matched well and their magnitude behaviour of the approximate model closely matched the full model. Table D.10; page 355 lists these values.

Similar to the clay loam soil type, the silty clay loam soils initially overestimates the infiltration capacity by 27%, but quickly recovers to less than 5% difference in the remaining timesteps as seen in Figures 4.24a – 4.22c. This initial infiltration absorption sees the runoff much reduced at the first timestep but then matches closely with the full models for the remaining part of the simulation. Table D.11

Applying the Sandy Clay soil parameters to the approximate model initially saw the infiltration capacity overestimate by 15.47%, but consistently decreased as the simulation continued to a little above 2.5%. This overestimate saw the runoff at the first timestep be underestimated in the approximate model, but the relative magnitudes between each

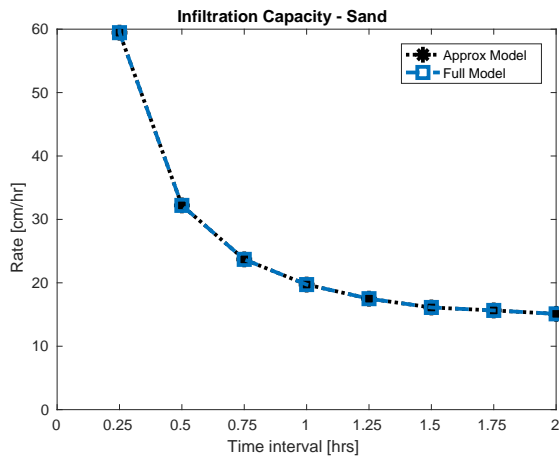


timestep closely match as seen in Figures 4.23a – 4.23c; page 174 and Table D.12; page 356.

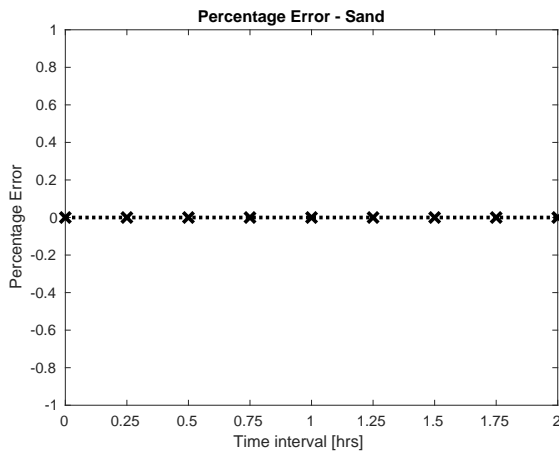
Like the Sandy Clay soil, when the approximate model applied the silty clay soil it initially overestimated the infiltration capacity by 27.16%, but quickly recovered to below 5%, as illustrated in Figures 4.24a – 4.24c; page 174 with values in D.13; 356.

Similar to the previous two soil types discussed, initially the approximate model overestimate the infiltration capacity by 52.17%, seeing the runoff output differ by 61.03%. However, after this the approximate model settles and the percentage error stabilises to 2-3% as seen in Figures 4.25a – 4.25c and Table D.14.

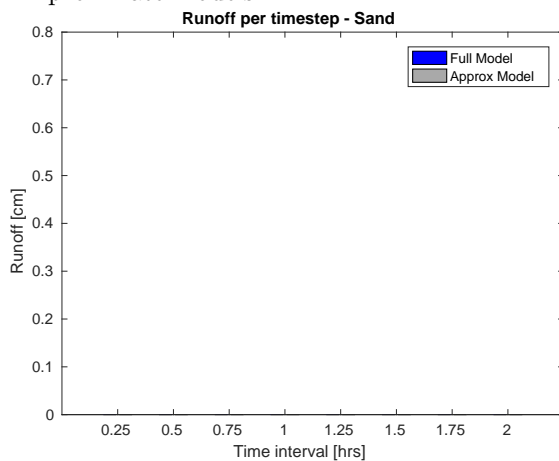
To conclude, the approximate model performs well enough to show the potential long term effect of infiltration of ponded conditions given a large enough run. Coarser soils work much better than finer soils in the initial timesteps, but comparisons of runoff magnitude between timestep intervals match well for both models. As the soils being modelled become more finer in porosity, the approximate model is less accurate but given enough time does provide a good substitute to the Newton-Raphson method.



(a) Absolute values for the infiltration capacity of the full and approximate models.

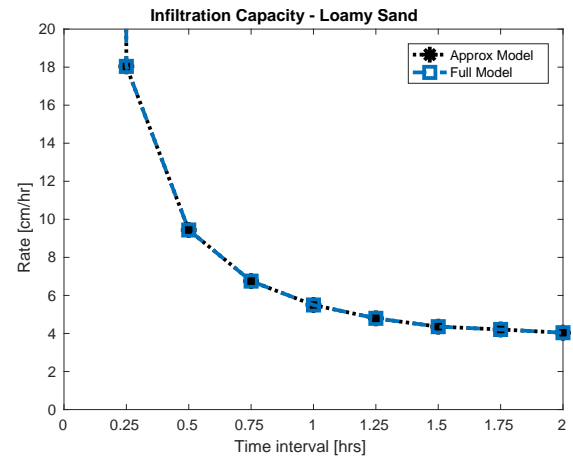


(b) Percentage error values for the infiltration capacity comparing the full and approximate models.

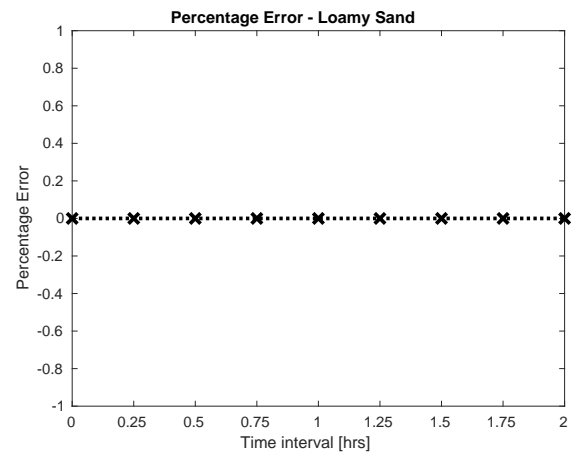


(c) Runoff rate per timestep comparison between the full and approximate models.

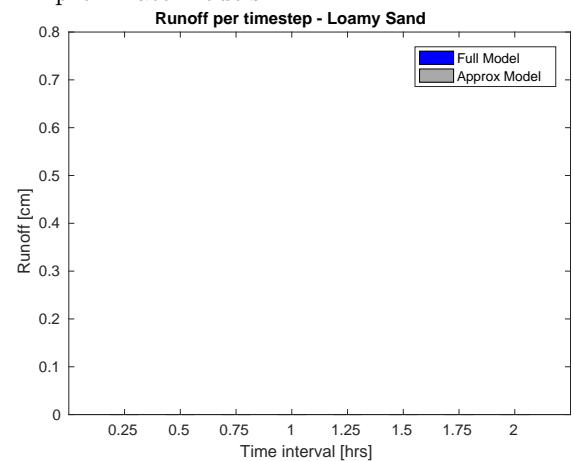
Figure 4.15.: A comparison between the full and approximate Green-Ampt model for the Sand soil parameter.



(a) Absolute values for the infiltration capacity of the full and approximate models.

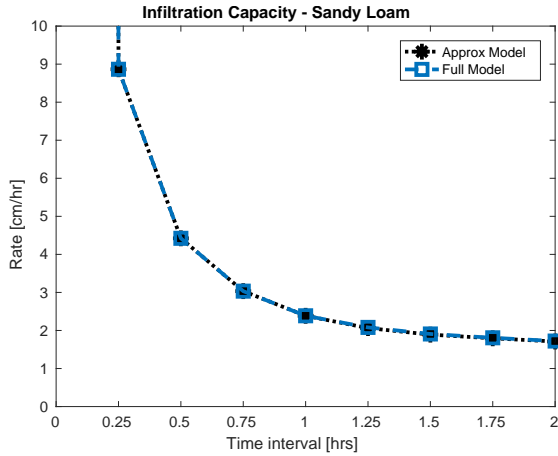


(b) Percentage error values for the infiltration capacity comparing the full and approximate models.

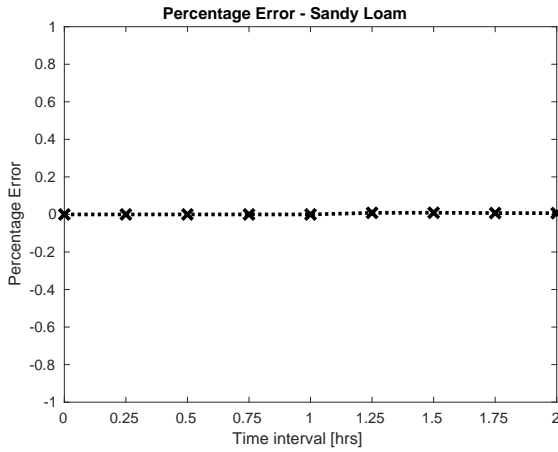


(c) Runoff rate per timestep comparison between the full and approximate models.

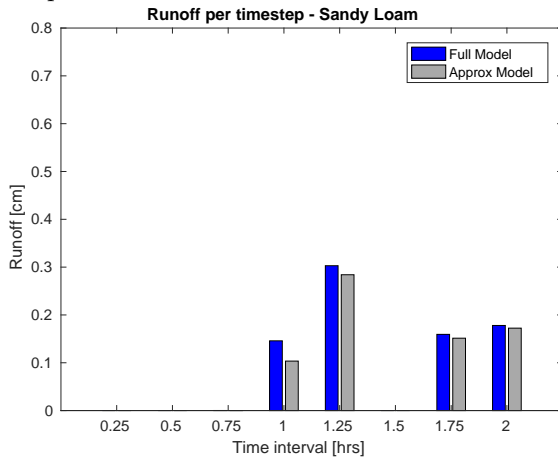
Figure 4.16.: A comparison between the full and approximate Green-Ampt model for the Loamy Sand soil parameter.



(a) Absolute values for the infiltration capacity of the full and approximate models.

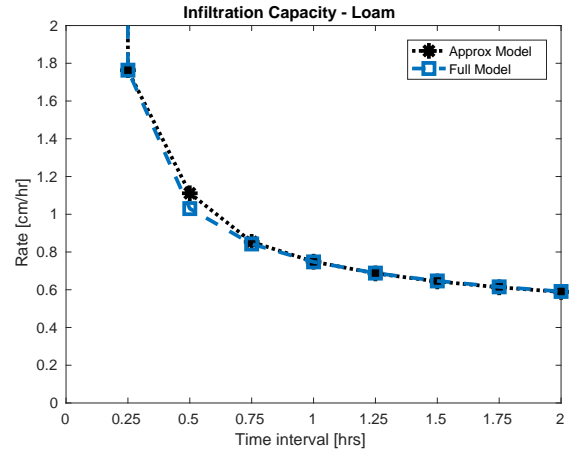


(b) Percentage error values for the infiltration capacity comparing the full and approximate models.

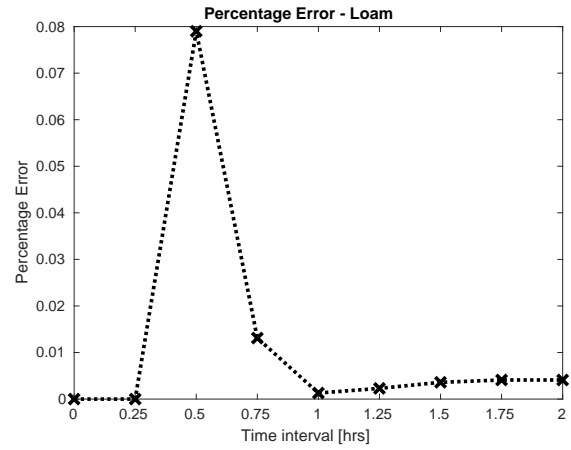


(c) Runoff rate per timestep comparison between the full and approximate models.

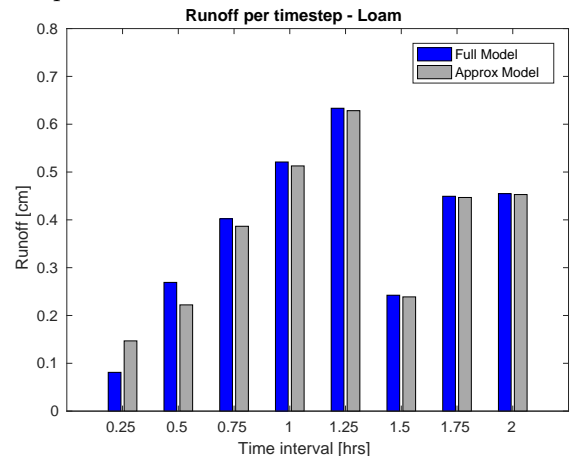
Figure 4.17.: A comparison between the full and approximate Green-Ampt model for the Sandy Loam soil parameter.



(a) Absolute values for the infiltration capacity of the full and approximate models.

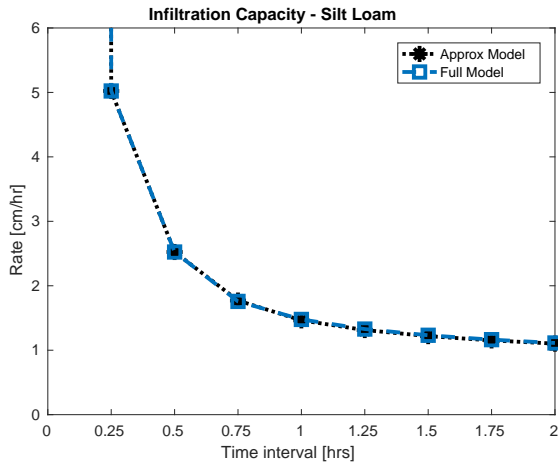


(b) Percentage error values for the infiltration capacity comparing the full and approximate models.

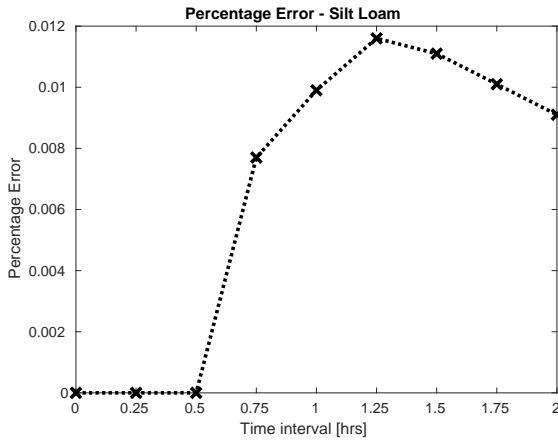


(c) Runoff rate per timestep comparison between the full and approximate models.

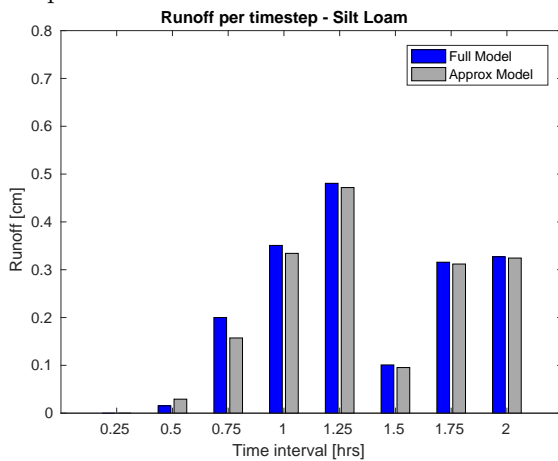
Figure 4.18.: A comparison between the full and approximate Green-Ampt model for the Loam soil parameter.



(a) Absolute values for the infiltration capacity of the full and approximate models.

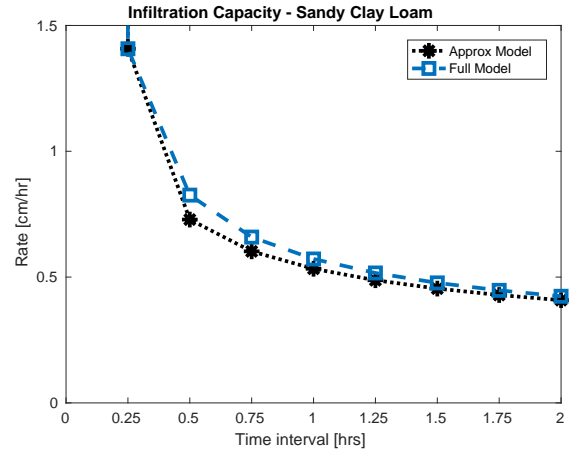


(b) Percentage error values for the infiltration capacity comparing the full and approximate models.

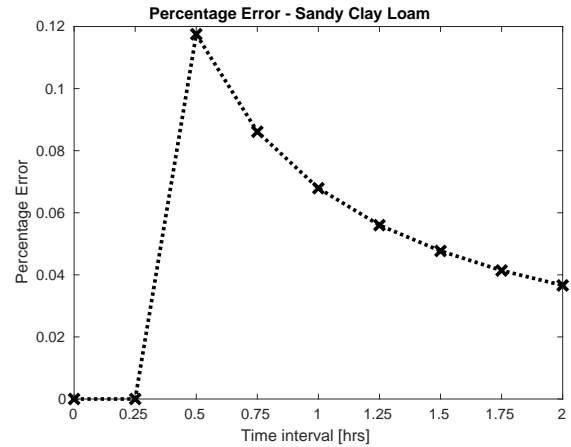


(c) Runoff rate per timestep comparison between the full and approximate models.

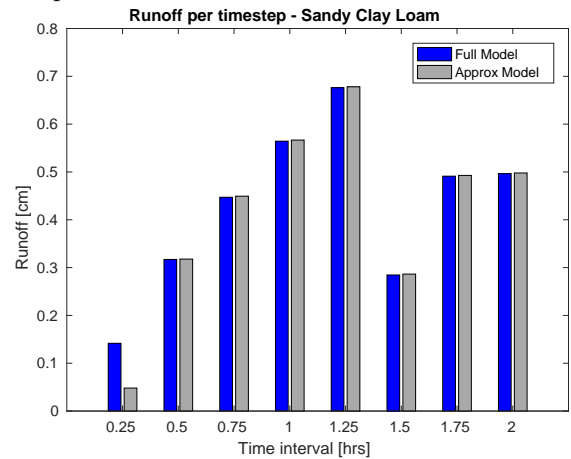
Figure 4.19.: A comparison between the full and approximate Green-Ampt model for the Silt Loam soil parameter.



(a) Absolute values for the infiltration capacity of the full and approximate models.

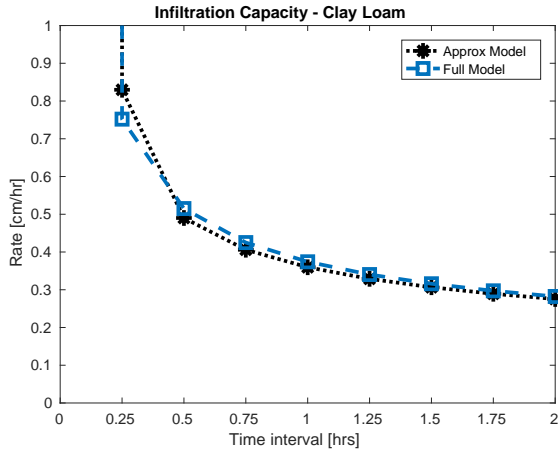


(b) Percentage error values for the infiltration capacity comparing the full and approximate models.

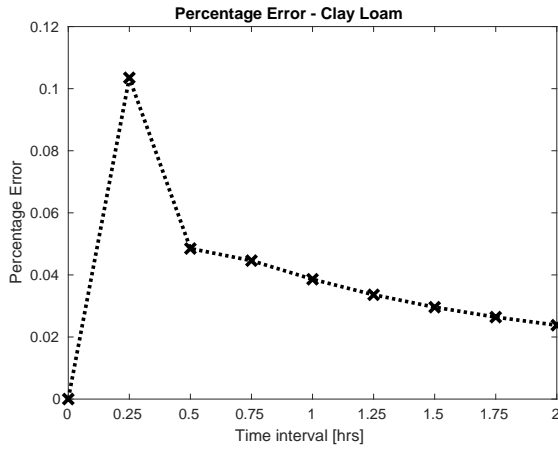


(c) Runoff rate per timestep comparison between the full and approximate models.

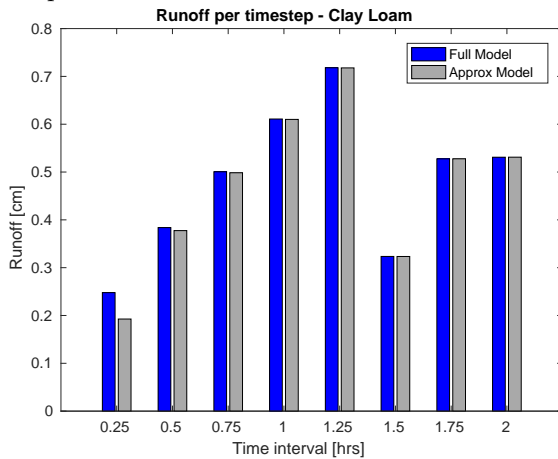
Figure 4.20.: A comparison between the full and approximate Green-Ampt model for the Sandy Clay Loam soil parameter.



(a) Absolute values for the infiltration capacity of the full and approximate models.

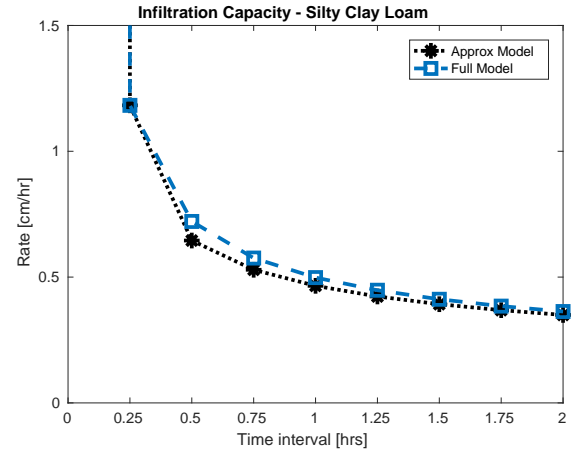


(b) Percentage error values for the infiltration capacity comparing the full and approximate models.

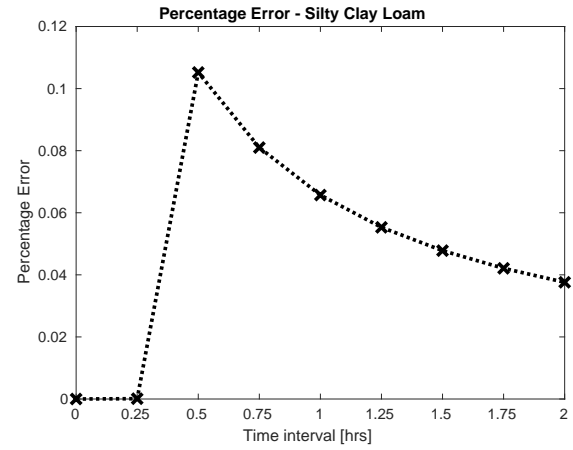


(c) Runoff rate per timestep comparison between the full and approximate models.

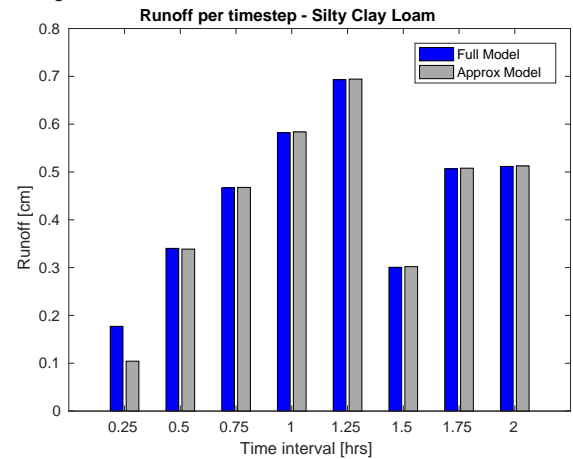
Figure 4.21.: A comparison between the full and approximate Green-Ampt model for the Clay Loam soil parameter.



(a) Absolute values for the infiltration capacity of the full and approximate models.

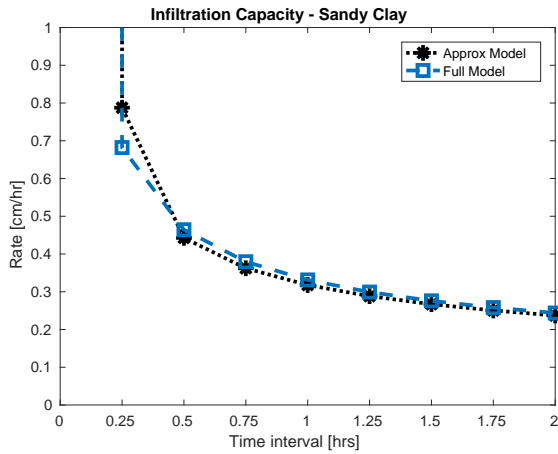


(b) Percentage error values for the infiltration capacity comparing the full and approximate models.

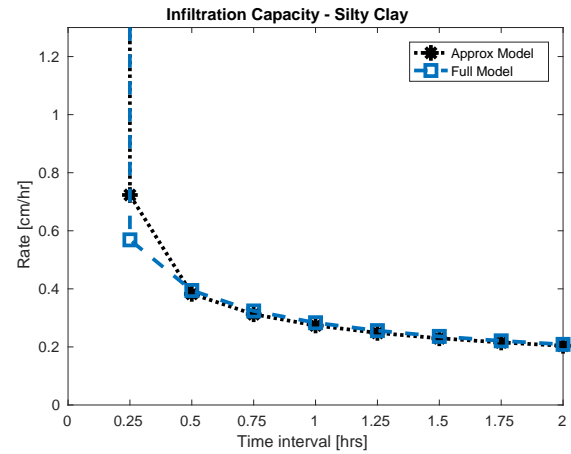


(c) Runoff rate per timestep comparison between the full and approximate models.

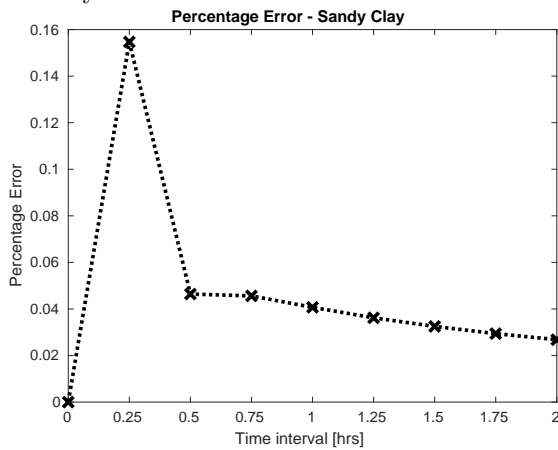
Figure 4.22.: A comparison between the full and approximate Green-Ampt model for the Silty Clay Loam soil parameter.



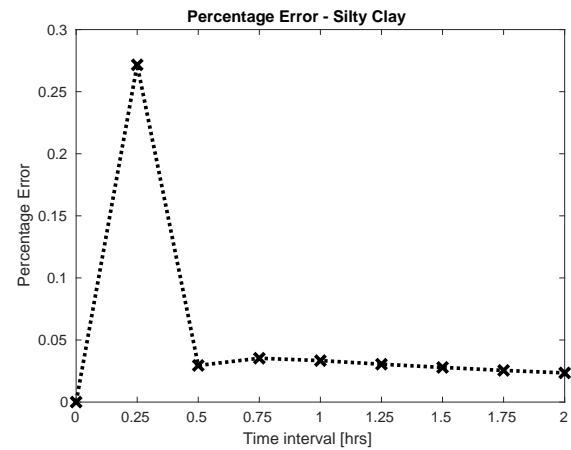
(a) Absolute values for the infiltration capacity of the full and approximate models.



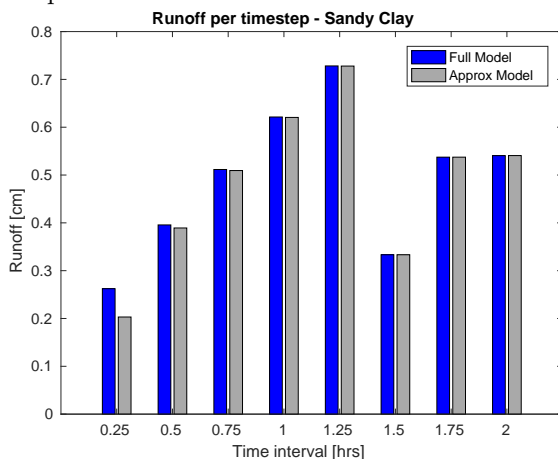
(a) Absolute values for the infiltration capacity of the full and approximate models.



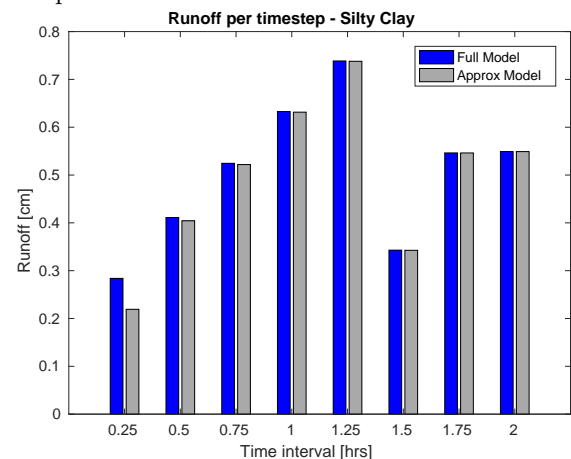
(b) Percentage error values for the infiltration capacity comparing the full and approximate models.



(b) Percentage error values for the infiltration capacity comparing the full and approximate models.



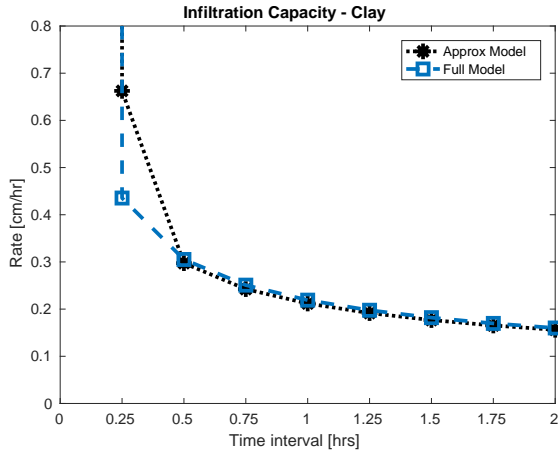
(c) Runoff rate per timestep comparison between the full and approximate models.



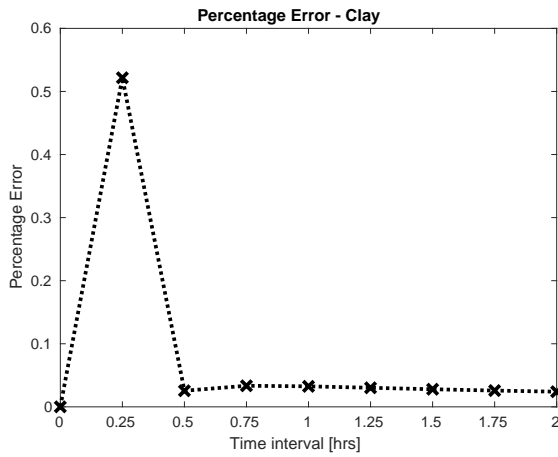
(c) Runoff rate per timestep comparison between the full and approximate models.

Figure 4.23.: A comparison between the full and approximate Green-Ampt model for the Sandy Clay soil parameter.

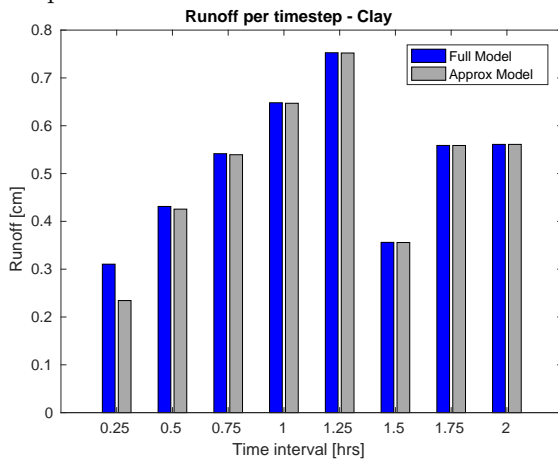
Figure 4.24.: A comparison between the full and approximate Green-Ampt model for the Silty Clay soil parameter.



(a) Absolute values for the infiltration capacity of the full and approximate models.



(b) Percentage error values for the infiltration capacity comparing the full and approximate models.



(c) Runoff rate per timestep comparison between the full and approximate models.

Figure 4.25.: A comparison between the full and approximate Green-Ampt model for the Clay soil parameter.

#### 4.3.5.2. Applying the SCS Method

Section 3.6 described the underlying theory used within the hydrological model. Specifically the Green-Ampt method for non-built up areas *Arable*, *Rough Grazing*, *Grassland* and *Woodland* was linearised to try and aid computational efficiency. Using the worked example from Tarboton (2003), Section 4.3.5.1 showed that the linearisation tracked well with the Newton-Raphson method, but significantly decreased the computational power used. Here a discussion on the final two land-use categories that will be used in this work and how they will be applied within the model using the theory outlined in Section 3.6.2 is given.

In this model an average antecedent moisture condition (AMC II) is assumed. A sub-urban land pixel will be defined to contain 50% residential, 30% woodland and 20% paved roads. Similarly the urban land-use category is assumed to be composed of 70% commercial space, 20% roads and 10% parklands. The calculations assume the area to be in units of acres. Table 4.3 highlights the total area in squared metres, its conversion to acres and the proportional area for each component of both land-use types, for each of the three model resolutions looked at in this work.

Using the curve numbers from Table 3.5 in Section 3.6.2, the curve number for the land-use pixel is calculated as highlighted in Table 4.5 below for each model resolution (rounded to the nearest integer). Applying Equation (3.77) using the curve numbers evaluated, the maximum potential storage is calculated as illustrated in Table 4.6. Finally, the total runoff is calculated using (3.75) on page 130 and listed in Table 4.7 below.

As mentioned in Section 3.6.2 an initial abstraction value of 0.2 was noted from empirical experiments. Lim et al. (2007) revised this value to  $I_a = 0.05$ . They discovered that it led to a more accurate long term prediction of direct runoff within urbanised areas. Since this method is solely being applied for the Sub-Urban and Urban land-use categories, this revised value is applied for every simulation run.

Table 4.3.: The total area of the model pixel resolutions in square metres and acres broken down into the sub-urban land-use components.

	<b>Total area</b> [m <sup>2</sup> ]	<b>Total area</b> [acres]	<b>Residential</b> (50%)	<b>Woodlands</b> (30%)	<b>Paved Roads</b> (20%)
<b>2</b> [m]	4	9.88422 x10 <sup>-4</sup>	4.94211 x10 <sup>-4</sup>	2.965266 x10 <sup>-4</sup>	1.976844 x10 <sup>-4</sup>
<b>20</b> [m]	400	9.88422 x10 <sup>-2</sup>	4.94211 x10 <sup>-2</sup>	2.965266 x10 <sup>-2</sup>	1.976844 x10 <sup>-2</sup>
<b>50</b> [m]	2500	0.6177635	0.3088175	0.18532905	0.1235527



Table 4.4.: The total area of the model pixel resolutions in square metres and acres broken down into the urban land-use components.

	<b>Total area</b> [m <sup>2</sup> ]	<b>Total area</b> [acres]	<b>Commercial</b> (50%)	<b>Paved Roads</b> (30%)	<b>Parklands</b> (20%)
<b>2 [m]</b>	4	9.88422 x10 <sup>-4</sup>	6.918954 x10 <sup>-4</sup>	1.976844 x10 <sup>-4</sup>	9.88422 x10 <sup>-5</sup>
<b>20 [m]</b>	400	9.88422 x10 <sup>-2</sup>	6.918954 x10 <sup>-2</sup>	1.976844 x10 <sup>-2</sup>	9.88422 x10 <sup>-3</sup>
<b>50 [m]</b>	2500	0.6177635	0.43243445	0.1235527	0.06177635

Table 4.5.: Curve number calculations for the sub-urban and urban regions, using the values from Table 3.5.

	<b>Sub-Urban</b>	<b>Urban</b>
<b>2 [m]</b>	$\frac{(4.94211 \times 90 + 2.965266 \times 73 + 1.376844 \times 98)}{9.88422} \times \frac{10^{-4}}{10^{-4}} = 87(86.5)$	93 (93.3)
<b>20 [m]</b>	87 (86.5)	93 (93.3)
<b>50 [m]</b>	87 (86.5)	93 (93.3)

Table 4.6.: The maximum potential storage for a sub-urban and urban land-use pixel.

	<b>[in]</b>	<b>[cm]</b>
<b>Sub-Urban</b>	$S = \frac{1000}{87} - 10 = 1.49425287356$	3.795
<b>Urban</b>	$S = \frac{1000}{93} - 10 = 0.75268172$	1.912

Table 4.7.: Formulae to calculate the total simulated runoff in a sub-urban and urban land-use pixel using the revised initial abstraction value  $I_a = 0.05$ .

	<b>Total simulation accumulated runoff [cm]</b>
<b>Sub-Urban</b>	$Q = \frac{(P - 0.18975)^2}{P + 3.60525}$
<b>Urban</b>	$Q = \frac{(P - 0.0956)^2}{P + 1.8164}$

The formulae from Table 4.7 determine the total amount of runoff a pixel will experience during a single simulation run. This total amount of input will be partitioned according to the rainfall intensity input at a given timestep. For example, if the rainfall rate is constant, then the infiltration amount per timestep will be equal. If the rainfall rate input is non-uniform, then the rainfall abstraction will be greatest during the timesteps with the heaviest rainfall rates.

#### 4.3.6. Boundary Conditions

In order to simplify the model further, a solid (slip) boundary condition is assumed to span across the entire perimeter of the region which is being simulated. Hence, for the western and eastern borders described in Section 4.2, the following condition is applied.

$$h_B = h_I, u_B = 0, v_B = v_I, \quad (4.50)$$

where subscripts B and I represent the prescribed condition and boundary pixel respectively.

Similarly for the northern and southern boundaries the following conditions are applied:

$$h_B = h_I, u_B = u_I, v_B = 0. \quad (4.51)$$

#### 4.3.7. Interception Parameters

Two thirds of precipitation is intercepted to be transpired, evaporated or infiltrated into the soil surface (Perlman, 2016). However, as stated in Section (2.7.1), this model is being run on my personal computer. The remit of this thesis is to introduce an analytical framework from the *facilities management* industry and apply it in a natural capital management context. Two of the key hydrological modelling components that lend themselves to flood risk management are surface routing and infiltration modelling. Sections 4.3.1 - 4.3.6 outline the fully-distributed hydrological model that has been constructed. Before any rainfall input is applied, the empirical approach taken to represent the interception component of the model is described. To minimise the computational expense on my machine, representative values of interception are outlined in this section. Sections 5.3 (page 191), 6.2 (page 233) and 7.2 (page 276) will outline the rainfall inputs used to illustrate the model performance according to their specific simulation contexts. In essence, rainfall inputs outlined in the aforementioned sections will reduce proportionally according to a percentage highlighted in the summary of the literature used below. These values are used to empirically represent the interception component in order to minimise the computational expenditure of the hydrological model.

Vegetation type, age, planting density and temporal season majorly influences the magnitude and proportion of precipitation that a given land area will likely experience. For example, averaged over a year, coniferous and broad-leaved forests likely catch between 15-35% and 9-25% of all precipitation respectively. Typically lower interception values have been observed for tropical rainforests and higher values noted for more temperate climates (Open University, 2022).

Similarly, interception magnitudes are crop dependent with oats, corn and clovers observed to capture 7%, 16% and 40% of rainfall respectively. For arid and semi-arid regions, as one might expect, interception phenomena are negligible (Open University, 2022).

Section 4.2.2 outlines the land-use categories which are defined within this model. Here a brief summary of the values and assumptions used to represent the interception component of the model according to current research is given.

161,000 hectares of arable farmland is used to farm the cereal crop wheat in southern western England (Department for Environment, Food & Rural Affairs, 2019). Within this work, it is assumed that all arable land-use types within the model farm this crop. A study conducted by Lull (1964) observed that on average 36% of rainfall was intercepted by wheat. So this value of 36% interception will be applied to all pixels which are defined to be arable.

Typically, grassland has been observed to intercept between 14-19% of rainfall (Open University, 2022). In this work, a parameter of 15% interception is utilised for rough grazing land-use and 20% interception for the grassland land-use category.

The UK has a *humid temperate oceanic climate* (Peel et al., 2007). From this definition it is assumed that woodland interception will lie in the range between 9-25% as highlighted previously. In this work, the value of 25% interception is used.

#### 4.3.8. Model Calibration

A vital stage of the model construction process is that of the model calibration. Model calibration is an important exercise to determine whether the initial parameterisation provides a good description of the system behaviour being investigated, or whether a new set of unique model parameters are required to minimise the errors between observed and predicted behaviour.

Unfortunately, no real data was available in order to calibrate the model that has been constructed for this thesis. Instead, this section gives an introductory discussion into how one would begin the model calibration process. It highlights the key hydrological parameters that will likely need calibrating for each sub-component of the model. An example of how one could begin calibrating the parameter is provided and what type of data one may need. It also discusses how one can utilise metrics to ascertain the quality of model calibration.

Section (4.3.8.1) discusses the key hydrological parameter needing calibration within the surface routing component of the model. Sections (4.3.8.2) and (4.3.8.3) outline the key considerations one has to take into account of the infiltration component of the model, namely the Green-Ampt model and SCS method respectively. Finally, the main parameters associated with interception modelling are noted in Section (4.3.8.4).

#### 4.3.8.1. Manning coefficient in the Shallow Water Equations

One key parameter within the surface routing component of the hydrological model that will need calibrating is the *roughness coefficient*. Within this work the Shallow Water Equations were utilised to govern this surface routing component (Section (4.3.1)). Within this set of equations is the Manning parameter, an empirical formula to estimate the average velocity of a fluid flowing within open channel flow. Section (4.3.4.1) outlined the initial considerations one has to make when determining the roughness coefficient. The values in the *Normal* column of Table (4.1; page 163) were used as estimates to the roughness coefficient. These values were obtained from (Chow et al., 1988, pg. 113).

Data from reliable flow gauge apparatus of the hydrological system one is modelling, aerial photography, topographic maps and real time satellite rainfall data would be extremely useful in the calibration process of this parameter. Hydrographs are a plotting tool to display how river discharge changes temporally in response to a storm event. They can be used to visualise and observe the peak discharge and response of a watershed during given storm events. These hydrographs could compare the observed event with an original model simulation event without calibration and then with calibration.

One common way to measure the potential improvement of a calibrated parameter is to use the root mean square error metric to compare the disparity between the model (uncalibrated and calibrated) against the observed event to determine whether the model prediction has been improved. A further discussion on calibration of the two-dimensional Shallow Water Equations is presented in (Bathurst and O'Connell, 1992). Within this paper it discusses the SHE hydrological modelling system which uses this surface routing method. It notes that physically based hydrological models parametrise the underlying physical meaning and hydrological characteristics of a watershed. Therefore calibration using field measurements can give more confidence in a model output than compared to a model without any physical process underpinning it. For the one-dimensional shallow water equations, the roughness parameter has been calibrated using a Monte Carlo method as well as gradient based optimisation methods (Lacasta et al., 2017).

#### 4.3.8.2. Green-Ampt

Four parameters of the Green-Ampt model need to be considered for calibration. These are *Wetting Front Soil Suction Head*, *Hydraulic Conductivity*, *Porosity* and *Initial Soil Moisture*. Ideally, field survey data of the watershed one is interested in would be acquired to attain the values of the parameters one is interested in through

experimentation, similar to the experiments conducted in Horton (1919) to obtain realistic parameter values. For a more general hydrological model this is impractical and so values determined within the literature are used in this work by first understanding the soil profile of the computational domain. The soil parameters related to the soil texture “Sandy Loam” were chosen as the default values as noted in Table (3.1; page 120). These values were originally obtained by Clapp and Hornberger (1978). The justification of this is presented in Section (4.2.4)

To calibrate these values, one could conduct a model sensitivity analysis for each parameter. To do so, one could determine a suitable gauged location within their desired watershed and run multiple simulations. Within each simulation, one would fix the value of three out of the four key parameters and then vary the final key parameter with representative low, middle (or mean) and high values. One could then compare the output of cumulative infiltration and the performance of each parameter relative to one another against the observed data to determine the importance of calibration for each parameter. This type of analysis was conducted for the Green-Ampt component of the TUFLOW hydrological model (TUFLOW, 2018). Here it found significant variations in runoff when the hydraulic conductivity parameter was varied throughout the simulated event. It also found the initial moisture content had influence on the runoff output at the beginning of a simulation. This was found to be consistent with results from within the literature.

In order to quantify the performance of the model calibration, one may use the root mean squared error (described in the previous section). Other quantitative methods include the percentage bias value, which measures the mean propensity of simulated values to deviate from the observation. Equally, one could use the Nash-Sutcliffe efficiency coefficient, originally used to measure the predictive quality of a hydrological model, it has also been found to be useful in measuring model accuracy.

#### 4.3.8.3. SCS

The key parameter for the SCS method is its *Initial abstraction* parameter  $I_a$ . Within its first conception was the proposal of the assumption that  $I_a = 0.2S$  as noted in Section (3.6.2; page 129). The original field data used to determine the runoff estimation method from the Soil Conservation Society (S.C.S, 1972) was never documented and subsequent literature could not replicate the original analysis from the Soil Conservation Society. Despite this, this method has become the de-facto approach for many software products, environmental impact estimation projects and engineering designs (Ling and Yusop, 2015). Many disagreements on this parameter value arose due to the reporting of many inconsistent results using this methodology (Ragan and Jackson, 1980; Ling and Yusop, 2014). Model fitting experiments conducted by Woodward et al. (2003) suggested a value of  $I_a = 0.05$  would be more appropriate as the value  $I_a = 0.2$  resulted output that was too high compared to observations. It is this value that was used throughout the hydrological model in this work.

Model calibration for this parameter is dependent on specific regional characteristics (Ling

and Yusop, 2014). Ling and Yusop (2015) developed a regional specific correction equation to amend the SCS method to be more suited to its three case study regions on the Universiti Teknologi Malaysia (UTM) Skudai campus in Malaysia. It assessed two null hypotheses given by SCS originally: 1.  $I_a = 0.2S$  globally; and 2.  $I_a = 0.2$  is constant. They adopted a bootstrapping, bias corrected and accelerated procedure to assess these hypotheses and help in utilising a numerical optimisation method to find the optimum initial abstraction value. In their work they rejected their null hypothesis after careful considerations of all the possible values of the initial abstraction parameter and found the hypothesis did not lie within one standard deviation of the range of optimal median or mean values. Utilising an optimal initial abstraction value, they constructed a modified runoff prediction model using the SCS method as a framework. To measure the calibration performance a comparison of the prediction of the SCS method against the non-inferential statistical approach was done. It found the new model reduced the residual sum of squares by 79%.

In order to adopt this calibration approach, experimental data of the watershed outlined in Section (4.2) would be required. However, the model in this work covers a large spatial area compared to the small experimental sites used in Ling and Yusop (2015) and would be impractical to implement. The application of the SCS method for this work is outlined in Section (4.3.5.2; page 176).

#### 4.3.8.4. Interception Parameter

Having an understanding of canopy interception and its effect on the water balance is vital in determining the correct input needed to accurately reflect the total amount of precipitation that reaches the ground surface. Total *net rainfall* (defined as the sum of *throughfall and stemflow*, outlined in Section (2.2.1; page 52)), the amount of precipitation that is not retained by vegetative surface, ultimately dictates the model input for the remaining components of a hydrological model. The interception phenomena is strongly correlated with rainfall intensity and timing, the structure of vegetation doing the intercepting as well as the weather conditions which control the evaporation process during and after a storm event (Rutter et al., 1975; Ward and Robinson, 1990; Dingman, 2002; Brutsaert, 2005; David et al., 2005). These correlates may account for up to 50% of total precipitation (Llorens et al., 1997; Roth et al., 2007; Siegert et al., 2017; Sadeghi et al., 2018).

The observations of interception events (as a percentage of rainfall) from specific studies outlined in Section (4.3.7) are used as a proxy for the interception component to save computational expense in the hydrological model within this work. One way in which data could be collected for calibration of an interception parameter is via *tipping-bucket* gauges. These devices are ubiquitous within interception literature and known to systematically underestimate gross rainfall and throughfall in forest areas. However, there are studies which outline a dynamic calibration procedure to correct these observations (Lida et al., 2018).

A study by Lida et al. (2018) outlines a dynamic calibration procedure to correct observa-

tions from these gauges. Five of these devices were measured with five different constant inflow intensities. The actual output was measured against the observations measured from the gauges and a correction equation was determined. The rain gauge was then compared against an Onset rain gauge and Ota rain gauge and correction applied to field data of canopy interception loss in a temperate forest in Japan. This correction procedure saw interception loss computed values change from -20% - +40%.

There exists many model types within the literature which simulate canopy interception. Such models include simple regression models (Helvey and Patric, 1965), physically-based models (Rutter et al., 1972; Gash, 1979) and stochastic models (Calder, 1996). Two physically-based models that are commonly used are the Rutter-type and Gash-type models (Muzylo et al., 2009). These are outlined in Section (2.2.1). Models of these types may be calibrated using a non-linear parameter estimator known as PEST (Parameter Estimation and Uncertainty Analysis) (Doherty, 2005; PEST, 2023). This method applied the Gauss-Marquardt-Levenberg method to find an optimal parameter set which minimises the sum of square errors between the measured and modelled data. PEST is an independent, free and open-source software that has been referenced numerously in the literature. One such study which employs this method is Linhoss and Siegert (2020) that calibrates five interception models (Gash, Gash Sparse, Rutter, Rutter Sparse and Liu models). Other advantages to this method is the fact that it is unbiased, it allows a comparison of optimised results and optimised parameter sets and gives good insight into a model's functionality. Goal of model calibration is to ensure that an estimated class probabilities are consistent with what would naturally occur.

#### 4.3.9. Model limitations and Future work

Due to a lack of appropriate data, the hydrological model could not be calibrated. As such one cannot be sure that the parameters used to demonstrate its function are a good representation of the hydrological system being investigated. One can overcome this issue by considering the points made in Section (4.3.8) noted above.

Since the model was not able to be calibrated due to a lack of real data there is little value in comparing it with existing models within the literature. Without any confidence that the hydrological model can represent a hydrological system robustly, it did not make sense to utilise further resources and time to conduct this comparison exercise. Should one wish this model to be used in flood management exercises, it would be necessary to conduct such a comparison after the calibration work has been conducted. The absence of comparisons of the model against models within the literature means that the confidence in the validity of the hydrological tool is limited.

Physically-based hydrological models require a large number of parameters and work best with a vast amount of data. Model calibration is required for each region and/or watershed one is interested in investigating. These data intensive models require a large amount of computational power. The model outlined in this chapter was limited to my personal computer. Thus the model was built pragmatically and not solely on need. High resolu-

tion physically-based hydrological models are most useful when run in a high-performing computer environment. High Performance Computing has enabled modellers the ability to attain resolutions that are not possible on a personal machine (Avesani et al., 2021).

The hydrological model constructed in this work comprises of four components. Each component in turn has underlying assumptions that one may wish to consider if trying to expand this work. For the surface routing component, the governing shallow water equations (Section 4.3.1), contains only one vertical component. As such, it is difficult to include a parameter which varies with height. Within the Green-Ampt model (Section 4.3.5.1), it assumes the soil to be isotropic and that the initial moisture content is uniform within the soil. This can lead to inaccuracies of infiltration-excess surface runoff calculations over a heterogeneous soil (Huo et al., 2020). To effectively use this model disaggregated daily precipitation data is best to use. However, this is very difficult to obtain (King et al., 1999).

When one applies the SCS method (discussed in Section 4.3.5.1), it requires the rainfall volume amount. It does not accept rainfall intensity and/or duration. As such one must determine an appropriate method to take into account this fact. Chapters 5 - 7 outline how this was overcome in this work. Essentially the total output obtained from this method was distributed according to rainfall intensity, as a percentage total input, at each timestep. The SCS method is also sensitive to curve number ( $CN$ ) values. Equally, expert judgement is needed in ascertaining the appropriate initial abstraction value ( $I_a$ ) and utilising the correcting antecedent moisture classification values.

Section 4.3.7 outlines the final hydrological model component discussed in this work, the infiltration parameter. In order to minimise computational expenditure, empirical values were used determined from field data highlighted in Section 4.3.7. As a result, the component does not have any physical basis embedded within it like the remaining three components. Finally, it is assumed that only one vegetation type will be present on specific land-use pixels. Again, while convenient computationally, it will not be truly representative of the interception mechanism present within the watershed.



## 4.4. Summary

Chapter 4 began by defining an orthogonal computational domain on which the hydrological model is built (Section 4.2). Section 4.2.2 highlighted the Dudley stamp maps at 1km resolution from the MAGIC platform. These maps defined the seven land-use categories that will be used in the work. The data for these maps was not available, so an image processing approach was justified and outlined in Section 4.2.3. Section 4.2.4 justified the use of “Soilscape 7” as a parameter within the Green-Ampt model. A lack of data availability and computational power meant that the hydrological model could not be run in its 2m resolution variant as justified in Section 4.2.5. The section also ruled out any model resolution variants at 100m and above as this would lose too much spatial variation needed to conduct land-use based policy planning and flood modelling. This work will use the 20m and 50m resolution variants and compare their outputs against each other.

Section 4.3 begins the explanation on the construction of the hydrological model. The first component to be constructing is the surface routing component. It first considers the governing equations themselves (Section 4.3.1) as well as how its integral form is applied to a finite volume numerical stencil (Section 4.3.1.1). The HLLC numerical solver is applied to numerically solve local Riemann problems (Section 4.3.2). The surface reconstruction method from Xia et al. (2017) is applied (Section 4.3.2.3) to aid in the determination of the Riemann states (Section 4.3.2.2). The source term discretisation is outlined in Section 4.3.3. The method constructed by Xia and Liang (2018) is utilised to explicitly calculated the friction term of the routing component in Section 4.3.4.

A justification on the use of the Green-Ampt model (for non-urban land-use categories) and SCS method (for urban land-use categories) begins Section 4.3.5. The implicit Newton-Raphson numerical solver embedded in the Green-Ampt model made the runtime for a single timestep of the model unfeasible. Thus Section 4.3.5.1 constructed a linear approximation to the method which provided extremely good agreement when an exercise from the literature was applied to compare the results of both methods for all parameter combinations outlined in Table 3.1 (page 120). To the best of my knowledge this approach has never been applied in the literature before and so is a novel application of this method. Section 4.3.5.2 outlines the application of the SCS Method for the sub-urban and urban areas. The model’s boundary conditions are highlighted in Section 4.3.6.

The justification of the use of empirical values to represent the interception component of the hydrological model begins Section 4.3.7. The values that determine this parameter for each land-use type was determined from the literature. Arable land will abstract 36% of water input. Rough grazing land-use categories, 15%. Grassland 20%. Finally, woodland land-use pixels will abstract 25% water input. Due to a lack of real data, calibration of the model could not be done. However, a discussion of how one may calibrate the model is given in Section 4.3.8. The chapter concludes with an overview of the model limitations and future work one can do to expand and improve this model in Section 4.3.9. This chapter outlined the modelling techniques that have been applied in the model construction (**RQ3**), how the model can be validated and calibrated (**RQ4**) and the key

considerations when deciding what model resolution is most suitable (**RQ5**).

# 5. Modelling Performance Analysis

## 5.1. Introduction

Humankind's need to equitably and sustainably use finite resources to meet its material, cultural and fundamental needs is outlined in Chapter 1. The academic parallels between the need for an “environmental management system”, as identified by Cornwall Council in its Environmental Growth Strategy (Section 1.1.5), and concepts within “facilities management” has led to the proposal of a computational tool to help policy makers in their longer term planning and to mitigate unintended adverse effects. One such computational tool is a hydrological model, which can aid decision makers in assessing the potential flood risks associated with local urbanisation projects. Chapter 2 considered the mathematical literature behind hydrological modelling. Chapter 3 presented the theory which is fundamental to the hydrological model constructed in Chapter 4.

Chapter 5 gives an initial comparison analysis between the model's (outlined in Chapter 4) 20m and 50m resolution model variants. The purpose of this chapter is to establish whether a coarser resolution model may be admissible for analysis, or otherwise ascertain possible differences between finer and coarser models. Section 5.2 begins by describing the two sub-regions which have been selected for the model performance analysis (Sections 5.4 and 5.5). This section will also orientate the reader in their understanding of how pixels within each model-resolution variant relate to a “patch” which in turn aids in the analysis exercise. Section 5.3 will define the common model input parameters that will be applied when conducting this comparison analysis. Sub-regions from the larger computational domain discussed in Section 4.2 have been extracted to enable the analysis. Section 5.4 considers a north-eastern sub-region of the domain while Section 5.5 looks to a northern part of the domain further west. Both of these sections are identical in their structure. First the local topographical and land-use pixel definitions between model variants are highlighted. The time taken to run multiple simulations for the 20m and 50m models are considered. Finally, an overview of the overland flow distribution within the extracted domain is reviewed before a more in depth analysis is given to selected patches within each sub-region. Additional material related to this chapter may be found in Appendices E, F, G, H and I. References to these sections are given throughout the chapter.

Table 5.1.: A summary of the orthogonal grid mesh utilised within the computational model.

Model Domain Structure	Value		Units
	20m	50m	
Domain area (Full)	5	5	[km <sup>2</sup> ]
# Pixels/Patch	25	4	[pixels / patch]
Pixel Grid (Full)	125 × 100	50 × 40	
Patch Grid (Full)	25 × 20	10 × 8	
Domain area (Extract)	0.64	0.64	[km <sup>2</sup> ]
Pixel Grid (Extract)	40 × 40	16 × 16	
Patch Grid (Extract)	8 × 8	8 × 8	
Spatial Interval: $\Delta x$ (W-E)	20	50	[m]
Spatial Interval: $\Delta y$ (N-S)	20	50	[m]

## 5.2. Sampled Computational Meshes

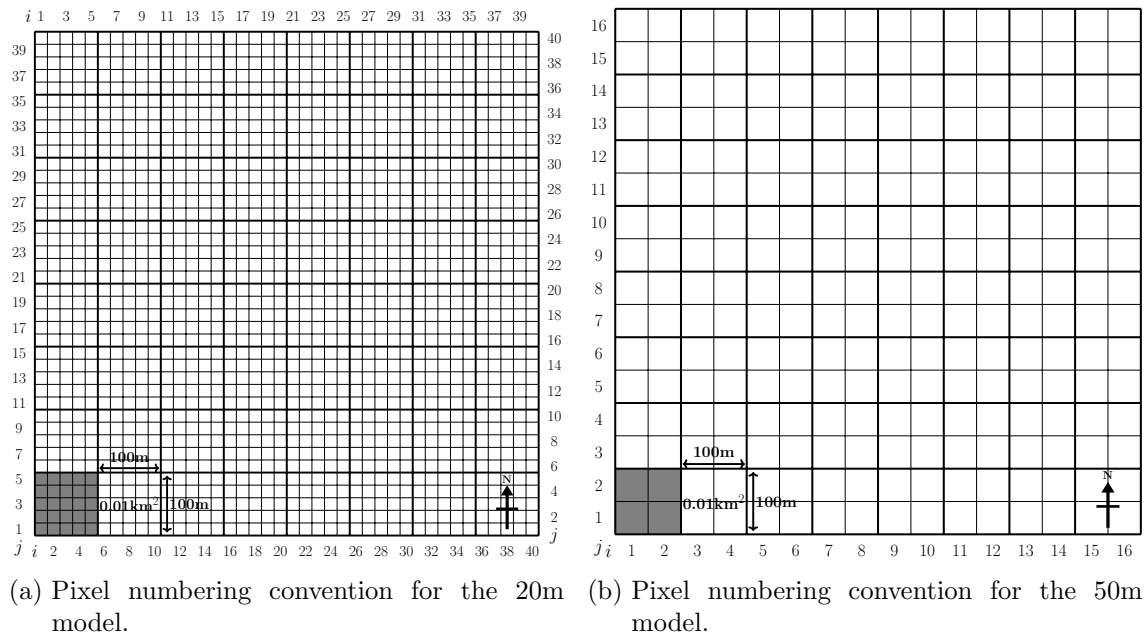
Section 4.2.5 (page 139) justifies why the 20m and 50m model resolutions were selected for comparison in the context of flood risk management in Cornwall. From both model resolutions processed in Section 4.2.3, two sub-regions comprising an area of 0.64km<sup>2</sup> are extracted. Section 5.4 looks at a north-eastern section of the full computational domain, whilst Section 5.5 looks at north-central region of the domain. Two separate regions are considered to ensure that every land-use defined in Section 4.2.3 are analysed in both model variants. The first model analysis region does not include the “woodland” land-use type whilst the second omits pixels defined as “water”.

Table 5.1 summarises the computational domain mesh structure utilised in its full configuration as well as the model analysis regions which have been extracted. Only the computational mesh which will be utilised in both the extracted regions used for model performance analysis will be discussed here. An orthogonal grid structure with dimensions 40 × 40 pixels defines the computational mesh for the 20m resolution model as seen in Figure 5.1a. Similarly, Figure 5.1b illustrates an orthogonal grid structure with dimensions 16 × 16 pixels defining the computational mesh for the 50m resolution model.

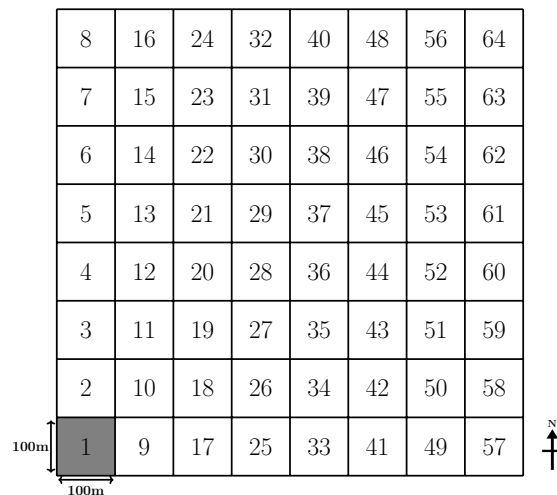
This domain is divided into further sub-regions of area 0.01km<sup>2</sup> to allow for an even comparison of model performance between the 20m and 50m resolutions. Each individual sub-region is referred to as a *patch*, where each patch grid has dimensions of 100m × 100m. Both model resolutions comprise of a computational domain with an 8 × 8 grid of patches. Each individual patch grid is comprised either a 5 × 5 orthogonal pixel grid with dimensions 20m × 20m, or a 2 × 2 pixel grid structure with dimensions of 50m × 50m. Figures 5.1a and 5.1b show this patch structure which comprises of the 5 × 5 and 2 × 2 pixel structures resolutions respectively.

Each patch is numbered from 1 to 64 to allow for a consistent referencing throughout this work. Patches 1 - 8 begin from the south to north in the furthest west column of the computational domain. Patches 9-16 again go from south to north in the column adjacent to the most western column. This numbering system continues until the most eastern columns where patches 57-64 go from south to north. Figure 5.1c highlights the numbering convention used. Patch #1 is shaded in grey in each sub-figure of figure 5.1 to

show that an equal area of the domain is being referenced in both resolutions. Each model is run at the pixel level and the outputs from each model simulation are then averaged at the patch level, at each timestep, to allow for a fair comparison between resolution outputs.



(a) Pixel numbering convention for the 20m model. (b) Pixel numbering convention for the 50m model.



(c) Patch numbering convention.

Figure 5.1.: A depiction of the computational mesh for the 20m 5.1a and 50m 5.1b resolution variants. Pixel column indices are located to the top and bottom of figure 5.1a and bottom of 5.1b. Pixel row indices are located to the left and right of 5.1a and left of the computational grid in 5.1b. The patch indexing convention used in this section is highlighted in figure 5.1c. Each patch is defined by the thicker black grid which overlays each respective pixel grid seen in grey. Patch #1, shaded in grey, is an example of a patch where the outputs are averaged to ensure an even comparison between both model resolutions. Patch dimensions and the area of the region are highlighted in each sub-figure.

### 5.3. Common Model Parameters & Inputs

Table 5.2 lists the constant model parameter inputs applied to both the 20m and 50m resolutions for both analyses discussed in Sections 5.4 and 5.5. A value of  $9.81\text{ms}^{-2}$  replaces the gravitational constant  $g$  wherever it is present in the methodology Chapter 4. Each of the four model simulations are run for a total time of  $T = 24$  hours and inputs are given in 30 minute intervals, or  $\Delta t = 0.5$  [hours]. Outputs are presented through 48 timesteps,  $t^{(k)}$ . Specific times may be found via  $t^{(k)} = k \times \Delta t$  [hours]. Each simulation begins with “Dry” initial conditions and no-slip boundary conditions from Section 4.3.6 are applied.

Where pixels defined as “Arable” in each model resolution, only 64% of the precipitation input reaches the surface at each timestep. As discussed in Section 4.3.7, rainfall interception processes in arable areas absorbed 36% of all input over a storm event. Similarly, the empirical interception parameters of 20%, 15% and 25% are applied for the land-use pixels defined as Grassland, Rough Grazing and Woodland respectively. Due to the complex composition of sub-urban and urban areas, the empirical method known as the *SCS runoff curve number* is applied to estimate the direct runoff from a specific rainfall event. A uniform unsaturated zone is defined for each pixel in all four models considered, where the total depth for absorption is 50cm and limited by the specific hydraulic conductivity of the sandy loam soil composition seen in Section 4.3.5.1.

Table 5.3.: Total precipitation input values for the entire simulation as well as a break down of input by timestep and pixel-definition.

Precipitation Input	Value	Units
Pixel avg. depth (Total)	5	[cm]
Pixel avg. depth / $\Delta t$	0.1042	[cm]
Arable avg. depth / $\Delta t$	0.0667	[cm]
Grassland avg. depth / $\Delta t$	0.0833	[cm]
Rough Grazing avg. depth / $\Delta t$	0.0886	[cm]
Woodland avg. depth / $\Delta t$	0.0782	[cm]
Sub-Urban avg. depth / $\Delta t$	0.0560	[cm]
Urban avg. depth / $\Delta t$	0.0735	[cm]

A total precipitation of 5cm is applied throughout the entire simulation. If no interception and absorption processes were present and the terrain is completely flat, then by the end of the simulation, an average water depth of 5cm would be recorded in each pixel and patch of every 20m and 50m model. This is listed in Table 5.3. With no hydrological processes interfering the total precipitation would equate to 0.1042cm of rainfall per timestep, or every 30 minutes. The equivalent timestep inputs for each land-use pixel is also listed in Table 5.3.

Table 5.2.: Input arguments for both simulation runs.

Common Parameters	Value	Units
Gravitational Constant	9.81	[ms <sup>-2</sup> ]
Simulation time	24	[hours]
# Timesteps	48	
Time interval ( $\Delta t$ )	30	[mins]
Initial Conditions	Dry	
Boundary Conditions	No-slip	
Interception: Arable	36	[%]
Interception: Grassland	20	[%]
Interception: Rough Grazing	15	[%]
Interception: Woodland	25	[%]
Interception: Sub-Urban	Runoff Curve Number	
Interception: Urban	Runoff Curve Number	
Unsaturated Zone depth	50	[cm]
Soil Composition	Sandy Loam	

## 5.4. North-Eastern Sub Region

### 5.4.1. Spatial Distribution: Local Terrain

Plots within Figure 5.2 on page 194 display the topological structure through surface plots 5.2a, 5.2b, 5.2c and 5.2d and contour diagrams 5.2e, 5.2f, 5.2g and 5.2h. sub-figures 5.2a, 5.2c, 5.2e and 5.2g shows the topology present within the 20m model. Equally, sub-figures 5.2b, 5.2d, 5.2f and 5.2h shows 50m model. Black boxes in sub-figures 5.2a, 5.2b, 5.2e and 5.2f highlight the respective regions extracted in the surf and contour plots and sub-figures 5.2c, 5.2d, 5.2g and 5.2h are zoomed in representations of these boxes. The elevation of each pixel is given in units of metres [m] above mean sea level (amsl). The colour map used in each of the eight plots depict the range from 0m - 110m and remain consistent throughout. Labels on the  $x$ - and  $y$ - axes in every sub-figure denote the column and row indices for each pixel within their respective domains. Labelling on the  $z$ - axes in the surface plots note the height above mean sea level of the terrain.

Focusing on the extracted computational domain, sub-figures 5.2c, 5.2d, 5.2g and 5.2h, some key features of the terrain within the region are highlighted. Travelling from north to south the height above mean sea level (amsl) decreases. The highest elevation in both resolutions is above 90m. The majority of the southern and eastern areas of both domains are below 1m. The coastline of the case-study region is evident via the depiction of the tightly packed contour lines in 5.2g and 5.2h. A small valley can also be seen between index columns 95 and 105 of sub-figure 5.2g as well as index columns 40 and 42 of sub-figure 5.2h.



### 5.4.2. Spatial Distribution: Land-Use

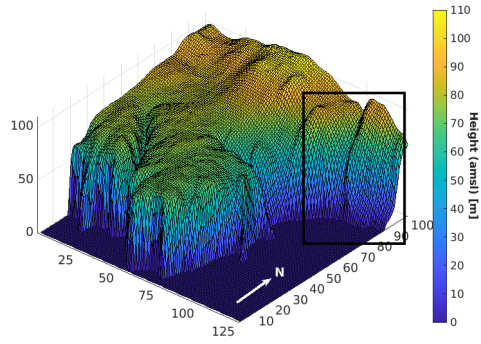
Figure 5.3 on page 195 demonstrates the spatial distribution of land-use pixels within the computational domain of the region being studied. Sub-figures 5.3a and 5.3b indicate what land-use is defined for each pixel for the 20m and 50m resolutions respectively. Each orange box in these sub-figures translate to zoomed in sub-figures 5.3c and 5.3d respectively. Land-use abbreviations are annotated to each colour bar within each sub-figure and are defined in Table 5.4. The proportion of land-use coverage is given as a percentage for the zoomed in computational domain utilised in the model performance analysis.

A plurality of pixels are categorised as water for both model resolutions at  $\sim 47\%$ . These pixels reside in the southern and eastern halves of the model variants. Rough grazing land-use categories constitutes the second most populous pixel type at  $\sim 25\%$  and  $\sim 27\%$  for the 20m and 50m models respectively. These are all evenly distributed among the land-based pixels within each model. Arable land-use is the next highest at  $\sim 14\%$  and  $\sim 13\%$ . The main bulk of arable land-use pixels are located in the north-western and northern areas of the computational domain. The fourth most ubiquitous land-utilisation pixel is grassland at  $\sim 12\%$  and  $\sim 11\%$  for the 20m and 50m resolutions. These pixels reside in the south-western/western areas as well as toward the east of both computational domains.

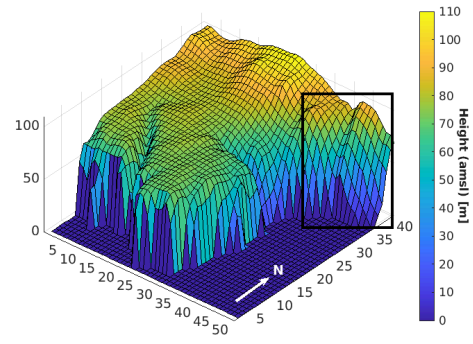
Table 5.4.: Land-use abbreviations, colour code, model parameter and spatial coverage of the sampled computational domain given as a percentage.

Land-Use	Abbreviation	Colour Code	Model Parameter	Proportion [%]	
				20m	50m
Arable	A	Brown	1	13.56	12.89
Grassland	G	Lime Green	2	12.44	11.33
Rough Grazing	RG	Yellow	3	24.94	27.34
Sub-Urban	SU	Purple	4	1.69	0.78
Urban	U	Red	5	0.0625	0
Woodland	Wo	Forest Green	6	0	0
Water	Wa	Blue	7	47.31	47.66

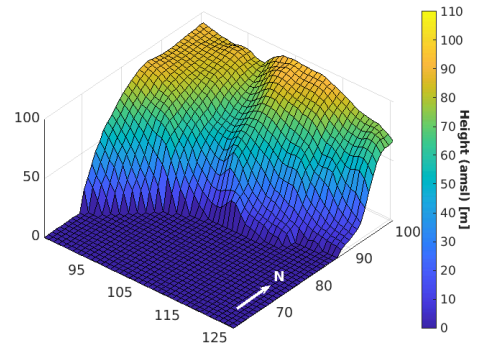
Sub-urban areas account for  $\sim 2\%$  and  $\sim 0.78\%$  within their respective domains. In the 20m resolution model, four pockets of sub-urban areas exist towards the western and northern regions. Three pixels exist in the 50m domain, one in the south-west at (35, 25), one in the west at (35, 35) and one in the north at (43, 40). Urban regions account for  $< 1\%$  of the domain toward the south-western regions within both model variants. The sub-urban and urban pixels to the south-west of both model resolutions are surrounded by water pixels only. It will be difficult to ascertain any significant insight between these pixels and as such, were re-defined as water pixels for this model performance analysis only. Zero woodland pixels were recorded in either model version for this analysis.



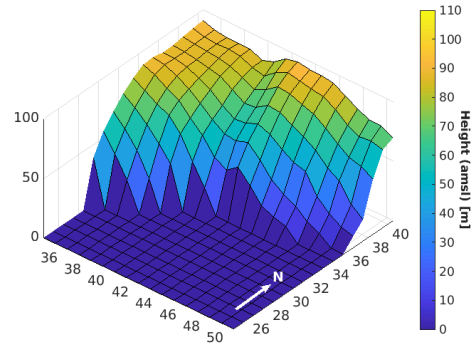
(a) Full domain surface elevation plot, 20m.



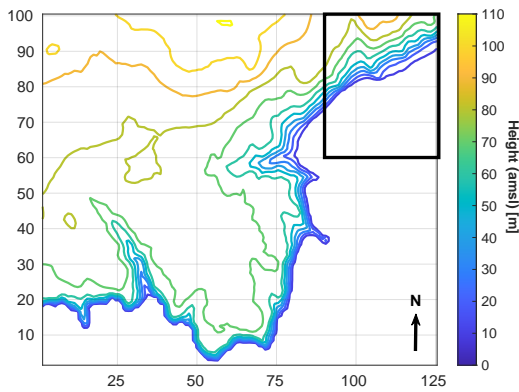
(b) Full domain surface elevation plot, 50m.



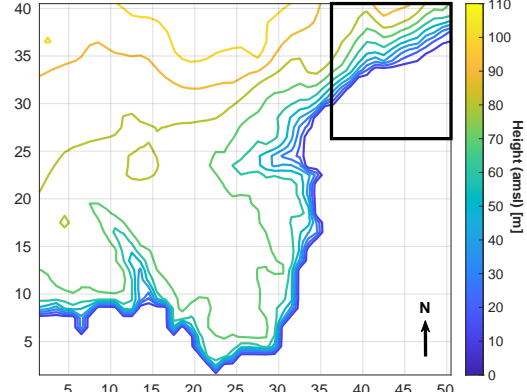
(c) Region 1 surface elevation, 20m.



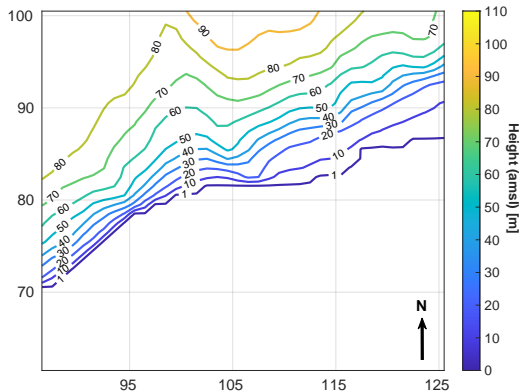
(d) Region 1 surface elevation, 50m.



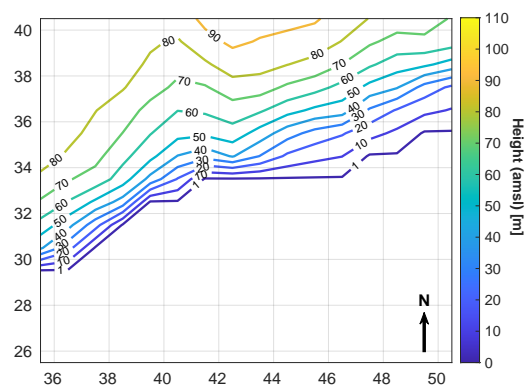
(e) Full domain contour elevation, 20m.



(f) Full domain contour elevation, 50m.



(g) Region 1 contour elevation, 20m.



(h) Region 1 contour elevation, 50m.

Figure 5.2.: A pictorial overview of the topological structure of the full computational domain as well as the first study region used for model analysis.

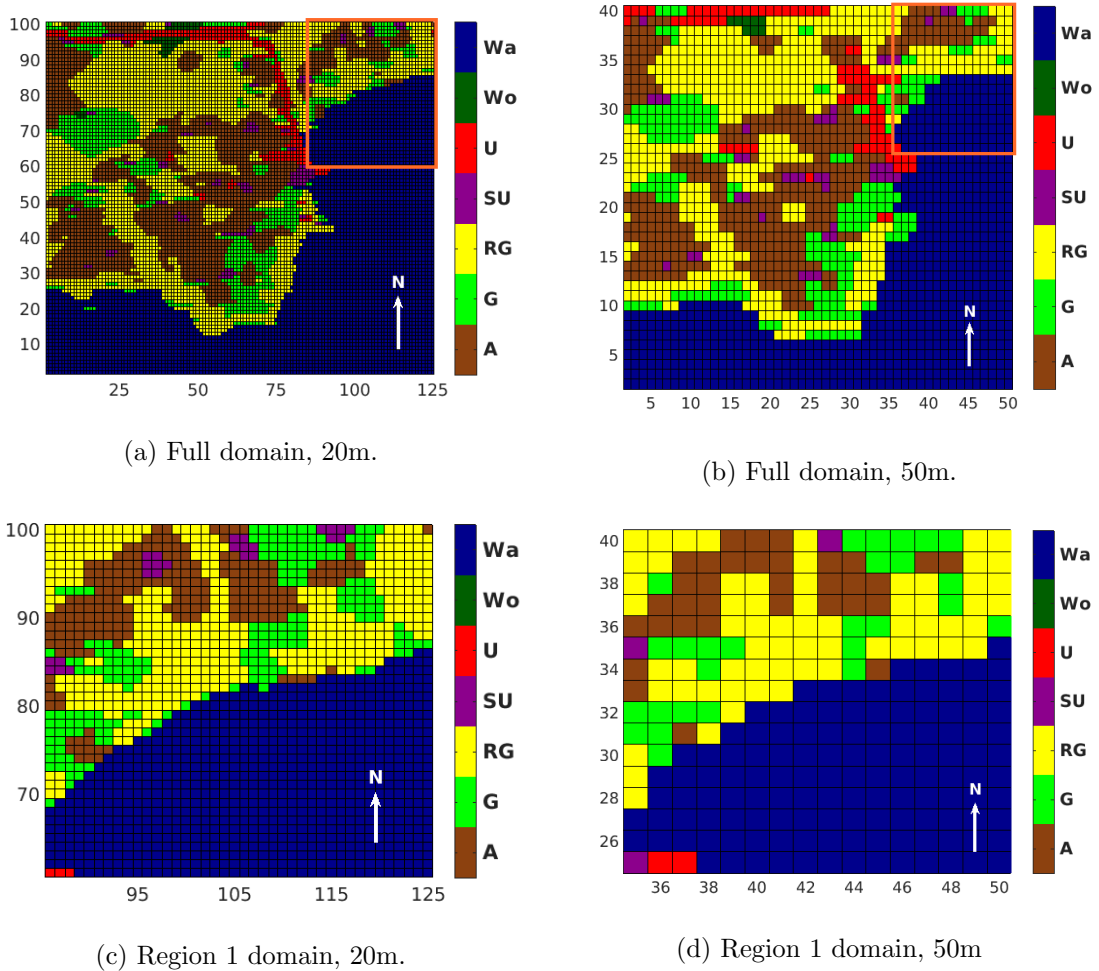


Figure 5.3.: The land-use spatial distributions used within each model variants. Labels on the axes represent the row and column indices for each pixel within the computational domain. Figure 5.3a shows the entire computational domain at 20m resolution. 5.3c is a zoomed in picture of the orange square in 5.3a. Similarly, figure 5.3b is the full computational domain at 50m resolution with its orange square highlighted in 5.3d. The land-use categories are abbreviated to the right of each figure. Table 5.4 defines each land-use category.

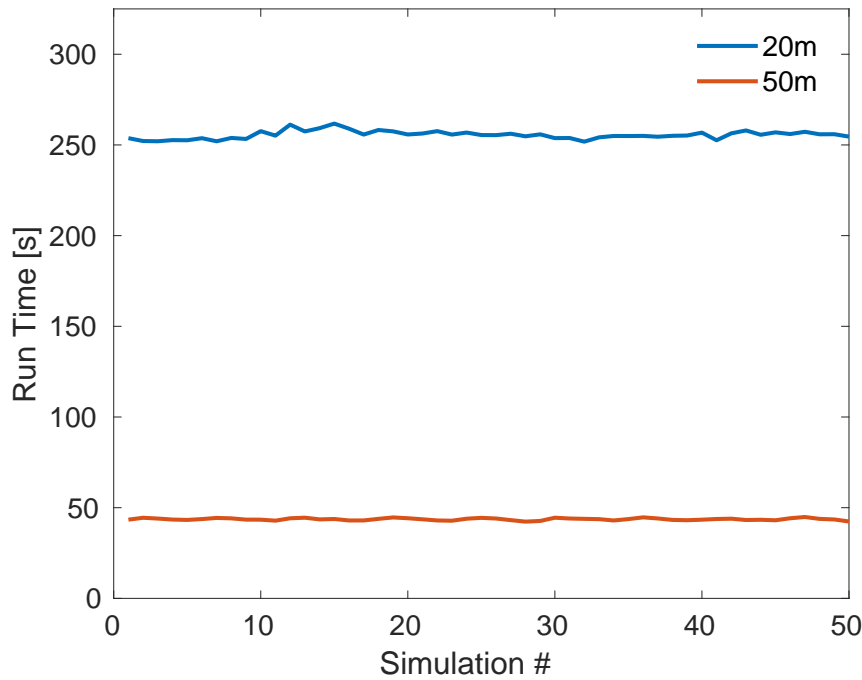


Figure 5.4.: The total time in seconds it took for each of fifty simulation runs for both the 20m (blue) and 50m (red) model resolutions to complete.

### 5.4.3. Simulation Run Times

Fifty simulations were run for both model versions recorded within the north-eastern domain discussed in Sections 5.4.1 and 5.4.2. The raw simulation times and the averages for this region are presented in Table E.1 in supplementary Section E. Figure 5.4 plots Table E.1, the total time taken for each model simulation to complete. The blue plot represents the 20m model variant and the red plot shows the 50m model. On average the 20m model took 255.6s to complete a single simulation whereas the 50m model spent 43.6s. From these simulation runs, the 50m model was 5.86 times faster than its 20m counterpart. Both models showed consistent simulation run times. The 20m simulations fell within a 10s range with a minimum and maximum time of 251.8s and 261.8s respectively. The 50m resolution was much more consistent with every simulation occurring within a 2.6s band between 42.3s and 44.9s. This distinct computational speed is not surprising given that the 50m model had 1344 pixels fewer to compute for each simulation run. If the 50m model's output is comparable to the 20m model, then it would be more prudent to utilise the 50m model to save on computational time for similar results.

### 5.4.4. Overland Flow Distribution

Figure 5.6 presents the temporal evolution and spatial distribution of overland flow throughout a simulation. Figures 5.6a, 5.6c, 5.6e and 5.6g highlight the evolution of flow for the 20m model. Similarly for the 50m model figures 5.6b, 5.6d, 5.6e and 5.6h shows the overland flow outputs at the equivalent timesteps to the 20m model. Similar figures at time periods 03:00, 09:00, 15:00 and 21:00 hours for both model resolutions have been included in Appendix Section G on page 366.

At every timestep within the simulation, overland flow is concentrated around urban and sub-urban areas. Two overlapping sub-urban areas between the 20m and 50m model versions occur in regions to the north and western part of both computational domains. The finer resolution of the 20m model shows another two regions of sub-urban pixels. The first region occurs from pixel columns (96-98) and pixel rows (95-97), surrounded by arable land. A second region exists between pixel columns (114-117) and rows (99-100).

Table 5.5.: Pixel column and row boundaries which defined analysis regions to calculate the minimum, maximum and average mean water depths at non-zero output pixels in Figures 5.5 and F.1 for the north-eastern sub-region.

Model Resolution	20m		50m	
Analysis Region	Columns	Rows	Columns	Rows
	86-125	61-100	34-50	24-40
Region 1	86-90	81-84	35-36	34-35
Region 2	94-99	92-97	38-40	37-40
Region 3	102-107	94-98	41-44	38-39
Region 4	113-119	96-100	46-48	38-40
Region 5	125	94-97	50	39-40

Figure 5.5 shows the minimum, maximum and mean averaged water depth at each pixel within their respective models at every timestep. Throughout the entire simulation the minimum values at each timestep fluctuated between 0.01 - 0.362cm for the 20m model and 0.01 - 0.567cm in the 50m model. Equally, the maximum values in both model resolutions ranged between 0.72 - 2.204cm and 0.055 - 1.227 respectively. The raw data of Figure 5.5 may be seen in Table F.1 in appendix Section F.

At 06:00 hours, the minimum and maximum averaged pixel depths recorded were 0.01cm and 0.798cm within the 20m model respectively. The mean value for average pixel water depth was noted as 0.432cm, where all dry pixels were excluded. For the 50m the minimum, maximum and mean data points were recorded at 0.537cm, 0.573cm and 0.555cm respectively.

Six hours later at 12:00 hours, values ranged between 0.011cm and 1.388cm with an average of 0.635cm within the 20m model. For the 50m model these data points were 0.096cm, 0.932cm and 0.322cm respectively.

After eighteen hours, the minimum value remained at 0.01cm with the maximum at 1.798cm with an average of 0.699cm for the 20m model. For its 50m counterpart the minimum, maximum and mean averaged water depth was 0.106cm, 1.130cm and 0.406cm respectively.

At the conclusion of the simulation, 24:00 hours, the minimum, maximum and mean values for the 20m resolution had risen to 0.023cm, 2.204cm and 0.714cm respectively. Within the 50m model these values were recorded at 0.063cm, 1.227cm and 0.413cm.

### 5.4.5. Patch Analysis

Given the different resolutions it is expected that absolute output values will vary. Normalising these results allows the comparison in how the behaviour may change between simulations. Each patch in the 50m model will contain four pixels (as outlined in Section 5.2). However, the finer resolution of the 20m model will contain 25 pixels within its patch. As a consequence of the model construction, when a flux transfer is estimated across a boundary of adjacent pixels (Section 4.3.2.1), it is implicitly assumed that the distance water can travel across a pixel is half of its resolution (e.g. 25m and 10m for the 50m and 20m models respectively) within an equal time interval. This behaviour is reflected in the patches with a similar proportion of pixels which are defined. For example, patch #46 contains a majority of rough grazing pixels in the 20m model whilst the 50m model is entirely made up of rough grazing pixels. Despite this, the output only shows non-zero values for the 50m version.

A similar observation is made with patches #22, #30, #31, #38, #39, #46, #47, #54, #55 and #63, where the pixels which compose each patch vary, but are similar between model variations. Between these patches, values reach a maximum of 1.346cm at #31 towards the end of the 50m simulation highlighted in Figure 5.7. Patches #31, #39 and #63 begin to show negligible amounts of output in the 20m model variation at the end of the simulation.

Remaining patches #5, #15, #16, #23, #24, #32, #40, #56 and #64 all contain at least one pixel that is sub-urban or urban in either, or both, resolutions. At some point in the simulation, an output within these patches is non-zero for the 20m model. A maximum value of 0.376cm and 2.104cm is reached by patches #32 and #56 for the 20m and 50m models respectively. Despite this, patches #5, #15 and #16 all do not record overland flow in their 50m variations. Patches #23 and #24 tend to have a larger output on average compared to the 50m variants. The opposite can be seen for patches #31 and #32 where the output is larger for the 50m version. Most interesting is patch #39. Despite varying outputs, which is to be expected, its normalised output values are virtually identical. The proportion of land-use pixels allocated at each model resolution is similar at  $\sim 76\%$  ( $\sim 75\%$ ) arable and  $\sim 24\%$  ( $\sim 25\%$ ) grassland for 20m (50m). Similarly for patch #40, despite the two pixels for sub-urban areas, the entirety of the patch is grassland. In the next section, the effect of the sub-urban and urban pixels are isolated in these patches and how they influence the overall output of the 20m version.

Figures 5.7 - 5.8 display the output of the average water depth per pixel in both the 20m and 50m resolution variants. Figure 5.7 presents the output scaled by its maximum at any point throughout the simulation. Table H.1 notes the land-utilisation pixels of each patch for each model resolution.

In order to assess the impact of sub-urban and urban pixels within the patches noted in the previous sections, the results from the original simulations will be compared against an altered land-use composition of the patches. For each patch, the compositional changes

are described and the normalised and absolute output values are listed through a table and figures. A separate temporal figure is provided to show the percentage change between model simulations to compare the impact of these pixel changes. For each patch that has been adjusted, the simulation run only contains this altered patch. When a simulation was run for an adjusted patch, the remaining patches and pixels stayed in their original spatial composition. For example, when a simulation was run for patch #32 where pixel  $\Omega_{41,40}$  was altered from rough-grazing to arable, the remaining patches kept their original composition. This same process was applied for each adjusted patch. These adjustments to the 50m model were made to better represent the 20m land-use coverage and to see if the output of the 50m is affected and more closely aligned with the 20m model.

#### 5.4.5.1. Patch #05

Figure 5.9 on page 206 shows the original pixel composition for the 20m and 50m models (sub-figures 5.9a and 5.9b respectively) assigned to patch #5. Sub-figure 5.9c presents the adjusted 50m model pixel composition. Sub-figure 5.9d shows the absolute output from each patch composition within each model. Finally, sub-figure 5.9e shows how the outputs from the original 50m model, the adjusted 50m model and the factored 50m model compare to the original 20m model output.

A blue triangle marker outlines the output from the 20m model. Overall, the average water depth rises linearly throughout the entire simulation. It reached a maximum average water depth of 0.3cm. The red dashed line shows the output from the original 50m model. Zero output was recorded throughout the entire simulation.

The presence of the three sub-urban pixels within the original 20m model and absence of them in the 50m model is the key reason for this gulf in output between the models. The land-use defined in pixel  $\Omega_{1,10}$  from the 50m model is changed from grassland to sub-urban. A yellow line with cross markers shows the output from the adjusted 50m model. Similar to the 20m model, the output from the adjusted 50m model has risen linearly. Yet, the output clearly overestimates the 20m model by nearly double, or 100% as seen in Figure 5.9e.

#### 5.4.5.2. Patch #15

Figure 5.10; page 207 shows the pixel composition within patch #15 for the 20m model 5.10a, the original 50m model 5.10b and the adjusted 50m model 5.10c. Sub-figure 5.10d shows the average water depth in patch #15 increasing at a steady rate within the original 20m model. Towards the second half of the simulation, the rate at which this water depth increases, begins to plateau. By the end of the simulation, a maximum average water depth of 0.183cm was reached. With the absence of sub-urban pixels in the original 50m model, there was no recorded presence of water within the patch. To include the sub-urban pixel, the arable pixel  $\Omega_{38,38}$  is replaced within the 50m model. This dramatically changes the output of the 50m model, where at the end of the simulation, the average water depth

is over double at 0.401cm.

#### 5.4.5.3. Patch #32

Average water depth within the 20m model for this patch monotonically increases throughout the simulation. The rate of increase in this average water depth slows towards the end. By the completion of the simulation, the average water depth had risen to a value of 0.350cm. In the 50m model, the rate of increase of average water depth was slightly faster in the first quarter of the simulation. This resulted in a small overestimation of output. The rate at which the 50m model output increased was much slower than the 20m model. As a result, the output of the 50m model recorded an average water depth of 0.306cm in the patch, a 12.5% decrease compared to the 20m model at the same timestep.

Pixels which were defined as rough-grazing cover 36% and 50% of the patch for the 20m and 50m model respectively. Similarly, the arable land-use pixels covered 44% and 25% respectively. Pixel  $\Omega_{41,40}$  is altered from rough-grazing to arable to better represent the 20m land-use coverage in the 50m model and to see if the output of the 50m is affected. As seen from sub-figure 5.11e; page 208, the output is identical and had zero influence.

#### 5.4.5.4. Patch #48

The land-use representation within the 50m model does not share the same proportionality as the 20m model. The sub-urban pixel coverage in the 50m model is 25%, a 7% decrease compared with the 32% present within the 20m model. These pixel compositions are seen in Figure 5.12; page 209, sub-figures 5.12a and 5.12b. It is difficult to justify an adjustment to the 50m model by including another sub-urban pixel. This is due to the accurate coverage of pixels  $\Omega_{45,39}$ ,  $\Omega_{45,40}$  or  $\Omega_{46,39}$  to the 20m grassland land-use. Again, the 20m model average water depth behaviourally increases linearly, reaching a maximum of 0.691cm, seen in Figure 5.12c. The rate at which the 50m model increases is much slower than its 20m counterpart and flattens out towards the second half of the simulation. An average water depth of 0.394cm was reached, underestimating the 20m model output by 43%.

#### 5.4.5.5. Patch #64

Within the 20m model, the average water depth input increases slowly throughout the simulation, reaching a maximum average water depth of 0.125cm in the patch. Given the absence of an urban pixel in the patch of the original 50m model, no water presence is recorded (sub-figure 5.13d; page 210). Pixel  $\Omega_{50,39}$  has its land-use designation changed from rough grazing to urban to reflect the singular urban pixel in the 20m model, illustrated in sub-figures 5.13a; 5.13b; and 5.13c. This inclusion sees the average water depth of the adjusted 50m model drastically overestimate its output compared to the 20m model,



reaching a maximum value of 0.550cm by the end of the simulation run, a 339% increase (sub-figure 5.13e).

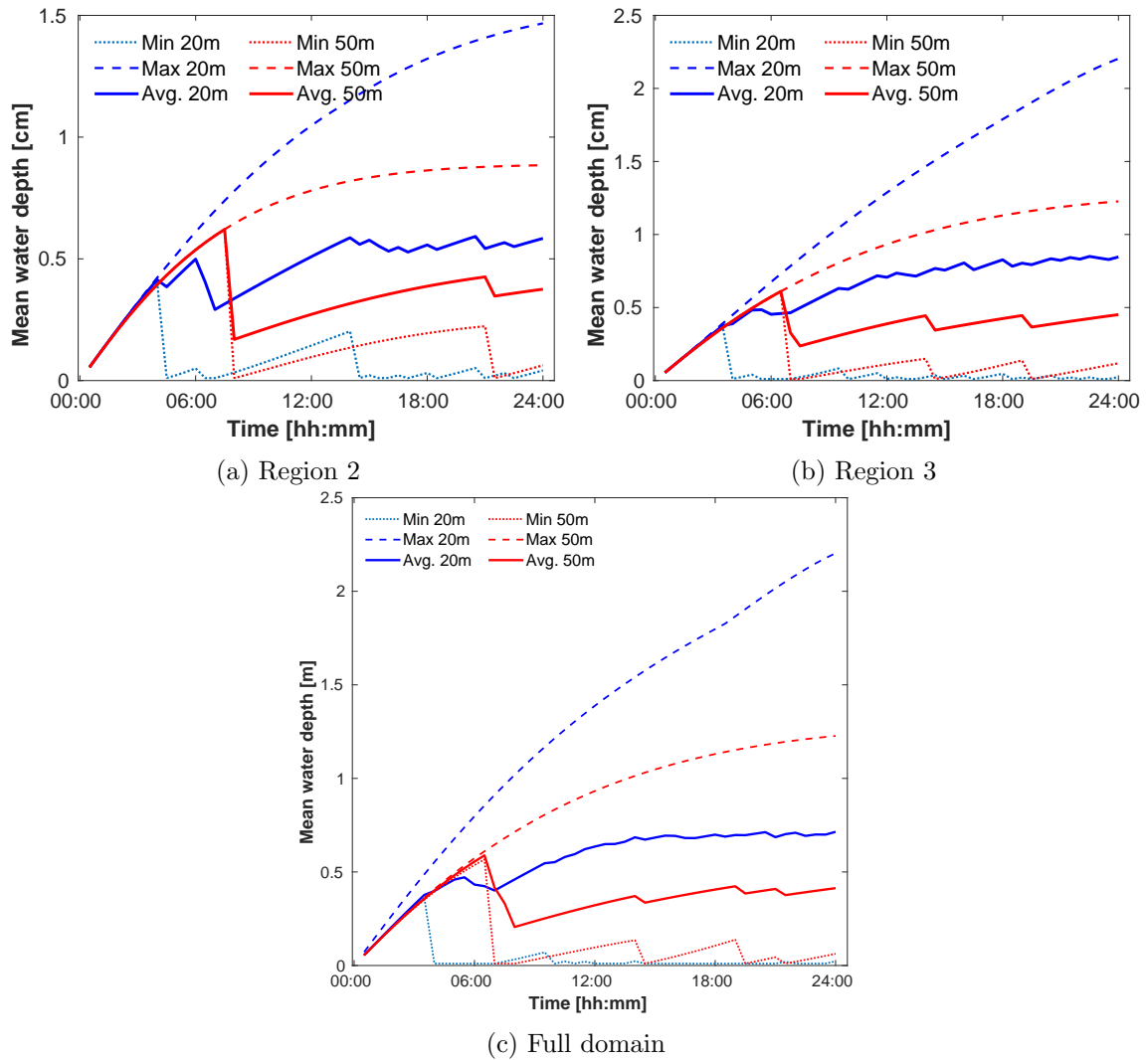


Figure 5.5.: The minimum, maximum and average mean water depths at non-zero output pixels within the north-eastern sub-region outlined in Figure 5.3 for both model resolutions. Sub-figures (a) and (b) show the values for two of the five regions where water is present as seen in Figure 5.6 as well as the entire domain (c).

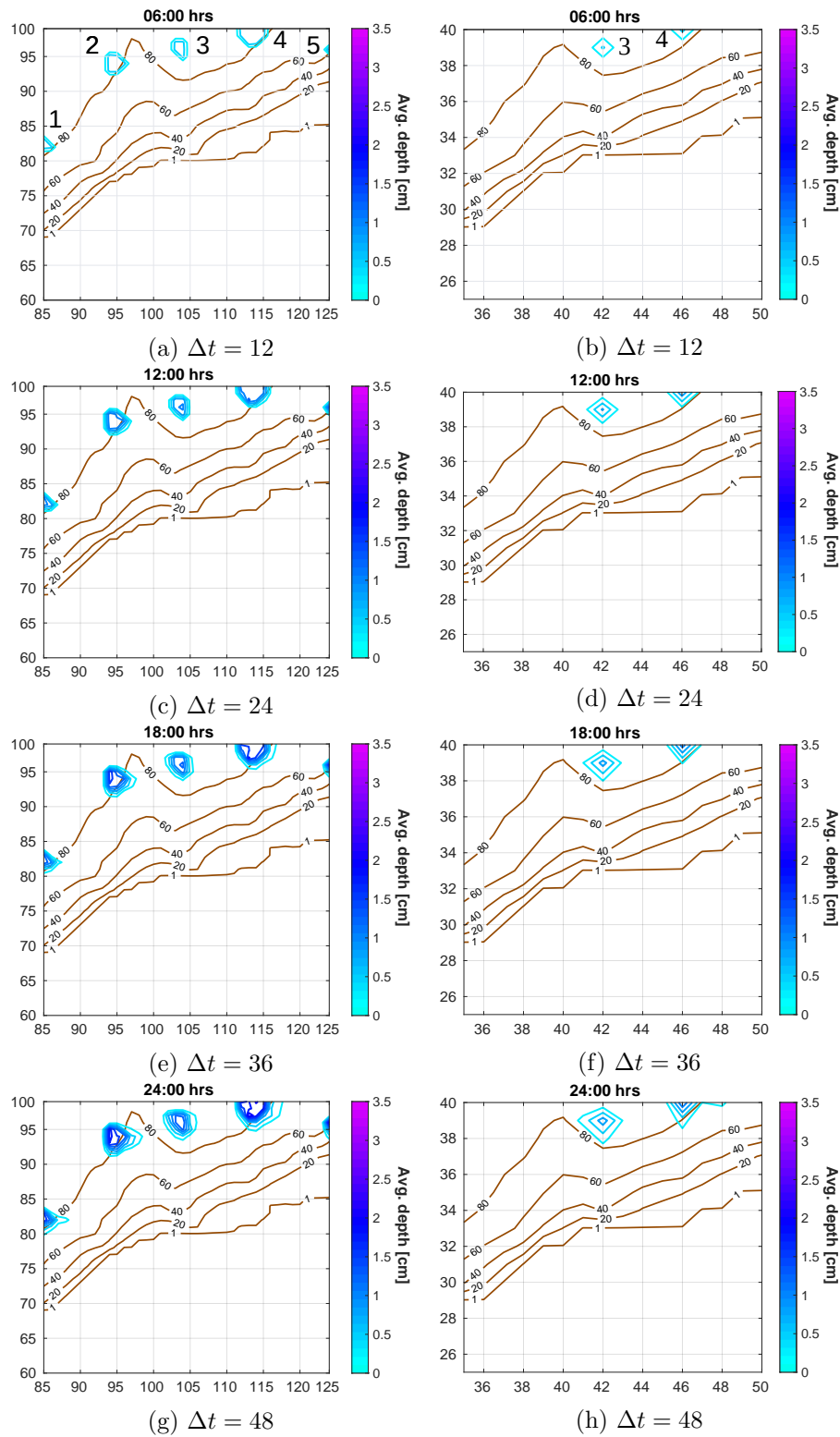


Figure 5.6.: An evolution of the average water depth overland flow throughout the 20m resolution model simulation.

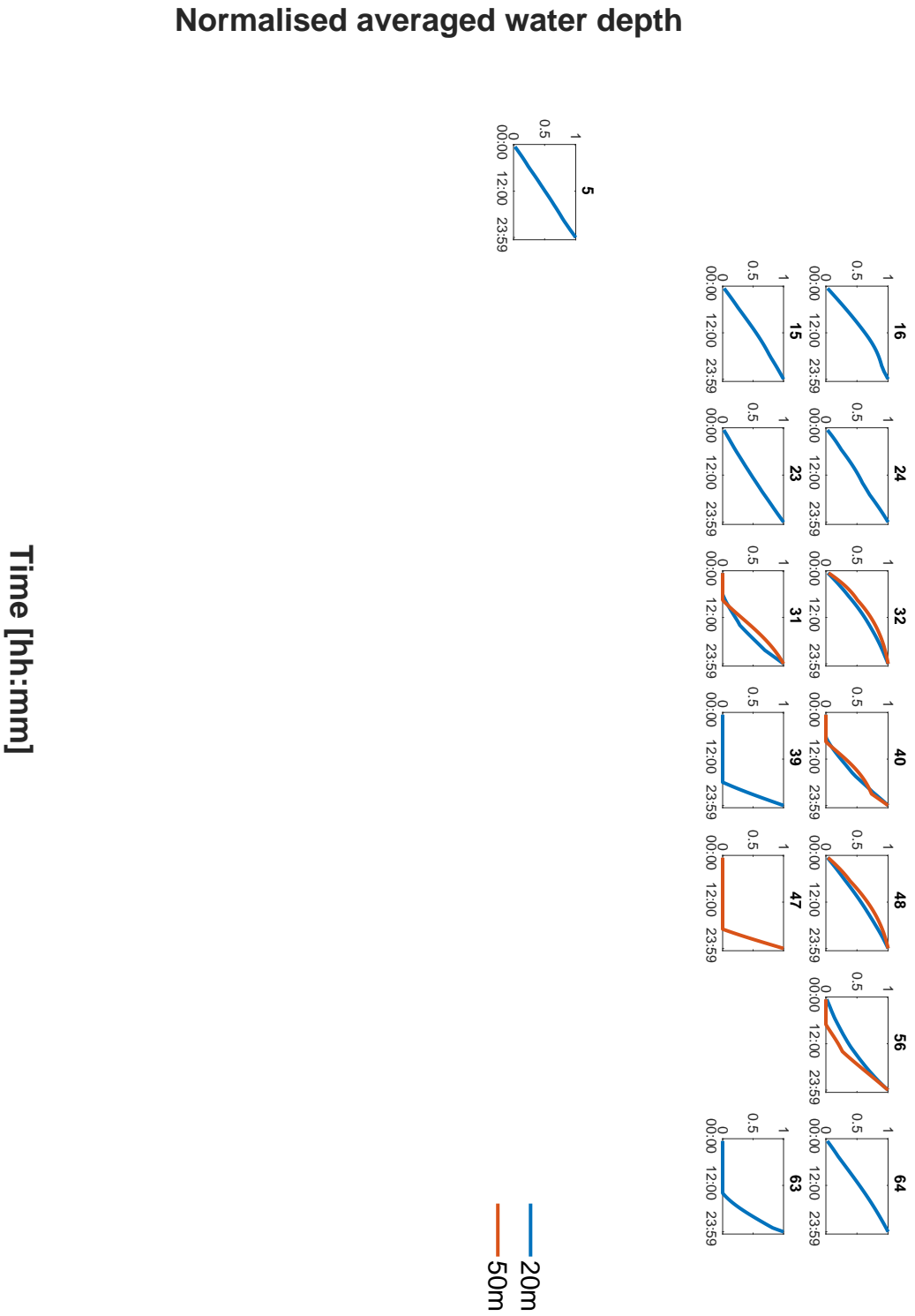


Figure 5.7.: A comparison of the normalised average water depth output between the 20m (blue) and 50m (red) resolutions. The normalisation utilises the maximum average value at any timestep within the patch. The number of timesteps goes across the  $x$ -axis of each subplot. Their plot placement corresponds to the patch numbers in figure 5.1c.

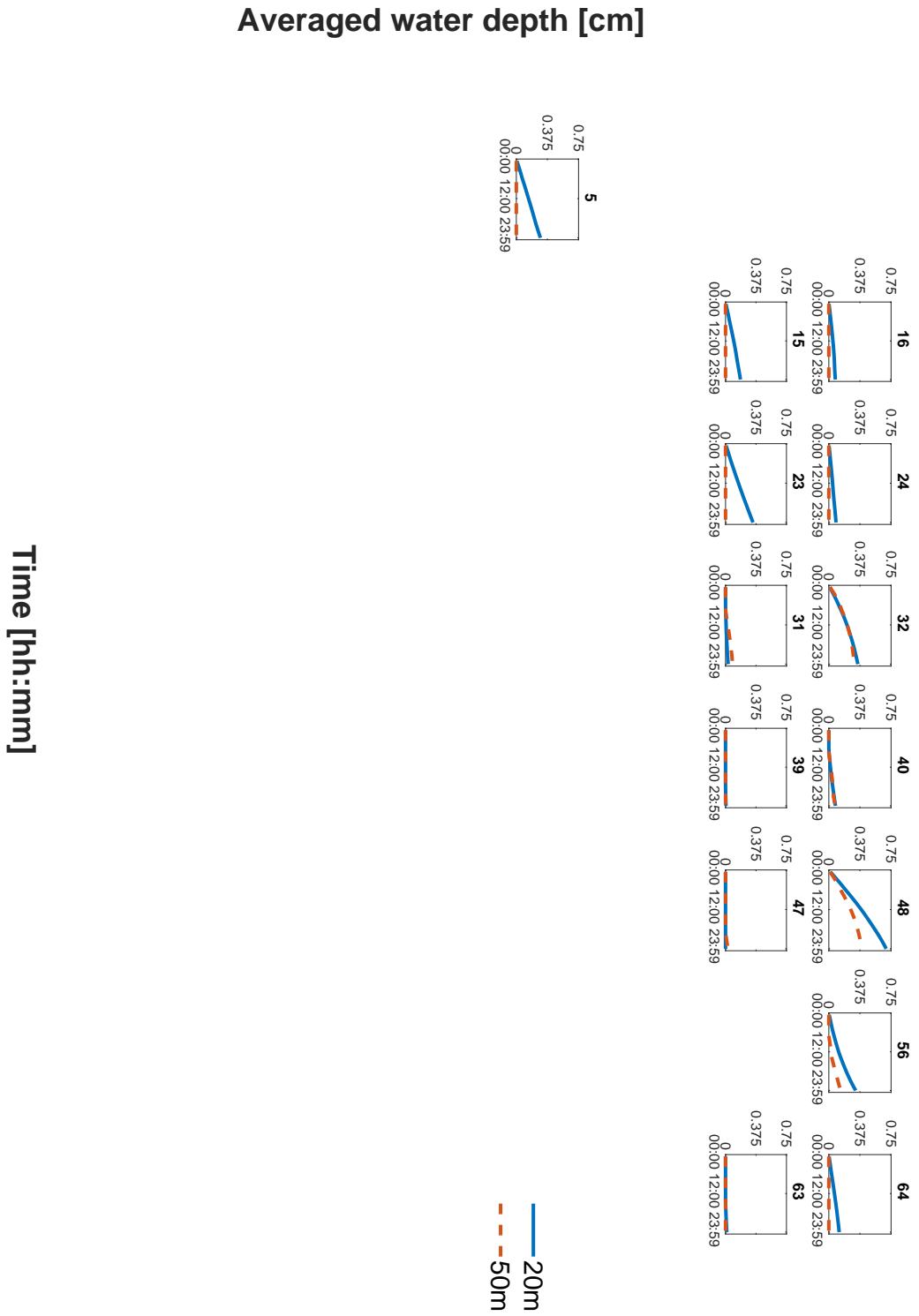
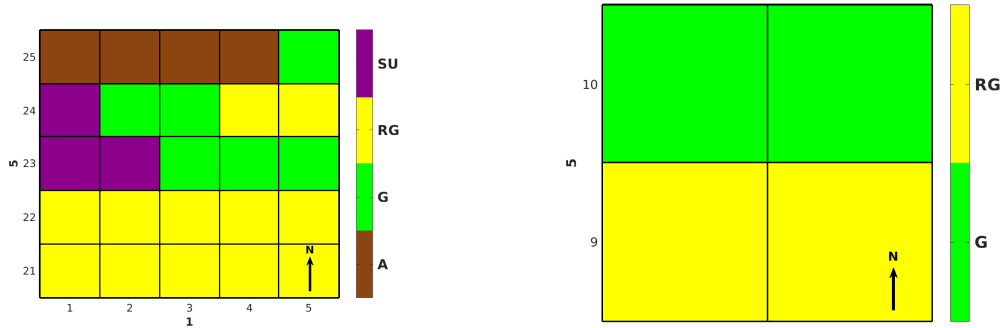
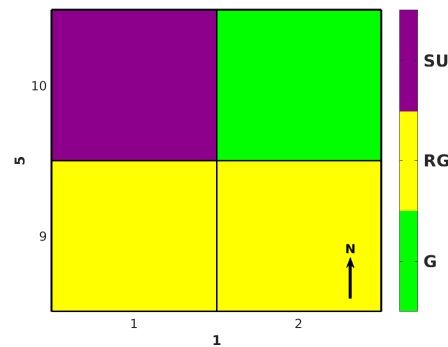


Figure 5.8.: A comparison of the absolute average water depth values between the 20m (blue) and 50m (red) resolutions.

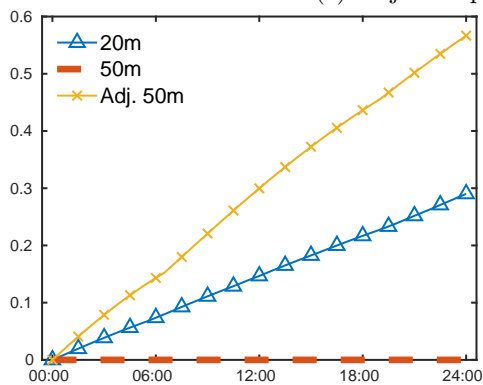


(a) Original patch composition, 20m.

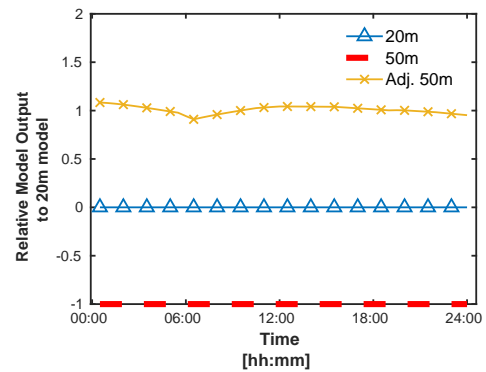
(b) Original patch composition, 50m.



(c) Adjusted patch composition, 50m.

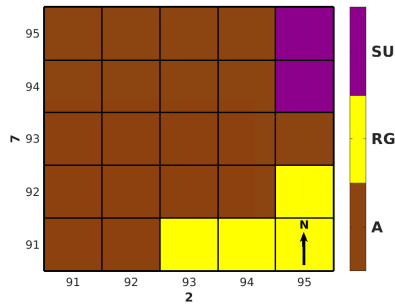


(d) Absolute water depth values for each patch composition.

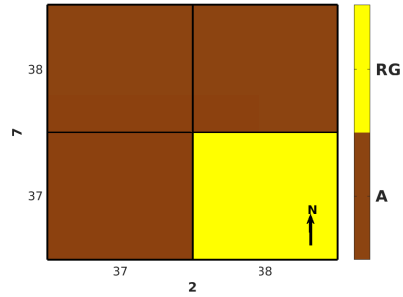


(e) 50m water depth values relative to 20m model composition.

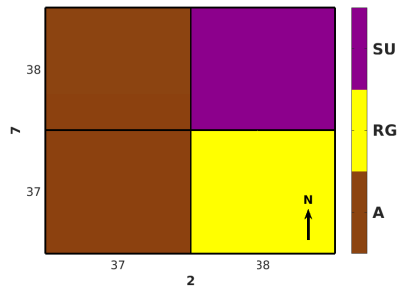
Figure 5.9.: Patch 5 - Original land composition within the 20m (5.9a) and 50m (5.9b) resolution models along with an adjusted 50m resolution patch (5.9c) with absolute water depth values for each model (5.9d) and relative 50m output values compared with the 20m model (5.9e).



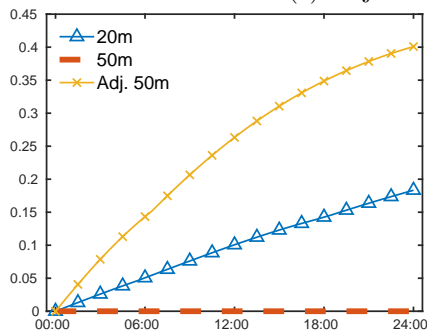
(a) Original patch composition, 20m.



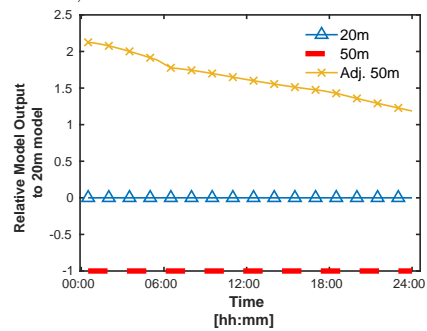
(b) Original patch composition, 50m.



(c) Adjusted patch composition, 50m.



(d) Absolute water depth values for each patch composition.



(e) 50m water depth values relative to 20m model composition.

Figure 5.10.: Patch 15 - Original land composition within the 20m (5.10a) and 50m (5.10b) resolution models along with an adjusted 50m resolution patch (5.10c) with absolute water depth values for each model (5.10d) and relative 50m output values compared with the 20m model (5.10e).

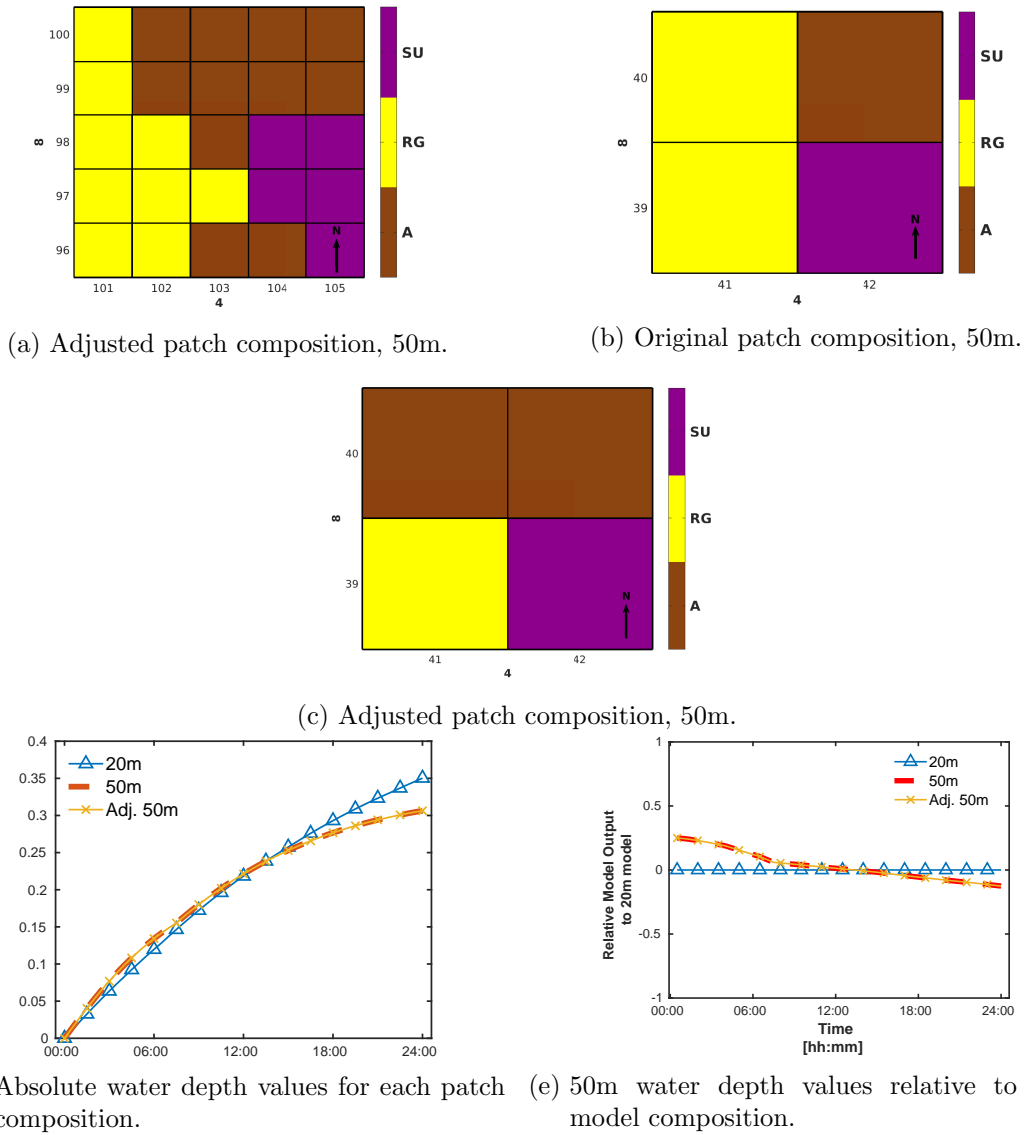


Figure 5.11.: Patch 32 - Original land composition within the 20m (sub-figure 5.11a) and 50m (5.11b) resolution models along with an adjusted 50m resolution patch (5.11c) with absolute water depth values for each model (5.11d) and relative 50m output values compared with the 20m model (5.11e).



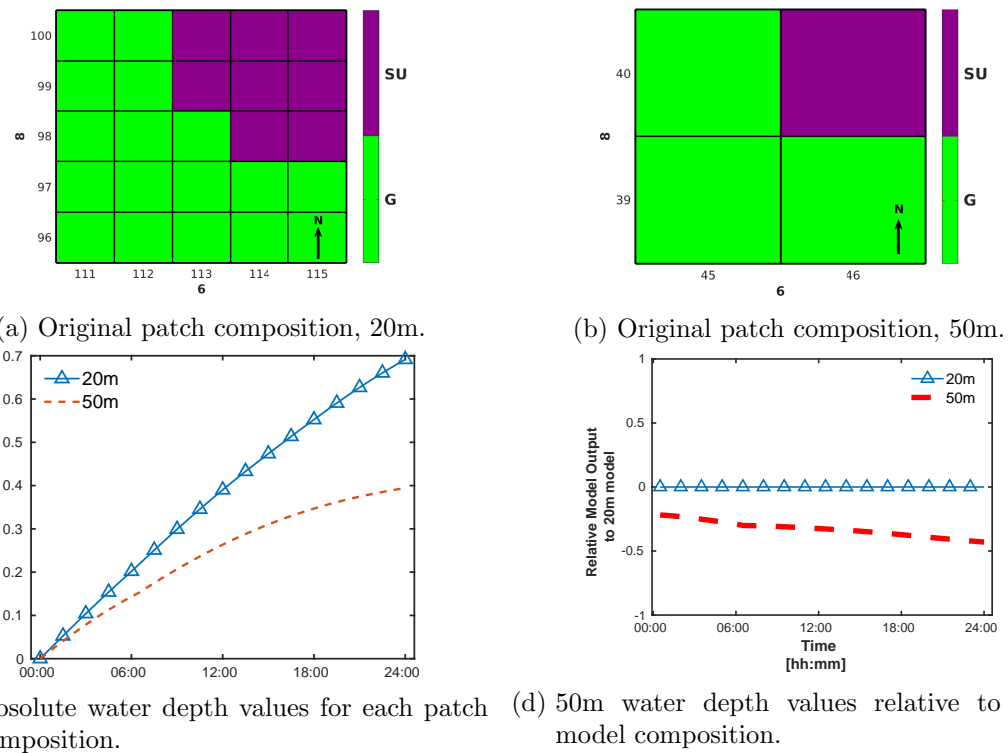
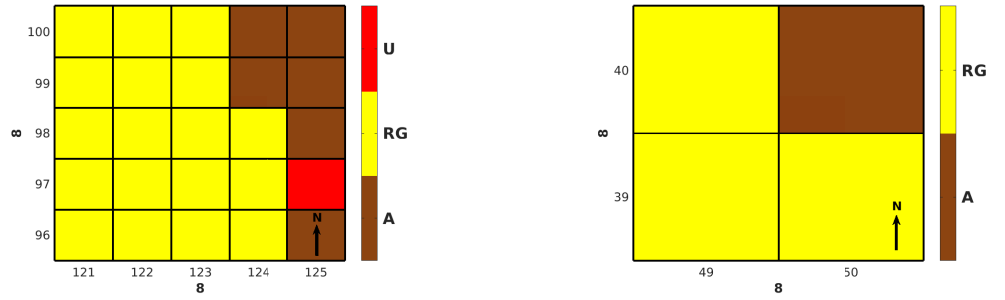
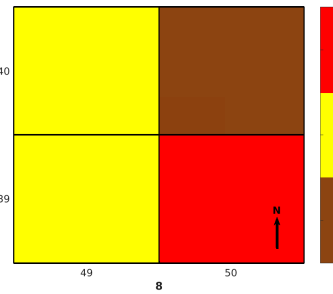


Figure 5.12.: Patch 48 - Original land composition within the 20m (5.12a) and 50m (5.12b) resolution models with absolute water depth values for each model (5.12c) and relative 50m output values compared with the 20m model (5.12d).

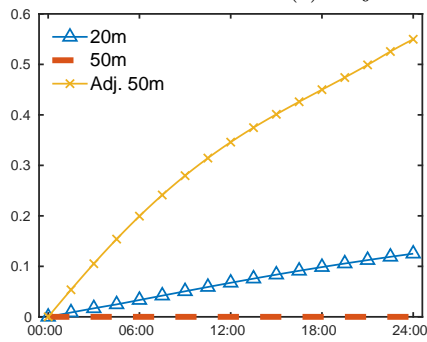


(a) Original patch composition, 20m.

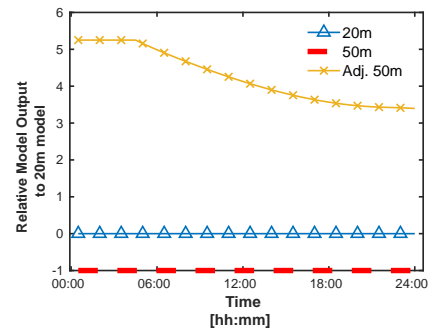
(b) Original patch composition, 50m.



(c) Adjusted patch composition, 50m.



(d) 50m water depth values relative to 20m model composition.



(e) Original patch composition, 20m.

Figure 5.13.: Patch 64 - Original land composition within the 20m (5.13a) and 50m (5.13b) resolution models along with an adjusted 50m resolution patch (5.13c) with absolute water depth values for each model (5.13d) and relative 50m output values compared with the 20m model (5.13e).

## 5.5. Northern Sub Region

### 5.5.1. Spatial Distribution: Local Terrain

Sub-figures in Figure 5.14 show the topological composition of the second model analysis region. The layout of this figure is identical to the layout of Figure 5.2 as described in the opening paragraph of Section 5.4.1. Again the focus will be on the topography of the concentrated computational domain shown in sub-figures 5.14c, 5.14d, 5.14g and 5.14h. The highest elevation points in both computation domains are above 105m, located to the north east of the computational domain. Elevation decrease predominately occurs from north to south, with some gradient elevation changes from east to west. The lowest elevation points in the domain are still above 70m. Unlike the first study area where gradient changes were steep, here the elevation decreases much more gently, highlighted by the spaced out contour lines in Figures 5.14g and 5.14h. There are no obvious topological features within this region like the valley seen in the first model analysis region.

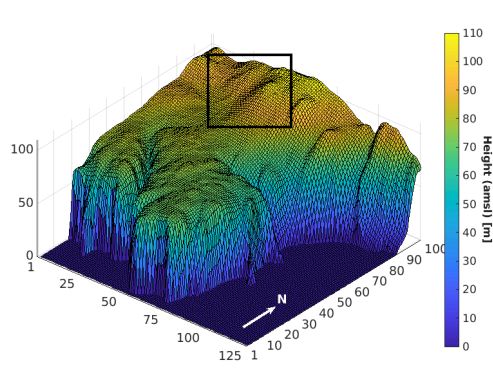
### 5.5.2. Spatial Distribution: Land-Use

Figure 5.15 highlights the spatial distribution of land-use pixels within the second computational domain being utilised for the model performance analysis. Once again, sub-figures 5.15a and 5.15b demonstrate the land-use distribution for the entire domain region. Each black box in these sub-figures corresponds to sub-figures 5.15c and 5.15d respectively, the sampled computational domains being used for the analyses. The land-use abbreviations are labelled on the colour bars within each sub-figure where abbreviation definitions may be found in Table 5.6 along with proportion of land-use pixels as a percentage.

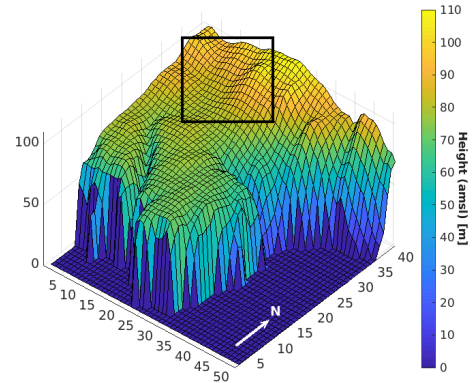
Table 5.6.: Land-Use abbreviations, colour code, model parameter and spatial coverage of the second sampled computational domain given as a percentage.

Land-Use	Abbreviation	Colour Code	Model Parameter	Proportion [%]	
				20m	50m
Arable	A	Brown	1	15.13	14.84
Grassland	G	Lime Green	2	19.63	20.70
Rough Grazing	RG	Yellow	3	56.75	57.03
Sub-Urban	SU	Purple	4	1.25	0.39
Urban	U	Red	5	3.63	3.91
Woodland	Wo	Forest Green	6	3.63	3.13
Water	Wa	Blue	7	0	0

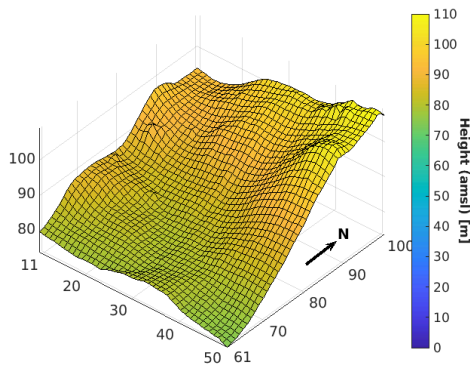
Rough grazing constitute the majority of the land-use pixels within the second computational domain. The main bulk of these pixels cover span from west to east across the domain. There also exists a sporadic distribution of rough grazing pixels along the boundary edges to the south west, south east and north of both the 20m and 50m variants. At  $\sim 20\%$  for both model variations grassland is the second most common land-use pixel type.



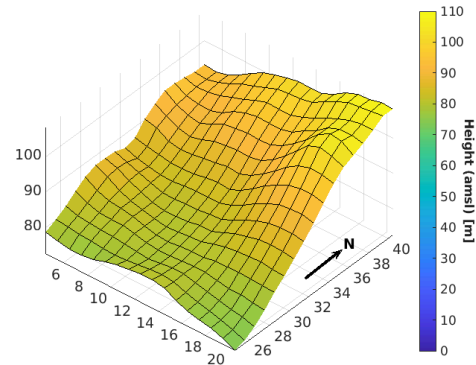
(a) Full domain surface elevation plot, 20m.



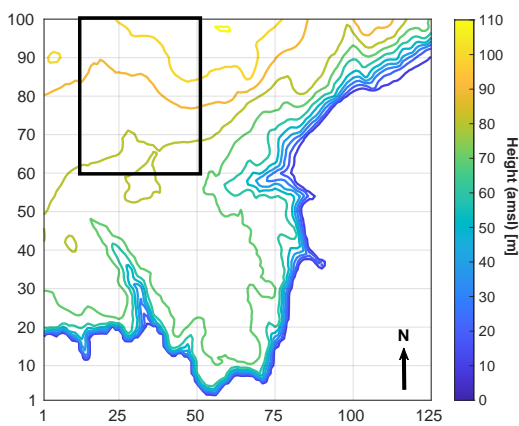
(b) Full domain surface elevation plot, 50m.



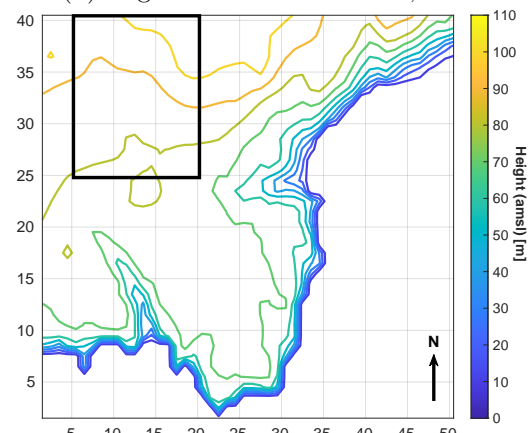
(c) Region 2 surface elevation, 20m.



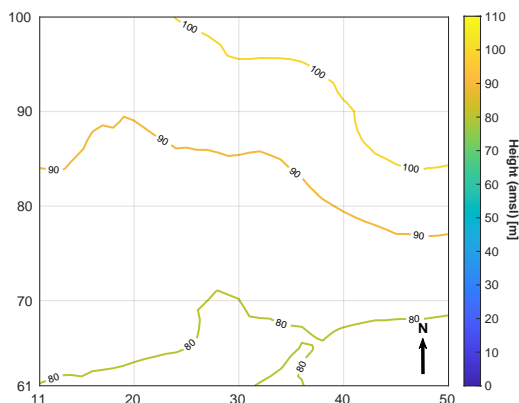
(d) Region 2 surface elevation, 50m.



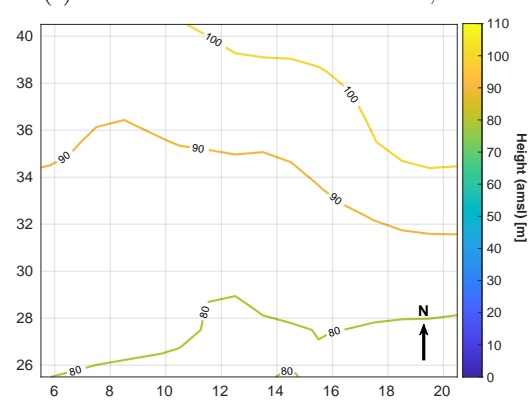
(e) Full domain contour elevation, 20m.



(f) Full domain contour elevation, 50m.



(g) Region 2 contour elevation, 20m.



(h) Region 2 contour elevation, 50m.

Figure 5.14.: A pictorial overview of the topological structure of the full computational domain as well as the second study region used for the model analysis.

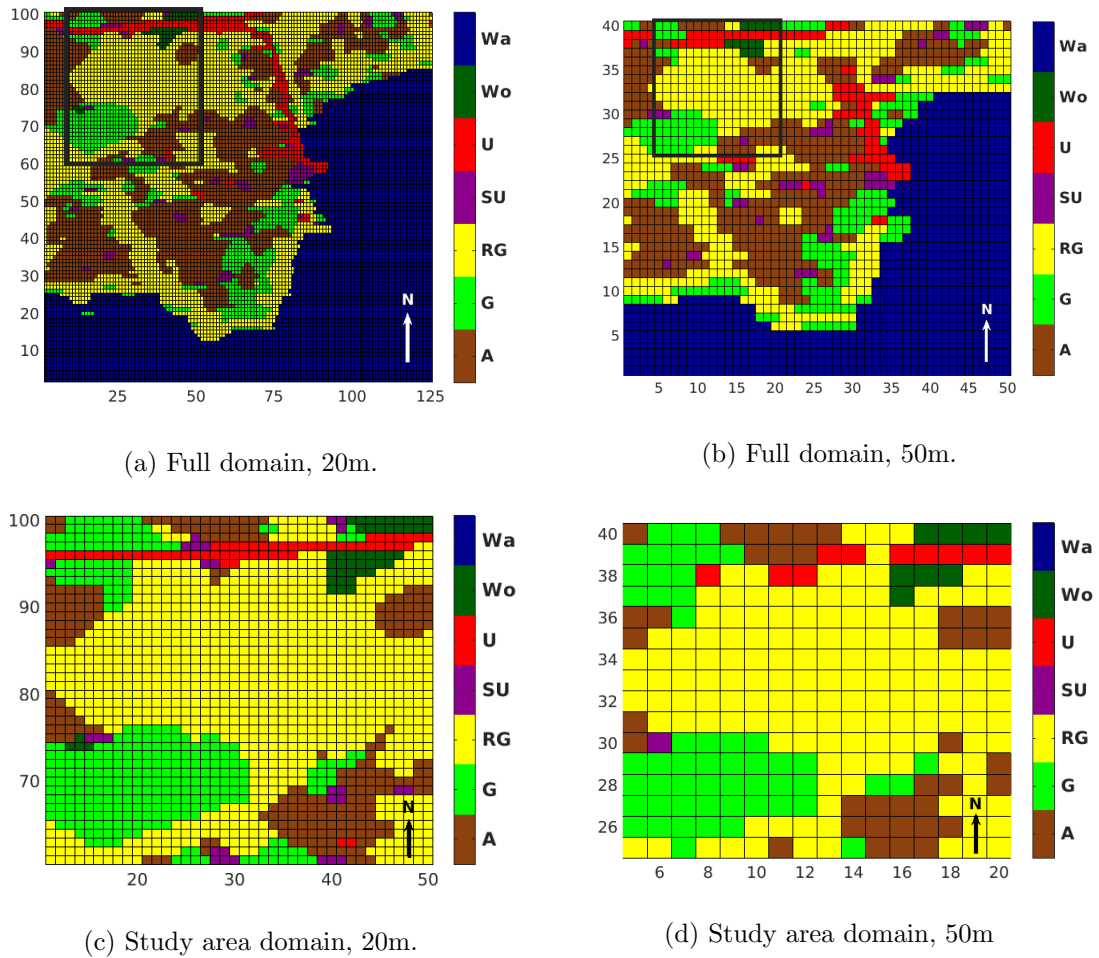


Figure 5.15.: The land-use spatial distributions used within each model variants. Labels on the axes represent the row and column indices for each pixel within the computational domain.

These pixels predominately reside in the south west and north west corners of both model resolutions. Thirdly is arable at  $\sim 15\%$  with the largest group of pixels to the south east and various groupings dotted around the perimeter of the region. Urban land-utilisation accounts for between  $\sim 3-4\%$  of both domains. A red band of pixels reach across north of the domain which is a road in the sampled region. There are also a couple of urban pixels to the south west in the 20m model. In the 50m model a similar, but disjointed, band is present towards the north. This is down to the resolution reduction process described in Section 4.2.3.1 on page 138. At  $\sim 3\%$  comes the woodland land-use type. A sole woodland pocket of pixels reside in the north-eastern part of the computational domain. Finally, the sub-urban pixels account for the final 1.25% and 0.39% respective to the 20m and 50m models. Only one sub-urban pixel is present to the west of the computational domain in the 50m model whereas more sub-urban pixels are distributed sporadically to the south, south east and north in the 20m model. In this model analysis domain, no areas of water pixels were noted.

### 5.5.3. Simulation Run Times

Once again, fifty simulations were run for both model versions within the north computational domain discussed in Sections 5.5.1 and 5.5.2. The time taken to complete each simulation was recorded and the raw data is provided in Table E.2 in supplementary Section E on page 359. Figure 5.16 is a plot of Table E.2, the total time taken for each model simulation to complete. The blue plot represents the 20m model variant and the red plot shows the 50m model. The mean time taken for the 20m model to fully complete a simulation was 228.2s and the 50m model took 37.4s. In this instance, the 50m model was typically 6.11 times faster. Again, both models showed consistency in the time taken to complete each simulation. The longest time the 20m model took was 232.5s and its fastest time was 227.5s, a 5s range. Once more, the 50m was more consistent with each model simulation laying within 1.6s from one another. Its slowest run was 38.7s and its fastest was 37.1s. As noted in Section ?? the speed differential in computational output is unsurprising given the vastly fewer pixels the 50m model is required to calculate. Again the outputs of both models will be compared and contrasted to see if their results agree with one another.

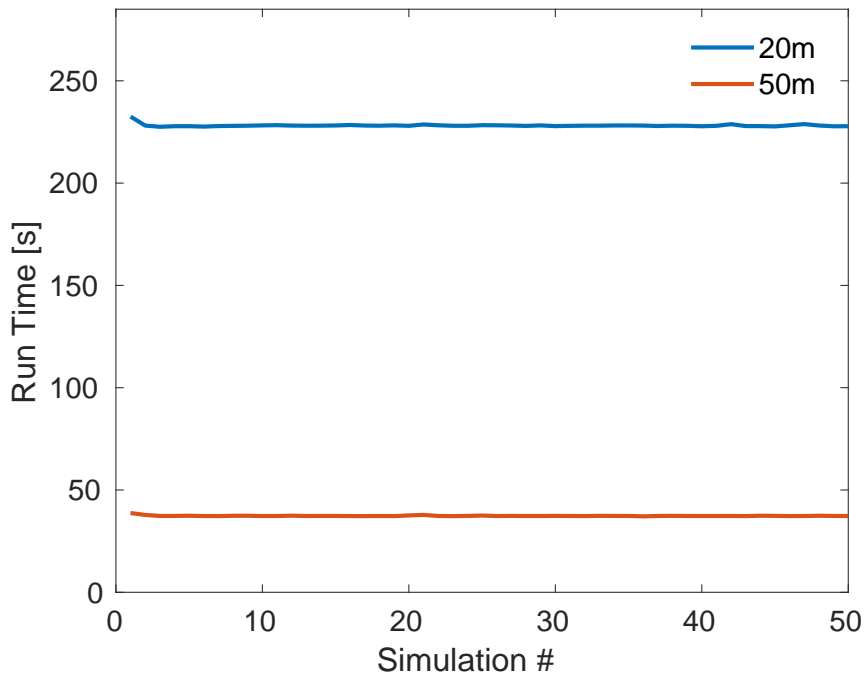


Figure 5.16.: The total time in seconds it took for each of fifty simulation runs for both the 20m (blue) and 50m (red) model resolutions to complete.

### 5.5.4. Overland Flow Distribution

The distribution of overland flow throughout the second sampled region is shown in Figure 5.17. Overland flow for the 20m and 50m models are given at time 06:00 hours 5.17a, 5.17b, 12:00 hours 5.17c, 5.17d, 18:00 hours 5.17e, 5.17f and 24:00 hours 5.17g, 5.17h. Figure

G.2 in Section G is identical in layout, presenting the evolution of water distribution at times 03:00, 09:00, 15:00 and 21:00 hours.

Output within the second simulation follows similarly to the first as overland flow is concentrated among urban and sub-urban areas. Within the 20m model, a large band of output spans the northern part of the computational domain from west to east. From Figure 5.15c (page 213), this output corresponds to the band of urban pixels which too spans from west to east. These urban pixels map to the B3293, which leads to the B3294, shown flooded in Figure 1.7a, on page 43 in Section 1.2. A coarser resolution from the 50m model separates this road into three discrete chunks with a total of ten discrete pixels as seen in Figure 5.15d. These separate areas see the model output present overland flow output as three disjointed regions. By the end of the simulation, two of these regions begin to merge, but not to the extent seen in its 20m counterpart.

A further ten regions contain zones of urban and sub-urban pixels in the 20m model. Three sets of sub-urban pixels are adjacent to the urban pixels which make up the B3293 and their output is merged in with these pixels. One sub-urban region resides in the north-eastern part of the domain at columns (40-41) and rows (99-100). The remaining six are dotted about toward the southern part of the domain at pixel regions (15-17, 74-75), (28-30, 61-62), (39-41, 61), (40-41, 68-69), (41-42, 63) and (47-48, 69). These seven areas correlate with the remaining sporadic outputs from the model. Within the 50m model only one sub-urban area filtered through from the 20m model at pixel (6, 30). This one sub-urban area towards the southern area of the 50m model accounts for the remainder of the 50m output.

Table 5.7.: Pixel column and row boundaries which defined analysis regions to calculate the minimum, maximum and average mean water depths at non-zero output pixels in Figures 5.17 and F.2 for the northern sub-region.

Model Resolution	20m		50m	
	Columns	Rows	Columns	Rows
	11-50	61-100	6-20	24-40
<b>Region 1</b>	13-18	73-75	7-9	29-31
<b>Region 2</b>	26-28	61-63	12-13	25-26
<b>Region 3</b>	39-43	61-63	17-18	25
<b>Region 4</b>	37-42	65-69	16-18	27-28
<b>Region 5</b>	45-48	77-78	19-20	27-28
<b>Region 6</b>	37-40	98-100	16-17	40
<b>Region 7</b>	11-50	91-97	6-20	37-40

Figure 5.18 on page 218 shows the minimum, maximum and mean averaged water depth at each pixel within their respective models at every timestep in this second model analysis. For the 20m and 50m models, the maximum values ranged between 0.074-3.077cm and 0.074-1.774cm respectively. The minimum values ranged between 0.010 - 0.314cm for both variants. The raw data for Figure 5.18 is located in Table F.2 on page 363 in appendix Section F.

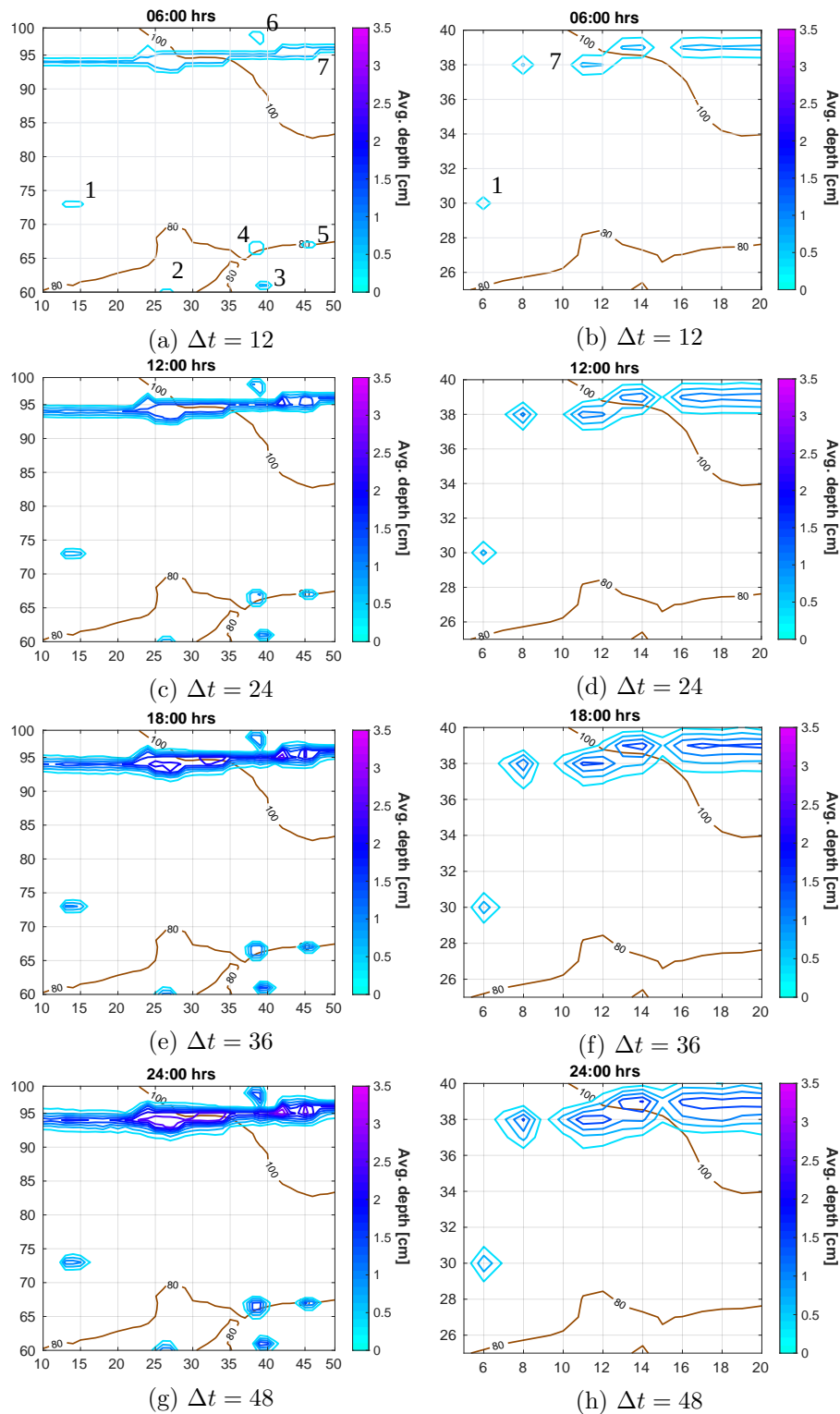


Figure 5.17.: An evolution of the average water depth overland flow throughout the 20m resolution model simulation.



At 06:00 hours, the minimum and maximum averaged pixel depths recorded were 0.01cm and 0.992cm within the 20m model respectively. The mean value for average pixel water depth was noted as 0.503cm. For the 50m the minimum, maximum and mean data points were recorded at 0.022cm, 0.821cm and 0.350cm respectively.

By 12:00 hours, values ranged between 0.01cm and 1.929cm with an average of 0.699cm within the 20m model. For the 50m model these data points were 0.031cm, 1.327cm and 0.538cm respectively.

Once eighteen hours had passed, the minimum value remained at 0.01cm whilst the maximum increased to 2.606cm with the average at 0.834cm for the 20m model. For its 50m counterpart the minimum, maximum and mean averaged water depth was 0.010cm, 1.592cm and 0.613cm respectively.

At the conclusion of the simulation, 24:00 hours, the minimum, maximum and mean values for the 20m resolution were 0.01cm, 3.3077cm and 0.929 respectively. Within the 50m model these values were recorded at 0.022cm, 1.774cm and 0.698cm.

#### **5.5.5. Patch Analysis**

Following the argument presented in Section 5.4.5, an analysis on the effect of sub-urban and urban patches is given below. Patches #3, #7, #11, #15, #23, #24, #25, #32, #39, #40, #41, #42, #49 and #58 all contain a least one land-use category pixel that is either sub-urban or urban in one of their model variants. Every patch except for #3 has an adjusted 50m model variant to compare against the original simulations to see if the output results between them can be closed.

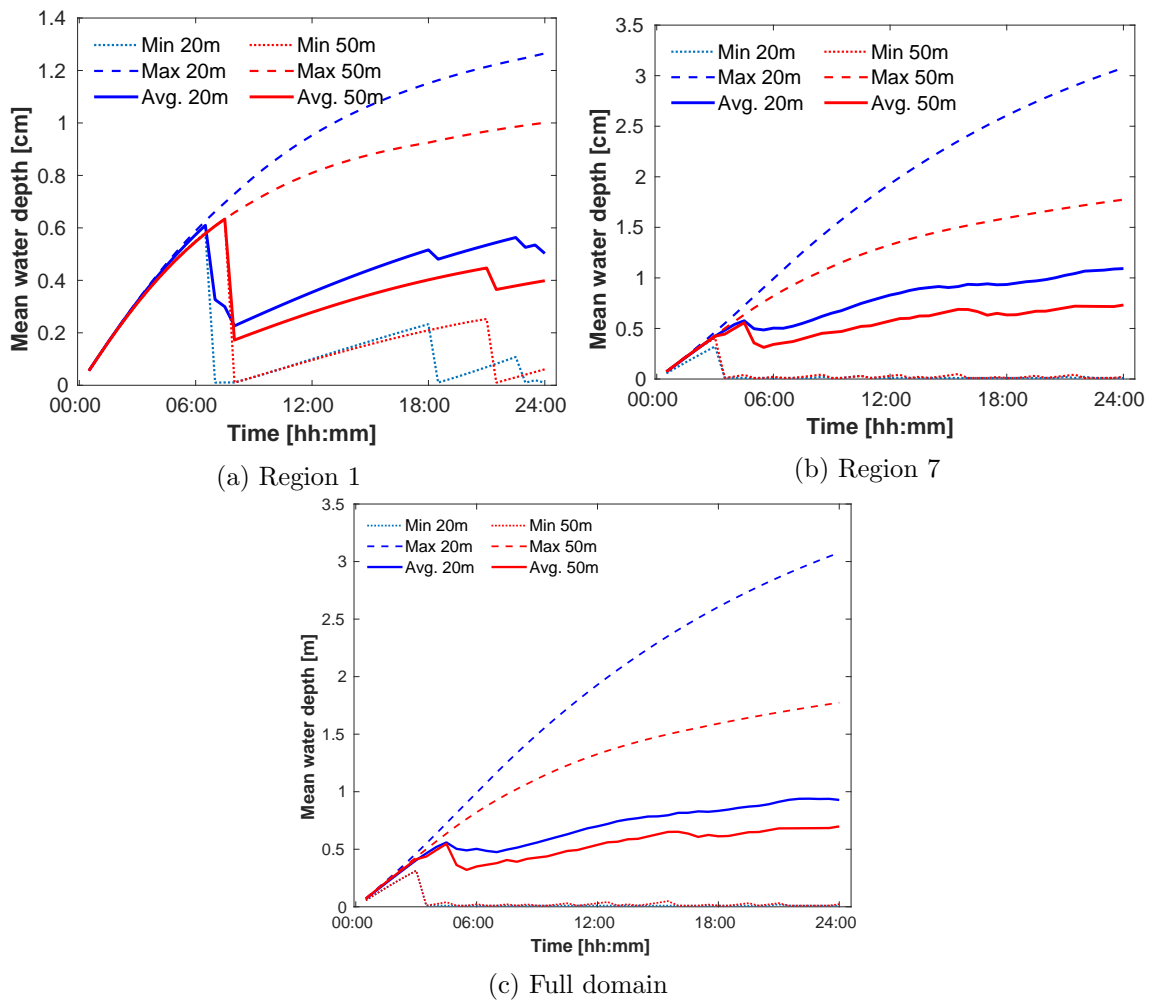


Figure 5.18.: The minimum, maximum and average mean water depths at non-zero output pixels within the northern sub-region outlined in Figure 5.14 for both model resolutions. Sub-figures (a) and (b) show the values for two of the seven regions where water is present as seen in Figure 5.17 as well as the entire domain (c).

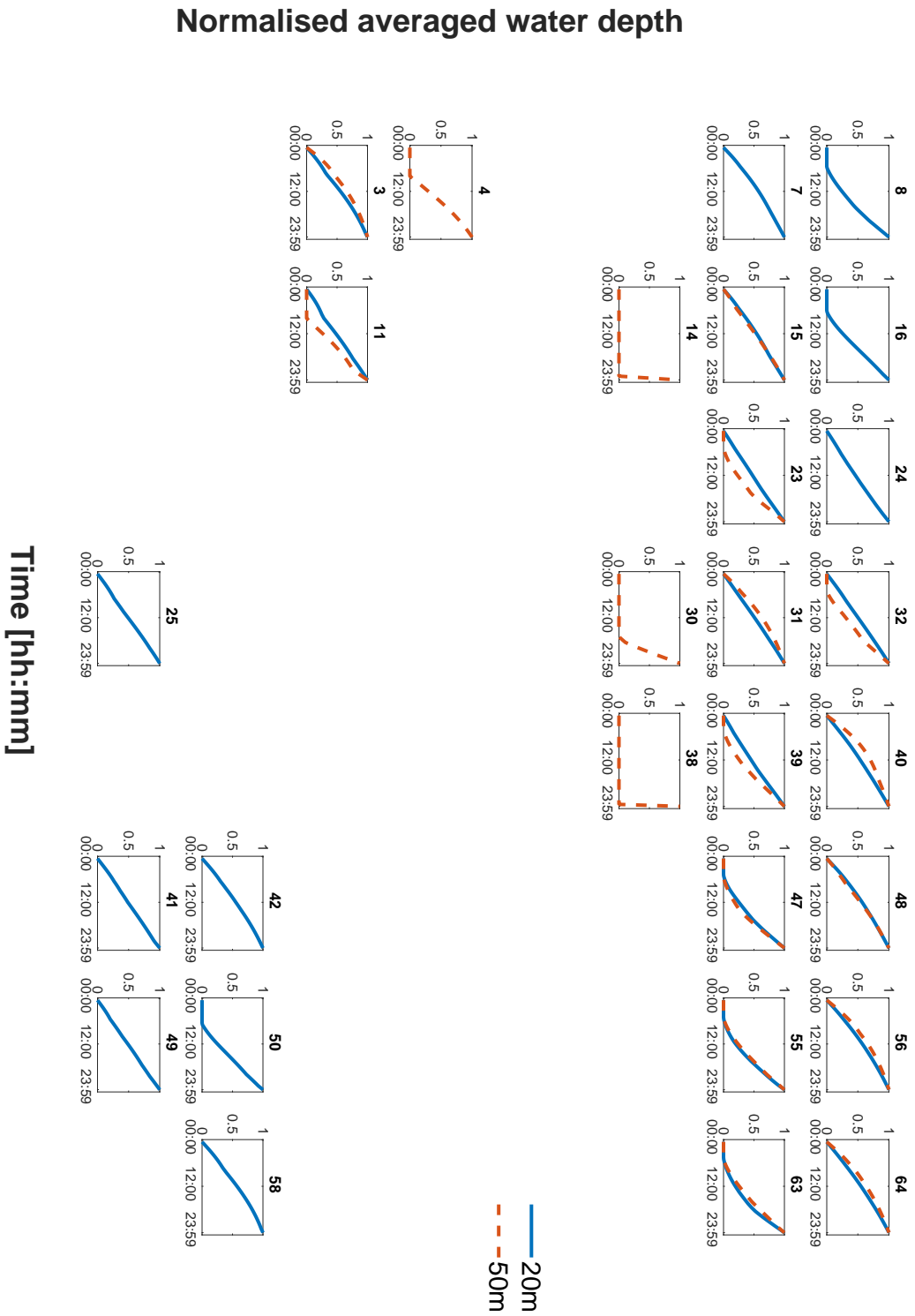


Figure 5.19.: A comparison of the normalised average water depth output between the 20m (blue) and 50m (red) resolutions. The normalisation utilises the maximum average value at any timestep within the patch. The number of timesteps goes across the  $x$ -axis of each subplot. Their plot placement corresponds to the patch numbers in figure 5.1c.

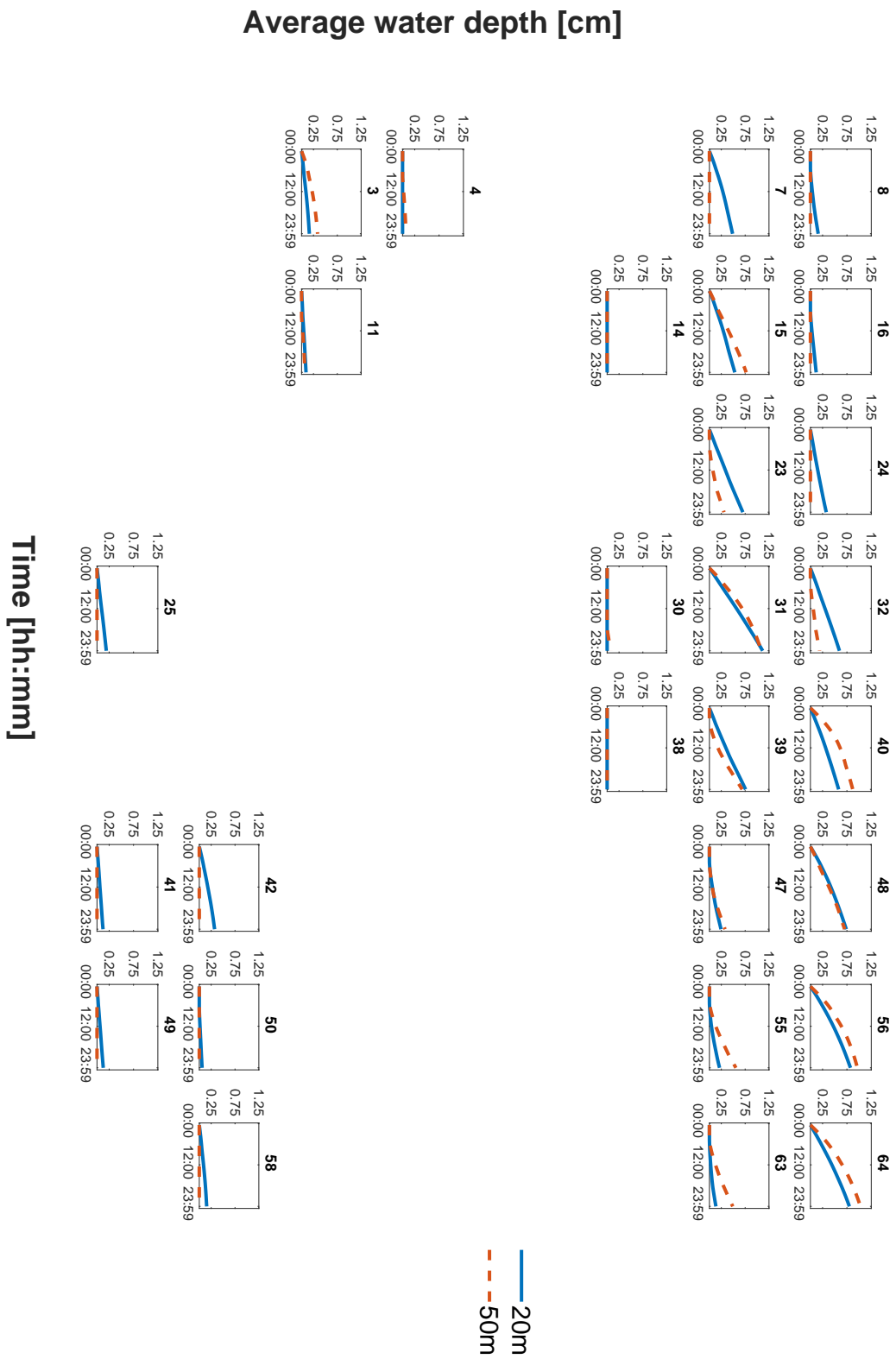


Figure 5.20.: A comparison of the absolute average water depth values between the 20m (blue) and 50m (red) resolutions.

#### 5.5.5.1. Patch #03

The central location of the woodland pixels in Figure 5.21a; page 222 does not cover a sufficient area in any one quadrant of the 20m model to justify adjusting the original 50m patch composition 5.21b. Grassland pixels are proportionally equitable at 48% and 50% respectively, as are the arable pixels at 28% to 25%. However, the sub-urban pixel in the 50m model variant does overestimate coverage at 25% compared with 8% of land-surface area in the 20m model. The 20m model average water depth increases linearly, with the rate of increase tailing off slightly after halfway through the simulation. It reaches a maximum of 0.495cm at the end (sub-figure 5.21c). The output of the 50m model overestimates water depth by over 200% initially. By the end of the simulation, it is still overestimating, by 100% compared with its 20m model counterpart (sub-figure 5.21d).

#### 5.5.5.2. Patch #07

Patch #07 within the 50m model is entirely grassland (sub-figure 5.22b; page 223). Within the 20m model there exists five urban and arable pixels each with the remaining pixels being grassland (sub-figure 5.22a). As urban land has less permeable hydrological characteristics compared to arable land, a grassland pixel in sub-figure 5.22c was replaced by an urban pixel in an attempt to better align the two model variants. Within the 20m model, the average water depth input monotonically increased with each timestep, reaching a maximum average water depth of 0.495cm. No water output was recorded in the original patch composition but the adjusted variant did (sub-figure 5.22d). Initially it overestimated the 20m model output by approximately 25%. This overestimation continued right throughout but did begin to slowly converge towards latter timesteps (sub-figure 5.22e).

#### 5.5.5.3. Patch #11

Patch #11 is also entirely grassland within the 50m model version (sub-figure 5.23b; page 224). However, two rough grazing and a single sub-urban pixel reside in the north-west corner of the original 20m patch (sub-figure 5.23a). Adjusting the 50m model to include a single sub-urban pixel (sub-figure 5.23c), a major overestimation in average water depth by 500% compared with the 20m model is observed (sub-figure 5.23e). However, the original 50m model does eventually catch up with the 20m model by the end of the simulation to 0.526cm (sub-figure 5.23d).

#### 5.5.5.4. Patch #23

Rough grazing defines 100% of the pixels within the 50m model (sub-figure 5.24b; page 225). For the 20m model, pixels land-use consists of urban and rough grazing with a 20%, 80% respectively (sub-figure 5.24a). Pixel  $\Omega_{(10,38)}$  was adjusted to an urban pixel within the 50m model to better reflect the 20m coverage (sub-figure 5.24c). Without the

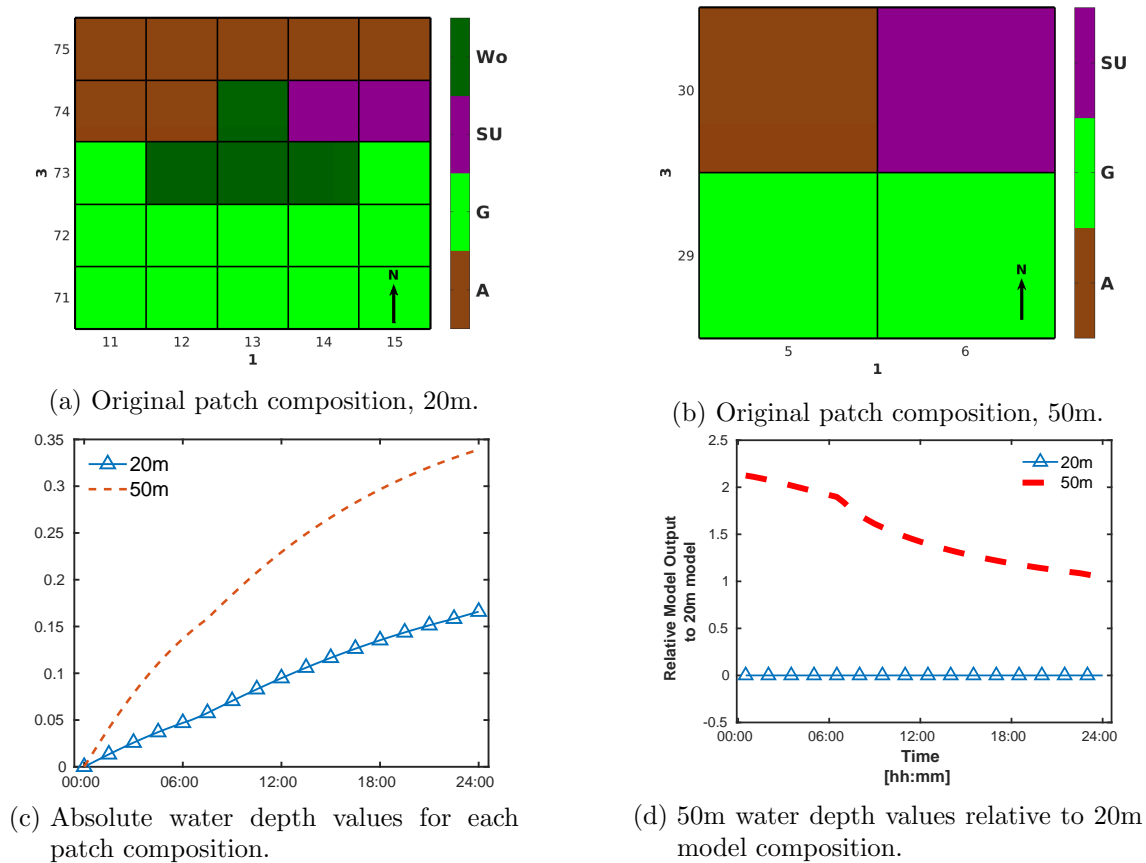


Figure 5.21.: Patch 3 - Original land composition within the 20m (5.21a) and 50m (5.21b) resolution models with absolute water depth values for each model (5.21c) and relative 50m output values compared with the 20m model (5.21d).

urban pixel, the 50m model underestimates the 20m resolution by 50% at the end of the simulation finishing with an average water depth of 0.316cm compared with 0.718cm in the 20m model (sub-figure 5.24e). However, for the 50m adjusted model, it overestimates the 20m model throughout each timestep concluding with an average water depth value of 0.966cm (sub-figure 5.24d).

#### 5.5.5.5. Patch #40

Patch #40's 20m model (sub-figure 5.25a; page 227) is made up of four land-use pixels: rough grazing (40%); arable (32%); urban (20%) and grassland (8%). However, half of the 50m model consists of urban pixels with an arable and rough grazing making up the rest of the patch (sub-figure 5.25b). This 50m model is adjusted by replacing an urban pixel  $\Omega_{14,39}$  with a rough grazing pixel (sub-figure 5.25c). The original 50m model initially overestimates the 20m model by 150% (sub-figure 5.25e). At the end of the simulation the original 50m model's average water depth is 0.879cm compared with the 20m model's output of 0.591cm, approximately a 50% increase. The adjusted 50m model matches the 20m model well for the first quarter of the simulation and only slightly overestimating it. As the simulation progressed, the rate of increase in average water depth of the adjusted variant does not keep pace with the 20m model. It finished with a value of 0.429cm, a

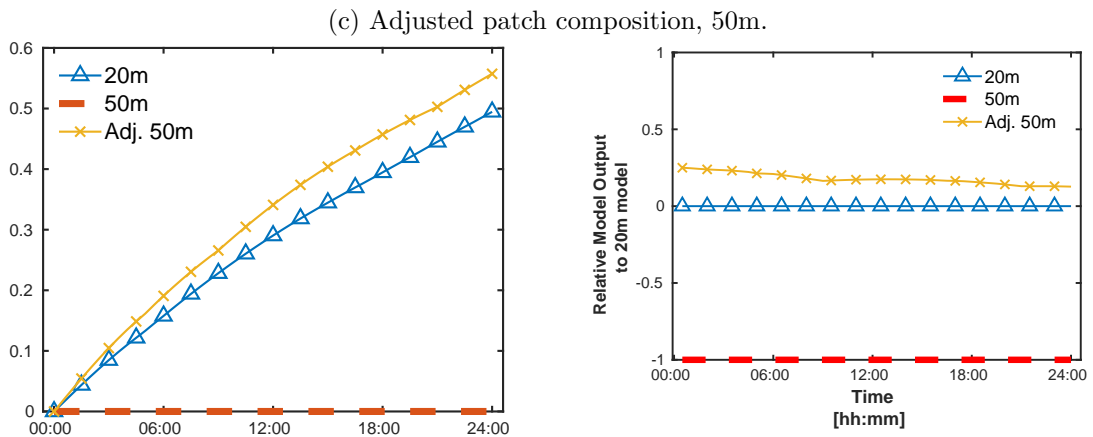
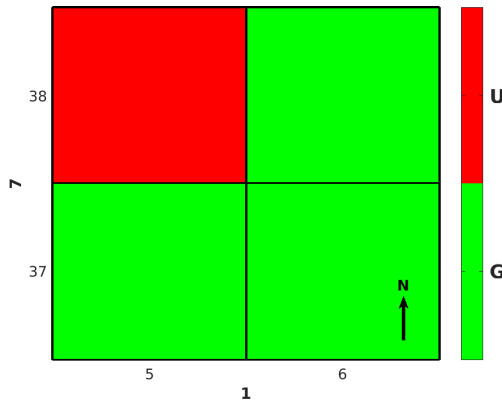
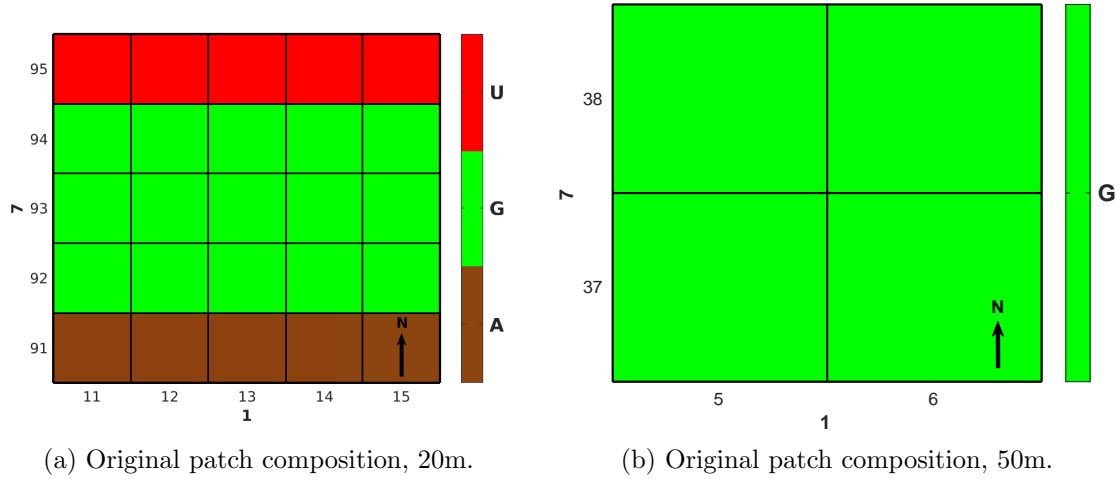
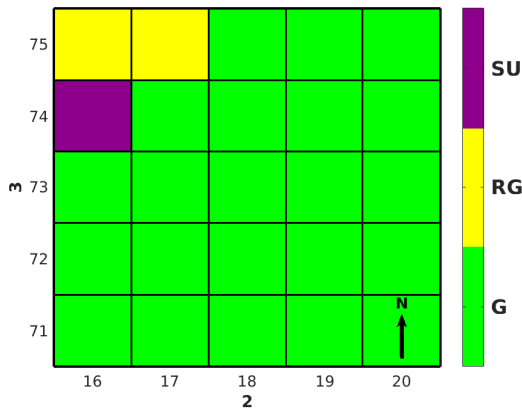
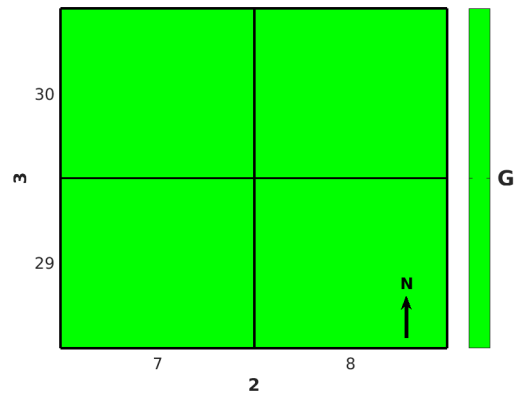


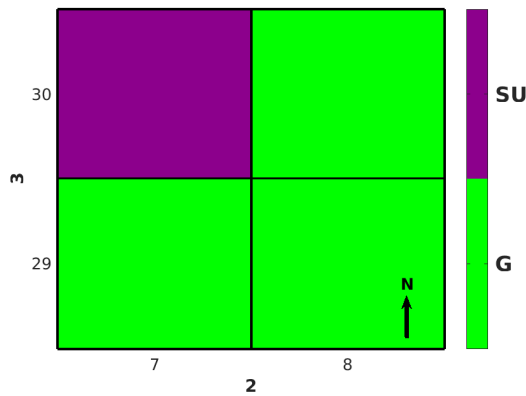
Figure 5.22.: Patch 7 - Original land composition within the 20m (5.22a) and 50m (5.22b) resolution models along with an adjusted 50m resolution patch (5.22c) with absolute water depth values for each model (5.22d) and relative 50m output values compared with the 20m model (5.22e).



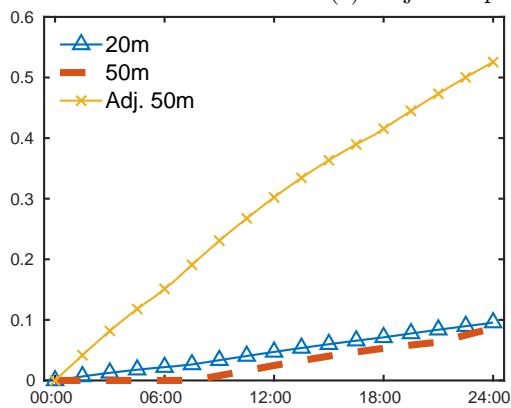
(a) Original patch composition, 20m.



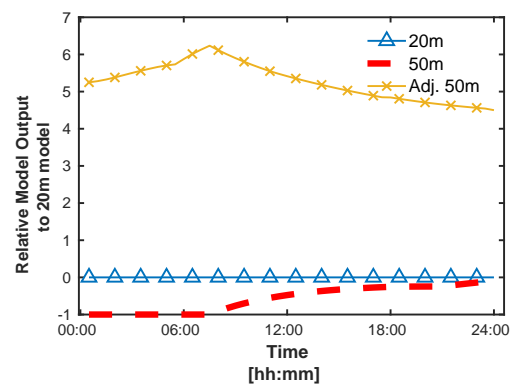
(b) Original patch composition, 50m.



(c) Adjusted patch composition, 50m.



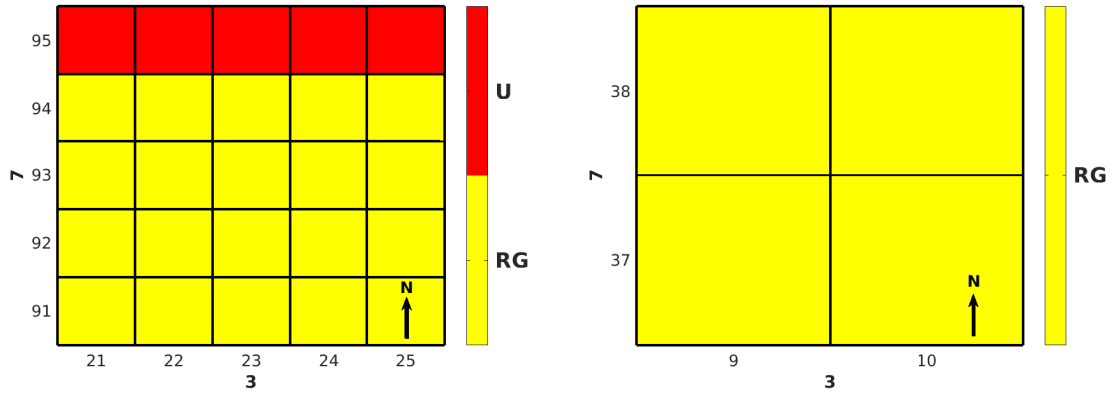
(d) Absolute water depth values for each patch composition.



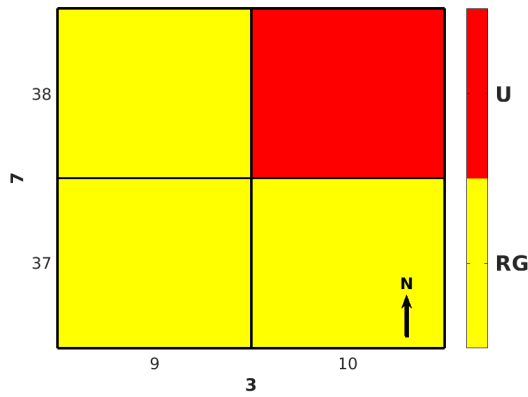
(e) 50m water depth values relative to 20m model composition.

Figure 5.23.: Patch 11 - Original land composition within the 20m (5.23a) and 50m (5.23b) resolution models along with an adjusted 50m resolution patch (5.23c) with absolute water depth values for each model (5.23d) and relative 50m output values compared with the 20m model (5.23e).

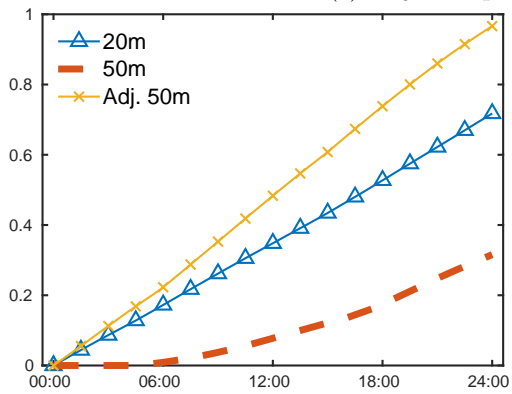




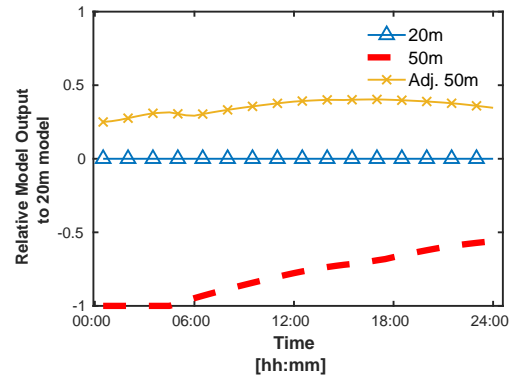
(a) Original patch composition, 20m. (b) Original patch composition, 50m.



(c) Adjusted patch composition, 50m.



(d) Absolute water depth values for each patch composition.



(e) 50m water depth values relative to 20m model composition.

Figure 5.24.: Patch 23 - Original land composition within the 20m (5.24a) and 50m (5.24b) resolution models along with an adjusted 50m resolution patch (5.24c) with absolute water depth values for each model (5.24d) and relative 50m output values compared with the 20m model (5.24e).

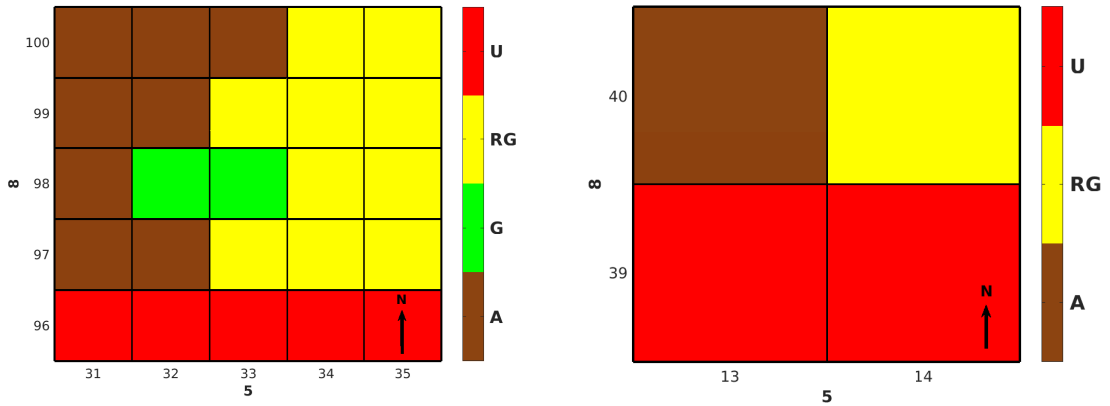
51% underestimation (sub-figure 5.25d).

#### **5.5.5.6. Patch #41**

Arable (92%), Grassland (4%) and Urban (4%) pixels make up the 20m model for patch #41 (sub-figure 5.26a; page 228). Arable pixels represent the entirety of the 50m model variant (sub-figure 5.26b). Arable land in pixel  $\Omega_{16,25}$  is replaced with an urban land pixel (sub-figure 5.26c). The original 50m model did not produce any output throughout the simulation (sub-figure 5.26d). When adjusted, the 50m model closely mirrored the rate of increase in average water depth from 06:00 onwards reaching an average water depth of 0.108cm at the end. Despite this, it did not catch up to the match the 20m model which finished at 0.127cm (sub-figure 5.26e).

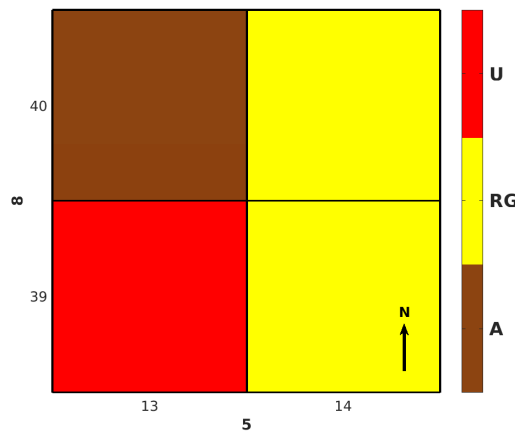
#### **5.5.5.7. Patch #42**

Arable, Grassland, Rough Grazing and Sub-Urban pixels of the 20m model cover 44%, 32%, 8% and 16% of patch #42 respectively (sub-figure 5.27a; page 229). In its 50m version, arable and grassland cover half of the patch each (sub-figure 5.27b). Due to the absorptive properties integrated into the model for arable and grassland, zero output was noted for the original 50m model (sub-figure 5.27d). As such a sub-urban pixel at  $\Omega_{(16,27)}$  replaces an arable pixel (sub-figure 5.27c). This replacement sees the output within the adjusted 50m model overestimating the 20m model by greater than 50% initially. The average water depth outputs between variants began to slowly converge as the simulation continued (sub-figure 5.27e), finishing at 0.354cm compared with 0.327cm for the 20m model.

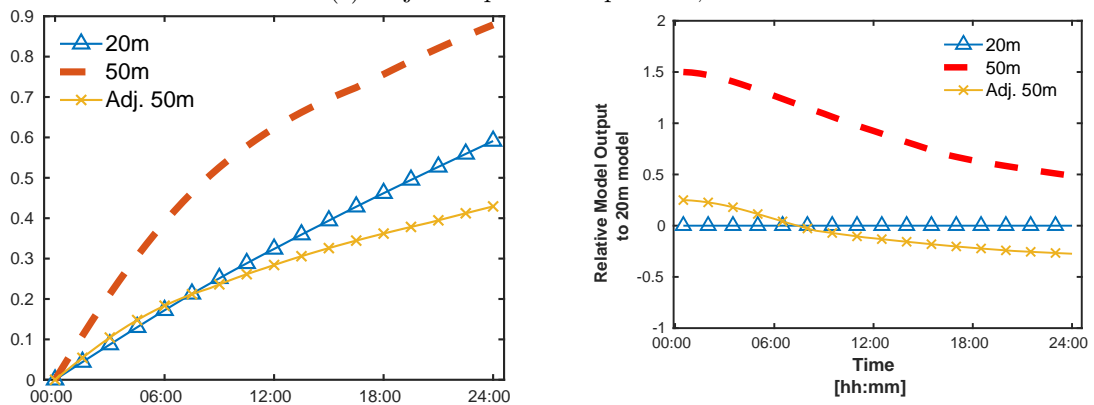


(a) Original patch composition, 20m.

(b) Original patch composition, 50m.



(c) Adjusted patch composition, 50m.



(d) Absolute water depth values for each patch composition.

(e) 50m water depth values relative to 20m model composition.

Figure 5.25.: Patch 40 - Original land composition within the 20m (5.25a) and 50m (5.25b) resolution models along with an adjusted 50m resolution patch (5.25c) with absolute water depth values for each model (5.25d) and relative 50m output values compared with the 20m model (5.25e).

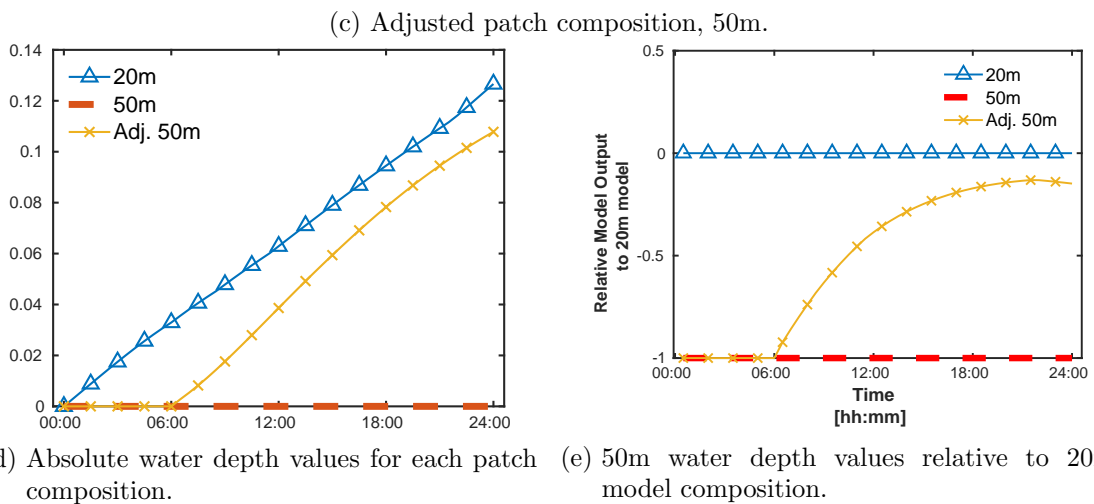
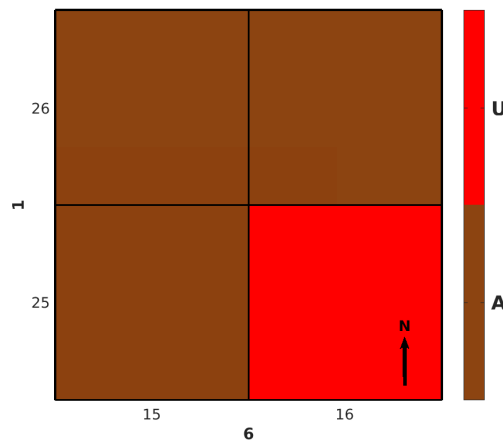
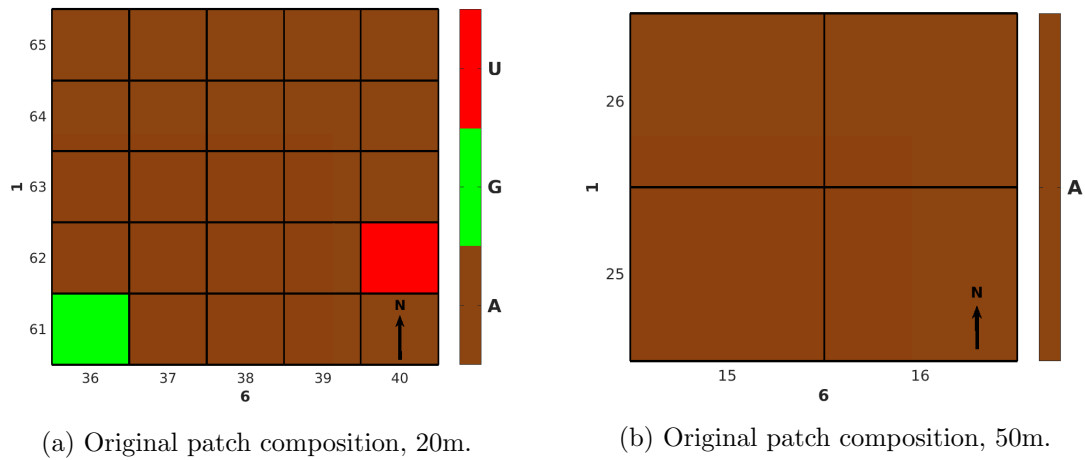
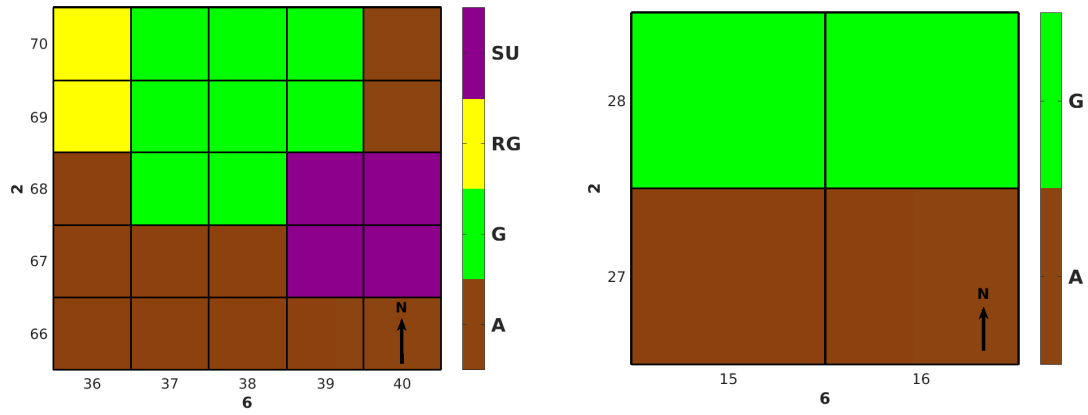
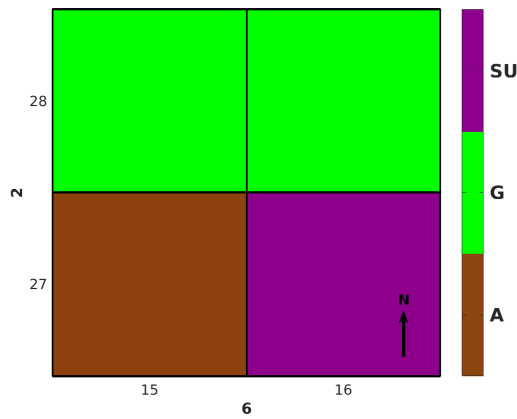


Figure 5.26.: Patch 41 - Original land composition within the 20m (5.26a) and 50m (5.26b) resolution models along with an adjusted 50m resolution patch to match more closely proportionally with the 20m model (5.26c) with absolute water depth values for each model (5.26d) and relative 50m output values compared with the 20m model (5.26e).

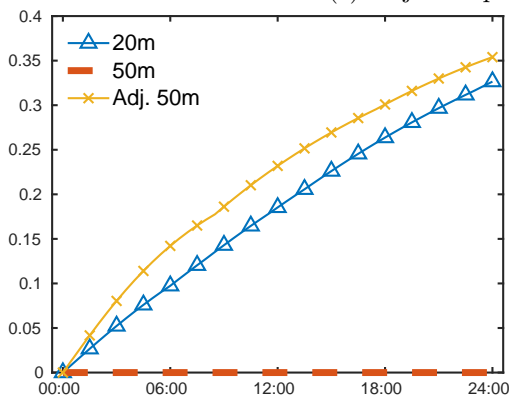


(a) Original patch composition, 20m.

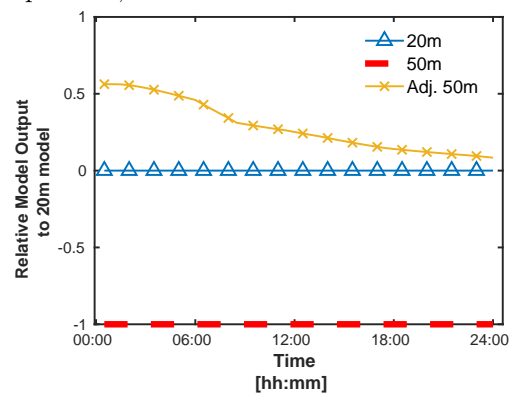
(b) Original patch composition, 50m.



(c) Adjusted patch composition, 50m.



(d) Absolute water depth values for each patch composition.



(e) 50m water depth values relative to 20m model composition.

Figure 5.27.: Patch 42 - Original land composition within the 20m (5.27a) and 50m (5.27b) resolution models along with an adjusted 50m resolution patch to match more closely proportionally with the 20m model (5.27c) with absolute water depth values for each model (5.27d) and relative 50m output values compared with the 20m model (5.27e).

## 5.6. Summary

This chapter compared two resolution variants of the model described in Chapter 4. The justification of selecting these resolutions is given in Section 4.2.5. A mesh structure was defined in Section 5.2 where two sub-regions with area  $0.64\text{km}^2$  were identified to conduct this comparison. The north-eastern and northern sub-regions covered all the land-use types defined within this work. A common “patch” of  $0.01\text{km}^2$  was defined to allow for an easy comparison. These patches consisted of a  $40 \times 40$  grid and  $16 \times 16$  grid for the 20m and 50m model resolutions respectively. The common model input parameters to conduct these analyses were outlined in Section 5.3.

The first model analysis discussed the north-eastern sub-region in Section 5.4. A summary of the local terrain and spatial variation of the land-use categories are given in Sections 5.4.1 and 5.4.2 respectively. A summary of the computation run time between both model resolutions is given in Section 5.4.3. The temporal and spatial evolution of the analysis is summarised in Section 5.4.4. The key behaviour noted in individual patches are highlighted in Section 5.4.5. Patches #5 (Section 5.4.5.1), #15 (Section 5.4.5.2), #32 (Section 5.4.5.3), #48 (Section 5.4.5.4) and #64 (Section 5.4.5.5) are reviewed. Additional patches with similar results are given in Appendix I.1.

The exact same analysis template is used for the northern sub-region in Section 5.5. Patches #3 (Section 5.5.5.1), #7 (Section 5.5.5.2), #11 (Section 5.5.5.3), #23 (Section 5.5.5.4), #40 (Section 5.5.5.5), #41 (Section 5.5.5.6), and #42 (Section 5.5.5.7) are reviewed. Additional patches with similar behaviour are provided in Appendix I.2. No conclusive results were obtained in this chapter. Chapter 6 repeats these analyses, but for a “storm-like” model input.

This chapter highlighted what the key considerations are when deciding what model resolution is most suitable (**RQ5**) and compared the model performance between the 20m and 50m model resolution variants (**RQ6**).

Table 5.8.: The minimum, maximum and average mean water depth value [cm] difference of the 50m and 50m adjusted model resolutions against the 20m model resolution for each patch reviewed in Section 5.4.

Patch	50m			Adjusted 50m		
	Min	Max	Average	Min	Max	Average
#5	0.0066	0.2902	0.1488	0.0071	0.2764	0.1493
#15	0.0044	0.1833	0.0988	0.0093	0.2176	0.1473
#23	0.0066	0.3381	0.1661	0.0071	0.2189	0.1289
#32	$3.7449 \times 10^{-4}$	0.0439	0.0141	$3.7449 \times 10^{-4}$	0.0439	0.0141
#48	0.0038	0.2972	0.1370	-	-	-
#56	0.0044	0.1837	0.0933	0.0093	0.4428	0.2334
#64	0.0029	0.1250	0.0670	0.0151	0.4247	0.2588

Table 5.9.: The minimum, maximum and average mean water depth value [cm] difference of the 50m and 50m adjusted model resolutions against the 20m model resolution for each patch reviewed in Section 5.5.

Patch	50m			Adjusted 50m		
	Min	Max	Average	Min	Max	Average
#3	0.0095	0.1732	0.1221	-	-	-
#7	0.0147	0.4945	0.2796	0.0037	0.0628	0.0451
#11	0.0022	0.0264	0.0184	0.0118	0.4299	0.2428
#15	0.0037	0.2412	0.1211	-	-	-
#23	0.0147	0.4019	0.2531	0.0037	0.2486	0.1342
#24	0.0067	0.3339	0.1635	0.0073	0.1349	0.0983
#25	0.0045	0.1945	0.1002	0.0095	0.2653	0.1604
#32	0.0140	0.4132	0.2455	0.0044	0.0991	0.0690
#39	0.0147	0.1670	0.1224	0.0037	0.4851	0.2524
#40	0.0221	0.3028	0.2482	0.0010	0.1619	0.0594
#41	0.0029	0.1266	0.0647	0.0029	0.0329	0.0208
#42	0.0090	0.3265	0.1821	0.0050	0.0466	0.0369
#49	0.0029	0.1313	0.0665	0.0154	0.5632	0.3278
#58	0.0045	0.1574	0.0897	0.0095	0.2829	0.1640

## Part III.

# Simulation & Analysis



## 6. Non-Uniform Model Input Analysis

### 6.1. Introduction

Chapter 1 discussed one of the challenges of our time, the need for humans to equitably and sustainably use finite resources in order to meet their material, cultural and fundamental needs. The academic parallels between an “environmental management system” identified by Cornwall Council’s “Environment Growth Strategy” (Section 1.1.5) and high level concepts within the “facilities management” industry has led to the proposal of a computational tool to aid policy makers in their longer term policy planning and assess any potential adverse effects. This thesis has described the need for a hydrological model to help decision makers in assessing the potential flooding risks associated with new urban developments needed to build new housing. Chapter 2 reviewed the literature relating to hydrological modelling. Chapter 3 described the fundamental mathematical theory which underpins the model that has been constructed in Chapter 4. Chapter 5 presented an initial performance analysis between the 20m and 50m variants of the model described in Chapter 4.

The analysis conducted in Chapter 5 assumed a uniform rainfall input. However, in reality such scenarios are not feasible. As such, Chapter 6 considers the model described in Chapter 4 but with a non-uniform input. Section 6.2 describes the methodology behind the input and how it was constructed to be more “storm like”. This new input will then be applied to the model for each resolution and then analysed through two scenarios where a ‘static’ and ‘moving’ storm are compared to one another. Section 6.3 looks at the storm as it falls across the centre of the domain. Finally, Section 6.4 compares the static and movement scenarios where the storm falls on the south-eastern part of the computational domain. An additional analysis was implemented where the where the fictitious storm falls on the north-western part of the domain. This is given in Appendix J (page 384).

### 6.2. Non-Uniform Model Input

Chapter 5 investigated whether the 50m model variant was able to perform as well as the 20m model. To do this a total of 5cm of rainfall input was applied evenly throughout the simulation per pixel i.e. each pixel received 0.1042cm input per timestep. If this model was to be used in plausible real world scenarios, one should not expect rainfall to fall in even increments. As such a fictitious storm was created to emulate what one could expect normally. The same total input described in Chapter 5 is used here, however the

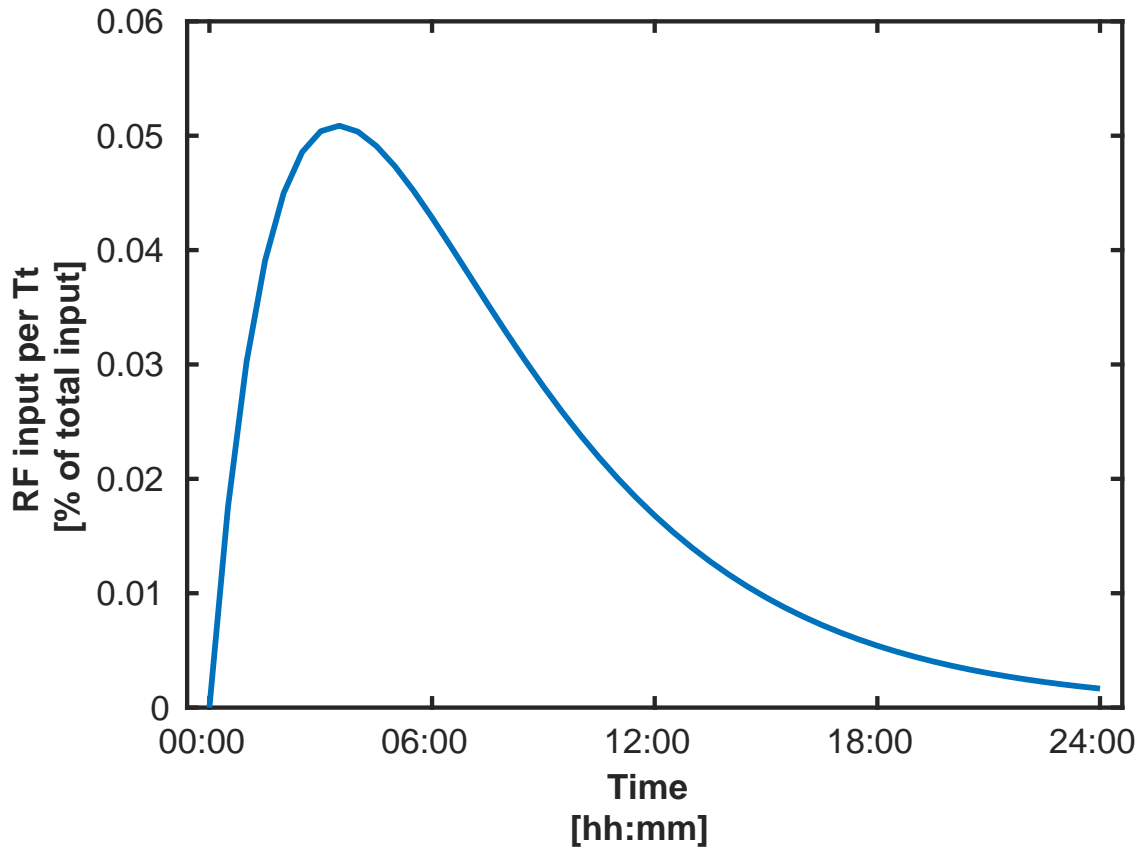
temporal and spatial distribution has been altered to be more “storm-like”. Figure 6.1(a) (page 235) shows the proportion of total input implemented into the model at the given timesteps. The majority of the rainfall pours over Coverack within the first quarter of the simulation. As its peak, 5% of the total input is applied at a given timestep.

To begin modelling the spatial distribution of the input, an  $m \times n$  evenly spaced mesh grid between -3 and 3 was developed. The cell values of this mesh grid were applied to the two-dimensional Gaussian function

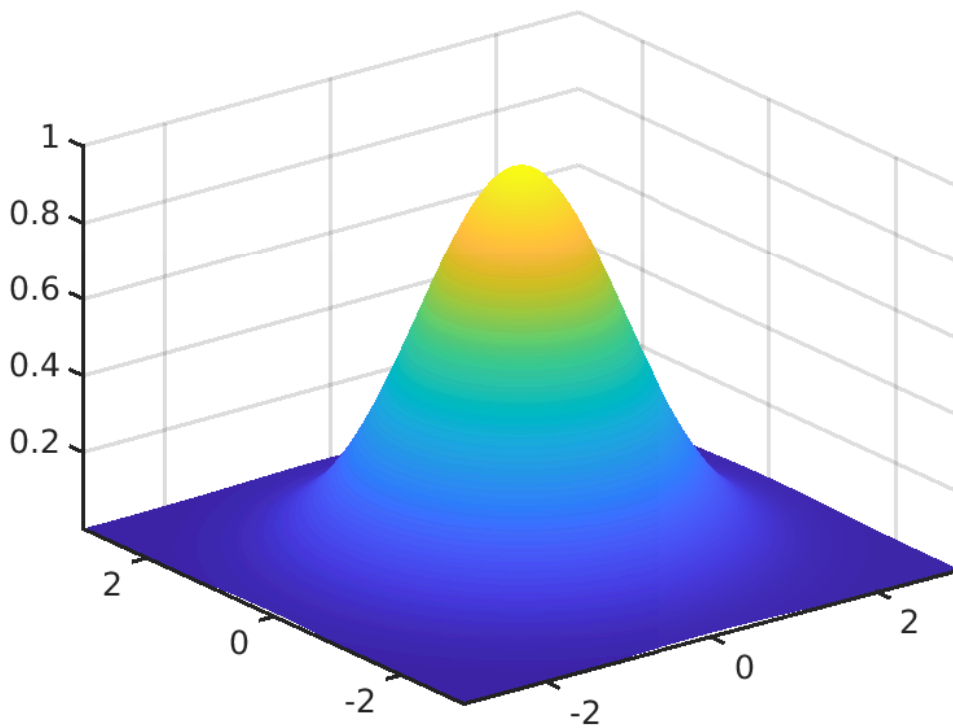
$$Z(x, y) = \frac{1000}{\sqrt{2\pi}} \exp \left\{ - \left( \frac{x^2}{2} \right) - \left( \frac{y^2}{2} \right) \right\}, \quad (6.1)$$

to create the storm’s shape seen in Figure 6.1(b).

Consider the timestep where the proportion of total input is at its peak of 5% as described above. For one pixel in either model this equates to 0.25cm. For all pixels in a 20m model this equates to 3750cm. This value is then applied proportionally distributed according to the two-dimensional Gaussian function in equation (6.1), to give the total input for that timestep. In this chapter, three fictitious storm scenarios are presented. A ‘static’ storm scenario is compared with a ‘moving’ storm scenario for both the 20m and 50m model using the original land-use definitions from Section 4.2.2. Three scenarios are explored where the location over the computational domain is changed.



(a) Temporal Signal



(b) Spatial Intensity

Figure 6.1.: Spatial and Temporal Inputs.

### 6.3. Scenario 1 - Central Region

#### 6.3.1. Movement 20m

Within this first scenario, the fictitious storm described in Section 6.1 travels from south-west to the north-east across the central part of the computational domain. Figure 6.2 shows the first quarter of the simulation run in 1.5 hour increments when the model input occurs. Its rainfall intensity is described by Figure 6.1(a) and the storm's shape is given by Figure 6.1(b). Sub-figures (a), (e) and (i) in the first column of Figure 6.2 and sub-figures (a) and (e) of Figure 6.3 show this storm evolution. Lighter blue colours show small rainfall inputs whilst deep purple and pink show heavy rainfall inputs at given time intervals.

Column two of Figure 6.2 contain sub-figures (b), (f) and (j) and column two of Figure 6.3 shows sub-figures (b) and (f). These show the average water depth overland flow experienced in the domain during this scenario. Due to the heavy initial input at the beginning of the simulation, pixels between  $\Omega_{(i,j)} = \Omega_{(1-10,25-40)}$  see an average water depth of at least 6cm within the south-west corner of the domain. As the model evolves, to timesteps  $\Delta t = 04 : 30$  and  $\Delta t = 06 : 00$  some overland flow is noticed along the B3293 urban pixels in the northern part of the computational domain. However, by the quarter-way stage of the simulation, the main bulk of overland flow is experienced in the south-west corner of the domain.

The final two columns of Figures 6.2 and 6.3 show the average unit-width horizontal velocity in the  $x$ - (sub-figures (c), (g) and (k) and sub-figures (c) and (g), respectively) and  $y$ - directions (sub-figures (d), (h) and (l) and sub-figures (d) and (h), respectively). Red shaded pixels depict the overland flow travelling eastwards. The deeper the shade of red the faster the velocity. Similarly, yellow shaded pixels show velocities travelling westwards. Shade intensity denotes the speed of the velocity. Within the final column of the figure, deeper shades of purple show faster northward unit width horizontal velocities, while deeper shades of green show faster southward unit width horizontal velocities. By  $\Delta t = 04 : 30$ , the overland flow in the south-west corner of the domain is travelling in a south-easterly direction and continues to do so throughout the first quarter of the simulation. The flooding experienced in the northern part of the domain is stagnant initially, but by  $\Delta t = 07 : 30$  it begins to move eastward and slowly southward.

The remainder of the simulation is illustrated through Figures 6.4 and 6.5. Sub-figures (a), (e) and (i) of 6.4 and (a) and (e) of 6.5 show no further rainfall input. After twelve hours, at  $\Delta t = 24 : 00$ , overland flow has dispersed over a greater area within the south-west region of the domain, while still predominately moving south eastwards (sub-figures 6.4(b), (c) and (d)). In the northern part of the domain, the overland flow unit width horizontal velocity moving southward is much stronger (sub-figure 6.4(d)), moving towards Coverack. By  $\Delta t = 42 : 00$  and six hours later at  $\Delta t = 48 : 00$ , some overland flow begins to dissipate in the northern part of the domain, but average water depth in the south-west remains even. One must keep in mind of the no-slip boundary condition imposed in the

simulation. Thus it is likely a factor in helping keep the presence of water in this region.

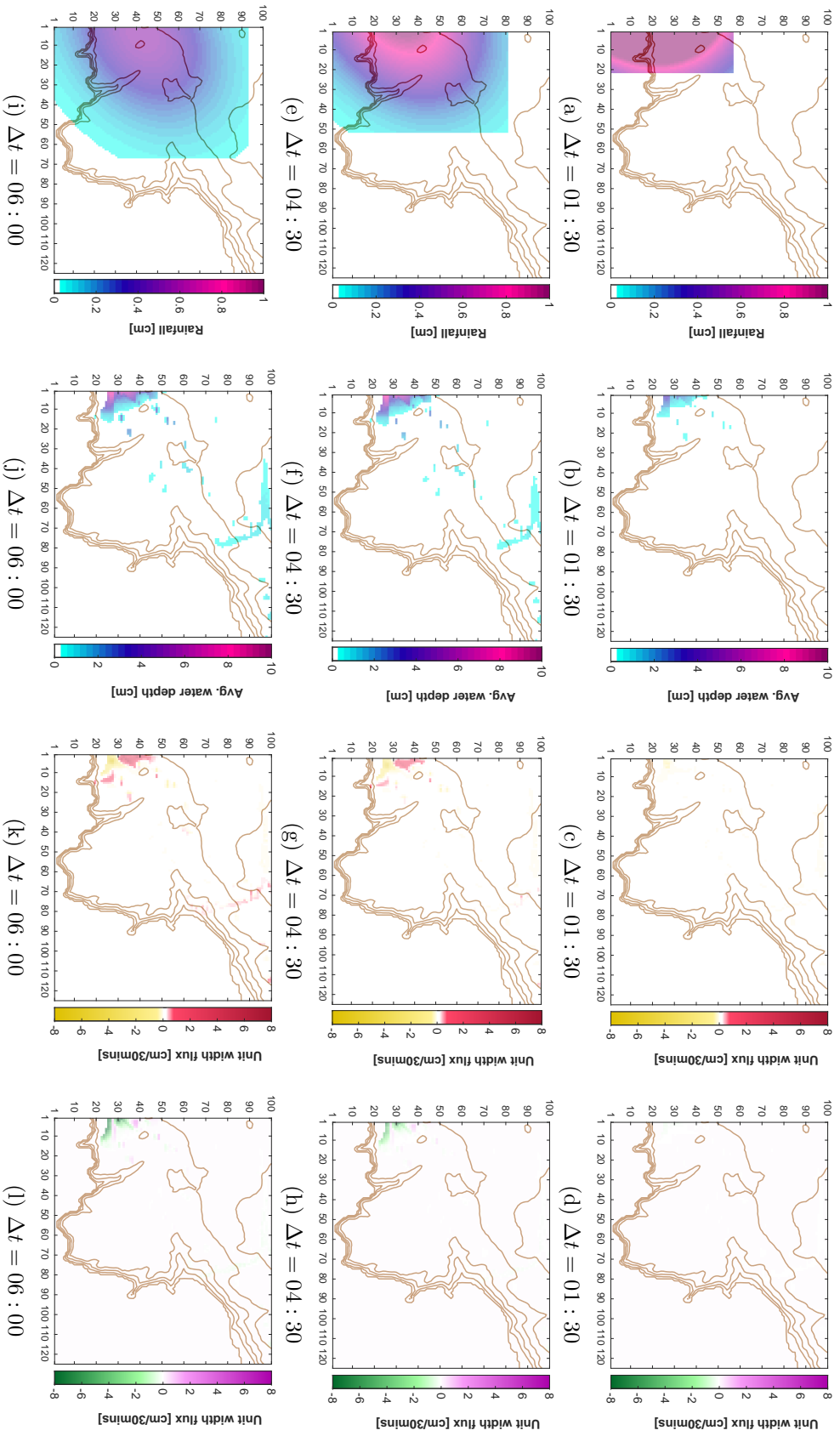


Figure 6.2: Scenario 1 - Central moving storm - 20m resolution model. Each row presents individual timesteps  $\Delta t = 01 : 30$ ,  $\Delta t = 04 : 30$  and  $\Delta t = 06 : 00$ . Sub-figures (a), (e) and (i) show the evolution of the fictitious storm during the simulation. Sub-figures (b), (f) and (j) show the average water depth at their given timesteps. Sub-figures (c), (g) and (k) depict the mean unit-width horizontal flux in the  $y$ -direction. Sub-figures (d), (h) and (l) depict the mean unit-width horizontal flux in the  $x$ -direction.

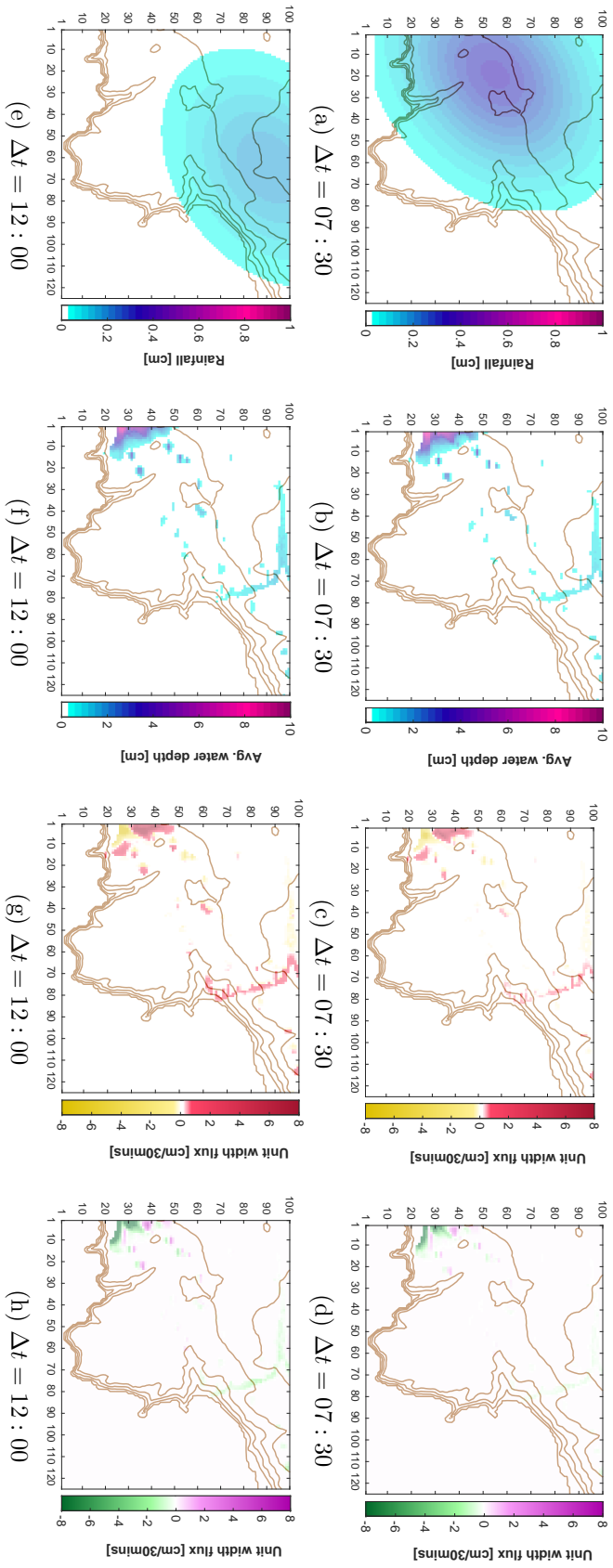


Figure 6.3.: Scenario 1 - Central moving storm - 20m resolution model. Each row presents individual timesteps  $\Delta t = 07 : 30$  and  $\Delta t = 12 : 00$ . Sub-figures (a) and (e) show the evolution of the fictitious storm during the simulation. Sub-figures (b) and (f) show the average water depth at their given timesteps. Sub-figures (c) and (g) depict the mean unit-width horizontal flux in the  $x$ -direction. Sub-figures (d) and (h) depict the mean unit-width horizontal flux in the  $y$ -direction.

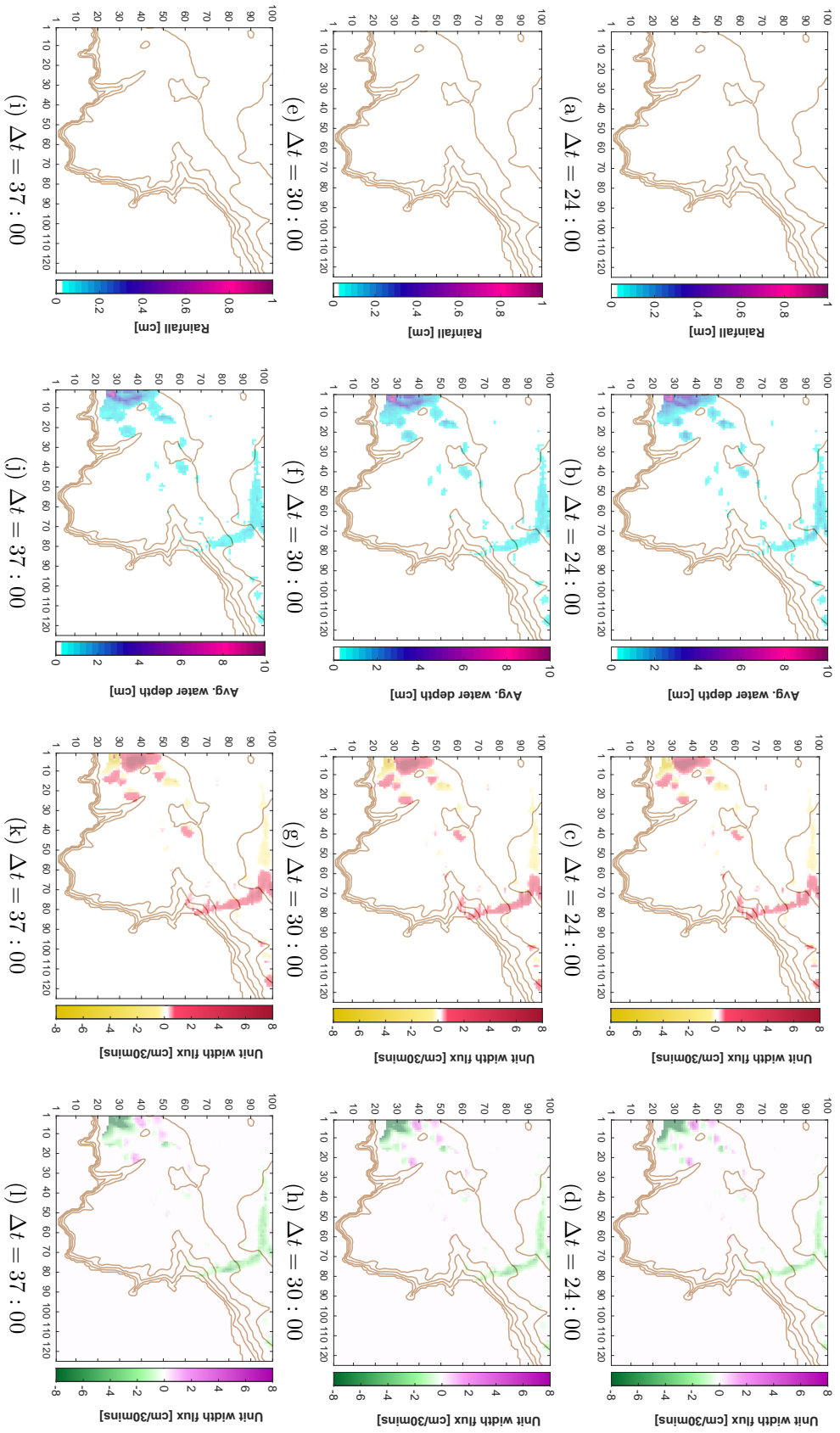


Figure 6.4: Scenario 1 - Central moving storm - 20m resolution model. Each row presents individual timesteps  $\Delta t = 24 : 00$ ,  $\Delta t = 30 : 00$  and  $\Delta t = 37 : 00$ . Sub-figures (a), (e) and (i) show the evolution of the fictitious storm during the simulation. Sub-figures (b), (f) and (j) show the average water depth at their given timesteps. Sub-figures (c), (g) and (k) depict the mean unit-width horizontal flux in the  $y$ -direction. Sub-figures (d), (h) and (l) depict the mean unit-width horizontal flux in the  $x$ -direction.



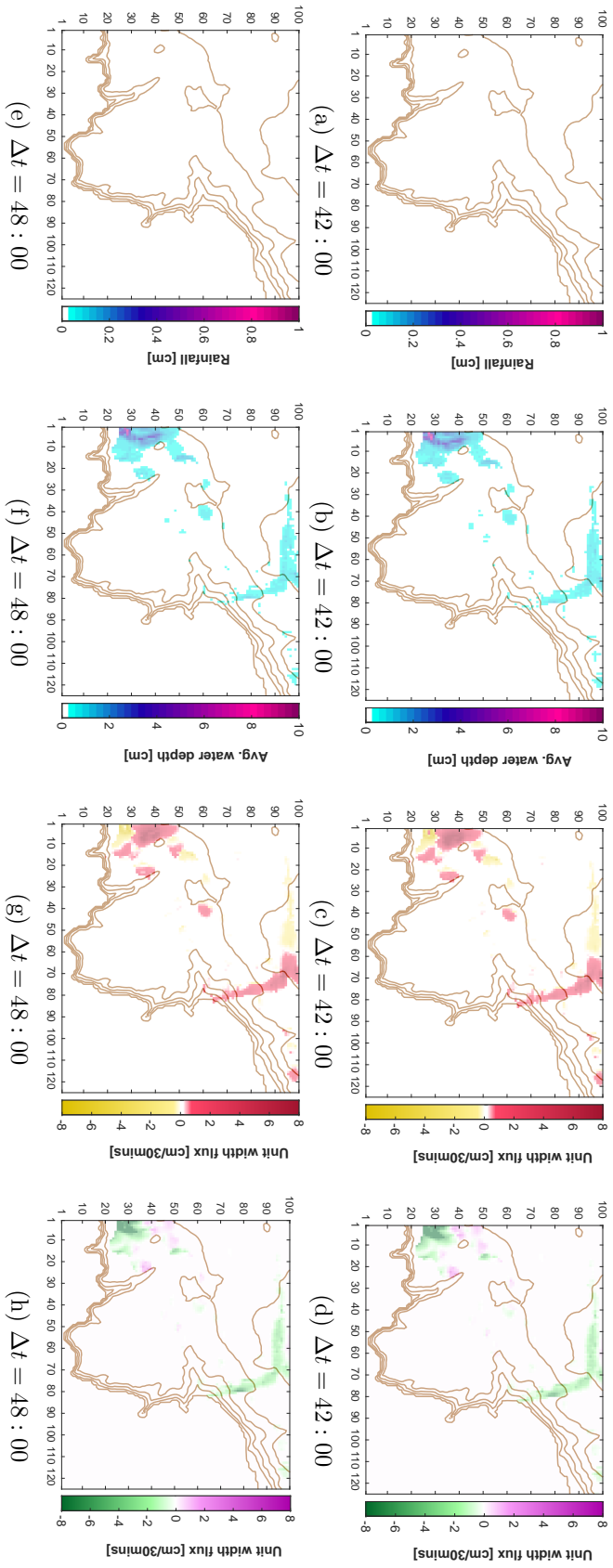


Figure 6.5.: Scenario 1 - Central moving storm - 20m resolution model. Each row presents individual timesteps  $\Delta t = 42:00$  and  $\Delta t = 48:00$ . Sub-figures (a) and (e) show the evolution of the fictitious storm during the simulation. Sub-figures (b) and (f) show the average water depth at their given timesteps. Sub-figures (c) and (g) depict the mean unit-width horizontal flux in the  $x$ -direction. Sub-figures (d) and (h) depict the mean unit-width horizontal flux in the  $y$ -direction.

### 6.3.2. Static 20m

Figures 6.6 and 6.7 have an identical format to Figures 6.2 and 6.3 respectively. The model input is shown in the first column. The resulting output is shown on the second column. The final two columns of the figure show the general unit-width velocity directions at the given timesteps. In this given scenario, the temporal and spatial distribution described in Section 6.1 is used. However, in this case the storm remains static.

As the bulk of the input did not fall in the south-west corner of the domain, there is an absence of overland flow there in comparison to the moving storm scenario presented in Section 6.3.1. Instead, overland flow is concentrated within the pixel region  $\Omega_{(i,j)} = \Omega_{(70-90,50-75)}$ . This is where Coverack is located. As the storm continues at timestep  $\Delta t = 06 : 00$ , average water depth rises to just below 4cm (sub-figure (j)). Generally, the water flow moves in a south-easterly direction (sub-figures (g) and (k)). At the end of the storm,  $\Delta t = 12 : 00$ , average water depth in some regions has reached 6cm (sub-figure (r)) moving eastwards (sub-figure 6.7(g)). Figure 6.7(h) presents a region in Coverack where dark green patches and dark purple patches are adjacent to one another. This suggests that overland water is flowing through this valley region and which is acting as a funnel to go into the sea.

At  $\Delta t = 24 : 00$  overland flow averages 6cm within Coverack and funneling through the town (sub-figures 6.8(a) – (d)). In particular, there is a strong southward unit-width horizontal velocity. This effect continues throughout and by the end of the simulation ( $\Delta t = 48 : 00$ ), overland flow is beginning to dissipate where most pixels are experiencing a mean average water depth of below 2cm (Figure 6.9(e) – (h)).

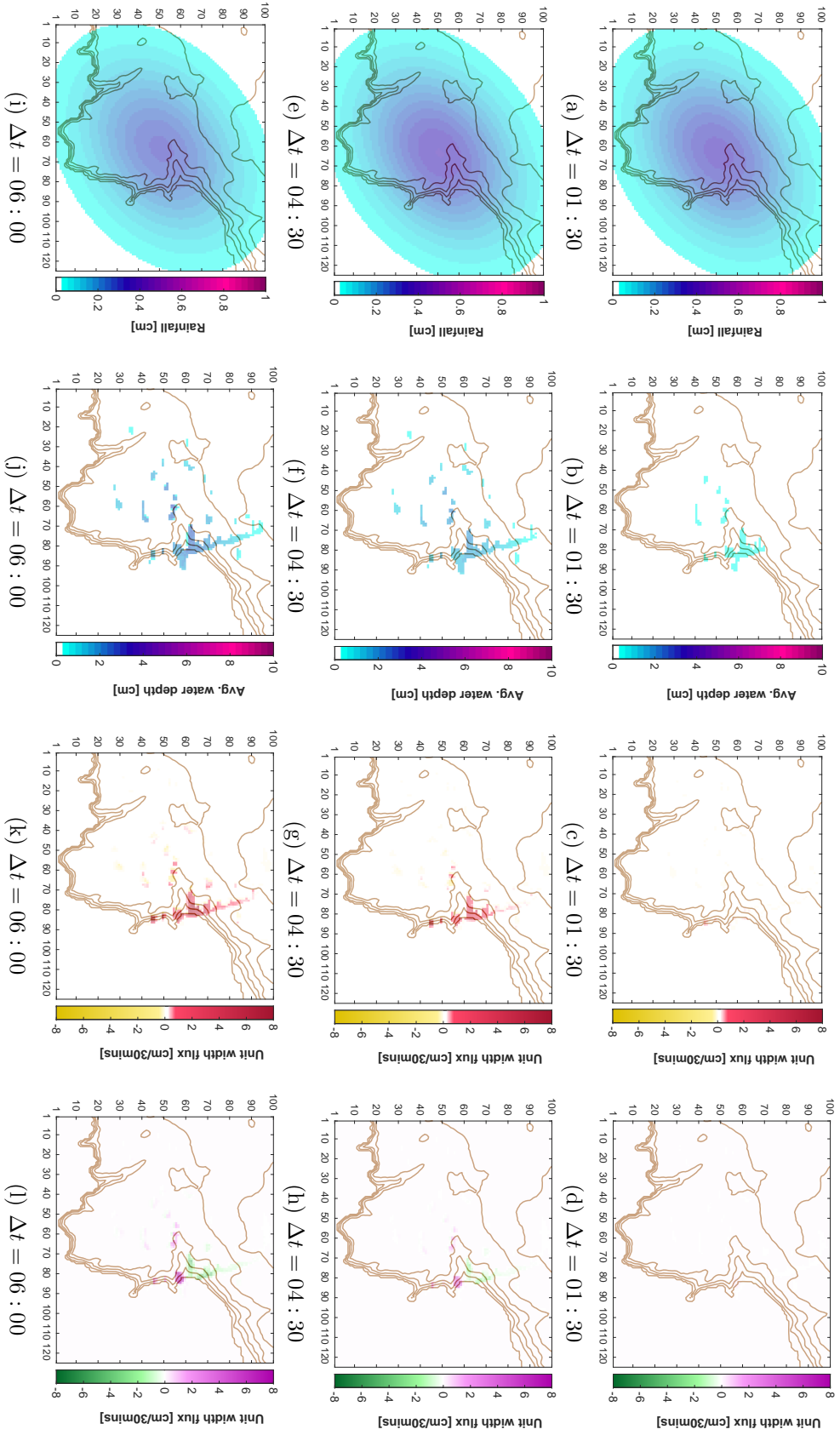


Figure 6.6.: Scenario 1 - Central static storm - 20m resolution model. Each row presents individual timesteps  $\Delta t = 01:30$ ,  $\Delta t = 04:30$  and  $\Delta t = 06:00$ . Sub-figures (a), (e) and (i) show the evolution of the fictitious storm during the simulation. Sub-figures (b), (f) and (j) show the average water depth at their given timesteps. Sub-figures (c), (g) and (k) depict the mean unit-width horizontal flux in the  $y$ -direction. Sub-figures (d), (h) and (l) depict the mean unit-width horizontal flux in the  $x$ -direction.

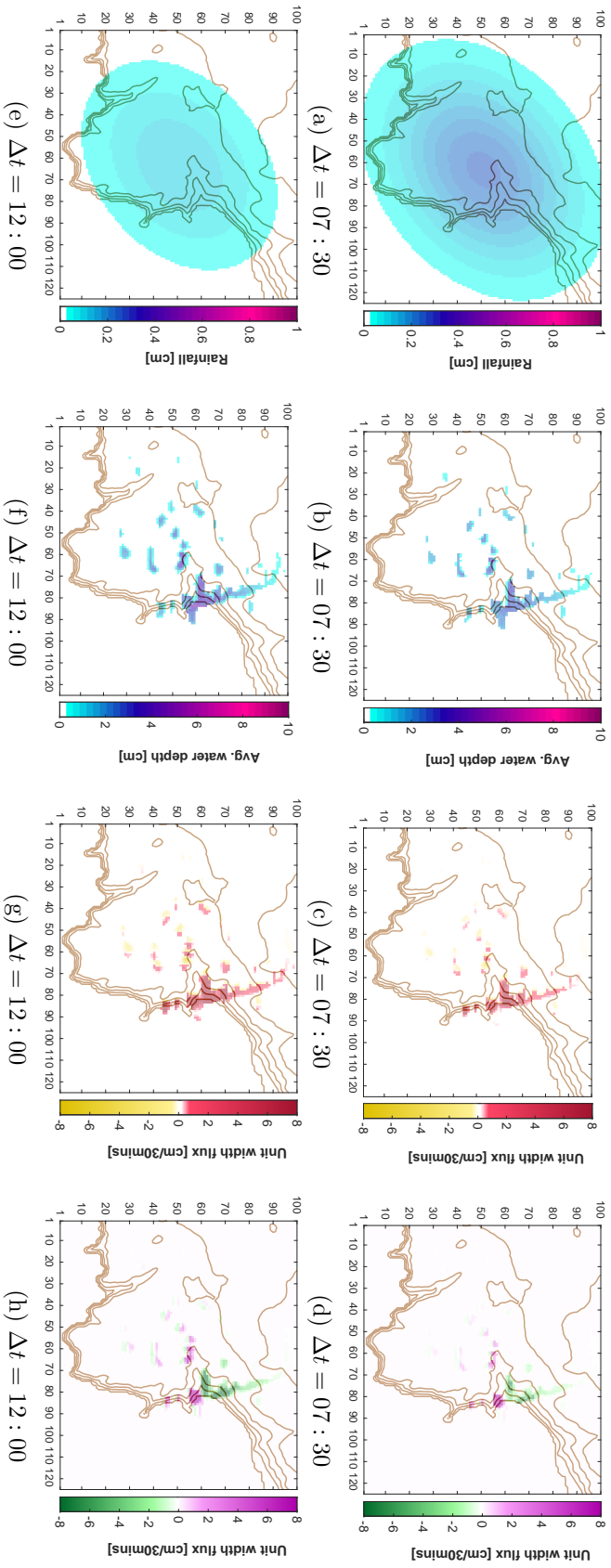


Figure 6.7.: Scenario 1 - Central static storm - 20m resolution model. Each row presents individual timesteps  $\Delta t = 07 : 30$  and  $\Delta t = 12 : 00$ . Sub-figures (a) and (e) show the evolution of the fictitious storm during the simulation. Sub-figures (b) and (f) show the average water depth at their given timesteps. Sub-figures (c) and (g) depict the mean unit-width horizontal flux in the  $x$ -direction. Sub-figures (d) and (h) depict the mean unit-width horizontal flux in the  $y$ -direction.

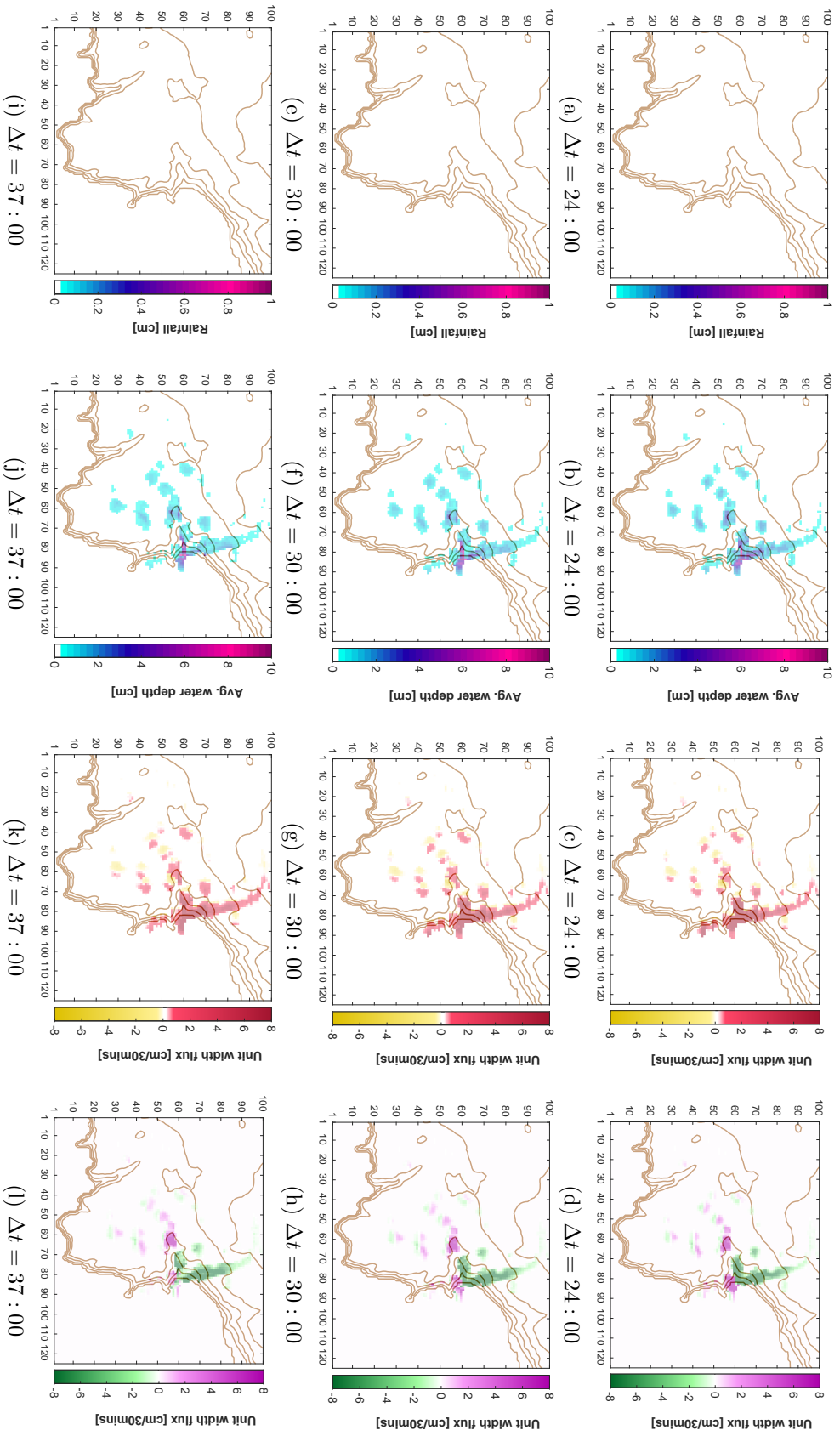


Figure 6.8: Scenario 1 - Central static storm - 20m resolution model. Each row presents individual timesteps  $\Delta t = 24 : 00$ ,  $\Delta t = 30 : 00$  and  $\Delta t = 37 : 00$ . Sub-figures (a), (e) and (i) show the evolution of the fictitious storm during the simulation. Sub-figures (b), (f) and (j) show the average water depth at their given timesteps. Sub-figures (c), (g) and (k) depict the mean unit-width horizontal flux in the  $y$ -direction. Sub-figures (d), (h) and (l) depict the mean unit-width horizontal flux in the  $x$ -direction.

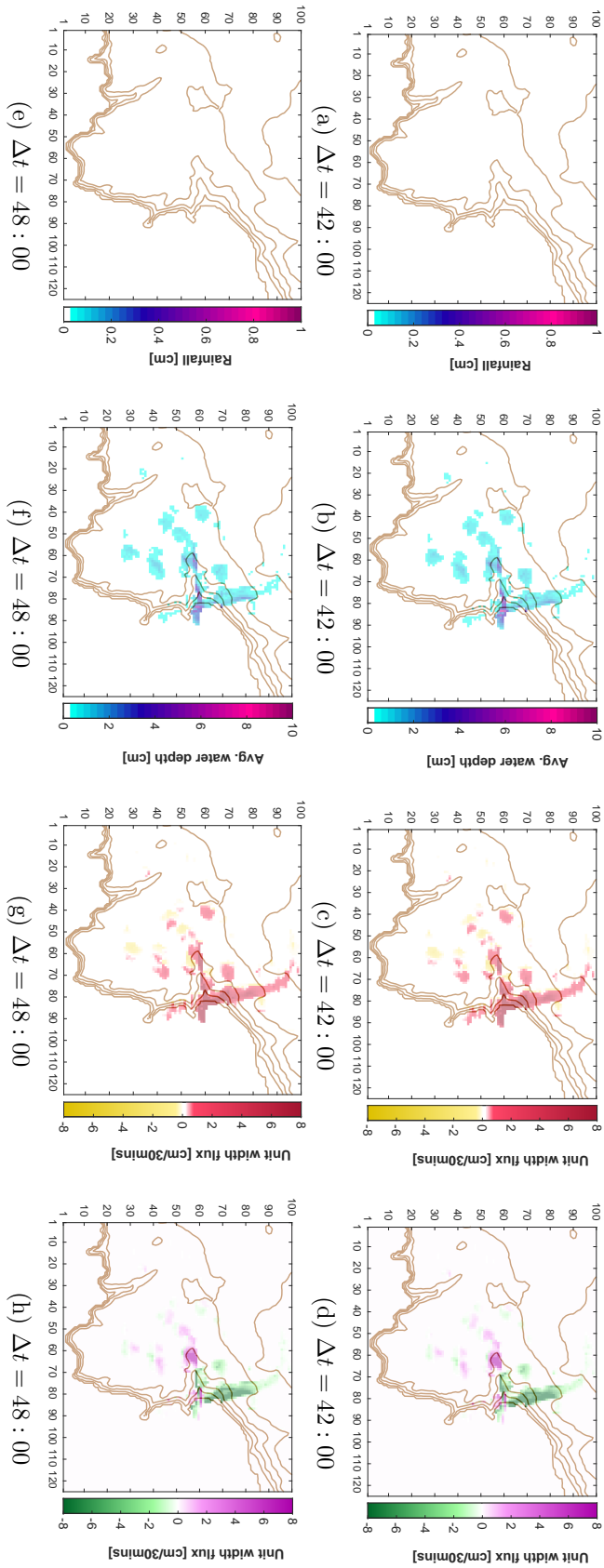


Figure 6.9.: Scenario 1 - Central static storm - 20m resolution model. Each row presents individual timesteps  $\Delta t = 42 : 00$  and  $\Delta t = 48 : 00$ . Sub-figures (a) and (e) show the evolution of the fictitious storm during the simulation. Sub-figures (b) and (f) show the average water depth at their given timesteps. Sub-figures (c) and (g) depict the mean unit-width horizontal flux in the  $x$ -direction. Sub-figures (d) and (h) depict the mean unit-width horizontal flux in the  $y$ -direction.

### 6.3.3. Movement 50m

Analysis of the output for the storm moving through the centre of the computational domain and its static equivalent will follow the same format as Sections 6.3.1 and 6.3.2 respectively. Figures 6.10 and 6.11 presents the storm movement scenario for the 50m model resolution variant. At  $\Delta t = 01 : 30$  initially begins with the bulk of the model input in the south-west corner of the domain. Given that sub-figure 6.10(b) shows water presence when it shouldn't clearly identifies that there is something wrong with the parameters when starting up this model variant. Due to various external factors, it was not possible to investigate this further to understand why. As the storm progressed, by the quarter stage of the simulation ( $\Delta t = 18 : 00$ ), the overland flow was far reaching across the domain. At the coastal regions of the south-west, average water depths were above 10cm (sub-figure (r)). There were some signs of large overland flow of approximately 5cm in the Coverack region too moving south easterly (sub-figures 6.11(f)-(h)). As the storm stopped, the water continued to flow in a south-easterly direction around Coverack (Figure 6.12) and by the end of the simulation, overland flow in the south-west part of the domain was beginning to disperse (sub-figure 6.13(f)).

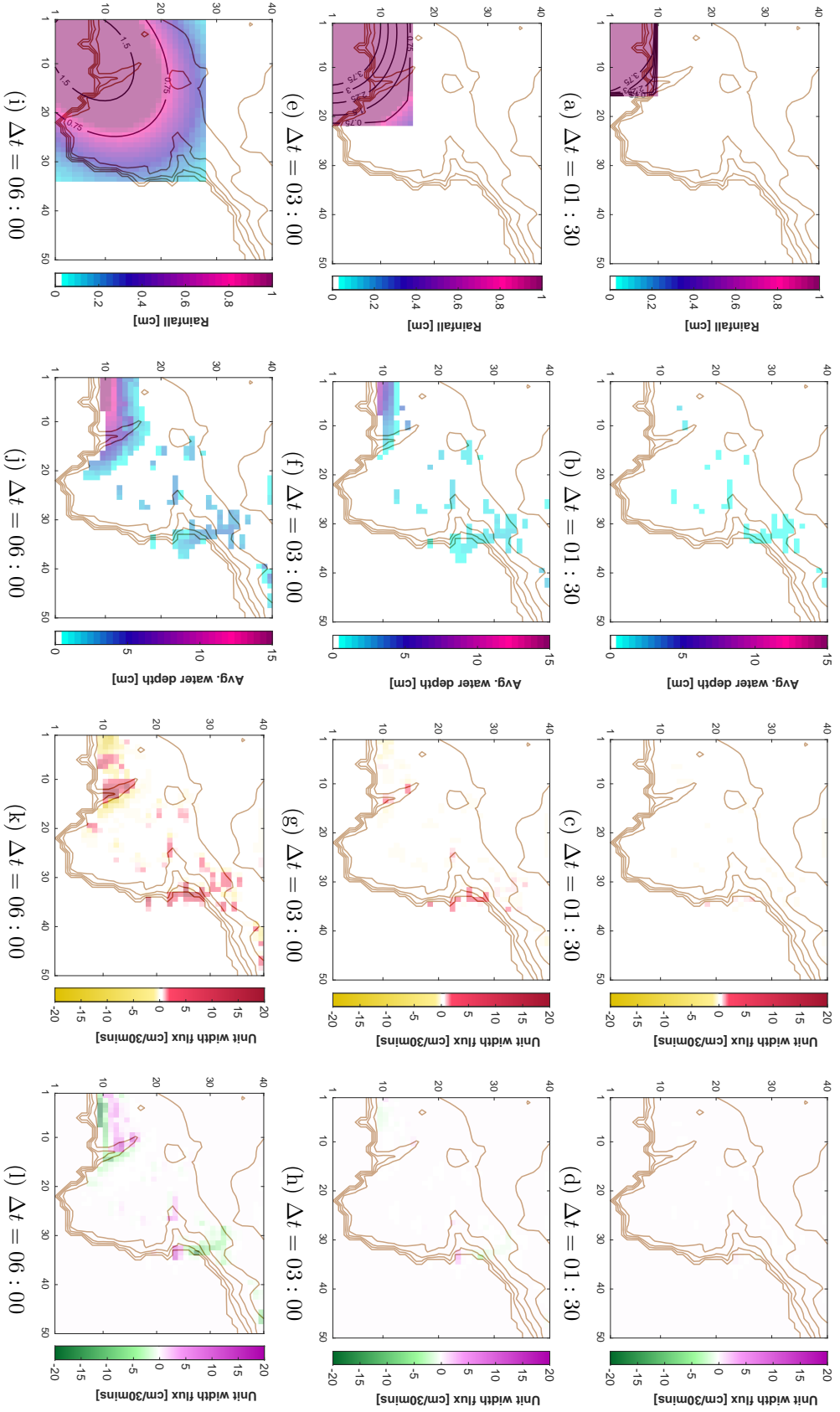


Figure 6.10.: Scenario 1 - Central moving storm - 50m resolution model. Each row presents individual timesteps  $\Delta t = 01:30$ ,  $\Delta t = 03:00$  and  $\Delta t = 06:00$ . Sub-figures (a), (e) and (i) show the evolution of the fictitious storm during the simulation. Sub-figures (b), (f) and (j) show the average water depth at their given timesteps. Sub-figures (c), (g) and (k) depict the mean unit-width horizontal flux in the  $y$ -direction. Sub-figures (d), (h) and (l) depict the mean unit-width horizontal flux in the  $x$ -direction.



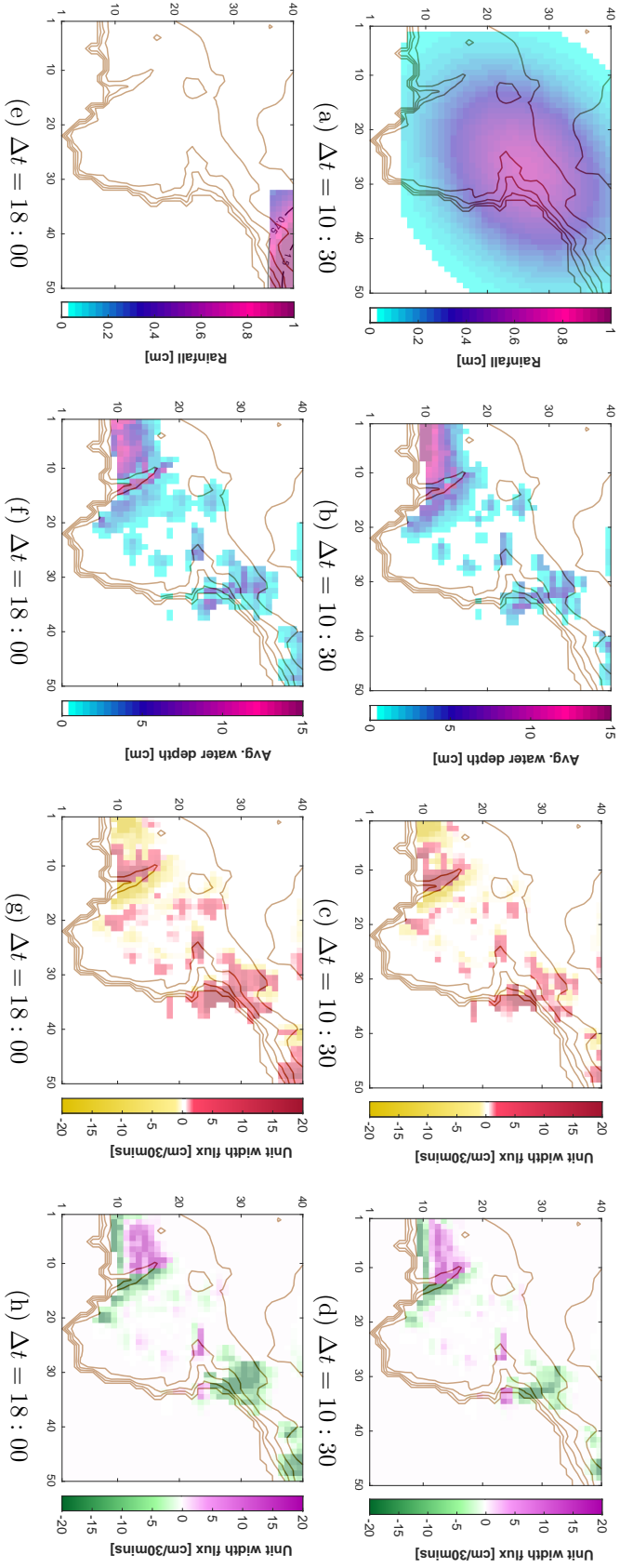


Figure 6.11.: Scenario 1 - Central moving storm - 50m resolution model. Each row presents individual timesteps  $\Delta t = 10:30$  and  $\Delta t = 18:00$ . Sub-figures (a) and (e) show the evolution of the fictitious storm during the simulation. Sub-figures (b) and (f) show the average water depth at their given timesteps. Sub-figures (c) and (g) depict the mean unit-width horizontal flux in the  $x$ -direction. Sub-figures (d) and (h) depict the mean unit-width horizontal flux in the  $y$ -direction.

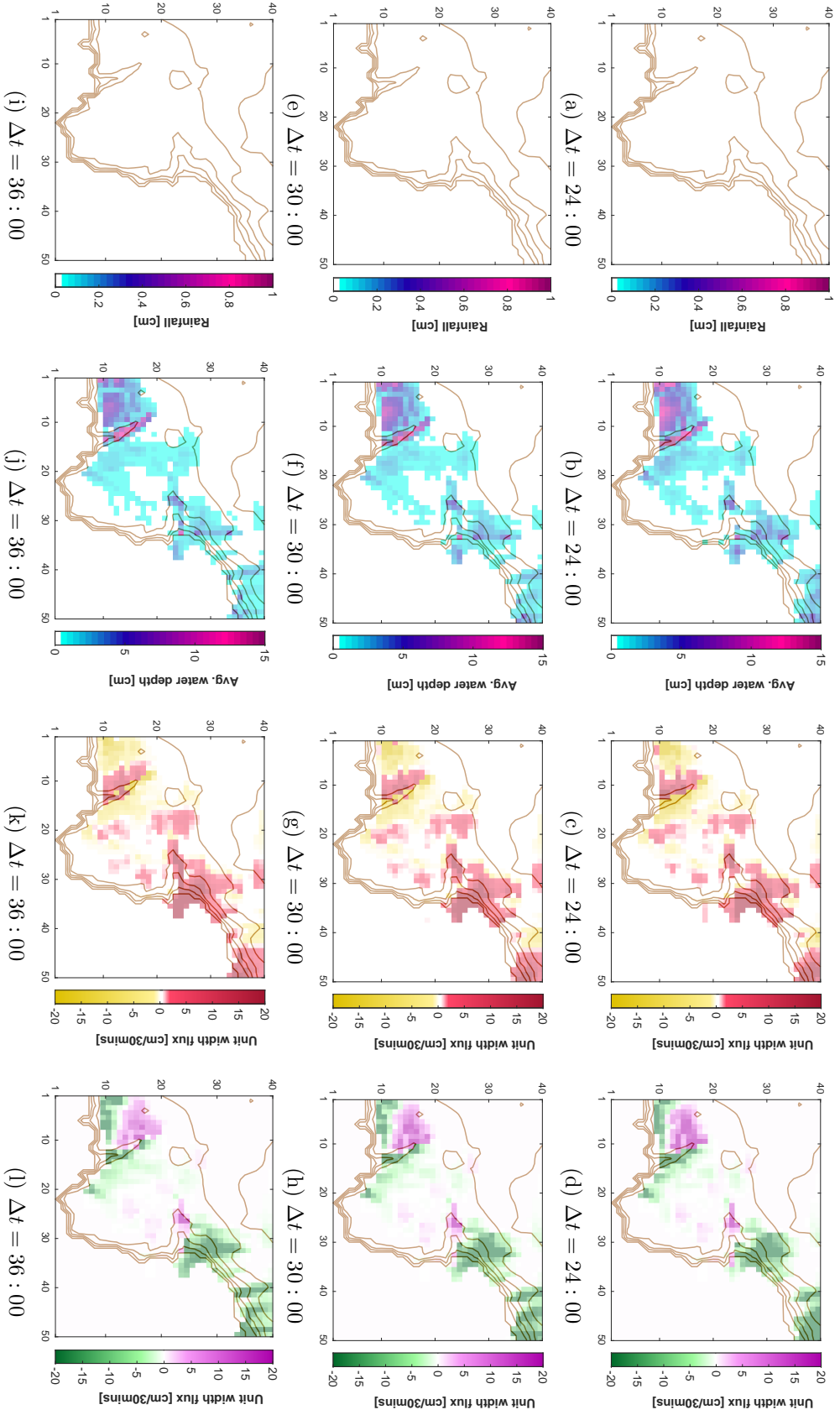


Figure 6.12.: Scenario 1 - Central moving storm - 50m resolution model. Each row presents individual timesteps  $\Delta t = 24 : 00$ ,  $\Delta t = 30 : 00$  and  $\Delta t = 36 : 00$ . Sub-figures (a), (e) and (i) show the evolution of the fictitious storm during the simulation. Sub-figures (b), (f) and (j) show the average water depth at their given timesteps. Sub-figures (c), (g) and (k) depict the mean unit-width horizontal flux in the  $y$ -direction. Sub-figures (d), (h) and (l) depict the mean unit-width horizontal flux in the  $x$ -direction.

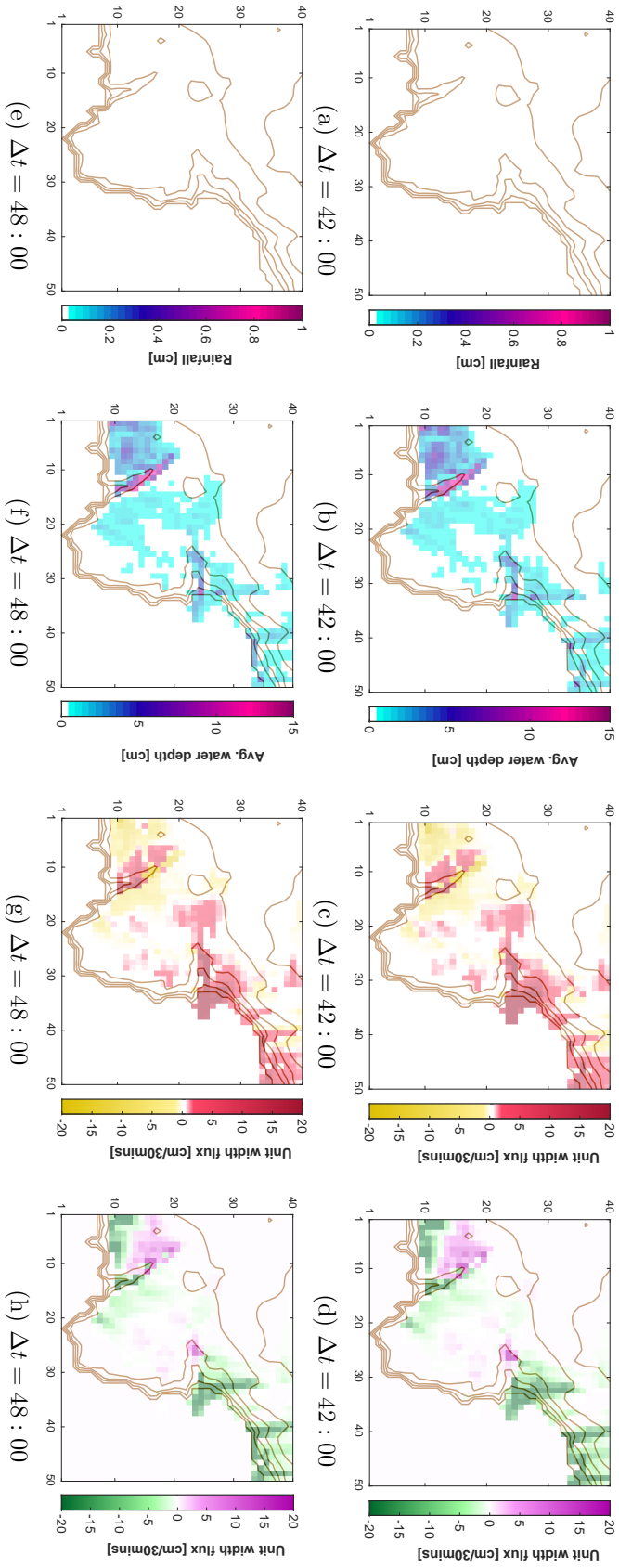


Figure 6.13: Scenario 1 - Central moving storm - 20m resolution model. Each row presents individual timesteps  $\Delta t = 42 : 00$  and  $\Delta t = 48 : 00$ . Sub-figures (a) and (e) show the evolution of the fictitious storm during the simulation. Sub-figures (b) and (f) show the average water depth at their given timesteps. Sub-figures (c) and (g) depict the mean unit-width horizontal flux in the  $x$ -direction. Sub-figures (d) and (h) depict the mean unit-width horizontal flux in the  $y$ -direction.

#### 6.3.4. Static 50m

When the storm is located centrally and remains static for the simulation, the overland flow is concentrated on the region surrounding Coverack. Figures 6.14 and 6.15 show the immediate response to the storm overhead. By  $\Delta t = 06 : 00$ , sub-Figures 6.14(i) – (l) show a large majority of the central domain flooded. Within urban and sub urban areas average water depths are above 10cm, flowing eastwards and funnelling through Coverack itself right throughout the storm event. The average water depth within the domain peaks at  $\Delta t = 24 : 00$ , travelling south-eastwards at greater than 20cm/30mins. This can be seen in sub-Figures 6.16(a)–(d). By  $\Delta t = 48 : 00$ , there exist some pixels still experiencing average water depths above 10cm and still flowing south-eastwards. However, most pixels have an average water depth of just above 0cm and are gently moving south-eastwards.

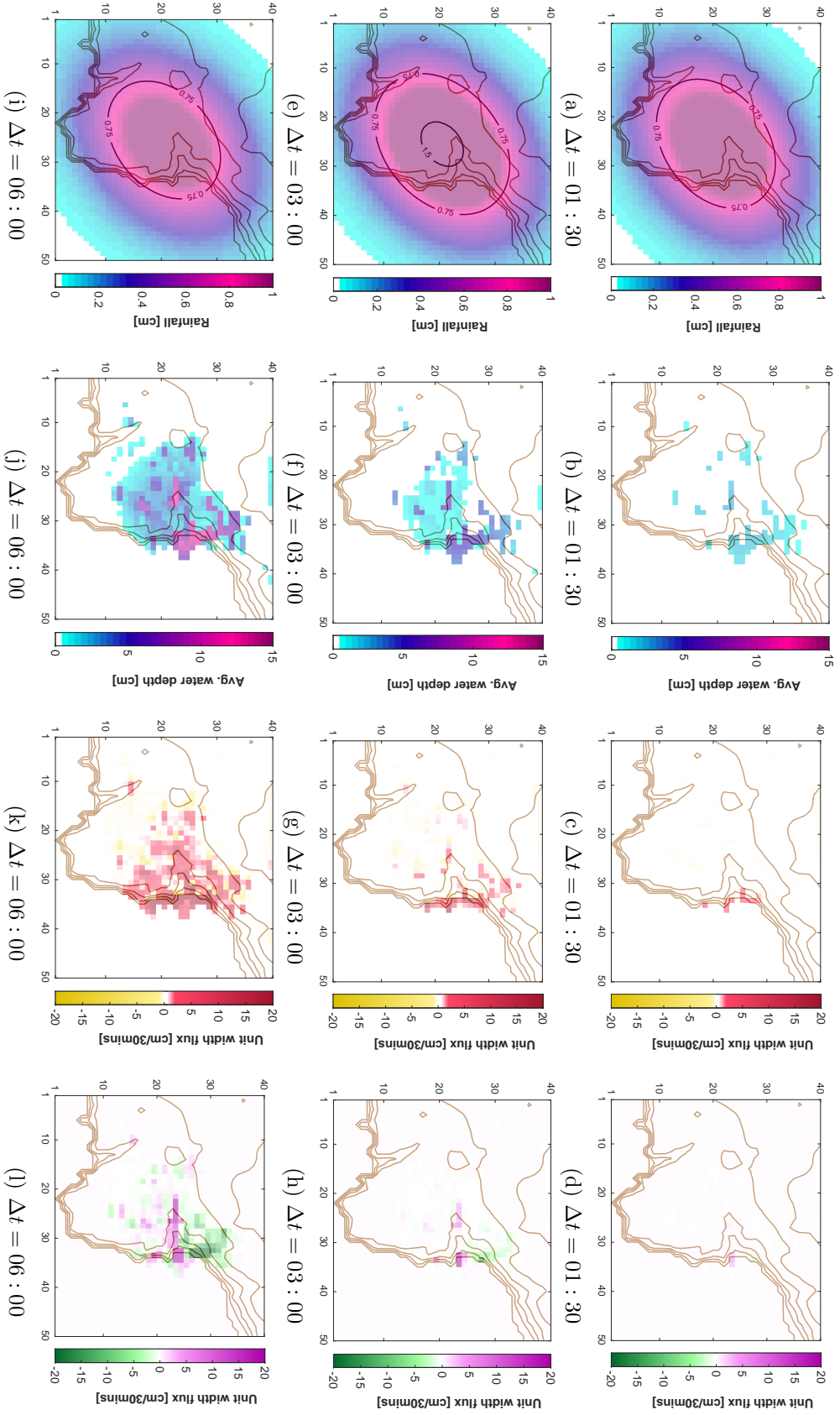


Figure 6.14.: Scenario 1 - Central static storm - 50m resolution model. Each row presents individual timesteps  $\Delta t = 01 : 30$ ,  $\Delta t = 03 : 00$  and  $\Delta t = 06 : 00$ . Sub-figures (a), (e) and (i) show the evolution of the fictitious storm during the simulation. Sub-figures (b), (f) and (j) show the average water depth at their given timesteps. Sub-figures (c), (g) and (k) depict the mean unit-width horizontal flux in the  $y$ -direction. Sub-figures (d), (h) and (l) depict the mean unit-width horizontal flux in the  $x$ -direction.

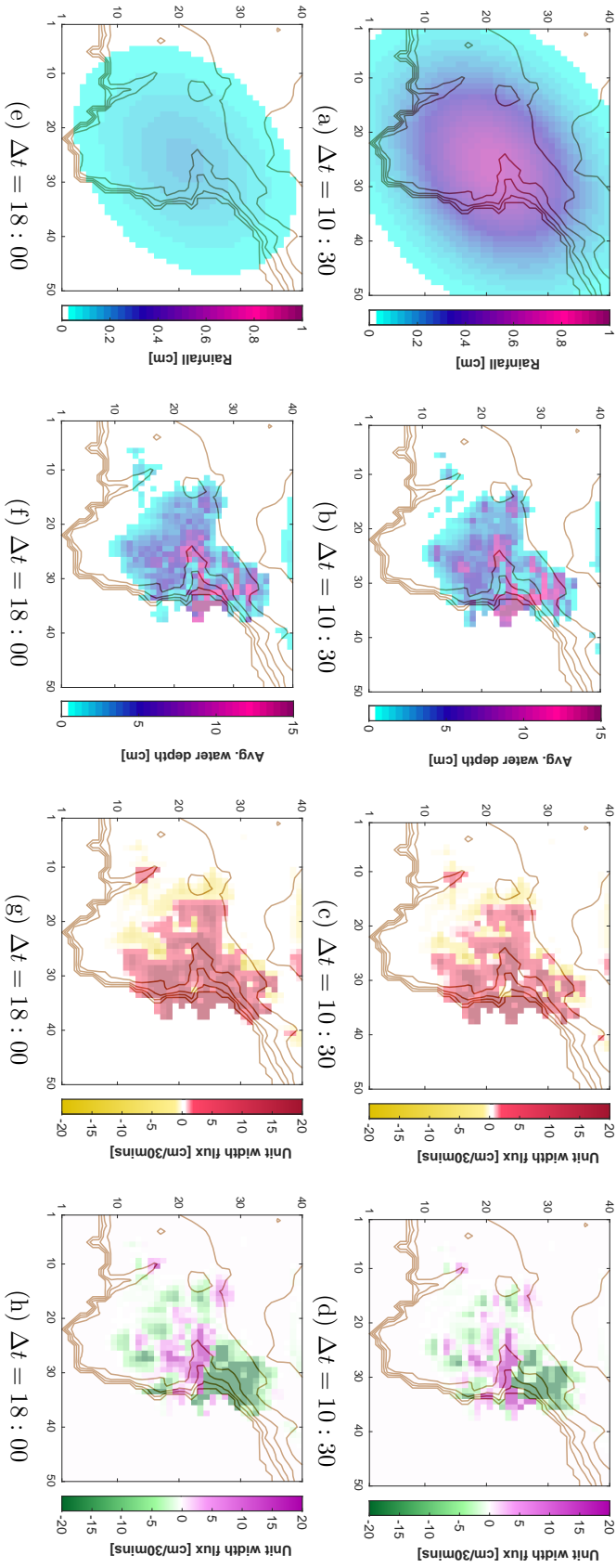


Figure 6.15.: Scenario 1 - Central static storm - 50m resolution model. Each row presents individual timesteps  $\Delta t = 10 : 30$  and  $\Delta t = 18 : 00$ . Sub-figures (a) and (e) show the evolution of the fictitious storm during the simulation. Sub-figures (b) and (f) show the average water depth at their given timesteps. Sub-figures (c) and (g) depict the mean unit-width horizontal flux in the  $x$ -direction. Sub-figures (d) and (h) depict the mean unit-width horizontal flux in the  $y$ -direction.

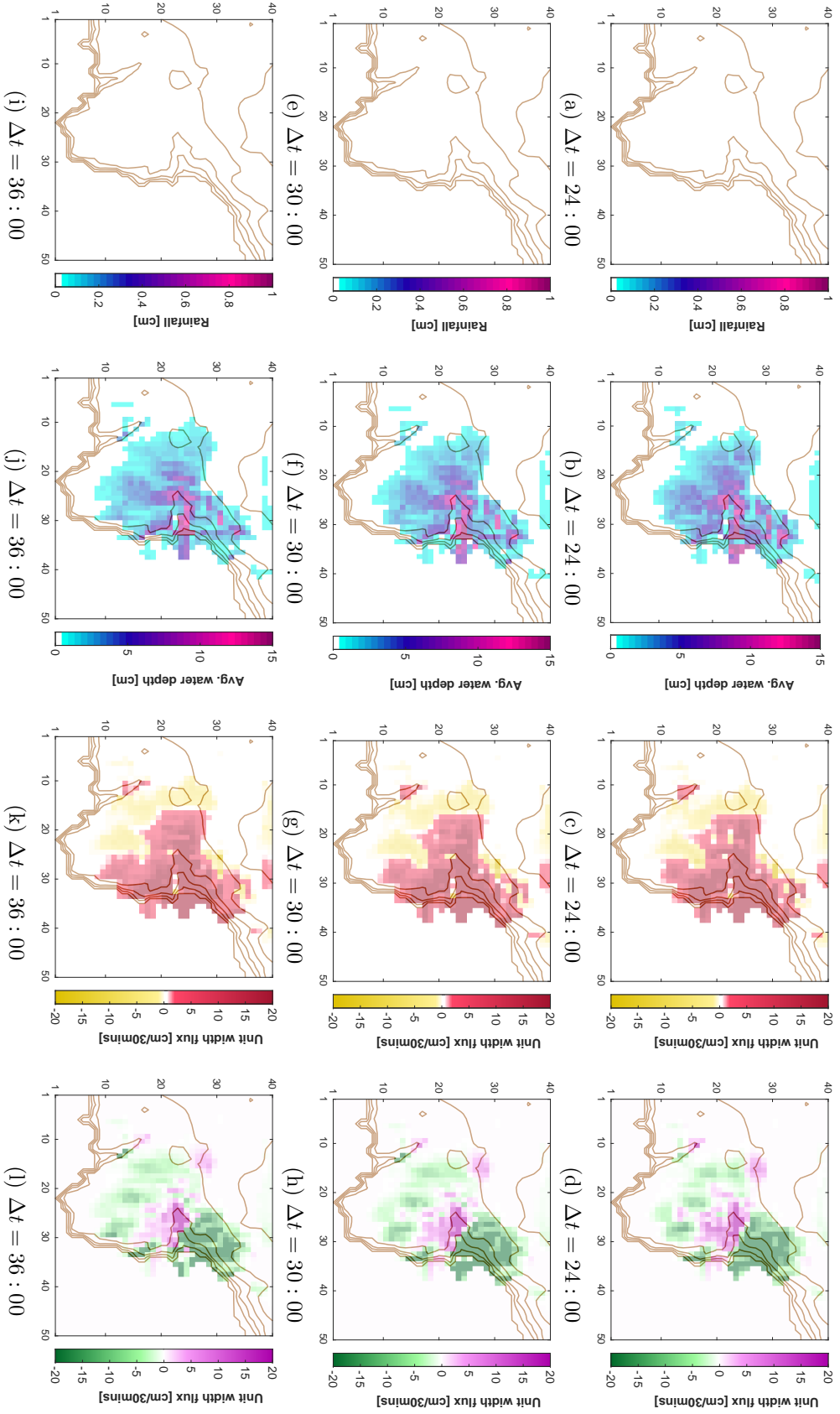


Figure 6.16.: Scenario 1 - Central static storm - 50m resolution model. Each row presents individual timesteps  $\Delta t = 24 : 00$ ,  $\Delta t = 30 : 00$  and  $\Delta t = 36 : 00$ . Sub-figures (a), (e) and (i) show the evolution of the fictitious storm during the simulation. Sub-figures (b), (f) and (j) show the average water depth at their given timesteps. Sub-figures (c), (g) and (k) depict the mean unit-width horizontal flux in the  $y$ -direction. Sub-figures (d), (h) and (l) depict the mean unit-width horizontal flux in the  $x$ -direction.

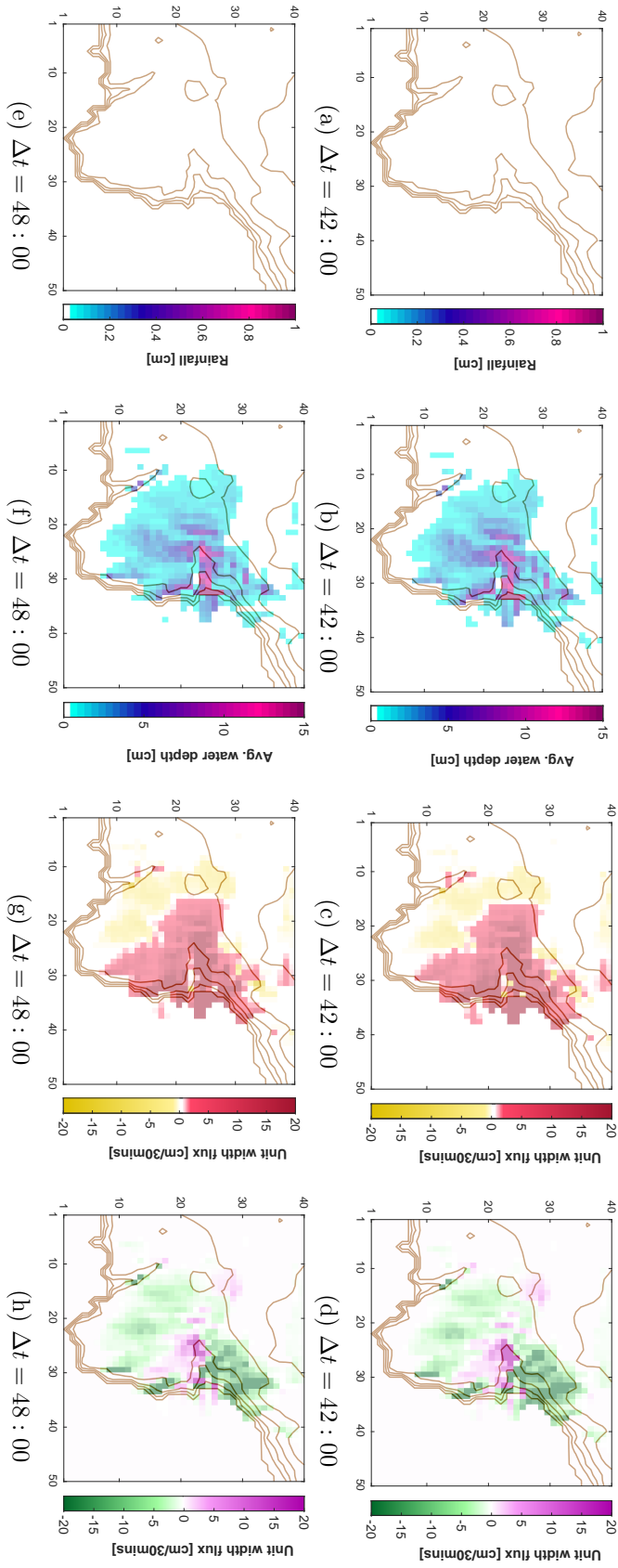


Figure 6.17.: Scenario 1 - Central static storm - 50m resolution model. Each row presents individual timesteps  $\Delta t = 42:00$  and  $\Delta t = 48:00$ . Sub-figures (a) and (e) show the evolution of the fictitious storm during the simulation. Sub-figures (b) and (f) show the average water depth at their given timesteps. Sub-figures (c) and (g) depict the mean unit-width horizontal flux in the  $x$ -direction. Sub-figures (d) and (h) depict the mean unit-width horizontal flux in the  $y$ -direction.



## 6.4. Scenario 2 - South Eastern Region

### 6.4.1. Movement 20m

For the final scenario of this chapter, the fictitious storm outlined in Section 6.1 concentrates its input in the south-eastern corner of the computational domain. Once again the movement simulations see the storm progress from south-west to north-east. The columns for all the figures in this section follow the same format as Sections 6.3 and ??.

With the largest rainfall intensity occurring at  $\Delta t = 01 : 30$ , very little overland flow is noticed due to the absorptive qualities of the land-use pixels present in the southern part of the domain (Figure 6.18). The storm reached Coverack by  $\Delta t = 06 : 00$  and some shallow average water depth values were observed (sub-figure 6.18(f)), moving in a north-easterly direction (sub-figures 6.18(g) and (h)). As the storm continued to travel north-eastwards, by  $\Delta t = 18 : 00$  average water depths in Coverack were approximately 0.5cm (Figure 6.19). This overland flow was being funnelled out to Coverack cove (sub-figure 6.19(h)). When the storm had stopped, the average water depth nearing 1cm at  $\Delta t = 24 : 00$  (Figure 6.20(b)) dwindled down to below 0.5cm 24 hours later at  $\Delta t = 48 : 00$  (sub-figure 6.20(j)).

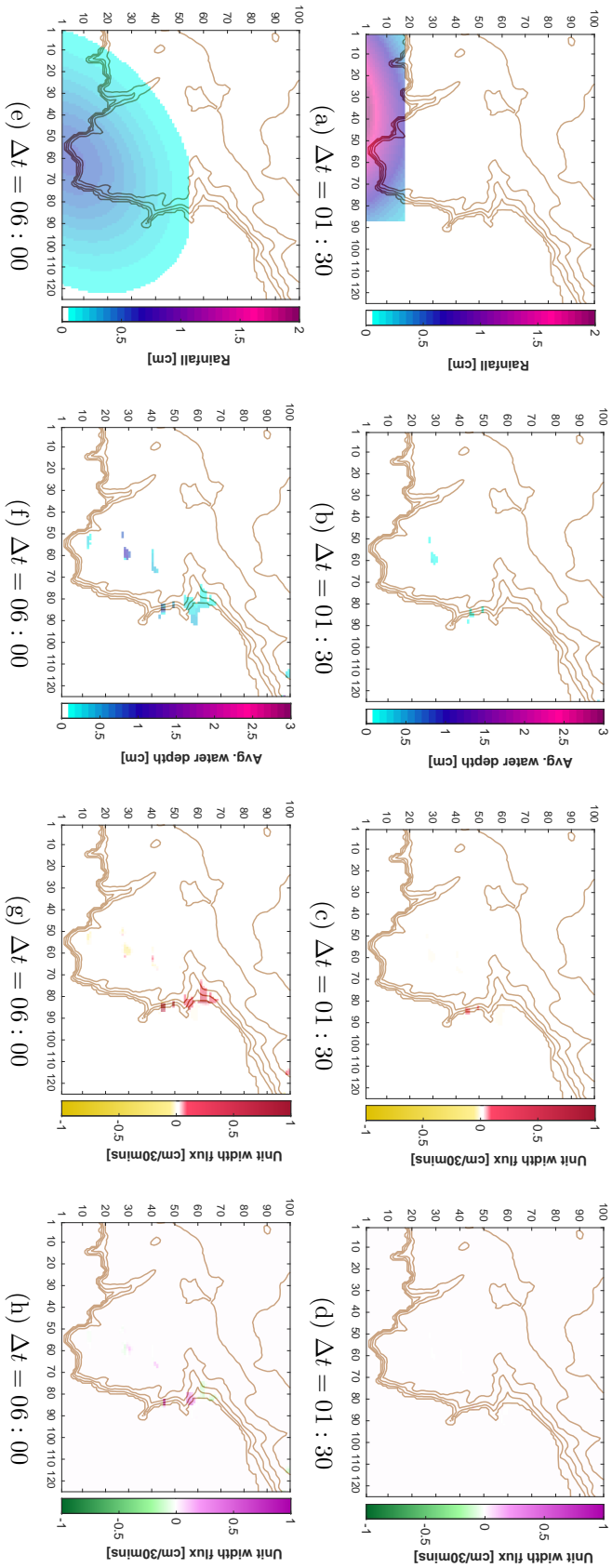


Figure 6.18.: Scenario 3 - South-eastern moving storm - 20m resolution model. Each row presents individual timesteps  $\Delta t = 01 : 30$  and  $\Delta t = 06 : 00$ . Sub-figures (a) and (e) show the evolution of the fictitious storm during the simulation. Sub-figures (b) and (f) show the average water depth at their given timesteps. Sub-figures (c) and (g) depict the mean unit-width horizontal flux in the  $x$ -direction. Sub-figures (d) and (h) depict the mean unit-width horizontal flux in the  $y$ -direction.

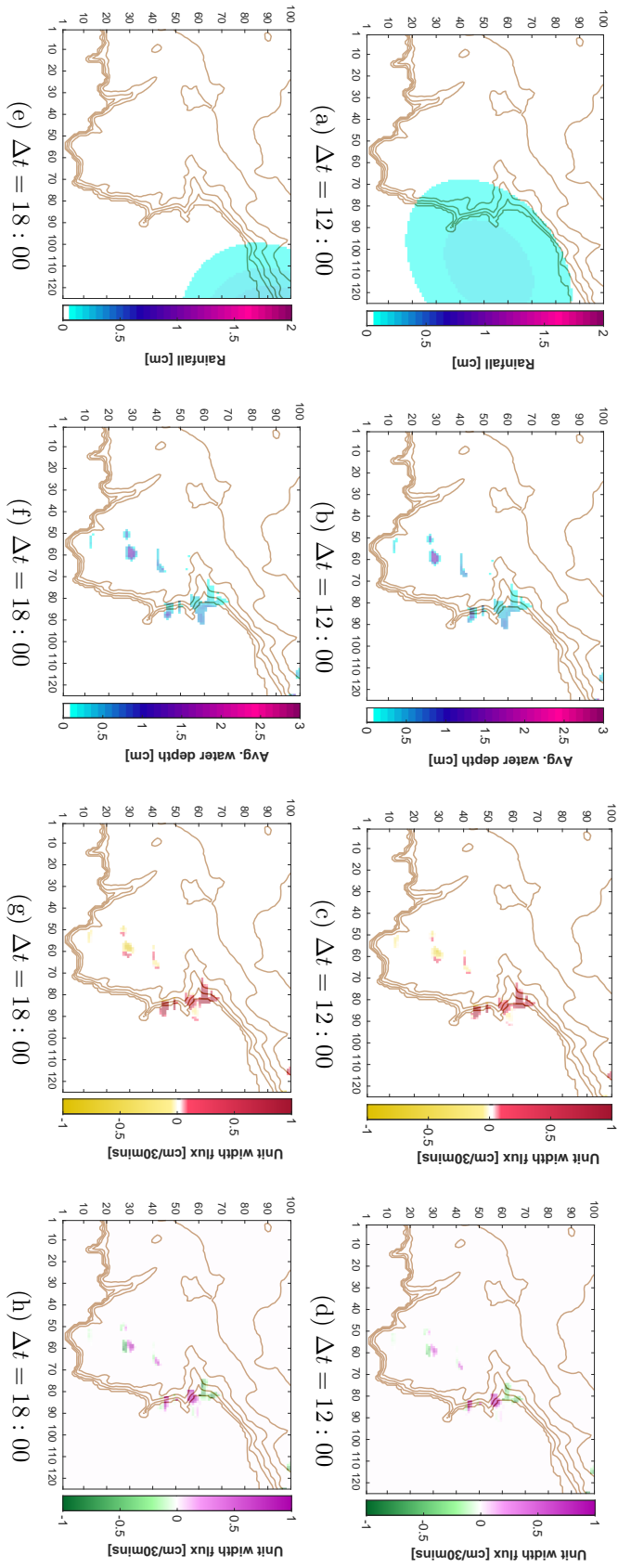


Figure 6.19.: Scenario 3 - South-eastern moving storm - 20m resolution model. Each row presents individual timesteps  $\Delta t = 12 : 00$  and  $\Delta t = 18 : 00$ . Sub-figures (a) and (e) show the evolution of the fictitious storm during the simulation. Sub-figures (b) and (f) show the average water depth at their given timesteps. Sub-figures (c) and (g) depict the mean unit-width horizontal flux in the  $y$ -direction. Sub-figures (d) and (h) depict the mean unit-width horizontal flux in the  $x$ -direction.

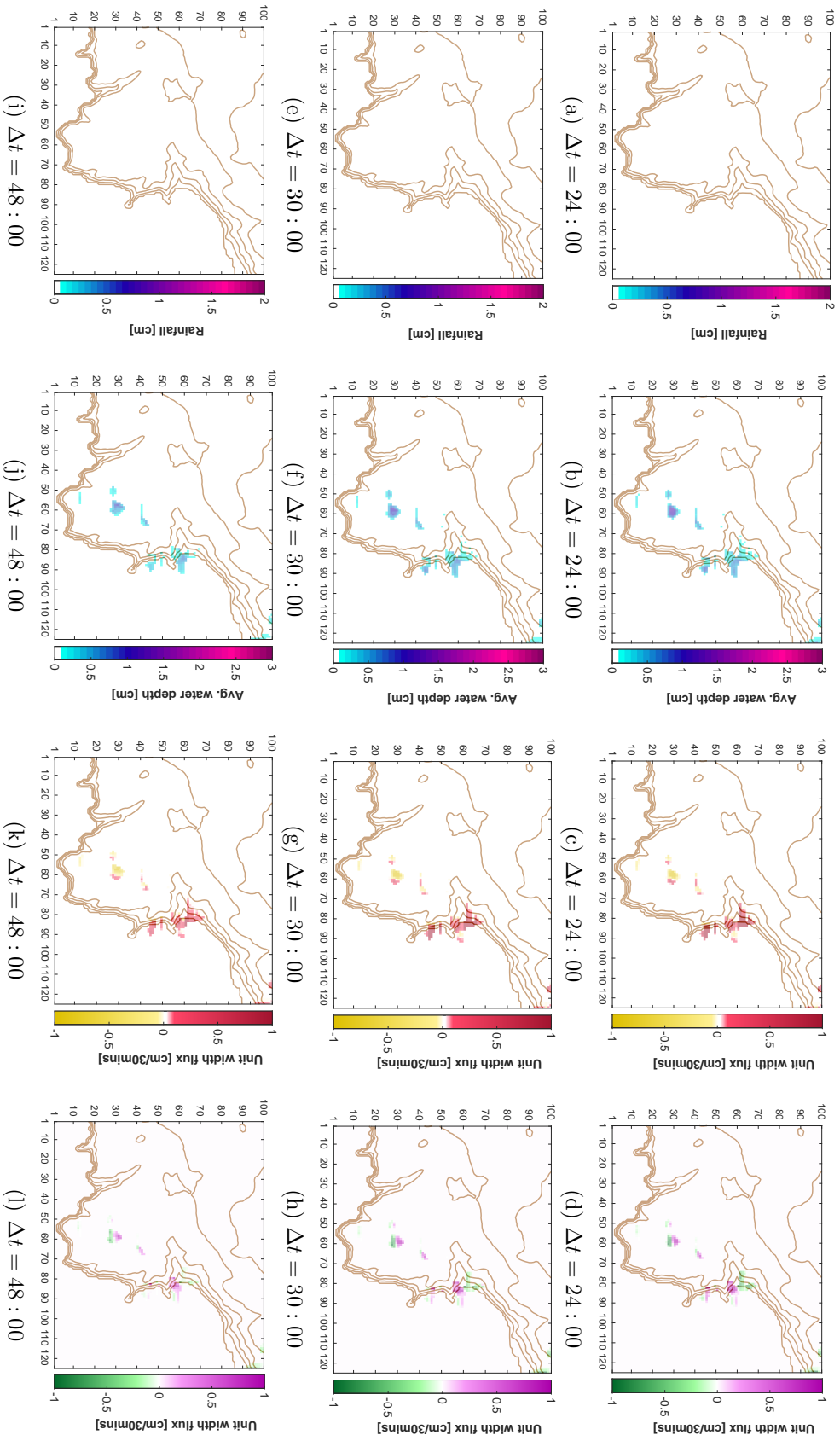


Figure 6.20.: Scenario 1 - Central moving storm - 20m resolution model. Each row presents individual timesteps  $\Delta t = 24 : 00$ ,  $\Delta t = 30 : 00$  and  $\Delta t = 48 : 00$ . Sub-figures (a), (e) and (i) show the evolution of the fictitious storm during the simulation. Sub-figures (b), (f) and (j) show the average water depth at their given timesteps. Sub-figures (c), (g) and (k) depict the mean unit-width horizontal flux in the  $y$ -direction. Sub-figures (d), (h) and (l) depict the mean unit-width horizontal flux in the  $x$ -direction.

### 6.4.2. Static 20m

Sub-figures 6.21(a), 6.21(e), 6.22(a) and 6.22(e) highlight the static fictitious storm. The centre of this storm is placed over the sea, however its periphery does reach the eastern coast of the Lizard peninsula. During the most intense period of the storm, average water depth values reach above 2cm in the Coverack region (Figure 6.21(f)). The overland flow concentrates itself over the B3294 (sub-figure 6.22(b)), with a greater number of pixels reaching average water depth values above 2.5cm.

As the storm stops, average water depth values reduce to approximately 2cm (Figure 6.23(b)). This reduction is predominately down to the funnelling of overland flow into Coverack cove at  $\Delta t = 24 : 00$  (sub-figure 6.23(d)). At  $\Delta t = 48 : 00$ , the end of the simulation, water continues to flow into Coverack cove (sub-figure 6.23(l)). The majority of pixels have very shallow water depth values, with a handful in Coverack having an approximate mean water depth of 2cm (sub-figure 6.23(j)).

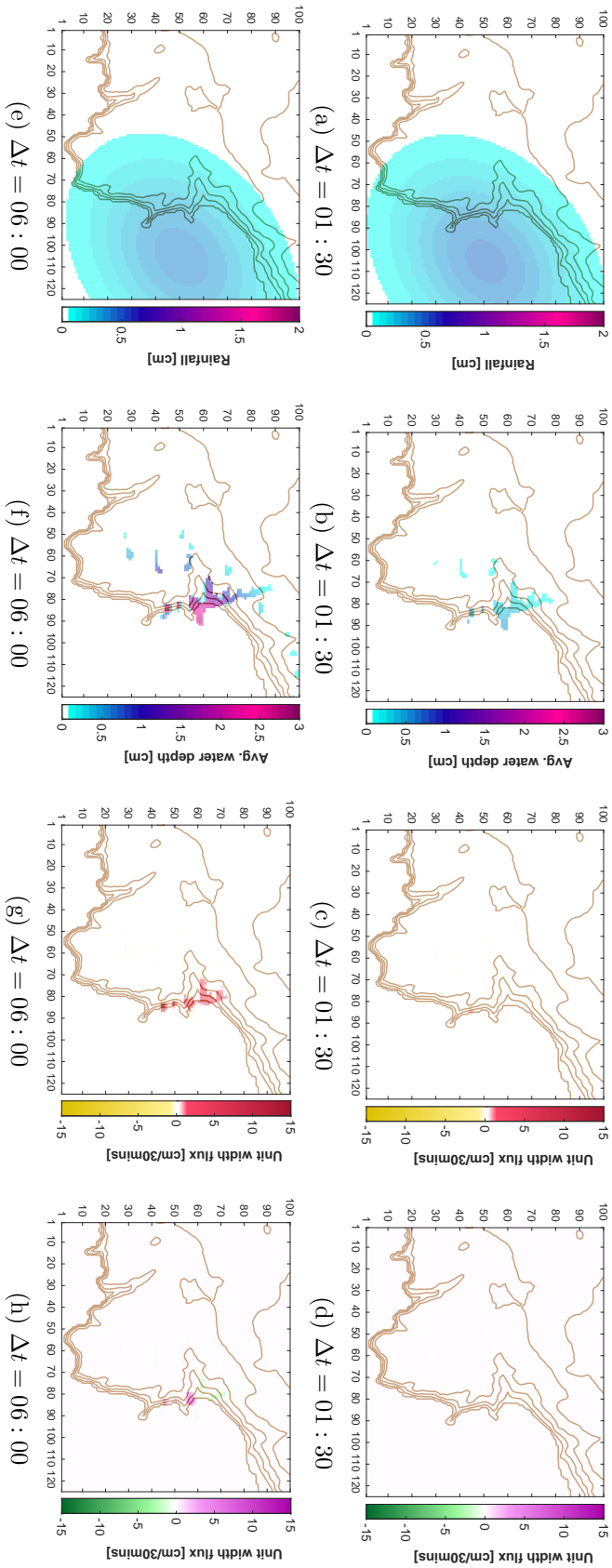


Figure 6.21.: Scenario 3 - South-eastern static storm - 20m resolution model. Each row presents individual timesteps  $\Delta t = 01 : 30$  and  $\Delta t = 06 : 00$ . Sub-figures (a) and (e) show the evolution of the fictitious storm during the simulation. Sub-figures (b) and (f) show the average water depth at their given timesteps. Sub-figures (c) and (g) depict the mean unit-width horizontal flux in the  $y$ -direction. Sub-figures (d) and (h) depict the mean unit-width horizontal flux in the  $x$ -direction.

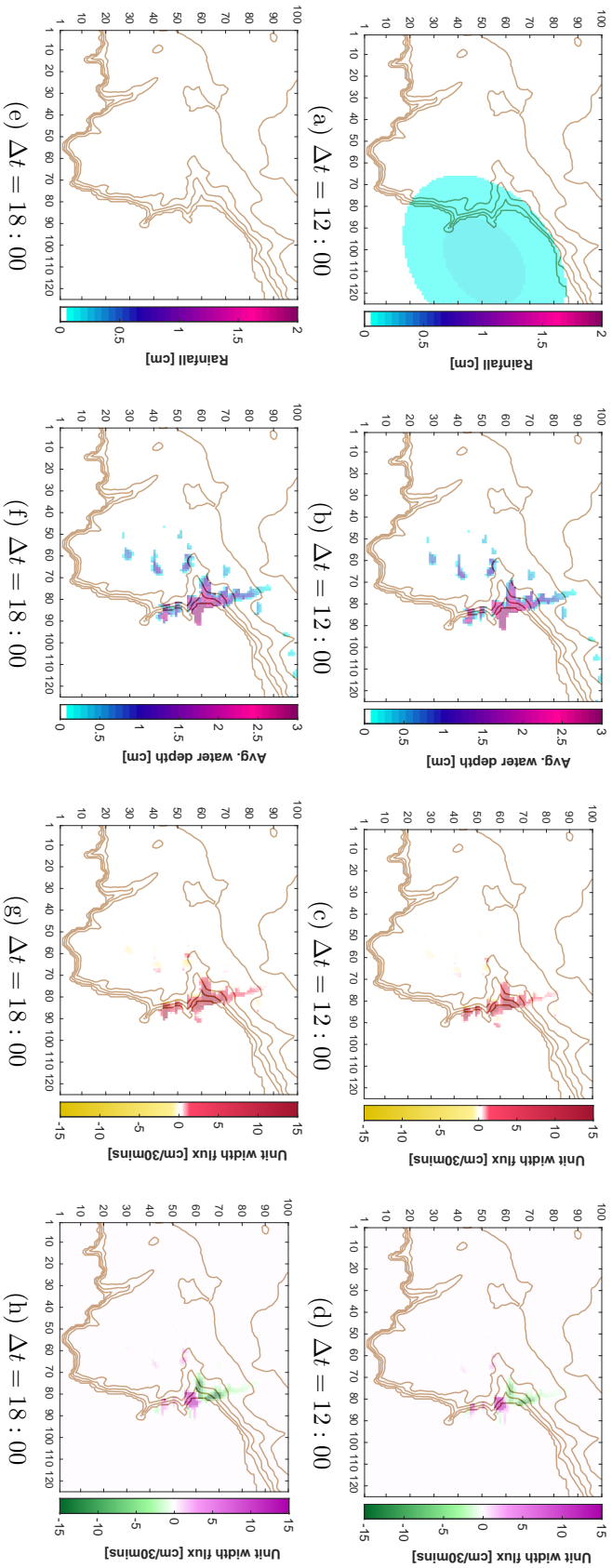


Figure 6.22.: Scenario 3 - South-eastern static storm - 20m resolution model. Each row presents individual timesteps  $\Delta t = 12 : 00$  and  $\Delta t = 18 : 00$ . Sub-figures (a) and (e) show the evolution of the fictitious storm during the simulation. Sub-figures (b) and (f) show the average water depth at their given timesteps. Sub-figures (c) and (g) depict the mean unit-width horizontal flux in the  $y$ -direction. Sub-figures (d) and (h) depict the mean unit-width horizontal flux in the  $x$ -direction.

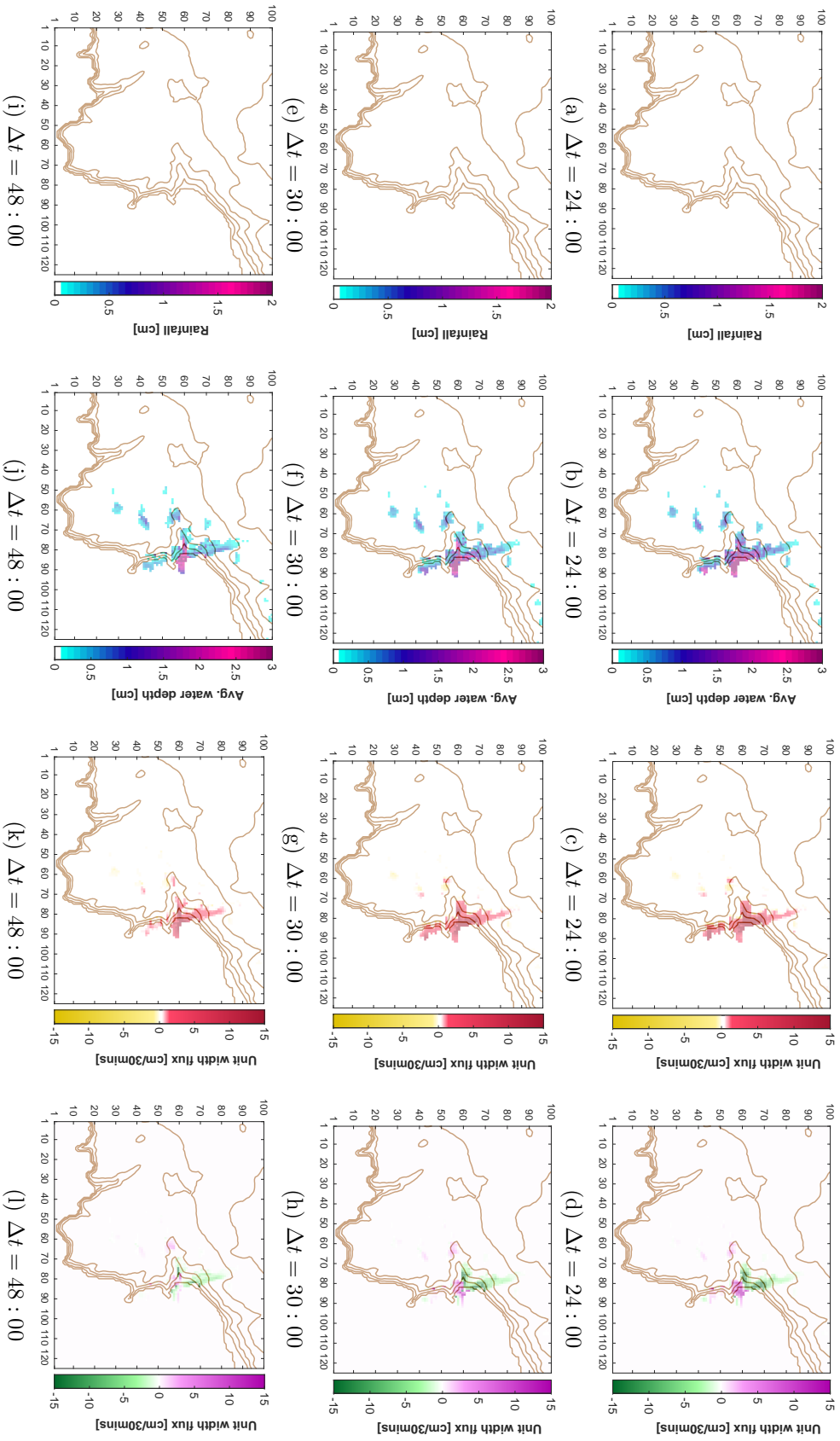


Figure 6.23: Scenario 3 - South-eastern static storm - 20m resolution model. Each row presents individual timesteps  $\Delta t = 24:00$ ,  $\Delta t = 30:00$  and  $\Delta t = 48:00$ . Sub-figures (a), (e) and (i) show the evolution of the fictitious storm during the simulation. Sub-figures (b), (f) and (j) show the average water depth at their given timesteps. Sub-figures (c), (g) and (k) depict the mean unit-width horizontal flux in the  $y$ -direction. Sub-figures (d), (h) and (l) depict the mean unit-width horizontal flux in the  $x$ -direction.



### 6.4.3. Movement 50m

For the 50m movement scenario, at  $\Delta t = 06 : 00$ , a vast amount of pixels in the southern part of the computational domain went above an average water depth of 10cm (Figure 6.24(f)). This is in contrast to the 20m movement scenario in Section 6.4.1, where very little overland flow was recorded. Overland flow was observed to be moving north-eastwards (sub-figures 6.24(g) and 6.24(h)). Some overland flow is also experienced within the Coverack region. By  $\Delta t = 13 : 30$  (sub-figure 6.25(b)), overland flow peaked and continued to travel north-eastwards (sub-figures 6.25(c) and (d)). Overland flow within the Coverack region also peaked at this timestep. At  $\Delta t = 24 : 00$ , average water depth values in the north-east corner of the computational domain reached above 10cm (sub-figure 6.25(f)), moving south-easterly (sub-figures 6.25(g) and (h)). During the period when the storm event finished, the southern region overland flow reduced to below 5cm for the majority of pixels at  $\Delta t = 42 : 00$  (Figure 6.26) and continued to move north-easterly. The average water depth in the north-eastern region of the computational domain also reduced to below 5cm for most pixels.

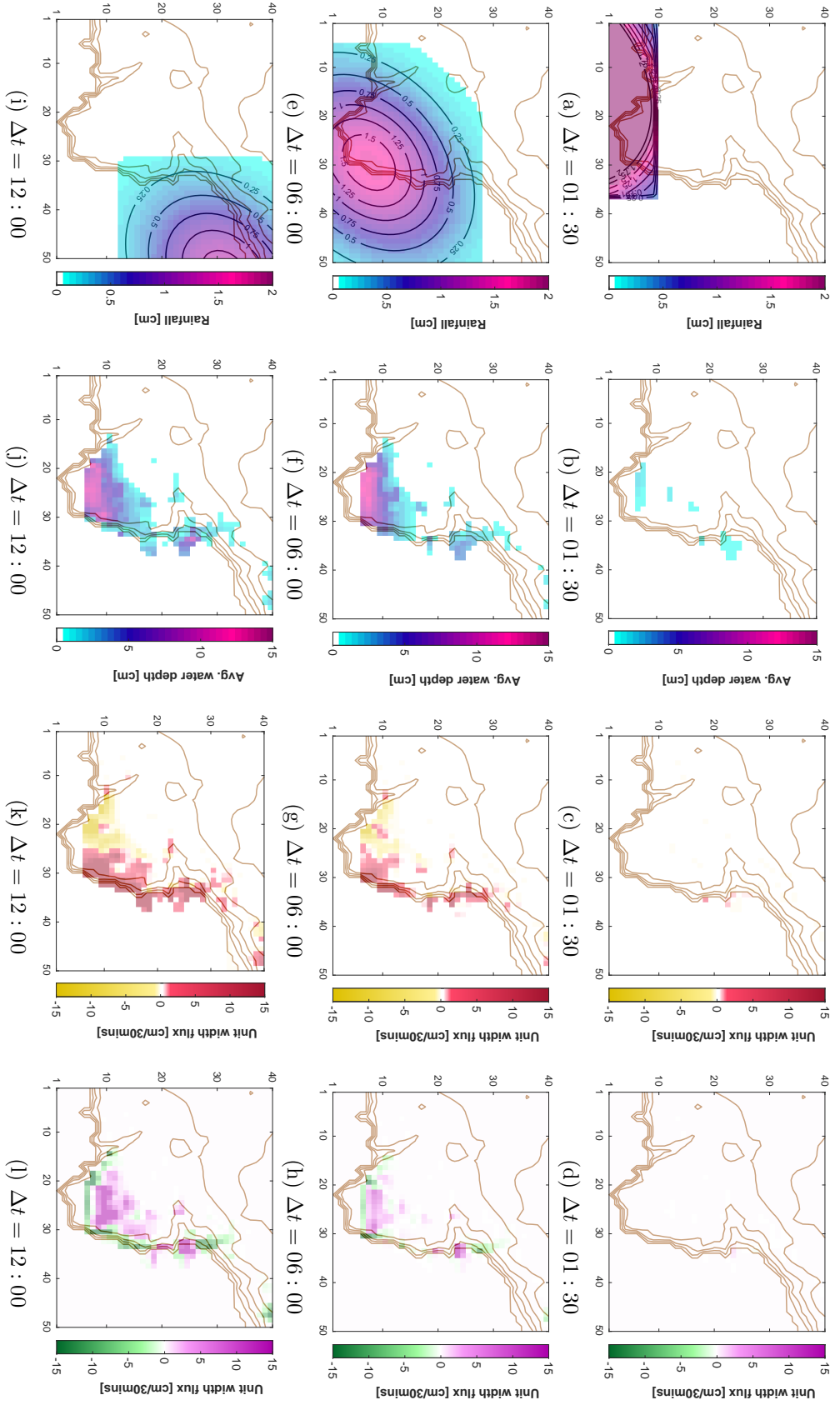


Figure 6.24: Scenario 3 - South-eastern moving storm - 50m resolution model. Each row presents individual timesteps  $\Delta t = 01 : 30$ ,  $\Delta t = 06 : 00$  and  $\Delta t = 12 : 00$ . Sub-figures (a), (e) and (i) show the evolution of the fictitious storm during the simulation. Sub-figures (b), (f) and (j) show the average water depth at their given timesteps. Sub-figures (c), (g) and (k) depict the mean unit-width horizontal flux in the  $y$ -direction. Sub-figures (d), (h) and (l) depict the mean unit-width horizontal flux in the  $x$ -direction.

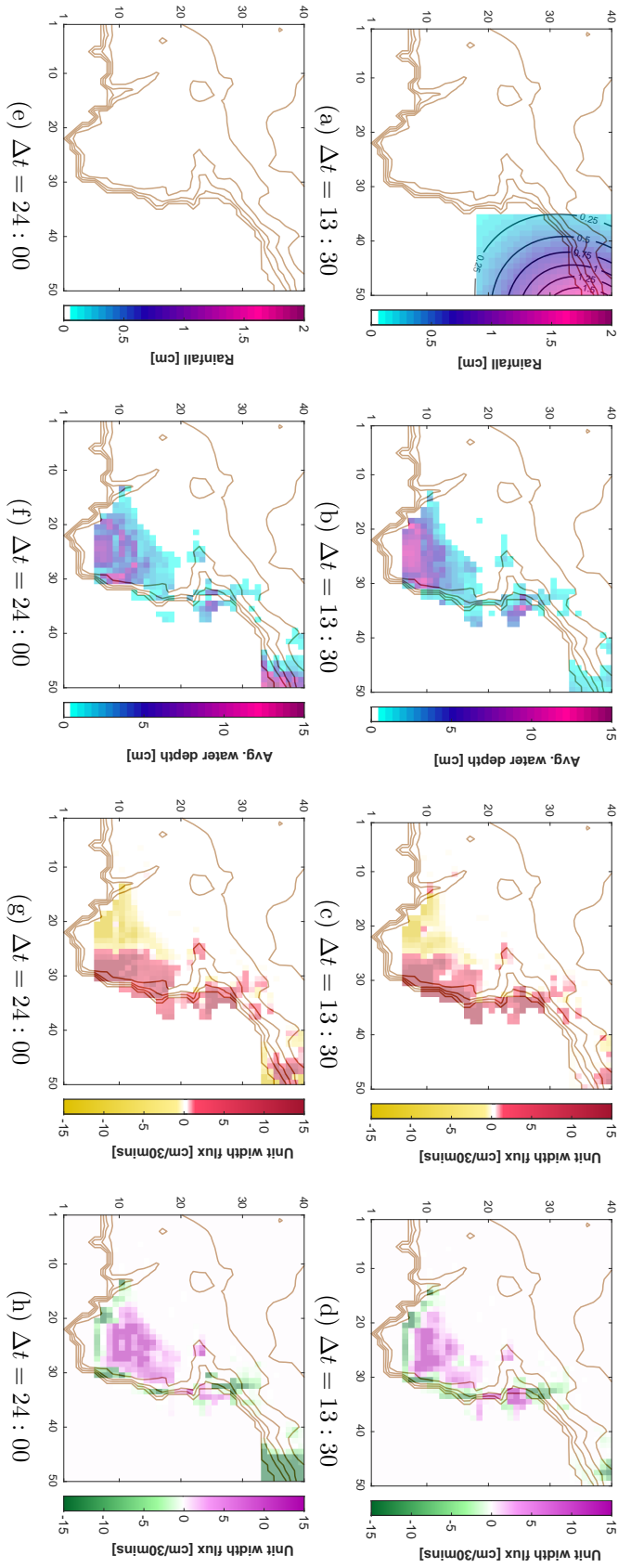


Figure 6.25: Scenario 3 - South-eastern moving storm - 50m resolution model. Each row presents individual timesteps  $\Delta t = 13:30$  and  $\Delta t = 24:00$ . Sub-figures (a) and (e) show the evolution of the fictitious storm during the simulation. Sub-figures (b) and (f) show the average water depth at their given timesteps. Sub-figures (c) and (g) depict the mean unit-width horizontal flux in the  $x$ -direction. Sub-figures (d) and (h) depict the mean unit-width horizontal flux in the  $y$ -direction.

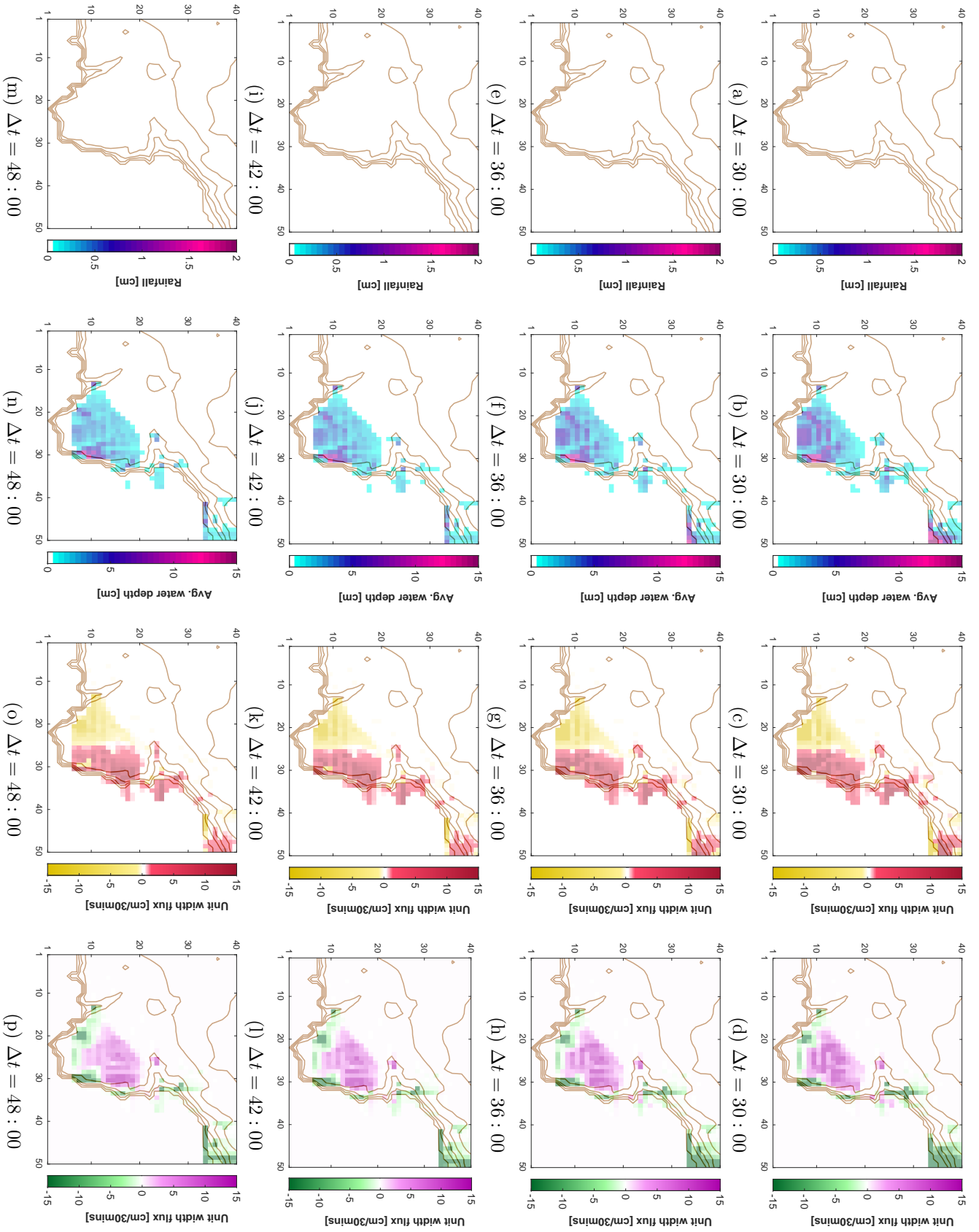


Figure 6.26.: Scenario 3 - South-eastern moving storm - 50m resolution model. Each row presents individual timesteps  $\Delta t = 30 : 00$ ,  $\Delta t = 36 : 00$ ,  $\Delta t = 42 : 00$  and  $\Delta t = 48 : 00$ . Sub-figures (a), (e), (i) and (m) show the evolution of the fictitious storm during the simulation. Sub-figures (b), (f), (j) and (n) show the average water depth at their given timesteps. Sub-figures (c), (g) (k) and (o) depict the mean unit-width horizontal flux in the  $x$ -direction. Sub-figures (d), (h), (l) and (p) depict the mean unit-width horizontal flux in the  $y$ -direction.

#### 6.4.4. Static 50m

Sub-figures 6.27(a), 6.27(e), 6.27(i), and 6.28(a) show the static storm centred over the sea to the east of the Lizard peninsula. By  $\Delta t = 06 : 00$  a large majority of pixels on the east of the peninsula were experiencing some overland flow. Peak overland flow as recorded in the Coverack region with values recorded above 10cm (sub-figure 6.27(f)). Between  $\Delta t = 13 : 30$  and  $\Delta t = 24 : 00$ , average water depth levels did decrease in some pixels, but at a slow pace (Figure 6.28). Similarly, between  $\Delta t = 30 : 00$  (Figure 6.29) and  $\Delta t = 48 : 00$  (Figure 6.30), overland values stayed at approximately 10cm within the Coverack region with water drainage being slow.

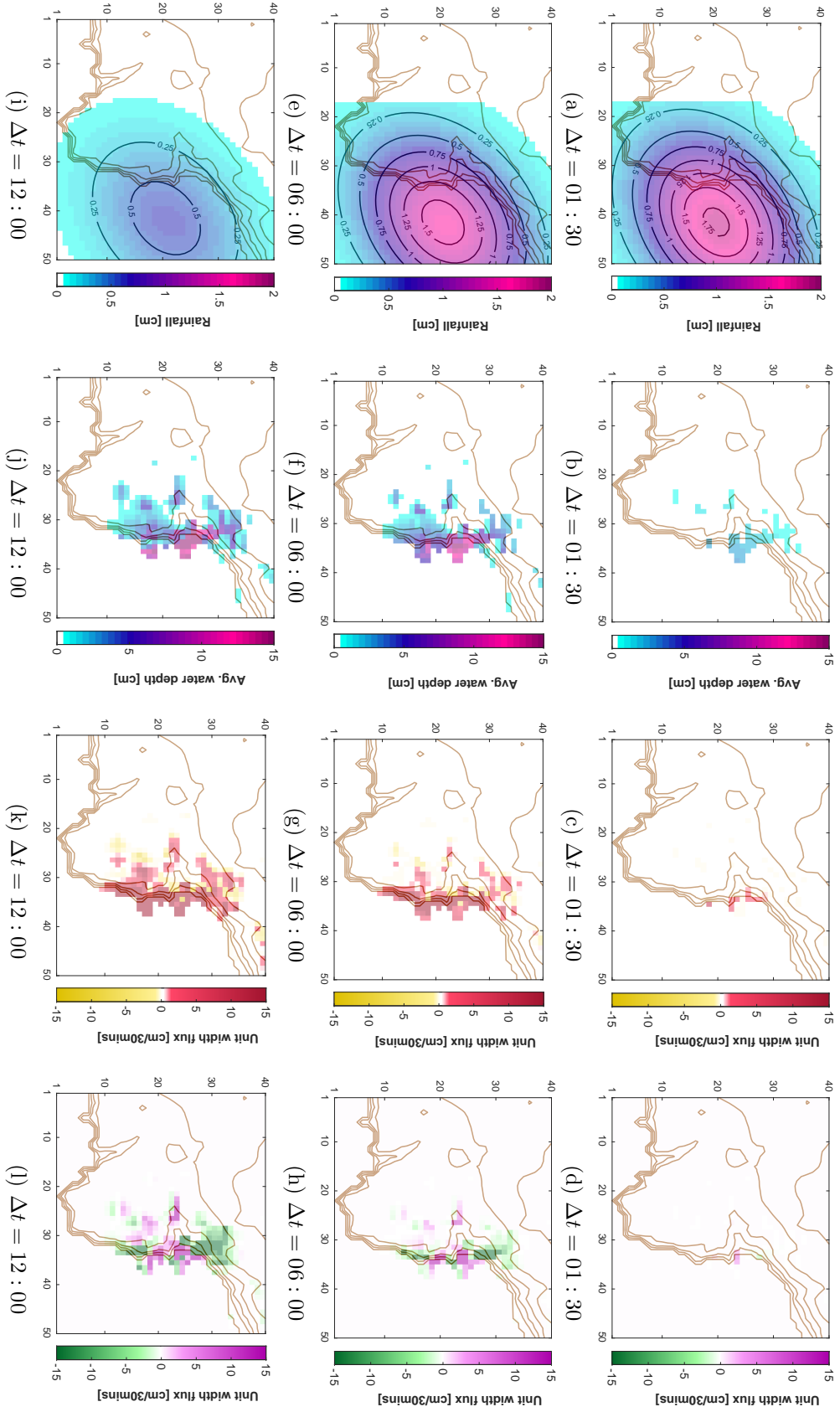


Figure 6.27: Scenario 3 - South-eastern static storm - 50m resolution model. Each row presents individual timesteps  $\Delta t = 01 : 30$ ,  $\Delta t = 06 : 00$  and  $\Delta t = 12 : 00$ . Sub-figures (a), (e) and (i) show the evolution of the fictitious storm during the simulation. Sub-figures (b), (f) and (j) show the average water depth at their given timesteps. Sub-figures (c), (g) and (k) depict the mean unit-width horizontal flux in the  $y$ -direction. Sub-figures (d), (h) and (l) depict the mean unit-width horizontal flux in the  $x$ -direction.

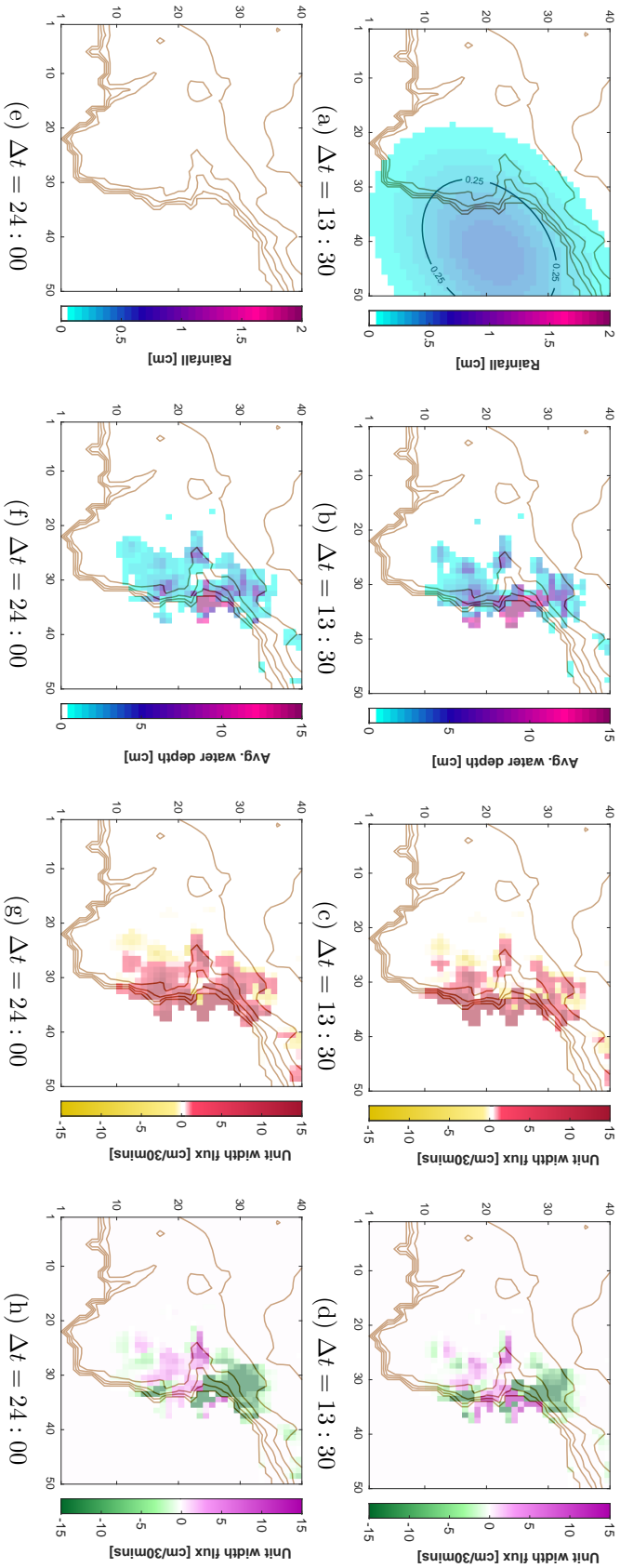


Figure 6.28: Scenario 3 - South-eastern static storm - 50m resolution model. Each row presents individual timesteps  $\Delta t = 13 : 30$  and  $\Delta t = 24 : 00$ . Sub-figures (a) and (e) show the evolution of the fictitious storm during the simulation. Sub-figures (b) and (f) show the average water depth at their given timesteps. Sub-figures (c) and (g) depict the mean unit-width horizontal flux in the  $x$ -direction. Sub-figures (d) and (h) depict the mean unit-width horizontal flux in the  $y$ -direction.

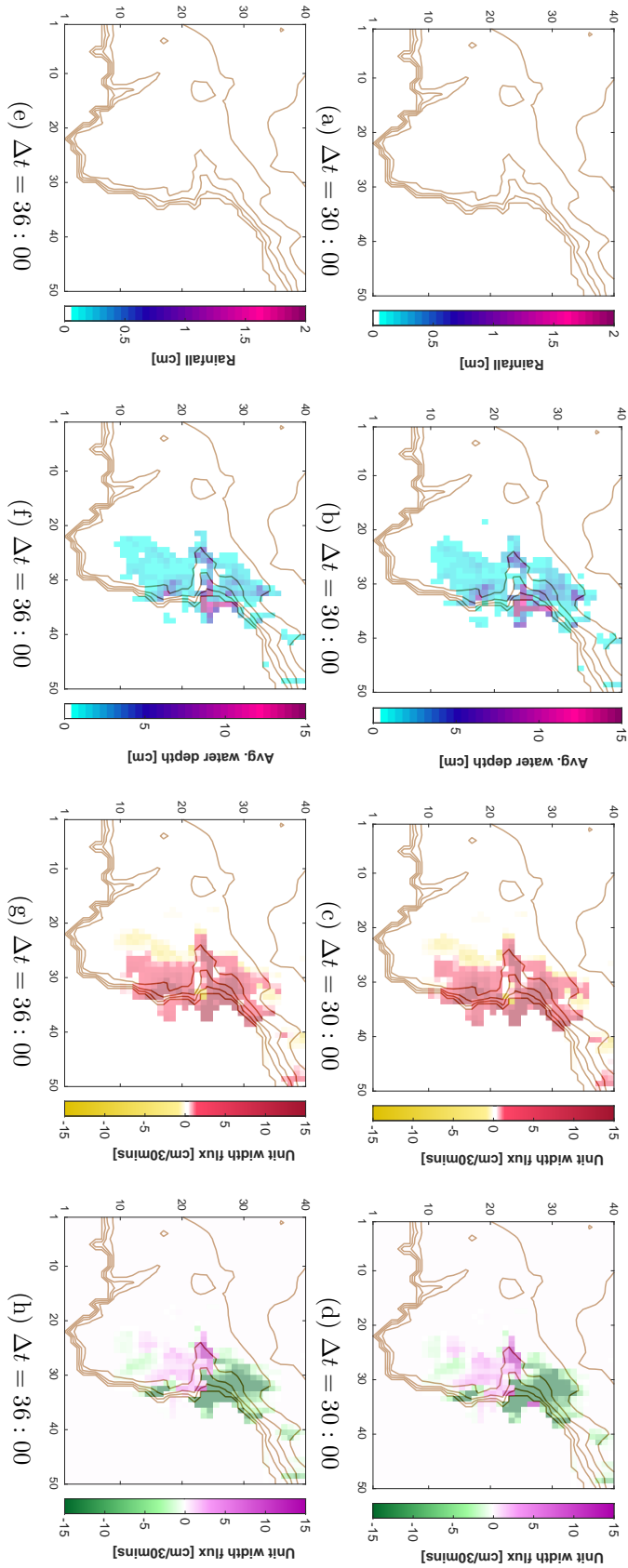


Figure 6.29.: Scenario 3 - South-eastern static storm - 50m resolution model. Each row presents individual timesteps  $\Delta t = 30 : 00$  and  $\Delta t = 36 : 00$ . Sub-figures (a) and (e) show the evolution of the fictitious storm during the simulation. Sub-figures (b) and (f) show the average water depth at their given timesteps. Sub-figures (c) and (g) depict the mean unit-width horizontal flux in the  $x$ -direction. Sub-figures (d) and (h) depict the mean unit-width horizontal flux in the  $y$ -direction.



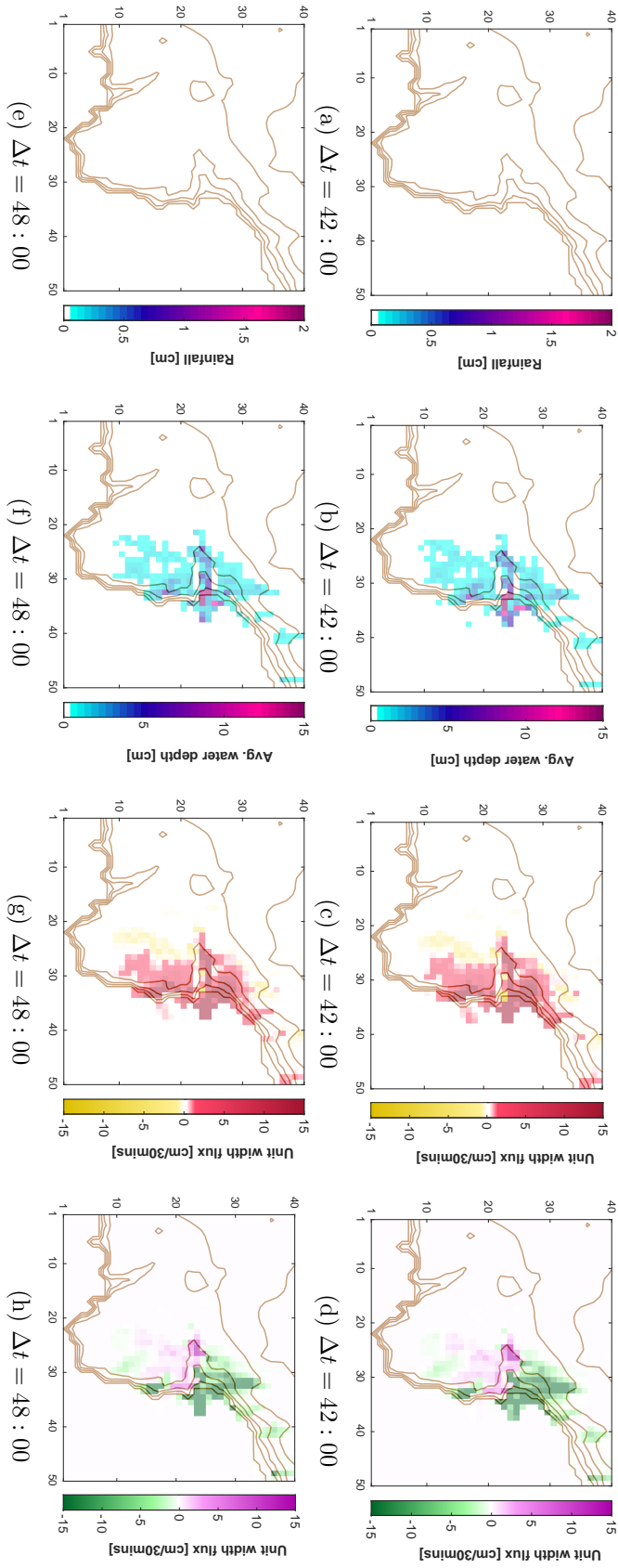


Figure 6.30.: Scenario 3 - South-eastern static storm - 50m resolution model. Each row presents individual timesteps  $\Delta t = 42 : 00$  and  $\Delta t = 48 : 00$ . Sub-figures (a) and (e) show the evolution of the fictitious storm during the simulation. Sub-figures (b) and (f) show the average water depth at their given timesteps. Sub-figures (c) and (g) depict the mean unit-width horizontal flux in the  $x$ -direction. Sub-figures (d) and (h) depict the mean unit-width horizontal flux in the  $y$ -direction.

## 6.5. Summary

The analysis conducted in Chapter 5 assumed that a storm would evenly distribute its precipitation across a river basin with an even intensity. In “real-world” scenarios, this assumption is unreasonable. Chapter 6 began by discussing the methodology used to define a fictitious storm in Section 6.2. Two storm scenarios were defined and analysed. Section 6.3 applied the fictitious storm centrally across the computational domain. Section 6.4 applied the fictitious storm to the south-east of the domain. Each storm scenario compared the outputs of a “static” storm with a “moving” storm for both model resolution variants. An additional analysis was implemented where the storm was placed in the north-west of the computational domain. This is provided in Appendix J.

A summary of the minimum, maximum and average differences between the 20m and 50m model of mean water depth for each scenario is given in Table 6.1. In general, the average difference between two resolutions within the first and third (Appendix J; page 384) static and moving scenarios are similar in magnitude. For the third scenario, the average difference in the movement case is slightly higher compared with the static case. Given the small differences in mean water depths between both model resolutions (as can also be seen in Tables 5.8 and 5.9, page 231), there is no strong evidence to choose one model variant over another. Patches with differing land-use compositions have produced differing results. Equally, patches with similar land-use compositions have given similar results on average.

It is up to the individual to determine which resolution of the model would be appropriate to use depending on the context in which the model is being run. The computational power needed run the 20m resolution model and produce the results outlined in Chapters 5 and 6 was reasonable. The Green-Ampt model (Section 4.3.5.1) and SCS method (Section 4.3.5.2) model small scale processes. As stated in Section 4.2.5, higher resolution models are preferred when modelling such systems as to reduce the uncertainty in model parameterisation. Thus the case study reviewed in Chapter 7 will be modelled using the 20m resolution model variant. This chapter highlighted what the key considerations are when deciding what model resolution is most suitable (**RQ5**) and compared the model performance between the 20m and 50m model resolution variants (**RQ6**).

As will be justified in Chapter 7, the storm scenario from Section 6.4.2 will be utilised as a template due to its similarities to the Coverack flooding event which will be implemented in the model next.

Table 6.1.: The minimum, maximum and average mean water depth output [cm] differences between the 20m and 50m model variants for different input and spatial scenarios reviewed in Sections 6.3, 6.4 and J.

Scenarios	Static			Movement		
	Min	Max	Average	Min	Max	Average
<b>S1</b>	0.0250	0.2560	0.2284	0.0109	0.2584	0.2108
<b>S2</b>	0.0019	0.1014	0.0519	$4.000 \times 10^{-5}$	0.0865	0.0555
<b>Appendix J</b>	0.0189	0.1477	0.1289	0.0292	0.1904	0.1638

# 7. Simulation Modelling: Coverack, Cornwall

## 7.1. Introduction

The motivation of the need for humans to equitably, sustainably and efficiently utilise finite resources to meet its material, cultural and fundamental needs was presented in Chapter 1. This motivation led to Cornwall Council’s justification of its “Environmental Growth Strategy” (Section 1.1.5). Parallels in high level management concepts between natural asset portfolio management and “facilities management” gave rise to the proposal of a computational tool, in the form of a hydrological model, to aid policy makers in their strategic long term planning goals and impact assessments (Section 1.3). Chapter 2 highlighted the literature related to hydrological modelling. Chapter 3 reviewed the fundamental mathematical knowledge that underpins the hydrological model which was described in Chapter 4.

This chapter will begin by reviewing incidents that took place during the Coverack flooding event on 18<sup>th</sup> July 2017 (Section 7.2). Section 7.3 re-defines the sub-regions from the computational domain discussed in Section 4.2 for the subsequent analyses. Section 7.4 envisages how this computational tool is intended to be applied in a land-use management context. This section justifies the potential policy proposals to mitigate another flooding event of a similar magnitude to the one experienced in Coverack. Section 7.5 outlines the seven scenarios that are analysed in Section 7.6 for each of the sub-regions. Specific parameter justifications for this model simulation have come from the initial model performance analysis (Chapter 5) and non-uniform model input analysis (Chapter 6) previously conducted and are presented below.

Chapter 5 analysed the 20m and 50m model resolution variants using a uniform precipitation input. The more coarse 50m model was less computationally expensive to execute. If there existed a parity in model output between the resolutions, it would have made sense to have used the 50m model in this case study simulation. Patches #3 and #7 in the northern sub-region analysed (Sections 5.5.5.1 and 5.5.5.2 respectively) demonstrated output parity when the land-use proportion of the 50m model matched the 20m model. However, the majority of patches analysed in the north-eastern (Section 5.4) and northern (Section 5.5) sub-regions did not. Given this, one cannot use the 50m model resolution variant in favour of the 20m model in order to reduce the computational work needed.

Chapter 6 looked to compare the model response of the 20m and 50m model variants for

differing non-uniform input scenarios. The spatial distribution of average water depth was much greater in the 50m model compared to the 20m model. The construction of the 50m model meant that the grid mesh was much more coarse. As a result, it would not be as useful in providing meaningful information to policy makers in the potential consequences of proposed policies. Sections 5 and 6 reviewed academic scenarios where there was little agreement between the two model resolutions looked at.

For these reasons, it is appropriate to consider a real life event using the highest resolution available. As such, this section will solely focus on simulating the Coverack flooding case study (Section 1.2) using the 20m resolution model variant.

## 7.2. The Coverack Flooding Event: An Overview

On 18<sup>th</sup> July 2017, southern England experienced torrential rainfall from thunderstorms. Coverack endured localised intense rainfall which led to a flash flooding event in the afternoon. The sheer volume of rainfall meant the river catchment could not cope. This resulted in river flooding, surface water and significant erosion. At least fifty properties were noted to be affected by this flash flood. The Environment Agency commissioned JBA Consulting, a leading water, environmental, urban design, engineering and risk management consultancy company, to review the underlying causes of this event (Environment Agency and Cornwall Council, 2018).

Initial findings from the review found that the flooding event began from:

“The most extreme storm event recorded in Cornwall and one of the most extreme three hour rainfall events experienced in the UK.”

A Met Office investigation concluded that between 165 and 201mm of rain fell over Coverack within three hours on the day. Figure 7.1 shows the Radar-gauged precipitation accumulation difference. The centre of the storm, where the greatest precipitation difference is, lies to the south-east of Coverack. Only the western half of the storm lies over land. It is most similar to the static storm scenarios in Section 6.4. From this information, the 20m static storm scenario from Section 6.4.2 will be used as the template for the spatial distribution of the storm input.

Figure 7.2 shows the hyetograph of the flooding event (blue) over Coverack between 13:30 and 16:30. It is compared with a 0.1% “Annual Exceedance Probability”, the probability of a natural hazard event occurring annually, hyetograph. The value listed in Table 7.1 has been read from Figure 7.2. Alongside it is the percentage of total input it represents as well as the lower bound, median and upper bound estimates from the Met Office’s conclusion. Applying the method discussed in Section 6.1, the values in Table 7.1 from Figure 7.2 will be distributed using the static storm scenario from Section 6.4.1.

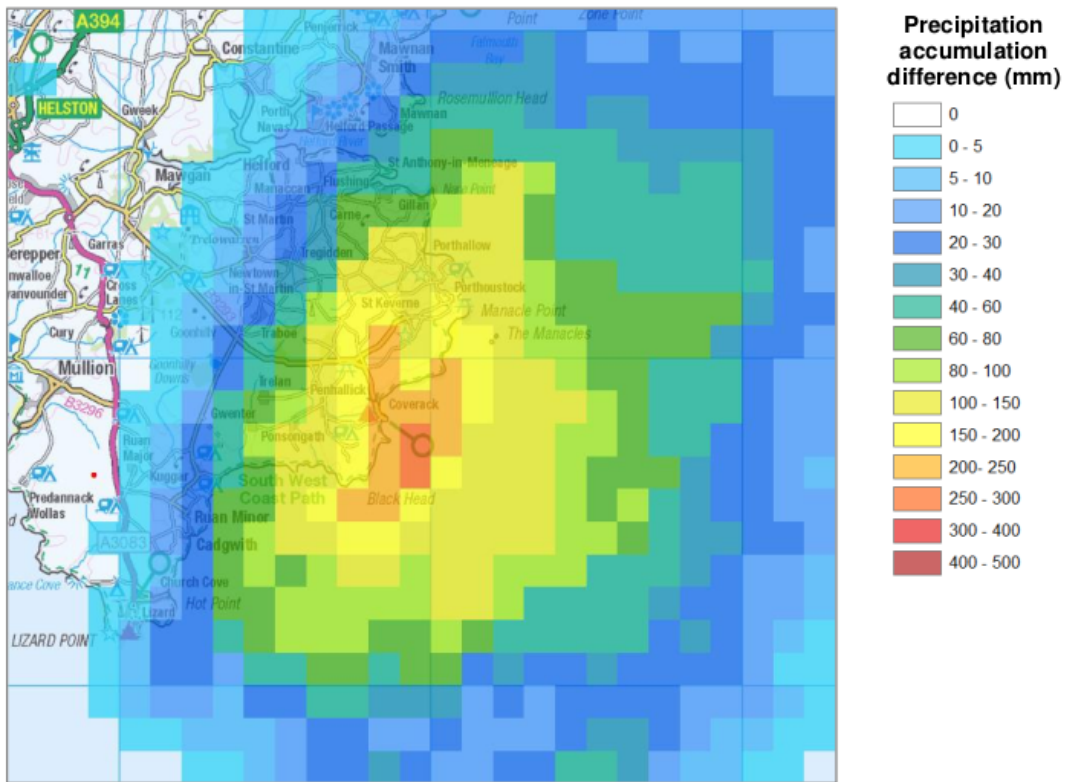


Figure 7.1.: A radar-gauge precipitation accumulation difference of the thunderstorm event over Coverack (Harrison et al., 2017; Environment Agency and Cornwall Council, 2018).

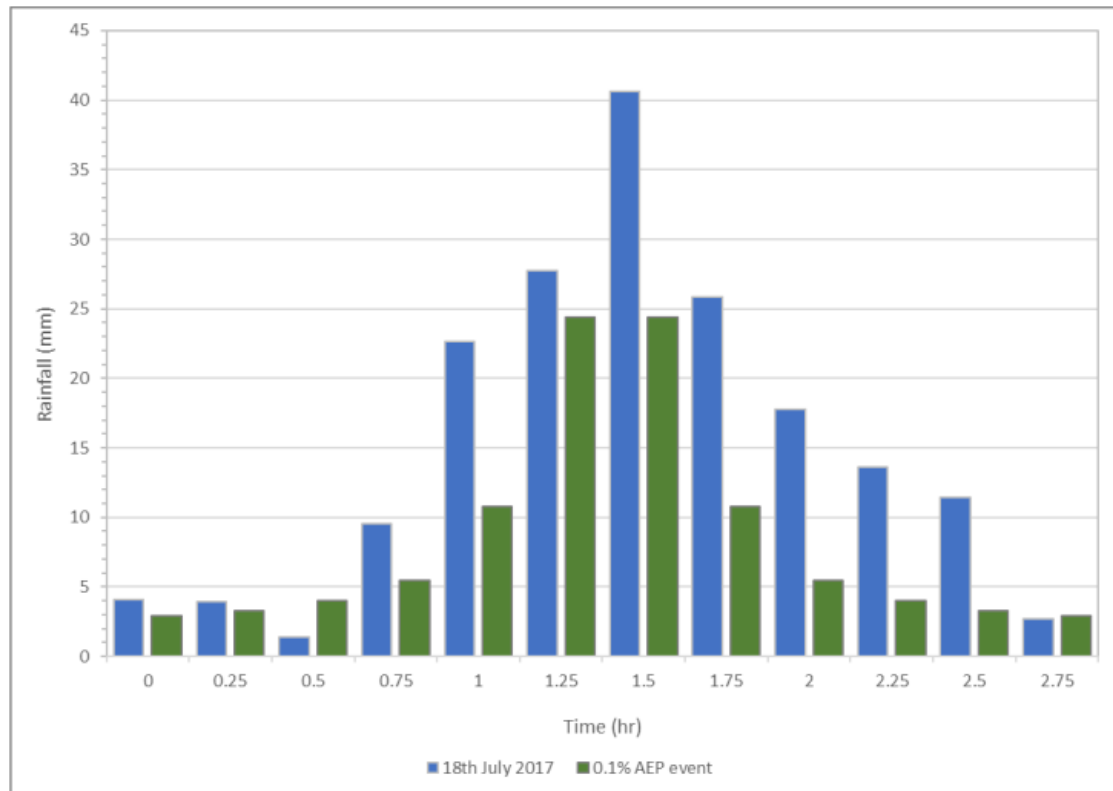


Figure 7.2.: Hyetographs for the Coverack storm event (blue) and the 0.1% Annual Exceedance Probability event (green) (Environment Agency and Cornwall Council, 2018).

Table 7.1.: Coverack Storm inputs estimated from Figure 7.2. Lower bound, upper bound and median estimates using the Met Office’s investigation.

Time [hh:mm]	RF Estimate (Hyteograph) [cm]	Percentage of Total	Lower Bound [cm]	Median [cm]	Upper bound [cm]
13:30	0.4	2.24	0.37	0.41	0.45
13:45	0.4	2.24	0.37	0.41	0.45
14:00	0.15	0.84	0.14	0.15	0.17
14:15	0.95	5.33	0.88	0.98	1.07
14:30	2.25	12.62	2.08	2.31	2.54
14:45	2.75	15.43	2.55	2.82	3.10
15:00	4.05	22.72	3.75	4.16	4.57
15:15	2.795	14.56	2.40	2.66	2.93
15:30	1.75	9.82	1.6203	1.80	1.97
15:45	1.15	6.45	1.06	1.18	1.30
16:00	1.125	6.31	1.04	1.15	1.27
16:15	0.25	1.40	0.23	0.26	0.28
<b>Total</b>	17.82	100	16.5	18.3	20.1

### 7.3. Sub-Region Domain Definitions

To obtain a better understand of the effect land-use categories have on the computational domain, the 20m resolution pixel categories (Figure 7.3), have been further sub-divided into five sub-regions (Figure 7.4). Any “undefined” pixels were defined as such because they did not produce any model output in the simulated scenarios defined in Section 7.5 below.

Table 7.2 defines the pixel boundaries of these sub-regions. Any urban or sub-urban pixels between  $\Omega_{(79-82, 53-64)}$  were included in the “Coverack” category. All other non-urban pixels were included in the “West Coverack” region.

Table 7.2.: Sub-region pixel boundary definitions (inclusive) for the 20m resolution model.

Sub-Region Name	Column Pixel Boundary $[\Omega_{(i,j)}]$	Row Pixel Boundary $[\Omega_{(i,j)}]$
<b>Coverack</b>	79–91	53–64
<b>North Coverack</b>	69–83	65–100
<b>North-East Coverack</b>	84–125	65–100
<b>South Coverack</b>	50–91	1–52
<b>West Coverack</b>	50–82	53–64

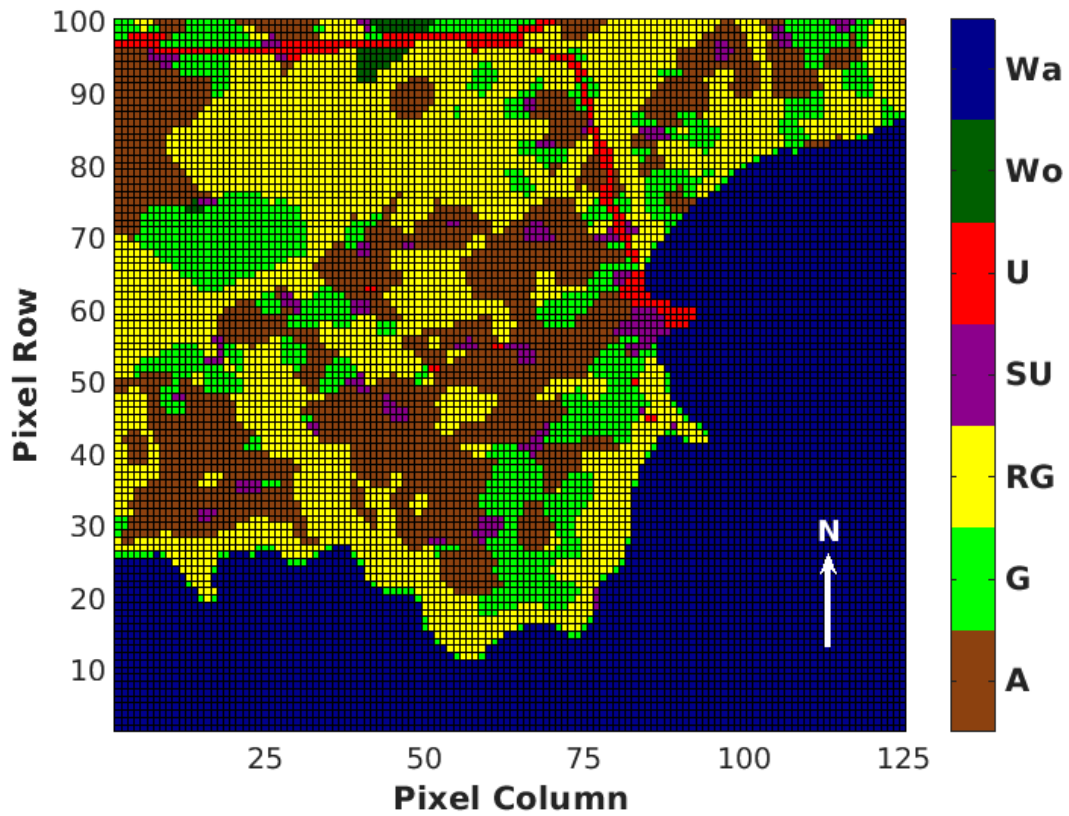


Figure 7.3.: Original 20m resolution land-use map.

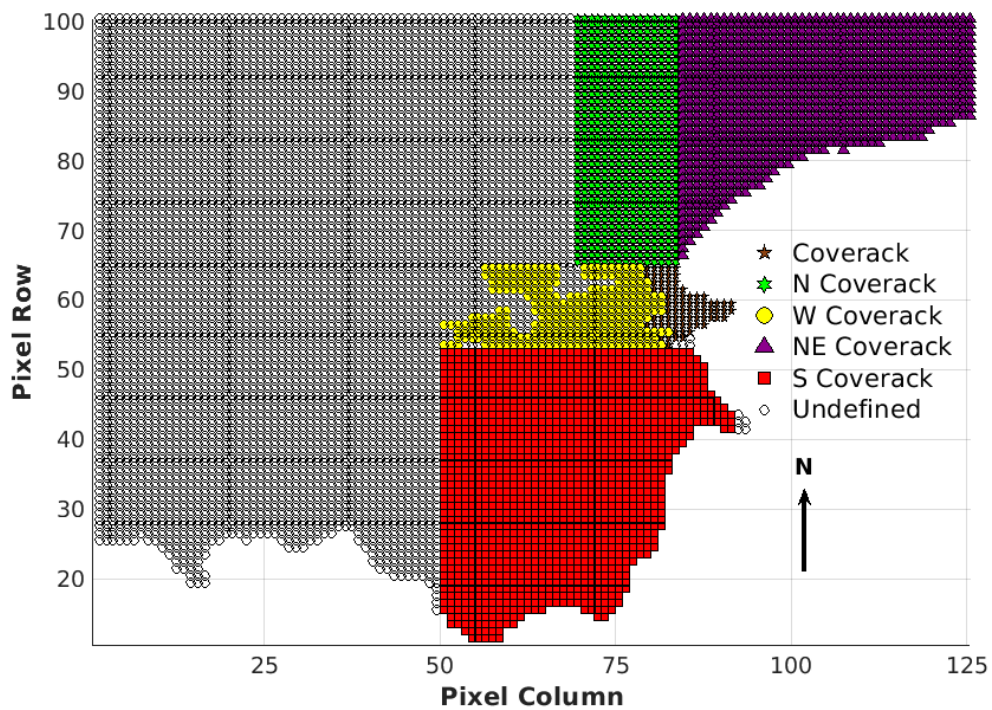


Figure 7.4.: Defined sub-regions for the 20m resolution computational domain.

## 7.4. A Perspective from a Hypothetical Cornwall Council Policy Planner

An in-depth understanding of how a hydrological model is structured and implemented is needed to ensure model outputs are robust and sensible. This knowledge can only be obtained through dedicated effort from individuals interested in applying themselves in this domain. Cornwall Councillors will not have had the opportunity to apply themselves deeply into the world of hydrological modelling.

Digital platforms are software-based infrastructures which can facilitate interactions and transactions between a given user through a front-end dashboard (such as ‘myFM’ discussed in Section 1.1.6; page 38) and model back-end, where a computational tool would reside (e.g. a hydrological model). When hydrological modelling tools are implemented in the back-end of such systems, this enables the access to the latest modelling techniques and knowledge. This will present policy makers with safe and secure access to the tool while minimising the possibility of incorrectly applying the hydrological model and misinterpreting its outputs.

The analysis of the modelling scenarios (Section 7.6; page 282) is done from the perspective of a Cornwall Council land-use policy planner. The planner reviews the Coverack flooding event (Section 7.2; page 276) through a front-end dashboard application (akin to the “myFM” dashboard seen in Figures 1.4 and 1.5; page 39). This is the control simulation (Section 7.5.1; page 281). Through the dashboard’s “plug-and-play” feature the planner defines the five sub-regions outlined in Section 7.3 which is illustrated in Figure 7.4. Through the same feature the planner defines three flood management suggestions. The first suggestion involves changing the watershed’s hydrological characteristics by altering the underlying soil from *Sandy Loam* to a more absorptive *Loamy Sand* for specific land-use pixels. This is detailed in Scenario I, Section 7.5.2. The planner’s second suggestion involves altering the land-use of the watershed for a given region from *Rough Grazing* to *Arable*. This is detailed in Scenario II, Section 7.5.3. The planner’s final suggestion is the implementation of a sluice gate on the coast of Coverack to drain excess surface water at a faster rate. This is outlined in Scenario III, Section 7.5.4. As well as being interested in how each intervention affects the Coverack flood risk, they are also interested in the combination of these interventions to see if they minimise the flood risk further. These are outlined in Sections 7.5.5, 7.5.6, 7.5.7 and 7.5.8. To begin their analysis they first look at the mean average water depth of the land-use pixels within the sub-regions of each watershed.



## 7.5. Modelling Simulation Scenarios

The thunderstorm which occurred on 18<sup>th</sup> July 2017 is represented by the storm scenario from Section 6.4.1 using the inputs outlined in the Environment Agency commissioned report (Environment Agency and Cornwall Council, 2018). Seven modelling scenarios are outlined here.

### 7.5.1. Control Simulation

The control simulation consists of the original 20m resolution model parameters defined in Table 5.2 using the initial land-use definitions picture in Figure 7.3.

### 7.5.2. Scenario I: Soil parameter changes

This first scenario changes soil parameters used in the Green-Ampt model (Section 3.6.1) from *Sandy Loam* to a more absorptive soil *Loamy Sand* listed in Table 3.1. These changes will be applied to the domain region  $\Omega_{(55-95,50-100)}$ . Only land-use pixels defined as *Arable*, *Grassland* and *Rough Grazing* will have this soil parameter change implemented.

### 7.5.3. Scenario II: Land-Use parameter change

For the second modelling scenario, any pixel defined as **Rough Grazing** within the domain region  $\Omega_{(55-95,50-100)}$  is altered to **Arable**.

### 7.5.4. Scenario III: Open “Sluice” parameter

For the final *individual* scenario, any *coastal urban* pixel within the range  $\Omega_{(81-91,46-100)}$  will have its hydrological properties altered so that it acts as an *open infinite sluice gate*. Any urban parameters on the Coverack coast will immediately drain any excess overland surface water.

### 7.5.5. Scenario IV: Soil and land-use parameter changes

Scenario IV is a combination of scenarios I (Section 7.5.2) and II (Section 7.5.3).

### 7.5.6. Scenario V: Soil parameter change with an open “Sluice”

Scenario V is a combination of scenarios I (Section 7.5.2) and III (Section 7.5.4).

### 7.5.7. Scenario VI: Land-use parameter change with an open “Sluice”

Scenario VI combines scenarios II (Section 7.5.3) and III (Section 7.5.4).

### 7.5.8. Scenario VII: Soil and land-use parameter changes with an open “Sluice”

Scenario VII is combines all the three individual scenarios; I (Section 7.5.2), II (Section 7.5.3) and III (Section 7.5.4).

## 7.6. Modelling Analysis

The thunderstorm which occurred on 18<sup>th</sup> July 2017 is represented by the storm scenario from Section 6.4.1 using the inputs outlined in the Environment Agency commissioned report (Environment Agency and Cornwall Council, 2018). The impact of the eight modelling scenarios outlined above on the five sub-regions are considered here. These regions are Coverack (Section 7.6.1), Northern Coverack (Section 7.6.2), North-Eastern Coverack (Section 7.6.3), Southern Coverack (Section 7.6.4) and Western Coverack (Section 7.6.5).

### 7.6.1. Coverack

Figure 7.5(a) on page 284 shows the layout of the coastal Coverack sub-region that is being analysed. The region is composed solely of sub-urban and urban land-use pixels. No discernable difference in output can be seen between the control scenario (Section 7.5.1) seen in Figure 7.5(b) and the first two scenarios (Sections 7.5.2 and 7.5.3) given in Figures 7.5(c) and 7.5(d) respectively. For each of these scenarios the mean average water depth of urban pixels reaches to just below 14cm at  $\Delta t = 09 : 00$ . The sub-urban value begins at an average water depth of approximately 13cm and sharply declines to just above 6cm at  $\Delta t = 15 : 00$  before plateauing throughout the remainder of the simulation. This sees the complete domain monotonically decrease from approximately 13cm to 7cm at the end of the simulation. Figure 7.5(e) demonstrates the third scenario which emulates a “sluice gate” for urban pixels which are adjacent to the coastline. Immediately noticeable is the starting mean average water depths of the domain. Sub-urban pixels begin just below 12cm at  $\Delta t = 16 : 30$  compared to the approximate 13cm in the control scenario. Similarly, urban pixels begin at just above 13cm in the control scenario at the same timestep but begins at just below 1cm in the third scenario. Throughout the entire simulation the mean average water depth of urban pixels remains at or below 1cm. When the first two individual scenarios are combined to make up Scenario IV (Section 7.5.5) no big difference can be found with the control scenario as seen in Figure 7.5(f). Figures 7.5(g), 7.5(h) and 7.5(i) depict the remaining three scenarios, Scenario V (Section 7.5.6), Scenario VI (Section 7.5.7) and Scenario VII (Section 7.5.8) respectively. These three scenarios contain

the third scenario mimicking the sluice gate and behave identically to this third modelling simulation.

### 7.6.2. Northern Coverack

The northern Coverack sub-region may be viewed in Figure 7.6(a) on page 285. The mean average water depth for each land-use type in the control scenario (Figure 7.6 (b)) peaked by  $\Delta t = 18 : 00$ . The sub-urban pixel's average was greatest at approximately 7cm, with urban land-use pixels just above 6cm. The mean average water depth experienced on Grassland pixels was approximately 4.7cm. Each of the aforementioned land-use types saw a sharp decline in their averages at some point in the simulation. The Arable land-use type reached to just below 3cm and remained steady throughout the simulation whilst the Rough-Grazing average started approximately at 2.5cm and steadily reduced to just above 1.5cm at the end. Each land-use type lay between a mean of 1.5cm and 3cm average water depth. No significant change in behaviour or magnitude was noted for the first scenario (Section 7.5.2). In scenario II (Section 7.5.3), the magnitudes of all the land-use types were decreased slightly. The sub-urban pixel saw its peak hit just above 6.5cm, less than the 7cm experienced in the control scenario. However its behaviour afterwards was very similar. This pixel finished with an average water depth of just above 2cm. The urban mean average water depth within this scenario peaked just above 6cm and declined dramatically before recovering slightly to approximately 2.5cm as can be seen in Figure 7.6(d). The Grassland pixel peaked at approximately 4.5cm before declining to just below 2cm at the end of the simulation. The remaining land-use pixels peaked between approximately 1.5cm and 3cm and remained within this range throughout the entirety of the simulation. A slight decrease in magnitude is noted for the sub-urban pixel for the third scenario (Section 7.5.4) with its maximum mean average water depth reaching just below 7cm. A full centimetre reduction can be seen for the urban land-use pixel average in Figure 7.6(e) compared with the control scenario. A similar magnitude reduction is observed between the grassland land-use average the control scenario.

When combining scenarios I and II to give scenario IV (Section 7.5.5), its output behaves similarly in magnitude to the second scenario for each land-use pixel as can be seen in Figure 7.6(g). As scenarios I and II are combined for scenario V (Section 7.5.6), the output of this scenario is most similar to the third individual scenario. This is equally the case for scenario VI (Section 7.5.7) which combines scenarios I and II and can be seen with Figure 7.6(h). When all three scenarios are combined to give scenario VII (Section 7.5.8) the individual sluice scenario (Section 7.5.4) has the largest influence in the model output.

### 7.6.3. North-Eastern Coverack

Figure 7.7 on page 287 shows the north-eastern Coverack sub-region of the computational domain. For the control scenario (Figure 7.7 (b)), the urban land-use pixels mean average

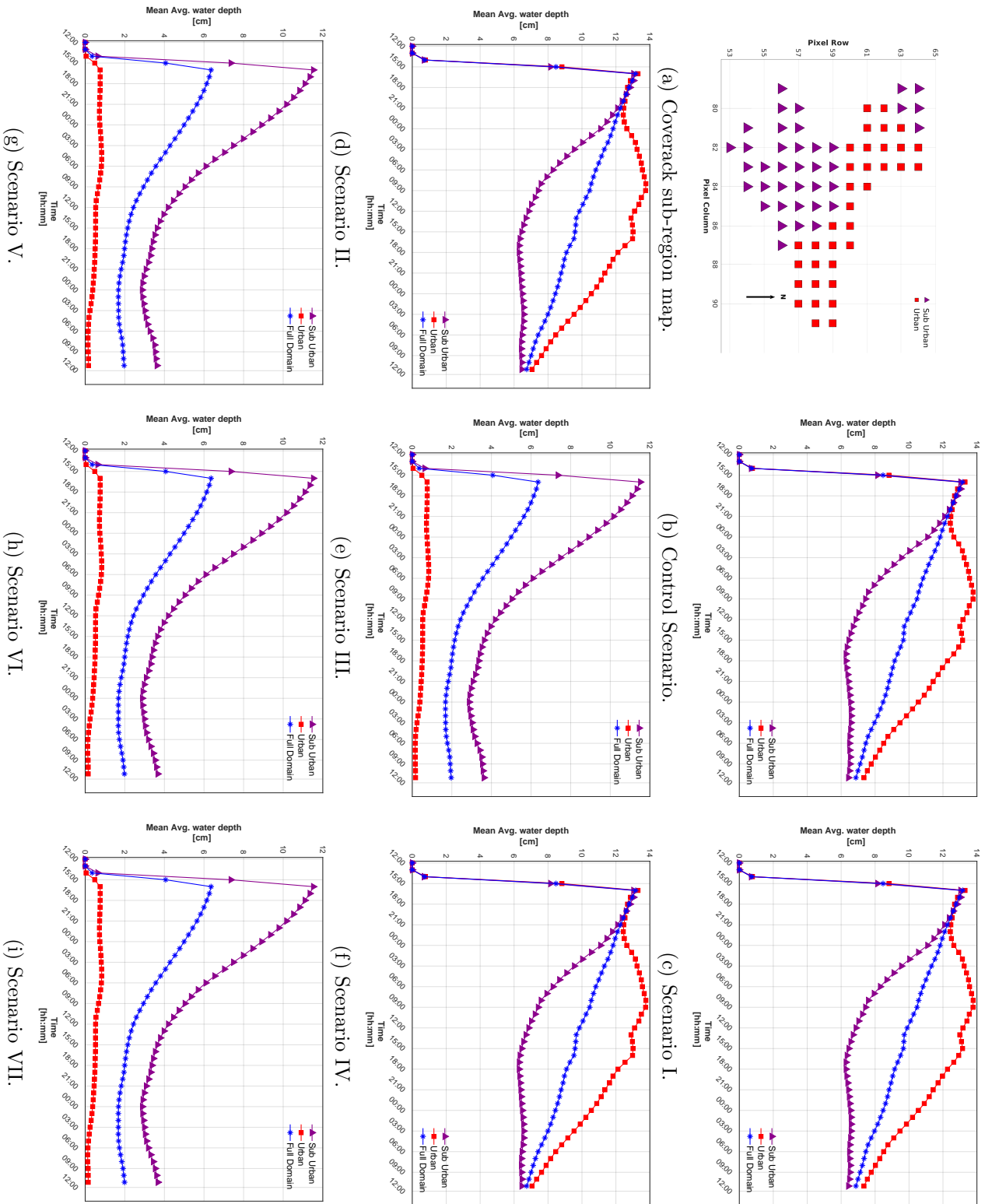


Figure 7.5.: Mean water depth values averaged across each land-use for each modelling scenario within the Coastal Coverack sub-region.

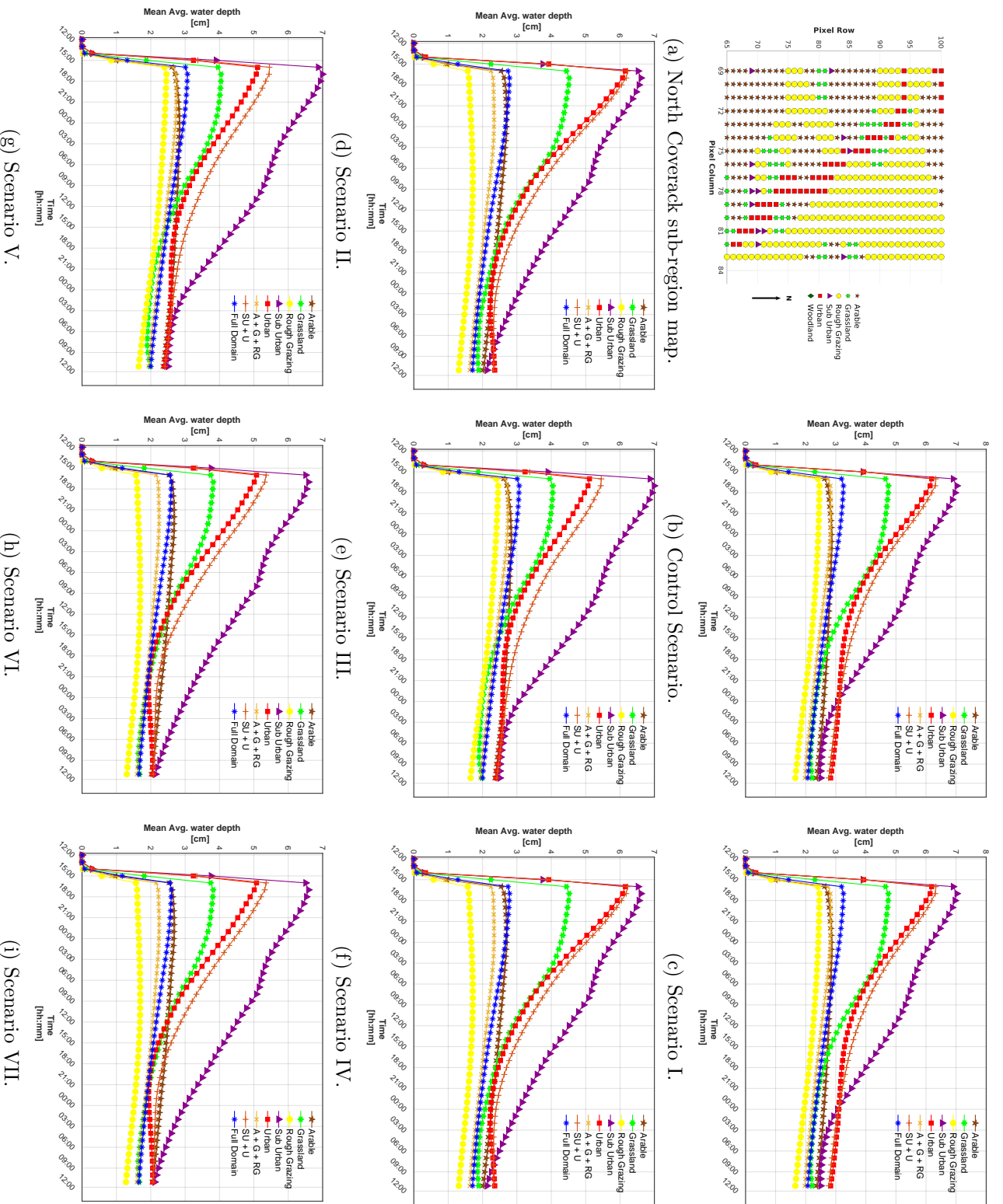


Figure 7.6.: Mean water depth values averaged across each land-use for each modelling scenario within the Northern Coverack sub-region.

water depth peaked just above 6cm and declined dramatically to below 0.25cm at  $\Delta t = 15 : 00$  and plateaued for the remainder of the simulation. Grassland, Rough Grazing and Sub-urban land-use pixels peaked at just above 4cm and declined more gently throughout the simulation reaching to just above 1cm, 1cm and approximately 0.75cm respectively. The arable land-use pixel peaked a little above 2cm and declined slowly to just above 1cm throughout the simulation. Looking at Figures 7.7(c)-(i), none of the modelling scenarios, nor their combinations had any effect on the overall magnitude or general behaviour on the mean average water depths of the land-use pixels within this region.

#### 7.6.4. Southern Coverack

The south Coverack region is depicted in Figure 7.8(a) on page 288. The largest peak average water depth occurred at  $\Delta t = 16 : 30$  at approximately 13.5cm for the urban land-use type within the control scenario (Figure 7.8(b)). Over the next 12 hours water depth for urban land-use dramatically declined to 2.5cm before stabilising at approximately 2cm at the end of the simulation. The sub-urban, grassland and rough grazing land-use types reached their maximum of approximately 8.5cm at the start of the simulation. Both the sub-urban and rough grazing land-use depths steadily decreased in value to approximately 3.5cm at the end of the simulation. A lesser decline in average water depth occurred in grassland pixels reaching 6cm at the end of the control scenario simulation. Finally the arable pixel began with a mean average water depth of roughly 5cm before peaking to just below 6cm at  $\Delta t = 15 : 00$  and reducing back to 5cm again by the end of the simulation. The magnitudes and behaviours of the land-use pixels in scenarios I, II and IV did not differ when compared to the control scenario as can be see in Figures 7.8(c), 7.8(d) and 7.8(f). No significant change in the behaviour and average water depth values occurred within the land-use pixels when scenario III was run except for in the urban land-use pixels (Figure 7.8(e)), which initially reached a peak of approximately 10cm. It then sharply declined to below 2cm by  $\Delta t = 04 : 30$ . The mean average water depth then slowly diminished to 1cm by the end of the simulation. This exact behaviour was also noted for scenarios V, VI and VII (Figures 7.8(g), (h) and (i)) where the sluice gate scenario was the dominant factor.

#### 7.6.5. Western Coverack

Figure 7.9(a) on page 290 shows the map of the west Coverack region within the computational domain. Within the control scenario (Figure 7.9(b)), both the urban and grassland begin with a mean average water depth of approximately 8.5cm. The urban pixel declines in three phases, to 7cm, 4.5cm and finally 2.5cm at  $\Delta t = 21 : 00$ ,  $\Delta t = 18 : 00$  and  $\Delta t = 12 : 00$  (at the end of the simulation), respectively. The grassland pixel declines to a value of roughly 6.5cm at  $\Delta t = 18 : 00$  but again rises to approximately 7.5cm at the end of the simulation. The average water depth on sub-urban land begins at approximately 7.5cm before steadily declining to 2cm by  $\Delta t = 18 : 00$ . It then begins increasing again to roughly 2.25cm at the end of the simulation. The mean average water depth recorded for

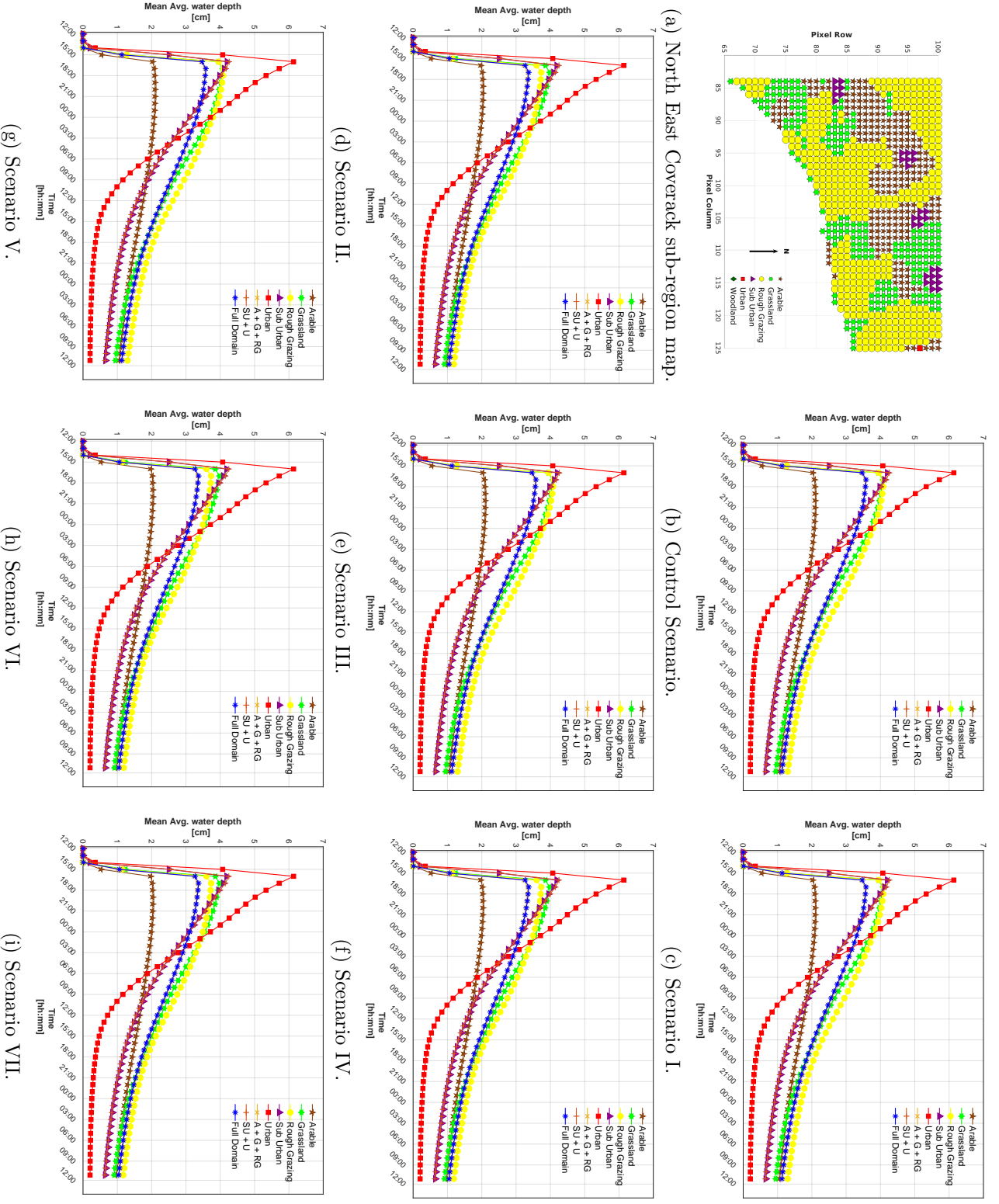


Figure 7.7.: Mean water depth values averaged across each land-use for each modelling scenario within the North-Eastern Coverack sub-region.

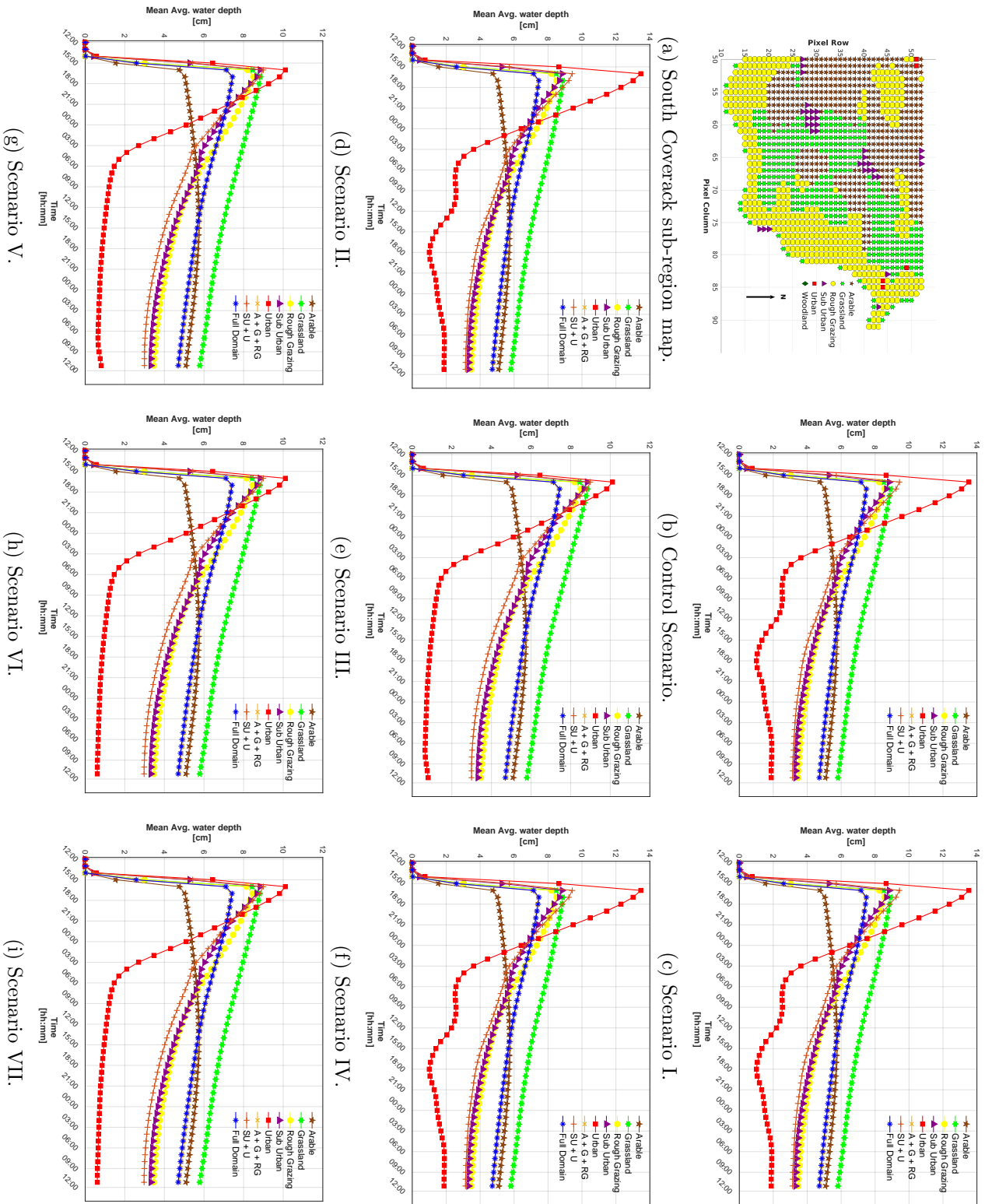


Figure 7.8.: Mean water depth values averaged across each land-use for each modelling scenario within the southern Coverack sub-region.



the arable pixels within the region began at approximately 4.5cm before rising to above 5.5cm and then declining to just above 5cm at the end of the simulation. No output was recorded for the rough-grazing category. Figures 7.8(c) - 7.8(i) all show the exact same magnitude and behaviour for each of the scenarios listed in Section 7.5, meaning that had no direct impact on the overland flow within this sub-region of the computational domain.

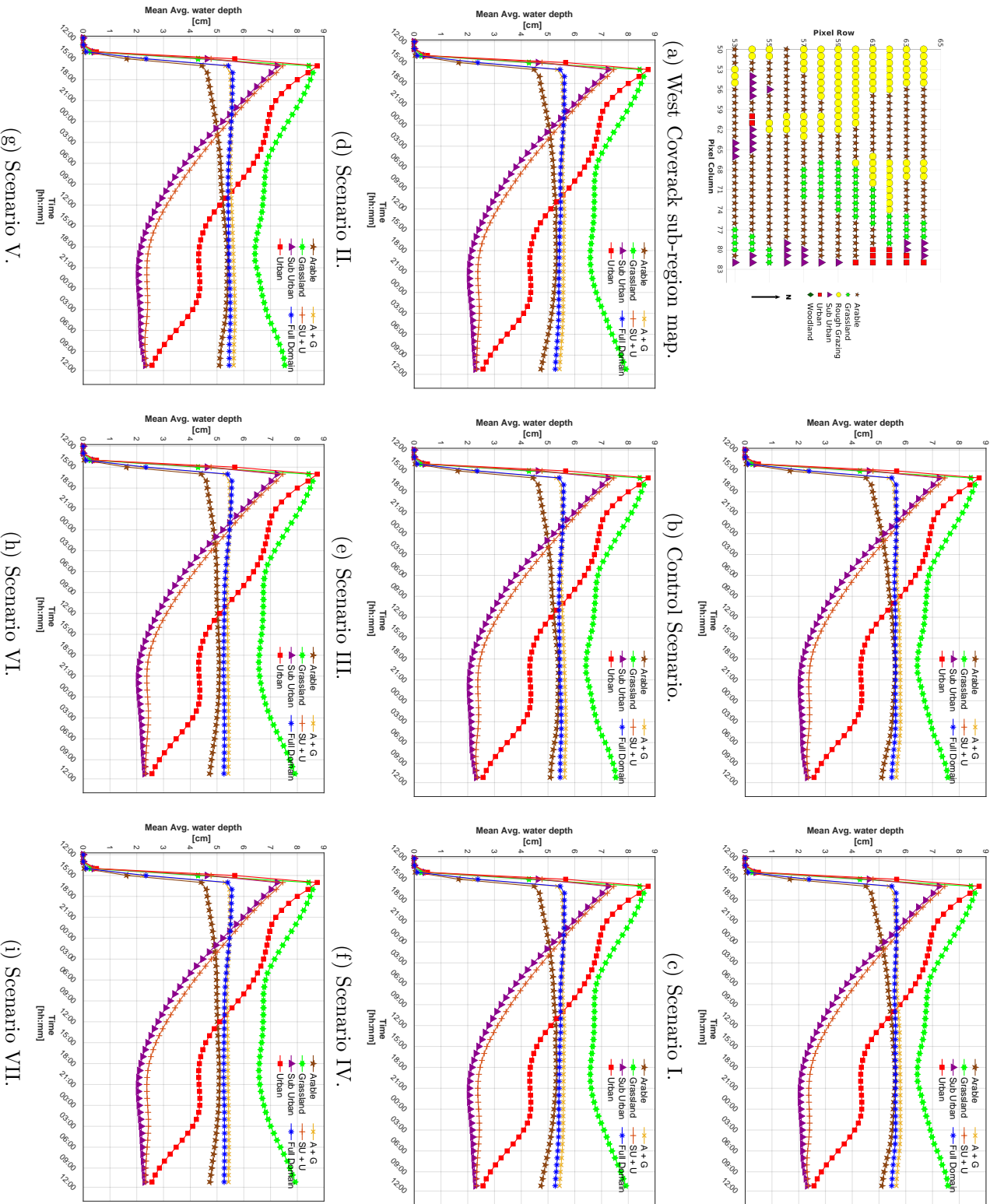


Figure 7.9.: Mean water depth values averaged across each land-use for each modelling scenario within the Western Coverack sub-region.

## 7.7. Discussion

The model data input used for the scenario analysis in Sections 7.5 and 7.6 came from a report written by JBA Consulting that was commissioned by the Environment Agency (Environment Agency and Cornwall Council, 2018). The average mean water depths reviewed in Section 7.6 are modest in nature. The data obtained from the JBA Consulting report was from a 2m resolution model and their simulations focused on Coverack itself (Environment Agency and Cornwall Council, 2018, Figure 7-2, page 58). The combination of having applied the incorrectly resolved input data to a coarser resolution and a wider area meant the average mean water depths per land-use reported were much smaller than what hydrological modellers would expect. To rectify this, one may either apply the model at 2m resolution and focus solely on the Coverack region outlined in Figure 7.4 (page 279), or identify more appropriate input data to use for the 20m resolution model.

The incorrect implementation of input data for the modelling scenario means that one cannot assume these outputs to be realistic. However, for three of the five regions analysed in Section 7.6 (Coverack (7.6.1), Northern Coverack (7.6.2), and Southern Coverack (7.6.4)), Scenario III (and the other scenarios in which it was included) proved the most effective at minimising the average mean water depth for the urban land-use category. This behaviour is representative of what one would expect a land-use management policy planner in the prospective management of a local watershed is looking for. The remaining discussion within this section will assume that the model has been implemented correctly and expand on how a platform outlined in Section 7.4 can be utilised for the management of *natural capital*.

Typically flooding risk assessments use an economic metric known as the *Expected Annual Damage* (EAD). This metric defines a damage-probability curve from the association between the damage estimated with the probability of flooding (Foudi et al., 2015; Sayers et al., 2022). This metric determines EAD through a combination of direct, indirect and intangible damage. Direct damage is calculated via the *Weighted Annual Average Damage method* (Penning-Rowsell et al., 2013; Sayers et al., 2015). This method is used to estimate the direct economic damage from a flood event. Indirect damage considerations are determined from the accumulation of disruption to economic networks and activities within the region due to the flood. Commonly they are assumed to be functions of direct damages. It is estimated that indirect damages add an additional 70% to EAD though this is debated within the literature (Sayers et al., 2015, 2022). Finally, intangible damages relate to the broader losses humans endure due to flooding. This includes the loss of treasured possessions, ill-health, loss of pets, trauma etc. Public Health England (2019) highlighted the significance and importance of these damages and add an extra 20% to the EAD metric.

Through the analysis conducted in Section 7.6, the policy planner has a good initial idea of how their suggested interventions would affect the wider watershed. With the policy proposal of over 50,000 new homes required in Cornwall to meet housing demand (Cornwall Council, 2016), Coverack and the wider region may be identified as a prime

region to contribute to this total in order to fulfil their policy objective. The policy planner could instruct the hydrological model of this proposal and conduct a similar analysis as Section 7.6. One could implement the economic metric, EAD, on the front-end dashboard and compare differing policy proposals to assess the optimal location for new housing developments. There is also scope to construct interesting optimisation problems that could seek to minimise the EAD and highlight the optimal locations for new housing developments that will also meet the Council’s environmental targets. On the other hand, if the location of new housing developments is restricted to a given area, the hydrological model can contribute in further land-use management modelling that present an optimal land-use composition which minimises the EAD metric which in turn minimises flood risk. Flooding has an environmental impact as well as economic. Flooding events exacerbate erosion and introduce more soil, organic matter and pollutants to the watershed. The number of plant biomass, fish and other species have reduced significantly with a greater number of extreme flood events (British Ecological Society, 2013). Population modelling could be modelled from the output of the flooding simulations to estimate the effect of suggested policy proposals, providing a more holistic understanding of the region.

From the perspective of Cornwall Council, the access to a hydrological model via a digital platform would give policy planners safe and secure access to cutting edge modelling techniques without the need for in-depth training on its application (assuming it is correctly implemented). A digital platform would consist of a front-end dashboard and a back-end where many potential natural capital management models could reside. This can empower the Council to investigate prospective policies through such a tool. A management framework could be adopted to ensure the tool is utilised effectively. For example, service level agreements are used in the facilities management industry to set contractual expectations between a service provider and the customer. A quasi-service level agreement framework could be used as a measure of performance for private and/or public entities on their intervention on the hydrological system (e.g. a farmer sewing a new crop which has greater water retention properties or a company constructing a new wetland) to improve the area. This could be facilitated through a front-end dashboard like “myFM”. Equally, this front-end dashboard could be used as a public interaction tool. This same tool could be put into the hands of the public to give them an insight of how policy decisions are made. They could also be used to justify that a car park (for example) is one of the leading causes of ecosystem degradation within the local community by pointing out the various assessment metrics one could use (such as EAD).

## 7.8. Summary

The model implemented for the case study presented in this chapter was developed using the knowledge attained from the literature review (Chapter 2). This informed the approach that was taken in this work. The model constructed in Chapter 4 applied the key mathematical concepts outlined in Chapter 3. Chapters 5 and 6 developed some initial analyses that justified the use of the 20m resolution model in this chapter.

This chapter has presented a plausible scenario in how this tool may be applied to advance the practices of holistically managing natural capital. This work can act as a template to build additional computational tools from different environmental domains. These tools can then be integrated into the “back-end” of a larger collection of devices that can aid policy planners.

Section 7.2 outlined the flooding event which took place in Coverack, Cornwall and how the fictitious storm discussed in Chapter 6 was implemented to emulate this. Section 7.3 defined five sub-regions within the computational domain to allow for a more purposeful analysis. Section 7.4 highlights how the tool discussed in this work is envisaged to be utilised to aid policy decision making. This sections justifies the seven modelling scenarios defined in Section 7.5.

Section 7.6 discussed the average mean water depth outputs per land-use type for each of the sub-regions. The most effective mitigation scenario in this section was Scenario III the ‘Open “Sluice” parameter’ described in Section 7.5.4. It greatly reduced the average mean water depth for the Urban and reduced slightly the values at sub-urban land-use types in the Coverack region (Section 7.6.1). This parameter change also saw a significant drop in output on Urban pixels in the northern (Section 7.6.2) and southern (Section 7.6.4) Coverack regions. Given that no discernable difference in output was noted in the north-eastern (Section 7.6.3) and western (Section 7.6.5) Coverack regions, this parameter change had the most impact on more local analysis regions. This chapter was used to highlight how such a hydrological model could be utilised to aid policy decision makers to manage natural capital whilst attending to the current and future needs of its population.

A discussion on how the hydrological model can be applied to support decision making related to flood risk management is given in Section 7.7 and concludes this chapter. It includes an overview of how metrics associated with “Expected Annual Damage” can be used to aid better decision making.

Through the case study of the Coverack flooding event, this chapter reviewed how flooding risk can be assessed via “Expected Annual Damage” (**RQ7**) and reviewed how mitigation measure suggestions could affect flood management through the seven proposed scenarios in Section 7.5 (**RQ8**).

Chapter 8 will summarise the work within this thesis, in context of the motivation and provide some direction on where this work can be built on.

**Part IV.**

**Conclusions**

## 8. Conclusion

### 8.1. Introduction

This thesis proposed a pilot computational tool which could enable and assist the planning and assessment of policy decisions by public and private stakeholders. Its key benefit was to aid officials in the strive toward the equitable and sustainable use of land to reach our material, cultural and fundamental needs. Utilising the knowledge and understanding of *Ecosystem Services* (Section 1.1.4), one could implement the policy proposals outlined in Cornwall Council's *Environmental Growth Strategy* (Section 1.1.5) by managing its natural asset portfolio in a holistic manner. This work was divided in four constituent parts. Part I laid out the motivational foundation on which this work is built. It reviewed the mathematical literature of hydrological modelling and the mathematics which underpinned the model constructed here. Part II focused on the hydrological model construction and an analysis of its performance over two variant resolutions. In Part III, specific modelling scenarios were assessed in preparation for the implementation of the Coverack flooding case study. Finally, Part IV, this chapter, summarises the work presented within this thesis. It outlines the research contribution and presents further avenues of research to build upon this work.

### 8.2. Thesis Summary

An initial hydrological literature review was carried out and presented in Chapter 2. Hydrological models consist of six key component parts (Section 2.2). An in-depth review of the key modelling methodologies and tools for each of these component parts are given in Sections 2.2.1 - 2.2.6. Section 2.3 gave a brief overview of the computational mesh options that have been used in various hydrological models. Sections 2.4 and 2.5 discussed the advantages and drawbacks of the most common hydrological model types, semi- and fully-distributed models respectively. Section 2.6 identified the research gap this work was attempting to fill. Finally, Section 2.7 utilised the knowledge attained from the literature review and the context in which it is being built to justify the modelling approach taken within this work.

Chapter 3 provided a summary of the mathematics which underpinned the hydrological model constructed in Chapter 4. The necessary mathematical definitions needed to build upon the theory within the chapter was given in Section 3.2. Key to understanding the model construction was the linear and multivariate Riemann Problem outlined

in Sections 3.2.2 and 3.2.3 respectively. Section 3.3 highlighted the value of conservation laws in hydrological modelling. In particular, the solution characteristic behaviours of the non-linear advection equation, wave-steepening, shockwaves and rarefaction waves. Godunov's numerical method is reviewed in Section 3.4 expanding on the theory of upwind methods. Key to understanding the implementation used for the surface routing component of the model constructed in Chapter 4 is the Godunov Finite Volume Method described in Section 3.4.6.1. Chapter 3 continued with Section 3.5, which introduced the theory behind "Total Variation Diminishing Methodology" and how it is applied to flux limiters. This chapter concluded with a review of the specific mathematical literature of infiltration modelling in Section 3.6.

The computational domain mesh on which the hydrological model was constructed commenced Chapter 4 in Section 4.2. The model construction began in Section 4.3 by considering the modelling of the governing equations themselves in Section 4.3.1. For the overland flow routing component of the model, the HLLC approximate Riemann solvers and its implementation were outlined in Section 4.3.2. The unsaturated zone component of the hydrological model focused on the infiltration methodology (Section 4.3.5). Specifically the Green-Ampt approximation model in Section 4.3.5.1 and the implementation of the SCS method in Section 4.3.5.2. The chapter continued with a description of the boundary conditions applied (Section 4.3.6) and the application of empirical parameters to represent the interception component of the hydrological model (Section 4.3.7). This chapter concluded with an overview of how calibration of the model should be conducted (Section 4.3.8) alongside the model limitations and future work needed to improve it (Section 4.3.9).

Two model variants of the model constructed in Chapter 4 were compared with one another, a 20m and 50m model, in Chapter 5. An analysis framework was described in Section 5.2 with two sub-regions within the computational domain identified to perform the analysis on. Section 5.3 outlined the common model inputs and parameters which were applied for the analysis. Section 5.4 compared the model performance between the two resolutions for the north-eastern sub-region. Similarly, Section 5.5 outlined the model performance comparison within the northern sub-region of the computational domain.

Chapter 6 developed a fictitious storm as a hydrological input, instead of a uniform input which was implemented in Chapter 5. The methodology in constructing the storm was presented in Section 6.2. Two storm scenarios were analysed for both the 20m and 50m hydrological model variants. For each scenario a "static" storm model input was compared with a "moving" storm. Section 6.3 considered the scenario where the storm moved centrally across the computational domain. Finally, Section 6.4 analysed the model outputs for the storm at the south-east of the domain.

Chapter 7 implemented the model constructed in Chapter 4 to demonstrate how such a hydrological model may be utilised to aid policy decision planners to manage natural capital along with other competing priorities. Section 7.2 discussed the flooding event of Coverack, Cornwall. The fictitious storm constructed in Section 6.4.2 was used as a blueprint to represent the storm event which took place in Coverack on that day. Five



sub-regions were defined in the computational domain for a more purposeful analysis in Section 7.3. Seven modelling scenarios were outlined in Section 7.5 with the parameter changes being implemented. The selection of these scenarios are highlighted in Section 7.4. Finally, the mean average water depth outputs per land-use type for each of the sub-regions defined in Section 7.3 were analysed.

### 8.3. Research Contribution

The broadest aim of this thesis was to explore and highlight the opportunity in widening computational tool access so that they may be utilised in the management of natural capital. This access will remove the need for expert practitioners to implement complex modelling techniques. A holistic computational tool to manage natural capital will aid in the monitoring of the sustainability, economic and social impacts proposed policies could have on a given region. A “front-end dashboard” templated on “MyFM” described in Section 1.1.6 is one possible way to widen the access to these models. Through “plug-and-play” features on the front facing UI, policy planners could test their proposed policies and gain an understanding of their potential impact before they are implemented. On the “back-end” of the computational tool the most up-to-date environmental models would reside, ready to implement the calculations needed to test a planner’s proposals.

To realise this broader aim, this work identified Cornwall Council’s “Environmental Growth Strategy” policy (Section 1.1.5). In essence this policy is focused on transitioning Cornwall’s economy to be less reliant on carbon based economic activity while promoting its natural capital assets. This policy document highlighted the need for an “environmental management system” to help monitor and support environmental growth within the county (Target outcome 4, Section 1.1.5.1).

A vast array of environmental models may have been applied to begin the construction of this environmental management system. However, this work noted the need for over 50,000 new homes in Cornwall by 2030. This would severely inhibit the hydrological properties of Cornish watersheds to adequately deal with potential flooding events. Due to the well-established field of hydrological modelling, it was decided that this tool was the natural choice in beginning the construction *towards a computational tool for the management of natural capital*. The research objectives listed in Section 1.3.1 guided the structure of this thesis and the research questions identified were answered in their respective chapters.

In striving to meet these aims and objectives, this work introduced the application and implementation of hydrological models in wider natural capital system management context. It highlighted the value of broadening access to current cutting-edge mathematical models to aid current policy implementation efforts. Secondly, a novel approach to implementing the Green-Ampt model was introduced. This effort saw a replacement of the Newton-Raphson methodology used for scenarios where ponding occurs. This replacement came in the form of a linear approximation where infiltration occurred at a constant

rate provided there was enough infiltration capacity in the soil (Section 4.3.5.1). The example used to justify this approach showed excellent agreement between the full model which included the Newton-Raphson component and its approximation. To the best of my knowledge, this method has not been implemented in the literature before.

## 8.4. Future Research Recommendations

There are three broad areas of research that may be pursued as a result of this work. The first area consists of work not completed within this thesis that should have been done. A comparison of the hydrological model constructed in this work should be compared with the hydrological models in the literature. A lack of real data during this work meant that the hydrological model was not calibrated. Calibration of this model with real data alongside a comparison with existing methods in the literature would provide extra confidence of the suitability of the model in its application to natural capital management. The Green-Ampt model approximation in Section 4.3.5.1, utilised an example from the literature to compare its performance against the full model. This model could be applied for different examples than the one used in this work to ensure that this method works in differing contexts. It would also benefit the research gap if the mathematical model constructed in this thesis was redesigned. The hydrological model constructed in this thesis produced an output with the unit of measurement in centimetres and not millimetres as is most common in hydrological literature. A unit of measurement in millimetres is also more physically intuitive. I faced many periods of interruptions which resulted in a disjointed research period. A consequence of this was the fact that the output was an order of magnitude out. In order to get the model to run successfully, the threshold described in Equation (4.28) had to be increased to  $\epsilon_h = 10^{-2}$ .

The second area of work consists of research that can improve on the work completed in this thesis. The model constructed utilised an empirical representation of the interception component. One could implement a fully working interception model and add the evapotranspiration component to provide a more complete hydrological model. Also, it has been suggested by Khakbaz et al. (2012) that semi-distributed models can perform at least as well, if not better than, fully-distributed hydrological models if built correctly. Section 2.5 on page 85 noted that coarse grid models may only be considered a generalisation. For scales which are larger than a few metres resolution, runoff depth and velocity have very little physical meaning. The small variations of those two parameters may not be that important due to the spatial variability inherent when considering a large river basin. Within this work a fully-distributed model was constructed. However, if a similar semi-distributed model was to be built, this would reduce the amount of computational effort and time needed to provide results for policy decision makers and limit the need for parameters with little physical meaning when considering coarser resolutions. Equally, if one is adamant on using a fully-distributed model, then running this model in a high performance computing environment should be seriously considered.

The final area of work focuses on how the tool constructed in this thesis can be imple-

mented to ensure it has a wider impact on policy making. Section 1.1.6 motivated this work by highlighting the parallels between the facilities management industry and natural capital accounting. There was an intent to translate the analytical framework and terminology from facilities management to natural capital management. Unfortunately midway through, I had lost contact with the main collaborators of this work. As such, this avenue was not pursued and there is an opportunity to develop this framework in future. There is also space to work with the “back-end” computational tool to define natural capital metrics which can be presented on the “front-end” dashboard. Having a pre-defined and well-understood decision framework will allow for comparison of policy proposals to provide additional insight. Additionally, this computational modelling tool concept may also be expanded to other ecological and natural phenomena. Other mathematical models may be constructed on the backend with their results presented on a dashboard for policy decision makers. This would allow such stakeholders an insight into the complexities of their local environment. The dynamic interaction and complexity of ecosystems can make it difficult to accurately predict the future of plant, animal and micro-organism communities due to their interdependence on one another. Such other models may include applying robust set-point regulation problems to ecological models with multiple management goals (Guiver et al., 2016), applying empirical models for effective conservation and population management (Stott et al., 2011) or implementing an adaptive switching feedback control scheme to ensure the persistence of managed resources (Franco et al., 2022). Finally, many interesting optimisation problems do arise from ecosystem management. In the context of this work, one can envisage a policy planner using the “front-end” of the dashboard to restrict a parameter space (e.g. by insisting a housing development is located in a specific region of a computational domain). Then an optimisation algorithm, using this restricted parameter space, look to minimise metrics that is important to the policy planner (e.g. the “Expected Annual Damage” for instance). Many variants of this optimisation and planning problem could be defined to inform a policy planner’s longer term strategic goals.

# Appendix

## A. Modelling foundations

### A.1. Fundamental properties of Hyperbolic Partial Differential Equations

The fundamental properties associated with hyperbolic partial differential equations is presented. Studying these properties will help to understand the underlying theory applied in the modelling process discussed in Chapter 4.

#### A.1.1. Quasi-Linear Equations

A system of first-order partial differential equations may be written in the form

$$\frac{\partial u_i}{\partial t} + \sum_{j=1}^m a_{ij}(x, t, u_1, \dots, u_m) \frac{\partial u_j}{\partial x} + b_i(x, t, u_1, \dots, u_m) = 0 \quad (.1)$$

where  $i \in \{1, \dots, m\}$ . Equation (.1) is a system of  $m$  equations with  $m$  unknown dependent variables  $u_i$ . These unknowns are expressed with the independent variables of space and time,  $x, t$  as  $u_i = u_i(x, t)$ ; the partial derivatives of the unknown variable with respect to time and space are  $\partial u_i / \partial t$  and  $\partial u_i / \partial x$  respectively. For brevity, these notations will be interchangeably used with their subscript counterparts  $u_t$  and  $u_x$ . One may also re-write (.1) in matrix form as

$$\mathbf{U}_t + \mathbf{A}\mathbf{U}_x + \mathbf{B} = \mathbf{0} \quad (.2)$$

where

$$\mathbf{U} = \begin{bmatrix} u_1 \\ u_2 \\ \vdots \\ u_m \end{bmatrix}, \quad \mathbf{B} = \begin{bmatrix} b_1 \\ b_2 \\ \vdots \\ b_m \end{bmatrix}, \quad \mathbf{A} = \begin{bmatrix} a_{11} & \cdots & a_{1m} \\ a_{21} & \cdots & a_{2m} \\ \vdots & \vdots & \vdots \\ a_{m1} & \cdots & a_{mm} \end{bmatrix}. \quad (.3)$$

Provided that each entry of matrix  $\mathbf{A}$ ,  $a_{ij}$ , is constant, as well as every entry of vector  $\mathbf{B}$ ,  $b_i$ , then the system may be described as *linear with constant coefficients*. If the entries of  $\mathbf{A}$  and  $\mathbf{B}$  are dependent on the independent variables  $x, t$  i.e.  $a_{ij} = a_{ij}(x, t)$  and  $b_i = b_i(x, t)$  then the system is considered to be *linear with variable coefficients*.

If  $\mathbf{B}$  is a function of vector  $\mathbf{U}$  so that  $\mathbf{B} = \mathbf{B}(\mathbf{U})$  the system is still considered to be linear. If  $\mathbf{B} = \mathbf{0}$  then we denote the system *homogeneous*. If  $\mathbf{A} = \mathbf{A}(\mathbf{U})$  then the system is *quasi-linear*. Quasi-linear systems are typically thought of as a subset of general systems of non-linear equations.

### A.1.2. Fundamentals of Hyperbolic Systems

A partial differential equation in the form of Equations (.2) and (.3) is defined as *hyperbolic* at the point  $(x, t)$  provided  $\mathbf{A}$  has  $m$  real eigenvalues  $\lambda^{(1)}, \dots, \lambda^{(m)}$  which correspond to a set of  $m$  linearly independent right eigenvectors  $\mathbf{e}^{(1)}, \dots, \mathbf{e}^{(m)}$ . If all eigenvalues  $\lambda^{(i)}$  are distinct, then the system is *strictly hyperbolic*. Strict hyperbolicity ensures hyperbolicity as real, distinct eigenvalues are accompanied with a set of linearly independent eigenvectors. If none of the eigenvalues of  $\mathbf{A}$  are real at a point  $(x, t)$  then the system is *elliptic* (Chow et al., 1988; Evans, 2010).

**A.1.2.1. Characteristic and the General Solution structure** One may define a *characteristic curve* or *characteristic* as a set of curves  $x = x(t)$  located in the  $t - x$  plane such that the initial PDE transforms into an ODE. As such the variable  $u$  is considered solely dependent on the temporal variable as  $u = u(x(t), t)$ .

$$\frac{du}{dt} = \frac{\partial u}{\partial t} + \frac{dx}{dt} \frac{\partial u}{\partial x}. \quad (.4)$$

Assuming the characteristic curve  $x = x(t)$  satisfies the ODE

$$\frac{dx}{dt} = a, \quad (.5)$$

combining the PDE from (3.1) with (.4) and (.5) yields

$$\frac{du}{dt} = \frac{\partial u}{\partial t} + a \frac{\partial u}{\partial x} = 0. \quad (.6)$$

Observing from (.6),  $u$  is constant as it traces the curve  $x = x(t)$ , or that the rate of change along the characteristic curve is zero. The wave propagation speed  $a$  is typically referred to as the *characteristic speed* and is defined as the gradient of the curve  $x = x(t)$  as stated in (.5). Figure A.1 shows a set of characteristic curves  $x = x(t)$  defined by the ODE in (.5) where  $a > 0$ . Setting an initial condition

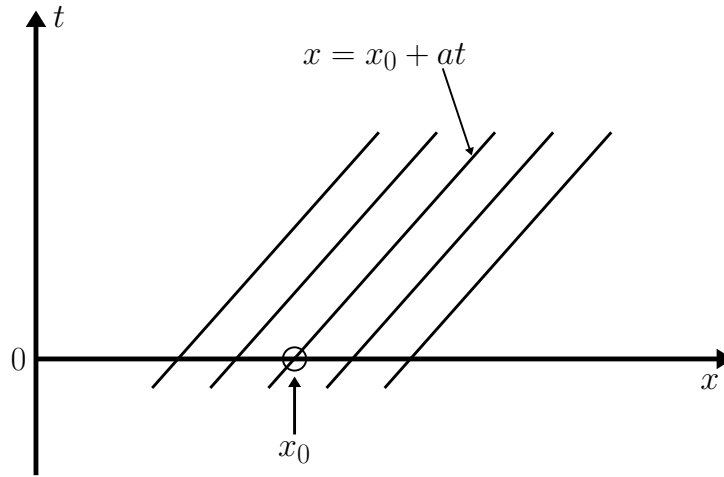


Figure A.1.: An illustration of the characteristics present for the linear advection equation with characteristic speed  $a > 0$ . The initial position  $x_0$  is a fixed initial condition at  $t = 0$ .

$$x(0) = x_0, \tag{.7}$$

a single characteristic curve is identified passing through the point  $(x_0, 0)$  using (.5) as

$$x = x_0 + at. \tag{.8}$$

Hyperbolic PDEs with constant coefficients all have curves which are parallel to one another. Using the result from (.6) that  $u$  is constant along characteristic curves a solution to the PDE (3.1) may be defined as

$$u(x, t) = u_0(x_0) = u_0(x - at). \tag{.9}$$

The solution in (.9) comes from defining an initial value  $u(x, 0) = u_0(x)$  at time  $t = 0$ . Thus the whole characteristic curve is defined as  $x(t) = x_0 + at$  which passes through  $x_0$  on the  $x$ -axis.

Hence, in context of the PDE in (3.1): given an initial value profile  $u_0(x)$ , this PDE will translate with velocity  $a$  to the right (left) provided  $a > 0$  ( $a < 0$ ). This PDE system contains the fundamental hallmarks associated with wave propagation behaviour which will be utilised in the work below.

### A.1.3. Linear Hyperbolic Systems

**A.1.3.1. Diagonalisation and Characteristic Variables** In order to analyse and resolve a general initial value problem it is beneficial to transform the dependent variables  $\mathbf{U}(x, t)$  to a new set of dependent variables  $\mathbf{W}(x, t)$ . A new definition known as a

diagonalisable system is required.

### A.1.3.2. A Diagonalisable System

The matrix  $\mathbf{A}$  is *diagonalisable* if it can be expressed as

$$\mathbf{A} = \mathbf{E}\mathbf{\Lambda}\mathbf{E}^{-1} \quad \text{or} \quad \mathbf{\Lambda} = \mathbf{E}^{-1}\mathbf{A}\mathbf{E}, \quad (.10)$$

in terms of a diagonal matrix  $\mathbf{\Lambda}$  and matrix  $\mathbf{E}$ . The diagonal entries of  $\mathbf{\Lambda}$  are the eigenvalues  $\lambda^{(i)}$  of  $\mathbf{A}$ . The columns  $\mathbf{E}^{(i)}$  of  $\mathbf{E}$  are the right eigenvectors of  $\mathbf{A}$  which correspond to their respective eigenvalues.

$$\mathbf{\Lambda} = \begin{bmatrix} \lambda^{(1)} & \cdots & 0 \\ 0 & \cdots & 0 \\ \vdots & \vdots & \vdots \\ 0 & \cdots & \lambda^{(m)} \end{bmatrix}, \quad \mathbf{E} = \left[ \mathbf{E}^{(1)}, \quad \dots, \quad \mathbf{E}^{(m)} \right], \quad \mathbf{A}\mathbf{E}^{(i)} = \lambda^{(i)}\mathbf{E}^{(i)}. \quad (.11)$$

Hence a system such as (3.4) is considered diagonalisable if its coefficient matrix  $\mathbf{A}$  is diagonalisable. From this concept, typically hyperbolic systems are set up with real eigenvalues and a diagonalisable matrix.

### A.1.3.3. Characteristic Variables

Using the inverse matrix  $\mathbf{E}^{-1}$ , a new set of dependent variables  $\mathbf{W} = (w_1, w_2, \dots, w_m)^T$  is defined using the transformation

$$\mathbf{W} = \mathbf{E}^{-1}\mathbf{U} \quad \text{or} \quad \mathbf{U} = \mathbf{E}\mathbf{W}. \quad (.12)$$

When this transformation is applied, the linear system (3.4) becomes entirely decoupled. These newly defined terms  $\mathbf{W}$  are referred to as the *characteristic variables*.

To rewrite the governing equations in terms of the characteristic variables provided consider writing  $\mathbf{U}_t$  and  $\mathbf{U}_x$  in terms of  $\mathbf{W}$ . Since  $\mathbf{A}$  is constant its eigenvectors are also constant and so

$$\mathbf{U}_t = \mathbf{E}\mathbf{W}_t, \quad \mathbf{U}_x = \mathbf{E}\mathbf{W}_x. \quad (.13)$$

By direct substitution the system may be expressed in terms of the characteristic variables as

$$\mathbf{E}W_t + \mathbf{A}EW_x = \mathbf{0}. \quad (.14)$$

Ascertaining the *characteristic* or *canonical form* of (3.4) by multiplying from the left  $\mathbf{E}^{-1}$  yields

$$\mathbf{W}_t + \mathbf{\Lambda}W_x = \mathbf{0}. \quad (.15)$$

Written fully the canonical form (.15) looks like

$$\begin{bmatrix} w_1 \\ w_2 \\ \vdots \\ w_m \end{bmatrix}_t + \begin{bmatrix} \lambda^{(1)} & \cdots & 0 \\ 0 & \cdots & 0 \\ \vdots & \vdots & \vdots \\ 0 & \cdots & \lambda^{(m)} \end{bmatrix} \begin{bmatrix} w_1 \\ w_2 \\ \vdots \\ w_m \end{bmatrix}_x = \mathbf{0}. \quad (.16)$$

Thus the  $i$ -th PDE of the system is

$$\frac{\partial w_i}{\partial t} + \lambda^{(i)} \frac{\partial w_i}{\partial x} = 0, \quad \text{where } i \in \{1, \dots, m\}. \quad (.17)$$

Equation (.17) contains a single unknown  $w_i(x, t)$  and hence is decoupled and identical to the linear advection equation discussed in (3.1) and Section A.1.2.1. As such there exists  $m$  characteristic curves which satisfy  $m$  ODEs each with characteristic speed  $\lambda^{(m)}$  i.e.

$$\frac{dx}{dt} = \lambda^{(m)}, \quad \text{for } i \in \{1, \dots, m\}. \quad (.18)$$

To illustrate the theory that is presented in Section 3.2.3.1 consider a general  $2 \times 2$  linear hyperbolic system. Figure 3.4 shows two waves emerging from the origin  $(0, 0)$  in the  $(x, t)$  plane with speeds equal to  $\lambda^{(1)}$  and  $\lambda^{(2)}$ .

Table A.1.: A comparison between the structures of the linear hyperbolic systems in Sections 3.2.1 and A.1.3.1.

Equation	PDE	ODE
<b>Linear Advection</b>	(.6): $u_t + au_x = 0$	(.5): $x_t = a$
<b>Characteristic Variable</b>	(.17): $(w_i)_t + \lambda^{(i)}(w_i)_x = 0$	(.18): $x_t = \lambda^{(i)}$

Table A.1 compares the structures of the linear hyperbolic systems discussed in Sections 3.2.1 and A.1.3.1.

To the left of  $dx/dt = \lambda^{(1)}$  is the initial state  $\mathbf{U}_l = a_1\mathbf{E}^{(1)} + a_2\mathbf{E}^{(2)}$ . Similarly, the initial state  $\mathbf{U}_r = b_1\mathbf{E}^{(1)} + b_2\mathbf{E}^{(2)}$  is the solution to the right of the ODE  $dx/dt = \lambda^{(2)}$ . The



section to the right of the left wave and left of the right wave is most commonly referred to as the *star region* with the solution denoted  $\mathbf{U}_*$ . Its value is determined by considering the pathway of the two waves which emanate from the origin of the initial discontinuity.

Starting from a point  $P_*(x, t)$  within the star region we trace along the characteristic curves with speeds  $\lambda^{(1)}$  and  $\lambda^{(2)}$ . These characteristics are represented by the dashed lines in Figure 3.4 and are parallel to the characteristics which pass through the origin. The characteristic curves which pass through  $P_*$  also pass through the initial points  $x_0^{(1)} = x - \lambda^{(1)}t$  and  $x_0^{(2)} = x - \lambda^{(2)}t$ .

The solution may be expressed in the form of (3.11) and now one must select the correct corresponding coefficients which satisfy these characteristic curves. A time  $t^*$  and point  $x_l$  to the left of the slowest wave is chosen so that  $\mathbf{U}(x_l, t^*) = \mathbf{U}_l$ . Highlighted in Figure 3.5 is the starting point  $(x_l, t^*)$ . Since this is to the left of the  $\lambda^{(1)}$ -wave every coefficient is  $a_i$ . As we trace the horizontal line  $t = t^*$  we eventually pass the wave  $dx/dt = \lambda^{(1)}$ , where  $x - \lambda^{(1)}t$  changes sign (as expressed in (3.10)). As such the constant coefficient changes from  $a_1$  to  $b_1$ . Hence, the solution within the entire star region between the two waves is

$$\mathbf{U}_*(x, t) = b_1 \mathbf{E}^{(1)} + a_2 \mathbf{E}^{(2)}. \quad (.19)$$

Continuing to move rightward one eventually crosses the  $\lambda^{(2)}$  wave where  $x - \lambda^{(2)}t$  changes from negative to positive. Again, utilising the result in (3.10) the right initial state i.e. the solution to the right of the fastest wave speed is obtained,

$$\mathbf{U}_r(x, t) = b_1 \mathbf{E}^{(1)} + b_2 \mathbf{E}^{(2)}. \quad (.20)$$

#### A.1.4. The Riemann Problem in Linearised Gas Dynamics

To solidify an understanding of the methodology presented in Sections A.1.3 - 3.2.3 consider the  $2 \times 2$  system present in the linearised Equations of Gas Dynamics. These equations are expressed as

$$\begin{aligned} \frac{\partial \rho}{\partial t} + \rho_0 \frac{\partial u}{\partial x} &= 0 \\ \frac{\partial u}{\partial t} + \frac{\alpha^2}{\rho_0} \frac{\partial \rho}{\partial x} &= 0 \end{aligned} \quad (.21)$$

In this system the unknowns are  $u_1 = \rho(x, t)$  and speed  $u_2 = u(x, t)$ ;  $\alpha$  is the speed of sound, a positive constant.  $\rho_0$  is a constant reference density.

Rewriting this system in matrix form as

$$\mathbf{U}_t + \mathbf{A}\mathbf{U}_x = \mathbf{0}, \quad (.22)$$

where

$$\mathbf{U} = \begin{bmatrix} u_1 \\ u_2 \end{bmatrix} = \begin{bmatrix} \rho \\ u \end{bmatrix}, \quad \mathbf{A} = \begin{bmatrix} 0 & \rho_0 \\ \alpha^2/\rho_0 & 0 \end{bmatrix}, \quad (.23)$$

with initial data

$$\mathbf{U}(x, 0) = \begin{cases} \mathbf{U}_l = [\rho_l \ u_l]^T, & \text{if } x < 0 \\ \mathbf{U}_r = [\rho_r \ u_r]^T, & \text{if } x > 0. \end{cases} \quad (.24)$$

Matrix  $\mathbf{A}$  has two distinct and real eigenvalues

$$\lambda^{(1)} = -\alpha, \quad \lambda^{(2)} = +\alpha, \quad (.25)$$

with corresponding right eigenvectors

$$\mathbf{E}^{(1)} = \begin{bmatrix} \rho_0 \\ -\alpha \end{bmatrix}, \quad \mathbf{E}^{(2)} = \begin{bmatrix} \rho_0 \\ \alpha \end{bmatrix}. \quad (.26)$$

Deconstructing the left Riemann state  $\mathbf{U}_l$  from (.24) into terms of constant coefficients  $a_1$  and  $a_2$  and the eigenvectors in (.26) gives

$$\mathbf{U}_l = \begin{bmatrix} \rho_l \\ u_l \end{bmatrix} = a_1 \begin{bmatrix} \rho_0 \\ -\alpha \end{bmatrix} + a_2 \begin{bmatrix} \rho_0 \\ \alpha \end{bmatrix}. \quad (.27)$$

Solving for the unknown constant coefficients

$$a_1 = \frac{\alpha\rho_l - \rho_0 u_l}{2\alpha\rho_0}, \quad a_2 = \frac{\alpha\rho_l + \rho_0 u_l}{2\alpha\rho_0}. \quad (.28)$$

Through analogous analysis the right Riemann state is expanded  $\mathbf{U}_r = [\rho_r \ u_r]^T$  to obtain the coefficients

$$b_1 = \frac{\alpha\rho_r - \rho_0 u_r}{2\alpha\rho_0}, \quad b_2 = \frac{\alpha\rho_r + \rho_0 u_r}{2\alpha\rho_0}. \quad (.29)$$

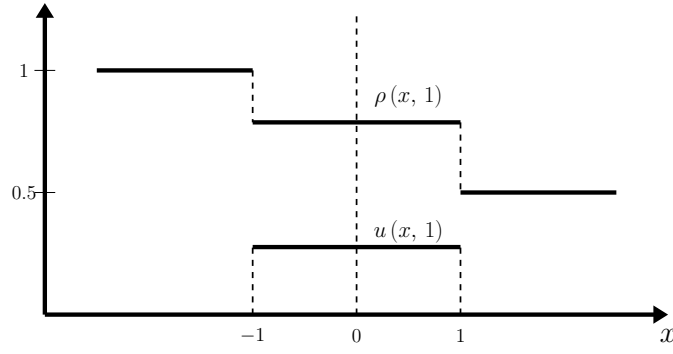


Figure A.2.: A diagrammatic version of the solution to the linearised gas dynamics Riemann problem. Here the density  $\rho(x, t)$  and velocity  $u(x, t)$  profiles at  $t = 1$  are shown. Initial parameter values are  $p_0 = 1$ ,  $\alpha = 1$  with  $(\rho_l, u_l) = (1, 0)$  and  $(\rho_r, u_r) = (0.5, 0)$ .

Applying the analysis from Section 3.2.3.2 and using the solution structure (.19) the solution for the star region is

$$\mathbf{U}_* = \begin{bmatrix} \rho_* \\ u_* \end{bmatrix} = b_1 \begin{bmatrix} \rho_0 \\ -\alpha \end{bmatrix} + a_2 \begin{bmatrix} \rho_0 \\ \alpha \end{bmatrix}, \quad (.30)$$

which yields after some algebraic manipulation

$$\begin{aligned} \rho_* &= \frac{1}{2}(\rho_l + \rho_r) - \frac{\rho_0}{2\alpha}(u_r - u_l) \\ u_* &= \frac{1}{2}(u_l + u_r) - \frac{\alpha}{2\rho_0}(\rho_r - \rho_l). \end{aligned} \quad (.31)$$

Hence in this example, for the entire domain where  $t > 0$  the piecewise constant solution is

$$\mathbf{U}(x, t) = \begin{bmatrix} \rho(x, t) \\ u(x, t) \end{bmatrix} = \begin{cases} \mathbf{U}_l, & \text{if } 0 < t \leq -x/\alpha \\ \mathbf{U}_*, & \text{if } 0 \leq |x|/\alpha \\ \mathbf{U}_r, & \text{if } 0 < t < x/\alpha. \end{cases} \quad (.32)$$

Figure A.2 shows a solution for  $\rho(x, t)$  and  $u(x, t)$  at time  $t = 1$ .

## A.2. Numerical Modelling and the Upwind Scheme

### A.2.1. Numerical Modelling and Discretisation

Challenges and opportunities in the real world often turn to mathematics to gain a better appreciation of a problem and potential solutions. Oftentimes these problems require an abstract mathematical representation, known as a model which, with clearly stated

assumptions, limitations and simplifications, can approximate the behaviours of real world phenomena. For example, the advection equation introduced in Section 3.2.1, equation (3.1) is an example of an abstract mathematical model describing the transportation of a given substance by bulk motion of a fluid.

It is often the case that these mathematical models cannot be solved in all generality. *Numerical modelling* is the process by which computational power is utilised to locate some of these solutions. *Numerical methods* are mathematical tools which are applied to find approximate solutions to models which cannot be solved analytically.

*Discretisation* is the process of translating continuous functions, models, variables and equations into distinct segments. Numerical methods utilise a set of finite discrete values in place of the continuous problem set by the mathematical model, for example the advection PDE equation on page 99.

The mathematical domain of the model one is interested in is discretised into a finite set of points or volumes known as a *mesh* or *grid*. Many discretisation approaches exist in the literature. Here the *finite difference* approach to introduce numerical method concepts will be discussed. Building on these concepts we then look at *finite volume* approaches.

### A.2.2. Derivative Approximations

A central component to finite difference methods are difference quotients, more commonly referred to as approximations to derivatives. Consider an illustrative example displayed in Figure A.3. Assuming a function  $f(x)$  is sufficiently smooth, define a derivative approximation about a defined point  $x_0$  and its neighbouring points  $x_0 \pm \Delta x$  which are all equally spaced. Three basic mathematical expressions of finite difference exist:

1. *Forward difference* takes the expression of the form

$$f^{(1)}(x_0) = \frac{f(x_0 + \Delta x) - f(x_0)}{\Delta x} + O(\Delta x). \quad (.33)$$

2. *Backward difference* uses the points  $x_0$  and  $x_0 - \Delta x$  to yield

$$f^{(1)}(x_0) = \frac{f(x_0) - f(x_0 - \Delta x)}{\Delta x} + O(\Delta x). \quad (.34)$$

3. *Central difference* utilises both points which neighbour  $x_0$  as follows

$$f^{(1)}(x_0) = \frac{f(x_0 + \Delta x) - f(x_0 - \Delta x)}{2\Delta x} + O(\Delta x^2). \quad (.35)$$

The forward (.33) and backward (.34) difference equations are a first-order approximation to the derivative of  $f(x)$ . These are *one-sided* approximations to the derivative, since the derivative is approximated by values to the right and left hand side of  $x_0$  respectively.

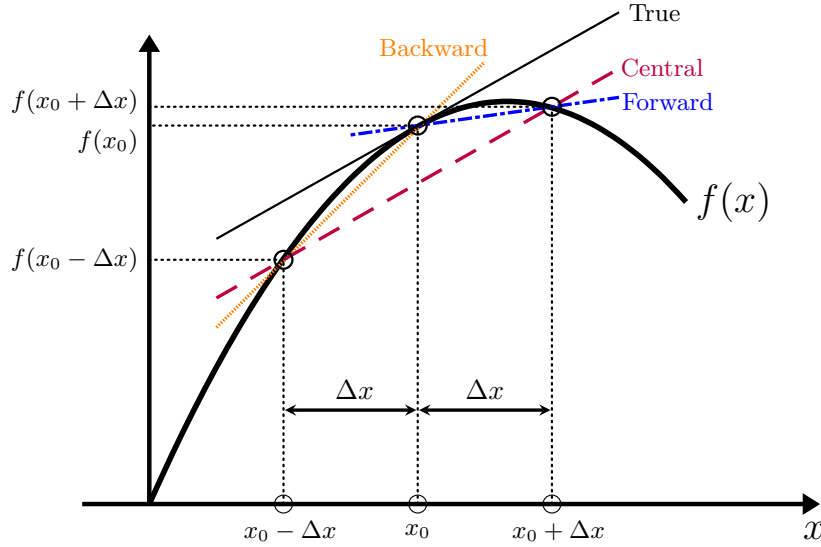


Figure A.3.: An illustration of all three finite difference approximations to the first derivative of function  $f(x)$  about the point  $x_0$ ; backward (orange), central (purple) and forward (blue). The true derivative is the line tangent to the curve at  $f(x_0)$  in black.

The central difference equation (.35) is second-order accurate, using the points  $x_0 \pm \Delta x$  simultaneously to estimate a derivative.

### A.2.3. A finite difference approximation to the advection equation

Consider again the linear advection equation (3.1) but now in the context of an *initial boundary value problem*

$$\begin{cases} \text{PDE:} & u_t + au_x = 0, \\ \text{IC:} & u(x, 0) = u_0(x), \\ \text{BCs:} & u(0, t) = u_l(t), \quad u(N, t) = u_r(t). \end{cases} \quad (.36)$$

To solve (.36) one begins by evolving a solution  $u(x, t)$  from the initial condition  $u_0(x)$  at  $t = 0$  subject to boundary conditions. One potential finite difference mesh where we may discretise the domain is shown in Figure A.4. Each grid has the dimension of  $(\Delta x, \Delta t)$  regularly spaced in the spatial ( $x$ -direction) and time,  $t$ , dimensions. If the spatial direction is discretised by  $n$  equally spaced points the spatial width of the grid would be

$$\Delta x = \frac{N}{n-1}. \quad (.37)$$

Each mesh point is located at  $u(x_i, t^{(k)}) \equiv (i\Delta x, k\Delta t)$  where  $i \in \{1, \dots, N\}$  and  $k \in \{1, \dots, T\}$ . Subscript  $i$  and superscript  $k$  denote the discrete spatial dimension and time-level respectively. The symbol  $u_i^{(k)}$  is defined as an approximation to the exact

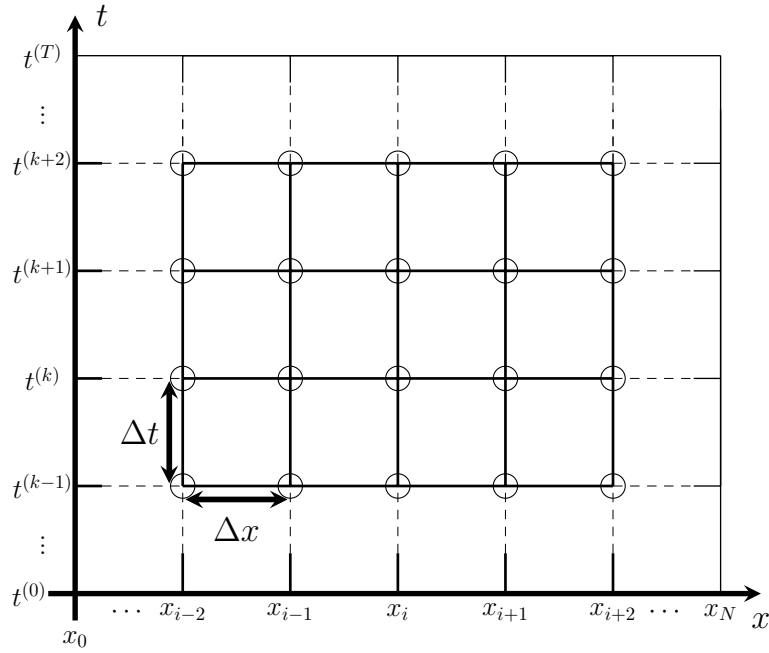


Figure A.4.: Discretisation of a finite difference approximation in the  $x - t$  domain, with a regular mesh of intervals  $\Delta x \times \Delta t$ .

mesh value  $u(x_i t^{(k)})$  where

$$u_i^{(k)} \equiv u(i\Delta x, k\Delta t) \equiv u(x_i, t^{(k)}). \quad (.38)$$

To solve (.36) the solution at the next time level  $k + 1$  is required. Boundary values  $u_0^{(k)}$  and  $u_N^{(k)}$  are defined before hand and applied at the appropriate time-level. For simplicity, we assume that these boundary conditions are constant at all time levels.

Applying the first-order forward finite difference approximation to  $u_t$  in (.36)

$$u_t \approx \frac{u_i^{(k+1)} - u_i^{(k)}}{\Delta t} \quad (.39)$$

One can either substitute a first-order backward or forward finite difference approximation depending on the propagation speed  $a$

$$u_x = \begin{cases} \frac{u_i^{(k)} - u_{i-1}^{(k)}}{\Delta x}, & \text{if } a > 0 \\ \frac{u_{i+1}^{(k)} - u_i^{(k)}}{\Delta x}, & \text{if } a < 0. \end{cases} \quad (.40)$$

Substituting the forward finite difference approximations for  $u_t$  and backward approximation for  $u_x$  into the PDE in (.36) gives

$$\frac{u_i^{(k+1)} - u_i^{(k)}}{\Delta t} + a \frac{u_i^{(k)} - u_{i-1}^{(k)}}{\Delta x} = 0. \quad (.41)$$

Equation (.41) is often referred to as an ***upwind scheme*** or ***first-order upwind method***. The discretisation of the spatial derivative is dependant on the sign of the wave speed  $a$ . This is the key distinguishing feature of the upwind scheme (Courant et al., 1928). ***Upwind*** refers to the process by which the spatial differencing within the finite difference approximation is calculated on the mesh from which the information (a.k.a wind) flows. Hyperbolic problems, such as the advection equation, has information which exists as waves along the characteristic of the partial differential equation. Using the knowledge of the solution structure a numerical flux function may be constructed. Upwind methods look to obtain this information on each characteristic variable by looking along the direction the information is coming from.

#### A.2.4. The CFL Condition

Equation (.41) is an example of an ***explicit time integration scheme***. Numerical solutions are often able to compute cheaply because the solution required only depends on values from previous timesteps. Despite this computational ease, the choice of timestep is restricted. Consider the computational blueprint in Figure A.5. Here,  $a > 0$ , where the three points on the mesh  $(x_{i-1}, t^{(k)})$ ,  $(x_i, t^{(k)})$  and  $(x_i, t^{(k+1)})$  are vertices on a right angled triangle. The base of the triangle at  $t = k$  spans the ***numerical domain of dependence*** of the scheme we wish to use.

Consider now the characteristic speed  $a$  through the point  $(x_i, t^{(k+1)})$  from Equation (.5),

$$\frac{dx}{dt} = a > 0, \quad (.42)$$

and that the true solution at this point takes the form

$$u_i^{(k+1)} = u(x_i, t^{(k+1)}) = u(x_p - a\Delta t, t^{(k)}), \quad (.43)$$

where  $x_p \in (x_{i-1}, x_i)$ . As the only data points which are available lie on the computational grid, we look to utilise the data at these points to estimate the information at  $x_p$ . Here, a linear interpolation function of the solution  $\hat{u}$  using the points  $(x_{i-1}^{(k)}, u_{i-1}^{(k)})$  and  $(x_i^{(k)}, u_i^{(k)})$  is developed. The distance between  $x_i$  and the point where the true solution resides is equal to the time taken for the solution to travel to the point  $(x_i, t^{(k+1)})$  multiplied by the characteristic speed i.e.

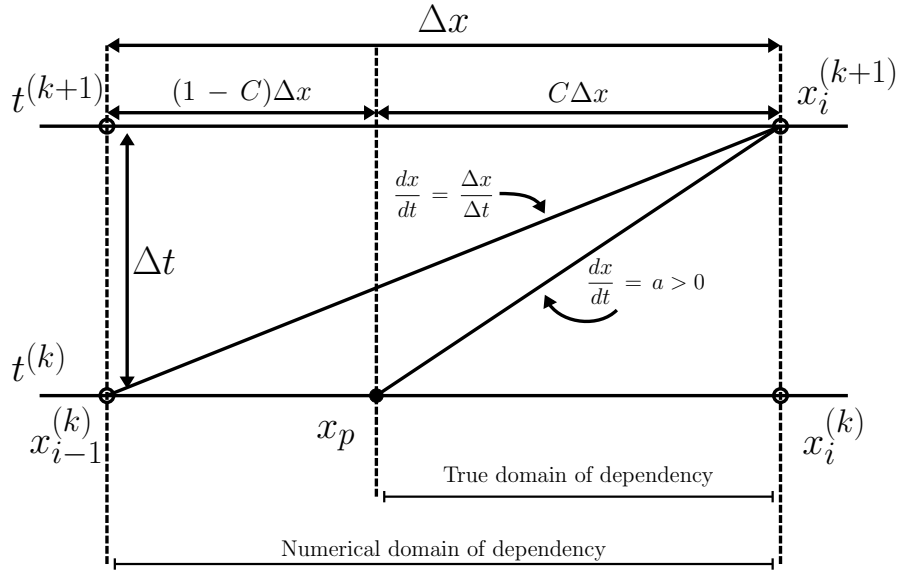


Figure A.5.: Grid mesh blueprint of the first-order upwind scheme with positive propagation speed  $a$ . Upwind direction is to the left.

$$\begin{aligned}
x_i - x_p &= a \Delta t \\
&= a \frac{\Delta t}{\Delta x} \Delta x \\
&= C \Delta x.
\end{aligned} \tag{.44}$$

Here  $C$  is known as the **CFL** or **Courant** number named after one of the authors who published this discovery (Courant et al., 1928).

As such the point  $x_p$  is at

$$x_p = (i - 1)\Delta x + (1 - C)\Delta x, \tag{.45}$$

and so the linearly interpolated solution takes the form

$$\hat{u}(x, t) = u_{i-1}^{(k)} + \frac{u_i^{(k)} - u_{i-1}^{(k)}}{\Delta x} (x - x_{i-1}). \tag{.46}$$

Substituting the definition of  $x_p$  into (.46), the solution function  $\hat{u}(x, t)$  gives



$$\begin{aligned}
\hat{u}(x_p, t) &= u_{i-1}^{(k)} + \frac{u_i^{(k)} - u_{i-1}^{(k)}}{\Delta x} [(i-1)\Delta x + (1-C)\Delta x] - (i-1)\Delta x \\
&= u_{i-1}^{(k)} + u_i^{(k)} - u_{i-1}^{(k)} - C \left( u_i^{(k)} - u_{(i-1)}^{(k)} \right) \\
&= u_i^{(k)} - C \left( u_i^{(k)} - u_{(i-1)}^{(k)} \right).
\end{aligned} \tag{.47}$$

The derivation outlined in (.47) is exactly the backward difference approximation in (.40).

At the outset,  $a$  is already prescribed and one determines  $\Delta x$  according to the level of accuracy one wishes to have. The choice of timestep  $\Delta t$  is restricted to the requirement that

$$0 \leq C = \frac{a\Delta t}{\Delta x} \leq 1. \tag{.48}$$

In other words, the grid speed  $\Delta x/\Delta t$  must be faster than the propagating information speed  $a$ . Simply, the *numerical domain of dependence must contain the true domain of dependence of the PDE within it, the single point  $x_p$  in this instance*. This is a necessary, but not sufficient, condition for a stable numerical scheme. If we decided to implement a fine mesh in the spatial dimension, larger timesteps would not be permissible and a larger computational effort would be required to reach any desired simulation time level.

### A.2.5. A Truncation Analysis

When one applies a finite difference approximation to a partial differential equation a disconnect develops between the analytical solution of the PDE and the approximate solution from the numerical integration. This disconnect is referred to as the ***truncation error***. This error is down to the approximating mathematical process. Consider again the advection equation using the backward finite difference approximation (.41) and replace the values  $u_i^{(k+1)}$  and  $u_{i-1}^{(k)}$  with its Taylor series expansion about the point  $(x_i, t^{(k)})$ :

$$u_i^{(k+1)} \approx u_i^{(k)} + \Delta t \frac{\partial u_i^{(k)}}{\partial t} + \frac{(\Delta t)^2}{2!} \frac{\partial^2 u_i^{(k)}}{\partial t^2} + O(\Delta t^3), \tag{.49}$$

$$u_{i-1}^{(k)} \approx u_i^{(k)} + \Delta x \frac{\partial u_i^{(k)}}{\partial x} + \frac{(\Delta x)^2}{2!} \frac{\partial^2 u_i^{(k)}}{\partial x^2} + O(\Delta x^3). \tag{.50}$$

Substituting (.49) and (.50) into (.41) yields

$$\frac{\partial u_i^{(k)}}{\partial t} + \frac{\Delta t}{2} \frac{\partial^2 u_i^{(k)}}{\partial t^2} + a \frac{\partial u_i^{(k)}}{\partial x} - a \frac{\Delta x}{2} \frac{\partial^2 u_i^{(k)}}{\partial x^2} + O(\Delta t^2) + O(\Delta x^2) = 0. \quad (.51)$$

Equation (.51) above is the Taylor series expansion for the backward finite difference approximation to the advection equation. Subtracting the analytical solution of the PDE

$$\frac{\partial u_i^{(k)}}{\partial t} + a \frac{\partial u_i^{(k)}}{\partial x} = 0, \quad (.52)$$

to this approximation to find the local truncation error

$$\tau := \frac{\Delta t}{2} \frac{\partial^2 u_i^{(k)}}{\partial t^2} + \frac{\Delta x}{2} \frac{\partial^2 u_i^{(k)}}{\partial x^2}. \quad (.53)$$

The order of a numerical scheme is defined by the lowest powers of  $\Delta t$  and  $\Delta x$  in  $\tau$ . In this truncation analysis the upwind method is defined as **first order** in time and space. If, as the limits  $\Delta t \rightarrow 0$  and  $\Delta x \rightarrow 0$  are taken, the truncation error  $\tau \rightarrow 0$ , then the numerical scheme is referred to as **consistent**. In other words, as we refine the spatial mesh and decrease the timesteps, the truncation error between the approximate and analytical solution decreases.

### A.2.6. Alternative Numerical Schemes

The upwind differencing method is not the only numerical scheme available to calculate an approximate solution. Three alternatives are listed here, however this list is by no means exhaustive. One alternative is a first-order scheme named after Peter Lax and Kurt O. Friedrichs is the **Lax-Friedrichs method** (Lax, 1954). A key difference between the upwind and this scheme is that the differencing calculation does not depend on the upwind direction the information is coming from. It is seen as a way of stabilising the central scheme, Equation (.35). An approximation for the partial time derivative is written as the mean value of the two points neighbouring  $u_i^{(k)}$  at  $t = k$

$$\frac{\partial u_i^{(k)}}{\partial t} \approx \frac{1}{2\Delta t} \left( u_{i-1}^{(k)} + u_{i+1}^{(k)} \right). \quad (.54)$$

Substituting the partial derivative approximation (.54) with the central spatial differencing approximation into the advection equation yields, when simplified

$$u_i^{(k+1)} \approx \frac{1}{2} (1 + C) u_{i-1}^{(k)} + \frac{1}{2} (1 - C) u_{i+1}^{(k)}. \quad (.55)$$

A von Neumann stability analysis shows that the scheme is stable provided the restriction

(.48) holds. One may apply a truncation analysis to confirm it is first-order accurate in both space and time. It is also known to have a second-order dissipation and third-order dispersion behaviours (Chu, 1979, pg. 304).

Peter Lax and Burton Wendroff developed the **Lax-Wendroff method**, which is second-order accurate in space and time (Lax and Wendroff, 1960). One uses a forward difference approximation for the time derivative

$$\frac{\partial u_i^{(k)}}{\partial t} \approx \frac{u_i^{(k+1)} - u_i^{(k)}}{\Delta t}. \quad (.56)$$

A weighted average between the upwind formula (.33), stable when  $a > 0$  and downwind (.34) unstable when  $a > 0$ , is used to estimate the spatial partial derivative

$$\frac{\partial u_i^{(k)}}{\partial t} \approx \beta_1 \left( \frac{u_i^{(k)} - u_{i-1}^{(k)}}{\Delta x} \right) + \beta_2 \left( \frac{u_{i+1}^{(k)} - u_i^{(k)}}{\Delta x} \right). \quad (.57)$$

When the coefficients are defined as

$$\begin{aligned} \beta_1 &= \frac{1}{2} (1 + C) \\ \beta_2 &= \frac{1}{2} (1 - C), \end{aligned} \quad (.58)$$

when simplified gives the Lax-Wendroff scheme

$$u_i^{(k+1)} \approx \frac{1}{2} C (1 + C) u_{i-1}^{(k)} + (1 - C^2) u_i^{(k)} - \frac{1}{2} C (1 - C) u_{i+1}^{(k)}. \quad (.59)$$

An interesting takeaway from this scheme is that despite every finite difference approximation being first-order accurate, the scheme itself is second-order accurate. As such, the accuracy of the approximations cannot be used to infer the accuracy of the scheme outright. Also, even with an unstable backward space approximation used in the spatial derivative approximation, the scheme itself is stable with the condition written in (.48) A more thorough overview of the Lax-Wendroff scheme is presented in Hirsch (1990).

Another upwind method for speed  $a > 0$  is the **Warming and Beam** scheme (Warming and Beam, 1976). This method is entirely one sided, meaning that every mesh point used in the calculation occurs to the left of the spatial point one is interested in, except for the central point. It is another example of a second-order accurate scheme which takes the form

$$u_i^{(k+1)} \approx \frac{1}{2}C(C-1)u_{i-1}^{(k)} + C(2-C)u_{i-1}^{(k)} + \frac{1}{2}(C-1)(C-2)u_i^{(k)}. \quad (.60)$$

The restriction boundary to ensure stability is doubled for this scheme

$$0 \leq |C| \leq 2. \quad (.61)$$

An enlarged stability region can result in more efficient schemes as one may advance times with larger timesteps. There exists an equivalent scheme for  $a < 0$ .

### A.3. Conservation Laws

Within this section a compact description of the basic properties of hyperbolic conservation laws are provided. The material considered is thought to be essential when discussing the application and development of numerical methods for conservation laws.

A system of  $m$  conservation laws may be written as a set of partial differential equations

$$\mathbf{U}_t + \mathbf{F}(\mathbf{U})_x = \mathbf{0} \quad (.62)$$

with

$$\mathbf{U} = \begin{bmatrix} u_1 \\ u_2 \\ \vdots \\ u_m \end{bmatrix}, \quad \mathbf{F}(\mathbf{U}) = \begin{bmatrix} f_1 \\ f_2 \\ \vdots \\ f_m \end{bmatrix}. \quad (.63)$$

Here  $\mathbf{U}$  is described as the vector of *conserved variables*.  $\mathbf{F} = \mathbf{F}(\mathbf{U})$  is a vector of fluxes with each component  $f_i$  a function of  $u_j$ , the components of  $\mathbf{U}$ . System (.63) is considered hyperbolic given the Jacobian matrix,

$$\mathbf{A}(\mathbf{U}) = \frac{\partial \mathbf{F}}{\partial \mathbf{U}}, \quad (.64)$$

has real eigenvalues  $\lambda^{(i)}(\mathbf{U})$  and a full set of eigenvectors  $\mathbf{E}^{(i)}(\mathbf{U})$ ,  $i \in \{1, \dots, m\}$  which are fully dependent on  $\mathbf{U}$ . Without loss of generality assume

$$\begin{aligned} \lambda^{(1)}(\mathbf{U}) &< \lambda^{(2)}(\mathbf{U}) < \dots < \lambda^{(m)}(\mathbf{U}) \\ \mathbf{E}^{(1)}(\mathbf{U}) &< \mathbf{E}^{(2)}(\mathbf{U}) < \dots < \mathbf{E}^{(m)}(\mathbf{U}). \end{aligned} \quad (.65)$$

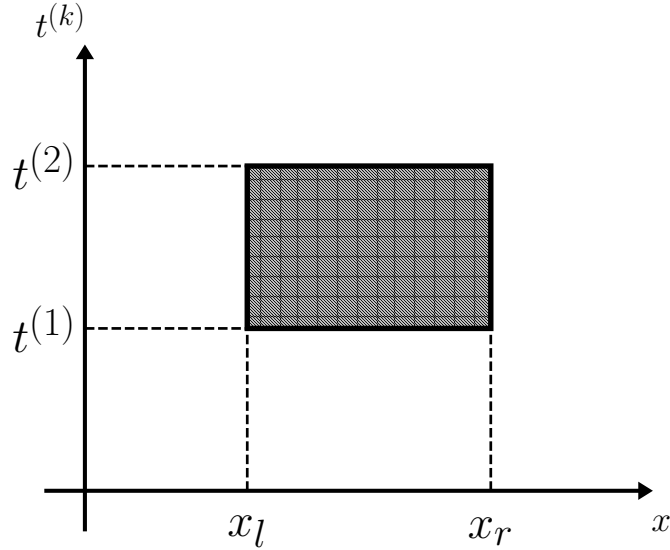


Figure A.6.: A control volume in the  $x$ - $t$  plane,  $V = [x_l, x_r] \times [t^{(1)}, t^{(2)}]$ .

### A.3.1. Integral Form of Conservation Laws

Systems of conservation may be expressed in a differential or integral form. The advection equation, first introduced in (3.1), is an example of a conservation law in differential form. Two reasons exist as to why it may be beneficial to consider the conservation law in its integral form: 1. The governing equations are derived from physical principles of conservation which are expressed as integral relations on control volumes, 2. Integral forms expand the span of admissible solutions to include discontinuous solutions as the assumption of smoothness is less critical.

Equation (.66) is a one-dimensional time dependent Euler equation system over a control volume  $V = [x_l, x_r] \times [t^{(1)}, t^{(2)}]$  shown in Figure A.6 where  $f = \rho u$  is the flux and

$$\frac{d}{dt} \int_{x_l}^{x_r} \rho(x, t) dx = f(x_l, t) - f(x_r, t). \quad (.66)$$

A complete system may be written as (.67) where  $\mathbf{F}(\mathbf{U})$  is a flux vector

$$\frac{d}{dt} \int_{x_l}^{x_r} \mathbf{U}(x, t) dx = \mathbf{F}(\mathbf{U}(x_l, t)) - \mathbf{F}(\mathbf{U}(x_r, t)). \quad (.67)$$

A second integral form exists by integrating (.62) between the time values  $t_1$  and  $t_2$  where  $t_1 \leq t_2$  which can be seen in (Toro, 1999, pg. 63, Eqn. 2.67). The derivation of the integral form may also be approached by integrating (.62) in any control volume  $V$  in  $x-t$  space and use Green's theorem (Riemann, 1851; Riley et al., 2010) to derive the result

$$\oint [\mathbf{U} dx - \mathbf{F}(\mathbf{U}) dt] = \mathbf{0}. \quad (.68)$$

Scalar conservation laws (where  $m = 1$ ) in differential form reads

$$\frac{\partial u}{\partial t} + \frac{\partial f(u)}{\partial x} = 0, \quad (.69)$$

where  $f(u)$  is a flux function. To have the ability to solve the conserved variable  $u(x, t)$  in its entirety, the flux function is required to be an algebraic function of the conserved variable, along with extra parameters which define a specific problem. In Section 3.2.1, the simplest example of a scalar conservation law, the advection equation (3.1) was introduced. Here the flux function is defined as a linear function of the conserved variable  $u$ ,  $f(u) = au$ .

### A.3.2. Non-linear hyperbolic conservation laws: Common Properties

Non-linear hyperbolic conservation laws exhibit key features known as *wave steepening* and *shock formation*. The scalar conservation law in (.69) assumes that  $f$  is a function of the solution  $u$  only. Typically this representation is insufficient in modelling the physical phenomena. Shock waves have viscous dissipation and heat conduction behaviours as well as the advective properties. A better flux function approximation requires a dependence on the spatial derivative of  $u$  so that (.69) would convert to

$$u_t + f(u)_x = \alpha u_{xx}, \quad (.70)$$

where  $\alpha$  is a positive coefficient of viscosity. Re-writing (.70) in the form of (.69) as

$$u_t + \lambda(u)u_x = 0, \quad (.71)$$

where the *characteristic speed* is defined as

$$\lambda(u) = \frac{df}{du} = f'(u). \quad (.72)$$

For the linear advection equation, considered in previous sections,  $\lambda(u) = a - \text{constant}$ . How the flux function  $f(u)$  behaves majorly influences the behaviour of the solution itself. One key property of the characteristic speed is its *monotonicity*. Three possible outcomes of monotonicity exist as

1. A convex flux, where  $\lambda(u)$  is a monotone increasing function of  $u$

$$\frac{d\lambda(u)}{du} = \lambda'(u) = f''(u) > 0$$

2. A concave flux, where  $\lambda(u)$  is a monotone decreasing function of  $u$

$$\frac{d\lambda(u)}{du} = \lambda'(u) = f''(u) < 0$$

3.  $\lambda(u)$  contains extrema which are non-convex and non-concave

$$\frac{d\lambda(u)}{du} = \lambda'(u) = f''(u) = 0$$

The equation of state within the non-linear systems of conservation laws define the characteristic of the flux function. Menikoff and Plohr (1989) presents a more thorough overview of these properties.

### A.3.3. Constructing Solutions on the Characteristic

An extension to the definition of the linear advection equation from Section A.1.2, Equation (3.1), to a non-linear advection equation (.73) is presented below. Consider an *inviscid* initial value problems for initial smooth data  $u_0(x) = u(x, 0)$

$$\begin{cases} u_t + \lambda(u)u_x = 0, \\ \lambda(u) = f'(u), \\ u(x, 0) = u_0(x). \end{cases} \quad (.73)$$

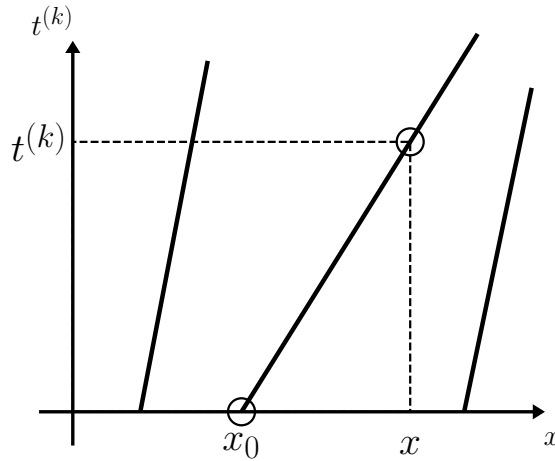


Figure A.7.: Standard characteristic curves for a non-linear hyperbolic conservation system.

The characteristic speed in this system is  $\lambda(u) = a = \text{constant}$ . To develop solutions for this system, the blueprint outlined in Section A.1.2.1 is followed. First consider the characteristic curves  $x = x(t)$  which satisfy the Initial Value Problem (.74)

$$\frac{dx}{dt} = \lambda(u), \quad x(0) = x_0. \quad (.74)$$

Now consider the variables  $u$  and  $x$  to be functions of  $t$  and locate the total derivative of  $u$  along the curve  $x(t)$

$$\frac{du}{dt} = u_t + \lambda(u)u_x = 0. \quad (.75)$$

$u$  is constant along the characteristic curve satisfying (.74) and as such the gradient  $\lambda(u)$  is also constant along the characteristic. Thus, the characteristic curves are straight lines. The solution along each curve is the value of  $u$  at the initial point  $x_0$

$$u(x, t) = u_0(x_0). \quad (.76)$$

A standard characteristic curve is presented in Figure A.7. The slope of the characteristic are evaluated at the initial point to determine the solution characteristic curves of the initial value problem (.74) which are

$$x = x_0 + \lambda(u_0(x_0))t. \quad (.77)$$

(.76) and (.77) are considered the analytical solution to the initial value problem. The point  $x_0$  depends on what point  $(x, t)$  is given. So the initial point is also a function of space and time  $x_0 = x_0(x, t)$ . Substituting (.77) into (.76) reveals that the solution is implicit.

$$u(x, t) = u_0[x - \lambda(u_0(x_0(x, t)))t]. \quad (.78)$$

The format of the solution (.78) is identical to the format of the solution to the linear advection Equation (.9) in Section A.1.2.1.

To verify the constructed solutions (.76) and (.77), first calculate the spatial and time derivative of the solution  $u(x, t)$  in (.76) which is

$$\begin{cases} u_t = u'_0(x_0) \frac{\partial x_0}{\partial t} \\ u_x = u'_0(x_0) \frac{\partial x_0}{\partial x} \end{cases} \quad (.79)$$

Then calculate the time derivative of (.77),



$$\begin{aligned}
\frac{\partial x}{\partial t} = 0 &= \frac{\partial x_0}{\partial t} + \frac{\partial \lambda(u_0(x_0))}{\partial t} t + \lambda(u_0(x_0)) \frac{\partial t}{\partial t} \\
&= \frac{\partial x_0}{\partial t} + \lambda'(u_0(x_0)) \frac{\partial u_0(x_0)}{\partial t} t + \lambda(u_0(x_0)) \\
&= \frac{\partial x_0}{\partial t} + \lambda'(u_0(x_0)) u'_0(x_0) t \frac{\partial x_0}{\partial t} + \lambda(u_0(x_0)) \\
\implies \frac{\partial x_0}{\partial t} &= -\frac{\lambda(u_0(x_0))}{1 + \lambda'(u_0(x_0)) u'_0(x_0) t}.
\end{aligned} \tag{.80}$$

Calculating the spatial derivative of (.78)

$$\begin{aligned}
\frac{\partial x}{\partial x} = 1 &= \frac{\partial x_0}{\partial x} + \frac{\partial \lambda(u_0(x_0) t)}{\partial x} \\
&= \frac{\partial x_0}{\partial x} + \lambda'(u_0(x_0)) \frac{\partial u_0(x_0)}{\partial x} t \\
&= \frac{\partial x_0}{\partial x} + \lambda'(u_0(x_0)) u'_0(x_0) t \frac{\partial x_0}{\partial x} \\
\implies \frac{\partial x_0}{\partial x} &= \frac{1}{1 + \lambda'(u_0(x_0)) u'_0(x_0) t}.
\end{aligned} \tag{.81}$$

By substituting (.80) and (.81) into (.79) yields

$$\begin{cases} u_t = -\frac{\lambda(u_0(x_0)) u'_0(x_0)}{1 + \lambda'(u_0(x_0)) u'_0(x_0) t} \\ u_x = \frac{u'_0(x_0)}{1 + \lambda'(u_0(x_0)) u'_0(x_0) t}. \end{cases} \tag{.82}$$

Applying the values in (.82) to (.73) show that partial derivatives of the solution in time and space satisfy the initial value problem.

#### A.3.4. Wave Steepening Behaviour

When the characteristic speed  $\lambda(u) = a = \text{constant}$ , initial data  $u_0(x)$  translates with speed  $a$  *without distortion* as illustrated in Figure A.1 on page 302. In a non-linear case, the characteristic speed is a function of the solution itself. As such, distortions are produced which is a key feature of non-linear conservative partial differential equation problems.

To understand this phenomena, consider the initial data  $u_0(x)$  with smooth problem in Figure A.8. Five initial points  $x_i^{(0)}$  are highlighted with their respective initial data values  $u_i^{(0)}$ . Without loss of generality, assume the flux function  $f(u)$  is convex so that  $\lambda'(u) =$

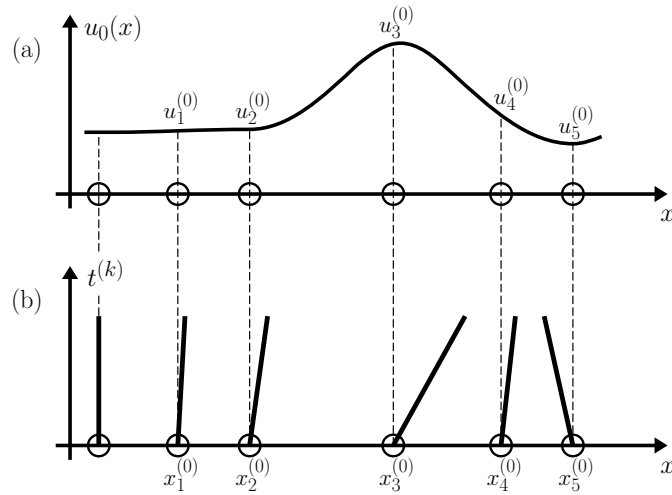


Figure A.8.: Wave steepening distortion phenomena in a non-linear hyperbolic conservation system. Part (a) shows the initial solution profile. Part (b) displays the corresponding characteristics of the initial solutions.

$f''(u) > 0$ . As a result the characteristic speed is an increasing function of the solution  $u$ .

The characteristic  $x_i^{(k)}$  evolve from initial points  $x_i^{(0)}$  carrying the constant values  $u_i^{(0)}$ . Since the flux function is assumed convex, larger magnitudes of  $u_0(x)$  will travel faster than initial solutions of lower magnitudes. Two regions of distortion are most evident in Figure A.8. The first region lies between the points  $[x_1^{(0)}, x_3^{(0)}]$ . Here,  $u_3^{(0)} > u_2^{(0)} > u_1^{(0)}$ . This relation is clearly reflected in the characteristics in part (b) of Figure A.8. As time evolves, this smooth profile will broaden and flatten out. The region is considered *expansive* if the characteristic speed  $\lambda_i > 0$  increases as the spatial index points increase.

A second distortion region in Figure A.8 exists between the points  $[x_3^{(0)}, x_5^{(0)}]$ . In contrast this region is *compressive*. The characteristic speeds decrease as the spatial indices increase  $\lambda_i < 0$ . Within this section the propagation speeds decrease as the spatial direction is traced,  $u_3^{(0)} > u_4^{(0)} > u_5^{(0)}$ . As time evolves, this region's profile will become more steep and narrow. This steepening behaviour will eventually see individual characteristics intersect one another and the solution will “fold over”. It is also worth noting that in the case of a concave flux where  $\lambda'(u) = f''(u) < 0$  the expansive and compressive behaviours are reversed for both regions described above.

Where two characteristics first intersect defined the **wave break**. The derivative  $u_x$  becomes infinite at the breaking time  $t_b$

$$t_b = -\frac{1}{\lambda_i(x_0)}. \quad (.83)$$

One may derive this equation from equations in (.82).

Equation (.70) shows that the rate of change of solution  $u$  is dependent on the balance between both the advection term  $f(u)_x$  and diffusion term  $\alpha u_{xx}$ . Highlighted in Figure

A.8(a) is the wave steepening effect within the region  $[x_3^{(0)}, x_4^{(0)}]$  due to the advective term is balanced by the wave easing of  $\alpha u_{xx}$  which is negative. These behaviours are reversed in the region  $[x_4^{(0)}, x_5^{(0)}]$ . A more comprehensive model of the physical process does not allow this folding behaviour, but would require a more complex viscous model. Despite this, the inviscid model in (.70) may be used by allowing the formation of discontinuities by the process of increasing compression, more commonly known as **shock waves**. A more complete presentation of this information may be found in Lax (1990), Smoller (1994) and Whitham (1999).

### A.3.5. Shockwaves

Extremely rapid changes of physical phenomena such as pressure, temperature and density in the air within compact transition regions are known as **shock waves**. An overview of the physical characteristics which make up shock waves may be found in (Landau and Lifshitz, 1987, pg. 337–341) and Whitham (1999). It is common place to use mathematical discontinuities as a reasonable approximation for shock wave behaviour.

Consider an integral form of the conservation law, such as Equation (.67) in one dimension. It has a solution  $u(x, t)$  where the flux  $f(u)$  and their derivatives are continuous within the entire domain except for the line  $s = s(t)$  where on the  $x - t$  plane  $u(x, t)$  has a jump discontinuity. Let  $x_l$  and  $x_r$  be fixed existing in the  $x$  spatial domain so that  $x_l < s(t) < x_r$ . Applying the conservation law on the control region  $[x_l, x_r]$  gives

$$f(u(x_l, t)) - f(u(x_r, t)) = \frac{d}{dt} \int_{x_l}^{s(t)} u(x, t) dx + \frac{d}{dt} \int_{s(t)}^{x_r} u(x, t) dx \quad (.84)$$

Rewriting (.84) as (Chow et al., 1988)

$$\begin{aligned} f(u(x_l, t)) - f(u(x_r, t)) &= [u(s_l, t) - u(s_r, t)] S \\ &+ \int_{x_l}^{s(t)} \frac{\partial u(x, t)}{\partial t} dx + \int_{s(t)}^{x_r} \frac{\partial u(x, t)}{\partial t} dx, \end{aligned} \quad (.85)$$

where  $S$  is the speed of the discontinuity and

$$u(s_l, t) = \lim_{x \rightarrow s(t)^-} u(s(t), t), \quad u(s_r, t) = \lim_{x \rightarrow s(t)^+} u(s(t), t), \quad S = \frac{ds}{dt}.$$

Since  $u_t(x, t)$  is constrained by the integrals as the discontinuity line  $s$  is approached from both sides, these cancel out identically so that

$$f(u(x_l, t)) - f(u(x_r, t)) = [u(s_l, t) - u(s_r, t)] S \quad (.86)$$

$$\Delta f = S \Delta u. \quad (.87)$$

The change in flux,  $\Delta f$  at the discontinuity is equal to the speed of the discontinuity  $S$  multiplied by the change in solution either side of the discontinuity  $\Delta u$ . This is known as the **Rankine-Hugoniot condition** typically expressed as (.87). One may use this equation to determine the speed of the discontinuity  $S$  by finding the quotient between the change in flux and solution disparity. Thus discontinuous solutions may be resolved by formulating conservation problems by PDEs in smooth solution regions and utilise Rankine-Hugoniot conditions through discontinuities.

**A.3.5.1. Examples of Discontinuous Solutions** To gain a better intuition of the theory presented in Section A.3.5, consider the initial-value problem for the inviscid Burgers equation

$$\begin{cases} u_t + f(u)_x = 0, & f(u) = \frac{1}{2}u^2 \\ u(x, 0) = u_0(x) = \begin{cases} u_l, & \text{if } x < 0 \\ u_r, & \text{if } x > 0. \end{cases} \end{cases} \quad (.88)$$

Assuming first that  $u_l > u_r$  so that the flux is convex and that  $\lambda'(u) = f''(u) > 0$ . As such the characteristic speeds to the left of the discontinuity are faster than those on the right.  $\lambda_l \equiv \lambda_{u_l} > \lambda_{u_r} \equiv \lambda_r$ . Section A.3.4 highlighted the difference between expansive and compressive regional behaviours. Based on this discussion, the initial data in (.88) can be immediately identified as compressive discontinuous data. This is highlighted in Figure A.9. Characteristics intersect immediately. From this information the solution to the initial-value problem may be written as

$$u(x, t) = \begin{cases} u_l & \text{if } x - St < 0 \\ u_r & \text{if } x - St > 0, \end{cases} \quad (.89)$$

where applying (.86) to find the discontinuity speed

$$S = \frac{1}{2}(u_l + u_r). \quad (.90)$$

This solution defines the shock wave which is compressive in nature. As such it adheres to the **entropy condition**  $\lambda_{u_l} > S > \lambda_{u_r}$ . A more thorough analysis and details on the entropy condition may be found in Chorin and Marsden (1990), Smoller (1994), Whitham

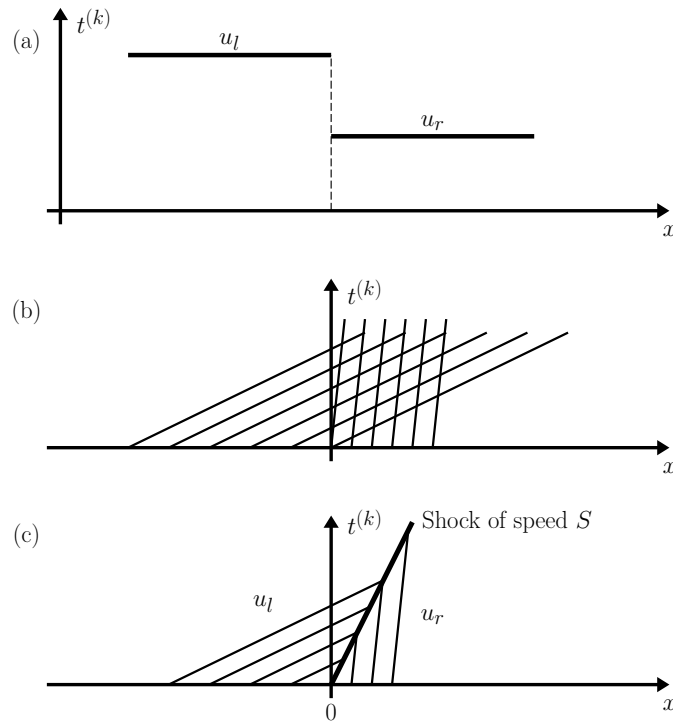


Figure A.9.: The initial discontinuous data (a), system characteristics (b) and solution on the  $x - t$  plane for the inviscid Burgers equation (c).

(1999) and LeVeque (2002).

Assuming  $u_l < u_r$  represents the case of an expansive region for convex flux function  $f(u)$ . One might expect an identical solution of the form given in (.89) and (.90) however this is physically impossible.

### A.3.6. Rarefaction Waves

The discontinuity shown in Figure A.10 has not resulted from the right hand characteristics intersecting with the left hand characteristics. Instead the characteristics are seen to be diverging away from the discontinuity.

This solution type is known as a *rarefaction shock*. As the entropy condition is not satisfied, it is known as an *entropy-violating shock*. Hence it must be rejected as a possible physical solution, even if it is mathematical solution. Given the expansive behaviour of the initial data, it would be a better assumption to think that the solution profile would flatten over time.

Consider initial-value problem (.88) again for a general convex flux function  $f(u)$  and expansive initial data where  $u_l < u_r$ . Instead of initial data listed in (.88), consider a linear dependence of  $u_0(x)$  between the two fixed points  $x_l < 0$  and  $x_r > 0$

$$u_0(x) = \begin{cases} u_l & \text{if } x \leq x_l \\ u_l + \frac{u_r - u_l}{x_r - x_l}(x - x_l) & \text{if } x_l < x < x_r \\ u_r & \text{if } x \geq x_r > 0. \end{cases} \quad (.91)$$

This initial data is presented in Figure A.11(a) with corresponding characteristics in Figure A.11(b). Once again the solution,  $u(x, t)$ , is written in terms of the two constant states  $u_l$  and  $u_r$ , but an area of smooth transition exists in between them. This area is known as the *rarefaction wave*.

Characteristics emanating from the right hand edge of the wave,  $x_r$  defines the *head* of the rarefaction, carrying the initial solution  $u_0(x_r) = u_r$

$$x = x_r + \lambda(u_r)t. \quad (.92)$$

Similarly, the left edge of the wave is defined via characteristics sourced from  $x_l$  known as the *tail* of the rarefaction containing the solution  $u_0(x_l) = u_l$

$$x = x_l + \lambda(u_l)t. \quad (.93)$$

The wave spreads and the profile flattens as time evolves due to the assumption of convexity,  $\lambda'(u) = f''(u) > 0$ . This assumption implies that larger values of initial solution  $u_0(x)$  propagate faster than smaller values.

From this information, the initial-value problem (.88), for general convex flux function  $f(u)$  and initial data (.91) has solution of the form

$$\begin{cases} u(x, t) = u_l & \text{if } \frac{x - x_l}{t} \leq \lambda_l \\ \lambda(u) = \frac{x - x_l}{t} & \text{if } \lambda_l < \frac{x - x_l}{t} < \lambda_r \\ u(x, t) = u_r & \text{if } \frac{x - x_l}{t} \geq \lambda_r. \end{cases} \quad (.94)$$

The rarefaction shock solution presented in (.89) with general discontinuity speed  $S = \Delta f / \Delta u$  is unstable for small distance  $\Delta x$ . Small perturbations of initial data would lead to large changes in solution due to the structure of the solution in the initial-value problem. However, the discontinuous data in the initial value problem (.91) takes into account the interval size between fixed points. Thus, the solution in (.94) is stable and as the limits  $x_l \rightarrow 0^-$  and  $x_r \rightarrow 0^+$  are taken to account, the initial value problem (.88) for general convex flux function  $f(u)$  converges.

In the limiting case,  $u_0(x)$  takes on all solution values between  $u_l$  and  $u_r$  at  $x = 0$ . As a

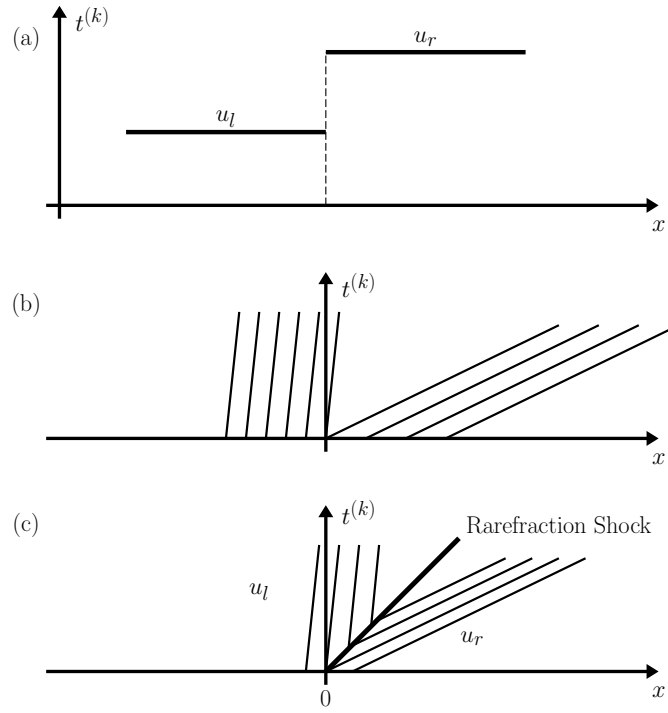


Figure A.10.: The initial expansive discontinuous data (a), system characteristics (b) and rarefaction shock solution on the  $x-t$  plane for the inviscid Burgers equation (c).

consequence,  $\lambda(u_0(x))$  takes all values between  $\lambda_l$  and  $\lambda_r$ . Since the flux function is convex, higher characteristic speeds propagate faster than lower values and initial data quickly settles highlighting a rarefaction solution. In this limiting case where all characteristics stem from a single point is known as a *centred rarefaction wave* with solution

$$\begin{cases} u(x, t) = u_l & \text{if } \frac{x}{t} \leq \lambda_l \\ \lambda(u) = \frac{x}{t} & \text{if } \lambda_l < \frac{x}{t} < \lambda_r \\ u(x, t) = u_r & \text{if } \frac{x}{t} \geq \lambda_r. \end{cases} \quad (.95)$$

This is illustrated by Figure A.12.

### A.3.7. A Riemann Problem for the Burgers Equation

To tie up the theory discussed from Sections A.3.5 - A.3.6, consider a solution to the Riemann problem where the flux function is  $f(u) = \frac{1}{2}u^2$ . This transforms the general initial value problem highlighted in Equation (.73) into the advective form of the inviscid Burgers' Equation

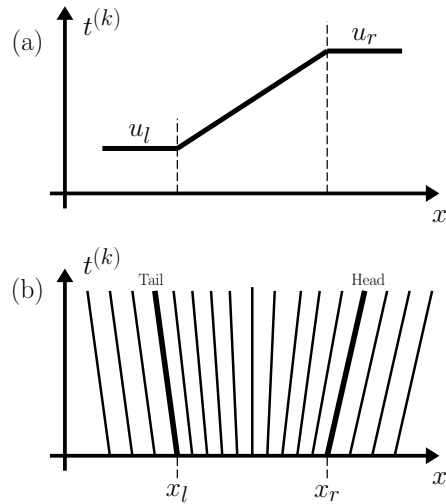


Figure A.11.: A non-centred rarefaction wave with expansive smooth initial data (a) and characteristics picture in  $x - t$  plane (b).

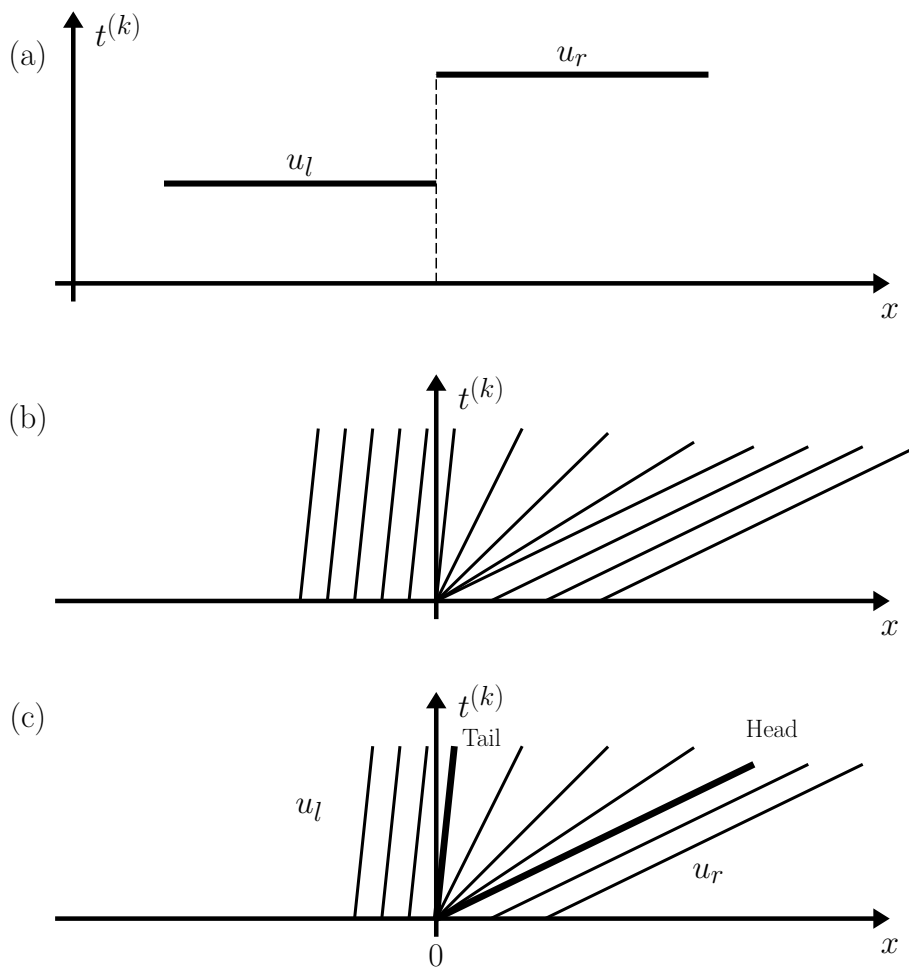


Figure A.12.: A centred rarefaction wave with expansive discontinuous initial data (a), characteristic picture (b) and the rarefaction solution on the  $x - t$  plane which satisfies the entropy condition (c).



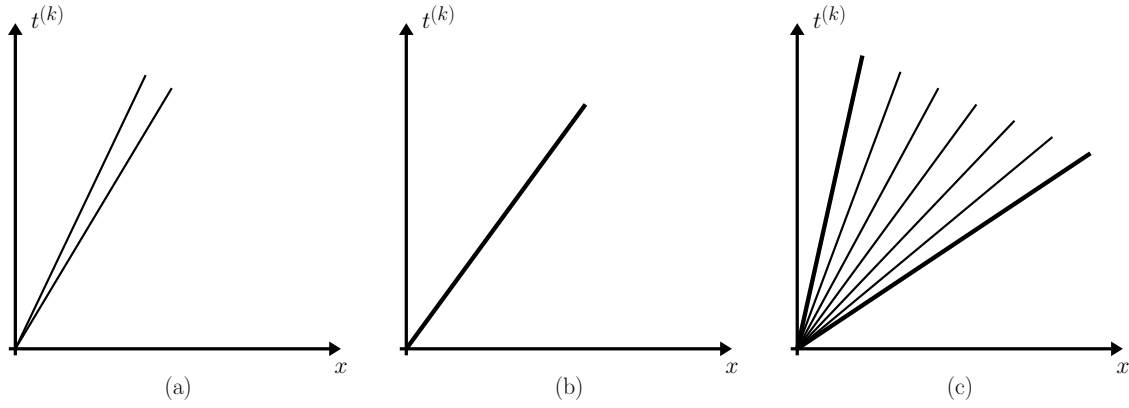


Figure A.13.: A typical solution for the inviscid Burgers equation where; (a) general solution structure (single wave, shock/rarefaction); (b) shock wave solution; (c) rarefaction wave solution.

$$\begin{cases} u_t + \left(\frac{u^2}{2}\right)_x = 0, \\ u(x, 0) = \begin{cases} u_l, & x < 0 \\ u_r, & x > 0. \end{cases} \end{cases} \quad (.96)$$

Figure A.13 shows a single wave projecting from the origin, which is the exact solution as discussed in Section A.3.5.1. Applying the entropy condition, the wave is a shockwave when  $u_l > u_r$  or a rarefaction wave when  $u_l \leq u_r$ . Using this information, a complete solution may be engineered.

Solution (.97) is depicted in Figure A.13 with a general solution and single wave (a), the shockwave case (b) and the rarefaction case (c).

$$\begin{aligned} \text{if } u_l > u_r \quad & \begin{cases} u(x, t) = \begin{cases} u_l & \text{if } x - St < 0 \\ u_r & \text{if } x - St > 0 \end{cases} \\ S = \frac{1}{2}(u_l + u_r), \end{cases} \\ \text{else } u_l \leq u_r \quad & u(x, t) = \begin{cases} u_l & \text{if } \frac{x}{t} \leq u_l \\ \frac{x}{t} & \text{if } u_l < \frac{x}{t} < u_r \\ u_r & \text{if } \frac{x}{t} \geq u_r. \end{cases} \end{aligned} \quad (.97)$$

**A.3.7.1. The Riemann Problem in Linearised Gas Dynamics: Part II** Consider again constructing a solution to the Riemann problem in linearised gas dynamics, but this time look to apply the Rankine-Hugoniot conditions. We look to solve for the unknowns  $\rho_*$  and  $u_*$  which lie in the star region, shown in Figure 3.4 on page 104.

Recall that the vector of conserved variables  $\mathbf{U}$  and coefficient matrix  $\mathbf{A}$  are given by

$$\mathbf{U} = \begin{bmatrix} u_1 \\ u_2 \end{bmatrix} = \begin{bmatrix} \rho \\ u \end{bmatrix}, \quad \mathbf{A} = \begin{bmatrix} 0 & \rho_0 \\ \alpha^2/\rho_0 & 0 \end{bmatrix}. \quad (.98)$$

The eigenvalues of matrix  $\mathbf{A}$  are

$$\lambda_1 = -\alpha, \quad \lambda_2 = +\alpha. \quad (.99)$$

With this information, apply the Rankine-Hugoniot conditions, shown in Equation (3.16), across the  $\lambda_1$ -wave of speed  $S_1 = \lambda_1$ , giving

$$\begin{bmatrix} 0 & \rho_0 \\ \frac{\alpha^2}{\rho_0} & 0 \end{bmatrix} \begin{bmatrix} p_* - \rho_l \\ u_* - u_l \end{bmatrix} = -\alpha \begin{bmatrix} p_* - \rho_l \\ u_* - u_l \end{bmatrix}. \quad (.100)$$

Expanding (.100) and resolving for  $u_*$  yields

$$u_* = u_l - \frac{\alpha}{\rho_0} (\rho_* - \rho_l). \quad (.101)$$

Apply the Rankine-Hugoniot conditions again, but across the  $\lambda_2$ -wave of speed  $S_2 = \lambda_2$  to attain

$$u_* = u_r + \frac{\alpha}{\rho_0} (\rho_* + \rho_r). \quad (.102)$$

Solving the two algebraic equations (.101) and (.102) for the two unknowns in the star region gives

$$\begin{aligned} \rho_* &= \frac{1}{2} (\rho_l + \rho_r) - \frac{\rho_0}{2\alpha} (u_r - u_l) \\ u_* &= \frac{1}{2} (u_l + u_r) - \frac{\alpha}{2\rho_0} (\rho_r - \rho_l) \end{aligned} \quad (.103)$$

which is precisely the solution in (.31) on page 307. This technique which expands the initial data through its eigenvectors utilising the Rankine-Hugoniot conditions is more direct than the derived result in Section A.1.4. Within the literature the Rankine-Hugoniot conditions are typically referred to as **Riemann states** owing to the fact that the conditions are specifically solving a Riemann problem at a jump discontinuity. This terminology will be used from here on out.

### A.3.8. Generalised Riemann Invariants

Given this construction, *Generalised Riemann Invariants* define relations which hold true for given waves across the entire wave structure. The waves lead to the following  $(m - 1)$  ordinary differential equations

$$\frac{d\omega_1}{k_1^{(i)}} = \frac{d\omega_2}{k_2^{(i)}} = \dots = \frac{d\omega_m}{k_m^{(i)}}. \quad (.104)$$

These relations are ratios between changes in  $d\omega_s$  to its associated component of the right eigenvector  $k_s^{(i)}$  (from Equation (.105)) for a given  $\lambda_i$ -wave group.

The behaviour of a wave linked with the  $i$ -characteristic field with eigenvalue  $\lambda_i$  and corresponding right eigenvector

$$\mathbf{K}^{(i)} = \left[ k_1^{(i)}, k_2^{(i)}, \dots, k_m^{(i)} \right]^T \quad (.105)$$

along with a more detailed description and analysis may be accessed from Jeffrey (1976).

**A.3.8.1. Shock Wave Solution** A single jump discontinuity in a non-linear field  $i$  connecting two constant Riemann states  $\mathbf{U}_l, \mathbf{U}_r$  results in a shock wave provided the following conditions are satisfied

- the Rankine-Hugoniot conditions are

$$\mathbf{F}(\mathbf{U}_r) - \mathbf{F}(\mathbf{U}_l) = S_i(\mathbf{U}_r - \mathbf{U}_l); \quad (.106)$$

- the entropy condition

$$\lambda_i(\mathbf{U}_l) > S_i > \lambda_i(\mathbf{U}_r). \quad (.107)$$

A shock wave with speed  $S_i$  is shown in Figure A.14(a). The compressive shock behaviour is illustrated by the characteristic  $dx/dt = \lambda_i$  on either side of the wave.

**A.3.8.2. Rarefaction Wave Solution** A smooth transition in a non-linear field  $i$  connecting two constant Riemann states  $\mathbf{U}_l, \mathbf{U}_r$  results in a rarefaction wave provided the following conditions are satisfied

- the parallel characteristic condition

$$\lambda_i(\mathbf{U}_l) < \lambda_i(\mathbf{U}_r); \quad (.108)$$

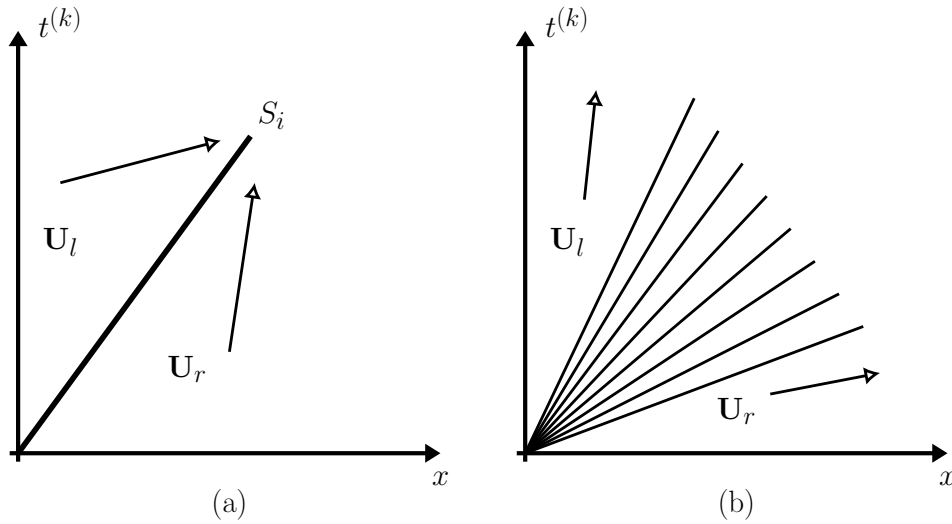


Figure A.14.: Two elementary wave solutions of the Riemann problem: (a) a shock wave characteristic with speed  $S_i$  and (b) a rarefaction wave.

- constancy of the general Riemann Invariants across the wave i.e.

$$\frac{d\omega_1}{k_1^{(i)}} = \frac{d\omega_2}{k_2^{(i)}} = \dots = \frac{d\omega_m}{k_m^{(i)}}. \quad (.109)$$

A rarefaction wave is shown in Figure A.14(b). Characteristics to the right and left of the wave diverge as well as the characteristics within the wave.

These elementary wave solutions of the Riemann problem are not exhaustive. Another solution that exists is known as the *contact wave* solution. However, this solution is not relevant to the numerical modelling work that has been embarked on and so is omitted from this thesis. Further information of this academic work may be followed through Whitham (1999); Smoller (1994); Chorin and Marsden (1990); Lax (1990); Lax and Wendroff (1960) and references therein.

## A.4. Godunov's Numerical Method

### A.4.1. One-dimensional finite volume method

Throughout the chapter so far a finite discretisation of the computational domain has been assumed, as discussed in section A.2.3, to determine a solution at an assigned point. This work may be extended by considering *cell averages* defined over a *finite control volume*.

Figure A.15 shows a discretisation of the computation domain of  $[0, N] \times [0, T]$ . The spatial dimension is divided into  $n$  *finite volumes*, often referred to as *cells* or *pixels*. The entire spatial domain may be expressed via the inequality

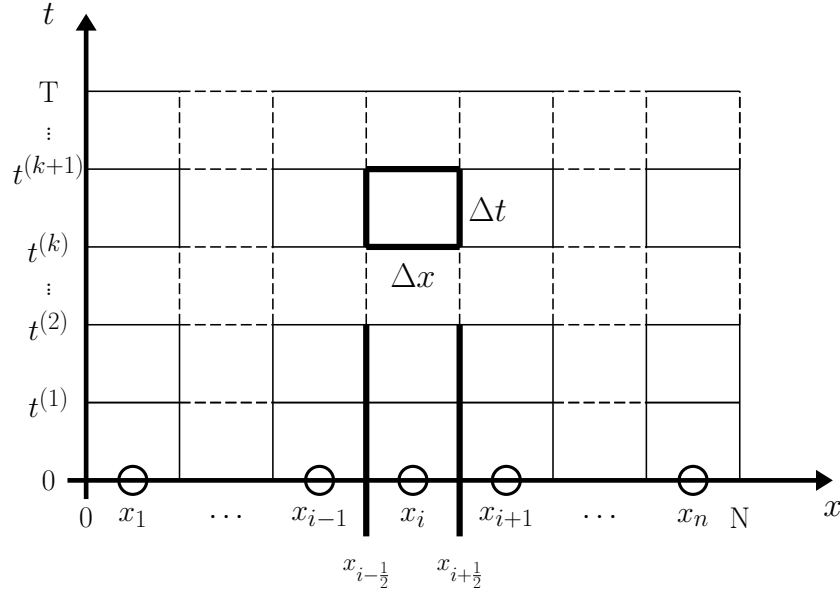


Figure A.15.: A discretisation illustration for the computational domain  $[0, N] \times [0, T]$  into  $n$  finite volumes.  $x_{i-\frac{1}{2}}$  and  $x_{i+\frac{1}{2}}$  denote the intercell boundaries of pixel  $x_i$ .

$$x_{i-\frac{1}{2}} = (i-1)\Delta x \leq x \leq i\Delta x = x_{i+\frac{1}{2}}. \quad (.110)$$

A given pixel  $i$  has boundary values  $x_{i-\frac{1}{2}}$  and  $x_{i+\frac{1}{2}}$  where intercell numerical fluxes are needed. The size of each pixel is defined as

$$\Delta x = x_{i+\frac{1}{2}} - x_{i-\frac{1}{2}} = \frac{N}{n}. \quad (.111)$$

One can define the average value of  $u(x, t)$  in pixel  $i$ , the cell average, at a fixed time  $t^{(k)} = k\Delta t$  as

$$u_i^{(k)} = \frac{1}{\Delta x} \int_{x_{i-\frac{1}{2}}}^{x_{i+\frac{1}{2}}} u(x, t^{(k)}) dx. \quad (.112)$$

The integral average value  $u_i^{(k)}$  defined in (.112) is a constant value. However one must remember that spatial variations of  $u(x, t)$  may exist within pixel  $i$ . This average value is assigned to the centre of the cell leading to its known terminology as a **cell-centred conservative method**. Computationally it is much more simple to deal with approximations to the pixel averages  $u_i^{(k)}$ . A set of pixel averages at a given time result in a piece-wise constant distribution of the solution as illustrated in Figure A.16.

In this section, pixels have been evenly discretised throughout the domain. One can split the domain into irregular sizes, but for simplicity, the modelling theory is applied solely within a rectangular domain.

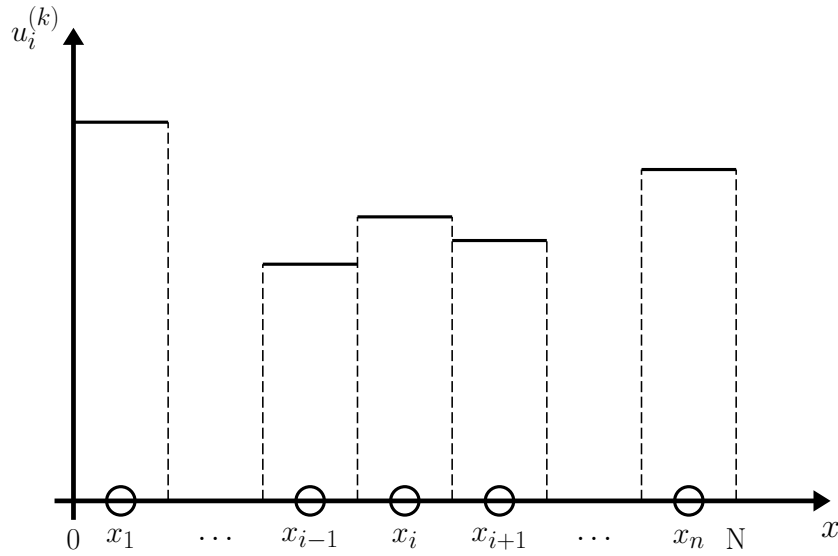


Figure A.16.: A representation of piece-wise constant distribution of information at time step  $t^{(k)}$ .

#### A.4.2. Godunov's Method: Interpretation 1

Godunov's proposed scheme begins by defining two local Riemann problems  $\text{RP} \left( u_{i-1}^{(k)}, u_i^{(k)} \right)$  at  $x_{i-\frac{1}{2}}$  and  $\text{RP} \left( u_i^{(k)}, u_{i+1}^{(k)} \right)$  at  $x_{i+\frac{1}{2}}$  using the conservation law in (3.27). Compute the two solutions of the local Riemann problems and take the integral average in pixel  $i$  of these solutions and assign it to  $u_i^{(k+1)}$ .

Figure A.17 illustrates the first Godunov method using the linear advection Equation 3.2.1. For positive  $a$  the exact solution to  $\text{RP} \left( u_{i-1}^{(k)}, u_i^{(k)} \right)$  is

$$u_{i-\frac{1}{2}}(x/t) = \begin{cases} u_{i-1}^{(k)} & \text{if } x/t < a, \\ u_i^{(k)} & \text{if } x/t > a, \end{cases} \quad (.113)$$

assuming the local origin of the problem is at  $(0, 0)$ . Similarly, the solution to  $\text{RP} \left( u_i^{(k)}, u_{i+1}^{(k)} \right)$  is

$$u_{i+\frac{1}{2}}(x/t) = \begin{cases} u_i^{(k)} & \text{if } x/t < a, \\ u_{i+1}^{(k)} & \text{if } x/t > a. \end{cases} \quad (.114)$$

One then applies the two solutions to the separate local Riemann problems to update Godunov's method with

$$u_i^{(k+1)} = \frac{1}{\Delta x} \left[ \int_0^{\frac{\Delta x}{2}} u_{i-\frac{1}{2}}(x/\Delta t) dx + \int_{-\frac{\Delta x}{2}}^0 u_{i+\frac{1}{2}}(x/\Delta t) dx \right]. \quad (.115)$$

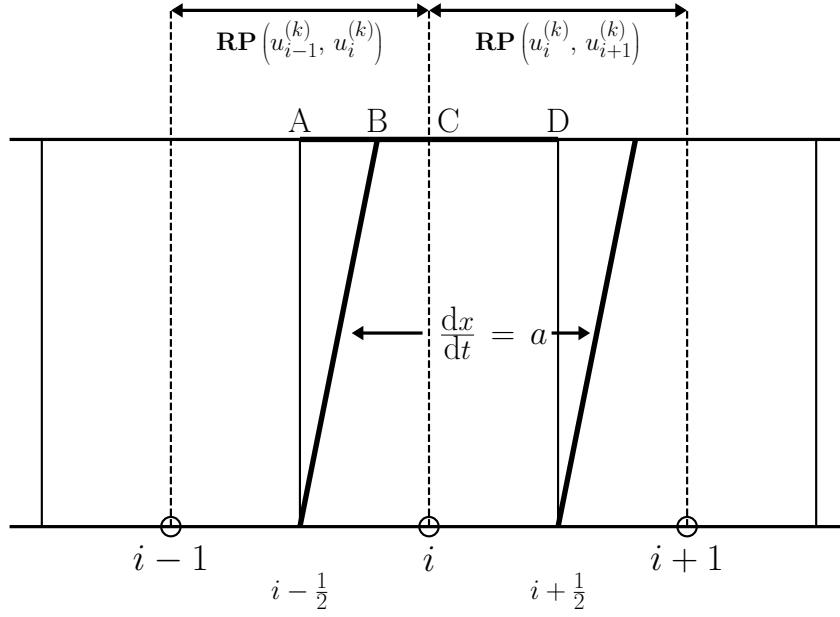


Figure A.17.: A stencil of Godunov's method for the linear advection equation where speed  $a > 0$ . Solutions to the Riemann problem are averaged within cell  $I_i$ .

(.115) is computed at time  $\Delta t$  between the intercell boundaries  $x_{i-\frac{1}{2}}$  and  $x_{i+\frac{1}{2}}$ . As illustrated in Figure A.17, only the right half of  $u_{i-\frac{1}{2}}$  and left half of  $u_{i+\frac{1}{2}}$  is applied. To compute the integral properly, restrictions are imposed on the timestep size  $\Delta t$  with

$$c = \frac{a \Delta t}{\Delta x} \leq \frac{1}{2}. \quad (.116)$$

Defining the interval lengths  $AB$  and  $BC$  as

$$l_{AB} = c\Delta x, \quad l_{BC} = \left(\frac{1}{2} - c\right) \Delta x, \quad (.117)$$

and using (.113) and (.114), re-write (.115) as

$$u_i^{(k+1)} = u_i^{(k)} + c \left( u_{i-1}^{(k)} - u_i^{(k)} \right). \quad (.118)$$

This is precisely the form to the CIR first order upwind method for positive speed  $a$  as seen in (.41) in Section A.2.3.

#### A.4.3. Godunov's Method: Interpretation 2

A second interpretation of Godunov's method can be developed by considering the solution of the Riemann problems  $\text{RP} \left( u_{i-1}^{(k)}, u_i^{(k)} \right)$  and  $\text{RP} \left( u_i^{(k)}, u_{i+1}^{(k)} \right)$  written as

$$u_i^{(k+1)} = \frac{1}{\Delta x} \int_{x_{i-\frac{1}{2}}}^{x_{i+\frac{1}{2}}} \tilde{u}(x, \Delta t) dx. \quad (.119)$$

$\tilde{u}(x, t)$  defines the combined solution between the two local Riemann problems. Since  $\tilde{u}$  is an exact solution to the fundamental conservation law (3.20), one may apply Equation (3.21) for the control volume  $[x_{i-\frac{1}{2}}, x_{i+\frac{1}{2}}] \times [0, \Delta t]$

$$\begin{aligned} \int_{x_{i-\frac{1}{2}}}^{x_{i+\frac{1}{2}}} \tilde{u}(x, \Delta t) dx &= \int_{x_{i-\frac{1}{2}}}^{x_{i+\frac{1}{2}}} \tilde{u}(x, 0) dx + \int_0^{\Delta t} f(\tilde{u}(x_{i-\frac{1}{2}}, t)) dt \\ &\quad - \int_0^{\Delta t} f(\tilde{u}(x_{i+\frac{1}{2}}, t)) dt. \end{aligned} \quad (.120)$$

Applying the definition for a cell average (.112) into (.120) and dividing by  $\Delta x$  yields Equation (3.25) (page 108)

$$u_i^{(k+1)} = u_i^{(k)} + \frac{\Delta t}{\Delta x} [f_{i-\frac{1}{2}} - f_{i+\frac{1}{2}}], \quad (.121)$$

where

$$f_{i-\frac{1}{2}} = \frac{1}{\Delta t} \int_0^{\Delta t} f(\tilde{u}(x_{i-\frac{1}{2}}, t)) dt, \quad f_{i+\frac{1}{2}} = \frac{1}{\Delta t} \int_0^{\Delta t} f(\tilde{u}(x_{i+\frac{1}{2}}, t)) dt \quad (.122)$$

are the intercell fluxes defined as time integral averages. Through utilising the integral form of the conservations laws on the finite volume  $[x_{i-\frac{1}{2}}, x_{i+\frac{1}{2}}] \times [0, \Delta t]$  in  $x-t$  space the conservation law (.120) is derived with intercell fluxes (3.25).

$f(\tilde{u}(x, t))$  is an integrand where each cell interface depends on the exact solution  $\tilde{u}(x, t)$  of the local Riemann problem as time evolves,

$$\tilde{u}(x_{i-\frac{1}{2}}, t) = u_{i-\frac{1}{2}}(0), \quad \tilde{u}(x_{i+\frac{1}{2}}, t) = u_{i+\frac{1}{2}}(0), \quad (.123)$$

with fluxes

$$f_{i-\frac{1}{2}} = f(u_{i-\frac{1}{2}}(0)), \quad f_{i+\frac{1}{2}} = f(u_{i+\frac{1}{2}}(0)). \quad (.124)$$

For flux  $f(u) = au$  and  $a > 0$  the intercell fluxes are defined as

$$f_{i-\frac{1}{2}} = au_{i-\frac{1}{2}}^{(k)}, \quad f_{i+\frac{1}{2}} = au_i^{(k)} \quad (.125)$$



which when substituted into (3.25) reproduces the CIR scheme. This second interpretation of Godunov's method is more widely applied since it is easier to implement in practice and avoids the restrictive CFL condition (.116).

### A.5. Total Variation Diminishing Methodology

The fundamental consideration one has when analysing numerical methods is that of the convergence problem. Modelling non-linear systems requires proofs which rely on non-linear stability theory. Total Variation Stable methods which are defined as mesh-dependent approximations within *compact sets* may be shown as convergent. Further details may be located in Harten (1983) and LeVeque (1992).

Ami Harten introduced the Total Variation Diminishing (TVD) concept (Harten, 1983), a subset of total variation stable methods. Mathematically, such approaches result in methods which do not increase in time. Consider once again the partial differential advection equation (3.1).

For  $u_j^{(k)} = u(x_j, t^{(k)})$  its total variation (TV) is defined as

$$TV(u(\cdot, t)) = \int \left| \frac{\partial u}{\partial x} \right| dx, \quad (.126)$$

or in the discrete case

$$TV(u^{(k)}) = TV(u(\cdot, t^{(k)})) = \sum_j \left| u_{j+1}^{(k)} - u_j^{(k)} \right|. \quad (.127)$$

A numerical method is considered to be *total variation diminishing* (TVD) provided

$$TV(u^{(k+1)}) \leq TV(u^{(k)}). \quad (.128)$$

Given  $u^{(k)}$  is monotonically increasing/decreasing in space, so is  $u^{(k+1)}$ . Harten (1983) showed that a monotone scheme is TVD and TVD methods are monotonicity preserving.

Within computational fluid dynamics applications, very fine computational grids are preferred to avoid any spurious oscillations in the solution which can result in a non-convergent numerical method. However, such fine resolutions are typically computationally cumbersome and inefficient time-wise. To combat this one may use more coarse grids utilising the upwind method (discussed in Section A.2) and other schemes. However, there is a high possibility of false shock predictions. A TVD method on a course mesh enables a more accurate prediction as it preserves monotonicity and so avoids spurious oscillations within the solution and saves computational expenditure. A summary of second order TVD limiters are highlighted in Table A.2 are second order TVD limiters. with its admissible

regions highlighted in Figure A.18.

Table A.2.: Common forms of flux/slope limiter functions  $\phi$ , the majority of which are second-order TVD.

Name	Symbol	Formula	Limit	Reference
<b>CHARM</b>	$\phi_{cm}(r)$	$\frac{r(3r+1)}{(r+1)^2}, r > 0, \quad 0$ otherwise	$\lim_{r \rightarrow \infty} \phi_{cm}(r) = 3$	Zhou (1995)
<b>HCUS</b>	$\phi_{hc}(r)$	$\frac{1.5(r+ r )}{r+2}$	$\lim_{r \rightarrow \infty} \phi_{hc}(r) = 3$	Waterson and Deconinck (1995)
<b>HQUICK</b>	$\phi_{hq}(r)$	$\frac{2(r+ r )}{r+3}$	$\lim_{r \rightarrow \infty} \phi_{hq}(r) = 4$	Waterson and Deconinck (1995)
<b>Koren</b>	$\phi_{kn}(r)$	$\max \left( 0, \min \left( 2r, \min \left( \frac{1+2r}{3}, 2 \right) \right) \right)$	$\lim_{r \rightarrow \infty} \phi_{kn}(r) = 2$	Koren (1993)
<b>minmod</b>	$\phi_{mm}(r)$	$\max [0, \min (0, r)]$	$\lim_{r \rightarrow \infty} \phi_{mm}(r) = 1$	Roe (1986)
<b>monotonised central</b>	$\phi_{mc}(r)$	$\max [0, \min (2r, 0.5(1+r)), 2]$	$\lim_{r \rightarrow \infty} \phi_{mc}(r) = 2$	van Leer (1977)
<b>Osher</b>	$\phi_{os}(r)$	$\max [0, \min (r, \beta)], \quad (1 \leq \beta \leq 2)$	$\lim_{r \rightarrow \infty} \phi_{os}(r) = \beta$	Chakravarthy and Osher (1983)
<b>ospre</b>	$\phi_{op}(r)$	$\frac{1.5(r^2+r)}{r^2+r+1}$	$\lim_{r \rightarrow \infty} \phi_{op}(r) = 1.5$	Waterson and Deconinck (1995)
<b>smart</b>	$\phi_{sm}(r)$	$\max [0, \min (2r, 0.25 + 0.75r, 4)]$	$\lim_{r \rightarrow \infty} \phi_{sm}(r) = 4$	Gaskell and Lau (1988)
<b>superbee</b>	$\phi_{sb}(r)$	$\max [0, \min (2r, 1), \min (r, 2)]$	$\lim_{r \rightarrow \infty} \phi_{sb}(r) = 2$	Roe (1986)
<b>Sweby</b>	$\phi_{sw}(r)$	$\max [0, \min (\beta r, 1), \min (r, \beta)], \quad 1 \leq \beta \leq 2$	$\lim_{r \rightarrow \infty} \phi_{sw}(r) = \beta$	Sweby (1984)
<b>UMIST</b>	$\phi_{um}(r)$	$\max [0, \min (2r, 0.25 + 0.75r, 0.75 + 0.25r, 2)]$	$\lim_{r \rightarrow \infty} \phi_{um}(r) = 2$	Lien and Leschziner (1994)
<b>van Albada 1</b>	$\phi_{va1}(r)$	$\frac{r^2+r}{r^2+1}$	$\lim_{r \rightarrow \infty} \phi_{va1} = 1$	van Albada et al. (1982)
<b>van Albada 2</b>	$\phi_{va2}$	$\frac{2r}{r^2+1}$	$\lim_{r \rightarrow \infty} \phi_{va2} = 0$	Kermani et al. (2003)

Table A.2.: Common forms of flux/slope limiter functions  $\phi$ , the majority of which are second-order TVD.

Name	Symbol	Formula	Limit	Reference
van Leer	$\phi_{vl}(r)$	$\frac{r +  r }{1 +  r }$	$\lim_{r \rightarrow \infty} \phi_{vl}(r) = 2$	van Leer (1974)

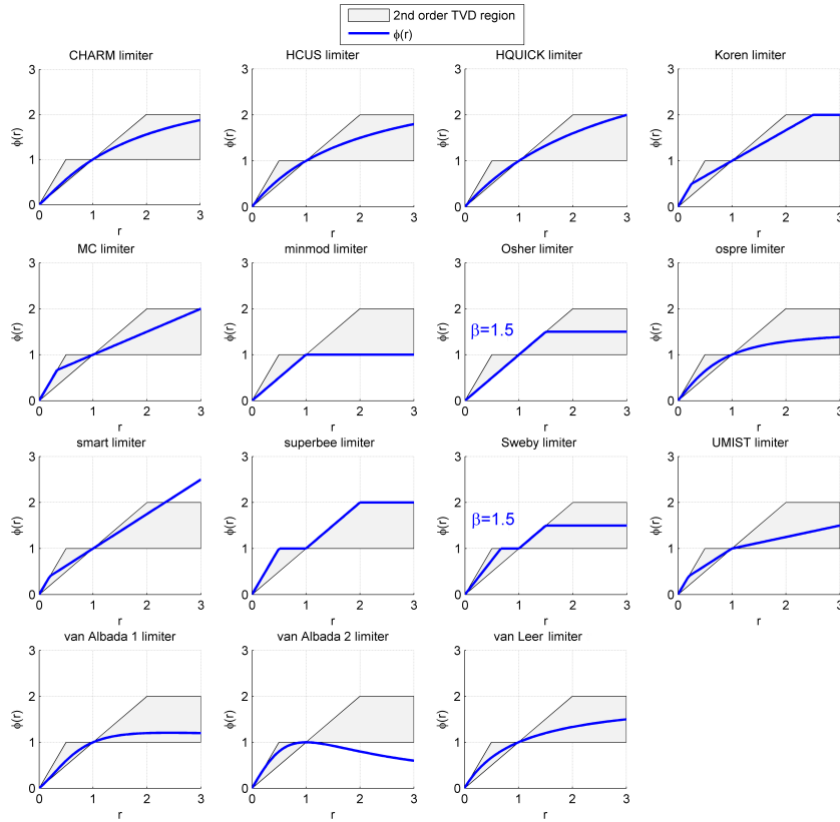


Figure A.18.: Graphical representation outputs (blue) along with the admissible second-order TVD region (grey). Obtained from Wikipedia (2022).

## B. Infiltration Modelling

The forces of gravity and capillarity which controls the movement of water into ground soil is a process known as *infiltration*. Viscous forces involved in the infiltration process limit the flow into soil pores. This *infiltration rate*,  $f$ , is a flow measured via *hydraulic conductivity* and/or *permeability*. This rate is dependent on soil characteristics, its amount and soil moisture distribution and total water availability at the ground surface. *Infiltration capacity*,  $f_c$ , is the maximum rate at which a given soil can absorb water in a given circumstance. If the infiltration capacity is greater than the surface water input over a period of time, then the infiltration rate will be equal to the surface water input rate  $w$ . If a soil's ability to absorb water is less than the rainfall intensity at a given time period then the infiltration at the surface occurs at the infiltration capacity rate. Hence, actual infiltration rate at a given time is

$$f = \min(f_c, w). \tag{.129}$$

Non-infiltrated water accumulates on the ground surface and adds to surface runoff processes B.19. Surface overland flow runoff rate,  $R$ , known as *precipitation excess* is defined as

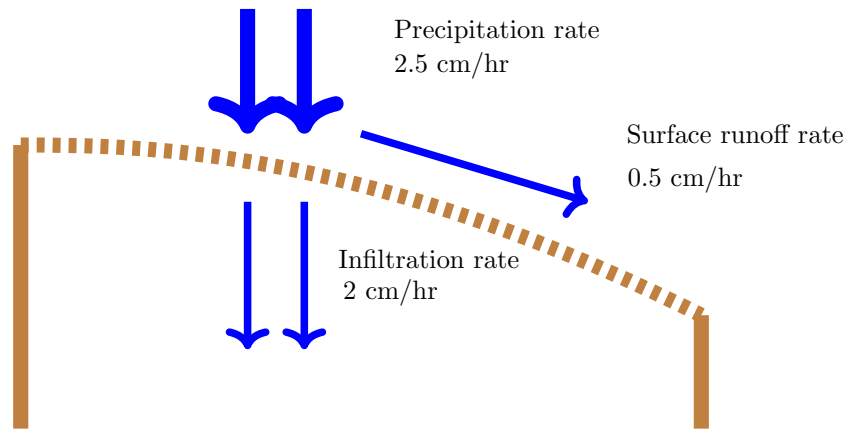


Figure B.19.: Surface runoff pictorial representation when water input is greater than infiltration capacity. Adapted from Dunne and Leopold (1978); Tarboton (2003).

$$R = w - f. \quad (.130)$$

Infiltration capacity is a dynamic characteristic. Surface runoff accumulation is directly affected by the decrease of infiltration capacity. *Point infiltration modelling* attempts to calculate surface runoff at given timesteps accounting for a changing infiltration capacity over a storm event. Using  $F$  as an independent variable known as *accumulated infiltration depth*, the infiltration capacity may be defined as a decreasing function  $f_c(F)$ . As  $F$  increases,  $f_c$  decreases over time.

Important factors in determining how much water may be stored before a soil is saturated include the soil's profile and initial moisture content. Well-drained, coarse and deep soils with large organic matter facilitate higher infiltration capacities compared to shallow soil profiles in clayey type soils which only accept low volumes of infiltration. Further details on physical phenomena which affect infiltration capacity may be seen in (Tarboton, 2003, pg. Chapter 5: 2) and references therein.

### B.1. From First Principles - Richards Equation

To begin calculating infiltration at a point, the physical conservation of mass principle through the continuity equation is combined with Darcy's equation which quantifies unsaturated flow through soils.

Consider the control volume in Figure B.20. The total volume of water in the control volume is the moisture content ( $\Delta\theta$ ) multiplied by its total volume  $V = \Delta x \Delta y \Delta z$ . The change in storage may be written as the specific discharge across the bottom surface  $q$  multiplied by its surface area minus the specific outflow discharge across the top surface  $q + \Delta q$  multiplied by the surface area during a given time interval.

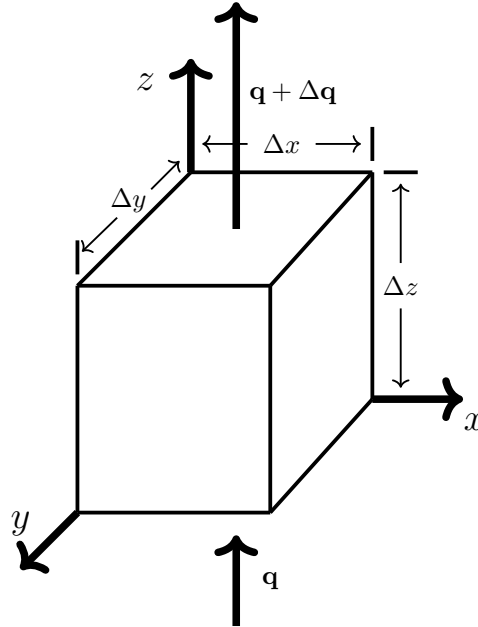


Figure B.20.: A control unsaturated soil volume considered when constructing the continuity equation. Adapted from Chow et al. (1988); Tarboton (2003).

$$\Delta\theta \Delta x \Delta y \Delta z = (q \Delta x \Delta y - (q + \Delta q) \Delta x \Delta y) \Delta t. \quad (.131)$$

Dividing (.131) by its volume at the time interval and letting  $\Delta z \rightarrow 0$  and  $\Delta t \rightarrow 0$  yields the continuity equation in the vertical direction

$$\frac{\partial\theta}{\partial t} = -\frac{\partial q}{\partial z}. \quad (.132)$$

Substituting Darcy's equation (.133) into (.132) gives Richards equation (.134) where  $\psi = h - z$  and **hydraulic conductivity**  $K$

$$\frac{\partial\theta}{\partial t} = \frac{\partial}{\partial z} K \frac{\partial h}{\partial z} \quad (.133)$$

$$\frac{\partial\theta}{\partial t} = \frac{\partial}{\partial z} \left( K \frac{\partial\psi}{\partial z} + K \right). \quad (.134)$$

Richards equation describes the vertical movement of water through unsaturated soil. Its complications arise from the necessity to model the characteristic relationships between moisture content and pressure head ( $\theta(\psi)$ ) as well as Hydraulic conductivity with pressure head ( $K(\psi)$ ) and/or moisture content ( $K(\theta)$ ).

Taking moisture content as an independent variable, Equation (.134) becomes

$$\frac{\partial \theta}{\partial t} = \frac{\partial}{\partial z} \left( D(\theta) \frac{\partial \theta}{\partial z} + K(\theta) \right), \quad (.135)$$

where  $D(\theta) = K(\theta) \frac{d\psi}{d\theta}$  is the *soil water diffusivity* due to its similarity with the diffusion term in the diffusion equation. Similarly, one may write Richards equation in terms of pressure head as

$$C(\psi) \frac{\partial \psi}{\partial t} = \frac{\partial}{\partial z} \left( K(\psi) \frac{\partial \psi}{\partial z} + K(\psi) \right), \quad (.136)$$

where  $C(\psi) \frac{d\theta}{d\psi}$  is known as the *specific moisture capacity*.

Philip (1969); Parlange et al. (1999); and Smith (2002) highlight analytical solutions for Richard's equation given specific parametrisations of  $K(\theta)$ ,  $D(\theta)$ ,  $K(\psi)$ , and  $C(\psi)$ . Numerical solutions based on moisture content are better at conserving moisture and dealing with dryer soil conditions. However, numerical computational methods using pressure head as an independent variable handle the change between saturated and unsaturated flow better close to the water table, but it is not as good at conserving mass. Celia and Bouloutas (1990) outlines methods which combines the representations for moisture content and pressure head.

## B.2. Richards Equation - A qualitative analysis

Accurate numerical results to Richards equation require complex and detailed soils data which are often scarce in practise. However, one may analyse the relationship between soil moisture and depth profiles qualitatively to construct an empirical model to determine soil infiltration.

Consider a soil block homogeneous with initial hydrostatic conditions ( $q = 0$ ,  $dh/dz = 0$  and  $h = \text{constant}$ ). Let  $\psi = -z$  where  $z$  is the height from the ground surface to the water table. Thus the initial moisture content at each depth  $z$  is

$$\theta(z) = \theta(\psi = -z). \quad (.137)$$

Initially, water reaches the ground surface at an input rate  $w$  which goes straight into the storage layer, increasing its moisture content. This in turn increases hydraulic conductivity and reduces the absolute value of negative pressure head. Thus a flux out of the surface layer into the layer below occurs. This process repeats at each timestep successively increasing moisture content as water input occurs, resulting in the water content profiles shown in Figure 3.11.

Capillary surface tension forces and gravitational forces, quantified by the pressure and



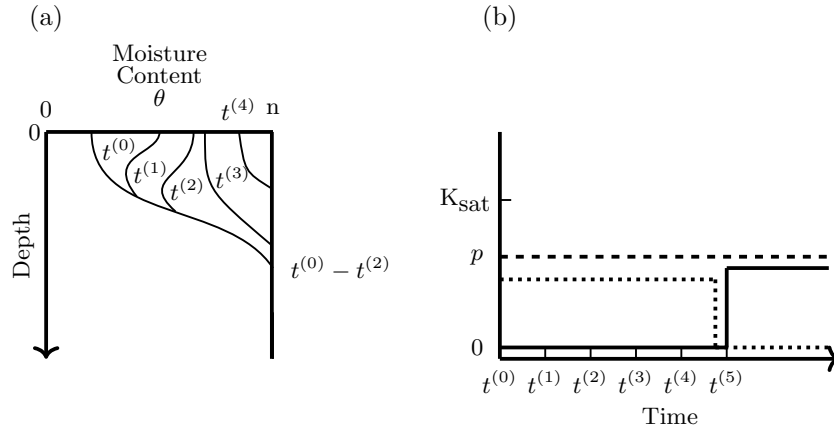


Figure B.21.: Saturation excess runoff generation illustration. (a) shows the moisture content vs. depth profile. (b) A time series of runoff generation when a soil is saturated. Adapted from Bras (1990); Tarboton (2003).

elevation head respectively, determines the downward hydraulic gradient which induces the infiltration. If water input rate is greater than saturated hydraulic conductivity ( $w > K_{sat}$ ), at some point in the process water content at the surface will reach saturation. This reduces infiltration capacity below the surface water input rate generating surface runoff. Shown in Figure 3.11,  $t^{(3)}$  is known as the **ponding time**. After this occurs, water continues to infiltrate and a zone of saturation propagates downward into the soil as seen at  $t^{(4)}$ . The wave of soil moisture from  $t^{(1)}$  to  $t^{(4)}$  is the **wetting front**. As the process increases the zone of saturation, there is a reduction in the contribution of suction head to gradient induced infiltration and in turn a reduction of infiltration capacity. Figure 3.11 (b) shows the relationship between water input, infiltration and surface runoff during ponding. In other words, the necessary conditions for runoff to occur are that the water input rate is greater than the saturated hydraulic conductivity of the soil ( $w > K_{sat}$ ) and that the surface water input duration is longer than the required ponding time for a given initial soil moisture profile and water input rate.

Provided that initial conditions are hydrostatic, at each depth  $z$ , soil moisture deficit below saturation is  $n - \theta(z)$ . The total soil moisture deficit may be found by integrating from the water table to the surface i.e.

$$D = \int_z^0 (n - \theta(z)) dz. \quad (.138)$$

This is the total amount of water which can infiltrate into a soil profile. Inputting surface water in this scenario results in a soil profile such as B.21. Yet, even if  $w < K_{sat}$  the accumulated surface water input reaches the soil moisture deficit and so the soil becomes completely saturated and infiltration capacity is zero. Any surface water input at this point generates runoff. The time series between surface water input, surface runoff and infiltration is illustrated in Figure B.21(b).

### B.3. The SCS Method: Terminology

#### B.3.1. Hydrological Soil Group

Hydrological soil groups (HSGs) reflect the runoff potential of the soils as determined by the NRCS. They have been defined as follows:

1. A: High infiltration (low runoff potential) when thoroughly wetted. High rate of water transmission through soils. Typically consisting of well-drained sands and gravels.
2. B: Moderate infiltration when thoroughly wetted. Chiefly make up soils which are moderately well-drained with moderately fine to coarse textures. Typically have water rate transmission between 3.8-7.6 mm / hr.
3. C: Slow infiltration rates when thoroughly wetted. Consists of soils with a layer which impedes vertical transfer of water downward. Soils have moderately fine to fine textures. Water transmission rates between 1.3-3.8 mm/hr.
4. D: Low infiltration (high runoff potential) when thoroughly wetted. Typically clay soils with high swelling potential. Very slow water transmission rate ( $< 1.3$  mm /hr).

Tables 2-2a - 2-2d from the Natural Resources Conservation Service (Natural Resources Conservation Service, 1986, Chapt. 2 pgs. 5-8) summarise the average moisture condition (antecedant moisture condition II) in Table 3.5. These values can be adjusted to reflect the below average and above average moisture conditions of which is discussed in the next section.

#### B.3.2. Antecedent Moisture Conditions

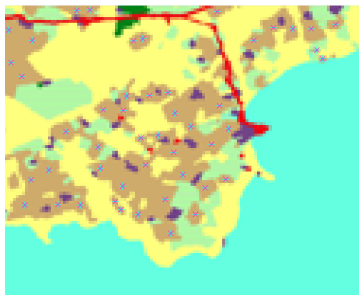
Soil moisture content before a precipitation event majorly influences the runoff experienced within a region. This phenomena is known as the *antecedent moisture condition* (AMC). The curve numbers for dry, average and moist soil moisture conditions are denoted  $CN_I$  (AMC I),  $CN_{II}$  (AMC II) and  $CN_{III}$  (AMC III) respectively. The dry soil moisture condition is calculated as a factor multiple of the average condition (AMC II), where this factor is less than one. This will have the effect of reducing the curve runoff number and decrease potential runoff. Similarly, the moist soil condition will be a factor greater than one and increase the curve number, increasing potential runoff. These factor adjustments are presented below in Table B.3 obtained from Ward and Trimble (2003).

Table B.3.: Adjustment scaling parameters for varying soil moisture conditions. Adapted from Ward and Trimble (2003).

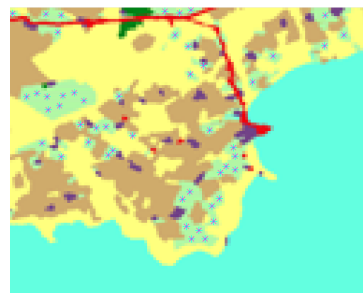
$CN_{II}$	Curve Number scaling parameters from $CN_{II}$	
	$CN_I$ (dry)	$CN_{III}$ (wet)
10	0.40	2.22
20	0.45	1.85
30	0.50	1.67
40	0.55	1.50
50	0.62	1.40
60	0.67	1.30
70	0.73	1.21
80	0.79	1.14
90	0.87	1.07
100	1.00	1.00

## C. Land-Use Image Processing

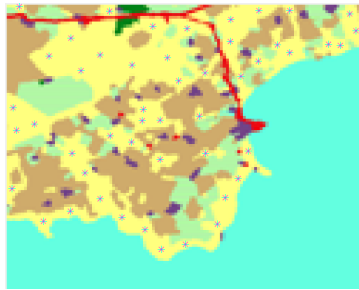
### C.1. 20m Resolution



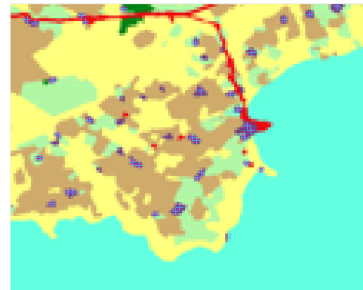
(a) Arable.



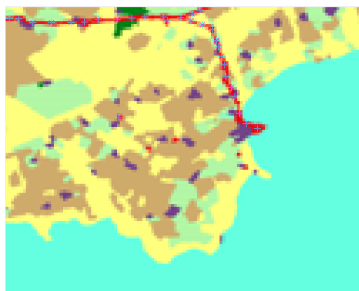
(b) Grassland.



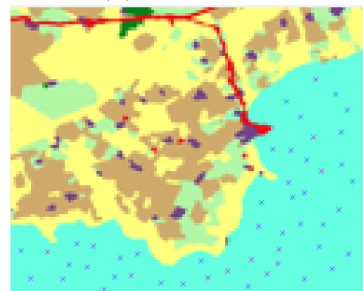
(c) Rough Grazing.



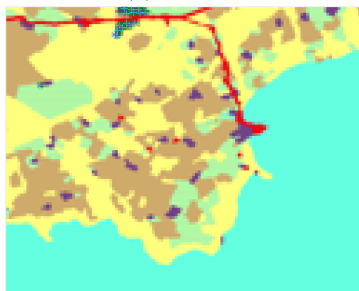
(d) Sub-Urban.



(e) Urban.

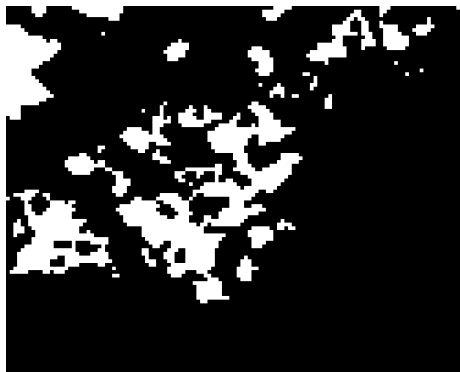


(f) Water.



(g) Woodland.

Figure C.22.: Locations of where RGB pixel samples were taken for image processing using the Dudley Stamp Map from Department for Environment, Food & Rural Affairs (2002c).



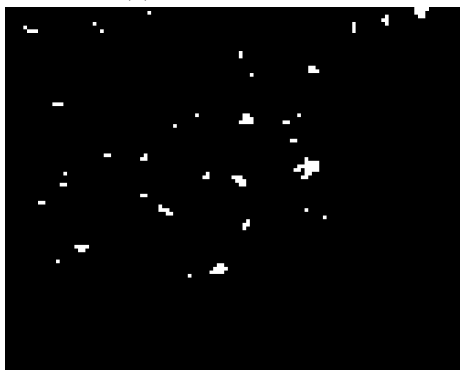
(a) Arable.



(b) Grassland.



(c) Rough Grazing.



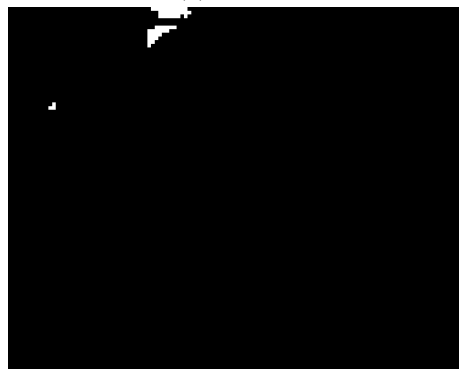
(d) Sub-Urban.



(e) Urban.



(f) Water.



(g) Woodland.

Figure C.23.: Binary outputs after image processing for each land use definition.

### C.2. 50m Resolution

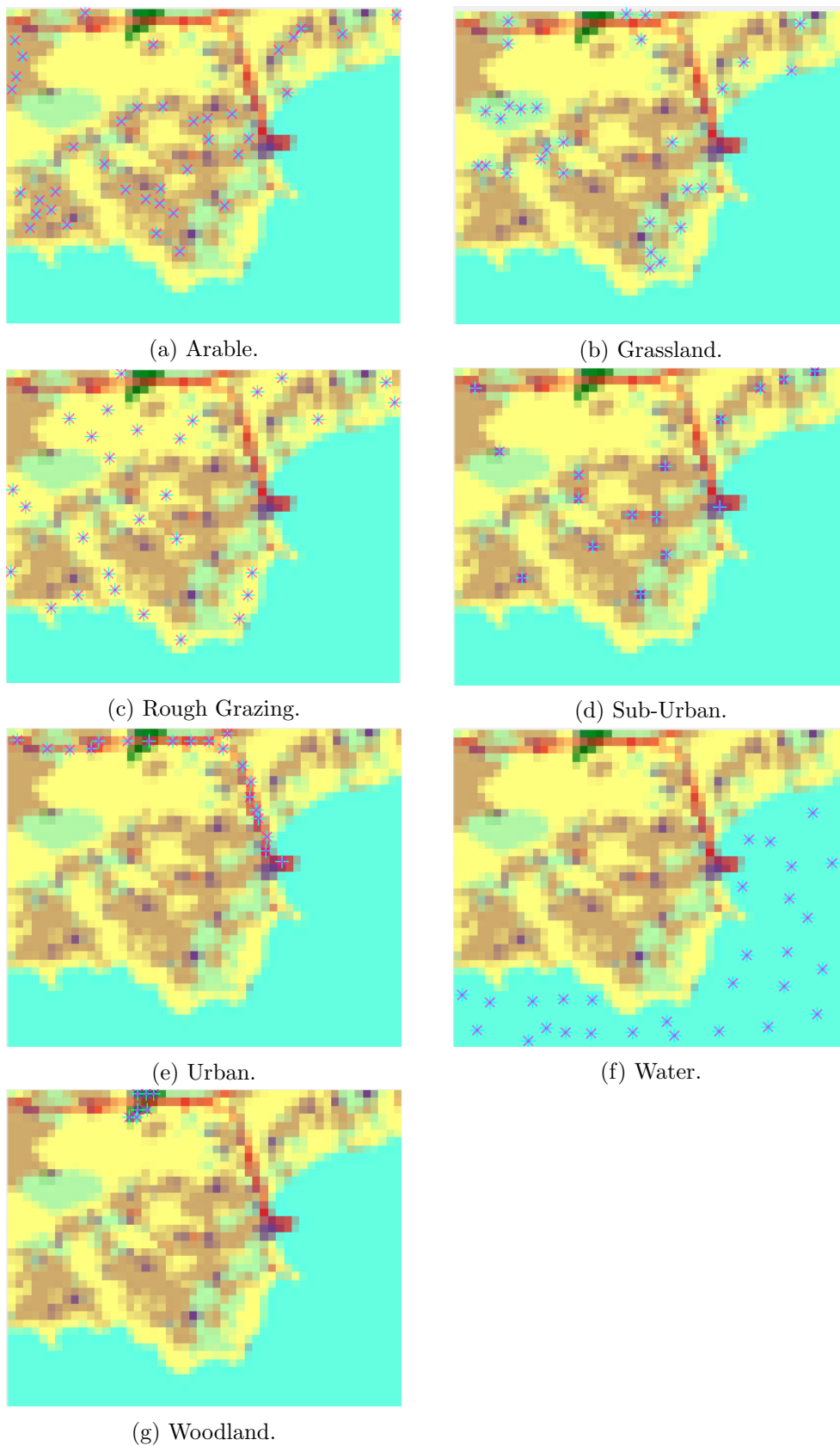
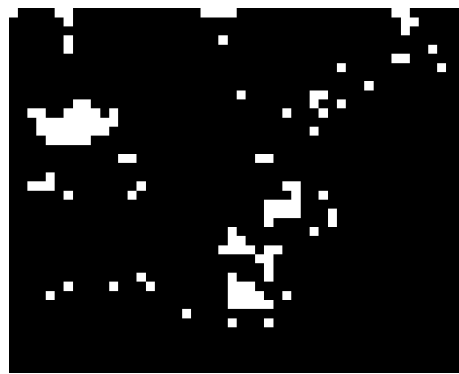


Figure C.1.: Locations of where RGB pixel samples were taken for image processing using the Dudley Stamp Map from Department for Environment, Food & Rural Affairs (2002c).



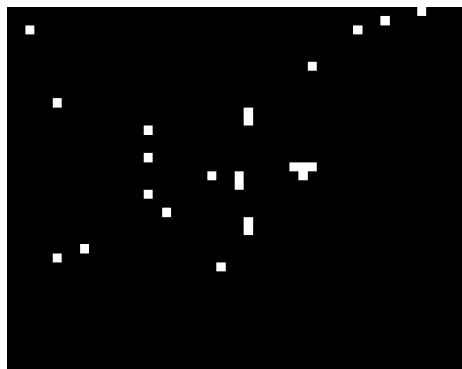
(a) Arable.



(b) Grassland.



(c) Rough Grazing.



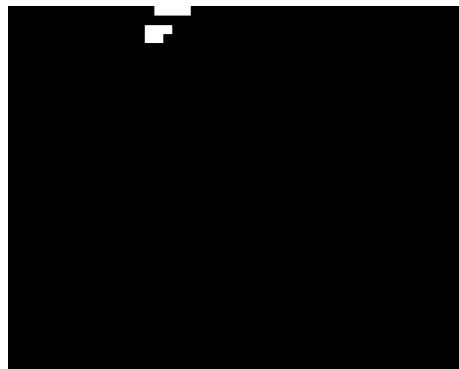
(d) Sub-Urban.



(e) Urban.



(f) Water.



(g) Woodland.

Figure C.2.: Binary outputs after image processing for each land use definition.

### D. Green-Ampt approximation Tabulated Data

Table D.4.: Raw value comparison between the full and approximate Green-Ampt infiltration model using the Sand parameter values.

Time	Rainfall	Rainfall Intensity			Cumulative Infiltration			Capacity			Infiltration			Runoff		
		0.3	0.4	0.5	Full	Approx	% Error	Full	Approx	% Error	Full	Approx	% Error	Full	Approx	% Error
0	0.3	1.2	0	0	0	0	∞	∞	-	0	0.3	0.3	0	0	0	0
0.25	0.4	1.6	0.3	0.3	0	0	59.4497	59.4497	0	0	0.4	0.4	0	0	0	0
0.5	0.5	2	0.7	0.7	0	0	32.2099	32.2099	0	0	0.5	0.5	0	0	0	0
0.75	0.6	2.4	1.2	1.2	0	0	23.6974	23.6974	0	0	0.6	0.6	0	0	0	0
1	0.7	2.8	1.8	1.8	0	0	19.725	19.725	0	0	0.7	0.7	0	0	0	0
1.25	0.8	3.2	2.5	2.5	0	0	17.5004	17.5004	0	0	0.8	0.8	0	0	0	0
1.5	0.4	1.6	3.3	3.3	0	0	16.1136	16.1136	0	0	0.4	0.4	0	0	0	0
1.75	0.6	2.4	3.7	3.7	0	0	15.6451	15.6451	0	0	0.6	0.6	0	0	0	0
2	0.6	2.4	4.3	4.3	0	0	15.1058	15.1058	0	0	0.6	0.6	0	0	0	0

Table D.5.: Raw value comparison between the full and approximate Green-Ampt infiltration model using the Loamy Sand parameter values.

Time	Rainfall	Rainfall Intensity			Cumulative Infiltration			Capacity			Infiltration			Runoff		
		0.3	0.4	0.5	Full	Approx	% Error	Full	Approx	% Error	Full	Approx	% Error	Full	Approx	% Error
0	0.3	1.2	0	0	0	0	∞	∞	-	0	0.3	0.3	0	0	0	0
0.25	0.4	1.6	0.3	0.3	0	0	18.0397	18.0397	0	0	0.4	0.4	0	0	0	0
0.5	0.5	2	0.7	0.7	0	0	9.4399	9.4399	0	0	0.5	0.5	0	0	0	0
0.75	0.6	2.4	1.2	1.2	0	0	6.7524	6.7524	0	0	0.6	0.6	0	0	0	0
1	0.7	2.8	1.8	1.8	0	0	5.4983	5.4983	0	0	0.7	0.7	0	0	0	0
1.25	0.8	3.2	2.5	2.5	0	0	4.7960	4.7960	0	0	0.8	0.8	0	0	0	0
1.5	0.4	1.6	3.3	3.3	0	0	4.3582	4.3582	0	0	0.4	0.4	0	0	0	0
1.75	0.6	2.4	3.7	3.7	0	0	4.2102	4.2102	0	0	0.6	0.6	0	0	0	0
2	0.6	2.4	4.3	4.3	0	0	4.04	4.04	0	0	0.6	0.6	0	0	0	0



Table D.6.: Raw value comparison between the full and approximate Green-Ampt infiltration model using the Sandy Loam parameter values.

Time	Rainfall	Rainfall Intensity	Cumulative Infiltration			Capacity			Infiltration			Runoff		
			Full	Approx	% Error	Full	Approx	% Error	Full	Approx	% Error	Full	Approx	% Error
0	0.3	1.2	0	0	0	$\infty$	$\infty$	-	0.3	0.3	0	0	0	0
0.25	0.4	1.6	0.3	0.3	0	8.8653	8.8653	0	0.4	0.4	0	0	0	0
0.5	0.5	2	0.7	0.7	0	4.4223	4.4223	0	0.5	0.5	0	0	0	0
0.75	0.6	2.4	1.2	1.2	0	3.0338	3.0338	0	0.5998	0.5997	0.01	$2 \times 10^{-4}$	$1 \times 10^{-4}$	53.98
1	0.7	2.8	1.7998	1.7997	0	2.3861	2.3861	0	0.5541	0.5965	7.65	0.1459	0.1035	29.07
1.25	0.8	3.2	2.3539	2.3962	1.80	2.0810	2.0634	0.84	0.4970	0.5159	3.80	0.3030	0.2841	6.24
1.5	0.4	1.6	2.8508	2.9121	2.15	1.9082	1.8910	0.90	0.4	0.4	0	0	0	0
1.75	0.6	2.4	3.2508	3.3121	1.88	1.8075	1.7943	0.73	0.4406	0.4486	1.80	0.1594	0.1514	4.98
2	0.6	2.4	3.6915	3.7607	1.87	1.7219	1.7103	0.68	0.422	0.4276	1.31	0.1780	0.1724	3.11

Table D.7.: Raw value comparison between the full and approximate Green-Ampt infiltration model using the Loam parameter values.

Time	Rainfall	Rainfall Intensity	Cumulative Infiltration			Capacity			Infiltration			Runoff		
			Full	Approx	% Error	Full	Approx	% Error	Full	Approx	% Error	Full	Approx	% Error
0	0.3	1.2	0	0	0	$\infty$	$\infty$	-	0.3	0.3	0	0	0	0
0.25	0.4	1.6	0.3	0.3	0	1.7635	1.7635	0	0.3189	0.2536	20.46	0.0811	0.1469	81.09
0.5	0.5	2	0.6189	0.5536	10.54	1.0300	1.1113	7.90	0.2308	0.2778	20.36	0.2692	0.2222	17.46
0.75	0.6	2.4	0.8497	0.8315	2.15	0.8426	0.8536	1.31	0.1977	0.2164	7.93	0.4023	0.3866	3.90
1	0.7	2.8	1.0474	1.0449	0.25	0.7477	0.7487	0.13	0.1790	0.1872	4.57	0.5210	0.5128	1.57
1.25	0.8	3.2	1.2264	1.2320	0.46	0.6882	0.6886	0.23	0.1666	0.1717	3.05	0.6334	0.6283	0.80
1.5	0.4	1.6	1.3930	1.4037	0.77	0.6466	0.6442	0.36	0.1576	0.1611	2.21	0.2424	0.2389	1.44
1.75	0.6	2.4	1.5506	1.5648	0.91	0.6154	0.6129	0.41	0.1507	0.1532	1.69	0.4493	0.4468	0.57
2	0.6	2.4	1.7013	1.7180	0.98	0.5910	0.5886	0.41	0.1452	0.1471	1.33	0.4548	0.4529	0.43

Table D.8.: Raw value comparison between the full and approximate Green-Ampt infiltration model using the Silt Loam parameter values.

Time	Rainfall	Rainfall Intensity	Cumulative Infiltration			Capacity			Infiltration			Runoff				
			Full	Approx	% Error	Full	Approx	% Error	Full	Approx	% Error	Full	Approx	% Error		
0	0.3	1.2	0	0	0	$\infty$	$\infty$	-	0.3	0.3	0	0	0	0	0	0
0.25	0.4	1.6	0.3	0.3	0	5.0223	5.0223	0	0.4	0.4	0	0	0	0	0	0
0.5	0.5	2	0.7	0.7	0	2.5239	2.5239	0	0.4846	0.4703	2.94	0.0154	0.0293	90.03	0.0154	0.03
0.75	0.6	2.4	1.1846	1.1703	1.20	1.7573	1.7708	0.77	0.4000	0.4427	10.67	0.2000	0.1573	21.34	0.2000	0.03
1	0.7	2.8	1.5846	1.6130	1.79	1.4778	1.4632	0.99	0.3492	0.3658	4.76	0.3508	0.3342	4.73	0.3508	0.03
1.25	0.8	3.2	1.9338	1.9788	2.33	1.3283	1.3129	1.16	0.3193	0.3282	2.79	0.4807	0.4718	1.86	0.4807	0.03
1.5	0.4	1.6	2.2531	2.3071	2.39	1.2322	1.2186	1.11	0.2991	0.3046	1.86	0.1009	0.0954	5.51	0.1009	0.03
1.75	0.6	2.4	2.5522	2.6117	2.33	1.1640	1.1522	1.01	0.2843	0.2881	1.33	0.3157	0.3119	1.20	0.3157	0.03
2	0.6	2.4	2.8364	2.8998	2.33	1.1124	1.1023	0.91	0.2729	0.2756	1.00	0.3271	0.3244	0.84	0.3271	0.03

Table D.9.: Raw value comparison between the full and approximate Green-Ampt infiltration model using the Sandy Clay Loam parameter values.

Time	Rainfall	Rainfall Intensity	Cumulative Infiltration			Capacity			Infiltration			Runoff				
			Full	Approx	% Error	Full	Approx	% Error	Full	Approx	% Error	Full	Approx	% Error		
0	0.3	1.2	0	0	0	$\infty$	$\infty$	-	0.3	0.3	0	0	0	0	0	0
0.25	0.4	1.6	0.3	0.3	0	1.4075	1.4075	0	0.2583	0.3519	36.25	0.1417	0.0481	66.05	0.1417	0.03
0.5	0.5	2	0.5583	0.6519	16.77	0.8258	0.7287	11.75	0.1829	0.1822	0.37	0.3171	0.3178	0.22	0.3171	0.03
0.75	0.6	2.4	0.7411	0.8341	12.54	0.6590	0.6023	8.61	0.1529	0.1506	1.54	0.4471	0.4494	0.53	0.4471	0.03
1	0.7	2.8	0.8941	0.9846	10.13	0.5720	0.5331	6.79	0.1356	0.1333	1.71	0.5644	0.5667	0.41	0.5644	0.03
1.25	0.8	3.2	1.0297	1.1179	8.570	0.5164	0.4875	5.60	0.1239	0.1219	1.66	0.6761	0.6781	0.30	0.6761	0.03
1.5	0.4	1.6	1.1536	1.2398	7.47	0.4770	0.4543	4.77	0.1154	0.1136	1.57	0.2846	0.2864	0.64	0.2846	0.03
1.75	0.6	2.4	1.2690	1.3534	6.65	0.4473	0.4288	4.14	0.1088	0.1072	1.47	0.4912	0.4928	0.32	0.4912	0.03
2	0.6	2.4	1.3777	1.405	6.01	0.4238	0.4083	3.66	0.1035	0.1021	1.37	0.4965	0.4979	0.28	0.4965	0.03

Table D.10.: Raw value comparison between the full and approximate Green-Ampt infiltration model using the Clay Loam parameter values.

Time	Rainfall	Rainfall Intensity	Cumulative Infiltration			Capacity			Infiltration			Runoff		
			Full	Approx	% Error	Full	Approx	% Error	Full	Approx	% Error	Full	Approx	% Error
0	0.3	1.2	0	0	0	$\infty$	$\infty$	-	0.2667	0.2383	10.36	0.0333	0.0614	84.54
0.25	0.4	1.6	0.2667	0.2383	10.66	0.7520	0.8298	10.35	0.1522	0.2074	36.33	0.2478	0.1926	22.31
0.5	0.5	2	0.4189	0.4457	6.41	0.5151	0.4901	4.85	0.1162	0.1225	5.42	0.3838	0.3775	1.64
0.75	0.6	2.4	0.5351	0.5683	6.19	0.4250	0.4060	4.46	0.0994	0.1015	2.13	0.5006	0.4985	0.42
1	0.7	2.8	0.6345	0.6698	5.56	0.3741	0.3596	3.86	0.0891	0.0899	0.97	0.6109	0.6101	0.14
1.25	0.8	3.2	0.7236	0.7597	4.99	0.3403	0.3289	3.36	0.0819	0.0899	0.42	0.7181	0.7178	0.05
1.5	0.4	1.6	0.8054	0.8419	4.53	0.3159	0.3066	2.96	0.0765	0.0766	0.13	0.3235	0.3234	0.03
1.75	0.6	2.4	0.8820	0.9186	4.15	0.2972	0.2893	2.64	0.0724	0.0723	0.04	0.5276	0.5277	0.01
2	0.6	2.4	0.9543	0.9909	3.83	0.2822	0.2755	2.38	0.0690	0.0689	0.14	0.5310	0.5311	0.02

Table D.11.: Raw value comparison between the full and approximate Green-Ampt infiltration model using the Silty Clay Loam parameter values.

Time	Rainfall	Rainfall Intensity	Cumulative Infiltration			Capacity			Infiltration			Runoff		
			Full	Approx	% Error	Full	Approx	% Error	Full	Approx	% Error	Full	Approx	% Error
0	0.3	1.2	0	0	0	$\infty$	$\infty$	-	0.3	0.3	0	0	$1 \times 10^{-4}$	0
0.25	0.4	1.6	0.3	0.3	0	1.1825	1.1827	0.01	0.2229	0.2957	32.66	0.1771	0.1043	41.09
0.5	0.5	2	0.5229	0.5957	13.91	0.7211	0.6453	10.52	0.1598	0.1613	0.94	0.3402	0.3387	0.44
0.75	0.6	2.4	0.6827	0.7570	10.87	0.5757	0.5291	8.10	0.1334	0.1323	0.85	0.4666	0.4677	0.24
1	0.7	2.8	0.8161	0.8893	8.96	0.4980	0.4653	6.57	0.1178	0.1163	1.28	0.5822	0.5837	0.26
1.25	0.8	3.2	0.9340	1.0056	7.67	0.4478	0.4230	5.53	0.1072	0.1058	1.39	0.6928	0.6942	0.21
1.5	0.4	1.6	1.0412	1.1113	6.73	0.4119	0.3923	4.78	0.0994	0.0981	1.39	0.3006	0.3019	0.46
1.75	0.6	2.4	1.2340	1.3015	6.03	0.3847	0.3686	4.21	0.0934	0.0921	1.34	0.5066	0.5079	0.25
2	0.6	2.4	1.0767	1.1258	5.47	0.3632	0.3496	3.76	0.0885	0.0874	1.29	0.5115	0.5126	0.22

Table D.12.: Raw value comparison between the full and approximate Green-Ampt infiltration model using the Sandy Clay parameter values.

Time	Rainfall	Rainfall Intensity	Cumulative Infiltration			Capacity			Infiltration			Runoff		
			Full	Approx	% Error	Full	Approx	% Error	Full	Approx	% Error	Full	Approx	% Error
0	0.3	1.2	0	0	0	$\infty$	$\infty$	-	0.2556	0.2185	14.5	0.0444	0.0817	84.06
0.25	0.4	1.6	0.2556	0.2185	14.5	0.6821	0.7876	15.47	0.1377	0.1969	42.97	0.2623	0.2031	22.56
0.5	0.5	2	0.3933	0.4154	5.62	0.4643	0.4427	4.64	0.1043	0.1107	6.13	0.3957	0.3893	1.62
0.75	0.6	2.4	0.4976	0.5261	5.73	0.3795	0.3622	4.56	0.0884	0.0906	2.44	0.5116	0.5094	0.42
1	0.7	2.8	0.5860	0.6167	5.23	0.3313	0.3178	4.07	0.0786	0.0795	1.11	0.6214	0.6205	0.14
1.25	0.8	3.2	0.6646	0.6961	4.75	0.2992	0.2884	3.62	0.0718	0.0721	0.48	0.7282	0.7279	0.05
1.5	0.4	1.6	0.7363	0.7682	4.33	0.2759	0.2670	3.25	0.0667	0.0667	0.13	0.3333	0.3333	0.03
1.75	0.6	2.4	0.8030	0.8350	3.98	0.2580	0.2504	2.94	0.0626	0.0626	0.07	0.5374	0.5374	0.01
2	0.6	2.4	0.8656	0.8976	3.69	0.2437	0.2371	2.68	0.0594	0.0953	0.19	0.5406	0.5407	0.02

Table D.13.: Raw value comparison between the full and approximate Green-Ampt infiltration model using the Silty Clay parameter values.

Time	Rainfall	Rainfall Intensity	Cumulative Infiltration			Capacity			Infiltration			Runoff		
			Full	Approx	% Error	Full	Approx	% Error	Full	Approx	% Error	Full	Approx	% Error
0	0.3	1.2	0	0	0	$\infty$	$\infty$	-	0.2312	0.1798	22.95	0.0688	0.1196	74.71
0.25	0.4	1.6	0.2312	0.1798	22.95	0.5784	0.7293	27.16	0.1179	0.1823	55.7	0.2821	0.2177	22.79
0.5	0.5	2	0.3491	0.3621	3.50	0.3999	0.3873	2.95	0.0900	0.0968	7.72	0.4100	0.4032	1.67
0.75	0.6	2.4	0.4391	0.4590	4.36	0.3282	0.3161	3.53	0.0765	0.0790	3.44	0.5235	0.5210	0.49
1	0.7	2.8	0.5156	0.5380	4.22	0.2869	0.2770	3.34	0.0681	0.0693	1.83	0.6319	0.6307	0.19
1.25	0.8	3.2	0.5837	0.6073	3.94	0.2593	0.2511	3.05	0.0622	0.0628	1.04	0.7378	0.7372	0.09
1.5	0.4	1.6	0.6459	0.6701	3.67	0.2391	0.2323	2.79	0.0578	0.0581	0.60	0.3422	0.3419	0.1
1.75	0.6	2.4	0.7036	0.7281	3.41	0.2236	0.2178	2.55	0.0543	0.0544	0.32	0.5457	0.5456	0.03
2	0.6	2.4	0.7579	0.7826	3.19	0.2112	0.2061	2.35	0.0515	0.0515	0.14	0.5485	0.5485	0.01

Table D.14.: Raw value comparison between the full and approximate Green-Ampt infiltration model using the Clay parameter values.

Time	Rainfall	Rainfall Intensity	Cumulative Infiltration			Capacity			Infiltration			Runoff		
			Full	Approx	% Error	Full	Approx	% Error	Full	Approx	% Error	Full	Approx	% Error
0	0.3	1.2	0	0	0	$\infty$	$\infty$	-	0.1908	0.1230	35.91	0.1092	0.1775	61.03
0.25	0.4	1.6	0.1908	0.1230	35.91	0.4381	0.6630	52.17	0.0901	0.1657	84.97	0.3099	0.2343	24.51
0.5	0.5	2	0.2810	0.2888	2.91	0.3072	0.2997	2.55	0.0692	0.0749	8.12	0.4308	0.4251	1.29
0.75	0.6	2.4	0.3502	0.3637	3.94	0.2524	0.2441	3.34	0.0588	0.0610	3.72	0.5412	0.5390	0.40
1	0.7	2.8	0.4090	0.4247	3.91	0.2204	0.2134	3.25	0.0523	0.0533	2.03	0.6477	0.6467	0.16
1.25	0.8	3.2	0.4612	0.4781	3.69	0.1988	0.1929	3.02	0.0476	0.0482	1.18	0.7524	0.7518	0.07
1.5	0.4	1.6	0.5089	0.5263	3.46	0.1830	0.1780	2.79	0.0442	0.0445	0.70	0.3558	0.3555	0.09
1.75	0.6	2.4	0.5531	0.5708	3.24	0.1708	0.1664	2.58	0.0414	0.0416	0.40	0.5608	0.5607	0.03
2	0.6	2.4	0.5945	0.6124	3.04	0.1610	0.1572	2.40	0.0392	0.0393	0.20	0.5608	0.5607	0.01

## E. Simulation Run Time Raw Data

Table E.1.: Model simulation times for each individual run for 20m and 50m resolutions in seconds with a scaling factor calculation for the north-eastern region.

Simulation No.	Resolution		Factor	Simulation No.	Resolution		Factor
	20m	50m			20m	50m	
1	253.7	43.4	5.85	27	256.2	43.1	5.94
2	252.2	44.4	5.68	28	254.8	42.3	6.02
3	252.0	44.0	5.73	29	255.8	42.7	5.99
4	252.7	43.5	5.81	30	253.8	44.5	5.70
5	252.6	43.3	5.83	31	253.8	44.0	5.77
6	253.7	43.7	5.81	32	251.8	43.8	5.75
7	252.0	44.4	5.68	33	254.2	43.7	5.82
8	253.9	44.1	5.76	34	254.9	43.0	5.93
9	253.3	43.4	5.84	35	254.9	43.7	5.83
10	257.6	43.4	5.94	36	255.0	44.7	5.70
11	255.1	42.9	5.95	37	254.5	44.1	5.77
12	261.2	44.2	5.91	38	255.0	43.3	5.89
13	257.4	44.5	5.78	39	255.2	43.1	5.92
14	259.2	43.5	5.96	40	256.8	43.4	5.92
15	261.8	43.8	5.98	41	252.6	43.8	5.77
16	259.0	43.0	6.02	42	256.4	43.9	5.84
17	255.7	43.0	5.95	43	258.0	43.2	5.97
18	258.2	43.8	5.89	44	255.6	43.3	5.90
19	257.5	44.6	5.77	45	256.9	43.1	5.96
20	255.8	44.2	5.79	46	256.0	44.2	5.79
21	256.3	43.6	5.88	47	257.3	44.9	5.73
22	257.6	43.0	5.99	48	255.9	43.8	5.84
23	255.7	42.8	5.97	49	255.9	43.5	5.88
24	256.8	43.9	5.85	50	254.6	42.4	6.00
25	255.4	44.4	5.75	Average	255.6	43.6	5.86
26	255.4	44.0	5.80				

Table E.2.: Model simulation times for each individual run for 20m and 50m resolutions in seconds with a scaling factor calculation for the northern region.

Simulation No.	Resolution		Factor	Simulation No.	Resolution		Factor
	20m	50m			20m	50m	
1	232.5	38.7	6.00	27	228.1	37.3	6.11
2	228.1	37.8	6.03	28	228.0	37.3	6.11
3	227.5	37.3	6.10	29	228.2	37.3	6.12
4	227.8	37.3	6.10	30	227.9	37.3	6.10
5	227.8	37.4	6.09	31	228.0	37.3	6.11
6	227.6	37.3	6.11	32	228.1	37.2	6.12
7	227.9	37.2	6.12	33	228.1	37.4	6.10
8	228.0	37.4	6.10	34	228.2	37.3	6.11
9	228.1	37.4	6.10	35	228.2	37.3	6.12
10	228.2	37.3	6.12	36	228.1	37.1	6.15
11	228.3	37.3	6.12	37	227.9	37.3	6.11
12	228.1	37.4	6.09	38	228.1	37.4	6.10
13	228.1	37.3	6.12	39	228.0	37.3	6.11
14	228.1	37.3	6.11	40	227.8	37.3	6.11
15	228.2	37.3	6.12	41	228.0	37.3	6.12
16	228.4	37.3	6.13	42	228.8	37.3	6.14
17	228.1	37.2	6.13	43	227.9	37.2	6.12
18	228.1	37.3	6.12	44	227.9	37.4	6.09
19	228.2	37.2	6.13	45	227.7	37.4	6.10
20	228.0	37.6	6.07	46	228.3	37.2	6.13
21	228.7	37.8	6.04	47	228.8	37.3	6.14
22	228.3	37.3	6.12	48	228.2	37.4	6.10
23	228.0	37.2	6.13	49	227.8	37.3	6.10
24	228.0	37.3	6.11	50	227.8	37.3	6.11
25	228.3	37.5	6.09	Average	228.2	37.4	6.11
26	228.3	37.3	6.12				

## F. Min, Max and Average Raw Data

Table F.1.: Min, Max and Average of mean water depths at non-zero pixels for north-eastern region.

Timestep $\Delta t$	Time	Resolution					
		20m			50m		
		Min	Max	Average	Min	Max	Average
<b>I.C.</b>	<b>00:00</b>	0.000	0.000	0.000	0.000	0.000	0.000
<b>1</b>	<b>00:30</b>	0.055	0.072	0.056	0.055	0.055	0.055
<b>2</b>	<b>01:00</b>	0.109	0.144	0.111	0.109	0.109	0.109
<b>3</b>	<b>01:30</b>	0.163	0.215	0.166	0.162	0.163	0.162
<b>4</b>	<b>02:00</b>	0.215	0.284	0.220	0.212	0.215	0.214
<b>5</b>	<b>02:30</b>	0.265	0.353	0.273	0.261	0.265	0.263
<b>6</b>	<b>03:00</b>	0.314	0.421	0.326	0.308	0.315	0.311
<b>7</b>	<b>03:30</b>	0.362	0.487	0.377	0.352	0.362	0.357
<b>8</b>	<b>04:00</b>	0.011	0.552	0.398	0.394	0.408	0.401
<b>9</b>	<b>04:30</b>	0.011	0.616	0.430	0.433	0.452	0.442
<b>10</b>	<b>05:00</b>	0.010	0.678	0.459	0.470	0.494	0.482
<b>11</b>	<b>05:30</b>	0.010	0.739	0.471	0.505	0.535	0.520
<b>12</b>	<b>06:00</b>	0.010	0.798	0.432	0.537	0.573	0.555
<b>13</b>	<b>06:30</b>	0.010	0.855	0.424	0.567	0.610	0.589
<b>14</b>	<b>07:00</b>	0.010	0.911	0.401	0.010	0.646	0.417
<b>15</b>	<b>07:30</b>	0.021	0.965	0.430	0.011	0.680	0.333
<b>16</b>	<b>08:00</b>	0.032	1.018	0.460	0.010	0.714	0.206
<b>17</b>	<b>08:30</b>	0.045	1.070	0.489	0.021	0.746	0.221
<b>18</b>	<b>09:00</b>	0.057	1.119	0.518	0.032	0.776	0.237
<b>19</b>	<b>09:30</b>	0.071	1.168	0.547	0.043	0.806	0.252
<b>20</b>	<b>10:00</b>	0.010	1.215	0.552	0.054	0.833	0.266
<b>21</b>	<b>10:30</b>	0.022	1.260	0.580	0.065	0.860	0.281
<b>22</b>	<b>11:00</b>	0.011	1.304	0.595	0.075	0.885	0.295
<b>23</b>	<b>11:30</b>	0.021	1.347	0.622	0.086	0.910	0.309
<b>24</b>	<b>12:00</b>	0.011	1.388	0.635	0.096	0.932	0.322
<b>⋮</b>	<b>⋮</b>	<b>⋮</b>	<b>⋮</b>	<b>⋮</b>	<b>⋮</b>	<b>⋮</b>	<b>⋮</b>



Timestep $\Delta t$	Time	Resolution					
		20m			50m		
		Min	Max	Average	Min	Max	Average
⋮	⋮	⋮	⋮	⋮	⋮	⋮	⋮
<b>25</b>	<b>12:30</b>	0.011	1.428	0.649	0.107	0.954	0.335
<b>26</b>	<b>13:00</b>	0.011	1.467	0.649	0.117	0.975	0.347
<b>27</b>	<b>13:30</b>	0.011	1.505	0.662	0.126	0.995	0.359
<b>28</b>	<b>14:00</b>	0.023	1.541	0.685	0.135	1.013	0.371
<b>29</b>	<b>14:30</b>	0.010	1.577	0.673	0.011	1.031	0.336
<b>30</b>	<b>15:00</b>	0.010	1.611	0.684	0.022	1.048	0.347
<b>31</b>	<b>15:30</b>	0.010	1.644	0.694	0.035	1.063	0.357
<b>32</b>	<b>16:00</b>	0.011	1.677	0.693	0.048	1.078	0.368
<b>33</b>	<b>16:30</b>	0.010	1.708	0.681	0.062	1.093	0.378
<b>34</b>	<b>17:00</b>	0.010	1.739	0.681	0.076	1.106	0.387
<b>35</b>	<b>17:30</b>	0.010	1.769	0.690	0.091	1.118	0.397
<b>36</b>	<b>18:00</b>	0.010	1.798	0.699	0.106	1.130	0.406
<b>37</b>	<b>18:30</b>	0.010	1.827	0.689	0.122	1.141	0.415
<b>38</b>	<b>19:00</b>	0.011	1.866	0.697	0.138	1.152	0.423
<b>39</b>	<b>19:30</b>	0.010	1.904	0.696	0.010	1.162	0.385
<b>40</b>	<b>20:00</b>	0.010	1.943	0.705	0.021	1.171	0.393
<b>41</b>	<b>20:30</b>	0.010	1.980	0.713	0.033	1.180	0.401
<b>42</b>	<b>21:00</b>	0.010	2.016	0.686	0.044	1.188	0.409
<b>43</b>	<b>21:30</b>	0.020	2.051	0.702	0.010	1.196	0.376
<b>44</b>	<b>22:00</b>	0.011	2.085	0.710	0.020	1.203	0.384
<b>45</b>	<b>22:30</b>	0.010	2.117	0.693	0.031	1.210	0.392
<b>46</b>	<b>23:00</b>	0.010	2.149	0.700	0.041	1.216	0.399
<b>47</b>	<b>23:30</b>	0.011	2.177	0.700	0.052	1.222	0.406
<b>48</b>	<b>00:00</b>	0.023	2.204	0.714	0.063	1.227	0.413

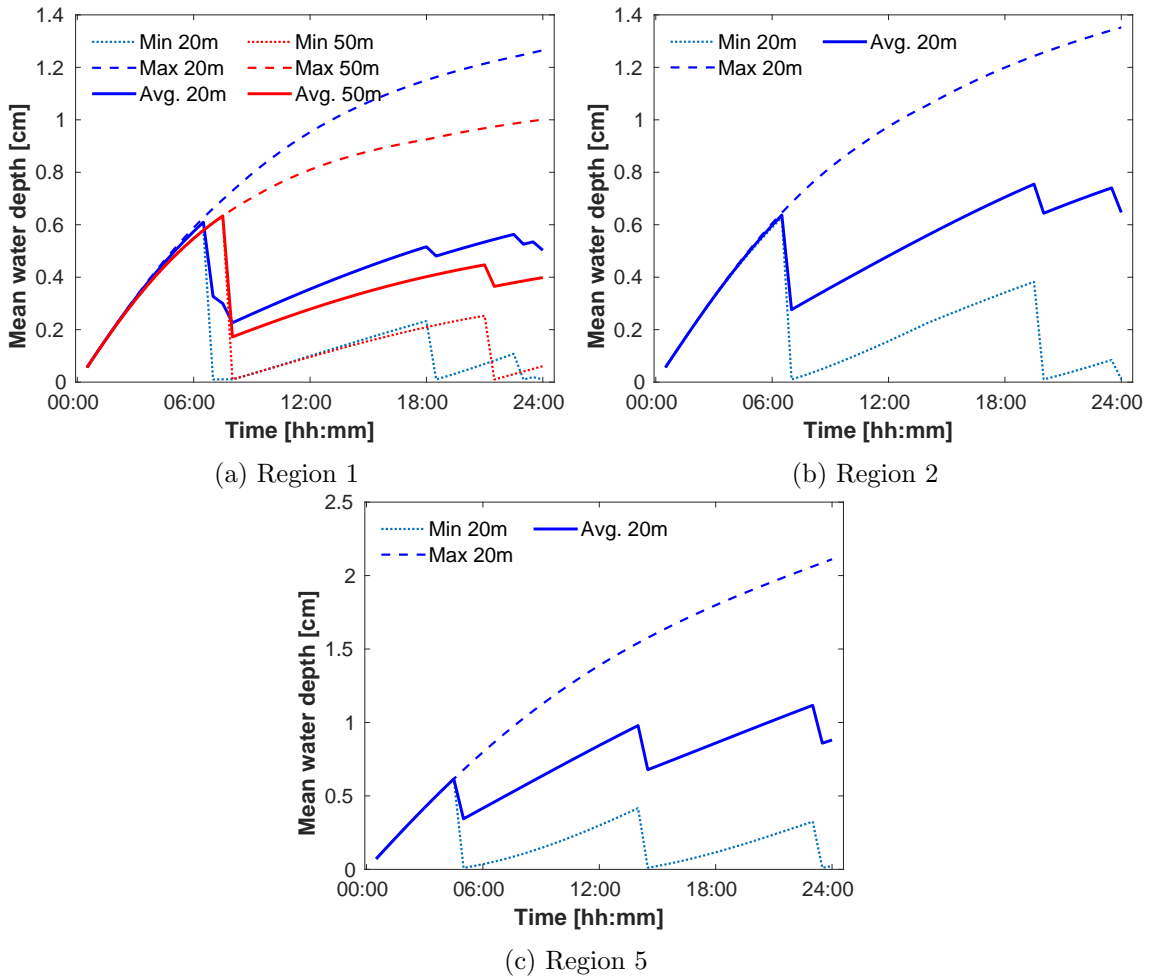


Figure F.1.: The minimum, maximum and average mean water depths at non-zero output pixels within the north-eastern sub-region outlined in Figure 5.3 for both model resolutions for the remaining three of the five regions not depicted in Figure 5.5.

Table F.2.: Min, Max and Average of mean water depths at non-zero pixels for northern region.

Timestep $\Delta t$	Time	Resolution					
		20m			50m		
		Min	Max	Average	Min	Max	Average
<b>I.C.</b>	<b>00:00</b>	0.000	0.000	0.000	0.000	0.000	0.000
<b>1</b>	<b>00:30</b>	0.056	0.074	0.069	0.056	0.074	0.072
<b>2</b>	<b>01:00</b>	0.111	0.148	0.138	0.111	0.147	0.143
<b>3</b>	<b>01:30</b>	0.165	0.224	0.206	0.165	0.219	0.213
<b>4</b>	<b>02:00</b>	0.217	0.302	0.274	0.217	0.290	0.282
<b>5</b>	<b>02:30</b>	0.267	0.382	0.340	0.266	0.361	0.349
<b>6</b>	<b>03:00</b>	0.314	0.465	0.406	0.314	0.431	0.413
<b>7</b>	<b>03:30</b>	0.010	0.550	0.464	0.011	0.500	0.437
<b>8</b>	<b>04:00</b>	0.012	0.637	0.520	0.024	0.569	0.493
<b>9</b>	<b>04:30</b>	0.010	0.726	0.559	0.040	0.636	0.547
<b>10</b>	<b>05:00</b>	0.010	0.815	0.504	0.010	0.702	0.364
<b>11</b>	<b>05:30</b>	0.010	0.903	0.490	0.010	0.763	0.321
<b>12</b>	<b>06:00</b>	0.010	0.992	0.503	0.022	0.821	0.350
<b>13</b>	<b>06:30</b>	0.010	1.079	0.486	0.011	0.876	0.365
<b>14</b>	<b>07:00</b>	0.010	1.168	0.475	0.011	0.928	0.379
<b>15</b>	<b>07:30</b>	0.010	1.254	0.497	0.021	0.977	0.407
<b>16</b>	<b>08:00</b>	0.011	1.337	0.514	0.010	1.023	0.391
<b>17</b>	<b>08:30</b>	0.010	1.418	0.537	0.021	1.067	0.417
<b>18</b>	<b>09:00</b>	0.010	1.497	0.559	0.010	1.111	0.428
<b>19</b>	<b>09:30</b>	0.010	1.574	0.583	0.011	1.153	0.438
<b>20</b>	<b>10:00</b>	0.010	1.649	0.607	0.020	1.192	0.462
<b>21</b>	<b>10:30</b>	0.011	1.722	0.630	0.031	1.229	0.485
<b>22</b>	<b>11:00</b>	0.011	1.793	0.656	0.011	1.263	0.493
<b>23</b>	<b>11:30</b>	0.011	1.862	0.682	0.021	1.296	0.516
<b>24</b>	<b>12:00</b>	0.010	1.929	0.699	0.031	1.327	0.538
<b>25</b>	<b>12:30</b>	0.011	1.995	0.720	0.041	1.356	0.560
<b>26</b>	<b>13:00</b>	0.011	2.059	0.744	0.011	1.383	0.565
<b>⋮</b>	<b>⋮</b>	<b>⋮</b>	<b>⋮</b>	<b>⋮</b>	<b>⋮</b>	<b>⋮</b>	<b>⋮</b>

Timestep $\Delta t$	Time	Resolution					
		20m			50m		
		Min	Max	Average	Min	Max	Average
⋮	⋮	⋮	⋮	⋮	⋮	⋮	⋮
<b>27</b>	<b>13:30</b>	0.010	2.121	0.759	0.022	1.409	0.587
<b>28</b>	<b>14:00</b>	0.010	2.181	0.770	0.011	1.433	0.590
<b>29</b>	<b>14:30</b>	0.010	2.240	0.784	0.022	1.457	0.611
<b>30</b>	<b>15:00</b>	0.010	2.297	0.786	0.035	1.478	0.631
<b>31</b>	<b>15:30</b>	0.010	2.352	0.795	0.049	1.499	0.651
<b>32</b>	<b>16:00</b>	0.010	2.406	0.816	0.010	1.519	0.652
<b>33</b>	<b>16:30</b>	0.010	2.458	0.817	0.010	1.537	0.636
<b>34</b>	<b>17:00</b>	0.010	2.509	0.829	0.010	1.555	0.607
<b>35</b>	<b>17:30</b>	0.010	2.558	0.826	0.019	1.574	0.625
<b>36</b>	<b>18:00</b>	0.010	2.606	0.834	0.010	1.592	0.613
<b>37</b>	<b>18:30</b>	0.010	2.652	0.845	0.010	1.609	0.615
<b>38</b>	<b>19:00</b>	0.010	2.697	0.860	0.021	1.626	0.632
<b>39</b>	<b>19:30</b>	0.010	2.740	0.870	0.032	1.643	0.648
<b>40</b>	<b>20:00</b>	0.010	2.783	0.877	0.011	1.659	0.650
<b>41</b>	<b>20:30</b>	0.010	2.823	0.891	0.021	1.674	0.666
<b>42</b>	<b>21:00</b>	0.020	2.863	0.912	0.032	1.690	0.681
<b>43</b>	<b>21:30</b>	0.011	2.901	0.929	0.010	1.705	0.682
<b>44</b>	<b>22:00</b>	0.010	2.939	0.938	0.010	1.719	0.682
<b>45</b>	<b>22:30</b>	0.010	2.975	0.939	0.011	1.733	0.683
<b>46</b>	<b>23:00</b>	0.010	3.010	0.937	0.010	1.747	0.684
<b>47</b>	<b>23:30</b>	0.010	3.044	0.938	0.011	1.761	0.684
<b>48</b>	<b>00:00</b>	0.010	3.077	0.929	0.022	1.774	0.698

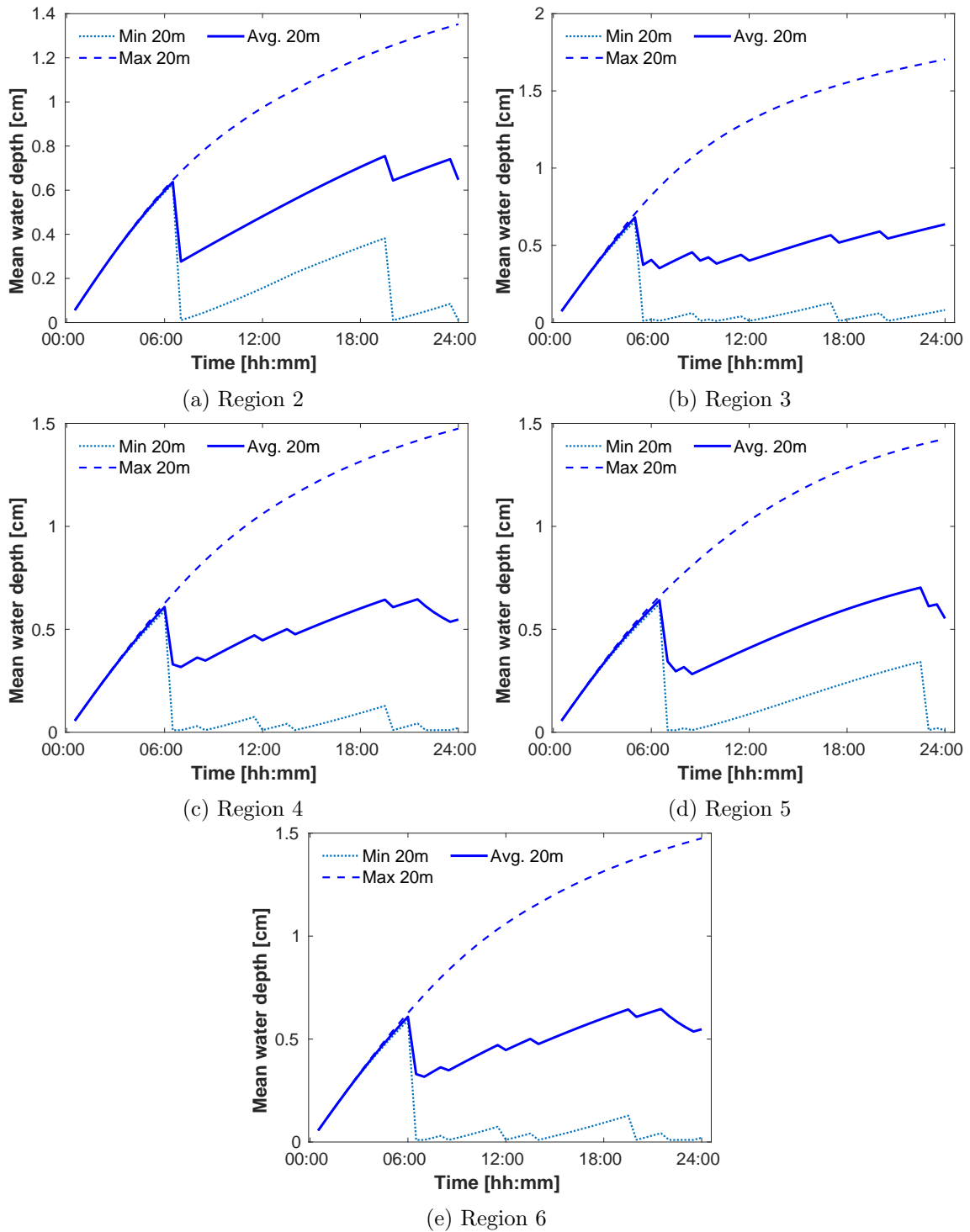


Figure F.2.: The minimum, maximum and average mean water depths at non-zero output pixels within the northern sub-region outlined in Figure 5.14 for both model resolutions for the remaining five of the seven regions not depicted in Figure 5.18.

## G. Contour Overland Flow II

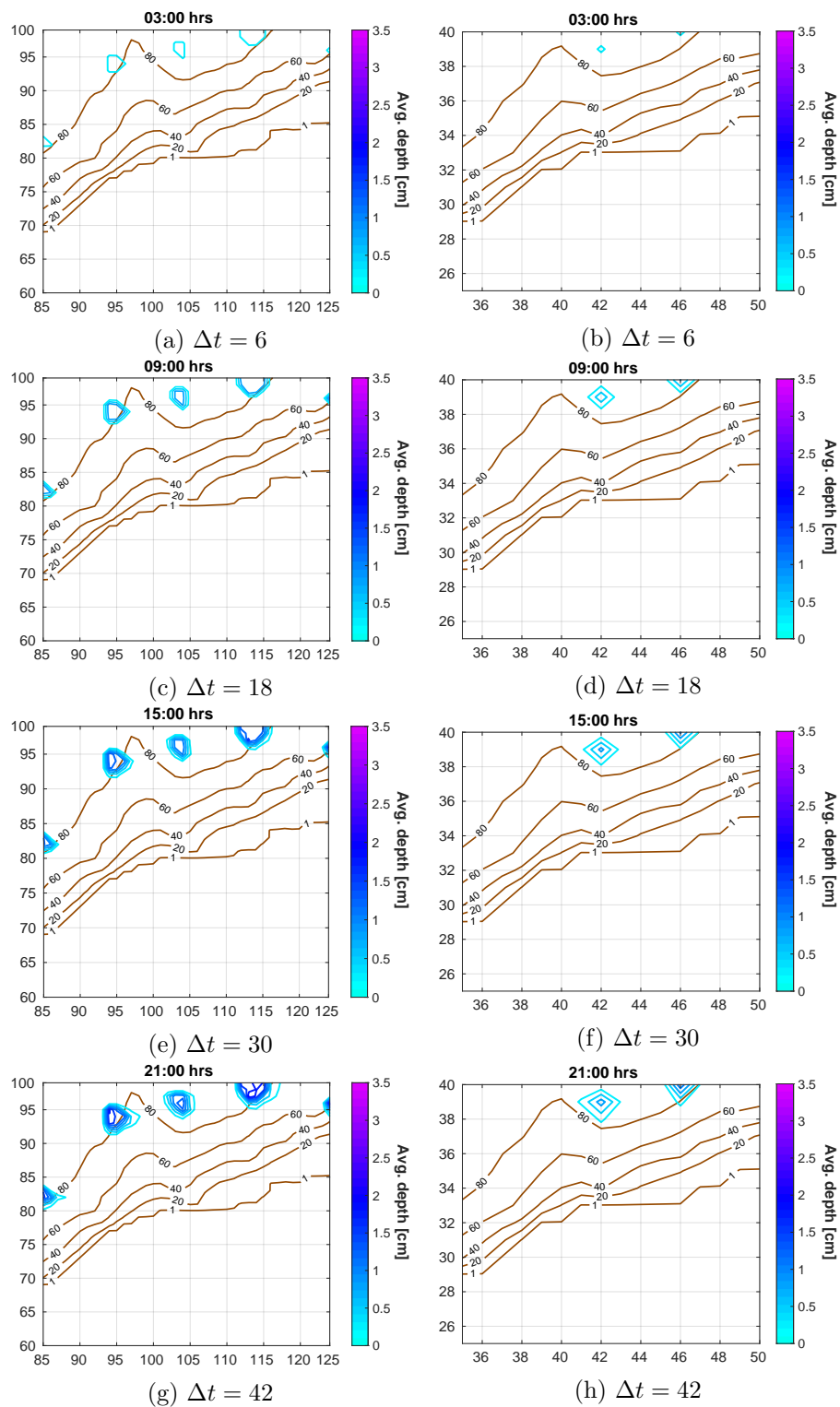


Figure G.1.: An evolution of the average water depth overland flow throughout the 50m resolution model simulation.

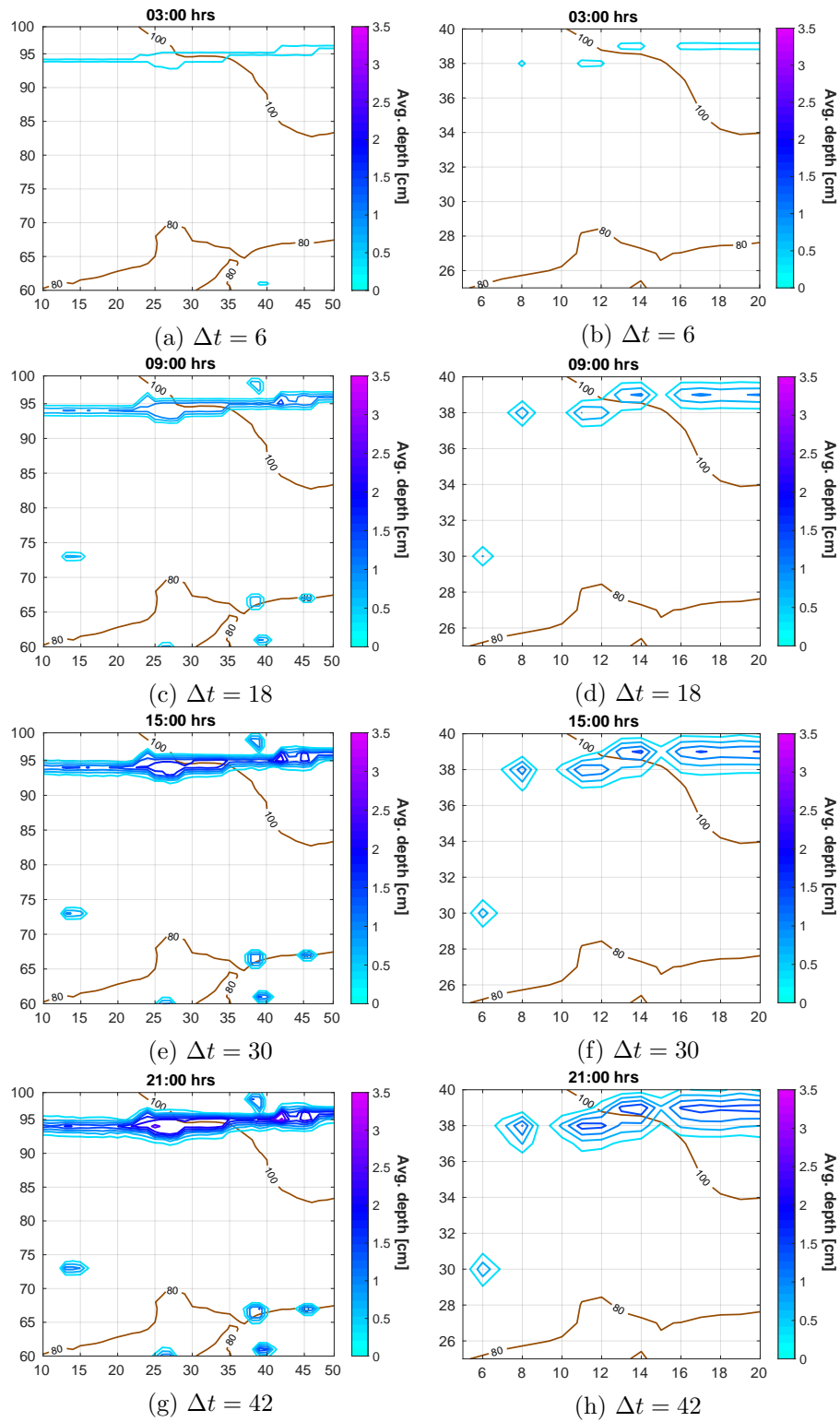


Figure G.2.: An evolution of the average water depth overland flow throughout the 50m resolution model simulation.

## H. Patch-Pixel Composition Raw Data

Table H.1.: Patch pixel composition split by land-use type for the north-eastern region.

Patch #	5		15		16		23		24	
	20m	50m	20m	50m	20m	50m	20m	50m	20m	50m
Arable	4	-	19	3	7	1	18	3	12	3
Grassland	6	2	-	-	-	-	-	-	-	-
Rough Grazing	12	2	4	1	17	3	4	1	12	1
Sub-Urban	3	-	2	-	1	-	3	-	1	-
Urban	-	-	-	-	-	-	-	-	-	-
Patch #	31		32		39		40		47	
	20m	50m	20m	50m	20m	50m	20m	50m	20m	50m
Arable	15	2	11	1	19	3	-	-	11	1
Grassland	-	-	-	-	6	1	23	4	6	1
Rough Grazing	10	2	9	2	-	-	-	-	8	2
Sub-Urban	-	-	5	1	-	-	2	-	-	-
Urban	-	-	-	-	-	-	-	-	-	-
Patch #	48		56		63		64			
	20m	50m	20m	50m	20m	50m	20m	50m		
Arable	-	-	2	-	1	-	6	1		
Grassland	17	3	13	2	-	-	-	-		
Rough Grazing	-	-	8	2	24	4	18	3		
Sub-Urban	8	1	2	-	-	-	-	-		
Urban	-	-	-	-	-	-	1	-		



Table H.2.: Patch pixel composition split by land-use type for the northern region.

Patch #	3		4		7		8		11	
	20m	50m	20m	50m	20m	50m	20m	50m	20m	50m
Arable	7	1	6	1	5	-	5	1	-	-
Grassland	12	2	-	-	15	4	20	3	22	4
Rough Grazing	-	-	19	3	-	-	-	-	2	-
Sub-Urban	2	1	-	-	-	-	-	-	1	-
Urban	-	-	-	-	5	-	-	-	-	-
Woodland	4	-	-	-	-	-	-	-	-	-
Patch #	14		15		16		23		24	
	20m	50m	20m	50m	20m	50m	20m	50m	20m	50m
Arable	-	-	-	-	4	-	-	-	13	3
Grassland	5	1	12	2	21	4	-	-	4	1
Rough Grazing	20	3	8	1	-	-	20	4	5	-
Sub-Urban	-	-	-	-	-	-	-	-	3	-
Urban	-	-	5	1	-	-	5	-	-	-
Woodland	-	-	-	-	-	-	-	-	-	-
Patch #	25		30		31		32		38	
	20m	50m	20m	50m	20m	50m	20m	50m	20m	50m
Arable	3	1	-	-	3	-	20	4	-	-
Grassland	-	-	-	-	-	-	-	-	-	-
Rough Grazing	20	3	25	4	13	2	-	-	25	4
Sub-Urban	2	-	-	-	2	-	1	-	-	-
Urban	-	-	-	-	7	2	4	-	-	-
Woodland	-	-	-	-	-	-	-	-	-	-

*Continued on next page*

Table H.2 – *Continued from previous page*

Patch #	39		40		41		42		47	
	20m	50m	20m	50m	20m	50m	20m	50m	20m	50m
Arable	-	-	8	1	23	4	11	2	-	-
Grassland	-	-	2	-	1	-	8	2	-	-
Rough Grazing	20	4	10	1	-	-	2	-	15	2
Sub-Urban	-	-	-	-	-	-	4	-	-	-
Urban	5	-	5	2	1	-	-	-	-	-
Woodland	-	-	-	-	-	-	-	-	10	2
Patch #	48		49		50		55		56	
	20m	50m	20m	50m	20m	50m	20m	50m	20m	50m
Arable	-	-	17	3	21	3	-	-	-	-
Grassland	1	-	-	-	-	-	-	-	3	-
Rough Grazing	15	3	7	1	4	1	10	2	-	-
Sub-Urban	3	-	-	-	-	-	-	-	-	-
Urban	5	1	1	-	-	-	-	-	8	2
Woodland	1	-	-	-	-	-	15	2	14	2
Patch #	58		63		64					
	20m	50m	20m	50m	20m	50m				
Arable	11	1	3	-	-	-				
Grassland	-	-	-	-	2	-				
Rough Grazing	12	3	21	4	3	-				
Sub-Urban	2	-	-	-	-	-				
Urban	-	-	-	-	7	2				
Woodland	-	-	1	-	13	2				

## I. Model Performance Analysis

### I.1. North Eastern Patch Analysis

#### I.1.1. Patch #23

A maximum water average depth of 0.338cm was reached in the original 20m model for patch #23. A steady linear increase of average water depth occurred as illustrated in sub-figure I.3d; page 375. Zero average water depth was recorded in the original 50m model. The absence of a sub-urban pixel within the original 50m model compared to the 20m model was the key difference in pixel patch composition which contributed to vastly

different outputs. This is seen in sub-figures I.3b and I.3a. Pixel  $\Omega_{39,38}$  was originally designated as arable. This was replaced with sub-urban pixel properties. With this adjusted 50m model, the average water depth was drastically overestimated compared with the original 20m model reaching a maximum of 0.557cm. This overestimation by 64.7% is illustrated in sub-figures I.3d and I.3e.

### **I.1.2. Patch #56**

Initially, the 20m model average water depth slowly increases linearly and from the start, reaching a maximum average water depth of 0.324cm, as seen in Figure I.4d; page 376. With the 50m model represented by two grassland and rough-grazing land-use pixels each (sub-figure I.4b), the average water depth of the patch does not begin to rise until 08:00 hours. This late increase in average water depth sees a noticeable underestimation of output compared to the 20m model. A peak average water depth of 0.141cm was reached in the 50m model, underestimating the 20m model by 56.7% (sub-figure I.4e). Pixel  $\Omega_{47,40}$  with grassland in the 50m model was replaced with a sub-urban category to better represent the 20m model. This alteration drastically overestimated the overall output compared to the 20m model by 137% with a value of 0.767cm.

## **I.2. Northern Patch Analysis**

### **I.2.1. Patch #15**

Land coverage within the 20m model comprises of 20% urban, 48% grassland and 32% rough grazing (sub-figure I.5a; page 377), whilst for the 50m model the respective percentages are 25%, 50% and 25% (sub-figure I.5b). As proportions are similar, no adjustments were made to the 50m model for this patch. Both model variant outputs monotonically increase throughout the simulation. The increase rate for the 50m model stays consistent compared to the 20m model (sub-figure I.5c). By the end the 50m model overestimated the 20m model output by almost 50% at a value of 0.784cm compared with 0.543cm (sub-figure I.5d).

**I.2.2. Patch #24**

For patch #24, there is no sub-urban nor rough-grazing pixels within the original 50m resolution (sub-figure I.6b; page 378) compared with its 20m model counterpart (sub-figure I.6a). The pixel  $\Omega_{10,39}$  is adjusted to include a sub-urban category instead of the arable pixel to reflect the limited absorptive properties within sub-urban areas (sub-figure I.6c). Due to the absorptive qualities of grassland and arable pixels, zero output was recorded within the original 50m model (sub-figure I.6d). However when a sub-urban pixel was included in the 50m model it overestimated the output by over double, with an average water depth of 0.448cm, compared to the 20m version which finished at 0.334cm. As the simulation ended the difference in output between models began to converge (sub-figure I.6e).

**I.2.3. Patch #25**

Within the 20m model, patch #25 contains three land-use categories. The majority is rough grazing (80%) with arable (12%) and sub-urban (8%) making up the rest of the patch (sub-figure I.7a; page 379). The original 50m patch is proportionally accurate for rough grazing parameters covering 75% of the area and also contains the arable land (sub-figure I.7b). However, no average water output was recorded in the original 50m model due to the good absorptive properties of the rough-grazing and arable land use categories (sub-figure I.7d). Adjusting the 50m model to include a sub-urban pixel (sub-figure I.7c) sees the model overestimate output by over 200% at some timesteps. An average water depth value of 0.460cm was recorded at the end of the simulation, compared to 0.195cm in the 20m model, an overestimation by 150%.

**I.2.4. Patch #32**

Three land-use types make up patch #32's 20m resolution model; arable (80%); urban (16%); and sub-urban (4%) (sub-figure I.8a; page 380). The 50m model is composed completely of arable pixels (sub-figure I.8b). Here one pixel in the 50m model is replaced with an urban pixel to balance the land-use proportions between the model variants (sub-figure I.8c). The 20m model output increases homogeneously reaching a maximum value

of 0.608cm. However, the 50m model only begins producing output a quarter of the way through the simulation (sub-figure I.8d), consistently underestimating the 20m model by more than 50% (sub-figure I.8e), finishing with an average water depth of 0.194cm. The adjusted 50m model consistently overestimates the 20m model, finishing at 0.670cm. Towards the end of the simulation the 20m and adjusted 50m model's output begin to converge.

### **I.2.5. Patch #39**

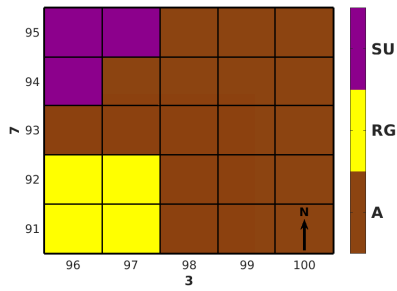
Patch #39 is composed of urban (20%) and rough grazing pixels (80%) (sub-figure I.9a; page 381). The original 50m model contains only rough grazing pixels (sub-figure I.9b). An urban pixel replaces a rough grazing pixel to more evenly represent the patch between model resolution variants (sub-figure I.9c). Once again the 50m model does not begin to record any output until roughly a quarter of the way through the simulation. It consistently underestimates the 20m model (sub-figure I.9d), reaching 0.709cm, but rapidly converged to match the average water depth output of the 20m model, which finished at 0.778cm. The adjusted 50m model overestimated the average water output by over 50% for the majority of the simulation (sub-figure I.9e) finishing with an average water depth of 1.263cm.

### **I.2.6. Patch #49**

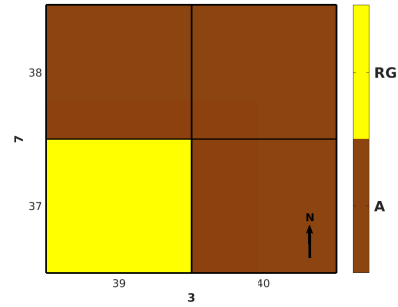
Three land-use types compose patch #49, namely arable (68%), rough-grazing (28%) and urban (4%) (sub-figure I.10a). However, urban representation is omitted from the original 50m model with just arable and rough-grazing being present (sub-figure I.10b). As such no average water depth output was recorded during the simulation of the original 50m model (sub-figure I.10d). Pixel  $\Omega_{23,61}$  was replaced with an urban land-use definition leading to the output sky-rocketing to over 500% for the first half the simulation. The adjusted model stayed well above 400% afterwards (sub-figure I.10e) finishing at 0.694cm compared with 0.131cm for the 20m model.

### **I.2.7. Patch #58**

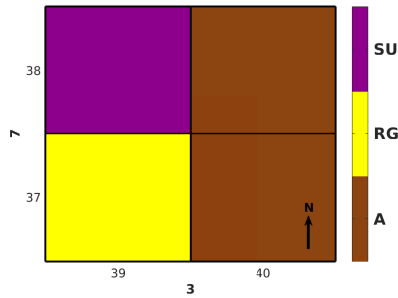
Finally, patch #58 is comprised of arable (44%), rough-grazing (48%) and sub-urban (8%) pixels within its 20m variant (sub-figure I.11a). The original 50m variant is made up from arable and rough-grazing pixels (sub-figure I.11b). From this the original 50m model does not record any output as seen in sub-figure I.11d. However, when a sub-urban pixel is included in  $\Omega_{19,28}$  for the adjusted 50m model (sub-figure I.11c), its output overestimates the 20m by over 200% initially. This output overestimation reduces slightly below 200% for the remaining simulation period (sub-figure I.11e). This adjusted patch concluded at an average water depth of 0.440cm compared with 0.157cm in the 20m model.



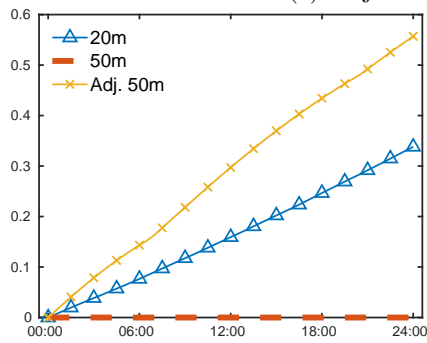
(a) Original patch composition, 20m.



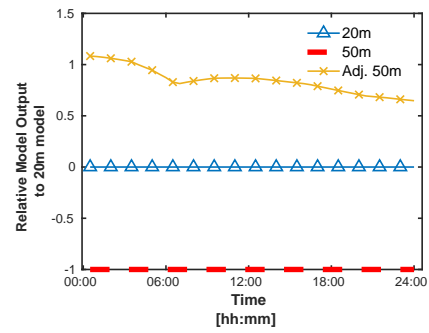
(b) Original patch composition, 50m.



(c) Adjusted patch composition, 50m.

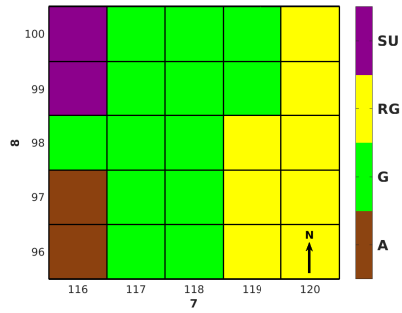


(d) Absolute water depth values for each patch composition.

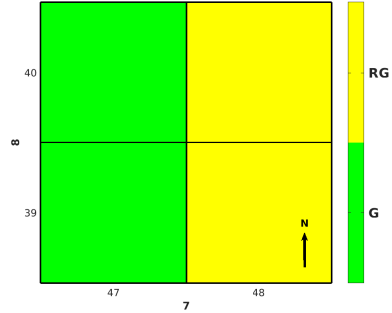


(e) 50m water depth values relative to 20m model composition.

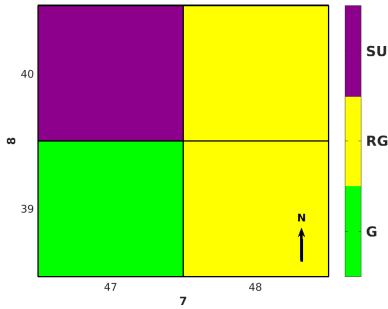
Figure I.3.: Patch 23 - Original land composition within the 20m (I.3a) and 50m (I.3b) resolution models along with an adjusted 50m resolution patch (I.3c) with absolute water depth values for each model (I.3d) and relative 50m output values compared with the 20m model (I.3e).



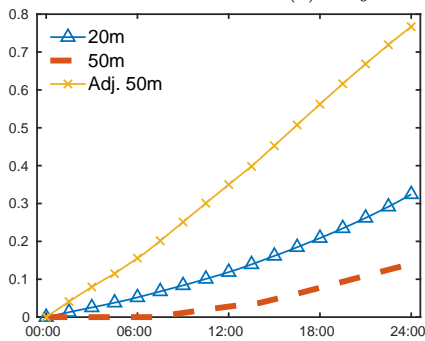
(a) Original patch composition, 20m.



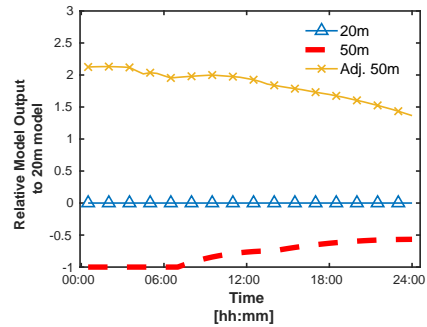
(b) Original patch composition, 50m.



(c) Adjusted patch composition, 50m.



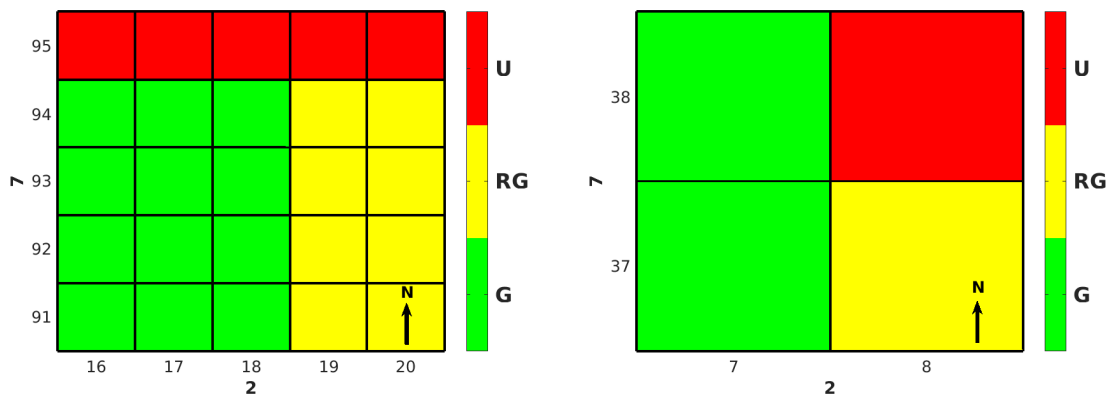
(d) Absolute water depth values for each patch composition.



(e) 50m water depth values relative to 20m model composition.

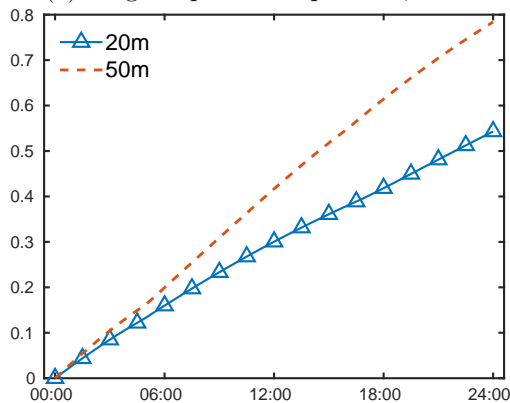
Figure I.4.: Patch 56 - Original land composition within the 20m (I.4a) and 50m (I.4b) resolution models along with an adjusted 50m resolution patch (I.4c) with absolute water depth values for each model (5.9d) and relative 50m output values compared with the 20m model (I.4e).



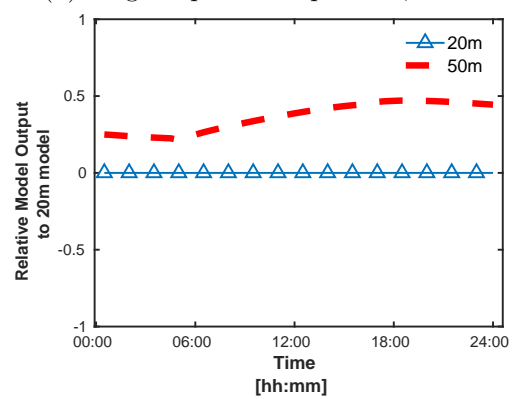


(a) Original patch composition, 20m.

(b) Original patch composition, 50m.

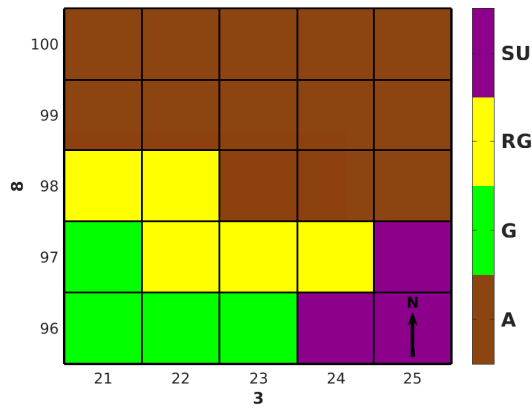


(c) Absolute water depth values for each patch composition.

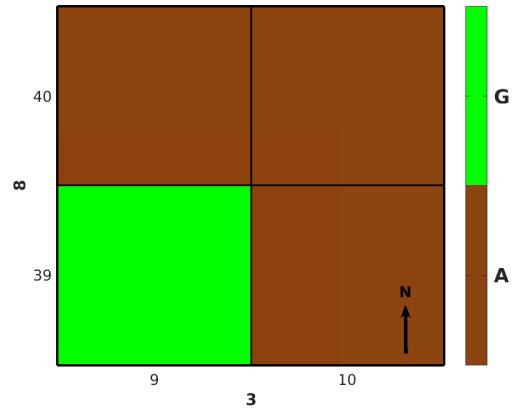


(d) 50m water depth values relative to 20m model composition.

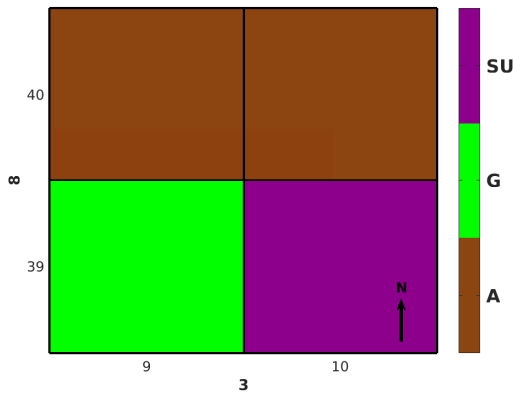
Figure I.5.: Patch 15 - Original land composition within the 20m (I.5a) and 50m (I.5b) resolution models with absolute water depth values for each model (I.5c) and relative 50m output values compared with the 20m model (I.5d).



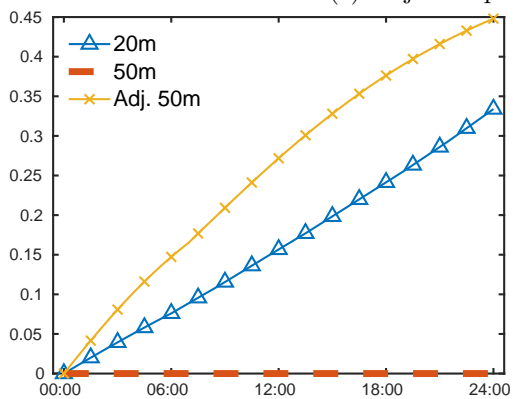
(a) Original patch composition, 20m.



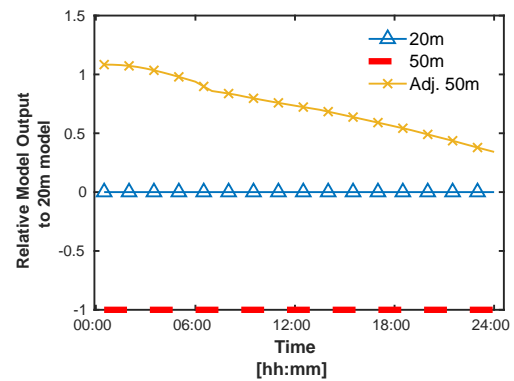
(b) Original patch composition, 50m.



(c) Adjusted patch composition, 50m.

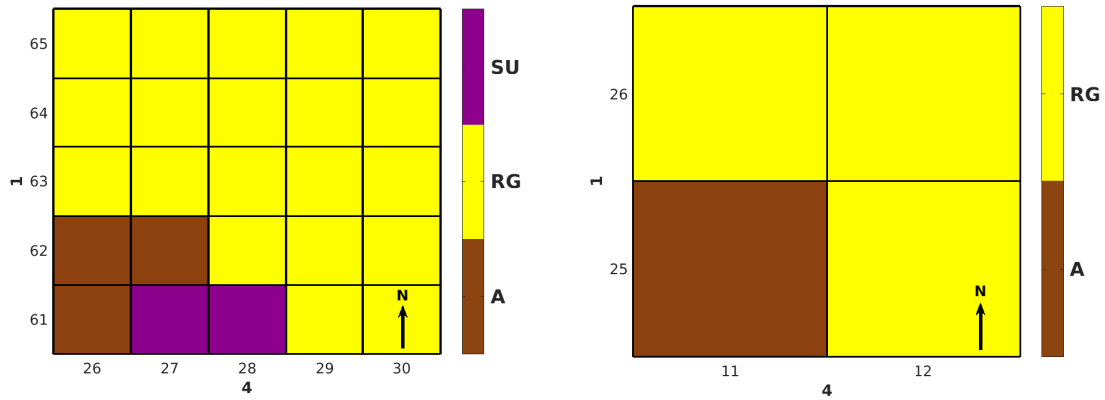


(d) Absolute water depth values for each patch composition.

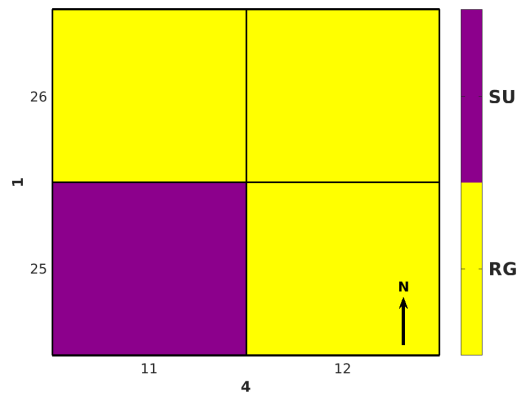


(e) 50m water depth values relative to 20m model composition.

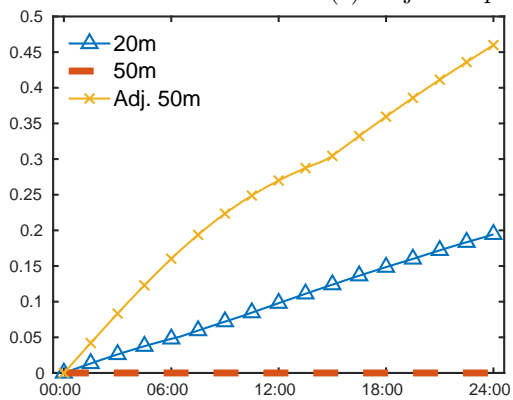
Figure I.6.: Patch 24 - Original land composition within the 20m (I.6a) and 50m (I.6b) resolution models along with an adjusted 50m resolution patch (I.6c) with absolute water depth values for each model (I.6d) and relative 50m output values compared with the 20m model (I.6e).



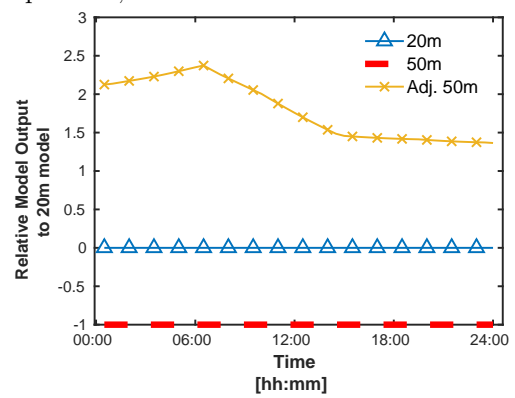
(a) Original patch composition, 20m. (b) Original patch composition, 50m.



(c) Adjusted patch composition, 50m.

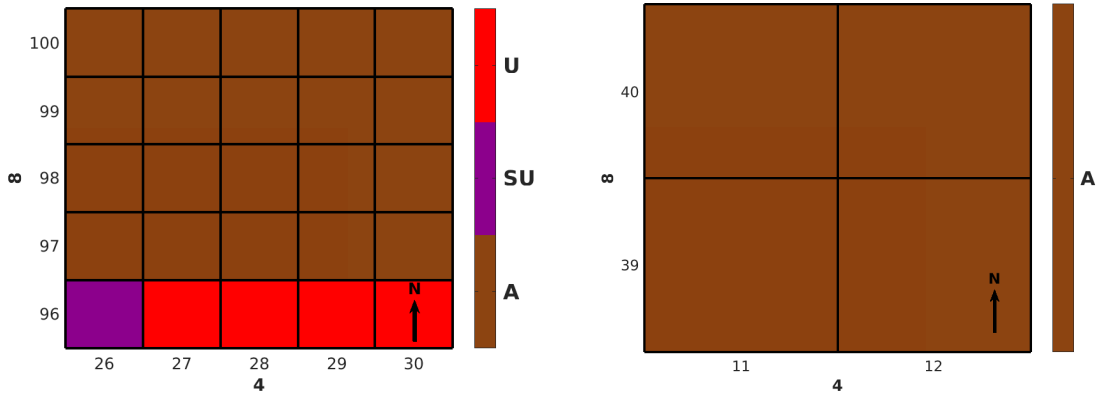


(d) Absolute water depth values for each patch composition.



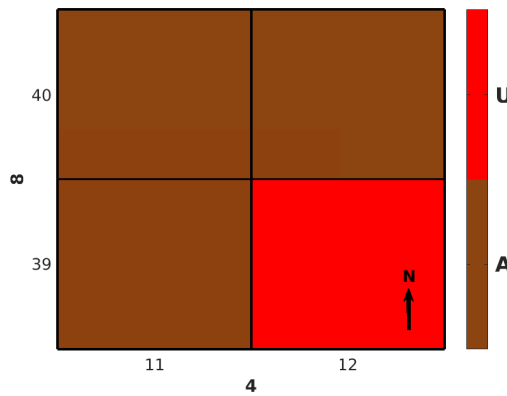
(e) 50m water depth values relative to 20m model composition.

Figure I.7.: Patch 25 - Original land composition within the 20m (I.7a) and 50m (I.7b) resolution models along with an adjusted 50m resolution patch (I.7c) with absolute water depth values for each model (I.7d) and relative 50m output values compared with the 20m model (I.7e).

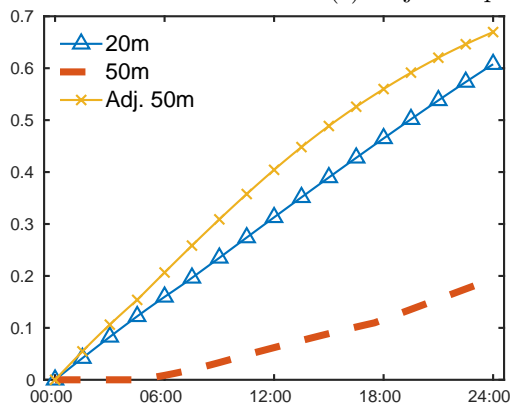


(a) Original patch composition, 20m.

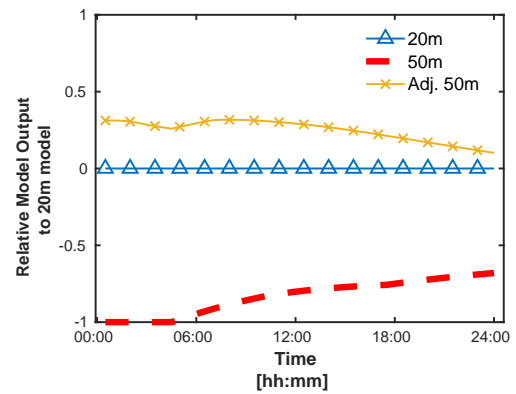
(b) Original patch composition, 50m.



(c) Adjusted patch composition, 50m.



(d) Absolute water depth values for each patch composition.



(e) 50m water depth values relative to 20m model composition.

Figure I.8.: Patch 32 - Original land composition within the 20m (I.8a) and 50m (I.8b) resolution models along with an adjusted 50m resolution patch (I.8c) with absolute water depth values for each model (I.8d) and relative 50m output values compared with the 20m model (I.8e).

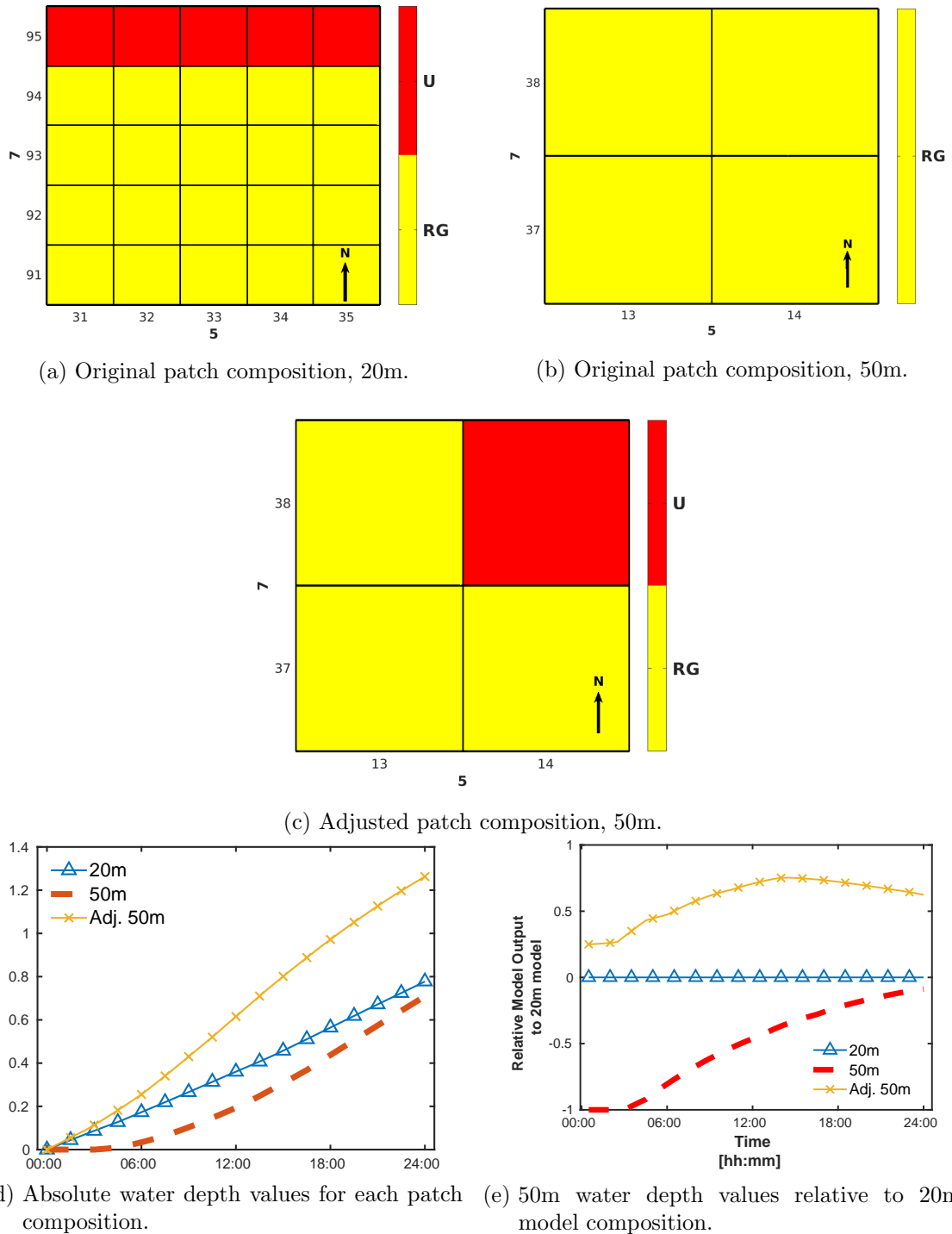


Figure I.9.: Patch 39 - Original land composition within the 20m (sub-figure I.9a) and 50m (sub-figure I.9b) resolution models along with an adjusted 50m resolution patch to match more closely proportionally with the 20m model (sub-figure I.9c) with absolute water depth values for each model (sub-figure I.9d) and relative 50m output values compared with the 20m model (sub-figure I.9e).

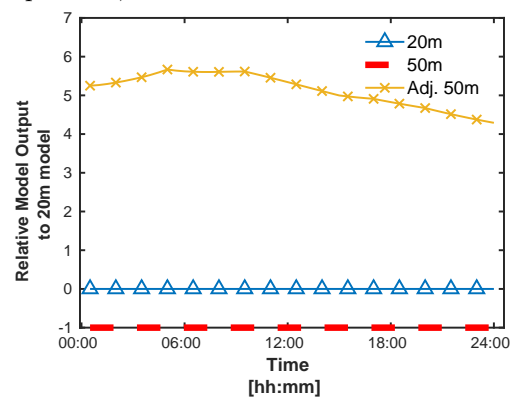
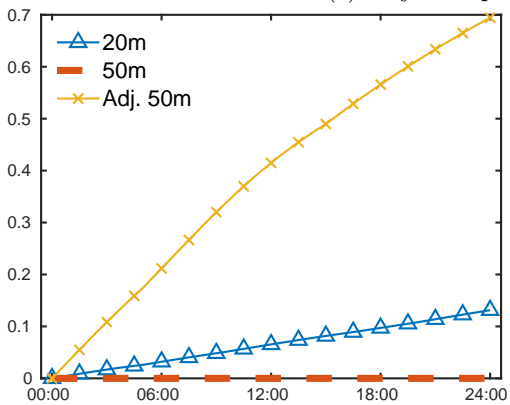
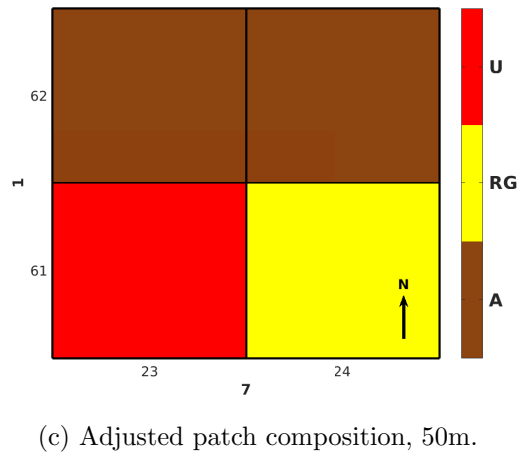
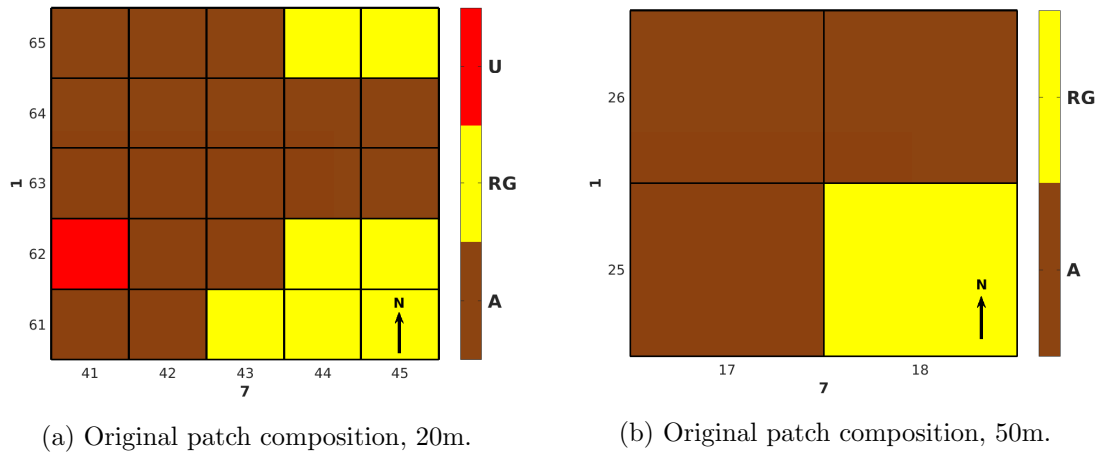
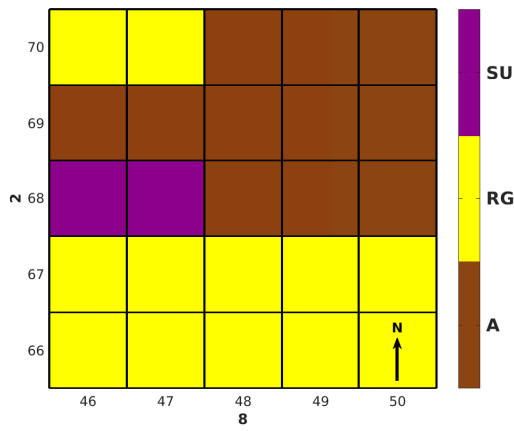
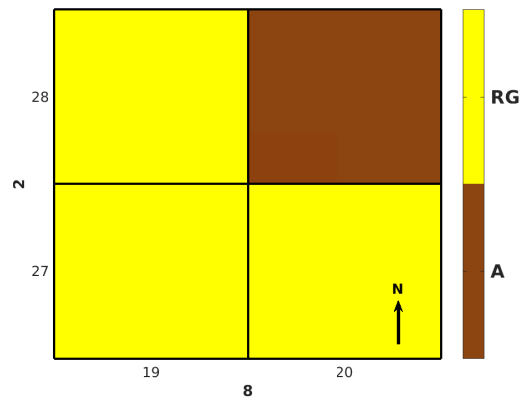


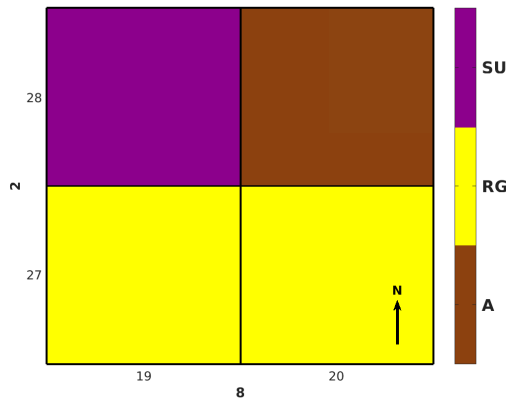
Figure I.10.: Patch 49 - Original land composition within the 20m (I.10a) and 50m (I.10b) resolution models along with an adjusted 50m resolution patch (I.10c) with absolute water depth values for each model (I.10d) and relative 50m output values compared with the 20m model (I.10e).



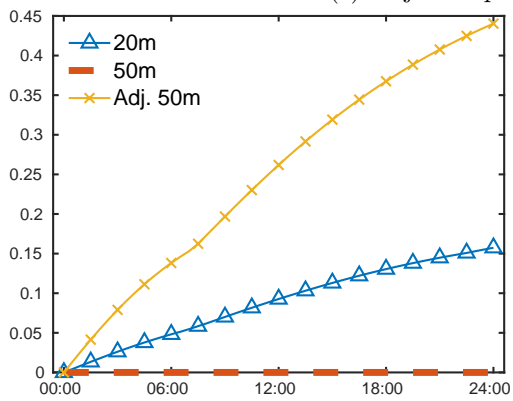
(a) Original patch composition, 20m.



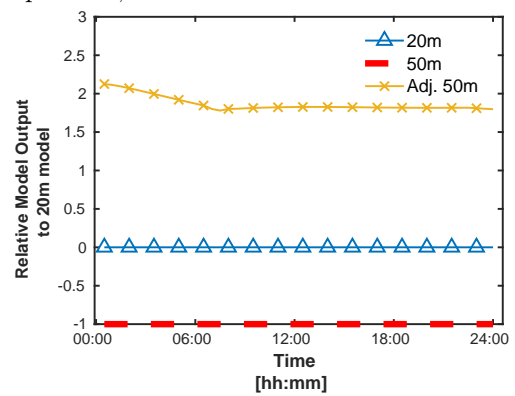
(b) Original patch composition, 50m.



(c) Adjusted patch composition, 50m.



(d) Absolute water depth values for each patch composition.



(e) 50m water depth values relative to 20m model composition.

Figure I.11.: Patch 58 - Original land composition within the 20m (I.11a) and 50m (I.11b) resolution models along with an adjusted 50m resolution patch (I.11c) with absolute water depth values for each model (I.11d) and relative 50m output values compared with the 20m model (I.11e).

## J. Non-Uniform Model Input Analysis: Scenario 3 - North West

### J.1. Movement 20m

The fictitious storm described in Section 6.1 again moves from south-west to north-east. However it concentrates its input in the north-west corner of the computational domain. Each column of Figures J.12, J.13, J.14 and J.15 illustrate the model input (sub-figures J.12(a), (e) and (i) and J.13(a) and (e)), average water depth (sub-figures J.12(b), (f) and (j) and J.13(b) and (r)), unit-width horizontal velocity in the  $x$ - direction (sub-figures J.12(c), (g) and (k) and J.13(c) and (g)) and unit-width horizontal velocity in the  $y$ -direction respectively (sub-figures J.12(d), (h) and (l) and J.13(p) and (t)).

With the bulk of the model input at  $\Delta t = 01 : 30$  coming between pixels columns 1-10, some overland flow is immediately noticeable on the western boundary of the domain (sub-figure J.12(b)). As the storm intensity decreases at  $\Delta t = 12 : 00$ , average water depth values in the western part of the domain are above 10cm, moving in a south-eastern direction (sub-figures J.12(j), (k) and (l)). Some shallow overland flow is working its way along the urban pixels in the north-western part of the domain also.

By  $\Delta t = 24 : 00$ , the average water depth along the north-west and dispersed longitudinally. There are also some signs that the western domain region of flooding is beginning to disperse. At  $\Delta t = 16 : 30$ , average water depths were above 10cm (sub-figure J.13(b)). However after 24 hours, some pixels' average water depths have gone below 10cm. The mean unit-width horizontal velocities continue to move in a south-easterly direction. These observations persist for timesteps  $\Delta t = 30 : 00, 36 : 00, 42 : 00, 48 : 00$  with negligible differences between them.



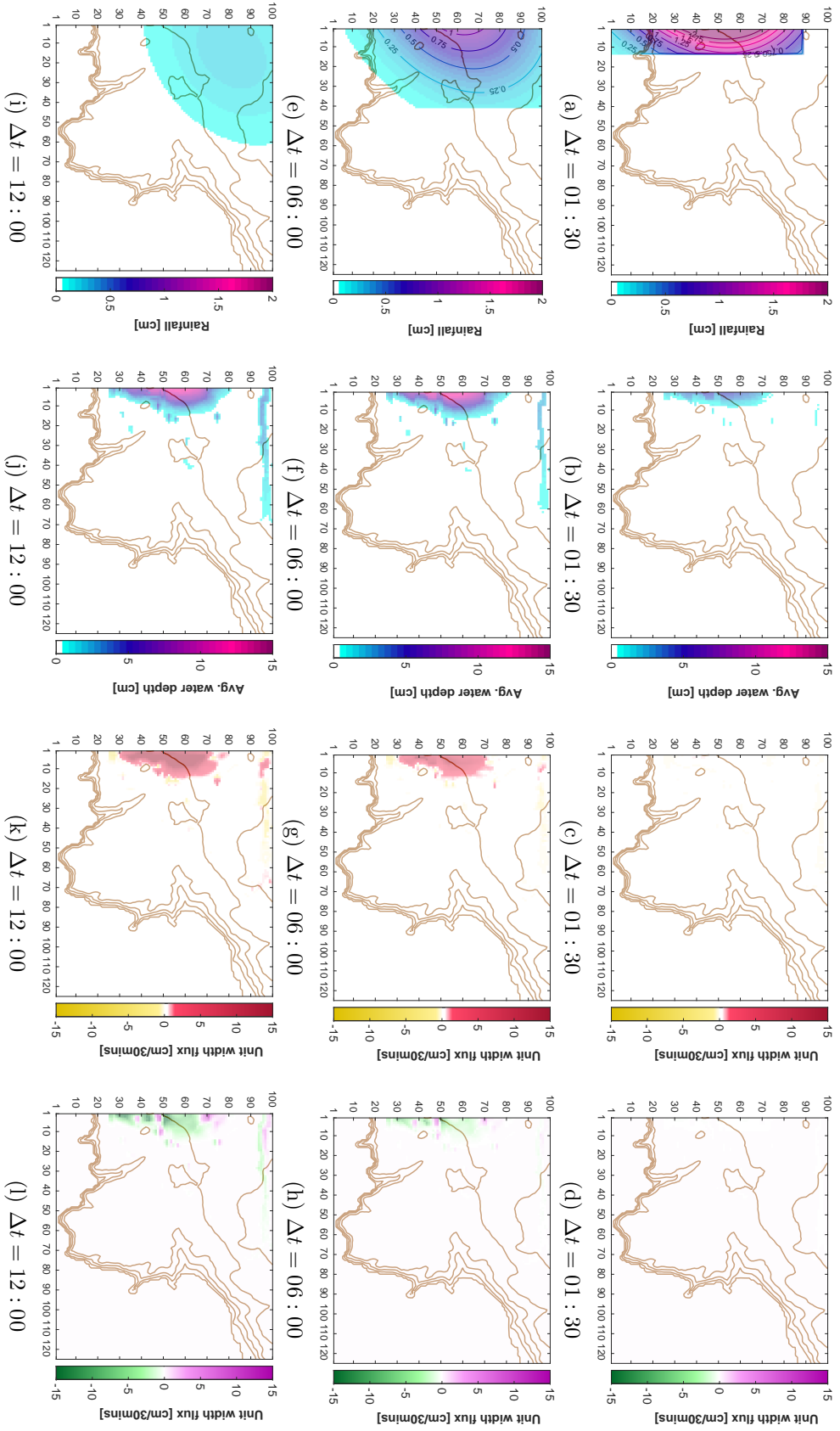


Figure J.12: Scenario 2 - North-western moving storm - 20m resolution model. Each row presents individual timesteps  $\Delta t = 01 : 30$ ,  $\Delta t = 06 : 00$  and  $\Delta t = 12 : 00$ . Sub-figures (a), (e) and (i) show the evolution of the fictitious storm during the simulation. Sub-figures (b), (f) and (j) show the average water depth at their given timesteps. Sub-figures (c), (g) and (k) depict the mean unit-width horizontal flux in the  $y$ -direction. Sub-figures (d), (h) and (l) depict the mean unit-width horizontal flux in the  $x$ -direction.

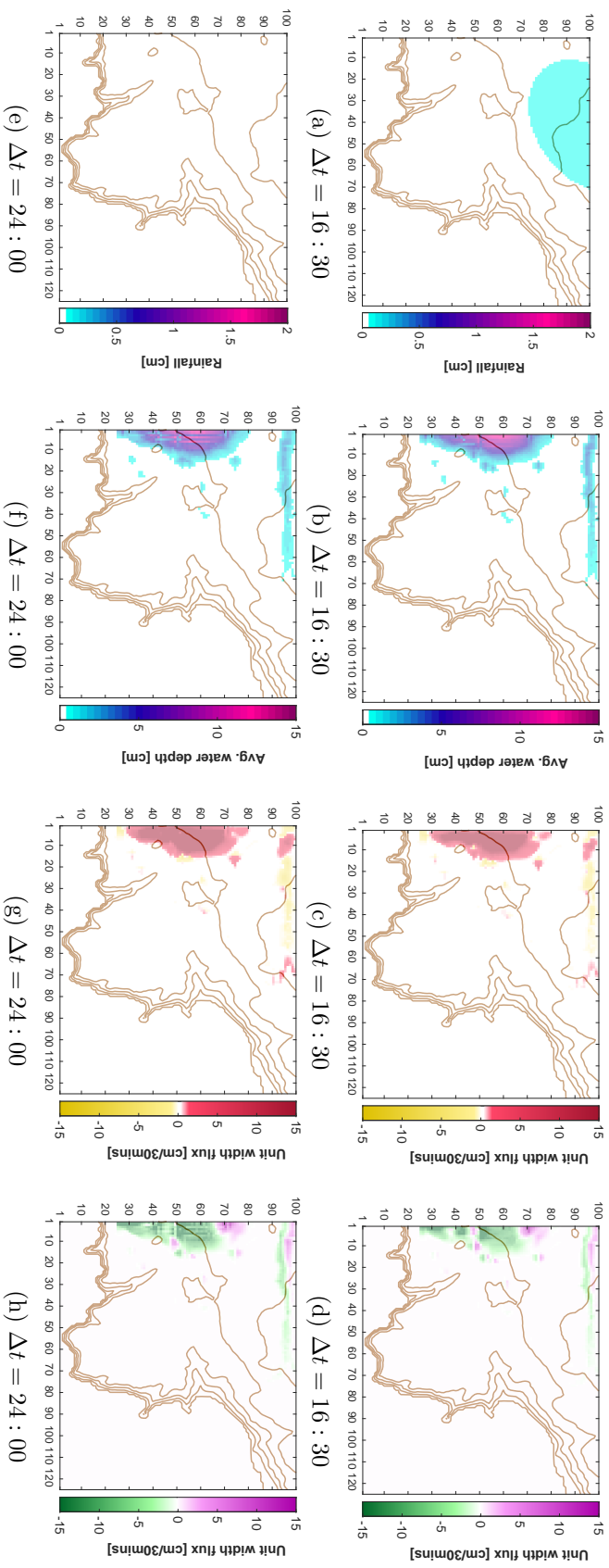


Figure J.13: Scenario 2 - North-western moving storm - 20m resolution model. Each row presents individual timesteps  $\Delta t = 16 : 30$  and  $\Delta t = 24 : 00$ . Sub-figures (a) and (e) show the evolution of the fictitious storm during the simulation. Sub-figures (b) and (f) show the average water depth at their given timesteps. Sub-figures (c) and (g) depict the mean unit-width horizontal flux in the  $y$ -direction. Sub-figures (d) and (h) depict the mean unit-width horizontal flux in the  $x$ -direction.

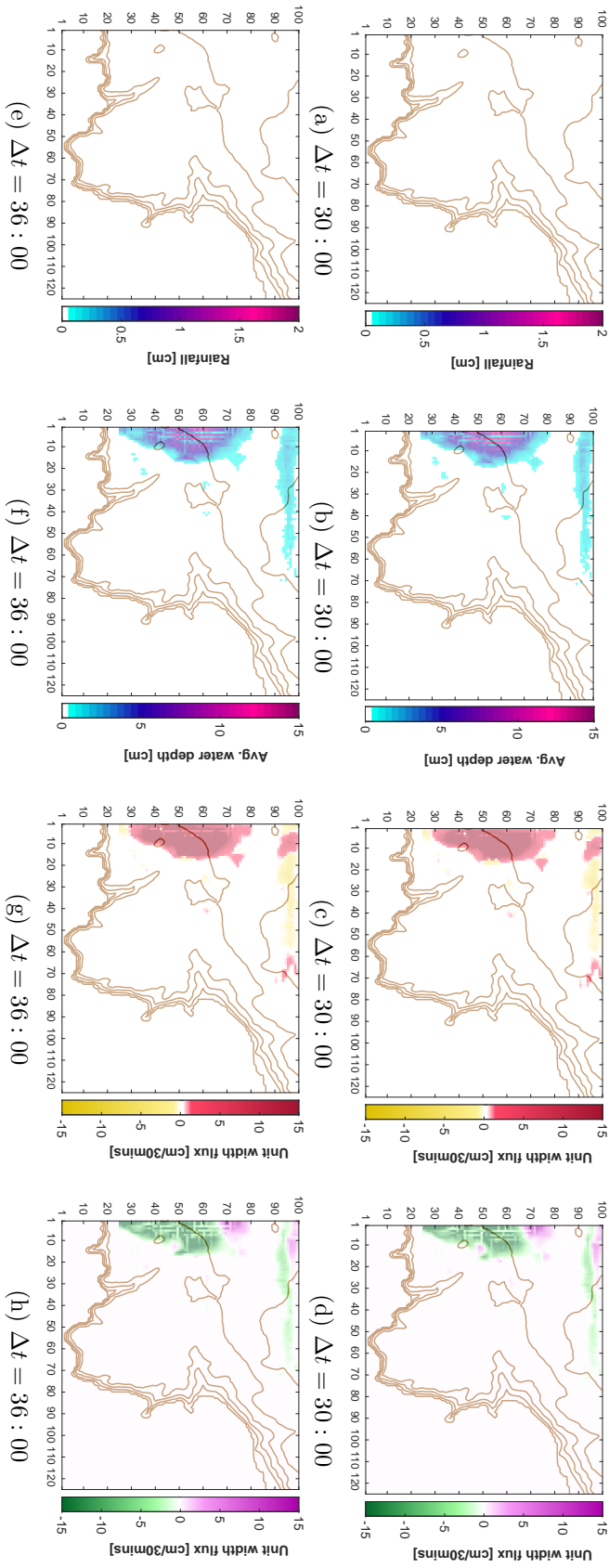


Figure J.14: Scenario 2 - North-western moving storm - 20m resolution model. Each row presents individual timesteps  $\Delta t = 30 : 00$  and  $\Delta t = 36 : 00$ . Sub-figures (a), (e) and (i) show the evolution of the fictitious storm during the simulation. Sub-figures (b), (f) and (j) show the average water depth at their given timesteps. Sub-figures (c), (g) and (k) depict the mean unit-width horizontal flux in the  $x$ -direction. Sub-figures (d), (h) and (l) depict the mean unit-width horizontal flux in the  $y$ -direction.

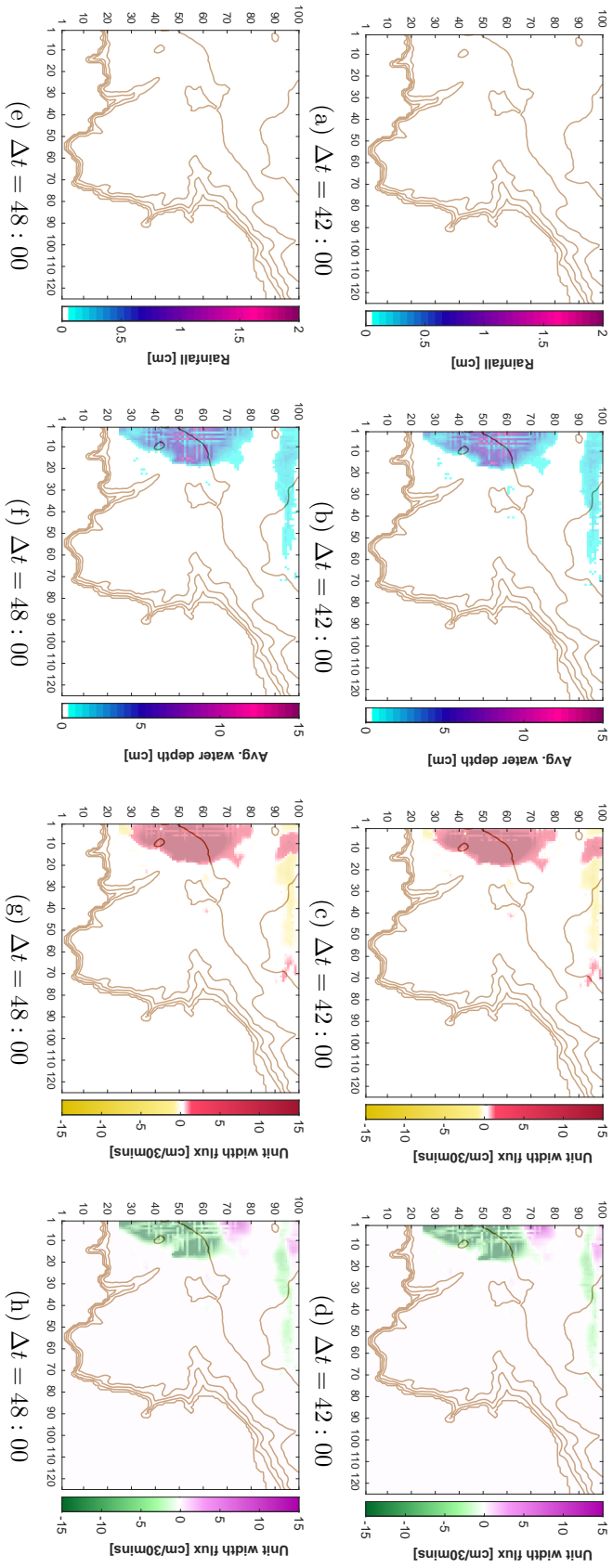


Figure J.15: Scenario 2 - North-western moving storm - 20m resolution model. Each row presents individual timesteps  $\Delta t = 42 : 00$  and  $\Delta t = 48 : 00$ . Sub-figures (a) and (e) show the evolution of the fictitious storm during the simulation. Sub-figures (b) and (f) show the average water depth at their given timesteps. Sub-figures (c) and (g) depict the mean unit-width horizontal flux in the  $y$ -direction. Sub-figures (d) and (h) depict the mean unit-width horizontal flux in the  $x$ -direction.

## J.2. Static 20m

In Figures J.16 and J.17, sub-figures J.16(a), (e) and (i) and sub-figure J.17(a) show the temporal and spatial location of the fictitious storm for the static scenario. This storm was placed in the north-west corner of the computational domain. Initially, the storm traced the urban land-use pixels in the northern part of the domain with a low average water depth (sub-figure J.16(b)). At  $\Delta t = 06 : 00$ , the average water depth rose above 5cm with further pixels to the south of the road also experiencing flooding. It is here also where one can see a divergence in the unit-width horizontal velocity in the  $y$ -direction (sub-figure J.16(h)). This continues at  $\Delta t = 12 : 00$  with average water depths breaching 10cm (sub-figure J.16(j)) and the divergence of the velocities strengthening (sub-figure J.16(l)). This pattern of behaviour continues throughout timesteps  $\Delta t = 16 : 30$  and  $\Delta t = 24 : 00$  (Figure J.17). Figures J.18 and J.19 show the flooding effect after the storm event. Average water depths have fallen below 10cm in the main by  $\Delta t = 30 : 00$  (sub-figure J.18(b)). The unit-width horizontal velocity in the  $y$ -direction is clearly visible too in the north-western part of the computational domain (sub-figure J.18(d)). This pattern continues throughout the remainder of the simulation. By  $\Delta t = 48 : 00$ , the overland flow has travelled south-eastward (sub-figure J.19(f)).

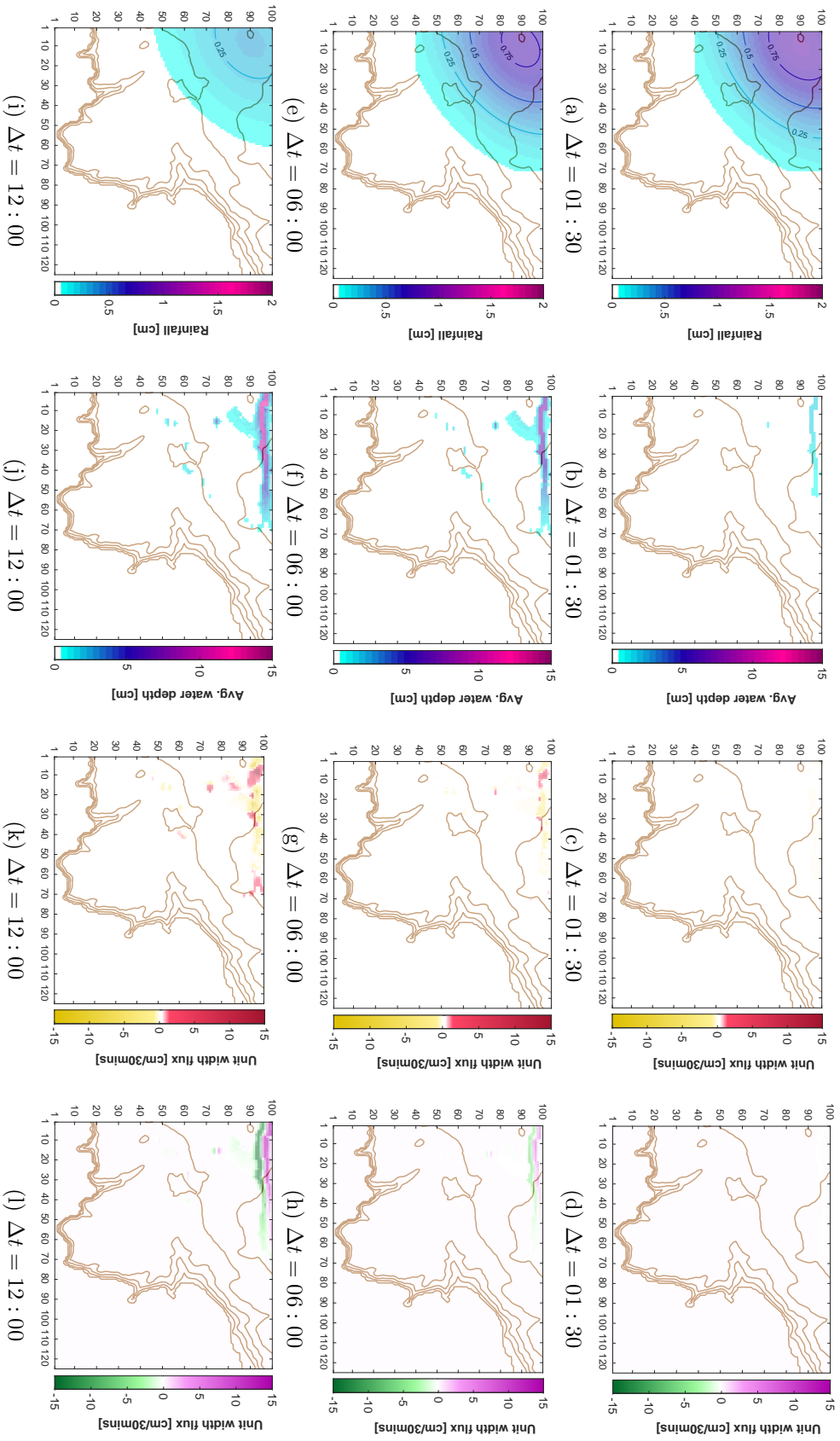


Figure J.16: Scenario 2 - North-western static storm - 20m resolution model. Each row presents individual timesteps  $\Delta t = 01 : 30$ ,  $\Delta t = 06 : 00$  and  $\Delta t = 12 : 00$ . Sub-figures (a), (e) and (i) show the evolution of the fictitious storm during the simulation. Sub-figures (b), (f) and (j) show the average water depth at their given timesteps. Sub-figures (c), (g) and (k) depict the mean unit-width horizontal flux in the  $y$ -direction. Sub-figures (d), (h) and (l) depict the mean unit-width horizontal flux in the  $x$ -direction.

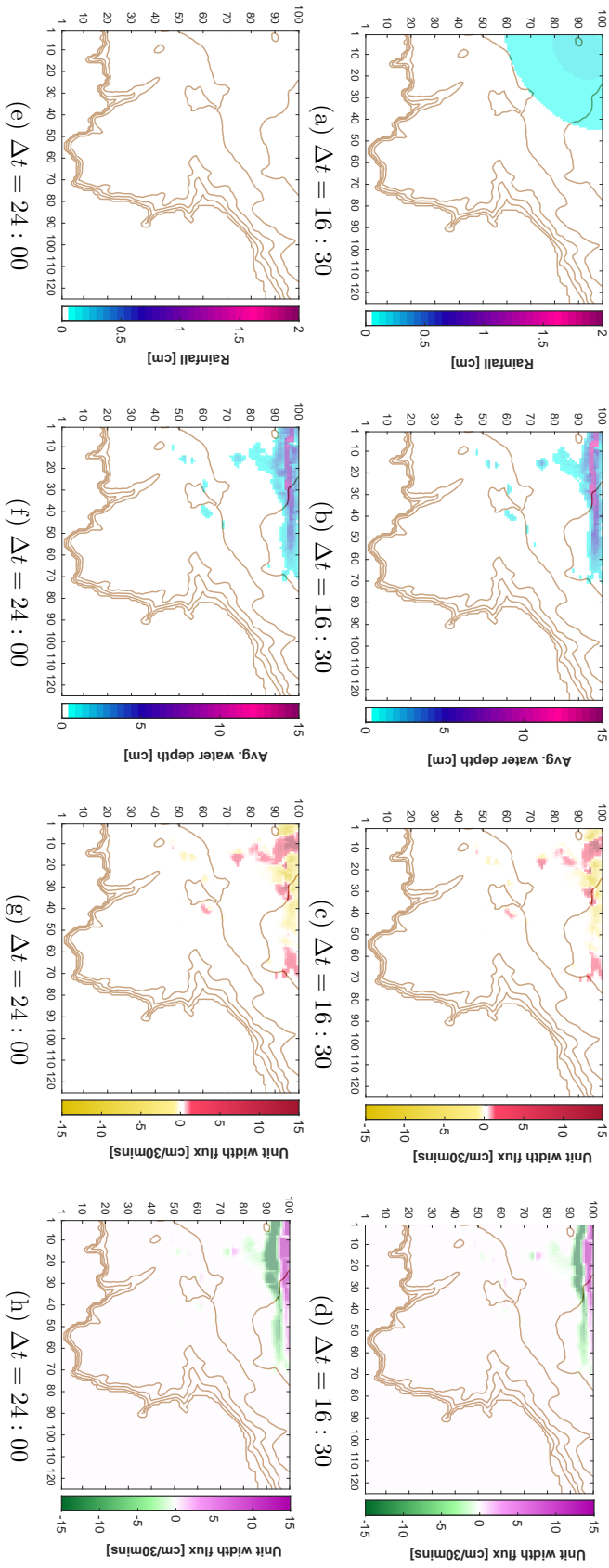


Figure J.17.: Scenario 2 - North-western static storm - 20m resolution model. Each row presents individual timesteps  $\Delta t = 16 : 30$  and  $\Delta t = 24 : 00$ . Sub-figures (a) and (e) show the evolution of the fictitious storm during the simulation. Sub-figures (b) and (f) show the average water depth at their given timesteps. Sub-figures (c) and (g) depict the mean unit-width horizontal flux in the  $y$ -direction. Sub-figures (d) and (h) depict the mean unit-width horizontal flux in the  $x$ -direction.

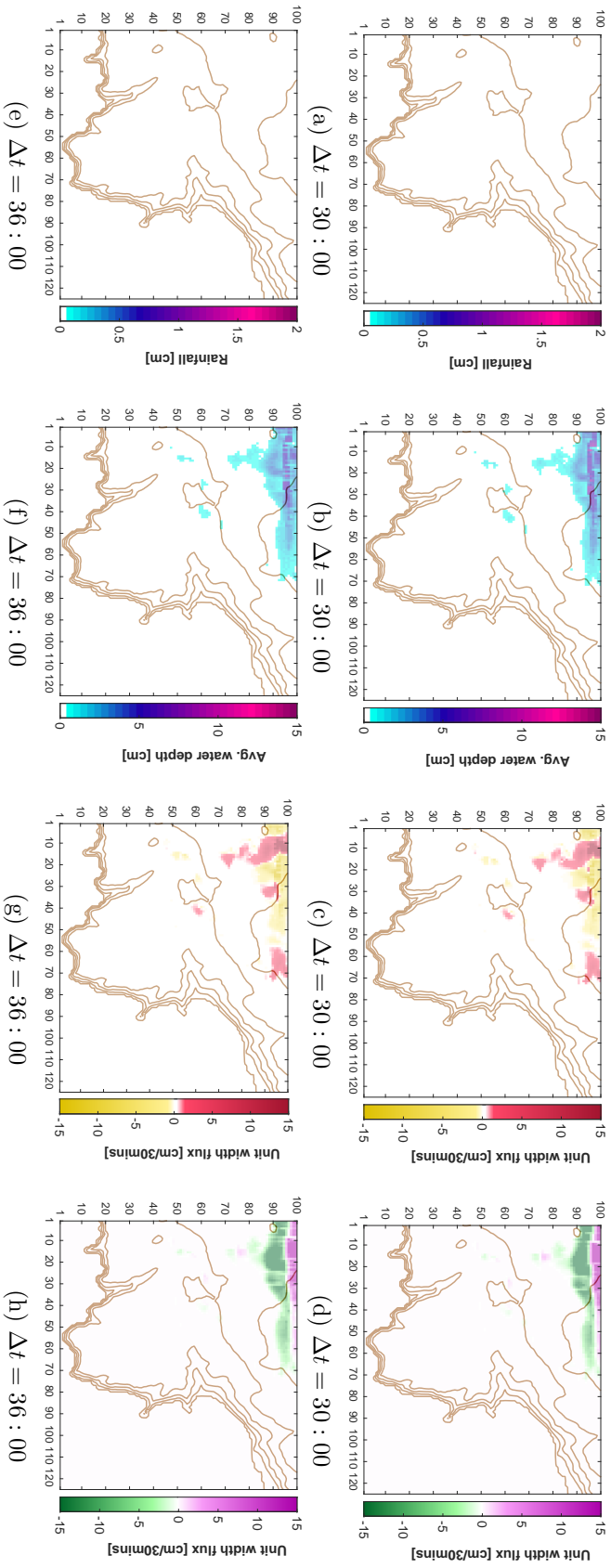


Figure J.18: Scenario 2 - North-western static storm - 20m resolution model. Each row presents individual timesteps  $\Delta t = 30 : 00$  and  $\Delta t = 36 : 00$ . Sub-figures (a), (e) and (i) show the evolution of the fictitious storm during the simulation. Sub-figures (b), (f) and (j) show the average water depth at their given timesteps. Sub-figures (c), (g) and (k) depict the mean unit-width horizontal flux in the  $x$ -direction. Sub-figures (d), (h) and (l) depict the mean unit-width horizontal flux in the  $y$ -direction.



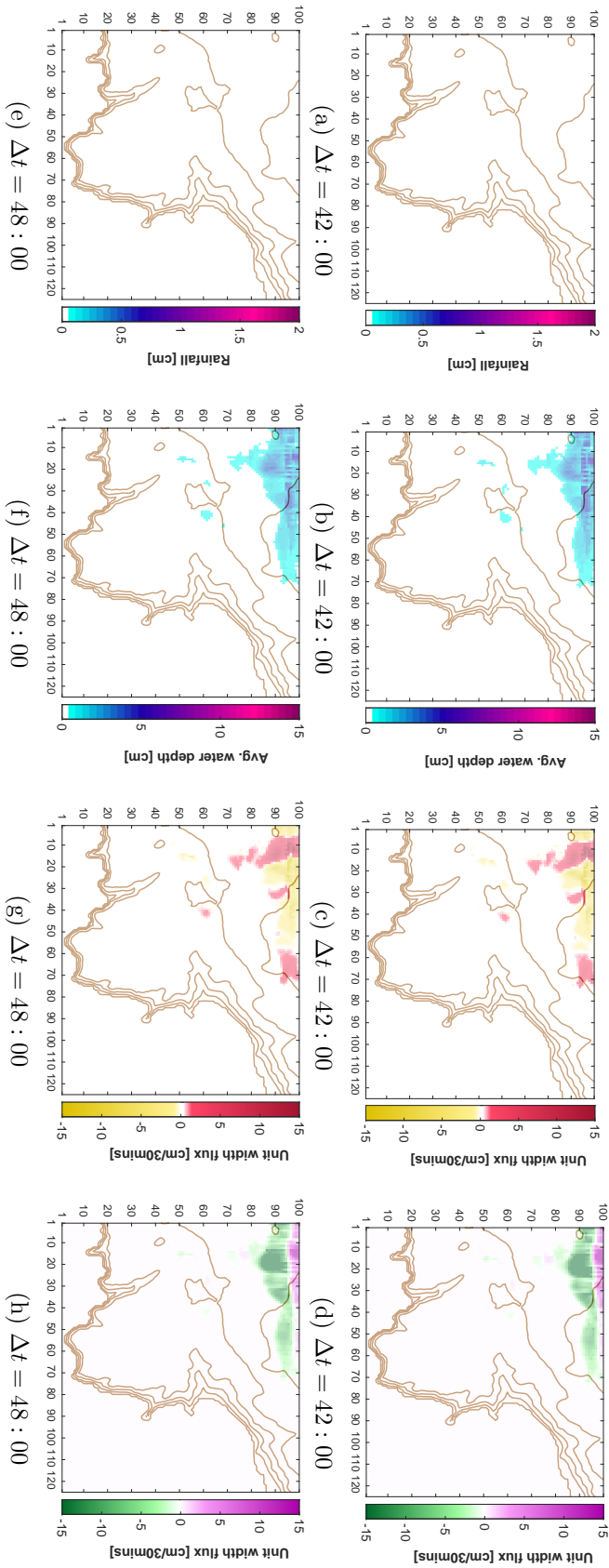


Figure J.19.: Scenario 2 - North-western static storm - 20m resolution model. Each row presents individual timesteps  $\Delta t = 42 : 00$  and  $\Delta t = 48 : 00$ . Sub-figures (a) and (e) show the evolution of the fictitious storm during the simulation. Sub-figures (b) and (f) show the average water depth at their given timesteps. Sub-figures (c) and (g) depict the mean unit-width horizontal flux in the  $y$ -direction. Sub-figures (d) and (h) depict the mean unit-width horizontal flux in the  $x$ -direction.

### J.3. Movement 50m

Figures J.20, J.21, J.22 and J.23 follow the same format as the figures discussed above. Initially the storm is concentrated within the first ten pixels of the 50m resolution mode (Figure J.20(a)) with an average water depth below 5cm (sub-figure J.20(b)). By  $\Delta t = 12 : 00$ , most of the storm has passed and a majority of the flooding occurs on the western boundary of the computational domain (sub-figure J.20(j)) reaching above 10cm in some parts. A strong unit-width horizontal velocities going in a south-easterly direction (sub-figures J.20(k) and J.20(l)) is easily identifiable. As the storm dissipates, the number of pixels with an average water depth above 10cm diminishes quickly by  $\Delta t = 24 : 00$ , with flood water moving in a south-easterly direction still (sub-figures J.21(f), (g) and (h)). Figures J.22 and J.23 depict the second half of the scenario. The majority of pixels contain an average water depth between 1 and 10cm (sub-figure J.22(b)). Throughout the timesteps these average water depths continue to diminish and by  $\Delta t = 48 : 00$  the majority of pixels are experiencing a mean water depth of below 5cm (sub-figure J.23(f)).

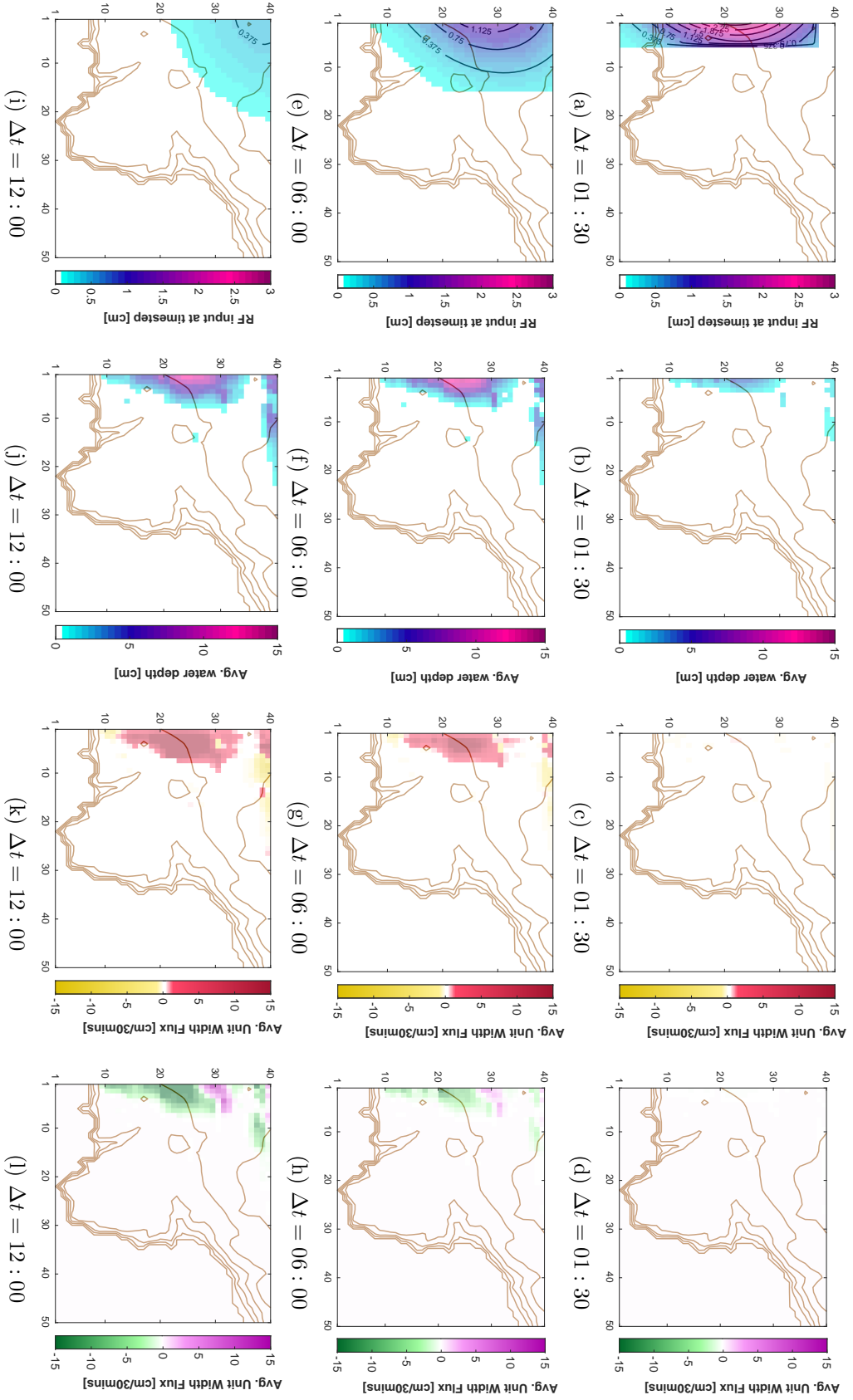


Figure J.20: Scenario 2 - North-western moving storm - 50m resolution model. Each row presents individual timesteps  $\Delta t = 01 : 30$ ,  $\Delta t = 06 : 00$  and  $\Delta t = 12 : 00$ . Sub-figures (a), (e) and (i) show the evolution of the fictitious storm during the simulation. Sub-figures (b), (f) and (j) show the average water depth at their given timesteps. Sub-figures (c), (g) and (k) depict the mean unit-width horizontal flux in the  $y$ -direction. Sub-figures (d), (h) and (l) depict the mean unit-width horizontal flux in the  $x$ -direction.

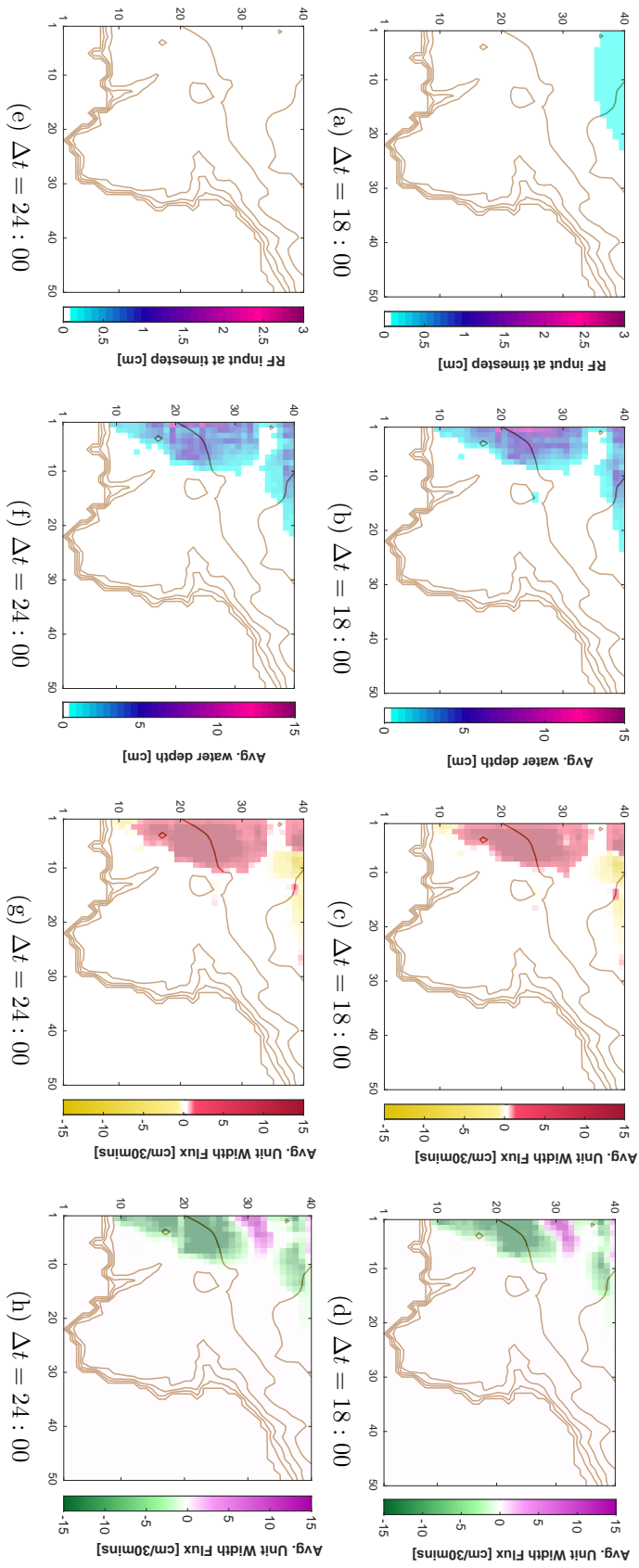


Figure J.21.: Scenario 2 - North-western moving storm - 50m resolution model. Each row presents individual timesteps  $\Delta t = 18 : 00$  and  $\Delta t = 24 : 00$ . Sub-figures (a) and (e) show the evolution of the fictitious storm during the simulation. Sub-figures (b) and (f) show the average water depth at their given timesteps. Sub-figures (c) and (g) depict the mean unit-width horizontal flux in the  $y$ -direction. Sub-figures (d) and (h) depict the mean unit-width horizontal flux in the  $x$ -direction.

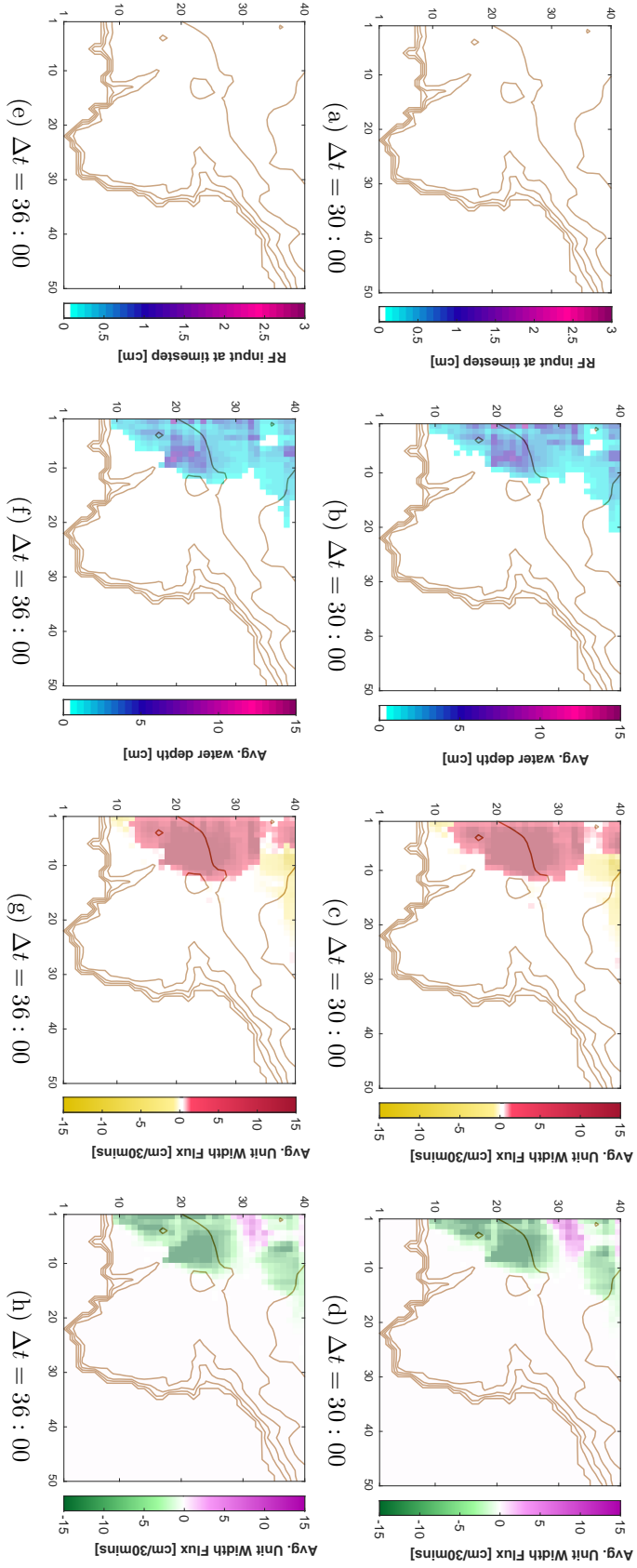


Figure J.22.: Scenario 2 - North-western moving storm - 50m resolution model. Each row presents individual timesteps  $\Delta t = 30 : 00$  and  $\Delta t = 36 : 00$ . Sub-figures (a) and (e) show the evolution of the fictitious storm during the simulation. Sub-figures (b) and (f) show the average water depth at their given timesteps. Sub-figures (c) and (g) depict the mean unit-width horizontal flux in the  $x$ -direction. Sub-figures (d) and (h) depict the mean unit-width horizontal flux in the  $y$ -direction.

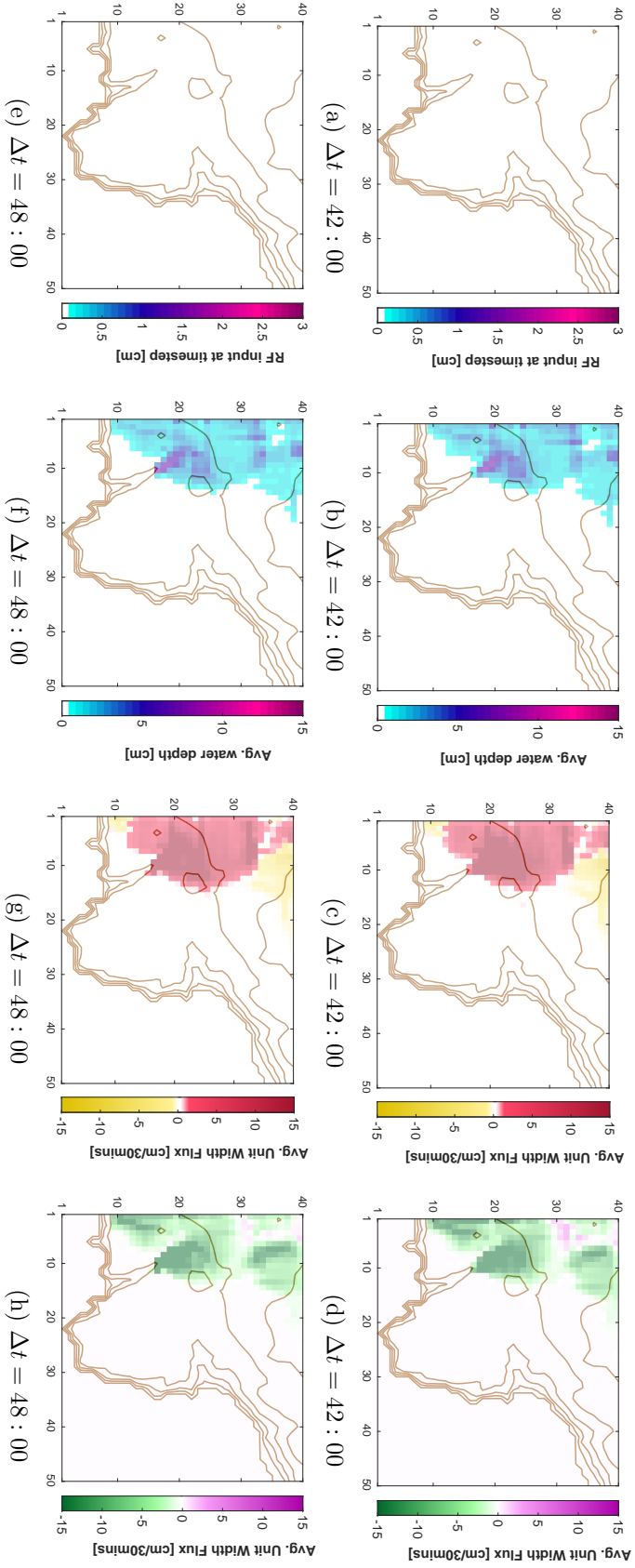


Figure J.23.: Scenario 2 - North-western moving storm - 50m resolution model. Each row presents individual timesteps  $\Delta t = 42 : 00$  and  $\Delta t = 48 : 00$ . Sub-figures (a) and (e) show the evolution of the fictitious storm during the simulation. Sub-figures (b) and (f) show the average water depth at their given timesteps. Sub-figures (c) and (g) depict the mean unit-width horizontal flux in the  $x$ -direction. Sub-figures (d) and (h) depict the mean unit-width horizontal flux in the  $y$ -direction.

#### J.4. Static 50m

For the static scenario, the storm is located in the north-west corner of the computational domain, as seen in Figures J.24 and J.25. At  $\Delta t = 12 : 00$  flooding is concentrated in the north-west corner of the computational domain with values between 10 and 15cm, moving in a south-westerly direction. This continues throughout and by  $\Delta t = 18 : 00$  a large majority of pixels near the computational boundary have an average water depth of 15cm (sub-figure J.25(b)). These pixels are moving at or beyond 15cm/30mins in a south-easterly direction (sub-figures J.25(c) and (d)). As the simulation continues the overland flow reaches pixels  $\Omega_{(i,j)} = \Omega_{(1-20,20-30)}$ , with a majority at a depth of between 10 and 15cm (Figure J.26(f)) at  $\Delta t = 36 : 00$ . At the end of the simulation (sub-figure  $\Delta t = 48 : 00$ ), this region continues to record overland flow, but at a lower depth of 5-10cm (sub-figure J.27(f)) and continues to move in a south-easterly direction at a strong pace (sub-figures J.27(f) and (g)).

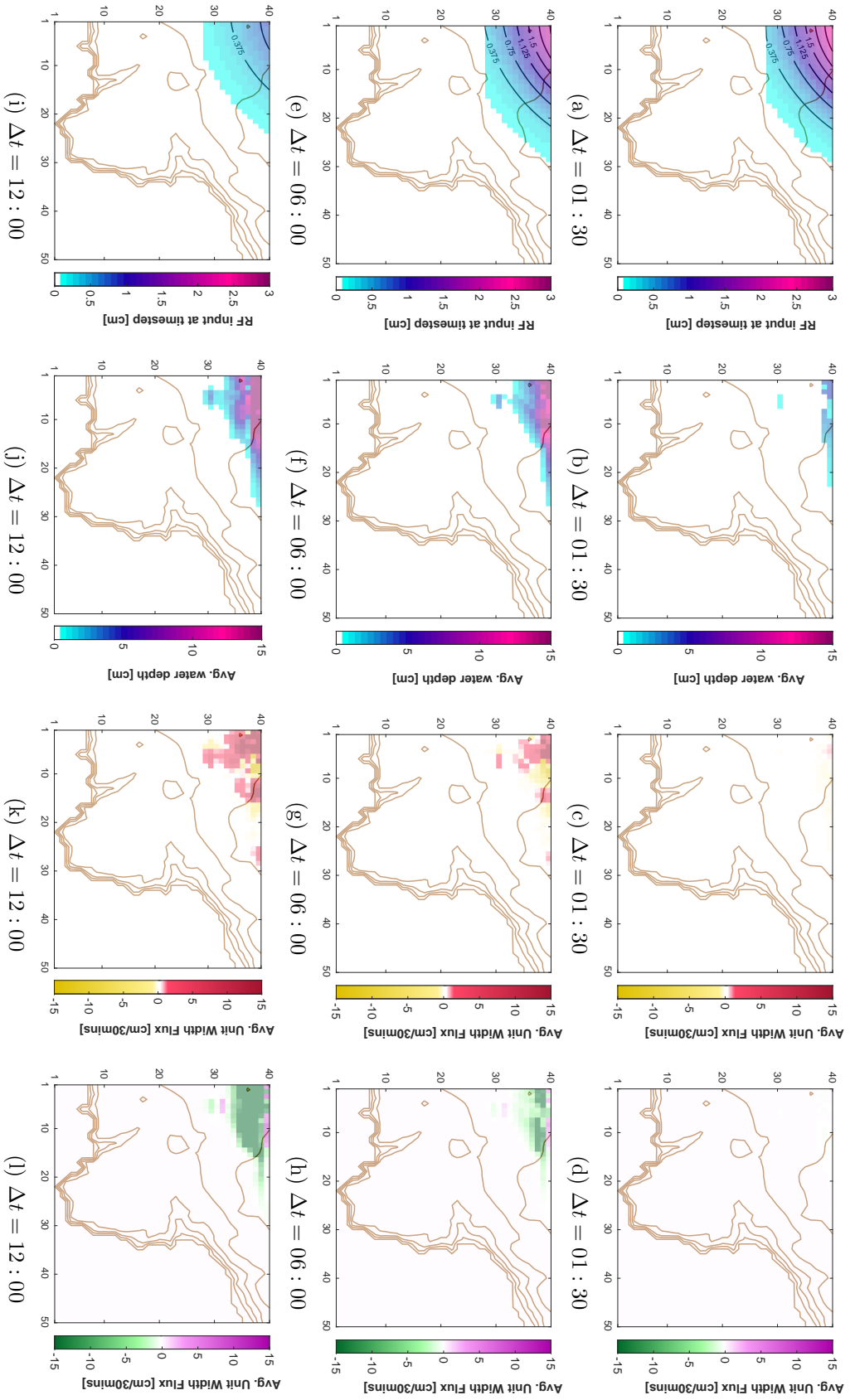


Figure J.24: Scenario 2 - North-western static storm - 50m resolution model. Each row presents individual timesteps  $\Delta t = 01 : 30$ ,  $\Delta t = 06 : 00$  and  $\Delta t = 12 : 00$ . Sub-figures (a), (e) and (i) show the evolution of the fictitious storm during the simulation. Sub-figures (b), (f) and (j) show the average water depth at their given timesteps. Sub-figures (c), (g) and (k) depict the mean unit-width horizontal flux in the  $y$ -direction. Sub-figures (d), (h) and (l) depict the mean unit-width horizontal flux in the  $x$ -direction.



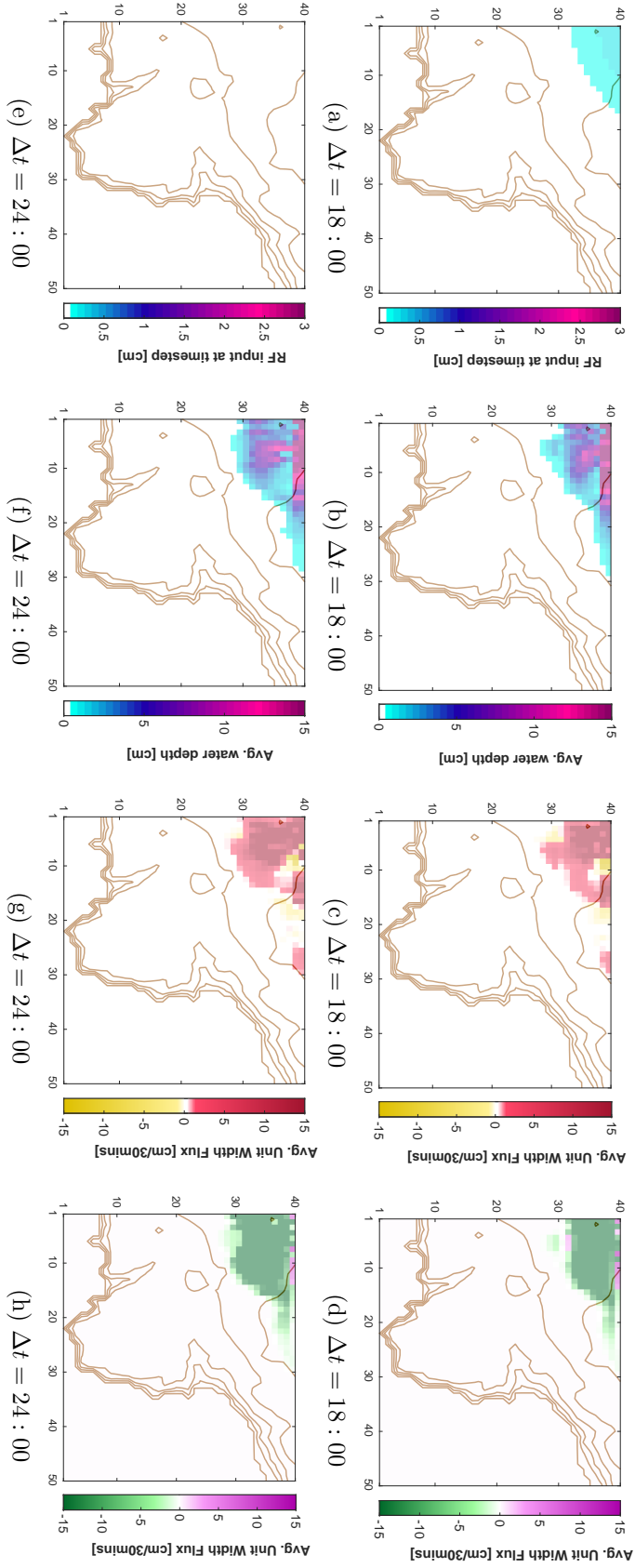


Figure J.25.: Scenario 2 - North-western static storm - 50m resolution model. Each row presents individual timesteps  $\Delta t = 18 : 00$  and  $\Delta t = 24 : 00$ . Sub-figures (a) and (e) show the evolution of the fictitious storm during the simulation. Sub-figures (b) and (f) show the average water depth at their given timesteps. Sub-figures (c) and (g) depict the mean unit-width horizontal flux in the  $x$ -direction. Sub-figures (d) and (h) depict the mean unit-width horizontal flux in the  $y$ -direction.

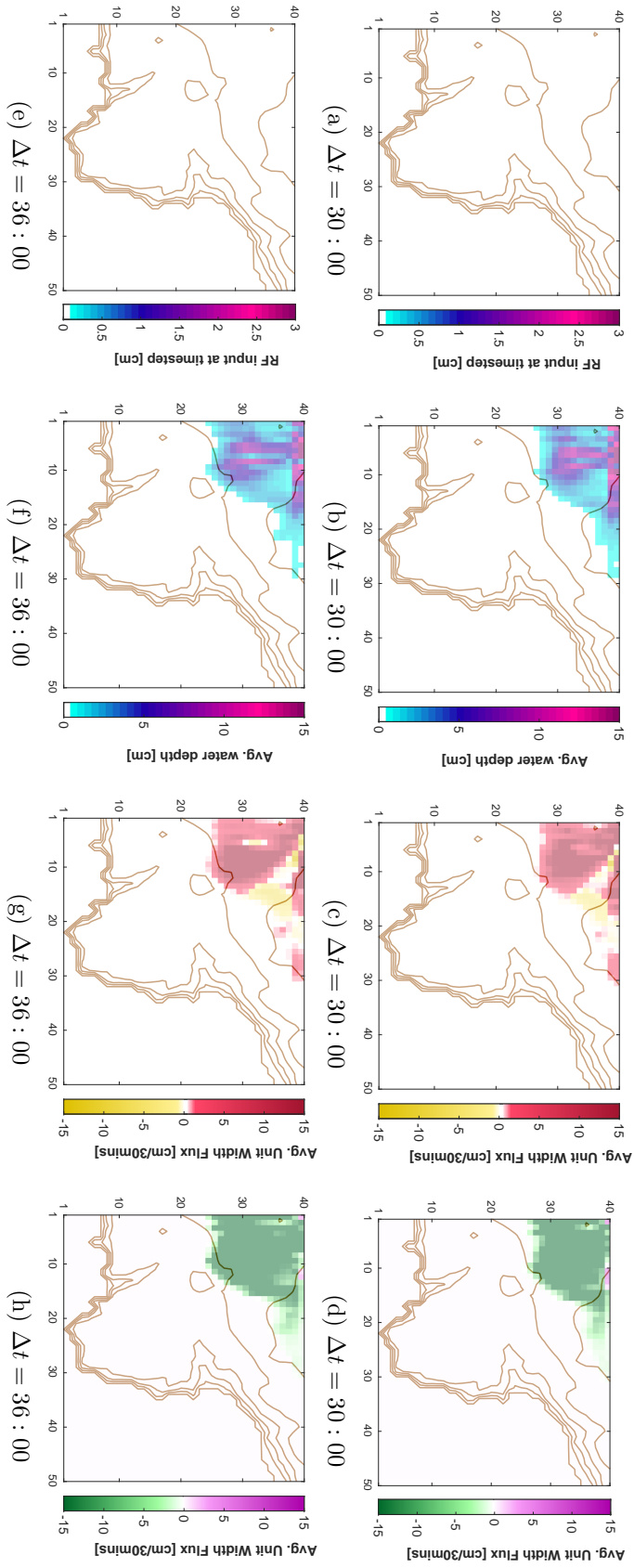


Figure J.26.: Scenario 2 - North-western static storm - 50m resolution model. Each row presents individual timesteps  $\Delta t = 30 : 00$  and  $\Delta t = 36 : 00$ . Sub-figures (a) and (e) show the evolution of the fictitious storm during the simulation. Sub-figures (b) and (f) show the average water depth at their given timesteps. Sub-figures (c) and (g) depict the mean unit-width horizontal flux in the  $x$ -direction. Sub-figures (d) and (h) depict the mean unit-width horizontal flux in the  $y$ -direction.

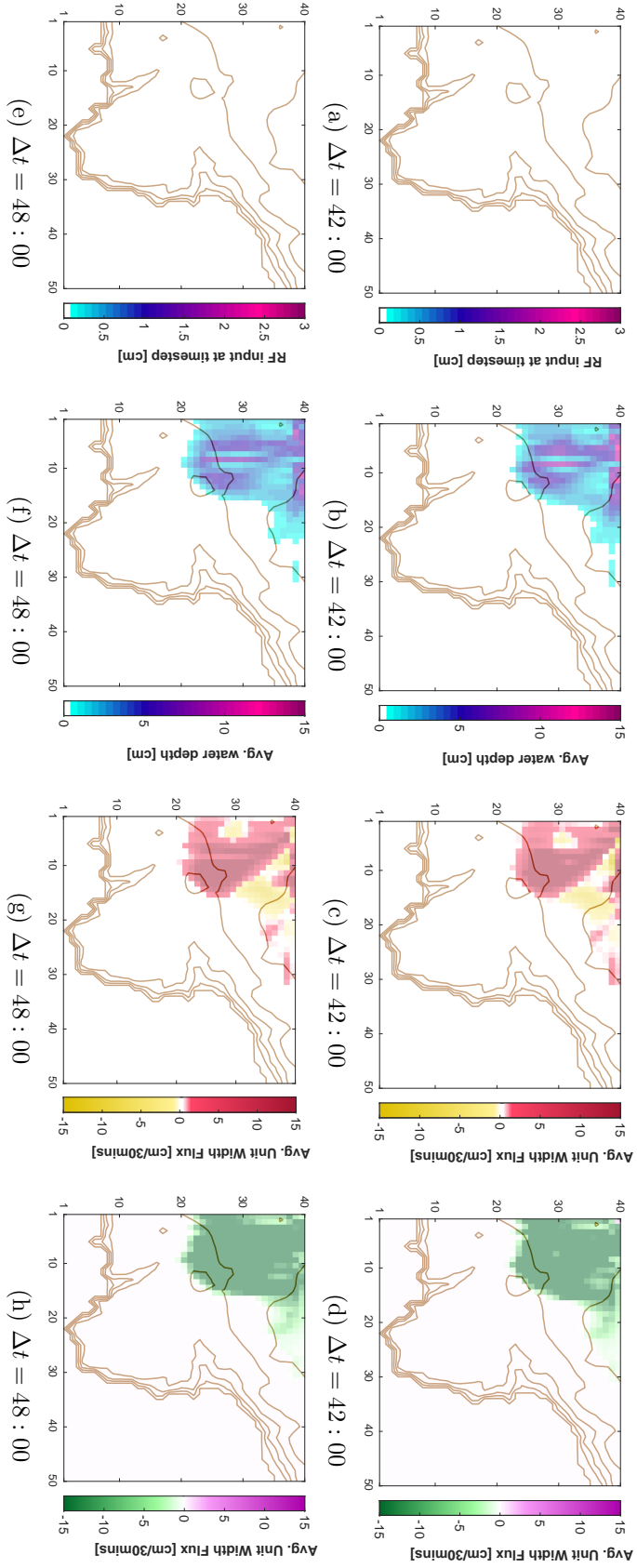


Figure J.27.: Scenario 2 - North-western static storm - 50m resolution model. Each row presents individual timesteps  $\Delta t = 42 : 00$  and  $\Delta t = 48 : 00$ . Sub-figures (a) and (e) show the evolution of the fictitious storm during the simulation. Sub-figures (b) and (f) show the average water depth at their given timesteps. Sub-figures (c) and (g) depict the mean unit-width horizontal flux in the  $x$ -direction. Sub-figures (d) and (h) depict the mean unit-width horizontal flux in the  $y$ -direction.

# Bibliography

- Abbott, M. B., Bathurst, J. C., Cunge, J. A., O'Connell, P. E., and Rasmussen, J. (1986a). An introduction to the European Hydrological System - Systeme Hydrologique Europeen, "SHE", 1: History and philosophy of a physically-based distributed modelling system. *Journal of Hydrology*, 87(1-2):45-59. DOI: [https://doi.org/10.1016/0022-1694\(86\)90114-9](https://doi.org/10.1016/0022-1694(86)90114-9).
- Abbott, M. B., Bathurst, J. C., Cunge, J. A., O'Connell, P. E., and Rasmussen, J. (1986b). An introduction to the European Hydrological System - Systeme Hydrologique Europeen, "SHE", 2: Structure of a physically-based, distributed modelling system. *Journal of Hydrology*, 87(1-2):61-77. DOI: [https://doi.org/10.1016/0022-1694\(86\)90115-0](https://doi.org/10.1016/0022-1694(86)90115-0).
- Akram, F., Rasul, M. G., Khan, M. M. K., and Amir, M. S. I. I. (2014). Comparison of Different Hydrograph Routing Techniques in XPSTORM Modelling Software: A Case Study. *International Journal of Environmental, Ecological, Geological and Mining Engineering*, 8(3):213-223. Retrieved from: <https://publications.waset.org/vol/87> [Accessed 17th February 2020].
- Alfieri, L., Burek, P., Dutra, E., Krzeminski, B., Muraro, D., Thielen, J., and Pappenberger, F. (2013). GloFAS - global ensemble streamflow forecasting and flood early warning. *Hydrology and Earth System Sciences*, 17(3):1161-1175. DOI: <https://doi.org/10.5194/hess-17-1161-2013>.
- Allen, R., Pereira, L., Raes, D., and Smith, M. (1998). Crop evapotranspiration: Guidelines for computing water requirements - FAO Irrigation and drainage paper. Technical Report 56, Food and Agriculture Organisation of the United Nations, Rome. ISBN-10: 9251042195.
- Angulo-Jaramillo, R., Vandervaere, J. P., Roulier, S., Thony, J., Gaudent, J., and Vauclin,

- 
- M. (2000). Field measurement of soil surface hydraulic properties by disc and ring infiltrometers: A review and recent developments. *Soil and Tillage Research*, 55(1–2):1–29. doi: [https://doi.org/10.1016/S0167-1987\(00\)00098-2](https://doi.org/10.1016/S0167-1987(00)00098-2).
- Aquanty Inc. (2015). HGS Theory Manual. Manual, Aquanty Inc., 600 Weber Street North, Unit B, Waterloo, Ontario, N2V 1K4. Retrieved from [https://aquanty-artifacts-public.s3.amazonaws.com/hgs/hydrosphere\\_theory.pdf](https://aquanty-artifacts-public.s3.amazonaws.com/hgs/hydrosphere_theory.pdf) [Accessed 16<sup>th</sup> July 2023].
- Arnell, N. W. (2002). *Hydrology and Global Environmental Change (Understanding Global Environmental Change)*. Routledge. ISBN-10: 0582369843.
- Arnold, J. G., Srinivasan, R., Muttiah, R. S., and Williams, J. R. (1998). Large Area Hydrologic Modelling and Assessment Part I: Model Development. *Journal of the American Water Resources Association*, 34(1):73–89. DOI: <https://doi.org/10.1111/j.1752-1688.1998.tb05961.x>.
- Aston, A. R. (1979). Rainfall interception by eight small trees. *Journal of Hydrology*, 42(3-4):383–396. DOI: [https://doi.org/10.1016/0022-1694\(79\)90057-X](https://doi.org/10.1016/0022-1694(79)90057-X).
- Audusse, E., Bouchut, F., Bristeau, M.-O., Klein, R., and Perthame, B. (2004). A fast and stable well-balanced scheme with hydrostatic reconstruction for shallow water flows. *SIAM Journal on Scientific Computing*, 25(6):2050–2065. DOI: <https://doi.org/10.1137/S1064827503431090>.
- Avesani, D., Galletti, A., Piccolroaz, S., Belling, A., and Majone, B. (2021). A dual-layer MPI continuous large-scale hydrological model including Human Systems. *Environmental & Software*, 139:105003. doi: <https://doi.org/10.1016/j.envsoft.2021.105003>.
- Baily, B. (2007). The extraction of digital vector data from historic land use maps of Great Britain using image processing techniques. *e-Perimtron*, 2(4):209–223.
- Bandaragoda, C., Tarboton, D. G., and Woods, R. (2004). Application of TOPNET in the distributed model intercomparison project. *Journal of Hydrology*, 298(1–4):178–201. DOI: <https://doi.org/10.1016/j.jhydrol.2004.03.038>.
- Bathurst, J. C. and O’Connell, P. E. (1992). Future of Distributed Modelling: The Systeme Hydrologique Europeen. *Hydrological Processes*, 6(3):265–277. doi: <https://doi.org/10.1002/hyp.3360060304>.

- 
- BBC News Website (2017). *Dick Powell Image BBC News*. Retrieved from <https://www.bbc.co.uk/news/uk-england-cornwall-40650406>. [Accessed 20th November 2021].
- Beven, K. (2019). How to make advances in hydrological modelling. *Hydrology Research*, 50(6):1481–1494. doi: <https://doi.org/10.2166/nh.2019.134>.
- Beven, K., Calver, A., and Morris, E. M. (1987). The Institute of Hydrology Distributed Model. Technical Report 98, Institute of Hydrology, Walingford, UK. Retrieved from <https://core.ac.uk/display/61684> [Accessed 15th February 2020].
- Beven, K. and Freer, J. (2001). A dynamic TOPMODEL. *Hydrological Processes*, 15(10):1993–2011. DOI: <https://doi.org/10.1002/hyp.252>.
- Beven, K., Lamb, R., Quinn, P., Romanowicz, R., and Freer, J. (1995). TOPMODEL. In Singh, V. P., editor, *Computer Models of Watershed Hydrology*, chapter 18, pages 627–668. Water Resources Publications, Highlands Ranch, CO. ISBN-10: 1887201742.
- Beven, K. J. and Kirkby, M. J. (1979). A physically based, variable contributing area model of basin hydrology. *Hydrological Sciences Journal*, 24(1):43–69. DOI: <https://doi.org/10.1080/02626667909491834>.
- Bhumralkar, C. M. (1975). Numerical experiments on the computation of ground surface temperatures in an atmospheric general circulation model. *Journal of Applied Meteorology*, 14(7):1246–1258. DOI: [https://doi.org/10.1175/1520-0450\(1975\)014<1246:NEOTCO>2.0.CO;2](https://doi.org/10.1175/1520-0450(1975)014<1246:NEOTCO>2.0.CO;2).
- Biftu, G. F. and Gan, T. Y. (2001). Semi-distributed, physical based, hydrologic modelling of the Paddle River Basin, using remotely sensed data. *Journal of Hydrology*, 244(3–4):137–156. DOI: [https://doi.org/10.1016/S0022-1694\(01\)00333-X](https://doi.org/10.1016/S0022-1694(01)00333-X).
- Biftu, G. F. and Gan, T. Y. (2004). A semi-distributed, physics-based hydrologic model using remotely sensed and Digital Terrain Elevation Data for semi-arid catchments. *International Journal of Remote Sensing*, 25(20):4351–4379. DOI: <https://doi.org/10.1080/01431160310001654374>.
- Blackadar, A. K. (1976). Modelling the nocturnal boundary layer. In *Proceedings of the Third Symposium on Atmospheric Turbulence, Diffusion and Air Quality*, pages 46–49, Boston, Massachusetts.

- 
- Bodman, G. B. and Colman, E. A. (1944). Moisture and Energy Conditions during downward entry of water into soils. *Soil Science Society of America*, 8:116–122. doi: <https://doi.org/10.2136/sssaj1944.036159950008000C0021x>.
- Bouilloud, L., Chancibault, K., Vincendon, B., Ducrocq, V., Habets, F., Saulnier, G.-M., Anquetin, S., Martin, E., and Noilhan, J. (2010). Coupling the ISBA Land Surface Model and the TOPMODEL Hydrological Model for Mediterranean Flash-Flood Forecasting: Description, Calibration and Validation. *Journal of Hydrometeorology*, 11(2):315–333. DOI: <https://doi.org/10.1175/2009JHM1163.1>.
- Bras, R. L. (1990). *Hydrology: An Introduction to Hydrologic Science*. Addison-Wesley Series in Civil Engineering. Addison-Wesley, 1<sup>st</sup> edition. ISBN-10: 0201059223.
- British Ecological Society (2013). Flooding in the UK: ecological impacts and an ecosystem approach. Webpage. <https://www.britishecologicalsociety.org/flooding-in-the-uk-ecological-impacts-and-an-ecosystem-approach/>.
- Brutsaert, W. (2005). *Hydrology: An Introduction*. Cambridge University Press, New York. ISBN-10: 0521824796.
- Bubnová, R., Hello, G., Bénard, P., and Gelyn, J.-F. (1995). Integration of the Fully Elastic Equations Cast in the Hydrostatic Pressure Terrain-Following Coordinate in the Framework of the ARPEGE/Aladin NWP System. *Monthly Weather Review*, 123(2):515–535. DOI: [https://doi.org/10.1175/1520-0493\(1995\)123<0515:IOTFEE>2.0.CO;2](https://doi.org/10.1175/1520-0493(1995)123<0515:IOTFEE>2.0.CO;2).
- Burkart, K. (2009). *How do you define a ‘green’ economy?* Retrieved from <https://www.mnn.com/green-tech/research-innovations/blogs/how-do-you-define-the-green-economy>. [Accessed 24th July 2019].
- Calder, I. (1996). Rainfall interception and drop size - development and calibration of the two-layer stochastic interception model. *Tree Physiology*, 16(8):727–732. doi: <https://doi.org/10.1093/treephys/16.8.727>.
- Causeway technologies (2022). *Causeway & NJW Limited*. Retrieved from <https://www.causeway.com/products/njw-limited>. [Accessed 1st July 2022].
- Celia, M. A. and Bouloutas, E. T. (1990). A General Mass-Conservative Numerical Solu-

- 
- tion for Unsaturated Flow Equation. *Water Resources Research*, 26(7):1483–1496. DOI: <https://doi.org/10.1029/WR026i007p01483>.
- Chakravarthy, S. R. and Osher, S. (1983). High resolution applications of the Osher upwind scheme for the Euler equations. In *Collection of Technical Papers*, number 6 in Computational Fluid Dynamics Conference, pages 363–372, New York. American Institute of Aeronautics and Astronautics. <https://web.archive.org/web/20110517180238/http://www.aiaa.org/content.cfm?pageid=406&gTable=mtgpaper&gID=55466>.
- Chorin, A. J. and Marsden, J. E. (1990). *A Mathematical Introduction to Fluid Mechanics*. Texts in Applied Mathematics. Springer-Verlag, New York, NY, 2<sup>nd</sup> edition. ISBN-10: 1468403664.
- Chow, V. T. (1959). *Open channel Hydraulics*. Mc-Graw Hill, New York.
- Chow, V. T., Maidment, D. R., and Mays, L. W. (1988). *Applied Hydrology*. McGraw Hill Publishing, New York. ISBN-10: 007070242X.
- Chu, C. K. (1979). Numerical Methods in Fluid Dynamics. In Yih, C.-S., editor, *Advances in Applied Mechanics*, volume 18 of *Advances in Applied Mechanics*, chapter 6, pages 285–331. Elsevier, Department of Mechanical Engineering and Plasma Physics Laboratory Columbia University New York, New York. DOI: [https://doi.org/10.1016/S0065-2156\(08\)70269-2](https://doi.org/10.1016/S0065-2156(08)70269-2).
- Clapp, R. B. and Hornberger, G. M. (1978). Empirical equations for some soil hydraulic properties. *Water Resources Research*, 14(4):601–604. DOI: <https://doi.org/10.1029/WR014i004p00601>.
- Colman, E. A. and Bodman, G. B. (1945). Moisture and Energy Conditions during Downward Entry of Water into Moist and Layered Soils. *Soil Science Society of America*, 9:3–11. doi: <https://doi.org/10.2136/sssaj1945.036159950009000C0001x>.
- Cornwall Council (2016). *Cornwall’s Environmental Growth Strategy: 2015 – 2065*. Retrieved from <http://www.cornwall.gov.uk/environmentalgrowth>. [Accessed 20th April 2017].
- Costabile, P., Costanzo, C., and Macchione, F. (2013). A storm event watershed model for surface runoff based on 2d fully dynamic wave equations. *Hydrological Processes*, 27(4):554–569. DOI: <https://doi.org/10.1002/hyp.9237>.



- 
- Courant, R., Friedrichs, K., and Lewy, H. (1928). Über die partiellen differenzengleichungen der mathematischen physik (about the partial difference equations of mathematical physics). *Mathematische Annalen*, 100(1):32–74. DOI: <https://doi.org/10.1007/BF01448839>.
- Courant, R., Isaacson, E., and Rees, M. (1952). On the Solution of Nonlinear Hyperbolic Differential Equations by Finite Differences. *Communications on Pure and Applied Mathematics*, 5(3):243–255. DOI: <https://doi.org/10.1002/cpa.3160050303>.
- Courtier, P. and Geleyn, J.-F. (1988). A global numerical weather prediction model with variable resolution: Application to the shallow-water equations. *Quarterly Journal of the Royal Meteorological Society*, 114(483):1321–1346. DOI: <https://doi.org/10.1002/qj.49711448309>.
- Cowan, W. L. (1956). Estimating hydraulic roughness coefficients. *Agricultural Engineering*, 37(7):473–475.
- Cranfield Soil and Agrifood Institute (2023). Soilscales. *landis*. <https://www.landis.org.uk/soilscales/index.cfm>.
- Cunge, J. A. (1969). On The Subject Of A Flood Propagation Computation Method (Muskingum Method). *Journal of Hydraulic Research*, 7(2):205–230. DOI: <https://doi.org/10.1080/00221686909500264>.
- Daly, H. E. (1991). *Steady-State Economics*. Island Press, 2<sup>nd</sup> edition. ISBN: 155963071X.
- David, J., Valente, F., and Gash, J. (2005). Evaporation of intercepted rainfall. In Anderson, M., editor, *Encyclopedia of Hydrological Sciences*, chapter 43, pages 627–634. John Wiley and Sons. ISBN-10: 0471491039.
- de Roo, A., van der Knijff, J., and Burek, P. (2013). LISFLOOD, distributed water balance and flood simulation model. User manual, Joint Research Centre, Institute for the Protection and Security of the Citizen, Publications Office. DOI: <https://data.europa.eu/doi/10.2788/24982>.
- Deardorff, J. W. (1978). Efficient prediction of ground surface temperature and moisture, with inclusion of a layer of vegetation. *Journal of Geophysical Research: Oceans*, 83(C4):1889–1903. DOI: <https://doi.org/10.1029/JC083iC04p01889>.

- 
- Delis, A. I. and Nikolos, I. K. (2021). Shallow Water Equations in Hydraulics: Modelling, Numerics and Applications. *Water*, 13(24):3598. doi: <https://doi.org/10.3390/w13243598>.
- Department for Communities and Local Government (2010). *Planning Policy Statement 25: Development and Flood Risk*. Her Majesty's Stationery Office (HMSO). ISBN: 9780117540996.
- Department for Communities and Local Government (2017). *Fixing our broken housing market*. Her Majesty's Stationery Office (HMSO). ISBN: 9781474137959.
- Department for Environment, Food & Rural Affairs (2002a). "MAGIC" map. <https://magic.defra.gov.uk/MagicMap.aspx>. [Accessed 16th February 2018].
- Department for Environment, Food & Rural Affairs (2002b). "MAGIC" map Data Sources. [https://magic.defra.gov.uk/Dataset\\_Download\\_Summary.htm](https://magic.defra.gov.uk/Dataset_Download_Summary.htm). [Accessed 16th February 2018].
- Department for Environment, Food & Rural Affairs (2002c). "MAGIC" platform. <https://magic.defra.gov.uk/>. [Accessed 16th February 2018].
- Department for Environment, Food & Rural Affairs (2019). *Defra statistics: Agricultural facts - South West*. [https://assets.publishing.service.gov.uk/government/uploads/system/uploads/attachment\\_data/file/972089/regionalstatistics\\_southwest\\_23mar21.pdf](https://assets.publishing.service.gov.uk/government/uploads/system/uploads/attachment_data/file/972089/regionalstatistics_southwest_23mar21.pdf). [Accessed 18th August 2022].
- Department for Environment Food and Rural Affairs (2013). *England Natural Environment Indicators*. Retrieved from [https://www.gov.uk/government/uploads/system/uploads/attachment\\_data/file/311680/England\\_Natural\\_Environment\\_Indicators\\_2013.pdf](https://www.gov.uk/government/uploads/system/uploads/attachment_data/file/311680/England_Natural_Environment_Indicators_2013.pdf). [Accessed 15th October 2016].
- Dingman, S. L. (2002). *Physical Hydrology*. Prentice Hall, Upper Saddle River, NJ, 2nd edition. ISBN-10: 0130996955.
- Doherty, J. (2005). Model-Independent Parameter Estimation User Manual: 5th Edition. User manual, Watermark Numerical Computing.
- Dréo, J. (2006). *Sustainable development*. Retrieved from [https://en.wikipedia.org/wiki/File:Sustainable\\_development.svg](https://en.wikipedia.org/wiki/File:Sustainable_development.svg). [Accessed 25th July 2019].

---

Duan, Q. Y., Gupta, V. K., and Sorooshian, S. (1993). Shuffled complex evolution approach for effective and efficient global minimization. *Journal of Optimization Theory and Applications*, 76(1):501–521. DOI: <https://doi.org/10.1007/BF00939380>.

Dunne, T. and Leopold, L. B. (1978). *Water in Environmental Planning*. W. H. Freeman, 1st edition. ISBN: 0716700794.

Environment Agency (2017). *LIDAR Composite Digital Terrain Model (DTM) - 2m: SW71NE*. Retrieved from <https://environment.data.gov.uk/dataset/c67f6085-1ef9-46c8-b908-67e9143deedf>. [Accessed 16th September 2018].

Environment Agency and Cornwall Council (2018). Flood Investigation Reports 2017. Technical report, Environment Agency - Cornwall. Retrieved from <https://www.cornwall.gov.uk/media/taidgftx/flood-investigation-reports-2017.pdf> [Accessed 20th November 2021].

EPA (2001). Risk Assessment Guidance for Superfund (RAGS) Volume III - Part A: Process for Conducting Probabilistic Risk Assessment. Technical report, Office of Emergency and Remedial Response, U.S. Environmental Protection Agency, Washington, DC, USA.

Evans, L. (2010). *Partial Differential Equations: Second Edition*, volume 19 of *Graduate Series in Mathematics*. American Mathematical Society, 201, Charles Street Providence, Rhode Island, U.S.A., 2<sup>nd</sup> edition. ISBN-10: 0-8218-4974-3.

Falmouth Packet Website (2017). *Frank Gzonka Image Falmouth Packet*. Retrieved from <https://www.falmouthpacket.co.uk/news/15418737-video-residents-airlifted-to-safety-as-st-keverne-and-coverack-area-heavily-flooded-so> [Accessed 20th November 2021].

Farthing, M. and Ogden, F. (2017). Numerical Solution of Richards' Equation: A Review of Advances and Challenges. *Soil Science Society of America*, 81(6):1257–1269. doi: <https://doi.org/10.2136/sssaj2017.02.0058>.

Ferguson, R. I. (1999). Snowmelt runoff models. *Progress in Physical Geography*, 23(2):205–227. DOI: <https://doi.org/10.1177/030913339902300203>.

Fiedler, F. R. and Ramirez, J. A. (2000). A numerical method for simulating discontinuous shallow flow over an infiltrating surface. *International Journal for Numerical Methods in*

- 
- Fluids*, 32(2):219–239. DOI: [https://doi.org/10.1002/\(SICI\)1097-0363\(20000130\)32:2<219::AID-FLD936>3.0.CO;2-J](https://doi.org/10.1002/(SICI)1097-0363(20000130)32:2<219::AID-FLD936>3.0.CO;2-J).
- Fodor, N., Sándor, R., Orfanus, T., Lichner, L., and Rajkai, K. (2011). Evaluation method dependency of measured saturated hydraulic conductivity. *Geoderma*, 165(1):60–68. doi: <https://doi.org/10.1016/j.geoderma.2011.07.004>.
- Foudi, S., Osés-Eraso, N., and Tamayo, I. (2015). Integrated spatial flood risk assessment: The case of Zargoza. *Land Use Policy*, 42(1):278–292. doi: <https://doi.org/10.1016/j.landusepol.2014.08.002>.
- Fraccarollo, L. and Toro, E. F. (1995). Experimental and numerical assessment of the shallow water model for two-dimensional dam-break type problems. *Journal of Hydraulic Research*, 33(6):843–864. DOI: <https://doi.org/10.1080/00221689509498555>.
- Franco, D., Guiver, C., Smith, P., and Townley, S. (2022). A switching feedback control approach for persistence of managed resources. *Discrete and Continuous Dynamical Systems - Series B*, 27(3):1765–1787. doi: <https://doi.org/10.3934/dcdsb.2021109>.
- Gash, J. (1979). An analytical model of rainfall interception by forests. *Quarterly Journal of the Royal Meteorological Society*, 105(443):43–55. doi: <https://doi.org/10.1002/qj.49710544304>.
- Gash, J. H. C. and Shuttleworth, W. J. (2007). *Evaporation: Benchmark Papers in Hydrology (IAHS Proceedings & Reports)*. International Associations of Hydrological Sciences. ISBN-10: 1901502988.
- Gaskell, P. H. and Lau, A. K. C. (1988). Curvature-compensated convective transport: SMART, A new boundedness-preserving transport algorithm. *Numerical Methods in Fluids*, 8(6):617–641. DOI: <https://doi.org/10.1002/flid.1650080602>.
- Georgescu-Roegen, N. (1971). *The Entropy Law and the Economic Process*. Cambridge: Harvard University Press. ISBN: 0674281640.
- Gerald, C. F. (1978). *Applied numerical analysis*. Addison-Wesley, Reading Massachusetts, 2 edition. ISBN-10: 0201026961.
- Germann, P. (2010). Theory for Source-Responsive and Free-Surface Film Modelling of Unsaturated Flow. *Vadose Zone Journal*, 9(4):1100–1101. doi: <https://doi.org/10.2136/vzj2010.0072>.

- 
- Google Maps (2017a). *Cornwall County- Google Maps*. Retrieved from <https://www.google.com/maps/@50.5608719,-4.2710443,9z>. [Accessed 9th August 2017].
- Google Maps (2017b). *Lizard Peninsula - Google Maps*. Retrieved from <https://www.google.com/maps/@50.0236543,-5.1425691,12z>. [Accessed 9th August 2017].
- Goring, D. (1994). Kinematic shocks and monoclinical waves in the waimakariri, a steep, braided, gravel-bed river. In Isaacson, M. and Quick, M., editors, *Proceedings of the International Symposium on Waves: Physical and Numerical Modelling*, volume 2, pages 336–345, Vancouver, Canada. Department of Civil Engineering, University of British Columbia. ISBN-10: 0888653646.
- Gray, D. M. and Male, D. H. (1981). *Handbook of Snow: Principles, Processes, Management and Use*. The Blackburn Press. ISBN-10: 1932846069.
- Gray, W. and Hassanizadeh, S. (1991). Paradoxes and Realities in Unsaturated Flow Theory. *Water Resources Research*, 27(8):1847–1854. doi: <https://doi.org/10.1029/91WR01259>.
- Grayson, R. B., Moore, I. D., and McMahon, T. A. (1992). Physically based hydrologic modelling: 1. A terrain-based model for investigative purposes. *Water Resources Research*, 28(10):2639–2658. DOI: <https://doi.org/10.1029/92WR01258>.
- Green, W. H. and Ampt, G. A. (1911). Studies on Soil Physics. Part I - the Flow of Air and Water through Soils. *Journal of Agricultural Science*, 4(1):1–24. DOI: <https://doi.org/10.1017/S0021859600001441>.
- Guiver, C., Mueller, M., Hodgson, D., and Townley, S. (2016). Robust set-point regulation for ecological models with multiple management goals. *Journal of Mathematical Biology*, 72:1467–1529. doi: <https://doi.org/10.1007/s00285-015-0919-7>.
- Gupta, R. S. (2017). *Hydrology and Hydraulic Systems*. Waveland Press, 4<sup>th</sup> edition. ISBN-10: 1-4786-3091-4.
- Habets, F., Noilhan, J., Golaz, C., Goutorbe, J. P., Lacarrère, P., Leblois, E., Ledoux, E., Martin, E., Ottlé, C., and Vidal-Madjar, D. (1999). The ISBA surface scheme in a macroscale hydrological model applied to the Hapex-Mobilhy area. Part I: Model and database. *Journal of Hydrology*, 217(1–2):75–96. DOI: [https://doi.org/10.1016/S0022-1694\(99\)00019-0](https://doi.org/10.1016/S0022-1694(99)00019-0).

- 
- Hamlin, L. P. B. (1996). Snowmelt Hydrologic Modelling of Northern Wetland Dominated River Basins. Master's thesis, University of Waterloo, Waterloo, ON.
- Hargreaves, G. H. and Samani, Z. A. (1982). Estimating potential evaporation. *ASCE, Journal of Irrigation and Drainage Division*, 108(3):225–230.
- Harrison, D., Jewell, S., and Best, S. (2017). High resolution precipitation estimates, Coverack Storm, 18th July 2017. Technical Report. Met Office, Radar Products Team, Observations R&D.
- Harten, A. (1983). High Resolution Schemes for Hyperbolic Conservation Laws. *Journal of Computational Physics*, 49(3):357–393. DOI: [https://doi.org/10.1016/0021-9991\(83\)90136-5](https://doi.org/10.1016/0021-9991(83)90136-5).
- Harvey, F. (2019). Labour's climate policies: what are they and what do they mean? *The Guardian*. Retrieved from <https://www.theguardian.com/politics/2019/sep/24/labours-climate-policies-what-are-they-and-what-do-they-mean> [Accessed 25th November 2019].
- Hawken, P., Amory B., L., and Lovins, L. H. (1999). *Natural Capitalism: Creating the Next Industrial Revolution*. Little, Brown & Company. ISBN: 9780316353168.
- Helvey, J. D. and Patric, J. H. (1965). Design criteria for interception studies. *International Association of Scientific Hydrology*, 67:131–137.
- Henderson, F. M. (1963). Flood waves in Prismatic Channels. *Journal of the Hydraulics Division of the American Society of Civil Engineers*, 89(4). doi: <https://doi.org/10.1061/JYCEAJ.000092>.
- Henderson, F. M. (1966). *Open-channel flow*. McMillan publishing, NewYork.
- Hirsch, C. (1990). *Computational Methods for Inviscid and Viscous Flows*, volume 2 of *Numerical Computation of Internal and External Flows*. Wiley, Hoboken, NJ, 1<sup>st</sup> edition. ISBN-10: 0471924520.
- Horton, R. E. (1919). Rainfall Interception. *Monthly Weather Review*, 47(9):603–623. DOI: [https://doi.org/10.1175/1520-0493\(1919\)47<603:RI>2.0.CO;2](https://doi.org/10.1175/1520-0493(1919)47<603:RI>2.0.CO;2).
- Horton, R. E. (1940). Approach toward a Physical Interpretation of Infiltration Capacity. *Soil Science of America Proceedings*, 23(3):399–417. Retrieved from

---

<http://soilphysics.okstate.edu/teaching/soil-6583/references-folder/horton%201940.pdf> [Accessed 15th February 2020].

Hou, T. Y. and LeFloch, P. G. (1994). Why non-conservative schemes converge to wrong solutions: Error analysis. *Mathematics of Computation*, 62(206):497–530. DOI: <https://doi.org/10.2307/2153520>.

Hromadka II, T. V. and Rao, P. (2021). Examination of Hydrologic Computer Programs DHM and EDHM. In Hromadka II, T. V. and Rao, P., editors, *Hydrology*, volume 1, chapter 3. IntechOpen. DOI: 10.5772/intechopen.94283, ISBN-10: 1839623306.

Hugoniot, H. (1887). Mémoire sur la propagation des mouvements dans les corps et spécialement dans les gaz parfaits (première partie) [Memoir on the propagation of movements in bodies, especially perfect gases (Part I)]. *Journal de l'École Polytechnique*, 57(1):3–97. ARK: <ark:/12148/bpt6k4337130>.

Hugoniot, H. (1889). Mémoire sur la propagation des mouvements dans les corps et spécialement dans les gaz parfaits (deuxième partie) [Memoir on the propagation of movements in bodies, especially perfect gases (Part II)]. *Journal de l'École Polytechnique*, 58(1):1–125. ARK: <ark:/12148/bpt6k4337130>.

Huo, W., Li, Z., Zhang, K., Wang, J., and Yao, C. (2020). GA-PIC: An improved Green-Ampt rainfall-runoff model with a physically based infiltration distribution curve for semi-arid basins. *Journal of Hydrology*, 586:124900. doi: <https://doi.org/10.1016/j.jhydrol.2020.124900>.

Ibbitt, R. (1971). Development of a conceptual model of interception, Unpublished Hydrological Research Progress Report No. 5. Technical report, Ministry of Works, New Zealand.

iFM (2022). *A brief introduction to Facilities Management*. Retrieved from <https://www.i-fm.net/fm-info>. [Accessed 1st July 2022].

Inoue, M., Šimůnek, J., Shiozawa, S., and Hopmans, J. W. (2000). Simultaneous estimation of soil hydraulic and solute transport parameters from transient infiltration experiments. *Advances in Water Resources*, 23(7):677–688. doi: [https://doi.org/10.1016/S0309-1708\(00\)00011-7](https://doi.org/10.1016/S0309-1708(00)00011-7).

- 
- International Chamber of Commerce (2016). *Green Economy Roadmap*. Technical report, International Chamber of Commerce. Retrieved from <https://web.archive.org/web/20160505222844/http://www.iccwbo.org/products-and-services/trade-facilitation/green-economy-roadmap/> [Accessed 24th July 2019].
- International Facility Management Association (1998). *What is Facility Management?* Retrieved from <https://www.ifma.org/about/what-is-facility-management/>. [Accessed 1st February 2019].
- Ivanov, V. Y., Vivoni, E. R., Bras, R. L., and Entekhabi, D. (2004a). Catchment hydrologic response with a fully distributed triangulated irregular network model. *Water Resources Research*, 40(11). DOI: <https://doi.org/10.1029/2004WR003218>.
- Ivanov, V. Y., Vivoni, E. R., Bras, R. L., and Entekhabi, D. (2004b). Preserving high-resolution surface and rainfall data in operational-scale basin hydrology: a fully-distributed physically-based approach. *Journal of Hydrology*, 298(1–4):80–111. DOI: <https://doi.org/10.1016/j.jhydro.2004.03.041>.
- Jayawardena, A. W. and Zhou, M. C. (2000). A modified spatial soil moisture storage capacity distribution curve for the Xinanjiang model. *Journal of Hydrology*, 227(1–4):93–113. doi: [https://doi.org/10.1016/S0022-1694\(99\)00173-0](https://doi.org/10.1016/S0022-1694(99)00173-0).
- Jeffrey, A. (1976). *Quasilinear Hyperbolic Systems and Waves*. Research Notes in Mathematics. Pitman Publishing, , 1<sup>st</sup> edition. ISBN-10: 0273001027.
- Kačergyé, I., Arlt, D., Berg, Å., Żmihorski, M., Knape, J., Rosin, Z., and Pärt, T. (2021). Evaluating created wetlands for bird diversity and reproductive success. *Biological Conservation*, 257:109084. doi: <https://doi.org/10.1016/j.biocon.2021.109084>.
- Kerkhoven, E. and Gan, T. Y. (2005). Modelling hydrological responses of the Athabasca River basin to climate change by the Modified ISBA Land Surface Scheme. In *Regional Hydrological Impacts of Climate Change*, Proceedings of symposium S6 held during the Seventh IAHS Scientific Assembly, Foz do Iguacu, Brazil. IAHS Publications 296.
- Kerkhoven, E. and Gan, T. Y. (2006). A modified ISBA surface scheme for modelling the hydrology of Athabasca River Basin with GCM-scale data. *Advances in Water Resources*, 29(6):808–826. DOI: <https://doi.org/10.1016/j.advwatres.2005.07.016>.



- 
- Kermani, M. J., Gerber, A. G., and Stockie, J. M. (2003). Thermodynamically Based Moisture Prediction Using Roe's Scheme. In *4th Conference of Iranian AeroSpace Society*, Amir Kabir University of Technology, Tehran, Iran.
- Khakbaz, B., Imam, B., Hsu, K., and Sorooshian, S. (2012). From lumped to distributed via semi-distributed: Calibration strategies for semi-distributed hydrologic models. *Journal of Hydrology*, 418–419:61–77. doi: <https://doi.org/10.1016/j.jhydrol.2009.02.021>.
- King, K., Arnold, J., and Bingner, R. (1999). Comparison of Green-Ampt and Curve Number Methods on Goodwin Creek Watershed using SWAT. *Transactions of the American Society of Agricultural Engineers*, 42(4):919–925. doi: <https://doi.org/10.13031/2013.13272>.
- Kirkby, M. J. and Weyman, D. R. (1974). Measurements of contributing area in very small drainage basins. In *Seminar Series B, No. 3*, Department of Geography, University of Bristol, Bristol.
- Kirkham, M. B. (2014). Potential Evaporation. In 2nd, editor, *Principles of Soil and Plant Water Relations*, chapter 28, pages 501–514. Academic Press, Madison, WI, 2nd edition. ISBN-10: 0124200222.
- Kite, G. (2019). *SLURP 12.9 Hydrologic Model*. Water Resources Publications LLC. ISBN-10: 1887201491.
- Kite, G. W. and Pietroniro, A. (1996). Remote sensing applications in hydrological modelling. *Hydrological Sciences Journal*, 41(4):563–591. DOI: <https://doi.org/10.1080/02626669609491526>.
- Kleczkowski, A., Ellis, C., Hanley, N., and Goulson, D. (2017). Pesticides and bees: Ecological-economic modelling of bee populations on farmland. *Ecological Modelling*, 360:53–62. doi: <https://doi.org/10.1016/j.ecolmodel.2017.06.008>.
- Köhne, J., Mohanty, B., and Šimøunek, J. (2006). Inverse Dual-Permeability Modelling of Preferential Water Flow in a Soil Column and Implications for Field-Scale Solute Transport. *Vadose Zone Journal*, 5(1):59–76. doi: <https://doi.org/10.2136/vzj2005.0008>.

- 
- Kondratyev, K. Y. (1969). *Radiation in the Atmosphere*, volume 12 of *International Geophysics Series*. Academic Press, New York and London. Retrieved from <https://www.sciencedirect.com/bookseries/international-geophysics/vol/12/suppl/C> [Accessed 15th February 2020].
- Koren, B. (1993). A robust upwind discretisation method for advection, diffusion and source terms. In Koren, B. and Vreugdenhil, C. B., editors, *Numerical Methods for Advection-Diffusion Problems*, volume 45 of *Notes on Numerical Fluid Mechanics*, page 117. Friedrich Vieweg & Sohn Verlagsgesellschaft mbH. ISBN-10:3528076453.
- Kouwen, N. (1986). WATFLOOD - Canadian Hydrological and Routing Model. User manual, Surveys and Information Branch, Ecosystem Science and Evaluation Directorate, Environment Canada. <http://www.civil.uwaterloo.ca/watflood/downloads/manual.pdf>.
- Kouwen, N. (1988). WATFLOOD: a Micro-Computer Based Flood Forecasting System Based on Real-Time Weather Radar. *Canadian Water Resources Journal*, 13(1):62–77. DOI: <https://doi.org/10.4296/cwrj1301062>.
- Kouwen, N. and Mousavi, S. F. (2002). WATFLOOD/SPL9 hydrological model & flood forecasting system. In Singh, V. P. and Frevert, D. K., editors, *Mathematical models of large watershed hydrology*, pages 649–685. Water Resources Publications, Highlands Ranch, CO. ISBN-10: 1887201343.
- Kristensen, K. J. and Jensen, S. E. (1975). A model for estimating actual evapotranspiration from potential evapotranspiration. *Hydrology Research*, 6(3):170–188. DOI: <https://doi.org/10.2166/nh.1975.0012>.
- Kuraz, M., Jačka, L., Blöcher, J., and Lepš, M. (2022). Automated calibration methodology to avoid convergence issues during inverse identification of soil hydraulic properties. *Advances in Engineering Software*, 173. doi: <https://doi.org/10.1016/j.advengsoft.2022.103278>.
- Lacasta, A., Morales-Hernández, M., Burguete, J., Brufau, P., and García-Navarro, P. (2017). Calibration of the 1D shallow water equations: a comparison of Monte Carlo and gradient-based optimisation methods. *Hydroinformatics*, 19(2):282–298. doi: <https://doi.org/10.2166/hydro.2017.021>.

- 
- Lafore, J. P., Stein, J., Asencio, N., Bougeault, P., Ducrocq, V., Duron, J., Fischer, C., Hérel, P., Mascart, P., Masson, V., Pinty, J. P., Redelsperger, J. L., Richard, E., and de Arellano, J. V.-G. (1998). The Meso-NH Atmospheric Simulation System. Part I: adiabatic formulation and control simulations. *Annales Geophysicae*, 16:90–109. DOI: <https://doi.org/10.1007/s00585-997-0090-6>.
- Landau, L. D. and Lifshitz, E. M. (1987). *Fluid Mechanics*, volume 6 of *Course on Theoretical Physics*. Pergamon Press, Headington Hall, Oxford, 2<sup>nd</sup> edition. ISBN-10: 0080339328.
- Lawton, J. H., Brotherton, P. N. M., Brown, V. K., Elphick, C., Fitter, A. H., Forshaw, J., Haddow, R. W., Hilborne, S., Leafe, R. N., Mace, G. M., Southgate, M. P., Sutherland, W. A., Tew, T. E., Varley, J., and Wynne, G. R. (2010). *Making Space for Nature: A Review of England's Wildlife Sites and Ecological Network*. Retrieved from <http://webarchive.nationalarchives.gov.uk/20130402170324/http://archive.defra.gov.uk/environment/biodiversity/documents/201009space-for-nature.pdf>. Report to Defra. [Accessed 5th May 2017].
- Lax, P. D. (1954). Weak Solutions of Nonlinear Hyperbolic Equations and their Numerical Computation. *Communications on Pure and Applied Mathematics*, 7(1):159–193. DOI: <https://doi.org/10.1002/cpa.3160070112>.
- Lax, P. D. (1990). *Hyperbolic Systems of Conservation Laws and the Mathematical Theory of Shock Waves*. Society of Industrial and Applied Mathematics, Philadelphia. ISBN-10: 0898711770.
- Lax, P. D. and Wendroff, B. (1960). Systems of Conservation Laws. *Communications on Pure and Applied Mathematics*, 13(2):217–237. DOI: <https://doi.org/10.1002/cpa.3160130205>.
- LeVeque, R. J. (1992). *Numerical Methods for Conservation Laws*. Lectures in Mathematics ETH Zürich. Birkhäuser Verlag, Basel. ISBN-10: 3764327235.
- LeVeque, R. J. (2002). *Finite Volume Methods for Hyperbolic Problems*. Cambridge texts in applied mathematics. Cambridge University Press, 32 Avenue of the Americas, New York NY 10013-2473, USA. ISBN-10: 0521009243.
- Liang, Q. and Borthwick, A. G. L. (2009). Adaptive quadtree simulation of shallow flows

- 
- with wet-dry fronts over complex topography. *Computers and Fluids*, 38(2):221–234. DOI: <https://doi.org/10.1016/j.compfluid.2008.02.008>.
- Liang, Q. and Marche, F. (2009). Numerical resolution of well-balanced shallow water equations with complex source terms. *Advances in Water Resources*, 32:873–884. DOI: <https://doi.org/10.1016/j.advwatres.2009.02.010>.
- Lida, S., Levia, D., Nanko, K., Sun, X., Shimizu, T., Tamai, K., and Shinohara, Y. (2018). Correction of Canopy Interception Loss Measurements in Temperate Forests: A Comparisons of Necessary Adjustments among Three Different Rain Gauges based on a Dynamic Calibration Procedure. *Journal of Hydrometeorology*, 19(3):547–553. doi: <https://doi.org/10.1175/JHM-D-17-0124.1>.
- Lien, F. S. and Leschziner, M. A. (1994). Upstream monotonic interpolation for scalar transport with application to complex turbulent flows. *Numerical Methods in Fluids*, 19(6):527–548. DOI: <https://doi.org/10.1002/flid.1650190606>.
- Lighthill, M. J. and Whitham, G. B. (1955). On Kinematic Waves I. Flood movement in long rivers. *Proceedings of the Royal Society A*, 229(1178):281–316. DOI: <https://doi.org/10.1098/rspa.1955.0088>.
- Lim, K., Engel, B. A., Muthukrishnan, S., and Harbor, J. (2007). Effects of Initial Abstraction and Urbanisation on Estimated Runoff using CN Technology. *Journal of the American Water Resources Association (JAWRA)*, 42(3):629–643. doi: <https://doi.org/10.1111/j.1752-1688.2006.tb04481.x>.
- Ling, L. and Yusop, Z. (2014). Inferential statistics of claim assessment. In *Proceedings of the 3<sup>rd</sup> International Conference on Quantitative Science and its Applications*, volume 1635 of 805–808, Langkawi, Kedah Malaysia. doi: <https://doi.org/10.1063/1.4903675>.
- Ling, L. and Yusop, Z. (2015). The calibration of the SCS runoff model. In *The 2<sup>nd</sup> IWA Malaysia, Young Water Professionals Conference*, Kuala Lumpur, Malaysia.
- Linhoss, A. and Siegart, C. (2020). Calibration reveals limitations in modelling rainfall interception at the storm scale. *Journal of Hydrology*, 584. doi: <https://doi.org/10.1016/j.jhydro.2020.124624>.

- 
- Linsey, R. K., Kohler, M. A., and Paulhus, J. L. H. (1982). *Hydrology for Engineers*. McGraw-Hill Series in Water Resources and Engineering. McGraw-Hill College, 1<sup>st</sup> edition. ISBN-10: 0070379564.
- Llorens, P., Poch, R., Latron, J., and Gallart, F. (1997). Rainfall intercession by *Pinus sylvestris* forest patch overgrown in a Mediterranean mountainous abandoned area I. Monitoring design and results down to the event scale. *Journal of Hydrology*, 199(3–4):331–345. doi: [https://doi.org/10.1016/S0022-1694\(96\)03334-3](https://doi.org/10.1016/S0022-1694(96)03334-3).
- Lull, H. W. (1964). Ecological and silvicultural aspects. In Chow, V. T., editor, *Handbook of Applied Hydrology*, chapter 6. McGraw-Hill, New York, 1 edition. ISBN-10: 0070107742.
- Mahfouf, J., Manzi, A. O., Noilhan, J., Giordani, H., and DéQué, M. (1995). The Land Surface Scheme ISBA within the Météo-France Climate Model ARPEGE Part I: Implementation and Preliminary Results. *Journal of Climate*, 8(8):2039–2057. DOI: [https://doi.org/10.1175/1520-0442\(1995\)008<2039:TLSSIW>2.0.CO;2](https://doi.org/10.1175/1520-0442(1995)008<2039:TLSSIW>2.0.CO;2).
- Maidment, D. R. and Hoogerwerf, T. N. (2002). Parameter Sensitivity in Hydrologic Modelling. Technical report, Center for Research in Water Resources, University of Texas, Austin, USA.
- Manning, R. (1891). On the flow of water in open channels and pipes. *Transactions of the Institution of Civil Engineers of Ireland*, 20(1):161–207. DOI: <https://doi.org/10.48495/r207ts96k>.
- McCabe, D. J. (2011). Rivers and Streams: Life in Flowing Water. *Nature Education Knowledge*, 3(10):19. <https://www.nature.com/scitable/knowledge/library/rivers-and-streams-life-in-flowing-water-23587918/>.
- McRae, B. H., Schumaker, N. H., McKane, R. B., Busing, R. T., Solomon, A. M., and Burdick, C. A. (2008). A multi-model framework for simulating wildlife population response to land-use and climate change. *Ecological Modelling*, 219:77–91. doi: <https://doi.org/10.1016/j.ecolmodel.2008.08.001>.
- Menikoff, R. and Plohr, B. J. (1989). The Riemann problem for fluid flow of real materials. *Reviews of Modern Physics*, 61(1):75–130. DOI: <https://doi.org/10.1103/RevModPhys.61.75>.

- 
- Merkel, W. H. (2002). Muskingum-Cunge Flood Routing Procedure in NRCS Hydrologic Models. In *NRCS Routing Procedure in NRCS Hydrologic Models, Second Federal Interagency Hydrologic Modeling Conference*.
- Merriam, R. A. (1960). A note on the interception loss equation. *Journal of Geophysical Research*, 65(11):3850–3851. DOI: <https://doi.org/10.1029/JZ065i011p03850>.
- Meteorological Office (2022). *UK snow and facts*. Retrieved from <https://www.metoffice.gov.uk/weather/learn-about/weather/types-of-weather/snow/snow-in-the-uk>. [Accessed 17th July 2022].
- Meyer, R. (2019). The Green New Deal Hits Its First Major Snag. *The Atlantic*. Retrieved from <https://www.theatlantic.com/science/archive/2019/01/first-fight-about-democrats-climate-green-new-deal/580543/> [Accessed 25th November 2019].
- Michigan Automated Weather Network (2010). Mawn: Michigan automated weather network, east lansing, michigan, 48823. Webpage. <http://www.agweather.geo.msu.edu/mawn/>.
- Millennium Ecosystem Assessment (2005). *Ecosystems and Human Well-being: Synthesis*. Ecosystems and human well-being: synthesis / Millennium Ecosystem Assessment. Island Press, Washington DC. ISBN:1597260401.
- Miller, J. (1994). Handbook for Agrohydrology. Handbook, Natural Resources Institute, Chatham, UK.
- Miller, J. E. (1984). Basic Concepts of Kinematic-Wave Models. Technical report, U.S. Department of the Interior. <https://pubs.usgs.gov/pp/1302/report.pdf>.
- Miller, R. D. (1951). A Technique for measuring soil-moisture tensions in rapidly changing systems. *Soil Science*, 72(4):291–302.
- Miller, R. D. and Richard, F. (1952). Hydraulic Gradients during Infiltration in Soils. *Soil Science Society of America*, 16(1):33–38. doi: <https://doi.org/10.2136/sssaj1952.03615995001600010011x>.
- Mishra, S. K. and Singh, V. P. (2003). SCS-CN Method. In *Soil Conservation Service Curve Number (SCS-CN) Methodology*, volume 42 of *Water Science and Technology*

- 
- Library*, chapter 2, pages 84–146. Springer, Dordrecht. doi: <https://doi.org/10.1007/978-94-017-0147-1>.
- Monteith, J. L. (1965). Evaporation and environment. *Symposia of the Society of Experimental Biology*, 19:205–234.
- Morton, F. I. (1983). Operational estimates of areal evapotranspiration and their significance to the science and practice of hydrology. *Journal of Hydrology*, 66(1–4):1–76. DOI: [https://doi.org/10.1016/0022-1694\(83\)90177-4](https://doi.org/10.1016/0022-1694(83)90177-4).
- Morton, R. D., Marston, C. G., O’Neil, A. W., and Rowland, C. S. (2020). Land Cover Map 2017 (20m classified pixels, GB). *NERC Environmental Information Data Centre*. DOI: <https://doi.org/10.5285/f6f86b1a-af6d-4ed8-85af-21ee97ec5333>.
- Muzylo, A., Llorens, P., Valente, F., Keizer, J. J., Domingo, F., and Gash, J. H. C. (2009). A review of rainfall interception modelling. *Journal of Hydrology*, 370(1–4):191–206. DOI: <https://doi.org/10.1016/j.jhydrol.2009.02.058>.
- Nash, J. E. and Sutcliffe, J. V. (1970). River flow forecasting through conceptual models part I - A discussion of principles. *Journal of Hydrology*, 10:282–290. DOI: [https://doi.org/10.1016/0022-1694\(70\)90255-6](https://doi.org/10.1016/0022-1694(70)90255-6).
- National Climatic Data Center (2010). Ncdc: National climatic data center. Webpage. <http://www.ncdc.noaa.gov/oa/climate/climatedata.html#daily>.
- National Institute of Water and Atmospheric Research (2011). *TopNet*. Retrieved from <http://tools.envirolink.govt.nz/dsss/topnet-/>. [Accessed 17th March 2021].
- Natural Resources Conservation Service (1986). Urban hydrology for small watersheds. Technical release 55, United States Department of Agriculture.
- Noilhan, J. and Mahfouf, J. F. (1996). The ISBA land surface parameterisation scheme. *Global and Planetary Change*, 13(1–4):145–159. DOI: [https://doi.org/10.1016/0921-8181\(95\)00043-7](https://doi.org/10.1016/0921-8181(95)00043-7).
- Noilhan, J. and Planton, S. (1989). A Simple Parameterisation of Land Surface Processes for Meteorological Models. *Monthly Weather Review*, 117:536–549. DOI: [https://doi.org/10.1175/1520-0493\(1989\)117<0536:ASPOLS>2.0.CO;2](https://doi.org/10.1175/1520-0493(1989)117<0536:ASPOLS>2.0.CO;2).

- 
- O'Loughlin, E. M. (1986). Prediction of Surface Saturation Zones in Natural Catchments by Topographic Analysis. *Water Resources Research*, 22(5):794–804. DOI: <https://doi.org/10.1029/WR022i005p00794>.
- Open University (2022). *Nature & Environment - Water use and the water cycle: Interception, evaporation and transpiration*. <https://www.open.edu/openlearn/nature-environment/environmental-studies/water-use-and-the-water-cycle/content-section-2.3>. [Accessed 16th August 2022].
- O'Riordan, T. (1988). The Politics of Sustainability. In Turner, R. K., editor, *Sustainable Environmental Management: Principles and Practice*, pages 48–54. Belhaven Press. ISBN: 1852930039.
- Overton, D. E. and Meadows, M. E. (1976). *Stormwater Modelling*. Academic Press, New York.
- Parlange, J. Y., Hogarth, W. L., Barry, D. A., Parlange, M. B., Haverkamp, R., Ross, P. J., Steenhuis, T. S., DiCarlo, D. A., and Katul, G. (1999). Analytical approximation to the solutions of Richards' equation with applications to infiltration, ponding and time compression approximation. *Advances in Water Resources*, 23(2):189–194. DOI: [https://doi.org/10.1016/S0309-1708\(99\)00022-6](https://doi.org/10.1016/S0309-1708(99)00022-6).
- Peel, M. C., Finlayson, B. L., and McMahon, T. A. (2007). Updated world map of the köppen-geiger climate classification. *Hydrology and Earth System Sciences*, 11(5):1633–1644. DOI: <https://doi.org/10.5194/hess-11-1633-2007>.
- Penman, H. L. (1948). Natural evaporation from open water, bare soil and grass. *Proceedings of the Royal Society A*, pages 120–145. DOI: <https://doi.org/10.1098/rspa.1948.0037>.
- Penman, H. L. and Long, I. F. (1960). Weather in wheat: An essay in micro-meteorology. *Quarterly Journal of the Royal Meteorological Society*, 86(367):16–50. DOI: <https://doi.org/10.1002/qj.49708636703>.
- Penning-Rowsell, E. C., Priest, S., Parker, D., Morris, J., Tunstall, S., Viavattene, C., Chatterton, J., and Owen, D. (2013). *Flood and Coastal Erosion Risk Management: A Manual for Economic Appraisal*. Routledge, 1 edition. ISBN-10: 0415815150.



- 
- Perez-Carmona, A. (2013). Growth: A Discussion of the Margins of Economic and Ecological Thought. In Meuleman, L., editor, *Transgovernance: Advancing Sustainability Governance*, pages 94–99. Springer, Heidelberg, Germany, 2013 edition. ISBN: 3642280080, doi: 10.1007/978-3-642-28009-2\_3.
- Perlman, H. (2016). The Water Cycle - USGS Water Science School. Webpage. <https://water.usgs.gov/edu/watercycle.html>.
- PEST (2023). PEST: Model-Independent Parameter Estimation and Uncertainty Analysis. Webpage. <https://pesthhomepage.org/>.
- Philip, J. R. (1954). An Infiltration Equation with Physical Significance. *Soil Science*, 77(2):153–158. DOI: <https://doi.org/10.1097/00010694-195402000-00009>.
- Philip, J. R. (1957a). The Theory of Infiltration: 2. The Profile of Infinity. *Soil Science*, 83(6):435–448.
- Philip, J. R. (1957b). The Theory of Infiltration: 3. Moisture Profiles and Relation to Experiment. *Soil Science*, 84(2):163–178.
- Philip, J. R. (1957c). The Theory of Infiltration: 4. Sorptivity and Algebraic Infiltration Equations. *Soil Science*, 84(3):257–264.
- Philip, J. R. (1957d). The Theory of Infiltration: 5. The Influence of the Initial Moisture Content. *Soil Science*, 84(4):329–340.
- Philip, J. R. (1969). Theory of Infiltration. In Chow, V. T., editor, *Advances in Hydroscience*, volume 5, pages 215–296. Academic Press, New York. DOI: <https://doi.org/10.1016/B978-1-4831-9936-8.50010-6>.
- Ponce, V. M. (1986). Diffusion Wave Modelling of Catchment Dynamics. *Journal of Hydraulic Engineering, ASCE*, 112(8):716–727. doi: [https://doi.org/10.1061/\(ASCE\)0733-9429\(1986\)112:8\(716\)](https://doi.org/10.1061/(ASCE)0733-9429(1986)112:8(716)).
- Preissmann, A. and Zaoui, J. (1979). Le module “écoulement de surface” due Système Hydrologique Européen (SHE). In *Proceedings of the 18<sup>th</sup> Congress International Association for Hydraulic Research*, volume 5, pages 193–199, Cagliari.
- Priestley, C. H. B. and Taylor, R. J. (1972). On the Assessment of Surface Heat Flux and Evaporation using Large-Scale Parameters. *Monthly Weather Review*, 100(2):81–92. DOI: [https://doi.org/10.1175/1520-0493\(1972\)100<0081:OTAOSH>2.3.CO;2](https://doi.org/10.1175/1520-0493(1972)100<0081:OTAOSH>2.3.CO;2).

- 
- Public Health England (2019). The long-term impacts of flooding on mental health. Technical report, Public Health England.
- Pyla, P. (2012). Beyond smooth talk. *Journal of the Design Studies Forum: Design and Culture*, 4(3). doi: 10.2752/175470812X13361292229032.
- Ragan, R. M. and Jackson, T. J. (1980). Runoff Synthesis using landsat and SCS model. *Journal of the Hydraulics Division*, 106(5):667–678. doi: <https://doi.org/10.1061/JYCEAJ.0005416>.
- Ralph M Parsons Laboratory (2000). tRIBS User Manual. User manual, Department of Civil and Environmental Engineering, Massachusetts Institute of Technology. [http://vivoni.asu.edu/tribs/userManual.html#:~:text=The%20tRIBS%20\(TIN%2Dbased%20%20Real,Triangulated%20Irregular%20Network%20\(TIN\).](http://vivoni.asu.edu/tribs/userManual.html#:~:text=The%20tRIBS%20(TIN%2Dbased%20%20Real,Triangulated%20Irregular%20Network%20(TIN).)
- Rankine, W. J. M. (1870). On the thermodynamic theory of waves of finite longitudinal disturbances. *Philosophical Transactions of the Royal Society of London*, 160(1):277–288. DOI: <https://doi.org/10.1098/rstl.1870.0015>.
- Rawls, W. J., Ahuja, L. R., Brakensiek, D. L., and Shirmohammadi, A. (1993). Infiltration of Soil Water Movement. In Maidment, D. R., editor, *Handbook of Hydrology*, chapter 5. McGraw-Hill, New York, 1<sup>st</sup> edition. ISBN-10: 0070397325.
- Rawls, W. J., Brakensiek, D. L., and Miller, N. (1983). Green-Ampt Infiltration Parameters from Soils Data. *Journal of Hydraulic Engineering*, 109(1):62–70. DOI: [https://doi.org/10.1061/\(ASCE\)0733-9429\(1983\)109:1\(62\)](https://doi.org/10.1061/(ASCE)0733-9429(1983)109:1(62)).
- Refsgaard, J. C. and Storm, B. (1995). MIKE SHE. In Singh, V. P., editor, *Computer Models of Watershed Hydrology*, chapter 23, pages 809–846. Water Resources Publications, Highlands Ranch, CO. ISBN-10: 1887201742.
- Refsgaards, J. C. and Knudsen, J. (1996). Operational Validation and Intercomparison of Different Types of Hydrological Models. *Water Resources Research*, 32(7):2189–2202. doi: <https://doi.org/10.1029/96WR00896>.
- Reynolds, O. (1895). IV. On the dynamical theory of incompressible viscous fluids and the determination of the criterion. *Philosophical Transactions of the Royal Society A: Mathematical, Physical and Engineering Sciences*, 186(1):123–164. DOI: <https://doi.org/10.1098/rsta.1895.0004>.

- 
- Richards, L. A. (1931). Capillary conduction of liquids through porous mediums. *Journal of Applied Physics*, 1(5):318–333. DOI: <https://doi.org/10.1063/1.1745010>.
- Richardson, O. C., Knapp, J. L., Lee, V. E., and Gaston, K. J. (2015). *ENVI-Indicators: Cornwall and the Isles of Scilly Natural Environment Indicator Report 2015*. Environment and Sustainability Institute, University of Exeter.
- Riemann, B. (1851). *Grundlagen für eine allgemeine Theorie der Functionen einer veränderlichen complexen Grösse (Basis for a general theory of functions of a variable complex quantity)*. PhD thesis, Göttingen, (Germany): Adalbert Rente 1867.
- Rifkin, J. and Howard, T. (1980). *Entropy: A New World View*. Viking Adult. ISBN: 0670297178.
- Riley, K. F., Hobson, M. P., and Bence, S. J. (2010). *Mathematical Methods for Physics and Engineering: A Comprehensive Guide*. Cambridge University Press, 3<sup>rd</sup> edition. ISBN: 0521861535.
- Roe, P. L. (1986). Characteristic-Based Schemes for the Euler Equations. *Annual Reviews of Fluid Mechanics*, 18:337–365. DOI: <https://doi.org/10.1146/annurev.fl.18.010186.002005>.
- Rosenberg, N. J., Blad, B. L., and Verma, S. B. (1983). *Microclimate: The Biological Environment*. Wiley-Interscience, 2nd edition. ISBN-10: 0471060666.
- Rossmiller, R. L. (1980). Rational formula revisited. In *International Symposium on Urban Storm Runoff*, University of Kentucky, Lexington, Kentucky - July 28-31.
- Roth, B. E., Slatton, K. C., and Cohen, M. J. (2007). On the potential for high-resolution lidar to improve rainfall interception estimates in forest ecosystems. *Frontiers in Ecology and the Environment*, 5(8):421–428. doi: [https://doi.org/10.1890/1540-9295\(2007\)5\[421:OTPFHL\]2.0.CO;2](https://doi.org/10.1890/1540-9295(2007)5[421:OTPFHL]2.0.CO;2).
- Runnalls, D. (2011). Environment and economy: joined at the hip or just strange bedfellows? *S.A.P.I.E.N.S.*, 4(2). Retrieved from <https://journals.openedition.org/sapiens/1150> [Accessed 24th July 2019].
- Rutter, A. J., Kersha, K. A., Robins, P. C., and Morton, A. J. (1971). A predictive model of rainfall interception in forests, I. Derivation of the model from observations

- 
- in a plantation of corsican pine. *Agricultural Meteorology*, 9:367–384. DOI: [https://doi.org/10.1016/0002-1571\(71\)90034-3](https://doi.org/10.1016/0002-1571(71)90034-3).
- Rutter, A. J., Kershaw, K. A., Robins, P. C., and Morton, A. J. (1972). A predictive model of rainfall interception in forests, 1. Derivation of the model from observations in a plantation of Corsican pine. *Agricultural Meteorology*, 9:367–384. doi: [https://doi.org/10.1016/0002-1571\(71\)90034-3](https://doi.org/10.1016/0002-1571(71)90034-3).
- Rutter, A. J. and Morton, A. J. (1977). A predictive model of rainfall interception in forests, III. Sensitivity of the model to Stand Parameters and Meteorological Variables. *Journal of Applied Ecology*, 14(2):567–588. DOI: <https://doi.org/10.2307/2402568>.
- Rutter, A. J., Robins, P. C., and Morton, A. J. (1975). A predictive model of rainfall interception in forests, II. Generalisation of the model and comparison with observations in some Coniferous and Hardwood Stands. *Journal of Applied Ecology*, 12:367–380. DOI: <https://doi.org/10.2307/2401739>.
- Sadeghi, S. M. M., Stan, J. T. V., Pypker, T. G., Tamjidi, J., Friesen, J., and Farah-naklangroudi, M. (2018). Importance of transitional leaf states in canopy rainfall partitioning dynamics. *European Journal of Forest Research*, 137:121–130. doi: <https://doi.org/10.1007/s10342-017-1098-4>.
- Salas, M. D. (2006). The curious events leading to the theory of shock waves. In *Proc. of the 17th Shock Interaction Symposium*, SIS, pages 1–20, Rome, Italy. NASA, Langley Research Center.
- Sayers, P. B., Horritt, M., Carr, S., Kay, A., Mauz, J., Lamb, R., and Penning-Rowell, E. (2022). Third UK Climate Change Risk Assessment (CCRA3): Future flood risk: Appendix B - Risk Metrics. Technical report, Committee on Climate Change, London. <https://www.ukclimaterisk.org/wp-content/uploads/2020/07/Future-Flooding-Appendix-B-Risk-metrics.pdf>.
- Sayers, P. B., Horritt, M., Penning-Rowell, E., and McKenzie, A. (2015). Climate Change Risk Assessment 2017: Projections of future flood risk in the UK. Technical report, Committee on Climate Change, London. Research undertaken by Sayers and Partners on behalf of the Committee on Climate Change.
- Schumacher, E. F. (2010). *Small is Beautiful: Economics as if People Mattered*. Harper Perennial, Reprint edition. ISBN: 0061997765.

- 
- Scottish Government (2023). Choosing a self-build home type: Plot size. <https://www.mygov.scot/self-build-type/plot-size>.
- S.C.S (1972). National Engineering Handbook, Section 4. Handbook, Soil Conservation Service, US Department of Agriculture, Washington, DC.
- Seity, Y., Brousseau, P., Malardel, S., Hello, G., Bénard, Bouttier, F., Lac, C., and Masson, V. (2011). The AROME-France Convective-Scale Operational Model. *Monthly Weather Review*, 139(3):976–991. DOI: <https://doi.org/10.1175/2010MWR3425.1>.
- Shaker, R. R. (2015). The spatial distribution of development in Europe and its underlying sustainability correlations. *Applied Geography*, 63:304–314. doi: 10.1016/j.apgeog.2015.07.009.
- Shen, C., , Niu, J., and Fang, K. (2014). Quantifying the effects of data integration algorithms on the outcomes of a subsurface-land surface processes model. *Environmental Modelling and Software*, 59:146–161. DOI: <https://doi.org/10.1016/j.envsoft.2014.05.006>.
- Shen, C., Niu, J., and Phanikumar, M. S. (2013). Evaluating controls on couple hydrologic and vegetation dynamics in a humid continental climate watershed using a subsurface-land surface processes model. *Water Resources Research*, 49(5):2552–2572. DOI: <https://doi.org/10.1002/wrcr.20189>.
- Shen, C. and Phanikumar, M. S. (2010). A process-based, distributed hydrologic model based on large-scale method for surface-subsurface coupling. *Advances in Water Resources*, 33(12):1524 – 1541. DOI: <https://doi.org/10.1016/j.advwatres.2010.09.002>.
- Short, D., Dawes, W., and White, I. (1995). The practicability of using Richards’ equation for general purpose soil-water dynamics models. *Environment International*, 21(5):723–730. doi: [https://doi.org/10.1016/0160-4120\(95\)00065-S](https://doi.org/10.1016/0160-4120(95)00065-S).
- Siegert, C. M., Levia, D. F., Stand, J. T. V., and Mitchell, M. J. (2017). Do storm synoptic patterns affect biogeochemical fluxes from temperate deciduous forest canopies? *Biogeochemistry*, 132:273–292. doi: <https://doi.org/10.1007/s10533-017-0300-6>.
- Singh, P. R., Gan, T. Y., and Gobena, A. K. (2009). Evaluating a hierarchy of snowmelt

- 
- models at a watershed in the Canadian Prairies. *Journal of Geophysical Research: Atmospheres*, 114(D4). DOI: <https://doi.org/10.1029/2008JD010597>.
- Sitterson, J., Knightes, C., Parmer, R., Wolfe, K., Muche, M., and Avant, B. (2017). An overview of rainfall-runoff model types. Report EPA/600/R-153, P29, US Environmental Protection Agency.
- Smith, M. (2002). Distributed model intercomparison project (DMIP). National Weather Service. World Wide Web. Retrieved from <http://www.nws.noaa.gov/oh/hrl/dmip/> [Accessed 22<sup>nd</sup> July 2023].
- Smoller, J. (1994). *Shock Waves and Reaction-Diffusion Equations*. Grundlehren der mathematischen Wissenschaften. Springer, New York, NY, 2 edition. ISBN-10: 3540907521.
- Soil Science Glossary Terms Committee (2008). *Glossary of Soil Science Terms 2008*. American Society of Agronomy. ISBN-10: 0891188517.
- Speers, D. D. and Versteeg, J. D. (1982). Runoff forecasting for reservoir operations - the past and the future. In *50th Annual Western Snow Conference*, Proceedings of the 50th Annual Western Snow Conferences, Reno, Nevada. Western Snow Conference. Retrieved from <https://westernsnowconference.org/node/933> [Accessed 15th February 2020].
- Stamp, L. D. (1937). The land of Britain. *The Report of Land Utilisation Survey of Britain*.
- Stott, I., Townley, S., and Hodgson, D. J. (2011). A framework for studying transient dynamics of population projection matrix models. *Ecology Letters*, 14(9):959–970. doi: <https://doi.org/10.1111/j.1461-0248.2011.01659.x>.
- Supit, I., Hooijer, A. A., and van Diepen, C. A. (1994). *System Description of the WOFOST 6.0 crop simulation model implemented in CGMS. Volume 1: Theory and Algorithms*. Office for the Official Publications of the European Communities, Luxembourg. EUR 15956.
- Supit, I. and Van Der Goot, E. (2003). *Updated System Description of the WOFOST Crop Growth Simulation Model as Implemented in the Crop Growth Monitoring System applied by the European Commission*. Treemail Publications.

- 
- Sweby, P. K. (1984). High Resolution Schemes using Flux Limiters for Hyperbolic Conservation Laws. *Society for Industrial and Applied Mathematics*, 21(5):995–1011. DOI: <https://doi.org/10.1137/0721062>.
- Szabó, J. A. (2006). An efficient hybrid optimisation procedure of adaptive partition-based search and downhill simplex methods for calibrating water resources models. In *Proceedings of the XXIII Conference of the Danubian Countries on the Hydrological Forecasting and Hydrological Basis of the Water Management*, Belgrade: Hydrometeorological Institute of Serbia.
- Tarboton, D. G. (2003). Rainfall Runoff Processes. *Civil and Environmental Engineering Faculty Publications*. Paper 2570. Retrieved from [https://digitalcommons.usu.edu/cee\\_facpub/2570/](https://digitalcommons.usu.edu/cee_facpub/2570/) [Accessed 15th February 2020].
- The Economics of Ecosystems and Biodiversity (2010). *The Economics of Ecosystems and Biodiversity: Ecological and Economic Foundations*. Routledge. ISBN: 9781849712125.
- Thielen, J., Bartholmes, J., Ramos, M.-H., and de Roo, A. (2009). The European Food Alert System - Part 1: Concept and development. *Hydrology and Earth System Sciences*, 13(2):125–140. DOI: <https://doi.org/10.5194/hess-13-125-2009>.
- Tipler, P. A. and Mosca, G. (2003). *Physics for Scientists and Engineers, Volume 1: Mechanics, Oscillations and Waves; Thermodynamics*. W. H. Freeman, 5th edition. ISBN: 0716708094.
- Tocci, M., Kelley, C., and Miller, C. (1997). Accurate and economical solution of the pressure-head form of Richards' equation by the method of lines. *Advances in Water Resources*, 20(1):1–14. doi: [https://doi.org/10.1016/S0309-1708\(96\)00008-5](https://doi.org/10.1016/S0309-1708(96)00008-5).
- Toro, E. F. (1999). *Riemann Solvers and Numerical Methods for Fluid Dynamics: A Practical Introduction*. Springer, 2<sup>nd</sup> edition. ISBN: 3540659668.
- Toro, E. F. (2001). *Shock-Capturing Methods for Free-Surface Shallow Flows*. Wiley. ISBN-10: 0471987662.
- Toro, E. F., Spruce, M., and Speares, W. (1994). Restoration of the contact surface in the HLL-Riemann solver. *Shock Waves*, 4(1):25–34. DOI: <https://doi.org/10.1007/BF01414629>.

---

TUFLOW (2018). TUFLOW Classic/HPC User Manual. Technical report, BMT. [https://downloads.tuflow.com/\\_archive/TUFLOW/Releases/2018-03/TUFLOW%20Manual.2018-03.pdf](https://downloads.tuflow.com/_archive/TUFLOW/Releases/2018-03/TUFLOW%20Manual.2018-03.pdf).

Turner, R. K. (1988). Sustainability, Resource Conservation and Pollution Control: An Overview. In Turner, R. K., editor, *Sustainable Environmental Management: Principles and Practice*, page 13. Belhaven Press. ISBN: 1852930039.

UK Labour Party (2022). Keir Starmer calls for new national champion in clean energy, Great British Energy, with a mission to cut bills, creat jobs, and deliver energy independence. Press Release. Retrieved from <https://labour.org.uk/press/keir-starmer-calls-for-new-national-champion-in-clean-energy-great-british-energy-with> [Accessed 30th October 2022].

UK National Ecosystem Assessment (2014). *The UK National Ecosystem Assessment: Synthesis of the Key Findings*. UNEP-WCMC, LWEC, UK.

United Nations Department of Economic and Social Affairs (2013). *A guidebook to the Green Economy*. Technical report, United Nations Department of Economic and Social Affairs. Retrieved from [https://web.archive.org/web/20130127180157/http://uncsd2012.org/content/documents/528Green%20Economy%20Guidebook\\_100912\\_FINAL.pdf](https://web.archive.org/web/20130127180157/http://uncsd2012.org/content/documents/528Green%20Economy%20Guidebook_100912_FINAL.pdf) [Accessed 24th July 2019].

United Nations Environment Programme (2011). *Towards a Green Economy: Pathways to Sustainable Development and Poverty Eradication - A Synthesis for Policy Makers*. Technical report, United Nations Environment Programme. Retrieved from <https://wedocs.unep.org/bitstream/handle/20.500.11822/12099/GL0CIGESummaryPolicyMakers.pdf?sequence=1&isAllowed=> [Accessed 24th July 2019].

US Army Corps of Engineers (1993). Introduction and Application of Kinematic Wave Routing Techniques using HEC-1. Technical report, Hydrologic Engineering Center.

van Albada, G. D., van Leer, B., and Roberts Jr., W. W. (1982). A comparative study of computational methods in cosmic gas dynamics. *Astronomy and Astrophysics*, 108(1):76–84.

Van Der Knijff, J. M., Younis, J., and Roo, A. P. J. D. (2010). LISFLOOD: a GIS-based distributed model for river basin scale water balance and flood simulation. *International*



- 
- Journal of Geographical Information Science*, 24(2):189–212. DOI: <https://doi.org/10.1080/13658810802549154>.
- van Genuchten, M. T. (1980). A Closed-form Equation for Predicting the Hydraulic Conductivity of Unsaturated Soils. *Soil Science Society of America*, 44(5):892–898. doi: <https://doi.org/10.2136/sssaj1980.03615995004400050002x>.
- van Leer, B. (1974). Towards the ultimate conservative difference scheme. II. Monotonicity and conservation combined in a second-order scheme. *Journal of Computational Physics*, 14(4):361–370. DOI: [https://doi.org/10.1016/0021-9991\(74\)90019-9](https://doi.org/10.1016/0021-9991(74)90019-9).
- van Leer, B. (1977). Towards the ultimate conservative difference scheme III. Upstream-centred finite-difference schemes for ideal compressible flow. *Journal of Computational Physics*, 23(3):263–275. DOI: [https://doi.org/10.1016/0021-9991\(77\)90094-8](https://doi.org/10.1016/0021-9991(77)90094-8).
- Varoufakis, Y. and Adler, D. (2019). It’s time for nations to unite around an International Green New Deal. *The Guardian*. Retrieved from <https://www.theguardian.com/commentisfree/2019/apr/23/international-green-new-deal-climate-change-global-response> [Accessed 25th November 2019].
- Vo, N. D. and Gourbesville, P. (2016). Application of deterministic distributed hydrological model for large catchment: a case study at Vu Gia Thu Bon catchment, Vietnam. *Journal of Hydroinformatics*, 18(5):885–904. doi: <https://doi.org/10.2166/hydro.2016.138>.
- Vogt, J., Barbosa, P., Hofer, B., Magni, D., Jager, A.-D., Singleton, A., Horion, S., Sepulcre, G., Micale, F., Sokolova, E., Calcagni, L., Marioni, M., and Antofie, T.-E. (2011). Developing the European Drought Observatory for Monitoring, Assessing and Forecasting Droughts across the European Continent. In *AGU Fall Meeting Abstracts*. European Commission Joint Research Centre, Institute for Environment and Sustainability.
- Wang, J., Hong, Y., Li, L., Gourley, J. J., Khan, S. I., Yilmaz, K. K., Adler, R. F., Policelli, F. S., Habib, S., Irwin, D., Limaye, A. S., Korme, T., and Okello, L. (2011). The coupled routing and excess storage (CREST) distributed hydrological model. *Hydrological Sciences Journal*, 56(1):84–98. DOI: <https://doi.org/10.1080/02626667.2010.543087>.
- Ward, A. D. and Trimble, S. W. (2003). *Environmental Hydrology*. CRC Press, 2<sup>nd</sup> edition. ISBN-10: 1566706165.

- 
- Ward, R. and Robinson, M. (1990). *Principles of Hydrology*. McGraw-Hill Publishing Co. ISBN-10:0077095022.
- Warming, R. F. and Beam, R. M. (1976). Upwind Second-Order Difference Schemes and Applications in Aerodynamic Flows. *AIAA Journal*, 14(9):1241–1249. DOI: <https://doi.org/10.2514/3.61457>.
- Waterson, N. P. and Deconinck, H. (1995). *A Unified Approach to the Design and Applications of Bounded Higher-Order Convection Schemes*. Preprint/Von Karman Institute for Fluid Dynamics.
- Watts, G., Battarbee, R., Bloomfield, J., Crossman, J., Daccache, A., Durance, I., Elliott, J. A., Garner, G., Hannaford, J., Hannah, D. M., Hess, T., Jackson, C., Kay, A., Kernan, M., Knox, J., Mackay, J., Monteith, D., Ormerod, S., Rance, J., Stuart, M., Wade, A., Wade, S., Weatherhead, K., Whitehead, P., and Wilby, R. (2015). Climate change and water in the UK - past changes and future prospects. *Progress in Physical Geography*, 39(1):6–28. DOI: <https://doi.org/10.1177/0309133314542957>.
- Whitaker, S. (1986). Flow in porous media I: A theoretical derivation of Darcy’s law. *Transport in Porous Media*, 1:3–25. doi: <https://doi.org/10.1007/BF01036523>.
- White, F. M. (2008). *Pressure Distribution in a Fluid*. Fluid Mechanics. McGraw-Hill, New York. ISBN-10: 0071286454.
- Whitham, G. B. (1999). *Linear and Nonlinear Waves*. Pure and applied mathematics. Wiley-Interscience, New York, 1 edition. ISBN-10: 0471359424.
- Whyte, C. (2019). Green New Deal proposal includes free higher education and fair pay. *New Scientist*, 3217. Retrieved from <https://www.newscientist.com/article/2193592-green-new-deal-proposal-includes-free-higher-education-and-fair-pay/> [Accessed 25th November 2019].
- Wieder, P., Butler, J. M., Theilmann, W., and Yahyapour, R. (2011). *Service Level Agreements for Cloud Computing*. Springer Science & Business Media. ISBN-10: 1461416132.
- Wikipedia (2021a). *Cornwall County - Wikipedia*. Retrieved from [https://en.wikipedia.org/wiki/Cornwall#/media/File:Cornwall\\_UK\\_locator\\_map\\_2010.svg](https://en.wikipedia.org/wiki/Cornwall#/media/File:Cornwall_UK_locator_map_2010.svg). [Accessed 20th November 2021].
-

- 
- Wikipedia (2021b). *Universal Transverse Mercator coordinate system - Wikipedia*. Retrieved from [https://en.wikipedia.org/wiki/Universal\\_Transverse\\_Mercator\\_coordinate\\_system](https://en.wikipedia.org/wiki/Universal_Transverse_Mercator_coordinate_system). [Accessed 20th November 2021].
- Wikipedia (2022). *Flux limiter - Wikipedia*. Retrieved from [https://en.wikipedia.org/wiki/Flux\\_limiter#/media/File:LimiterPlots1.png](https://en.wikipedia.org/wiki/Flux_limiter#/media/File:LimiterPlots1.png). [Accessed 20th July 2022].
- Wood, E. F., Sivapalan, M., Beven, K., and Band, L. (1988). Effects of spatial variability and scale with implications to hydrologic modelling. *Journal of Hydrology*, 102(1–4):29–47. DOI: [https://doi.org/10.1016/0022-1694\(88\)90090-X](https://doi.org/10.1016/0022-1694(88)90090-X).
- Woodward, D. E., Hawkins, R. H., JIang, R., and Hjelmfelt, Jr., A. T. (2003). Runoff curve number method: Examinations of the initial abstraction ratio. In *World Water and Environmental Resources Congress 2003*, Philadelphia, Pennsylvania, United States. DOI: [https://doi.org/10.1061/40685\(2003\)308](https://doi.org/10.1061/40685(2003)308).
- World Commission on Environment and Development (1987). *Our Common Future*. Oxford University Press. ISBN-10: 019282080X.
- Xia, X. and Liang, Q. (2018). A new efficient implicit scheme for discretising the stiff friction terms in the shallow water equations. *Advances in Water Resources*, 117:87–97. doi: 10.1016/j.advwatres.2018.05.004.
- Xia, X., Liang, Q., Ming, X., and Hou, J. (2017). An efficient and stable hydrodynamic model with novel source term discretization schemes for overland flow and flood simulations. *Water Resources Research*, 53:3730–3759. DOI: <https://doi.org/10.1002/2016WR020055>.
- Yang, W., Li, D., Sun, T., and Ni, G. (2015). Saturation-excess and infiltration excess runoff on green roofs. *Ecological Engineering*, 74(1):327–336. doi: <https://doi.org/10.1016/j.ecoleng.2014.10.023>.
- Yates, D. (1994). Watbal - an integrated water balance model for climate impact assessment of river basin runoff. *IIASA Working Paper*.
- Younes, A., Mara, T., Fahs, M., Grunberger, O., and Ackerer, P. (2017). Hydraulic and transport parameter assessment using column infiltration experiments. *Hydrology and Earth System Sciences*, 21(5):2263–2275. doi: <https://doi.org/10.5194/hess-21-2263-2017>.

---

Zhao, R. J. (1992). The Xinanjiang model applied in China. *Journal of Hydrology*, 135(1–4):371–381. DOI: [https://doi.org/10.1016/0022-1694\(92\)90096-E](https://doi.org/10.1016/0022-1694(92)90096-E).

Zhou, G. (1995). *Numerical simulations of physical discontinuities in single and multi-fluid flows for arbitrary Mach numbers*. PhD thesis, Chalmers University of Technology, Goteborg, Sweden.

Zinke, P. J. (1967). Forest Interception Studies in the United States. In W. E. Sopper and H. W. Lull, editor, *International Symposium on Forest Hydrology*, pages 137–161. Pergamon Press, New York.